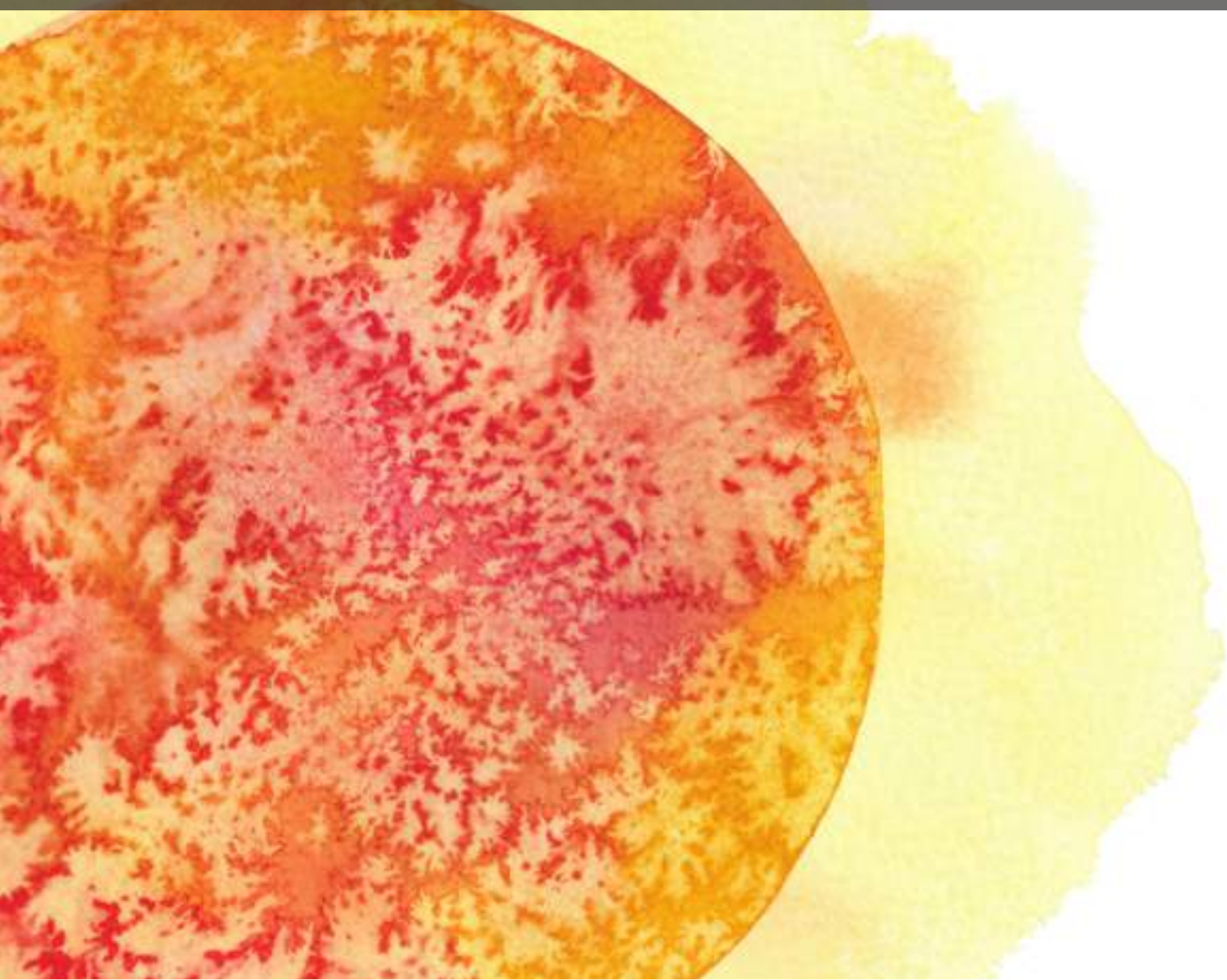


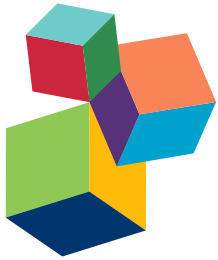
# CORONAL MAGNETOMETRY

EDITED BY: Sarah E. Gibson, Laurel A. Rachmeler and Stephen M. White

PUBLISHED IN: *Frontiers in Astronomy and Space Sciences*



**frontiers** Research Topics



# frontiers

## **Frontiers Copyright Statement**

© Copyright 2007-2017 Frontiers Media SA. All rights reserved.

All content included on this site, such as text, graphics, logos, button icons, images, video/audio clips, downloads, data compilations and software, is the property of or is licensed to Frontiers Media SA ("Frontiers") or its licensees and/or subcontractors. The copyright in the text of individual articles is the property of their respective authors, subject to a license granted to Frontiers.

The compilation of articles constituting this e-book, wherever published, as well as the compilation of all other content on this site, is the exclusive property of Frontiers. For the conditions for downloading and copying of e-books from Frontiers' website, please see the Terms for Website Use. If purchasing Frontiers e-books from other websites or sources, the conditions of the website concerned apply.

Images and graphics not forming part of user-contributed materials may not be downloaded or copied without permission.

Individual articles may be downloaded and reproduced in accordance with the principles of the CC-BY licence subject to any copyright or other notices. They may not be re-sold as an e-book.

As author or other contributor you grant a CC-BY licence to others to reproduce your articles, including any graphics and third-party materials supplied by you, in accordance with the Conditions for Website Use and subject to any copyright notices which you include in connection with your articles and materials.

All copyright, and all rights therein, are protected by national and international copyright laws.

The above represents a summary only. For the full conditions see the Conditions for Authors and the Conditions for Website Use.

**ISSN 1664-8714**

**ISBN 978-2-88945-220-0**

**DOI 10.3389/978-2-88945-220-0**

## **About Frontiers**

Frontiers is more than just an open-access publisher of scholarly articles: it is a pioneering approach to the world of academia, radically improving the way scholarly research is managed. The grand vision of Frontiers is a world where all people have an equal opportunity to seek, share and generate knowledge. Frontiers provides immediate and permanent online open access to all its publications, but this alone is not enough to realize our grand goals.

## **Frontiers Journal Series**

The Frontiers Journal Series is a multi-tier and interdisciplinary set of open-access, online journals, promising a paradigm shift from the current review, selection and dissemination processes in academic publishing. All Frontiers journals are driven by researchers for researchers; therefore, they constitute a service to the scholarly community. At the same time, the Frontiers Journal Series operates on a revolutionary invention, the tiered publishing system, initially addressing specific communities of scholars, and gradually climbing up to broader public understanding, thus serving the interests of the lay society, too.

## **Dedication to Quality**

Each Frontiers article is a landmark of the highest quality, thanks to genuinely collaborative interactions between authors and review editors, who include some of the world's best academicians. Research must be certified by peers before entering a stream of knowledge that may eventually reach the public - and shape society; therefore, Frontiers only applies the most rigorous and unbiased reviews.

Frontiers revolutionizes research publishing by freely delivering the most outstanding research, evaluated with no bias from both the academic and social point of view.

By applying the most advanced information technologies, Frontiers is catapulting scholarly publishing into a new generation.

## **What are Frontiers Research Topics?**

Frontiers Research Topics are very popular trademarks of the Frontiers Journals Series: they are collections of at least ten articles, all centered on a particular subject. With their unique mix of varied contributions from Original Research to Review Articles, Frontiers Research Topics unify the most influential researchers, the latest key findings and historical advances in a hot research area! Find out more on how to host your own Frontiers Research Topic or contribute to one as an author by contacting the Frontiers Editorial Office: [researchtopics@frontiersin.org](mailto:researchtopics@frontiersin.org)

# CORONAL MAGNETOMETRY

Topic Editors:

**Sarah E. Gibson**, High Altitude Observatory, National Center for Atmospheric Research, United States

**Laurel A. Rachmeler**, Marshall Space Flight Center, National Aeronautics and Space Administration, United States

**Stephen M. White**, Air Force Research Labs., Kirtland Air Force Base, United States



Artistic rendition of the sun and solar corona [L. A. Rachmeler]

Copyright released under: Attribution-NonCommercial 4.0 International (CC BY-NC 4.0), <https://creativecommons.org/licenses/by-nc/4.0/>  
Coronal Magnetometry is to provide a forum for comparing and coordinating these research methods, and for discussing future opportunities.

**Citation:** Gibson, S. E., Rachmeler, L. A., White, S. M., eds. (2017). Coronal Magnetometry. Lausanne: Frontiers Media. doi: 10.3389/978-2-88945-220-0

Magnetism defines the complex and dynamic solar corona. It determines the magnetic loop structure that dominates images of the corona, and stores the energy necessary to drive coronal eruptive phenomena and flare explosions. At great heights the corona transitions into the ever-outflowing solar wind, whose speed and three-dimensional morphology are controlled by the global coronal magnetic field. Coronal magnetism is thus at the heart of any understanding of the nature of the corona, and essential for predictive capability of how the Sun affects the Earth.

Coronal magnetometry is a subject that requires a concerted effort to draw together the different strands of research happening around the world.

Each method provides some information about the field, but none of them can be used to determine the full 3D field structure in the full volume of the corona. Thus, we need to combine them to understand the full picture.

The purpose of this Frontiers Research Topic on Coronal Magnetometry is to provide a forum for comparing and coordinating these research methods, and for discussing future opportunities.

# Table of Contents

## 05 Editorial: Coronal Magnetometry

Sarah E. Gibson, Laurel A. Rachmeler and Stephen M. White

## Section 1: Measuring coronal magnetic fields

### 07 Infrared Dual-Line Hanle Diagnostic of the Coronal Vector Magnetic Field

Gabriel I. Dima, Jeffrey R. Kuhn and Svetlana V. Berdyugina

### 16 Diagnostics of Coronal Magnetic Fields through the Hanle Effect in UV and IR Lines

Nour E. Raouafi, Pete Riley, Sarah Gibson, Silvano Fineschi and Sami K. Solanki

### 26 Measuring Coronal Magnetic Fields with Remote Sensing Observations of Shock Waves

Alessandro Bemporad, Roberto Susino, Federica Frassati and Silvano Fineschi

## Section 2: Coronal plasma diagnostics

### 30 Line-of-Sight Velocity As a Tracer of Coronal Cavity Magnetic Structure

Urszula Bąk-Stęślicka, Sarah E. Gibson and Ewa Chmielewska

### 40 Evidence for a Magnetic Flux Rope in Observations of a Solar Prominence-Cavity System

Patricia R. Jibben, Katharine K. Reeves and Yingna Su

### 55 Lifecycle of a Large-Scale Polar Coronal Pseudostreamer/Cavity System

Chloé Guennou, Laurel A. Rachmeler, Daniel B. Seaton and Frédéric Auchère

### 76 3D Global Coronal Density Structure and Associated Magnetic Field near Solar Maximum

Maxim Kramar, Vladimir Airapetian and Haosheng Lin

## Section 3: Numerical models of coronal magnetic fields

### 84 Analyses of the Photospheric Magnetic Dynamics in Solar Active Region 11117 Using an Advanced CESE-MHD Model

Chaowei Jiang, Shi T. Wu and Xueshang Feng

### 92 A Comparative Study of Divergence Cleaning Methods of Magnetic Field in the Solar Coronal Numerical Simulation

Man Zhang and Xueshang Feng

## Section 4: From forward to inverse techniques

### 106 FORWARD: A Toolset for Multiwavelength Coronal Magnetometry

Sarah E. Gibson, Therese A. Kucera, Stephen M. White, James B. Dove, Yuhong Fan, Blake C. Forland, Laurel A. Rachmeler, Cooper Downs and Katharine K. Reeves

**127 *Forward Modeling of EUV and Gyrosynchrotron Emission from Coronal Plasmas with FoMo***

Tom Van Doorsselaere, Patrick Antolin, Ding Yuan, Veronika Reznikova and Norbert Magyar

**136 *ROAM: A Radial-Basis-Function Optimization Approximation Method for Diagnosing the Three-Dimensional Coronal Magnetic Field***

Kevin Dalmasse, Douglas W. Nychka, Sarah E. Gibson, Yuhong Fan and Natasha Flyer

### **Section 5: Future instruments**

**150 *Waves and Magnetism in the Solar Atmosphere (WAMIS)***

Yuan-Kuen Ko, John D. Moses, John M. Laming, Leonard Strachan, Samuel Tun Beltran, Steven Tomczyk, Sarah E. Gibson, Frédéric Auchère, Roberto Casini, Silvano Fineschi, Michael Knoelker, Clarence Korendyke, Scott W. McIntosh, Marco Romoli, Jan Rybak, Dennis G. Socker, Angelos Vourlidas and Qian Wu

**163 *mxCSM: A 100-slit, 6-Wavelength Wide-Field Coronal Spectropolarimeter for the Study of the Dynamics and the Magnetic Fields of the Solar Corona***

Haosheng Lin



# Editorial: Coronal Magnetometry

**Sarah E. Gibson<sup>1\*</sup>, Laurel A. Rachmeler<sup>2</sup> and Stephen M. White<sup>3</sup>**

<sup>1</sup> High Altitude Observatory, National Center for Atmospheric Research, Boulder, CO, USA, <sup>2</sup> Marshall Space Flight Center, NASA, Huntsville, AL, USA, <sup>3</sup> Air Force Research Labs., Kirtland Air Force Base, Albuquerque, NM, USA

**Keywords:** coronal magnetic fields, solar corona, space weather, sun, coronal mass ejections

## Editorial on the Research Topic

### Coronal Magnetometry

Magnetism defines the complex and dynamic solar corona. It determines the magnetic loop structure that dominates images of the corona, and stores the energy necessary to drive coronal eruptive phenomena and flare explosions. At great heights the corona transitions into the ever-outflowing solar wind, whose speed and three-dimensional morphology are controlled by the global coronal magnetic field. Coronal magnetism is thus at the heart of any understanding of the nature of the corona, and essential for predictive capability of how the Sun affects the Earth.

Such an understanding will ultimately come from knowing the time-evolving vector magnetic field throughout the solar corona. Given this knowledge, it becomes possible to determine where magnetic free energy is stored, what triggers the eruptive events that release this energy, where solar energetic particles are accelerated and how they propagate, and how coronal mass ejection (CME) internal magnetic structure evolves in response to interactions with the surrounding corona and solar wind.

Until recently, our knowledge of magnetism in the corona was primarily limited to extrapolations of solar surface observations in conjunction with purely morphological coronal observations. There are several reasons that obtaining more direct observations of the coronal magnetic field is difficult; foremost among them is that the corona is optically thin and relatively dim compared to the solar disk. However, current and planned coronal polarimetric measurements are changing this paradigm, making the development of coronal magnetometric techniques a priority.

Coronal magnetometry is a subject that requires a concerted effort to draw together the different strands of research happening around the world. Each method provides some information about the field, but none of them can be used to determine the full 3D field structure in the full volume of the corona. Thus, we need to combine them to understand the full picture. The purpose of this Frontiers Research Topic on Coronal Magnetometry is to provide a forum for comparing and coordinating these research methods. We now briefly summarize the papers it contains.

A key development of recent years has been the availability of coronal polarimetric measurements, in particular at visible and infrared wavelengths. Dima et al. presents a method for combining linear-polarization measurements from near-infrared permitted and forbidden coronal emission lines to calculate the coronal vector magnetic field. Raouafi et al. similarly argues for multiwavelength linear-polarization diagnostics, using forward modeling of global MHD models to demonstrate the complementary diagnostic power of ultraviolet and infrared lines. Moving away from polarimetric measurements, Bemporad et al. discusses the extent to which the magnetic field strength of CMEs in the outer corona might be deduced from white-light and ultraviolet observations assumed to correspond to shock fronts.

Observations of both coronal morphologies and thermal plasma properties contribute clues to the nature of the underlying magnetic structure. Jibben et al. presents a case study, and Bąk-Stęślicka et al. presents a statistical analysis of thermal and velocity structure within quiescent

### OPEN ACCESS

**Edited and reviewed by:**  
Michael J. Thompson,  
National Center for Atmospheric  
Research (UCAR), USA

**\*Correspondence:**  
Sarah E. Gibson  
sgibson@ucar.edu

**Specialty section:**

This article was submitted to  
Stellar and Solar Physics,  
a section of the journal  
*Frontiers in Astronomy and Space  
Sciences*

**Received:** 17 March 2017

**Accepted:** 28 April 2017

**Published:** 15 May 2017

**Citation:**

Gibson SE, Rachmeler LA and  
White SM (2017) Editorial: Coronal  
Magnetometry.  
*Front. Astron. Space Sci.* 4:3.  
doi: 10.3389/fspas.2017.00003

(non-erupting) coronal prominence cavities, finding evidence for a magnetic flux-rope topology. Guennou et al. uses solar-rotational tomography to characterize the evolution of a pseudostreamer-cavity system and its thermodynamic properties. Kramar et al. uses tomography to model the 3D density and emissivity of the global corona for one rotation, and compares morphological features to a potential-field model of the rotation.

The ultimate goal is to build a 3D global coronal magnetic field. To do so will necessarily draw upon the observations and diagnostics described above, but also is likely to require the explicit utilization of boundary-driven numerical models. Jiang et al. presents an MHD model driven by the time-evolving photospheric boundary vector magnetic field, in the presence of a stratified atmosphere. Zhang and Feng describes how such MHD simulations must be kept divergence-free. Jibben et al. presents a nonlinear-force-free-field model based on the photospheric line-of-sight magnetic boundary, with currents added to match coronal observations of a prominence cavity system. Forward modeling then allows direct comparison to coronal polarimetric data.

Methodologies for drawing together models and observations in an efficient fashion need to be developed, including forward and inverse techniques. Gibson et al. presents the FORWARD software suite for model-data comparison, and discusses how multiwavelength data might be used to constrain models of the physical state of the corona. Van Doorsselaere et al. presents the FoMo software for forward modeling of emission from coronal plasma, which has been applied to the study of coronal wave models in EUV and radio gyrosynchrotron emission. Dalmasse et al. presents a new Radial-basis-function Optimization Approximation Method (ROAM) for obtaining orders-of-magnitude increases in speed vs a full grid search of parameter space, and applies it to fitting synthetic polarimetric data obtained through forward modeling a magnetic-flux-rope model.

Finally, new telescopes are needed to fully realize the potential of coronal magnetometry. Limitations of ground-based coronal polarimetric observations might be overcome by a

balloon-borne mission, such as the Waves and Magnetism in the Solar Atmosphere (WAMIS) investigation, consisting of a 20 cm coronagraph with a visible-IR spectropolarimeter focal plane assembly (Ko et al.) Difficulties measuring the weak circular polarization signal in the corona require larger aperture telescopes; alternatively, technological advances may substantially increase the efficiency of coronal spectropolarimeters, as described for the mxCSM, a proposed 100-slit, 6-Wavelength wide-field coronal spectropolarimeter (Lin).

In conclusion, the field of coronal magnetometry is a young one, with new observations, models, and methodologies continuing to be developed, and with rich potential for substantial scientific discovery over the next decade.

## AUTHOR CONTRIBUTIONS

SG, SW, and LR all wrote and revised this editorial.

## FUNDING

NCAR is supported by the National Science Foundation. SEG acknowledges support from the Air Force Office of Space Research, FA9550-15-1-0030.

## ACKNOWLEDGMENTS

We acknowledge all the authors, reviewers, editors, and publishers who have supported this Research Topic.

**Conflict of Interest Statement:** The authors declare that the research was conducted in the absence of any commercial or financial relationships that could be construed as a potential conflict of interest.

*Copyright © 2017 Gibson, Rachmeler and White. This is an open-access article distributed under the terms of the Creative Commons Attribution License (CC BY). The use, distribution or reproduction in other forums is permitted, provided the original author(s) or licensor are credited and that the original publication in this journal is cited, in accordance with accepted academic practice. No use, distribution or reproduction is permitted which does not comply with these terms.*



# Infrared Dual-Line Hanle Diagnostic of the Coronal Vector Magnetic Field

Gabriel I. Dima<sup>1\*</sup>, Jeffrey R. Kuhn<sup>1</sup> and Svetlana V. Berdyugina<sup>1,2,3</sup>

<sup>1</sup> Institute for Astronomy, University of Hawaii, Pukalani, HI, USA, <sup>2</sup> Kiepenheuer Institut fuer Sonnenphysik, Freiburg, Germany, <sup>3</sup> Predictive Science Inc., San Diego, CA, USA

## OPEN ACCESS

### Edited by:

Sarah Gibson,  
National Center for Atmospheric Research/High Altitude Observatory,  
USA

### Reviewed by:

Veronique Bommier,  
Observatoire de Paris, France  
Roberto Casini,  
High Altitude Observatory-National Center for Atmospheric Research,  
USA

### \*Correspondence:

Gabriel I. Dima  
gdima@hawaii.edu

### Specialty section:

This article was submitted to  
Stellar and Solar Physics,  
a section of the journal  
*Frontiers in Astronomy and Space Sciences*

Received: 03 January 2016

Accepted: 01 April 2016

Published: 20 April 2016

### Citation:

Dima GI, Kuhn JR and Berdyugina SV (2016) Infrared Dual-Line Hanle Diagnostic of the Coronal Vector Magnetic Field. *Front. Astron. Space Sci.* 3:13.  
doi: 10.3389/fspas.2016.00013

Measuring the coronal vector magnetic field is still a major challenge in solar physics. This is due to the intrinsic weakness of the field (e.g.,  $\sim 4\text{G}$  at a height of  $0.1R_{\odot}$  above an active region) and the large thermal broadening of coronal emission lines. We propose using concurrent linear polarization measurements of near-infrared forbidden and permitted lines together with Hanle effect models to calculate the coronal vector magnetic field. In the unsaturated Hanle regime both the direction and strength of the magnetic field affect the linear polarization, while in the saturated regime the polarization is insensitive to the strength of the field. The relatively long radiative lifetimes of coronal forbidden atomic transitions implies that the emission lines are formed in the saturated Hanle regime and the linear polarization is insensitive to the strength of the field. By combining measurements of both forbidden and permitted lines, the direction and strength of the field can be obtained. For example, the SiX 1.4301  $\mu\text{m}$  line shows strong linear polarization and has been observed in emission over a large field-of-view (out to elongations of  $0.5 R_{\odot}$ ). Here we describe an algorithm that combines linear polarization measurements of the SiX 1.4301  $\mu\text{m}$  forbidden line with linear polarization observations of the HeI 1.0830  $\mu\text{m}$  permitted *coronal* line to obtain the vector magnetic field. To illustrate the concept we assume that the emitting gas for both atomic transitions is located in the plane of the sky. The further development of this method and associated tools will be a critical step toward interpreting the high spectral, spatial and temporal infrared spectro-polarimetric measurements that will be possible when the Daniel K. Inouye Solar Telescope (DKIST) is completed in 2019.

**Keywords:** corona, magnetic fields, spectro-polarimetry, magnetometry, infrared, Hanle effect

## 1. INTRODUCTION

Magnetometry using optical spectropolarimetry has yielded some of the most precise direct measurements of coronal magnetic fields (Kuhn, 1995; Lin et al., 2000, 2004; Tomczyk et al., 2008). Earlier infrared (IR) coronal Zeeman observations (e.g., Arnaud and Newkirk, 1987; Kuhn, 1995) have used forbidden FeXIII transitions near 1 micron. The larger context of all coronal magnetometry techniques has been reviewed elsewhere (e.g., Penn, 2014), but the great promise of the Daniel K. Inouye Solar Telescope (DKIST) will be to use near-IR coronal lines to routinely observe the so far seldom measured weak solar coronal magnetic field. Up until now attempts from the ground to measure the magnetic field strength have depended on the ability to detect very weak Zeeman splitting through Stokes-V (circular) polarization observations. A Gauss-scale coronal magnetic field creates very weak Stokes-V signals (typically  $10^{-4}$ ) in spectral lines that are

dominated by much stronger linear scattering polarization amplitudes (e.g., Stokes-Q and U of order  $10^{-2}$  and sometimes up to  $10^{-1}$ , Lin et al., 2004).

Most recently linear polarization observations of permitted lines combined with forward calculations of field configurations have been productive tools for understanding solar prominence magnetic fields (Bommier et al., 1981; López Ariste and Casini, 2003; Merenda et al., 2006). A powerful coronal field diagnostic follows from simultaneous measurements of the optical scattering linear polarization of combined forbidden and permitted spectral lines. Early work on the possibility of using lines with different Hanle sensitivity used the HeI 0.5875  $\mu\text{m}$  and HeI 1.0830  $\mu\text{m}$  (hereafter HeI1083) lines for measuring the magnetic field in a prominence located in the plane of the sky (Bommier et al., 1981). Recently space spectropolarimetric observations of the permitted coronal Ly $\alpha$  line have been attempted (Ishikawa et al., 2011). The discovery of HeI1083 line far into the corona (Kuhn et al., 1996, 2007) has now made it feasible to measure coronal fields in the 0.1 – 10G range using only linear polarimetry of the HeI1083 line and another forbidden coronal line—such as the newly characterized SiX 1.4301  $\mu\text{m}$  (hereafter SiX1430) line.

For practical reasons the IR spectrum is particularly useful for ground-based studies of the corona because spurious background noise from both the atmosphere and optical scattering in telescopes and instruments decreases with increasing wavelength (Kuhn et al., 2003). Terrestrial thermal emission below 1.8  $\mu\text{m}$  is also inconsequential. Observations (Kuhn et al., 1996) and calculations (Judge, 1998) have described new IR forbidden lines that could be useful as spectropolarimetry diagnostics. Only the HeI1083 line has been observed as a promising IR permitted line for Hanle magnetometry. Some earlier measurements revealed diffuse coronal neutral triplet-state Helium associated with streamers (Kuhn et al., 1996). This initial measurement was eventually confirmed to have solar origin through ground-based spectro-polarimetric observations using the Scatter-free Observatory for Limb, Active Regions, and Coronae (SOLARC) telescope on Haleakala (Kuhn et al., 2007; Moise et al., 2010). The diffuse HeI emission is generated by scattering of photospheric radiation by the triplet state of HeI. The narrow line-width observed for this emission is consistent with the triplet states being produced primarily through electron collisional excitation of singlet-state neutral He in the higher density K-corona, rather than collisional recombination of He $^+$  ions (Moise et al., 2010).

## 2. DUAL-LINE HANLE MAGNETIC DIAGNOSTICS

The Hanle effect causes a change in the polarization of atomically scattered optical radiation due to the presence of a magnetic field. The magnetic field splits atomic levels into  $2J+1$  magnetic sublevels ( $J$  is the total angular momentum) via the Zeeman effect. If sublevels of the upper level are unevenly populated through their coupling to an anisotropic solar radiation field, then the emission line can be polarized. When the Zeeman splitting is comparable to the energy spread of the upper level

(i.e., the Larmor frequency is smaller than or comparable to the total line emission transition rate), quantum mechanically induced wavefunction interferences will modify the scattering polarization magnitude and rotate the polarization plane by an amount that depends on the field—this is the unsaturated Hanle effect.

The coronal vector magnetic field at a point in the corona is uniquely described by the magnetic flux density  $|\mathbf{B}| \equiv B$ , the inclination angle  $\theta_B$  (with respect to the local outward solar radial direction) and the azimuth angle  $\chi_B$  in a plane perpendicular to the radial direction (Figure 1). For a scattering geometry where the emission takes place in the plane-of-sky (POS) we can freely choose the reference axis for the  $\chi_B$  angle to coincide with the line of sight axis. In the unsaturated Hanle regime, when the atomic Larmor frequency is comparable to the inverse upper-level lifetime, the linear polarization of an emission line is sensitive to all three B-vector parameters, while in the saturated Hanle regime (when the Larmor frequency is much larger than the inverse lifetime) only the angles  $(\theta_B, \chi_B)$  influence the linear polarization. The  $B$  value at which the transition between the two regimes takes place is not a sharp value. In fact, a gradual loss of sensitivity takes place above the critical field strength  $B_H$ , which depends on the Lande factor  $g'$  and the lifetime  $\tau'$  of the upper level:

$$B_H = \frac{\hbar}{\mu_B g' \tau'} \quad (1)$$

where  $\mu_B$  is the Bohr magneton.

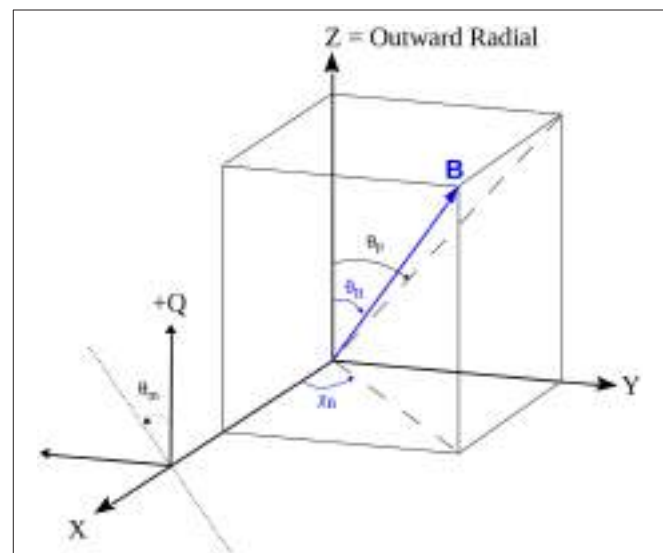


**FIGURE 1 | Observing geometry for a magnetic field located in the plane of the sky (corresponding to the ZY plane).** The  $+Z$  direction indicates the local outward radial direction so moving around the solar limb corresponds to a rotation about the  $X$  axis which is taken to coincide with the line of sight. The projected angle of magnetic field on the plane sky  $\theta_B$  is measured clockwise, while the angle of polarization  $\theta_m$  is measured counter-clockwise adhering to the common polarimetric convention. The reference direction for the polarization measurement is oriented along the outward radial direction.

The dual-line vector magnetometry technique we propose here relies on simultaneous observations of both permitted and forbidden coronal lines. Near-IR observable coronal lines such as SiX1430, FeXIII 1.0747  $\mu\text{m}$  (hereafter FeXIII1075) and HeI1083 have good polarized atomic modeling available (e.g., House, 1974; Sahal-Brechot, 1977; Casini and Judge, 1999; Asensio Ramos et al., 2008). The critical field strength  $B_{\text{H}}$  for the HeI1083 transition is 0.77G (Bommier et al., 1981) while the forbidden lines have critical field strengths in the  $10^{-5}\text{G}$  range (House, 1974). The two forbidden lines are firmly in the saturated Hanle regime, while the permitted HeI line maintains Hanle sensitivity up to  $\sim 8\text{G}$ . In their analysis, Bommier et al. (1981) found the unsaturated Hanle magnetic sensitivity of the HeI1083 line to be significant between  $0.1B_{\text{H}} < B < 10B_{\text{H}}$ .

The only known visible or IR coronal permitted line is HeI1083. Using current observatories like SOLARC, it is possible to combine near-IR observations of HeI1083 with the FeXIII1075 or SiX1430 lines. When DKIST comes online, potentially longer wavelength IR spectropolarimetry in the near-thermal IR will be possible. To date, emphasis has been placed on FeXIII1075 observations for coronal spectropolarimetry (Tomczyk et al., 2008), although observations during the total solar eclipse on March 29, 2006 (Dima et al., 2016, in preparation) show that SiX1430 emission can be significantly brighter than FeXIII1075. The experiment for that eclipse used a wide-field fiber fed spectropolarimeter. **Figure 2** gives a comparative view of the line signal/noise in each of the fibers. During the same eclipse HeI1083 emission was also observed, although that spectropolarimeter did not have the sensitivity to demonstrate Hanle magnetometry. Nevertheless, these IR measurements clearly point to the importance of the SiX1430 line. Since the FeXIII and SiX ion abundances peak at different temperatures this result highlights the need to have multiple coronal lines accessible for polarimetry that sample different temperature regimes of the corona. While the analysis and examples presented below discuss the SiX1430 line, they can apply equally well to FeXIII1075 observations since the two

lines have very similar polarization properties (Judge et al., 2006).

### 3. ALGORITHM DESCRIPTION

Forbidden lines like FeXIII1075 and SiX1430 have radiative decay rates that are not so different from the electron collision rate at coronal densities. Thus, isotropic collisions can depolarize the Zeeman substate populations in the upper levels of the lines. Mixing occurs through both electron collisions and indirectly through cascades from excited higher levels that can have substantially higher downward transition rates (Sahal-Brechot, 1977; Judge et al., 2006). This collisional depolarization has a density dependence which is difficult to accurately model, but only affects the amplitude of the forbidden line polarization (Judge and Casini, 2001). Consequently, our method in its current form only employs the polarization angle in the forbidden lines which is independent of isotropic collisional effects.

Lines in the saturated Hanle regime maintain a fixed angular relationship between the linear polarization plane (characterized by the polarization angle  $\theta_{\text{m}}$ ) and the projected magnetic field orientation on the plane of the sky (characterized by the projected angle  $\theta_{\text{p}}$ ) as shown in **Figure 1**. The magnetic field orientation angles ( $\theta_{\text{B}}$ ,  $\chi_{\text{B}}$ ) are related to the projected angle  $\theta_{\text{p}}$  by

$$\tan\theta_{\text{p}} = \tan\theta_{\text{B}}\sin\chi_{\text{B}} \quad (2)$$

For magnetic dipole transitions like SiX1430 the polarization plane is parallel to the magnetic field when  $\theta_{\text{B}} < \theta_{\text{VV}}$  or  $\theta_{\text{B}} > 180^{\circ} - \theta_{\text{VV}}$  and perpendicular when  $\theta_{\text{VV}} < \theta_{\text{B}} < 180^{\circ} - \theta_{\text{VV}}$ , where  $\theta_{\text{VV}} = 54.7^{\circ}$  is the Van Vleck angle. This effect leads to the Van Vleck ambiguity (e.g., House, 1974): one measured pair of Stokes Q, U corresponds to at least two pairs of possible magnetic field orientation angles. This ambiguity only applies to a subset of possible field inclinations: all linearly polarized emission from

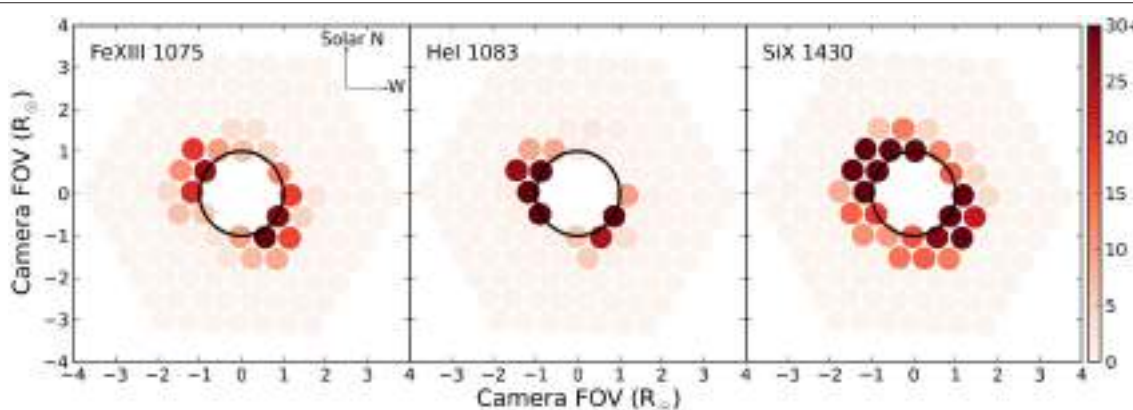


**FIGURE 2 | Spatial sampling of the corona during the March 29, 2006 total eclipse.** A hexagonal array of 127 fibers sparsely sampled the coronal image plane. Each plot shows the signal/noise measured in each fiber for the lines indicated. One key result from these measurements is the large spatial extent of bright SiX1430 emission compared to FeXIII1075 emission.

**TABLE 1 | Summary of parameters and algorithm solutions for two example magnetic field cases.**

	<b>Assumed values (<math>B</math>, <math>\theta_B</math>, <math>\chi_B</math>)</b> <b>Height(<math>R_\odot</math>) Density(<math>\text{cm}^{-3}</math>)</b>	<b>SiX1430 polarization</b> <b>(angle<sup>b</sup>, amplitude<sup>c</sup>)</b>	<b>HeI1083 polarization</b> <b>(angle<sup>b</sup>, amplitude)</b>	<b>Solutions<sup>a</sup></b> <b>(<math>B</math>, <math>\theta_B</math>, <math>\chi_B</math>)</b>
Field I	(0.65G, 156°, -90°) 0.26 $0.2 \times 10^8$	( $-24 \pm 2^\circ$ , $0.097 \pm 0.005$ )	( $78 \pm 1^\circ$ , $0.128 \pm 0.005$ )	( $0.65_{-0.15G}^{+0.15G}$ , $156_{-10^\circ}^{+1^\circ}$ , $-90_{-150^\circ}^{+10^\circ}$ ) ( $0.65_{-0.15G}^{+0.15G}$ , $24_{-10^\circ}^{+1^\circ}$ , $90_{-10^\circ}^{+15^\circ}$ ) ( $0.35_{-0.10G}^{+0.15G}$ , $152_{-2^\circ}^{+3^\circ}$ , $-125_{-5^\circ}^{+10^\circ}$ ) ( $0.35_{-0.10G}^{+0.15G}$ , $27_{-2^\circ}^{+3^\circ}$ , $125_{-10^\circ}^{+5^\circ}$ )
Field II	(1.3G, 76°, -63°) 0.08 $2 \times 10^8$	( $-16 \pm 14^\circ$ , $0.01 \pm 0.005$ )	( $-90 \pm 6^\circ$ , $0.024 \pm 0.005$ )	( $1.3_{-0.3G}^{+0.4G}$ , $76_{-1^\circ}^{+1^\circ}$ , $-63_{-7^\circ}^{+8^\circ}$ ) ( $1.3_{-0.3G}^{+0.4G}$ , $104_{-1^\circ}^{+1^\circ}$ , $63_{-8^\circ}^{+7^\circ}$ ) ( $3.2_{-0.9G}^{+1.8G}$ , $141_{-1^\circ}^{+1^\circ}$ , $-22_{-3^\circ}^{+3^\circ}$ ) ( $3.2_{-0.9G}^{+1.8G}$ , $39_{-1^\circ}^{+1^\circ}$ , $22_{-3^\circ}^{+3^\circ}$ )

<sup>a</sup>Parameter errors only account for polarization errors in the HeI1083 line. The error contributions from SiX1430 polarization angle uncertainty is discussed in the text.

<sup>b</sup>Polarization angles are given in the [-90°, 90°] domain and the reference direction is along the local solar radial.

<sup>c</sup>Polarization amplitude for SiX1430 are given to show amplitude/noise for each case, but the values themselves are not part of the algorithm.

fields with  $\theta_{VV} < \theta_B < 180^\circ - \theta_{VV}$  is ambiguous with respect to a set of field inclinations outside this inclination domain.

In contrast, the HeI1083 permitted line has an upper level lifetime six orders of magnitude shorter. Collisions have a negligible effect on polarization amplitudes permitted lines at coronal densities. Thus, both the polarization angle and amplitude can be modeled without detailed knowledge of the coronal electron density. In our analysis synthetic Stokes I, Q, U profiles for the HeI1083 line are created using the Hanle and Zeeman Light (HAZEL)<sup>1</sup> code (Asensio Ramos et al., 2008). The HeI1083 line is a multiplet between the 2p<sup>3</sup>S and 2s3S terms of the triplet system of HeI. The upper term has three levels with  $J = 0, 1, 2$  while the lower term has one level with  $J = 1$  with corresponding transition wavelengths: 10829.09Å, 10830.25Å and 10830.34Å. The blue component is not polarizable in emission because the upper level with  $J = 0$  has only one magnetic sublevel and is intrinsically unpolarizable. The final Stokes parameters are obtained from integrating the synthetic line profiles over the two red components which typically appear blended due to the small wavelength separation. For the analysis we choose to work in terms of the concepts of linear polarization angle and amplitude (degree) which are related to the line-profile integrated Stokes I, Q, U by the simple relations:

$$\text{Polarization amplitude} = \frac{\sqrt{Q^2 + U^2}}{I} \quad (3)$$

$$\text{Polarization angle} = 0.5 \tan^{-1} \left( \frac{U}{Q} \right) \quad (4)$$

To ensure the polarization angle is correctly calculated an “arctan2”-type function should be applied. This function accounts for the signs of the U and Q values and correctly maps the polarization angle over the domain [-90°, 90°].

<sup>1</sup><http://www.iac.es/proyecto/magnetism/pages/codes/hazel.php>

The algorithm steps for co-spatial sources in the plane of the sky proceed as follows:

1. From the measured forbidden line linear polarization angle  $\theta_m$  we generate two sets of angle pairs ( $\theta_B$ ,  $\chi_B$ ) satisfying (Equation 2) with  $\theta_p = -\theta_m$  or  $\theta_p = -(\theta_m + 90^\circ)$ . The two sets correspond to the situations where the plane of polarization is respectively parallel or perpendicular to the projected magnetic field direction.
2. HAZEL is used to generate two model Stokes profile grids for each set of angle pairs together with a suitably chosen value range for the magnetic field strength ( $0 < B < 8G$ ). Thus, each point on the grid corresponds to one or more ( $B$ ,  $\theta_B$ ,  $\chi_B$ ) magnetic fields. The two dimensional grids are expressed in terms of polarization angles and amplitudes calculated using Equations (3) and (4).
3. The measured HeI1083 polarization angle and amplitude are now compared to each of the model grids to find the magnetic field solution grid points consistent with the measurements and errors. If the measured linear polarization parameters only intersects the parallel model grid and lie outside the perpendicular model grid then the deduced magnetic field solution is not affected by the Van Vleck uncertainty. Alternatively if the measured value intersects both grids the deduced magnetic field has at least two degenerate solutions due to the Van Vleck uncertainty.

### 3.1. Example Application

To demonstrate the method we use as examples two magnetic fields with different ( $B$ ,  $\theta_B$ ,  $\chi_B$ ) parameters that are typical of coronal fields (Table 1). The fields, named Fields I and II are influencing scattering points located in the plane of the sky at different heights,  $0.26R_\odot$  and  $0.08R_\odot$  respectively. We synthesize “measurements” using the assumed magnetic field parameters and height. HeI1083 measurements are calculated using the HAZEL code, while SiX1430 measurements are

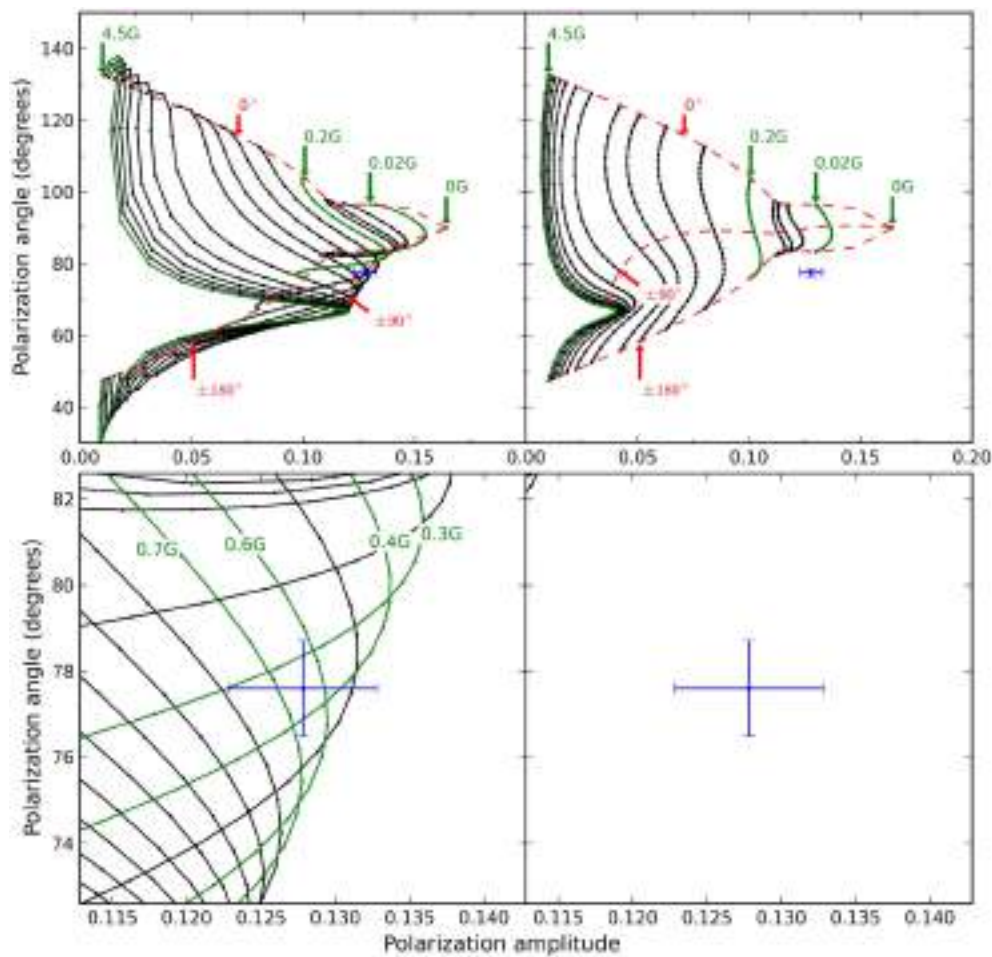


**FIGURE 3 | Field I model grids for HeI1083 linear polarization with polarization angle drawn against polarization amplitude.** B-isocontours are drawn as solid black lines. The top panel shows the entire solution space with some B-isocontours highlighted and labeled in green three  $x_B$ -isocontours drawn with red dashed. The bottom panel shows an enhanced region around the measured value for Field I with some B-isocontours highlighted in green. The B-isocontours in the bottom panel are all separated by 0.1G. For both the top and bottom panels the left plot shows the model grids for plane of polarization parallel to the field projection, while the right plot shows the grid for the plane of polarization perpendicular to the field projection. The measured HeI1083 polarization value for Field I is drawn in blue with errors bars corresponding in size to intensity errors  $\sim 0.5\%$ . For Field I the measurement intersects only the parallel grid. This is consistent with an inclination measurement outside the Van Vleck uncertainty region.

calculated using the FORWARD<sup>2</sup> code (Gibson et al., 2010) which generates polarized emission from a multi-level SiX atomic model (Judge and Casini, 2001). To synthesize the SiX1430 polarized emission we also assumed coronal electron densities typical of the heights at which the two fields are located:  $0.2 \times 10^8 \text{ cm}^{-3}$  for Field I and  $2 \times 10^8 \text{ cm}^{-3}$  for Field II. The larger exciting radiation anisotropy and lower densities found at larger heights leads to an increase in the amplitude of the SiX1430 polarization. For observations that are not photon limited this leads to improved accuracy for measurements higher above the solar limb.

Following our algorithm two angle/amplitude grids are generated separately for Field I and II from the SiX1430 polarization angle measurement. Figures 3, 4 show the model

grids generated for Field I and II respectively. By convention the polarization angle is defined over  $[-90^\circ, 90^\circ]$ , but we redefine it for display purposes over the interval  $[0^\circ, 180^\circ]$  without any loss of information. This is done because the model grids shown below are easier to interpret over the modified domain. While the algorithm grid are arbitrarily dense, only some of the grid points are shown to avoid overcrowding the plot space. To visualize the variation with magnetic field strength B-isocontours are highlighted. The errors in the HeI1083 measurement are typical measurement errors of  $\sim 0.5\%$  in the line intensity, although more accurate measurements are possible. The solution grids are not uniform so the same measurement error translates differently into inverted magnetic field errors depending on the strength of the field. Visually this is evident in the way the B-isocontours become closer together as the field strength increases. The top panel in each figure shows the full model domain while the lower

<sup>2</sup><http://www.hao.ucar.edu/FORWARD/>

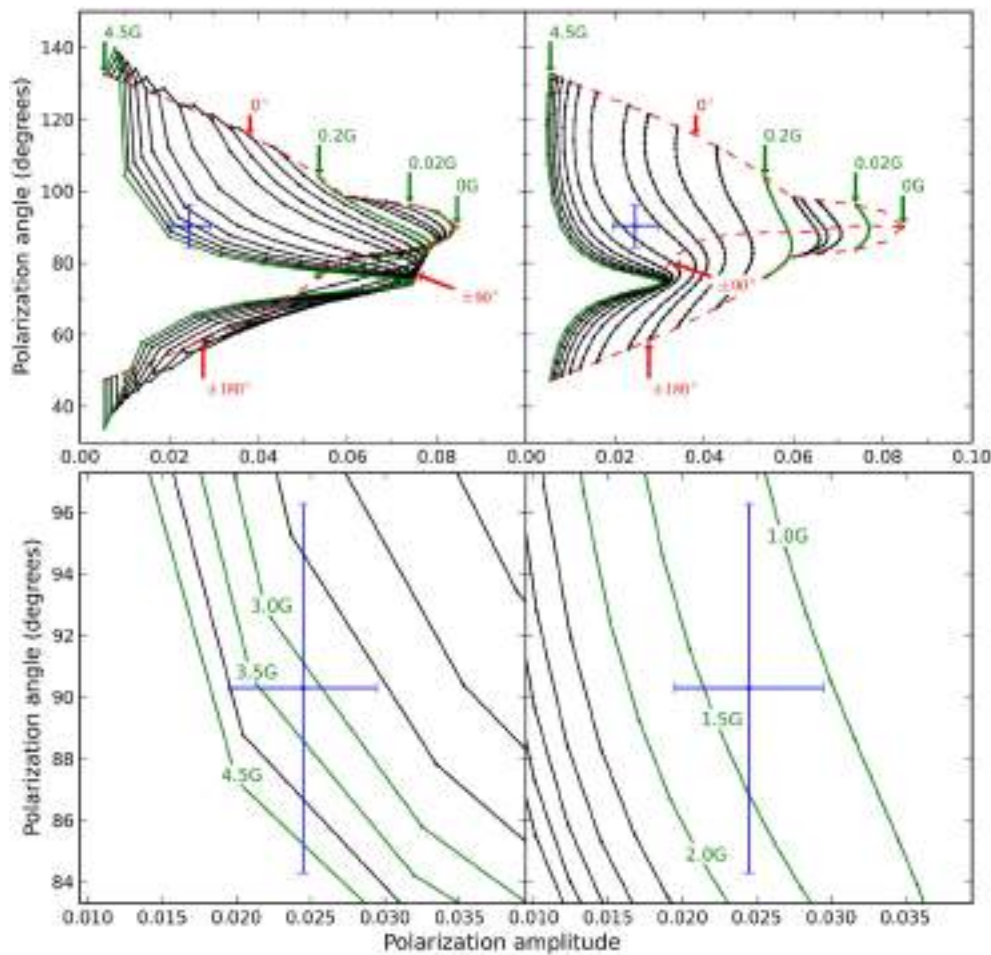


**FIGURE 4 | The same as Figure 3 for the Field II model grids.** For the bottom panel only the B-isocontours spaced by 0.5G are drawn. For Field II the HeI1083 polarization measurement intersects both model grids which is consistent with inclination solutions inside the Van Vleck uncertainty region.

panels show an enhanced view of each grid near the measured values.

For Field I four independent solutions are obtained as shown in **Table 1**. The four solutions can be divided into two solution pairs with unique values of the magnetic field strength  $B$ . For each pair with a unique  $B$  there are two degenerate solutions for the angle variables  $\theta_B$  and  $\chi_B$ . This “classical degeneracy” is independent of the Van Vleck degeneracy and is inherent in the matter-radiation interaction problem and plane of sky scattering geometry (Bommier, 1980). The two ambiguous solutions can be obtained from each other by reflection of the  $B$  vector through the line of sight. For Field I it is evident that the measured polarization value does not intersect the solution grid for the case where the polarization plane is perpendicular to the magnetic field vector. This shows that the magnetic field is not in the Van Vleck degeneracy region.

The recovered solution space for Field II also consists of four independent solutions which can be broken down into two pairs of solutions with unique  $B$  values. Same as for Field I each pair with a unique  $B$  has two degenerate solutions for the angle variables due to the classical degeneracy. However, for Field II the

origin of the different solutions for the magnetic field strength  $B$  lies in the Van Vleck degeneracy. This is seen from the fact that the measured polarization value intersects both model grids.

An important source of error in the analysis is the uncertainty in measuring the SiX1430 polarization angle. This uncertainty can be quite large as is the case for Field II due to the low radiation anisotropy and higher electron density. This uncertainty changes the parallel and perpendicular sets of  $(\theta_B, \chi_B)$  angles that satisfy Equation (2). The effect this uncertainty has on the model grids is shown in **Figures 5, 6** for Field I and II respectively. To produce the variation shown the maximum uncertainty is added and subtracted to the measured SiX1430 polarization angle and new model grids are created using HAZEL. For Field I solutions the errors given in **Table 1** are roughly one and a half time larger for all the parameters. Field II has a much larger uncertainty in measured SiX1430 polarization angle so the effect is larger but mostly concentrated in the angle determination with the variation in the angles increasing to  $\pm 25^\circ$  while the magnetic field strength  $B$  uncertainty increases by one and a half times the values given in **Table 1**.

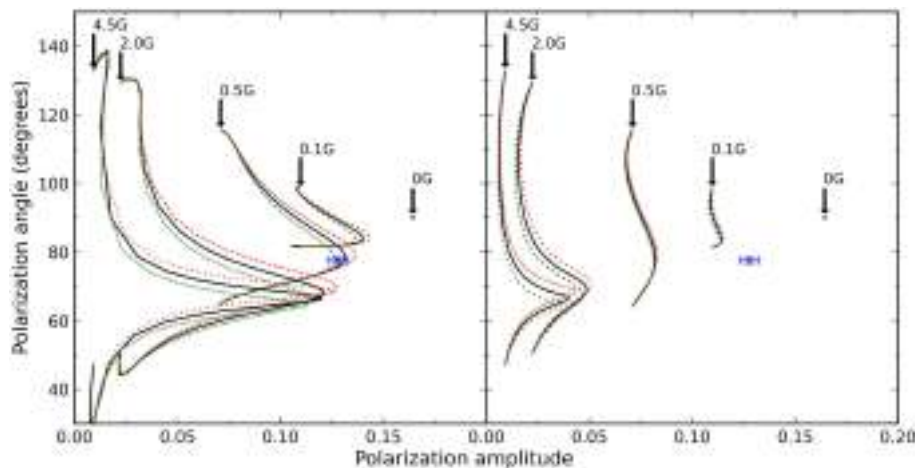


**FIGURE 5 |** Shown in black are the parallel(left) and perpendicular(right) model grids for Field I as they also appear in Figure 3. The dotted lines represent added (red) and subtracted (green) uncertainties in the SiX1430 polarization angle. Only a few B-isocontours are shown and labeled to avoid overcrowding due to intersecting contour lines. The measured HeI1083 polarization parameters are shown with corresponding measurement uncertainties. Propagating the SiX1430 uncertainty requires new grids to be computed since the shapes of the grid changes as seen by the bending and crossing of model contours.

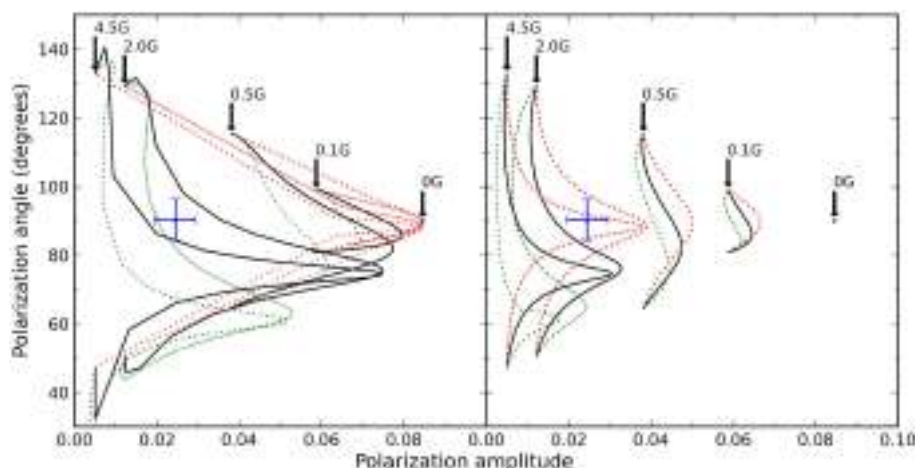


**FIGURE 6 |** The same as Figure 5 but for the Field II model grids and corresponding errors. The SiX1430 linear polarization signal for Field II is weak and thus relatively uncertain for the selected realistic measurement accuracy. This uncertainty leads to the large distortions in the model grids. High accuracy forbidden line polarization directions will be required in this regime.

For these test cases we assume the line intensity measurement to be  $\sim 0.5\%$  for both situations. Since the polarized signal for Field II is ten times weaker than the signal for Field I this translates into a significant increase in the error of the calculated magnetic field strength. However, there is nothing fundamentally limiting about the uncertainty we adopted since the source of the uncertainty is random rather than systematic. For weak polarimetric signals we can increase the integration time to improve the the uncertainty to acceptable levels for errors in the calculated parameters. To achieve the quoted  $0.5\%$  accuracy using the current spectrograph on the  $0.45\text{ m}$  SOLARC telescope around  $12\text{ min}$  of integration time is needed assuming a SiX1430 line brightness of  $5 \times 10^{-6}\text{B}_\odot$  and a spatial resolution element  $7''$  in diameter. The larger  $4\text{ m}$  telescope DKIST will have improved light collecting power as well

as improved signal throughput. It will make this type of accuracy possible for an observation region  $1''$  in diameter in less than  $1\text{ s}$  of integration time.

## 4. DISCUSSION AND CONCLUSIONS

The method proposed provides important constraints on the coronal magnetic field and shows promise as a detailed magnetic field diagnostic, since it drastically constrains the coronal source region local magnetic field to four independent solutions using potentially high signal-to-noise IR linear polarization measurements. This is achieved without knowledge of polarization amplitudes for the forbidden lines that depends

on the coronal electron density. It is interesting to note that the method obtains four degenerate solutions for magnetic fields located inside or outside the Van Vleck degeneracy region. Merenda et al. (2006) proposed a chromospheric algorithm that uses measured HeI1083 linear and circular polarization to determine the vector magnetic field for prominences located in the POS. Their method recovered two degenerate solutions for a magnetic field outside the Van Vleck region and four degenerate solutions for a field inside the Van Vleck region. However, all the examples analyzed by them were for field strengths in excess of 10G, which means the HeI1083 emission is in the saturated Hanle regime. From our solutions for Field I we conclude that the extra degeneracy (not related to the classical degeneracy) that appears even for fields outside the Van Vleck regions is due to the unsaturated Hanle effect. Independent knowledge of the electron density (or the forbidden line polarization amplitude) can reduce the degeneracy outside the Van Vleck region from four to two and uniquely recover the magnetic field strength B. For future work we are testing how accurate the density estimate needs to be in order to reliably distinguish between the degenerate solutions. It may be possible to exclude one pair of solutions even with an average electron model consistent with coronal white light observations.

In principle, the information on the electron density is contained in the polarization amplitude of the forbidden line which we excluded from the present algorithm. If it is possible to distinguish between the two solution pairs, we can then recover information about the electron density from the measured polarization amplitude.

Resolving the final ambiguity from the radiation field geometry requires more information. One solution to this problem is through forward modeling, using 3D coronal MHD models, perhaps constrained by photospheric magnetic field measurements. It is noticeable that these degenerate solutions have complementary values for the inclination angle, so constraints just from the photospheric magnetic polarity changes may provide the key to breaking this degeneracy. Note that similar degeneracies are encountered when measuring vector magnetic fields near the photosphere. Leka et al. (2009) summarizes the types of algorithms used to break the ambiguities in photospheric vector magnetograms. Another possibility involves using tomographic inferences from observing the same region over a few days of solar rotation. Bommier et al. (1981) successfully distinguished between ambiguous solutions by observing a prominence as it rotates through the plane of the sky.

## REFERENCES

- Arnaud, J., and Newkirk, Jr. G. (1987). Mean properties of the polarization of the Fe XIII 10747 Å coronal emission line. *Astron. Astrophys.* 178, 263–268.  
 Asensio Ramos, A., Trujillo Bueno, J., and Landi Degl'Innocenti, E. (2008). Advanced forward modeling and inversion of stokes profiles resulting from the joint action of the Hanle and Zeeman effects. *Astrophys. J.* 683, 542–565. doi: 10.1086/589433  
 Bommier, V. (1980). Quantum theory of the Hanle effect. II - Effect of level-crossings and anti-level-crossings on the polarization of the D3 helium line of solar prominences. *Astron. Astrophys.* 87, 109–120.

While detections of coronal HeI1083 emission shows strong correlation with streamers (Moise et al., 2010) more polarimetric observations of this line are needed to determine the exact geometry and line formation mechanisms of the emitting region. One of our principal assumptions is that the HeI1083 and forbidden line emission is co-spatial but a relaxed version of this assumption is that the emitters experience the same magnetic field. Since the magnetic field expands to fill the coronal volume it is not unreasonable to assume that some large volumes of the corona will experience the same magnetic field. However, obtaining a better understanding and characterization of the HeI1083 coronal signal in the context of simultaneous forbidden line emission measurements will provide more information toward understanding the validity of this assumption. Currently we are pursuing a dedicated campaign to obtain co-spatial and quasi-simultaneous spectropolarimetric observations of the FeXIII1075, SiX1430 and HeI1083 lines in the solar corona using the SOLARC telescope on Haleakala. These observations will form the data set needed to test the proposed method.

## AUTHOR CONTRIBUTIONS

The bulk of the effort in testing and implementing this algorithm has been done by GD in the course of developing his PhD thesis. JK conceived and advised the primary concept. SB provided support in the Hanle effect theory. SB and JK developed the funding and work plan and contributed ideas and material to the manuscript.

## FUNDING

We gratefully acknowledge support from the NSF through grant number ATM-1358270.

## ACKNOWLEDGMENTS

We are grateful to Tom Schad for useful clarifying discussion on the HeI spectropolarimetry. SB thanks Predictive Science Inc. and IfA, University of Hawaii for the opportunity to carry out this project as a visiting scientist. The algorithm has benefited from discussion at NSF SHINE program meetings and at the International Space Science Institute (ISSI) International Team Coronal Magnetism meetings in 2013 and 2014.

- Bommier, V., Sahal-Brechot, S., and Leroy, J. L. (1981). Determination of the complete vector magnetic field in solar prominences, using the Hanle effect. *Astron. Astrophys.* 100, 231–240.  
 Casini, R., and Judge, P. G. (1999). Spectral lines for polarization measurements of the coronal magnetic field. II. Consistent treatment of the stokes vector for magnetic-dipole transitions. *Astrophys. J.* 522, 524–539. doi: 10.1086/307629  
 Gibson, S. E., Kucera, T. A., Rastawicki, D., Dove, J., de Toma, G., Hao, J., et al. (2010). Three-dimensional morphology of a coronal prominence cavity. *Astrophys. J.* 724, 1133–1146. doi: 10.1088/0004-637X/724/2/1133  
 House, L. L. (1974). The theory of the polarization of coronal forbidden lines. *Pub. Astron. Soc. Pacific* 86, 490. doi: 10.1086/129637

- Ishikawa, R., Bando, T., Fujimura, D., Hara, H., Kano, R., Kobiki, T., et al. (2011). "A sounding rocket experiment for spectropolarimetric observations with the Ly line at 121.6 nm (CLASP)," in *Solar Polarization 6, Vol. 437 of Astronomical Society of the Pacific Conference Series*, eds J. R. Kuhn, D. M. Harrington, H. Lin, S. V. Berdyugina, J. Trujillo-Bueno, and S. L. Keil (San Francisco, CA: Astronomical Society of the Pacific), 287.
- Judge, P. G. (1998). Spectral lines for polarization measurements of the coronal magnetic field. I. Theoretical intensities. *Astrophys. J.* 500, 1009–1022. doi: 10.1086/305775
- Judge, P. G., and Casini, R. (2001). "A synthesis code for forbidden coronal lines," in *Advanced Solar Polarimetry – Theory, Observation, and Instrumentation, Vol. 236 of Astronomical Society of the Pacific Conference Series*, ed M. Sigwarth (San Francisco, CA: Astronomical Society of the Pacific), 503.
- Judge, P. G., Low, B. C., and Casini, R. (2006). Spectral lines for polarization measurements of the coronal magnetic field. IV. Stokes signals in current-carrying fields. *Astrophys. J.* 651, 1229–1237. doi: 10.1086/507982
- Kuhn, J. R. (1995). "Infrared coronal magnetic field measurements," in *Infrared Tools for Solar Astrophysics: What's Next?*, eds J. R. Kuhn and M. J. Penn (Singapore: World Scientific), 89–94.
- Kuhn, J. R., Arnaud, J., Jaeggli, S., Lin, H., and Moise, E. (2007). Detection of an extended near-sun neutral helium cloud from ground-based infrared coronagraph spectropolarimetry. *Astrophys. J.* 667, L203–L205. doi: 10.1086/522370
- Kuhn, J. R., Coulter, R., Lin, H., and Mickey, D. L. (2003). "The SOLARC off-axis coronagraph," in *Innovative Telescopes and Instrumentation for Solar Astrophysics, Vol. 4853 of Society of Photo-Optical Instrumentation Engineers (SPIE) Conference Series*, eds S. L. Keil and S. V. Avakyan (Bellingham, WA), 318–326.
- Kuhn, J. R., Penn, M. J., and Mann, I. (1996). The near-infrared coronal spectrum. *Astrophys. J.* 456:L67. doi: 10.1086/309864
- Leka, K. D., Barnes, G., Crouch, A. D., Metcalf, T. R., Gary, G. A., Jing, J., et al. (2009). Resolving the 180° ambiguity in solar vector magnetic field data: evaluating the effects of noise, spatial resolution, and method assumptions. *Sol. Phys.* 260, 83–108. doi: 10.1007/s11207-009-9440-8
- Lin, H., Kuhn, J. R., and Coulter, R. (2004). Coronal magnetic field measurements. *Astrophys. J.* 613, L177–L180. doi: 10.1086/425217
- Lin, H., Penn, M. J., and Tomczyk, S. (2000). A new precise measurement of the coronal magnetic field strength. *Astrophys. J.* 541, L83–L86. doi: 10.1086/312900
- López Ariste, A., and Casini, R. (2003). Improved estimate of the magnetic field in a prominence. *Astrophys. J.* 582, L51–L54. doi: 10.1086/367600
- Merenda, L., Trujillo Bueno, J., Landi Degl'Innocenti, E., and Collados, M. (2006). Determination of the magnetic field vector via the Hanle and Zeeman effects in the He I  $\lambda$ 10830 multiplet: evidence for nearly vertical magnetic fields in a polar crown prominence. *Astrophys. J.* 642, 554–561. doi: 10.1086/501038
- Moise, E., Raymond, J., and Kuhn, J. R. (2010). Properties of the diffuse neutral helium in the inner heliosphere. *Astrophys. J.* 722, 1411–1415. doi: 10.1088/0004-637X/722/2/1411
- Penn, M. J. (2014). Infrared Solar Physics. *Living Rev. Solar Phys.* 11:2. doi: 10.12942/lrsp-2014-2
- Sahal-Brechot, S. (1977). Calculation of the polarization degree of the infrared lines of Fe XIII of the solar corona. *Astrophys. J.* 213, 887–899. doi: 10.1086/155221
- Tomczyk, S., Card, G. L., Darnell, T., Elmore, D. F., Lull, R., Nelson, P. G., et al. (2008). An instrument to measure coronal emission line polarization. *Sol. Phys.* 247, 411–428. doi: 10.1007/s11207-007-9103-6

**Conflict of Interest Statement:** The authors declare that the research was conducted in the absence of any commercial or financial relationships that could be construed as a potential conflict of interest.

The reviewer RC declared a past co-authorship with one of the authors JK to the handling Editor, who ensured that the process met the standards of a fair and objective review.

Copyright © 2016 Dima, Kuhn and Berdyugina. This is an open-access article distributed under the terms of the Creative Commons Attribution License (CC BY). The use, distribution or reproduction in other forums is permitted, provided the original author(s) or licensor are credited and that the original publication in this journal is cited, in accordance with accepted academic practice. No use, distribution or reproduction is permitted which does not comply with these terms.



# Diagnostics of Coronal Magnetic Fields through the Hanle Effect in UV and IR Lines

Nour E. Raouafi<sup>1\*</sup>, Pete Riley<sup>2</sup>, Sarah Gibson<sup>3</sup>, Silvano Fineschi<sup>4</sup> and Sami K. Solanki<sup>5,6</sup>

<sup>1</sup> The John Hopkins University Applied Physics Laboratory, Laurel, MD, USA, <sup>2</sup> Predictive Science Inc., San Diego, CA, USA,

<sup>3</sup> High Altitude Observatory, National Center for Atmospheric Research, Boulder, CO, USA, <sup>4</sup> The Astrophysical Observatory of Turin, National Institute for Astrophysics, Turin, Italy, <sup>5</sup> Max-Planck-Institut für Sonnensystemforschung, Göttingen, Germany, <sup>6</sup> School of Space Research, Kyung Hee University, Yongin, South Korea

## OPEN ACCESS

### Edited by:

Xueshang Feng,  
National Space Science Center, China

### Reviewed by:

Keiji Hayashi,  
Naogya University, Japan

Meng Jin,

University Corporation for  
Atmospheric Research and Lockheed  
Martin Solar and Astrophysics  
Laboratory, USA

### \*Correspondence:

Nour E. Raouafi  
[noureddine.raouafi@jhuapl.edu](mailto:noureddine.raouafi@jhuapl.edu)

### Specialty section:

This article was submitted to  
Stellar and Solar Physics,  
a section of the journal  
Frontiers in Astronomy and Space  
Sciences

Received: 11 February 2016

Accepted: 10 May 2016

Published: 22 June 2016

### Citation:

Raouafi NE, Riley P, Gibson S,  
Fineschi S and Solanki SK (2016)  
Diagnostics of Coronal Magnetic  
Fields through the Hanle Effect in UV  
and IR Lines.  
Front. Astron. Space Sci. 3:20.  
doi: 10.3389/fspas.2016.00020

The plasma thermodynamics in the solar upper atmosphere, particularly in the corona, are dominated by the magnetic field, which controls the flow and dissipation of energy. The relative lack of knowledge of the coronal vector magnetic field is a major handicap for progress in coronal physics. This makes the development of measurement methods of coronal magnetic fields a high priority in solar physics. The Hanle effect in the UV and IR spectral lines is a largely unexplored diagnostic. We use magnetohydrodynamic (MHD) simulations to study the magnitude of the signal to be expected for typical coronal magnetic fields for selected spectral lines in the UV and IR wavelength ranges, namely the H I Ly- $\alpha$  and the He I 10,830 Å lines. We show that the selected lines are useful for reliable diagnosis of coronal magnetic fields. The results show that the combination of polarization measurements of spectral lines with different sensitivities to the Hanle effect may be most appropriate for deducing coronal magnetic properties from future observations.

**Keywords:** sun: corona, sun: magnetic fields, sun: UV radiation, sun: infrared, polarization, scattering, atomic processes, plasmas

## 1. INTRODUCTION

Our understanding of coronal phenomena, such as plasma heating and acceleration, particle energization, and explosive activity, faces major hurdles due to the lack of reliable measurements of key parameters such as densities, temperatures, velocities, and particularly magnetic fields. The knowledge of key plasma parameters, particularly the magnetic field and plasma velocity, in the solar corona is a prerequisite to advance our understanding of coronal manifestations that greatly affect and modulate the interplanetary medium, particularly the Earth's environment.

Spectroscopic diagnostics in the ultraviolet (UV) and extreme ultraviolet (EUV) wavelength regimes provide measurements of plasma densities, temperatures, and partial information on the velocity. But they cannot provide any insight into the coronal magnetic field, which is the key player in the structuring of the solar corona and in dominating most (if not all) physical processes underlying the multi-scaled solar activity. For instance, the abundant mechanical energy that is available in the convection zone is partially transferred to the corona, where it is stored in complex magnetic field structures and dissipated in the form of heat, acceleration, and energization of the plasma during activity events occurring at different spatial and temporal scales. The magnetic activity manifests itself in different forms such as Coronal Mass Ejections [CMEs], flares, jets, waves and instabilities, magnetic reconnection, and turbulence.

Magnetic fields measurements in the photosphere and, to a lesser degree, in the chromosphere, which are based mainly on the Zeeman effect, have been a routine exercise for decades. The Zeeman effect in the higher layers of the solar atmosphere, particularly the corona, are limited to regions of relatively strong magnetic fields (i.e., above active regions) and to infrared lines due to the wavelength squared scaling of this effect and the relatively large widths of coronal lines (Lin et al., 2004). Other methods based on radio emissions could provide constraints on the magnetic field in the corona (White, 1999; Gibson et al., 2016). Coronal magnetic fields are usually approximated through MHD modeling and extrapolation of photospheric measurements (e.g., Wiegelmans et al., 2014). These approaches have, however, their limitations. For instance, extrapolation models are based on the assumption that the magnetic field is force-free at the lower boundary of the calculation, which is not the case in the photosphere. Additionally, large-scale MHD models of the solar corona are based on synoptic maps of the photospheric magnetic fields, which are built up from images taken by near-Earth observatories recorded over a whole solar rotation. Finally, the MHD models may underestimate the magnetic field strength in the corona (Riley et al., 2012). Moreover, coronal plasma parameters obtained through the models cannot be constrained without direct measurements. For more details on methods for the measurements of magnetic fields in upper solar atmosphere, see reviews by Fineschi (2001) and Raouafi (2005, 2011).

In this paper, we focus on the diagnostics of coronal magnetic fields through the linear polarization of selected spectral lines (i.e., H I Ly- $\alpha$  and He I 10,830 Å) that are sensitive to the “Hanle effect.” Other spectral lines are also of interest, but the analysis of their polarization is left for future publications.

## 2. THE HANLE EFFECT

The Hanle effect (Hanle, 1924), which is the modification of the linear polarization of a spectral line by a local magnetic field,

may provide strong diagnostics of regions of weak magnetic fields such as the solar corona, where a number of spectral lines with different but complementary sensitivity ranges are present. Unlike the Zeeman effect, the Hanle effect does not create polarization but requires its presence through other physical processes such as radiation scattering. The Hanle effect is a purely quantum phenomenon and has no classical equivalent. However, for brevity, to provide a simplified illustration of such a complex effect, it can be explained by approximating the excited atom/ion to a damped oscillator with Larmor frequency that is scattering incident non-polarized radiation (see Figure 1). The Larmor frequency,  $\omega_L$ , of the precession motion around the magnetic field vector is directly related to the magnetic field strength. The damping is proportional to the finite lifetime,  $\tau$ , of the upper level of the atomic transition. We note that this classical description could explain only the case of the normal Zeeman triplet (i.e., two-level atom  $J_u = 1; J_l = 0$ ). Significant advances in the theory of radiation scattering in the presence of magnetic fields have been achieved in the last four decades (Sahal-Bréchot et al., 1977; Bommier, 1980; Landi Degl’Innocenti, 1982; Casini and Judge, 1999; López Ariste and Casini, 2002; Raouafi, 2002; Trujillo Bueno et al., 2002a; Landi Degl’Innocenti and Landolfi, 2004).

The sensitivity of a given spectral line to the Hanle effect is a function of the lifetime of the atomic transition and  $|B|$ . Ideally, a spectral line is sensitive to magnetic field strengths satisfying the relation

$$\gamma B \tau \approx 1, \quad (1)$$

where  $\gamma = g_{J_u} \mu_B / \hbar$ ,  $g_{J_u}$  is the Landé factor of the upper atomic level,  $\mu_B$  is the Bohr magneton, and  $\hbar$  is the reduced Planck constant. Practically, the Hanle effect is measurable for  $0.2 \leq \omega_L \tau \leq 10$  (Bommier and Sahal-Bréchot, 1978, 1982). Table 1 provides the magnetic field strengths corresponding to the ideal sensitivity of the different spectral lines to the Hanle effect.

Theoretically, direct determination of the magnetic field in the solar corona could be achieved through linear polarization

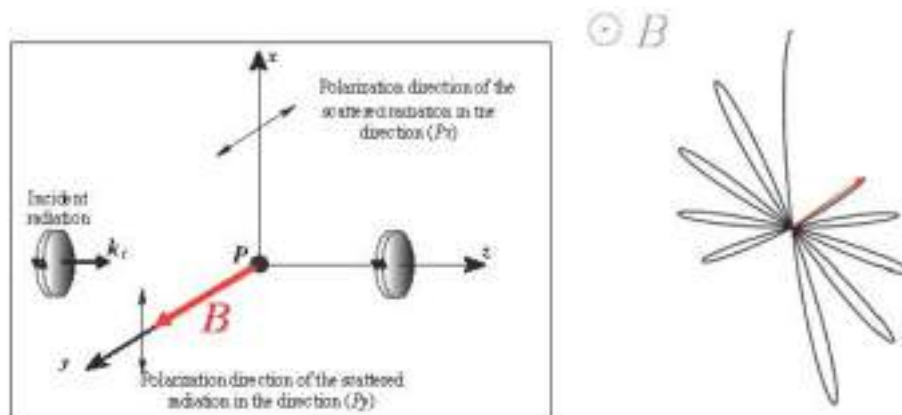


**FIGURE 1 | Illustration of the Hanle effect due to a magnetic field aligned with the line of sight (Py).** In the absence of a magnetic field, the direction of the linear polarization of the scattered light is parallel to the (Px) axis (left panel). In the presence of a magnetic field, the combination of the precession around the magnetic field and the damping of the atomic dipole results in a modification of linear polarization that depends on both the strength and direction of the field vector (right panel).

**TABLE 1 | Magnetic field strengths corresponding to the ideal Hanle effect for a number of spectral lines (column 4).**

Spectral line	Wavelength (Å)	$A_{ul}$ ( $10^8 \text{ s}^{-1}$ )	B (Gauss)
H I Ly- $\alpha$	1215.16	6.265	53.43
H I Ly- $\beta$	1025.72	1.672	14.26
H I Ly- $\gamma$	972.53	0.682	5.81
H I Ly- $\delta$	949.74	0.344	2.93
O vi	1031.91	4.16	35.48
He I	10,830.0	0.344	0.82

$A_{ul}$  is the Einstein coefficient of spontaneous emission of the upper level of the corresponding transitions.

of spectral lines with suitable sensitivity to the Hanle effect. The Hanle effect in selected spectral lines yields a powerful diagnostic tool for magnetic fields typically ranging from a few milli-Gauss to several hundred Gauss (depending strongly on the chosen line and the strength and direction of the magnetic field). Unlike the Zeeman effect, the depolarization of spectral lines by turbulent magnetic fields can be detected in the Hanle regime allowing the determination of the strength of the field in mixed-polarity regions (e.g., Stenflo, 1982; Trujillo Bueno et al., 2004).

In the solar corona, the Hanle effect manifests itself primarily through a depolarization and a rotation of the plane of linear polarization, with respect to the zero-field case where the plane of polarization is parallel to the local solar limb. Bommier et al. (1981) studied various measurement scenarios allowing for the complete diagnostic of the coronal magnetic field vector. The Hanle effect diagnostic of magnetic fields has been successful in solar prominences (Leroy et al., 1977; Sahal-Bréchot et al., 1977; Bommier, 1980; Landi Degl'Innocenti, 1982; Querfeld et al., 1985; López Ariste and Casini, 2002; Trujillo Bueno et al., 2002b), as well as in arch filament systems (Solanki et al., 2003; Lagg et al., 2004; Xu et al., 2010; Merenda et al., 2011).

## 2.1. Prominence Magnetic Fields

Bommier et al. (1994) and previous related papers (Sahal-Bréchot et al., 1977; Bommier and Sahal-Bréchot, 1978) have successfully demonstrated the power of the Hanle effect method for measuring the magnetic fields in solar prominences. Leroy et al. (1983, 1984) used observations obtained with the coronagraph polarimeter at the Pic du Midi observatory (France) to study the magnetic field of several hundreds of prominences based on the Hanle effect of spectral lines such as H- $\alpha$ , H- $\beta$ , and He I 5876 Å. Leroy et al. (1983) found that magnetic field strengths increased with the rise of the solar cycle. They reported an average field strength of  $\sim 6$  Gauss at the beginning of the cycle and about twice this value near solar maximum. Furthermore, Leroy et al. (1984) found that the magnetic field strength and direction depend also on the prominence height: prominences with heights lower than 30 Mm have  $\sim 20$  Gauss fields with  $\alpha \sim 20^\circ$  and prominences higher than 30 Mm have 5 – 10 Gauss fields with  $\alpha \sim 25^\circ$  ( $\alpha$  is the angle between the magnetic field vector and the prominence spine).

More recently, the He I 10,830 Å triplet has provided additional, very detailed diagnostics of the magnetic field in filaments. Thus, Kuckein et al. (2009, 2012), Sasso et al. (2011), and Xu et al. (2012) found that active region filaments have hectoGauss field strengths, i.e., an order of magnitude larger than the quiet filaments and prominences studied earlier. The spectropolarimetry of this set of lines even revealed the complex multicomponent structure of an activated filament, with the different components displaying magnetic vectors with different field strengths and directions and gas flowing at different speeds and in different directions (Sasso et al., 2014).

## 2.2. Polarization of Coronal Forbidden Lines

Charvin (1965) has shown that the direction of polarization of some forbidden lines is expected to be either parallel or perpendicular to the local magnetic field projected onto the plane of the sky. This provides a useful approach to study the orientation (direction) of coronal magnetic fields. No information on the field strength can, however, be obtained from such diagnostics.

The polarization of forbidden lines such as Fe XIV 530.3 nm and Fe XIII 1074.7 nm have been studied for more than three decades during solar eclipses and using coronagraph observations (Querfeld, 1974, 1977; Querfeld and Elmore, 1976; Arnaud and Newkirk, 1987, etc.). The relatively low resolution observations show a striking evidence of a predominant radial orientation of the polarization, found everywhere independently of the phase of the solar cycle, which depicts the direction of the coronal field projected on the plane of the sky (see Arnaud, 1982a,b; Arnaud and Newkirk, 1987). This may, however, be attributed to the low resolution of the instruments used in the above studies. In addition due to the van Vleck ambiguity, the magnetic field can also be perpendicular to the direction of the linear polarization. This is likely the case at tops of large coronal loops where the magnetic field is nearly horizontal.

Habbal et al. (2001) analyzed intensity and polarization maps with better resolution of the Fe XIII 1074.7 nm line. They found evidence for two magnetic components in the corona: a non-radial field associated with the large-scale structures known as streamers (with loop-like structures at their base) and a more pervasive radial magnetic field, which corresponds to the open coronal magnetic field. More recent observations from the CoMP telescope (Tomczyk et al., 2008) with higher resolutions show significant non-radiality of the coronal magnetic field projected on the plane of the sky. For examples of CoMP observations, see Gibson et al. (2016).

## 2.3. Polarization of FUV and EUV Coronal Lines

Several lines in the far UV (FUV) and EUV wavelength ranges have suitable sensitivity to determine the coronal magnetic field via the Hanle effect. The coronal Hanle effect in the FUV and EUV wavelength ranges is largely unexplored despite the high potential of this diagnostic. Li-like ion lines (O VI, N V, C IV, ...)

are presumed to be observed high in the corona due to their broad abundance curves (Sahal-Bréchot et al., 1986). Li-like ion lines are very intense lines of the chromosphere-corona transition region (the O VI 103.2 nm line is one of the most intense lines after H I Ly- $\alpha$ ). For instance, the observed emission of the O VI ion by Vial et al. (1980) at 30'' above the limb (as well as Reeves and Parkinson, 1970) has shown that the O VI emission extends out into the corona to a few *arcmin* above the limb. Observations from the Ultraviolet Coronagraph Spectrometer (UVCS; Kohl et al., 1995) on the The Solar and Heliospheric Observatory (SOHO; Domingo et al., 1995) show that the O VI emission extends several solar radii above the limb, with a line ratio and line widths sensitive to Doppler dimming and anisotropic velocity distributions (Kohl et al., 1998; Li et al., 1998). Such lines have small natural widths and short lifetimes of the upper levels of the corresponding atomic transitions. The magnetic field strength corresponding to their sensitivity to the Hanle effect ranges from a few Gauss to more than 300 Gauss. This interval contains the expected magnitude of the magnetic field strength in the solar corona.

In a series of papers, Fineschi et al. (1991, 1993) and Fineschi and Habbal (1995) studied both theoretically and from an instrumental point of view the feasibility of coronal magnetic field diagnostics through the Hanle effect. In particular, they considered the case of the strongest UV coronal line, H I Ly- $\alpha$ . One of the advantages of using H I Ly- $\alpha$  is the very broad line profile of transition region incident radiation, which makes it insensitive to effects of the solar wind velocity at low coronal heights. Additionally, H I Ly- $\alpha$  has a negligible collisional component compared to that of the other H I Lyman series. This results in a H I Ly- $\alpha$  zero-field polarization larger than that of the other H I Lyman lines, increasing the overall line sensitivity to the Hanle effect (see Fineschi et al., 1999).

Raouafi et al. (1999a) used spectroscopic observations from the SOHO Solar Ultraviolet Measurements of Emitted Radiation spectrometer (SUMER; Wilhelm et al., 1995) to measure the linear polarization of the O VI 103.2 nm line. SUMER calibration before launch shows that the instrument is sensitive to the linear polarization of the observed light (Hassler et al., 1997). The observations were made during the roll manoeuvre of the SOHO spacecraft on March 19, 1996, in the southern coronal polar hole at  $1.3 R_{\odot}$ . For more details on the observations see Raouafi et al. (1999a,b). The data show in particular that the plane of polarization has an angle of  $\sim 9^{\circ}$  with respect to the solar limb. In contrast, the polarization direction is expected to be tangent to the local solar limb in the absence of the magnetic field effect. Raouafi et al. (1999a,b, 2002) interpreted these measurements in terms of the Hanle effect due to the coronal magnetic field. They developed models to simulate the observational results and inferred a field strength of  $\sim 3$  Gauss at  $1.3 R_{\odot}$  above the solar pole. The main result from this work is a clear evidence for the Hanle effect in the strong O VI 103.2 nm coronal lines. This opens a window for direct diagnostic of the coronal magnetic field by using different FUV-EUV lines with complementary sensitivities to the magnetic field.

Manso Sainz and Trujillo Bueno (2009) discussed the possibility of mapping the on-disk coronal magnetic fields using forward scattering in permitted lines at EUV wavelengths (e.g., the Fe X 17.4 nm line).

### 3. SIMULATION DATA: MAGNETIC FIELD CONFIGURATION AND PLASMA PARAMETERS

To develop useful model solutions for the solar corona, we use the magnetohydrodynamic (MHD) approximation, which is appropriate for long-scale, low-frequency phenomena in magnetized plasmas. In the past, we employed a "polytropic approximation" for treating the heating of the coronal plasma and the acceleration of the solar wind (Riley et al., 2001; Riley and Luhmann, 2012). While this approach produces remarkably good solutions for the structure of the coronal magnetic field, this is at the expense of poorer velocity and density profiles. In this study, however, we use our "thermodynamic" model, which relies on coronal heating functions that are guided by observational constraints (Lionello et al., 2009; Riley et al., 2015). Detailed comparisons with EUV and X-ray observations from several spacecraft have allowed us to constrain the likely functional forms for this heating, such that they reproduce the observed emission.

Most (if not all) of the Hanle effect studies in the literature were based on well-defined magnetic field configurations (e.g., theoretical models or extrapolated photospheric magnetic fields), which were lacking well-defined plasma parameters such as densities, temperatures, and velocities. These quantities enter directly into the definition of the Stokes parameters encompassing the magnetic field signature that is the Hanle effect. *Ad-hoc* approximations may provide valuable results and order of magnitude estimates of different quantities as well as estimates of linear polarization of a given spectral line, but they cannot yield physically meaningful estimates of the coronal magnetic field through the Hanle effect. These assumptions can be improved upon by considering self-consistent magnetic fields and plasma parameters obtained through MHD simulations.

To obtain realistic estimates of the polarization parameters of the UV H I Ly- $\alpha$  (1216 Å), we utilize high-resolution MHD simulations using Predictive Science's state-of-the-art MAS code. The simulation includes a full thermodynamic description of the plasma. All parameters needed for the calculation of the polarization of the spectral line are obtained in a self-consistent fashion, thus removing any need for heuristic assumptions. All quantities are provided on the nodes of spherical grids whose resolution changes with the heliodistance. **Figure 2** displays the magnetic field configuration of the solar corona corresponding to Carrington rotation 2130. The synthetic white-light coronal emission is shown in the right-hand-side panel.

For the coronal Hanle effect of the different spectral lines, we use the magnetic field, density, temperature, and velocity data cube. Line-of-sight (LOS) integration is taken into account. All quantities at any given point on the LOS are obtained by interpolation of the simulation data.

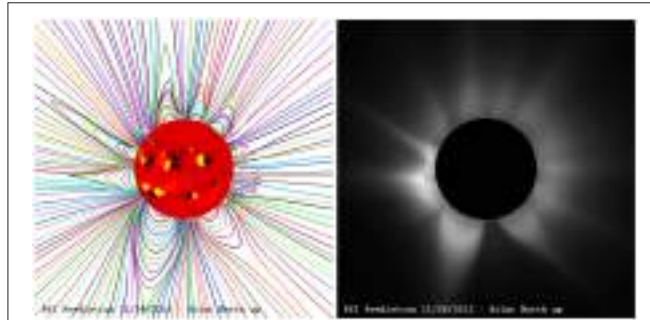


**FIGURE 2 | Predictions of the coronal magnetic field configuration (left) and white-light synthetic image (right) for the solar eclipse of November 13, 2012.** The images shown below are aligned such that solar north is vertically upward and includes the tilt due to the solar  $B_0$  angle. The date on the panels is when the prediction was made. PSI have been providing predictions for solar eclipses for many years, which can be found at: <http://www.predsci.com/corona/>.

## 4. H I LY- $\alpha$ SOLAR DISK RADIATION

The H I Ly- $\alpha$  line is formed in the transition region at a temperature  $\sim 1$  MK. The coronal counterpart is formed by scattering of this incident radiation, resulting in the most intense UV coronal line. The solar disk radiation of this line is characterized by very little to no center-to-limb variations (Bonnet et al., 1980). The line profile is substantially wider than other lines and is typically complex. Figure 3 shows an average H I Ly- $\alpha$  line profile as observed by SOHO/SUMER (Lemaire et al., 1998). It is characterized by an inverted peak at the center of the line, making a single Gaussian fit meaningless. For the present study, this profile is fitted with four Gaussians whose parameters are shown in the same figure. Numerically, we assume four individual Gaussian spectral lines (Figure 3) at different frequencies and with different widths and intensities. This assumption is, we believe, the best way to realistically mimic the incident radiation from the solar transition region.

We consider a two level atomic model for the H I Ly- $\alpha$  line. This assumption is sufficient to describe the light scattering by hydrogen atoms in the solar corona. The spectral line has two components,  $2p\ ^2P_{3/2}^o \rightarrow 1s\ ^2S_{1/2}$  (polarizable) and  $2p\ ^2P_{1/2}^o \rightarrow 1s\ ^2S_{1/2}$  (non-polarizable), with virtually the same Einstein coefficients of spontaneous emission,  $A_{ul} \approx 6.2648 \times 10^8\ s^{-1}$ . The coronal electron collisional component represents less than 1% of the total intensity (Raymond et al., 1997). We neglect this component and assume that the H I Ly- $\alpha$  coronal line results only from the scattering of incident radiation from the transition region. Since we are interested in the magnetic field, we also neglect the effect of the solar wind velocity. This assumption is justified by the fact that the polarization calculations presented in this paper are achieved at coronal heights lower than  $1 R_\odot$ , where the solar wind speed is lower than  $100\ km\ s^{-1}$ . Considering the line width of the incident line, the Doppler distribution effects are neglected. The incident radiation from the solar transition region is unpolarized and the radiation field is assumed to be cylindrically symmetric around the solar vertical, with half-cone

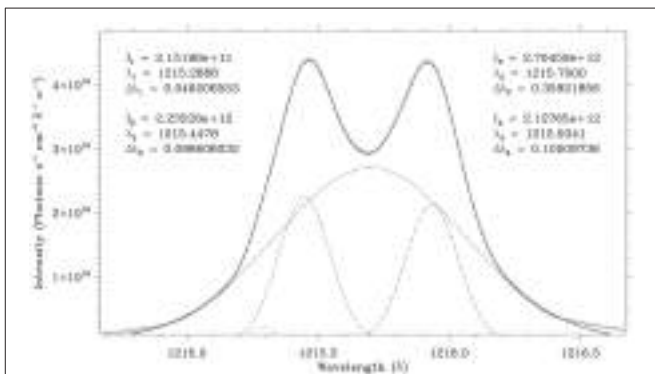


**FIGURE 3 | Average transition region profile (Solid profile) of the H I Ly- $\alpha$  profile as observed by SOHO/SUMER (Lemaire et al., 1998).** The “+” signs are the best 4-Gaussian fit of the observed profile. The individual Gaussians are given by the dotted, dashed, dot-dashed, and triple-dot-dashed profiles. The incident H I Ly- $\alpha$  radiation is assumed to be composed of four individual Gaussian profiles. The parameters of the individual profiles (i.e., amplitude [in photons cm $^{-2}$  s $^{-1}$  Å $^{-1}$  sr $^{-1}$ ], central wavelength [in Å] and width [in Å]) are also displayed.

angle  $\alpha_r$  (i.e., solar disk radiation inhomogeneities [e.g., active regions] are also neglected).

### 4.1. The Atomic Model and Polarization

We consider the case of a two-level atom ( $\alpha_l J_l, \alpha_u J_u$ ) in the presence of a magnetic field  $B$ . We also assume a non-polarizable lower level, such as that of the H I Ly- $\alpha$  line whose spherically symmetric lower level  $^2S_{1/2}$  (that is not polarizable). Within the frame of the density matrix formalism, the lower level is described only by its population represented by  $\alpha_l J_l \rho_0^0$  within the frame of density matrix formalism.

We assume that the incident radiation is characterized by a Gaussian spectral profile

$$\mathcal{I}(\Omega, \nu) = \frac{\mathcal{I}_c f(\Omega)}{\sqrt{\pi} \sigma_i} e^{-\left(\frac{\nu-\nu_0}{\sigma_i}\right)^2}, \quad (2)$$

where  $\mathcal{I}_c$  is the solar disk center radiance (in erg cm $^{-2}$  s $^{-1}$  sr $^{-1}$  Hz $^{-1}$ ),  $\nu_0$  and  $\sigma_i$  are the line center frequency and width of the incident profile, and  $f(\Omega)$  describes the center-to-limb variation of the incoming radiation field. In the case of Ly- $\alpha$ ,  $f(\Omega) \approx 1$  (see Bonnet et al., 1980). In the solar frame, the properties of the incident radiation field are given by

$$\begin{aligned} \mathfrak{J}_0^0(\nu) &= \oint \frac{d\Omega}{4\pi} \mathcal{I}(\Omega, \nu) \\ \mathfrak{J}_0^2(\nu) &= \oint \frac{d\Omega}{4\pi} \frac{1}{2\sqrt{2}} (3 \cos^2 \alpha_r - 1) \mathcal{I}(\Omega, \nu) \end{aligned} \quad (3)$$

All other multipoles (i.e.,  $\mathfrak{J}_{0,\pm 1}^1$  and  $\mathfrak{J}_{\pm 1,\pm 2}^2$ ) are zero since the incident radiation is not polarized. The density matrix multipoles of the incident radiation have to be re-written in the magnetic field reference frame, which is obtained from the solar frame by a rotation  $\mathcal{R}(\psi, \eta, 0)$ , where  $\psi$  and  $\eta$  are, respectively, the azimuth and co-latitude of the vector magnetic field with respect to the solar vertical reference frame.

For a two-level atom with unpolarized lower level, the atomic polarization properties of the upper level are given by the atomic density matrix:

$$\begin{aligned} \alpha_u J_u \rho_Q^K(\nu, \Omega) = & \frac{\alpha_l J_l \rho_0^0(\nu)}{A_{ul} + i Q \omega_L} \sqrt{3(2J_l + 1)} B_{lu} (-1)^{1+J_l+J_u+Q} \\ & \left\{ \begin{array}{ccc} 1 & 1 & K \\ J_u & J_u & J_l \end{array} \right\} {}^B \mathfrak{J}_{-Q}^K(\nu, \Omega) \\ = & \sqrt{\frac{2J_l + 1}{2J_u + 1}} \frac{B_{lu}}{A_{ul} + i Q \omega_L} \frac{\alpha_l J_l \rho_0^0(\nu)}{\omega_L} w_{ul}^{(K)} (-1)^Q {}^B \mathfrak{J}_{-Q}^K(\nu, \Omega) \end{aligned} \quad (4)$$

where  $K = 0, \dots, 2J_u$  and  $Q = -K, \dots, K$ .  $\omega_L = 2\pi g_u \nu_L$  is the Larmor angular frequency. For details on the derivation of Equation (4), see Landi Degl'Innocenti and Landolfi (2004).  $\nu_L$  is the Larmor frequency and reflects the Hanle effect due to the presence of the magnetic field,  $g_u$  is the Landé factor of the upper level, and  $A_{ul}$  and  $B_{lu}$  are the Einstein coefficients for the spontaneous emission and absorption from the lower to upper levels. The symbol between the brackets is the Wigner 6j-symbol.

Equation (4) is the solution of the statistical system of linear equations of the atomic system in the steady-state case.

## 5. HANLE EFFECT OF THE H I Ly- $\alpha$ CORONAL LINES

The results of the forward modeling of the linear polarization of the coronal H I Ly- $\alpha$  line are shown in Figure 4. In the absence of the effect of the coronal magnetic field (i.e., Hanle effect), the direction of polarization is parallel to the local solar limb regardless of coronal altitude. The fractional linear polarization increases as a function of altitude because of the increased anisotropy of the incident solar disk radiation. The LOS integration is also more important with increasing altitude above the solar limb. This is due to the increasingly shallower density gradient. For the present calculations, the LOS integration is done for a range of  $5 R_\odot$  centered on the plane of the sky.

The top panels of Figure 4 illustrated the altitude variation of the Stokes parameters ( $\log_{10} I$ ,  $Q/I$ , and  $U/I$ , respectively). The lowest coronal altitude of the calculations is  $1.015 R_\odot$ . The bottom panels show the degree of linear polarization (in %, left), the polarization degree in zero magnetic field ( $P/P_0$ , middle), and the rotation of the plane of polarization with respect to the local solar limb ( $H$  in degrees, right).

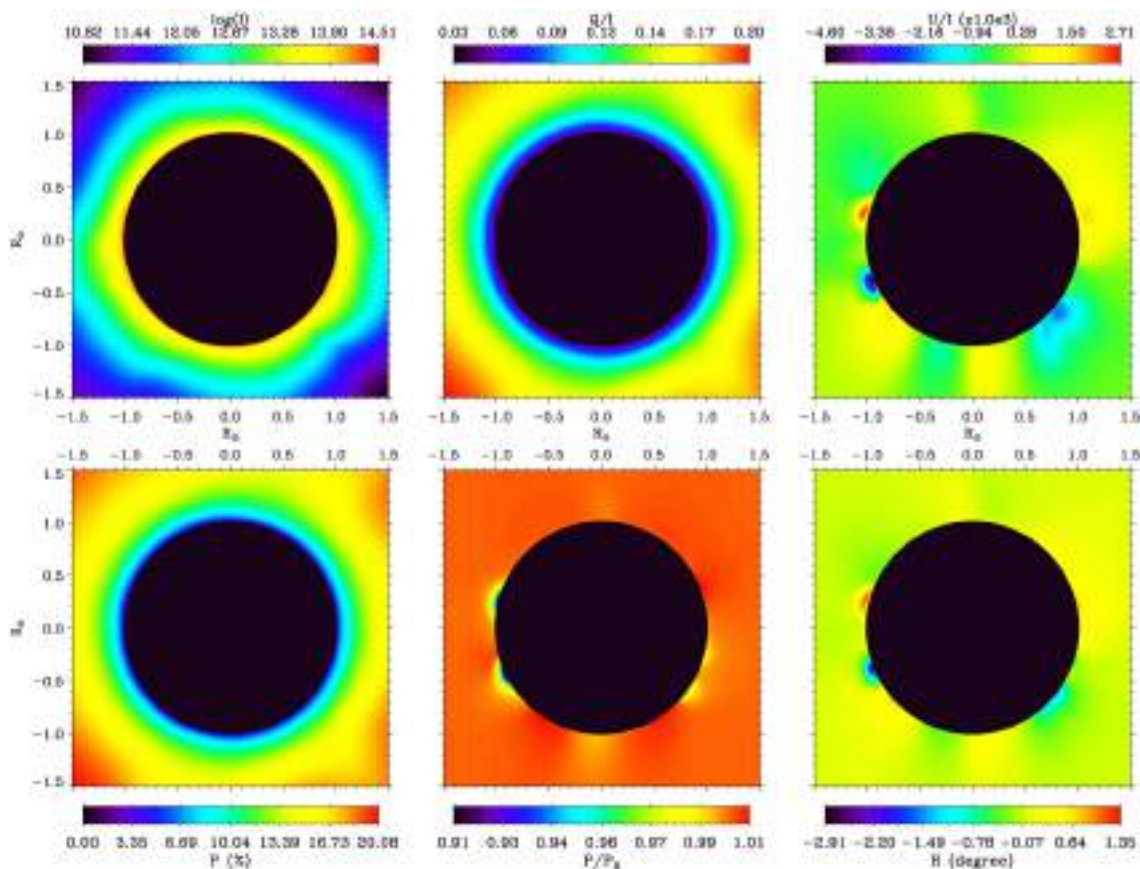


**FIGURE 4 | Line-profile-integrated Stokes parameters (top) and linear polarization (bottom) of the coronal H I Ly- $\alpha$  line.**  $P$ ,  $P_0$ , and  $R$  are the polarization degree, the polarization degree in zero magnetic field, and the rotation of the plane of polarization with respect to the local solar limb, respectively. Above regions of relatively strong coronal magnetic fields the Hanle depolarization attains about 10% and the rotation of the plane of polarization is about  $3^\circ$ . This illustrates that although this line is not the best in terms of sensitivity to the Hanle effect, the effects of the magnetic field on the linear polarization are significant.

depolarization (i.e., the ratio of the degree of polarization to that in the absence of magnetic field, middle), and the rotation of the plane of linear polarization with respect to the local solar limb (in degrees). It is clear that the signature of the Hanle effect, which is given primarily by the depolarization and the rotation of plane of polarization, is limited to low-altitude regions where the magnetic field is relatively strong. This is expected because of the sensitivity of this line to the Hanle effect.

Although these results are still preliminary, they suggest that the H I Ly- $\alpha$  line could be very useful for measuring the coronal magnetic field, particularly at low latitude, and in strong field regions (i.e., above active regions). Theoretical polarization rates (not shown here) in these coronal line are reasonably high and could be easily measured. The depolarization with respect to the zero magnetic field case attains  $\sim 10\%$  in some areas. The main parameter that limits the measurability of the Hanle effect in this line is the rotation of the plane of polarization. Above active regions, a rotation of about  $3^\circ$  is obtained, and rotations of more than  $1^\circ$  are obtained in larger areas. These results show that this line is promising in terms of constraining the coronal magnetic field, despite the fact that it is not the most suitable line in terms of sensitivity to the coronal Hanle effect. In combination with other spectral lines with complementary sensitivities to the effect of the coronal magnetic field, the Hanle effect could provide reliable constraints on the coronal magnetic field.

## 6. HANLE EFFECT OF THE He I 10,830 Å CORONAL LINE

Kuhn et al. (2007) showed evidence for an extended diffuse surface brightness flux at the He I 10,830 Å line using observations from the SOLARC coronagraph. The observations show that emissions result from cold helium (i.e., narrow line

profiles), which is unlikely to be scattered by the solar wind helium that is presumably significantly hotter. The authors argue that cold helium atoms form on dust grains, which provide an atomic population different to that of the solar wind. The importance of these observations stems from the sensitivity of the He I 10,830 Å line to the Hanle effect, which corresponds to magnetic field strength ranging from  $\sim 0.2$  Gauss to  $<10$  Gauss. This line may be the most suitable line for the diagnostic of coronal magnetic fields through the Hanle effect.

**Figure 5** shows forward modeling results of the linear polarization of the He I 10,830 Å. The LOS-integration scheme is the same as for H I Ly- $\alpha$ . Unlike H I Ly- $\alpha$  where the Hanle effect is limited to low-height, strong field regions, the linear polarization of He I 10,830 Å shows more variations as it depicts coronal structures, such as streamers, closed field regions. The variation of the polarization parameters spreads over larger intervals, which make their measurement easier. This is expected because of the higher sensitivity of this line to the relatively weak coronal magnetic fields. Dima et al. (2016) present a complementary analysis of the polarization of the He I 10,830 Å line.

We believe that the linear polarization of the He I 10,830 Å line could provide valuable constraints on the coronal magnetic field. In combination with UV lines such as H I Ly- $\alpha$ , - $\beta$ , and O VI 103.2 nm, as well as IR forbidden lines, the coronal Hanle effect could provide reliable diagnostic of the coronal magnetic field and consequently to extrapolation and MHD models.

## 7. SUMMARY AND CONCLUSIONS

The preliminary results of the forward modeling of the linear polarization of two coronal spectral lines (i.e., H I Ly- $\alpha$  and He I 10,830 Å) with different sensitivities to the Hanle effect

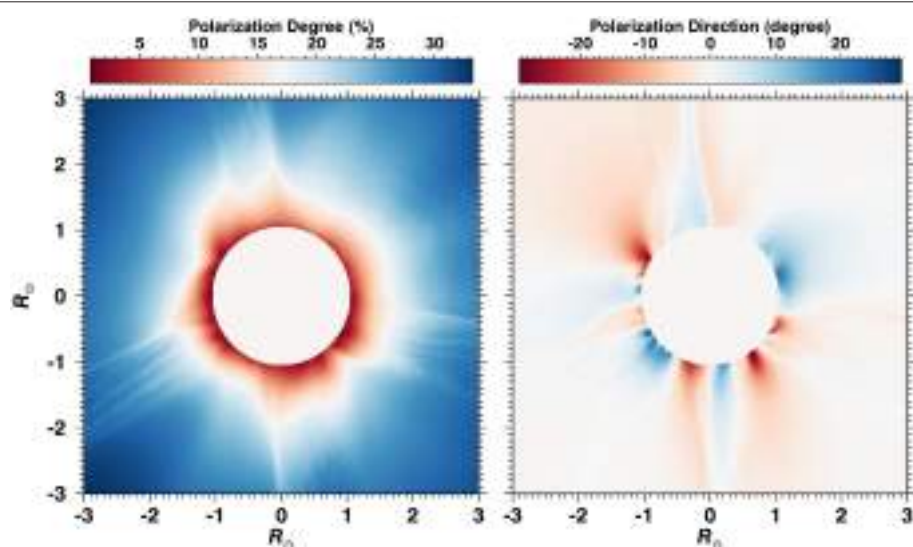


**FIGURE 5 |** Polarization parameters of the He I 10,830 line. (Left) polarization degree (in %) and (Right) rotation of the plane of polarization (in degrees) with respect to the local tangent to the solar limb.

are promising. The UV H I Ly- $\alpha$  line is mainly sensitive to low-height, strong magnetic fields above active regions. The polarization of the He I 10,830 Å line, which is sensitive to magnetic fields ranging roughly from  $\sim 0.2$  Gauss up to  $<10$  Gauss, shows more variations with coronal height and traces different coronal structures with different magnetic topologies (e.g., streamers and closed field regions).

Forward modeling of the Hanle effect is an important step in our quest for direct measurements of the magnetic field in the solar corona, which is a very difficult problem that includes different issues that observations will be subject to (e.g., 180° and Van Vleck 90° ambiguities and LOS-integration). Forward modeling will allow us to fully understand these problems and develop the necessary tools to analyze the observations. It also shows the potential of the Hanle effect in different wavelength regimes, which can be utilized for future space solar missions with UV and IR polarimeters (e.g., Peter et al., 2012).

We believe that the combination of the linear polarization of coronal lines with complementary sensitivities to the Hanle effect is promising and could provide long-sought measurements of the coronal magnetic field. The Hanle effect is a powerful tool that

may provide the most reliable diagnostics of the magnetic field at relatively low coronal heights. Radio observations along with polarimetric measurements in the Zeeman and saturated Hanle regimes may provide complementary constraints that could help piece together the coronal magnetic field structure.

## AUTHOR CONTRIBUTIONS

All authors listed, have made substantial, direct and intellectual contribution to the work, and approved it for publication.

## ACKNOWLEDGMENTS

We, the authors, would like to thank the reviewers for the constructive comments and criticism that helped improving the quality of the manuscript. This work was enabled by discussions with members of the International Space Science Institute (ISSI) working group on coronal magnetism (2013–2014), particularly J. Kuhn. SG acknowledges support from the Air Force Office of Space Research, FA9550-15-1-0030; NCAR is supported by the National Science Foundation.

## REFERENCES

- Arnaud, J. (1982a). Observed polarization of the Fe xiv 5303 coronal emission line. *Astron. Astrophys.* 112, 350–354.
- Arnaud, J. (1982b). The analysis of Fe xiv 5303 coronal emission-line polarization measurements. *Astron. Astrophys.* 116, 248–254.
- Arnaud, J., and Newkirk, G. Jr. (1987). Mean properties of the polarization of the Fe XIII 10747 Å coronal emission line. *Astron. Astrophys.* 178, 263–268.
- Bommier, V. (1980). Quantum theory of the hanle effect. II - effect of level-crossings and anti-level-crossings on the polarization of the D<sub>3</sub> helium line of solar prominences. *Astron. Astrophys.* 87, 109–120.
- Bommier, V., and Sahal-Bréchot, S. (1978). Quantum theory of the hanle effect - calculations of the stokes parameters of the D<sub>3</sub> helium line for quiescent prominences. *Astron. Astrophys.* 69, 57–64.
- Bommier, V., and Sahal-Bréchot, S. (1982). The Hanle effect of the coronal L- $\alpha$  line of hydrogen: theoretical investigation. *Sol. Phys.* 78, 157–178. doi: 10.1007/BF00151151
- Bommier, V., Sahal-Bréchot, S., and Leroy, J. L. (1981). Determination of the complete vector magnetic field in solar prominences, using the Hanle effect. *Astron. Astrophys.* 100, 231–240.
- Bommier, V., Landi Degl'Innocenti, E., Leroy, J.-L., and Sahal-Bréchot, S. (1994). Complete determination of the magnetic field vector and of the electron density in 14 prominences from linear polarization measurements in the He I D<sub>3</sub> and H- $\alpha$  lines. *Sol. Phys.* 154, 231–260.
- Bonnet, R. M., Decaudin, M., Bruner, E. C. Jr., Acton, L. W., and Brown, W. A. (1980). High-resolution Lyman- $\alpha$  filtergrams of the sun. *Astrophys. J. Lett.* 237, L47–L50. doi: 10.1086/183232
- Casini, R., and Judge, P. G. (1999). Spectral lines for polarization measurements of the coronal magnetic field. II. Consistent treatment of the stokes vector for magnetic-dipole transitions. *Astrophys. J.* 522, 524–539. doi: 10.1086/307629
- Charvin, P. (1965). Étude de la polarisation des raies interdites de la couronne solaire. Application au cas de la raie verte  $\lambda$ 5303. *Ann. d'Astrophys.* 28:877.
- Dima, G. I., Kuhn, J. R., and Berdyugina, S. V. (2016). Infrared dual-line hanle diagnostic of the coronal vector magnetic field. *Front. Astron. Space Sci.* 3:13. doi: 10.3389/fspas.2016.00013
- Domingo, V., Fleck, B., and Poland, A. I. (1995). The SOHO mission: an overview. *Sol. Phys.* 162, 1–37. doi: 10.1007/BF00733425
- Fineschi, S. (2001). Space-based instrumentation for magnetic field studies of solar and stellar atmospheres, in magnetic fields across the Hertzsprung-Russell diagram. *ASP Conf. Ser.* 248:597.
- Fineschi, S., Chiuderi, C., Poletto, G., Hoover, R. B., and Walker, A. B. C. Jr. (1993). LY-A-CO-PO (LY- $\alpha$  coronograph/polarimeter): an instrument to measure coronal magnetic fields. *Memorie della Societ Astronomia Italiana* 64, 441.
- Fineschi, S., Gardner, L. D., Kohl, J. L., Romoli, M., Pace, E., Corti, G., et al. (1999). “Polarimetry of the UV Solar Corona with ASCE”, in *Ultraviolet and X-Ray Detection, Spectroscopy, and Polarimetry III*, Vol. 3764, eds S. Fineschi, B. E. Woodgate, and R. A. Kimble (Denver, CO: Proceedings of SPIE), 147–160. doi: 10.1117/12.371079
- Fineschi, S., and Habbal, S. R. (1995). Coronal magnetic field diagnostics via the Hanle effect of Lyman series lines. *Proc. Solar Wind* 8:68.
- Fineschi, S., Hoover, R. B., Fontenla, J. M., and Walker, A. B. C. Jr. (1991). Polarimetry of extreme ultraviolet lines in solar astronomy. *Opt. Eng.* 30, 1161–1168. doi: 10.1117/12.55922
- Gibson, S. E., Kucera, T. A., White, S. M., Dove, J. B., Fan, Y., Forland, B. C., et al. (2016). FORWARD: a toolset for multiwavelength coronal magnetometry. *Front. Astron. Space Sci.* 3:8. doi: 10.3389/fspas.2016.00008
- Habbal, S. R., Woo, R., and Arnaud, J. (2001). On the predominance of the radial component of the magnetic field in the solar corona. *Astrophys. J.* 558, 852–858. doi: 10.1086/322308
- Hanle, W. (1924). Über magnetische Beeinflussung der Polarisation der Resonanzfluoreszenz. *Zeitschrift für Physik* 30, 93. doi: 10.1007/BF01331827
- Hassler, D. M., Lemaire, P., Longval, Y. (1997). Polarization sensitivity of the SUMER instrument on SOHO. *Appl. Opt.* 36, 353–359. doi: 10.1364/AO.36.000353
- Kohl, J. L., Esser, R., Gardner, L. D., Habbal, S., Daigneau, P. S., Dennis, E. F., et al. (1995). The ultraviolet coronagraph spectrometer for the solar and heliospheric observatory. *Sol. Phys.* 162, 313–356. doi: 10.1007/BF00733433
- Kohl, J. L., Noci, G., Antonucci, E., Tondello, G., Huber, M. C. E., Cranmer, S. R., et al. (1998). UVCS/SOHO empirical determinations of anisotropic velocity distributions in the solar corona. *Astrophys. J. Lett.* 501:L127. doi: 10.1086/311434
- Kuckein, C., Centeno, R., Martínez Pillet, V., Casini, R., Manso Sainz, R., and Shimizu, T. (2009). Magnetic field strength of active region filaments. *Astron. Astrophys.* 501, 1113–1121. doi: 10.1051/0004-6361/200911800

- Kuckein, C., Martínez Pillet, V., and Centeno, R. (2012). An active region filament studied simultaneously in the chromosphere and photosphere. I. Magnetic structure. *Astron. Astrophys.* 539:A131. doi: 10.1051/0004-6361/20111765
- Kuhn, J. R., Arnaud, J., Jaeggli, S., Lin, H., and Moise, E. (2007). Detection of an extended near-sun neutral helium cloud from ground-based infrared coronagraph spectropolarimetry. *Astrophys. J. Lett.* 667:L203. doi: 10.1086/522370
- Lagg, A., Woch, J., Krupp, N., Solanki, S. K. (2004). Retrieval of the full magnetic vector with the He I multiplet at 1083 nm. Maps of an emerging flux region. *Astron. Astrophys.* 414, 1109–1120. doi: 10.1086/522370
- Landi Degl'Innocenti, E. (1982). The determination of vector magnetic fields in prominences from the observations of the Stokes profiles in the D<sub>3</sub> line of helium. *Sol. Phys.* 79, 291–322.
- Landi Degl'Innocenti, E., and Landolfi, M. (2004). “Polarization in spectral lines,” in *Astrophysics and Space Science Library*, Vol. 307 (Dordrecht: Springer).
- Lemaire, P., Emerich, C., Curdt, W., Schuehle, U., and Wilhelm, K. (1998). Solar H I Lyman- $\alpha$  full disk profile obtained with the SUMER/SOHO spectrometer. *Astron. Astrophys.* 334, 1095–1098.
- Leroy, J. L., Ratier, G., and Bommier, V. (1977). The polarization of the D<sub>3</sub> emission line in prominences. *Astron. Astrophys.* 54, 811–816.
- Leroy, J. L., Bommier, V., and Sahal-Bréchot, S. (1983). The magnetic field in the prominences of the polar crown. *Sol. Phys.* 83, 135–142. doi: 10.1007/BF00148248
- Leroy, J. L., Bommier, V., and Sahal-Bréchot, S. (1984). New data on the magnetic structure of quiescent prominences. *Astron. Astrophys.* 131, 33–44.
- Li, X., Habbal, S. R., Kohl, J. L., and Noci, G. (1998). The effect of temperature anisotropy on observations of doppler dimming and pumping in the inner corona. *Astrophys. J. Lett.* 501, L133–L137. doi: 10.1086/311428
- Lionello, R., Linker, J. A., and Mikić, Z. (2009). Multispectral emission of the sun during the first whole sun month: magnetohydrodynamic simulations. *Astrophys. J.* 690, 902–912. doi: 10.1088/0004-637X/690/1/902
- Lin, H., Kuhn, J. R., and Coulter, R. (2004). Coronal magnetic field measurements. *Astrophys. J. Lett.* 613:L177. doi: 10.1086/425217
- López Ariste, A., and Casini, R. (2002). Magnetic fields in prominences: inversion techniques for spectropolarimetric data of the He I D<sub>3</sub> line. *Astrophys. J.* 575, 529–541. doi: 10.1086/341260
- Manso Sainz, R., and Trujillo Bueno, J. (2009). A possible polarization mechanism of EUV coronal lines, in solar polarization 5. *ASP Conf. Ser.* 405:423.
- Merenda, L., Lagg, A., and Solanki, S. K. (2011). The height of chromospheric loops in an emerging flux region. *Astron. Astrophys.* 532:A63. doi: 10.1051/0004-6361/201014988
- Peter, H., Abbo, L., Andretta, V., Auchère, F., Bemporad, A., Berrilli, F., et al. (2012). Solar magnetism eXplorer (SolmeX). Exploring the magnetic field in the upper atmosphere of our closest star. *Exp. Astron.* 33, 271–303. doi: 10.1007/s10686-011-9271-0
- Querfeld, C. W. (1974). The high altitude observatory coronal-emission polarimeter, in planets, stars, and nebulae: studied with photopolarimetry. *IAU Colloq.* 23:254.
- Querfeld, C. W., and Elmore, D. E. (1976). Observation of polarization in Fe XIII 10747 Å coronal emission line. *Bull. Am. Astron. Soc.* 8, 368.
- Querfeld, C. W. (1977). Observations of Fe XIII 10747 Å coronal emission-line polarization. *Rep. Lund Observ.* 12:109.
- Querfeld, C. W., Smartt, R. N., Bommier, V., Landi Degl'Innocenti, E., and House, L. L. (1985). Vector magnetic fields in prominences. II - He I D<sub>3</sub> stokes profiles analysis for two quiescent prominences. *Sol. Phys.* 96, 277–292.
- Raouafi, N.-E., Lemaire, P., and Sahal-Bréchot, S. (1999a). Detection of the O VI 103.2 nm line polarization by the SUMER spectrometer on the SOHO spacecraft. *Astron. Astrophys.* 345, 999–1005.
- Raouafi, N.-E., Sahal-Bréchot, S., Lemaire, P., and Bommier, V. (1999b). Doppler redistribution of resonance polarization of the O VI 103.2 nm line observed above a polar hole, Proc. of Solar Polarization 2. *Astroph. Space Sci. Library* 243:349.
- Raouafi, N.-E. (2002). Stokes parameters of resonance lines scattered by a moving, magnetic medium. Theory of the two-level atom. *Astron. Astrophys.* 386, 721–731. doi: 10.1051/0004-6361:20020113
- Raouafi, N.-E., Sahal-Bréchot, S., and Lemaire, P. (2002). Linear polarization of the O VI lambda 1031.92 coronal line. II. Constraints on the magnetic field and the solar wind velocity field vectors in the coronal polar holes. *Astron. Astrophys.* 396, 1019–1028.
- Raouafi, N.-E. (2005). Measurement methods for chromospheric and coronal magnetic fields, in chromospheric and coronal magnetic fields. *ESA Spec. Publ.* 596:3.
- Raouafi, N.-E. (2011). Coronal polarization, proceedings of solar polarization 6. *ASP Conf. Ser.* 437, 99.
- Raymond, J. C., Kohl, J. L., Noci, G., Antonucci, E., Tondello, G., Huber, M. C. E., et al. (1997). Composition of coronal streamers from the SOHO ultraviolet coronagraph spectrometer. *Sol. Phys.* 175, 645–665. doi: 10.1023/A:1004948423169
- Reeves, E. M., and Parkinson, W. H. (1970). An atlas of extreme-ultraviolet spectroheliograms from OSO-IV. *Astrophys. J. Suppl.* 21, 1. doi: 10.1086/190217
- Riley, P., Linker, J. A., and Mikić, Z. (2001). An empirically-driven global MHD model of the solar corona and inner heliosphere. *J. Geophys. Res.* 106, 15889–15901. doi: 10.1029/2000JA000121
- Riley, P., and Luhmann, J. G. (2012). Interplanetary signatures of unipolar streamers and the origin of the slow solar wind. *Sol. Phys.* 277, 355–373. doi: 10.1007/s11207-011-9909-0
- Riley, P., Linker, J. A., Lionello, R., and Mikić, Z. (2012). Corotating interaction regions during the recent solar minimum: the power and limitations of global MHD modeling. *J. Atmos. Solar Terrestr. Phys.* 83, 1–10. doi: 10.1016/j.jastp.2011.12.013
- Riley, P., Lionello, R., Linker, J. A., Cliver, E., Balogh, A., Beer, J., et al. (2015). Inferring the structure of the solar corona and inner heliosphere during the maunder minimum using global thermodynamic magnetohydrodynamic simulations. *Astrophys. J.* 802:105. doi: 10.1088/0004-637X/802/2/105
- Sahal-Bréchot, S., Bommier, V., and Leroy, J. L. (1977). The hanle effect and the determination of magnetic fields in solar prominences. *Astron. Astrophys.* 59, 223–231.
- Sahal-Bréchot, S., Malinovsky, M., and Bommier, V. (1986). The polarization of the O VI 1032 Å line as a probe for measuring the coronal vector magnetic field via the Hanle effect. *Astron. Astrophys.* 168, 284–300.
- Sasso, C., Lagg, A., and Solanki, S. K. (2011). Multicomponent He I 10830 Å profiles in an active filament. *Astron. Astrophys.* 526, A42. doi: 10.1051/0004-6361/200912956
- Sasso, C., Lagg, A., and Solanki, S. K. (2014). Magnetic structure of an activated filament in a flaring active region. *Astron. Astrophys.* 561:A98. doi: 10.1051/0004-6361/201322481
- Solanki, S. K., Lagg, A., Woch, J., Krupp, N., and Collados, M. (2003). Three-dimensional magnetic field topology in a region of solar coronal heating. *Nature* 425, 692–695. doi: 10.1038/nature02035
- Stenflo, J. O. (1982). The Hanle effect and the diagnostics of turbulent magnetic fields in the solar atmosphere. *Sol. Phys.* 80, 209–226. doi: 10.1007/BF00147969
- Tomczyk, S., Card, G. L., Darnell, T., Elmore, D. F., Lull, R., Nelson, P. G., et al. (2008). An instrument to measure coronal emission line polarization. *Sol. Phys.* 247, 411–428. doi: 10.1007/s11207-007-9103-6
- Trujillo Bueno, J., Casini, R., Landolfi, M., and Landi Degl'Innocenti, E. (2002a). The physical origin of the scattering polarization of the Na I D lines in the presence of weak magnetic fields. *Astrophys. J. Lett.* 566:L53.
- Trujillo Bueno, J., Landi Degl'Innocenti, E., Collados, M., Merenda, L., and Manso Sainz, R. (2002b). Selective absorption processes as the origin of puzzling spectral line polarization from the sun. *Nature* 415, 403–406.
- Trujillo Bueno, J., Shchukina, N., and Asensio Ramos, A. (2004). A substantial amount of hidden magnetic energy in the quiet sun. *Nature* 430, 326–329. doi: 10.1038/nature02669
- Vial, J. C., Lemaire, P., Artzner, G., and Gouttebroze, P. (1980). O VI ( $\lambda = 1032 \text{ \AA}$ ) profiles in and above an active region prominence, compared to quiet sun center and limb profiles. *Sol. Phys.* 68, 187–206. doi: 10.1007/BF00153276
- White, S. M. (1999). Radio versus EUV/X-ray observations of the solar atmosphere. *Sol. Phys.* 190, 309–330. doi: 10.1023/A:1005253501584

- Wiegelmann, T., Thalmann, J. K., and Solanki, S. K. (2014). The magnetic field in the solar atmosphere. *Astron. Astrophys. Rev.* 22:78. doi: 10.1007/s00159-014-0078-7
- Wilhelm, K., Curdt, W., Marsch, E., Schühle, U., Lemaire, P., Gabriel, A., et al. (1995). SUMER – solar ultraviolet measurements of emitted radiation. *Sol. Phys.* 162, 189–231. doi: 10.1007/BF00733430
- Xu, Z., Lagg, A., and Solanki, S. K. (2010). Magnetic structures of an emerging flux region in the solar photosphere and chromosphere. *Astron. Astrophys.* 520:13. doi: 10.1051/0004-6361/200913227
- Xu, Z., Lagg, A., Solanki, S. K., and Liu, Y. (2012). Magnetic fields of an active region filament from full stokes analysis of Si I 1082.7 nm and He I 1083.0 nm. *Astrophys. J.* 749:138. doi: 10.1088/0004-637X/749/2/138

**Conflict of Interest Statement:** The authors declare that the research was conducted in the absence of any commercial or financial relationships that could be construed as a potential conflict of interest.

Copyright © 2016 The Johns Hopkins University Applied Physics Laboratory LLC. This is an open access article distributed under the terms of the Creative Commons Attribution License (CC BY). The use, distribution or reproduction in other forums is permitted, provided the original author(s) or licensor are credited and that the original publication in this journal is cited, in accordance with accepted academic practice. No use, distribution or reproduction is permitted which does not comply with these terms.



# Measuring Coronal Magnetic Fields with Remote Sensing Observations of Shock Waves

Alessandro Bemporad\*, Roberto Susino, Federica Frassati and Silvano Fineschi

INAF, Turin Astrophysical Observatory, Pino Torinese, Italy

**Keywords:** coronal magnetic field, remote sensing, MHD and plasma physics, shock waves, coronal mass ejections

## INTRODUCTION

### State of the Art

Our limited knowledge of the magnetic fields structuring in the solar corona represents today the main hurdle in our understanding of its structure and dynamic. Over the last decades significant efforts have been dedicated to measure these fields, by approaching the problem on many different sides and in particular: (i) by improving our theoretical understanding of the modification (via Zeeman and Hanle effects) induced by these fields on the polarization of coronal emission lines, (ii) by developing new instrumentation to measure directly with spectro-polarimeters these modifications, (iii) by improving the reliability of the extrapolated coronal fields starting from photospheric measurements, (iv) by developing new techniques to analyse existing remote sensing data and infer properties of these fields, or by combining all these different approaches (e.g., Chifu et al., 2015).

In this paper we focus on the fourth method, discussing the advantages and disadvantages of techniques recently developed. Over the last few years it has been shown that coronagraphic white light (WL) observations of major Coronal Mass Ejections (CMEs) show the presence of hemispherical regions expanding ahead of the CME fronts (Figure 1) where faint increases in the WL intensity are detected (e.g., Vourlidas et al., 2003; Ontiveros and Vourlidas, 2009). More recently similar features have also been detected in the early stages of CME developments observed with EUV imagers (e.g., Kozarev et al., 2011). Usually these slightly brighter regions are interpreted as the coronal plasma compressed by the transit of the shock wave driven by the super-alfvénic expansion of the CME, a region called “shock sheath.” This interpretation has also been supported by MHD simulations (e.g., Manchester et al., 2008) and forward modeling of synthetic observations (Vourlidas et al., 2013) showing the formation of an arch shaped feature very similar to what is observed in WL coronagraphs. In this scenario, it has been recently demonstrated that measurements of coronal fields can be successfully derived from remote sensing observations of interplanetary shocks with at least two techniques, briefly described in the next Sections.

## OPEN ACCESS

### Edited by:

Laurel Anne Rachmeler,  
National Aeronautics and Space  
Administration, USA

### Reviewed by:

Robin Colaninno,  
Naval Research Lab, USA  
Neel P. Savani,  
UMBC/NASA GSFC, USA

### \*Correspondence:

Alessandro Bemporad  
bemporad@oato.inaf.it

### Specialty section:

This article was submitted to  
Stellar and Solar Physics,  
a section of the journal  
Frontiers in Astronomy and Space  
Sciences

Received: 15 January 2016

Accepted: 04 May 2016

Published: 27 May 2016

### Citation:

Bemporad A, Susino R, Frassati F and  
Fineschi S (2016) Measuring Coronal  
Magnetic Fields with Remote Sensing  
Observations of Shock Waves.  
*Front. Astron. Space Sci.* 3:17.  
doi: 10.3389/fspas.2016.00017

## The Shock Standoff Distance Technique

Gopalswamy and Yashiro (2011) first applied to remote sensing observations of CMEs this technique based on the measurement of the so called shock “standoff distance”  $\Delta$ , i.e., the distance between the shock driver (i.e., the expanding flux-rope) and the shock wave. Given  $\Delta$  and the radius of curvature  $R$  of the flux-rope, a semi-empirical formula relates the  $\Delta/R$  ratio with the value of the shock sonic Mach number  $M_s$ . The  $M_s$  value derived from the observed  $\Delta/R$  ratio can be combined with the measured shock speed  $v_{sh}$  to provide a measurement of the upstream Alfvén speed  $v_A$ , by assuming that the Alfvénic Mach number  $M_A \sim M_s$ , and by assuming a value for the pre-shock solar wind speed  $v_{out}$ . Given also the measured pre-shock coronal electron density  $n_e$ , the magnetic

field strength is provided by  $B = v_A (\mu m_p n_e)^{1/2}$ . Various authors applied this method to shocks observed with WL coronagraphs (Kim et al., 2012), EUV full disk imagers (Gopalswamy et al., 2012) and heliospheric imagers (Poomvises et al., 2012), providing measurements of the coronal field up to heliocentric distances larger than 120 solar radii.

Nevertheless, this technique has various limitations. As pointed out by Savani et al. (2012) there are some uncertainties in the expression of the semi-empirical relationship between the  $\Delta/R$  ratio with  $M_s$  which has two expressions:

$$\frac{\Delta}{R} = k \frac{(\gamma - 1) M_s^2 + 2}{(\gamma + 1) M_s^2} \text{ and } \frac{\Delta}{R} = k \frac{(\gamma - 1) M_s^2 + 2}{(\gamma + 1) (M_s^2 - 1)},$$

where, the first expression was originally derived by Priest (1984) for the hydrodynamic (HD) shock case, while the second one is an adjustment made on intuitive basis by Farris and Russell (1994) to avoid the fact that the first expression is not valid under low Mach number regime ( $M_s < 3$ ). A second problem is that (as discussed in Savani et al., 2012) the value of the constant  $k$  can vary depending on the oblateness of the shock driver (hence of the CME flux rope), which is usually a poorly constrained parameter (because of projection effects and unknown 3D shape of the CME) and is also expected to change as function of time/distance (Savani et al., 2011). The third problem is that (even though more appropriate MHD formulas were provided by Priest and Forbes, 2007) the above expression holds for the HD case, and can be applied in the magneto-hydrodynamic (MHD) case if one assumes that  $M_A \sim M_s$ , hence  $v_A \sim v_s$ , while usually in the solar corona  $v_A \gg v_s$ . The HD solution is a good approximation for the MHD case when the magnetic pressure is much smaller than the plasma pressure ( $\beta \gg 1$ ), but this is not the case for the lower corona and is true only for the interplanetary medium, hence for the analysis of heliospheric images or in situ measurements (Fairfield et al., 2001). Moreover, the application of the above method to CMEs observed with WL coronagraphs requires the assumption of another free parameter, the solar wind speed, to convert the measured shock speed into an upstream speed. Also, this technique is able to provide only a 1D radial profile of the magnetic field strength in the direction of propagation of the shock.

## The WL-UV Technique

To overcome these limitations, an alternative technique to derive coronal magnetic fields from shocks has been developed by the Group in Turin. In particular, Bemporad and Mancuso (2010) first demonstrated that WL and UV observations of a coronal shock (Figure 1) can be combined to infer the magnetic field strength and deflection across the shock front. In the technique pre- and post-shock densities are derived as usual from WL, while pre-shock solar wind velocities and plasma temperatures are derived from UV with standard techniques. The WL images are also used to estimate the shock speed and the inclination angle  $\vartheta_{Bn}$  between the normal to the shock surface (projected on the plane of the sky) and the pre-shock magnetic field, assuming that above two solar radii it's radial. Given

the shock compression ratio, shock inclination and velocity derived from WL, and the pre-shock plasma temperature and outflow velocity derived from UV, the MHD Rankine-Hugoniot equations written for the general case of an oblique shock provide not only the post-shock plasma temperatures, but also the post-shock outflow velocities, pre- and post-shock magnetic field strengths, as well as the velocity and magnetic field vector deflections across the shock. This technique, being a combination of WL and UV data, is very promising for application on future observations by the Metis coronagraph (Antonucci et al., 2012; Fineschi et al., 2012) on-board the forthcoming ESA-Solar Orbiter mission.

In a following work (Bemporad and Mancuso, 2013) we introduced an empirical relationship to derive the Alfvénic Mach number  $M_{A\angle}$  for the general case of an oblique shock directly from WL observations of shocks as

$$M_{A\angle} = \sqrt{(M_{A\perp} \sin \vartheta_{Bn})^2 + (M_{A//} \cos \vartheta_{Bn})^2}$$

where  $M_{A\perp}$  and  $M_{A//}$  are the Alfvénic Mach numbers for the special cases of perpendicular and parallel shocks, respectively, that are easily estimated from the shock compression ratio by assuming low plasma  $\beta$  condition. This empirical relationship, tested observationally (Bemporad et al., 2014) and numerically (Bacchini et al., 2015), allowed the authors to derive for the first time the magnetic field strength in the corona crossed by a shock over a huge region covering 10 solar radii in altitudes and  $110^\circ$  in latitudes (Susino et al., 2015).

This technique has also some uncertainties. First, it assumes that the pre-shock magnetic field is radial, an hypothesis which is more reliable above coronal streamer regions and usually not acceptable above polar regions, where super-radial expansion of the solar wind occurs. Second, it assumes that all the plasma parameters are derived on the plane of the sky, and (as it happens usually for remote sensing observations) it is hard to estimate the effect of the line of sight (LOS) integration in the determination of the shock compression ratio and all the other parameters derived from this quantity. Issues related with LOS integration are present in all kinds of remote sensing observations of optically thin plasmas. Nevertheless, we point out that in the above determinations of the shock compression ratios from WL the authors showed how to take into account different LOS extensions of the shocked plasmas at different altitudes (see e.g., Bemporad and Mancuso, 2010), thus improving the simplistic usual assumption by previous authors of a constant LOS thickness (e.g., Ontiveros and Vourlidas, 2009).

## PRESENT DEBATES ON MAGNETIC FIELD MEASUREMENTS WITH SHOCK

After a first excitement by part of the community for the possibility to directly observe the propagation of shocks in the corona, the validity of these results are becoming more debated. It has been pointed out that the observed hemispherical WL features expanding ahead of CMEs could not be unambiguously differentiated from the front of compression waves, due to the

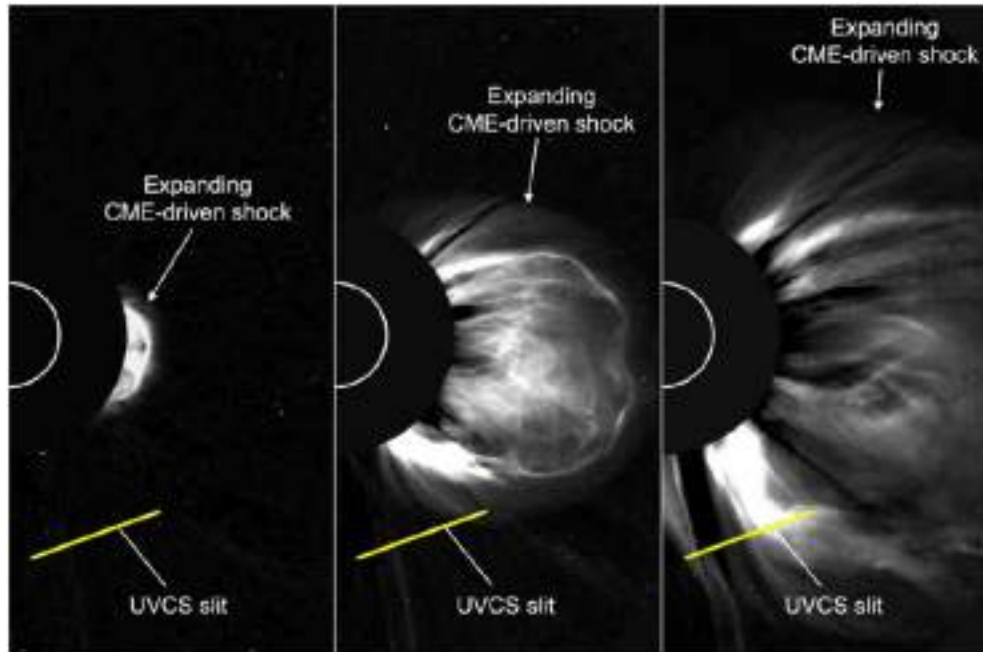


**FIGURE 1 |** The expansion of a CME-driven shock wave as observed in the LASCO/C2 WL coronagraph (Bemporad and Mancuso, 2010).

pileup of coronal plasma lying above the expanding CME. The hypothesis that these features are really shocks is better supported when at the same time at least one of these observational features is also reported:

1. remote sensing observation in radio data of a type-II burst;
2. remote sensing observation on EUV-UV spectroscopic data of non-thermal line broadening ahead of the CME front;
3. *in situ* observation of a gradual SEP event.

Another observational property supporting the real formation of a CME-driven shock is provided directly by the speed of the CME front as observed in WL images. In fact, the formation of a shock is expected only when the driver (i.e., the expanding CME) is moving in the corona faster than the local Alfvén, sound and/or magneto-sonic speeds. In agreement with this, faster CMEs are also statistically more associated with type-II radio bursts (Gopalswamy et al., 2010) and a good correlation exists between CME speeds and SEP fluxes (Kahler and Vourlidas, 2013). In any case, the detection of one or more of these features is not telling us where the shock is formed in the corona, and the possibility that the observed WL feature is not the real shock cannot be completely ruled out.

A criticism often also pointed out is that, if these hemispherical features are really the shocks, then the intensity variation plotted perpendicular to the shock should contain a steep discontinuity, similar to those observed in density measurements acquired by *in situ* spacecraft at shock transit. On the other hand, radial plots of the WL intensity across

these hemispherical features can show a gradual increase of the WL, hence a gradual increase in the electron column density of the plasma. Nevertheless, this is only an apparent inconsistency due to a combination of the 3D geometry of the shock surface and the integration along the LOS through the optically thin coronal plasma. In fact, the shock surface will have an almost hemispherical shape (as demonstrated by 3D numerical simulations), and the location of the shock boundary in the 2D projected view will correspond to the pixels where the lines of sight graze this surface. Then, moving radially into the shock sheath, the fraction of the LOS intercepting the sheath region will progressively increase, leading to the observed progressive increase in the WL intensity, as nicely shown by Manchester et al. (2008).

More in general, the above techniques require many assumptions to derive the magnetic fields from the observed WL images, making it difficult to estimate the real accuracy of these measurements. We suggest that these uncertainties will be better constrained by combining data analysis with forward modeling of synthetic observations (e.g., Gibson, 2015).

## CONCLUSIONS AND FUTURE PERSPECTIVES

Despite the uncertainties discussed here, both the “standoff” and “WL-UV” techniques (recently applied for inter-comparison to the same event by Susino et al., 2015) are now providing reasonable measurements of the coronal magnetic fields over

broad intervals in altitudes and latitudes never reached before. Comparison with other observational methods and the analysis of synthetic data will likely help us to improve and optimize these techniques in the future. A limit of these techniques is that field measurements are provided only after the eruption responsible for the shock wave: hence these methods give an “*a posteriori*” knowledge of the pre-CME coronal fields, and likely will be applicable for forecasting purposes only when statistical analyses will be carried out.

## REFERENCES

- Antonucci, E., Fineschi, S., Naletto, G., Romoli, M., Spadaro, D., Nicolini, G., et al. (2012). “Multi element telescope for imaging and spectroscopy (metis) coronagraph for the solar orbiter mission,” in *Proceedings of SPIE*, Vol. 8443 (Amsterdam).
- Bacchini, F., Susino, R., Bemporad, A., and Lapenta, G. (2015). Plasma physical parameters along CME-driven Shocks. II. Observation-simulation comparison. *Astrophys. J.* 809, 58–70. doi: 10.1088/0004-637X/809/1/58
- Bemporad, A., and Mancuso, S. (2010). First complete determination of plasma physical parameters across a coronal mass ejection-driven shock. *Astrophys. J.* 720, 130–143. doi: 10.1088/0004-637X/720/1/130
- Bemporad, A., and Mancuso, S. (2013). Super- and sub-critical regions in shocks driven by radio-loud and radio-quiet CMEs. *J. Adv. Res.* 4, 287–291. doi: 10.1016/j.jare.2012.09.005
- Bemporad, A., Susino, R., and Lapenta, G. (2014). Plasma physical parameters along coronal-mass-ejection-driven shocks. I. Ultraviolet and white-light observations. *Astrophys. J.* 784, 102–112. doi: 10.1088/0004-637X/784/2/102
- Chifu, I., Inhester, B., and Wiegelmann, T. (2015). Coronal magnetic field modeling using stereoscopy constraints. *Astronom. Astrophys.* 577, 8. doi: 10.1051/0004-6361/201322548
- Fairfield, D. H., Cairns, I. H., Desch, M. D., Szabo, A., Lazarus, A. J., and Aellig, M. R. (2001). The location of low Mach number bow shocks at Earth. *J. Geophys. Res.* 106, 25361–25376. doi: 10.1029/2000ja000252
- Farris, M. H., and Russell, C. T. (1994). Determining the standoff distance of the bow shock: mach number dependence and use of models. *J. Geophys. Res.* 99, 17681–17689. doi: 10.1029/94JA01020
- Fineschi, S., Antonucci, E., Naletto, G., Romoli, M., Spadaro, D., and Nicolini, G. (2012). “METIS: a novel coronagraph design for the Solar Orbiter mission,” in *Proceedings of SPIE*, Vol. 8443 (Amsterdam).
- Gibson, S. (2015). Data-model comparison using FORWARD and CoMP. *Proc. Int. Astron. Union* 305, 245–250. doi: 10.1017/S1743921315004846
- Gopalswamy, N., Nitta, N., Akiyama, S., Mäkelä, P., and Yashiro, S. (2012). Coronal magnetic field measurement from EUV images made by the solar dynamics observatory. *Astrophys. J.* 744, 7. doi: 10.1088/0004-637X/744/1/72
- Gopalswamy, N., Xie, H., Mäkelä, P., Akiyama, S., Yashiro, S., Kaiser, M. L., et al. (2010). Interplanetary shocks lacking type ii radio bursts. *Astrophys. J.* 710, 1111–1126. doi: 10.1088/0004-637X/710/2/112
- Gopalswamy, N., and Yashiro, S. (2011). The strength and radial profile of the coronal magnetic field from the standoff distance of a coronal mass ejection-driven shock. *Astrophys. J.* 736, 5. doi: 10.1088/2041-8205/736/1/L17
- Kahler, S. W., and Vourlidas, A. (2013). A comparison of the intensities and energies of gradual solar energetic particle events with the dynamical properties of associated coronal mass ejections. *Astrophys. J.* 769, 12. doi: 10.1088/0004-637X/769/2/143
- Kim, R.-S., Gopalswamy, N., Moon, Y.-J., Cho, K.-S., and Yashiro, S. (2012). Magnetic field strength in the upper solar corona using white-light shock structures surrounding coronal mass ejections. *746*, 8. doi: 10.1088/0004-637X/746/2/118
- Kozarev, K. A., Korreck, K. E., Lobzin, V. V., Weber, M. A., and Schwadron, N. A. (2011). Off-limb solar coronal wavefronts from SDO/AIA extreme-ultraviolet observations—implications for particle production. *Astrophys. J.* 733L, 7. doi: 10.1088/2041-8205/733/2/L25
- Manchester, W. B. I. V., Vourlidas, A., Tóth, G., Lugaz, N., Roussey, I., Sokolov, I., et al. (2008). Three-dimensional MHD simulation of the 2003 October 28 coronal mass ejection: comparison with LASCO coronagraph observations. *Astrophys. J.* 684, 1448–1460. doi: 10.1086/590231
- Ontiveros, V., and Vourlidas, A. (2009). Quantitative measurements of coronal mass ejection-driven shocks from LASCO observations. *Astrophys. J.* 693, 267–275. doi: 10.1088/0004-637X/693/1/267
- Poomvises, W., Gopalswamy, N., Yashiro, S., Kwon, R.-Y., and Olmedo, O. (2012). Determination of the heliospheric radial magnetic field from the standoff distance of a CME-driven shock observed by the STEREO spacecraft. *Astrophys. J.* 758, 6. doi: 10.1088/0004-637X/758/2/118
- Priest, E. (1984). *Solar Magneto-Hydrodynamics*. Geophysics and Astrophysics Monographs. Dordrecht: Reidel.
- Priest, E., and Forbes, T. (2007). *Magnetic Reconnection: MHD Theory and Application*. Cambridge, UK: Cambridge University Press.
- Savani, N. P., Owens, M. J., Rouillard, A. P., Forsyth, R. J., Kusano, K., Shiota, D., et al. (2011). Evolution of coronal mass ejection morphology with increasing heliocentric distance. I. Geometrical analysis. *Astrophys. J.* 731, 6. doi: 10.1088/0004-637X/731/2/109
- Savani, N. P., Shiota, D., Kusano, K., Vourlidas, A., and Lugaz, N. (2012). A study of the heliocentric dependence of shock standoff distance and geometry using 2.5D magnetohydrodynamic simulations of coronal mass ejection driven shocks. *Astrophys. J.* 759, 11. doi: 10.1088/0004-637X/759/2/103
- Susino, R., Bemporad, A., and Mancuso, S. (2015). Physical conditions of coronal plasma at the transit of a shock driven by a coronal mass ejection. *Astrophys. J.* 812, 13. doi: 10.1088/0004-637X/812/2/119
- Vourlidas, A., Lynch, B. J., Howard, R. A., and Li, Y. (2013). How many cmes have flux ropes? Deciphering the signatures of shocks, flux ropes, and prominences in coronagraph observations of CMEs. *Solar Phys.* 284, 179–201. doi: 10.1007/s11207-012-0084-8
- Vourlidas, A., Wu, S. T., Wang, A. H., Subramanian, P., and Howard, R. A. (2003). Direct detection of a coronal mass ejection-associated shock in large angle and spectrometric coronagraph experiment white-light images. *Astrophys. J.* 598, 1392–1402. doi: 10.1086/379098

## AUTHOR CONTRIBUTIONS

All authors listed, have made substantial, direct and intellectual contribution to the work, and approved it for publication.

## ACKNOWLEDGMENTS

RS acknowledges support from ASI contract I/013/12/0-1; FF acknowledge support from INAF Ph.D. Grant.

**Conflict of Interest Statement:** The authors declare that the research was conducted in the absence of any commercial or financial relationships that could be construed as a potential conflict of interest.

Copyright © 2016 Bemporad, Susino, Frassati and Fineschi. This is an open-access article distributed under the terms of the Creative Commons Attribution License (CC BY). The use, distribution or reproduction in other forums is permitted, provided the original author(s) or licensor are credited and that the original publication in this journal is cited, in accordance with accepted academic practice. No use, distribution or reproduction is permitted which does not comply with these terms.



# Line-of-Sight Velocity As a Tracer of Coronal Cavity Magnetic Structure

**Urszula Bąk-Stęślicka<sup>1\*</sup>, Sarah E. Gibson<sup>2</sup> and Ewa Chmielewska<sup>1</sup>**

<sup>1</sup> Astronomical Institute, University of Wrocław, Wrocław, Poland, <sup>2</sup> High Altitude Observatory, National Center for Atmospheric Research, Boulder, CO, USA

We present a statistical analysis of 66 days of observations of quiescent (non-erupting) coronal cavities and associated velocity and thermal structures. We find that nested rings of LOS-oriented velocity are common in occurrence and spatially well correlated with cavities observed in emission. We find that the majority of cavities possess multiple rings, and a range in velocity on the order of several km/sec. We find that the tops of prominences lie systematically below the cavity center and location of largest Doppler velocity. Finally, we use DEM analysis to consider the temperature structure of two cavities in relation to cavity, prominence, and flows. These observations yield new constraints on the magnetic structure of cavities, and on the conditions leading up to solar eruptions.

## OPEN ACCESS

### Edited by:

Xueshang Feng,  
National Space Science Center, China

### Reviewed by:

Gordon James Duncan Petrie,  
National Solar Observatory, USA  
Chaowei Jiang,  
Chinese Academy of Sciences, China

### \*Correspondence:

Urszula Bąk-Stęślicka  
*bak@astro.uni.wroc.pl*

### Specialty section:

This article was submitted to  
Stellar and Solar Physics,  
a section of the journal  
*Frontiers in Astronomy and Space  
Sciences*

**Received:** 08 January 2016

**Accepted:** 19 February 2016

**Published:** 18 March 2016

### Citation:

Bąk-Stęślicka U, Gibson SE and Chmielewska E (2016) Line-of-Sight Velocity As a Tracer of Coronal Cavity Magnetic Structure. *Front. Astron. Space Sci.* 3:7.  
doi: 10.3389/fspas.2016.00007

## 1. INTRODUCTION

Solar coronal cavities are regions of rarefied density and elliptical cross-section (Fuller and Gibson, 2009; Gibson et al., 2010; Forland et al., 2013). They are often observed in eruption as a component of the classic three-part structure of a Coronal Mass Ejections (CME), as they surround the CME's bright core formed by the dense material from the eruptive prominence (Illing and Hundhausen, 1986; Tandberg-Hanssen, 1995). Cavities exist not only as eruptive phenomena, however. Non-erupting, or quiescent cavities may exist in equilibrium for many days or weeks (Gibson et al., 2006). They usually surround quiescent prominences (Tandberg-Hanssen, 1995), especially in the polar crown regions, but in some cases cavities are observed in the absence of prominences. Cavities are mostly observed when a filament or filament channel is large and oriented along the line-of-sight, and where there are no bright neighboring structures (Gibson, 2015; McCauley et al., 2015).

The first recorded observations of cavities were made in white light (WL) during the solar eclipse of January 22, 1898 (Wesley, 1927) and since then cavities have been studied many times (Waldmeier, 1941; von Kluber, 1961; Williamson et al., 1961; Waldmeier, 1970; Gibson et al., 2006). The first explanation of the cavity phenomena as an area of reduced electron density was proposed by Waldmeier (1941). Cavities have been observed in a wide wavelength range, not only in WL, but also in radio, EUV and SXR (Vaiana et al., 1973a,b; Hudson et al., 1999; Hudson and Schwenn, 2000; Marqué et al., 2002; Marqué, 2004; Heinzel et al., 2008; Berger et al., 2012; Reeves et al., 2012). Observations in WL are particularly useful for larger cavities; smaller cavities are better viewed in EUV (Gibson, 2015). *Yohkoh*/Soft X-ray Telescope observations revealed hot central cores within cavities (Hudson et al., 1999; Hudson and Schwenn, 2000). Other analyses also suggest the existence of hotter plasma inside cavities (Fuller et al., 2008; Habbal et al., 2010; Reeves et al., 2012).

Cavities have been modeled as a flux rope (Low, 1994; Low and Hundhausen, 1995), but the physical nature of cavities is still under investigation. Although quiescent cavities are long-lived and their structure evolves slowly with time, they have been observed to bodily erupt as a CME

(Marićić et al., 2004; Vršnak et al., 2004; Gibson et al., 2006; Régnier et al., 2011; Forland et al., 2013; Su et al., 2015). Understanding the magnetic structure of such cavities may be essential for establish the pre-CME configurations and for choosing between models for CME eruptive drivers.

The Coronal Multi-channel Polarimeter (CoMP) observes the full-Sun lower coronal magnetic field via spectropolarimetric measurements of the the forbidden lines of Fe XIII. These observations give us information about line intensity (polarized and unpolarized), Doppler shift, and line width. These in turn constrain coronal density, temperature, velocity, and through the polarization measurements, magnetic field. Observations of linear polarization in particular diagnose the direction of the magnetic field in the plane of sky (POS), and are well-suited for analysis of the magnetic configuration in polar-crown prominence cavities. CoMP observations have revealed that polar-crown cavities showed characteristic structures in linear polarization (**Figure 1**) which we termed “lagomorphic,” due to their resemblance to rabbit heads seen in silhouette. This characteristic structure may be explained by a magnetic flux-rope model (Bąk-Stęślicka et al., 2013). Lagomorphic structures are very common, and they may be observed in most of the cavities oriented along the line of sight (LOS). The size of the CoMP lagomorphic signature generally scales with the cavity size seen in EUV (Bąk-Stęślicka et al., 2014).

The first CoMP observations of cavities, taken while it was placed at the National Solar Observatory in 2005, revealed interesting results. Schmit et al. (2009) found, for the first time, Doppler velocities in the range of  $5 - 10 \text{ km s}^{-1}$  within a coronal cavity. In our previous paper (Bąk-Stęślicka et al., 2013) we showed another example of LOS flows within cavities. What was the most interesting about these flows was that they occurred in the form of nested ring-like structures with apparently counterstreaming velocities.

In the present work we present a statistical analysis of Doppler velocities within cavities. In Section 2 we describe the data used in our study of 66 days of cavity flow observations. In Section 3 we present our results, and discuss relations between cavities, flows,

associated prominences, and hot cores. In Section 4 we give our conclusions.

## 2. INSTRUMENTS AND DATA ANALYSIS

### 2.1. Instruments

The Atmospheric Imaging Assembly (AIA, Lemen et al., 2012) on board *Solar Dynamics Observatory* (SDO, Pesnell et al., 2012) continuously makes full-disk images of the Sun through ten passbands with a spatial resolution  $\sim 1 \text{ arcsecond}$ , temporal cadence of 12 s, and FOV of  $1.3 R_\odot$ . AIA consists of four telescopes and provides narrow-band imaging of seven extreme ultraviolet (EUV) band passes centered on lines: Fe XVIII (94 Å), Fe VIII, XXI (131 Å), Fe IX (171 Å), Fe XII, XXIV (193 Å), Fe XIV (211 Å), He II (304 Å), and Fe XVI (335 Å). For effective temperature diagnostics of EUV emissions these cover the range from 0.6 to 20 MK.

The CoMP was installed in 2010 at the Mauna Loa Solar Observatory (MLSO) in Hawaii. Since 2010 October CoMP has made daily (subject to weather conditions) observations of the coronal magnetic field in the lower corona with a field of view (FOV) of about  $1.04 - 1.4$  solar radii and a spatial resolution of  $4.46''/\text{pixel}$ . CoMP measures a polarimetric signal (Stokes I, Q, U, V) of the forbidden lines of Fe XIII at 1074.7 and at 1079.8 nm (Tomczyk et al., 2008). The line-of-sight (LOS) directed strength of the magnetic field can be obtained from the circular polarization (Stokes V) although such observations require long integration times on the order of multiple hours due to the very low intensity of circular polarization. As discussed above, the direction of the magnetic field in the POS – subject to a (resolvable)  $90^\circ$  ambiguity – can be determined from the observations in the linear polarization. LOS velocity is obtained via Doppler line shift measurements. All measurements are integrated along the LOS since the corona is optically thin; however forward modeling and CoMP observations have demonstrated that for extended structures such as polar-crown cavities critical information is preserved (see Gibson et al., 2016).

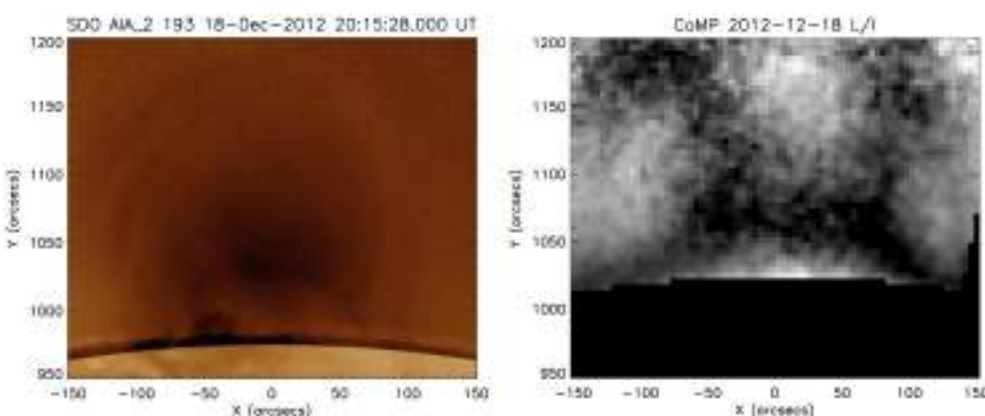


**FIGURE 1 | Left:** Cavity observed on 2012 December 18 by SDO/AIA 193 Å. **Right:** LOS-integrated linear polarization fraction ( $L/I$ ) from CoMP showing lagomorphic, or rabbit-head shaped, structure. The occulting disk of CoMP extends to  $1.05 R_\odot$ .

## 2.2. Data Analysis

Using daily AIA 193 Å images and CoMP data we examined multiple years of polar-crown cavities and analyzed their properties. In particular, we investigated Doppler velocity patterns, quiescent prominences, and hot cores in relation to cavities.

In the set of CoMP observations between January 2012 and October 2015, we analyzed more than 70 days for which a coherent Doppler velocity pattern was observed in the cavity. For the purpose of our analysis we excluded those for which the cavity center was at a height lower than the CoMP occulter, and cavities positioned too close to the telescope occulter arm where there was no possibility of obtaining complete intensity and velocity profiles. This left us with 66 days of cavity flow observations, of which 46 appear to be independent cavity systems. We note that it is difficult to determine whether cavities are truly “independent,” since they are extended along the line of sight and may go in and out of view with a curve of the neutral line (see Gibson et al., 2006 for further discussion). For the purposes of this paper we consider distinct days of observation as data points.

From CoMP observations we used intensity (Stokes-I) images and Doppler shift maps. We mainly used the Level 2 three-point data of the Fe XIII 1074.7 nm line taken between January 2012 and October 2015 available on the MLSO web page (<http://mlso.hao.ucar.edu>). The zero point for CoMP Doppler velocity is not currently well established (*G. de Toma, private communication*); we therefore used the median value of Doppler shift in each map as our zero point in the scale (Tian et al., 2013). In addition, both intensity and Doppler shifts images were averaged over tens of minutes to hours, to improve the signal-to-noise ratio. Such averaging may affect our obtained velocity gradient (average values are likely to be smaller than for individual moments of time). Doppler velocity for Level 2 is also partially corrected for solar rotation through a model described by Tian et al. (2013);

this model assumption may be source of uncertainty. Since cavities are relatively small compared to the velocity gradients of the Tian model, and since our analysis depends on relative velocity values rather than absolute ones, our conclusions will be generally robust to these uncertainties.

AIA 193 Å images were used to measure the height of the cavity center [a detailed description of this method can be found in Gibson et al. (2010)]. For each cavity we extracted polar-angle cuts in the averaged CoMP intensity image at the same height as the AIA cavity center height (Figure 2, left). Using such CoMP intensity profiles we measured an average signal at the cavity rim on both sides of the cavity, and fit a straight line between those points. We defined a cavity width using an area where the signal decreased more than  $3\sigma$  in relation to the fitted line. We repeated this analysis three times. The width, presented in this paper, is the average value from those measurements and the error is their standard deviation. We note that the cavity width obtained in this manner is somewhat larger than for widths in previously reported results based on AIA data (Forland et al., 2013).

We applied the same polar-angle cuts to the Doppler velocity images and used the same averaging as for the CoMP intensity images (Figure 2, right). Using these cavity-center velocity profiles, we measured the velocity range (minimum to maximum) within the cavity and the position of the strongest flow. Since many cavities show a nested-rings pattern in Doppler velocity images, we also calculated the slope of the velocity profiles and number of the velocity gradient changes. We also smoothed velocity profiles (using 2, 3, and 4 points), then measured the number of the velocity gradient changes. The values presented in this paper are the averaged value (from smoothed and unsmoothed profiles), error is their standard deviation.

For two cavities we used six of the AIA filters (94, 131, 171, 193, 211, and 335 Å) to calculate Differential Emission

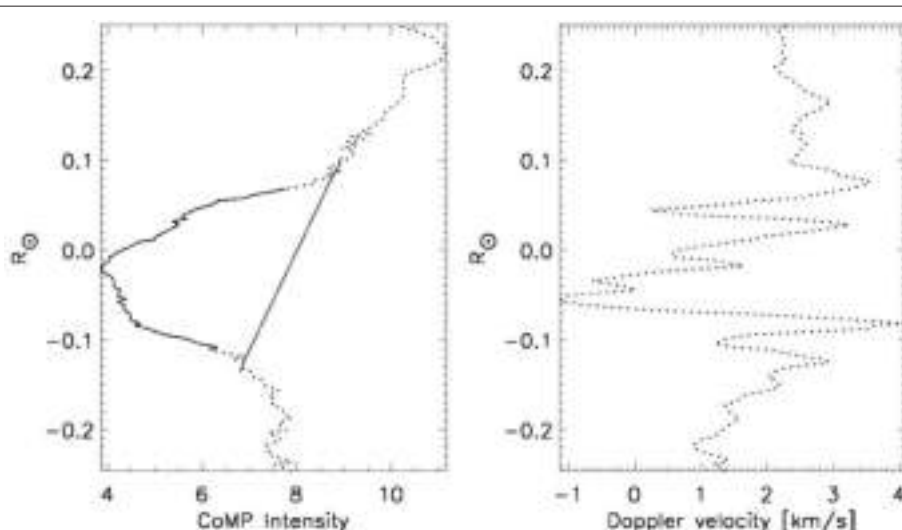


**FIGURE 2 | Left:** CoMP intensity profile across polar-angle cuts at the height equal to the cavity center height for the 20 March 2012 cavity. Solid line shows  $3\sigma$  depletion under the fitted straight line. **Right:** Observed Doppler velocity profile.

Measure (DEM). We calculated response functions for all six filters using the CHIANTI database (Dere et al., 1997). In order to calculate DEM profiles and maps we used the iterative forward-fitting method originally developed for *HINODE/XRT* data (Weber et al., 2004). This XRT method of DEM calculation is available through SSW and was slightly modified by Cheng et al. (2012) to work with the AIA filters (see Appendix of Cheng et al., 2012). In this forward fitting method the differences between fitted and the observed intensities in six EUV AIA filters are minimized. For each pixel in the map we calculated the DEM-weighted average temperature. This parameter characterizing the overall temperature was introduced by Cheng et al. (2012):

$$\bar{T} = \frac{\int DEM(T) \times T dT}{\int DEM(T) dT} \quad (1)$$

Finally, for the full set of cavities with flows, we used AIA 304 Å images to calculate the height of any associated prominence (at the top as measured in an averaged image).

### 3. RESULTS

First of all, we find that coherent – often ring-shaped – flows in Doppler velocity are almost as common within cavities as the “lagomorphic” signature in linear polarization discussed in our previous paper (Bąk-Stęślicka et al., 2013), although the visibility of both depends upon the orientation and extent of the cavity; see Jibben et al. (2016) for an example of a cavity which does not have a clear lagomorph/quiescent velocity structure. The flows in the 66 days we analyzed are usually in the form of the characteristic concentric rings within the cavity (**Figures 3, 4**), and may be observed to persist for a few days (as is also true for lagomorphic

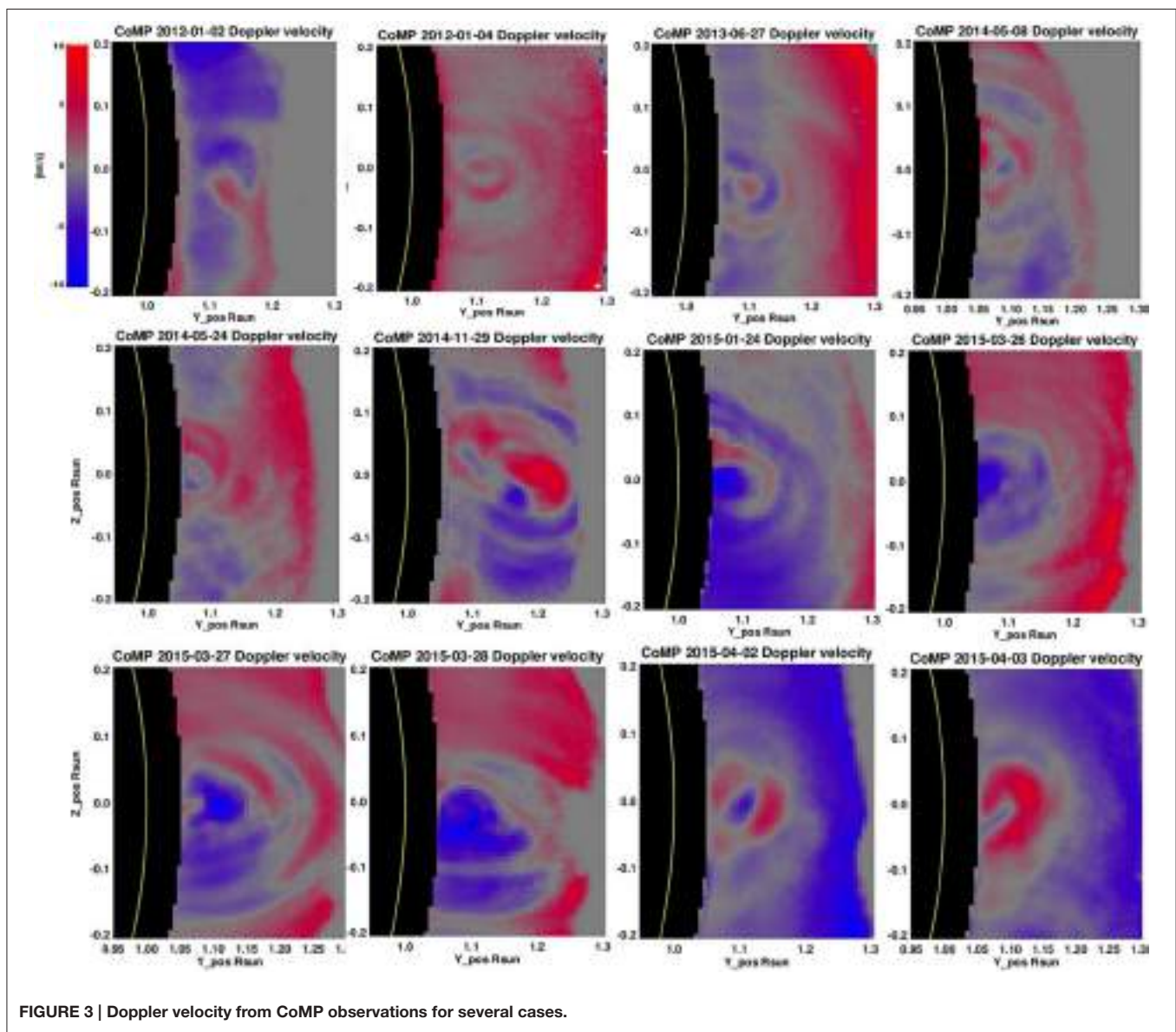
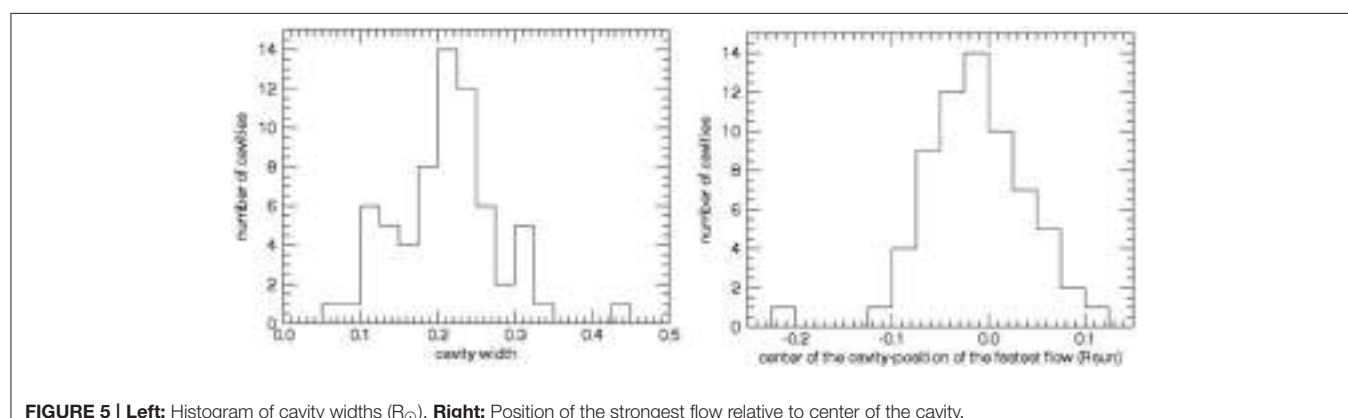
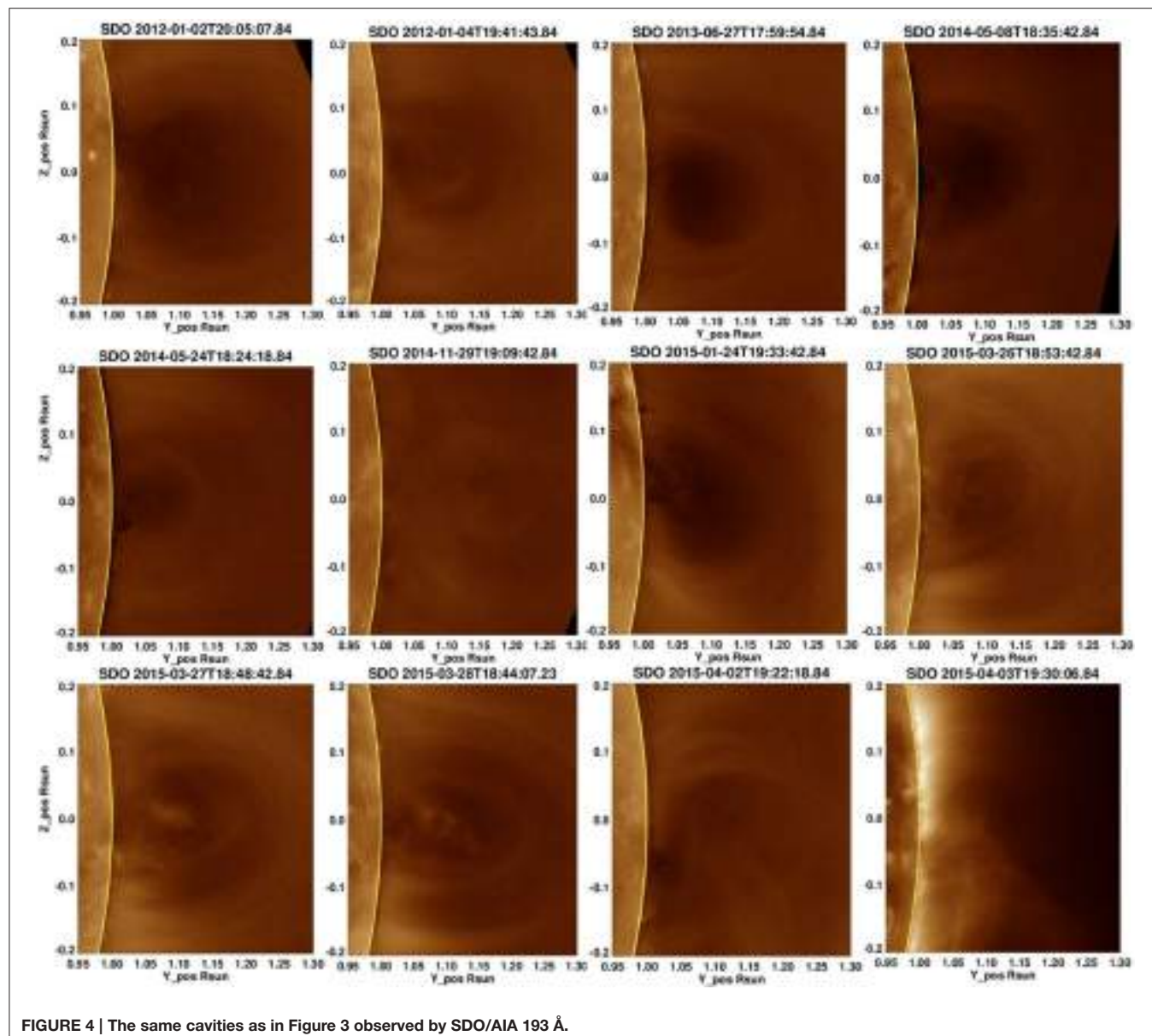


**FIGURE 3 |** Doppler velocity from CoMP observations for several cases.



structures). Eventually, the change of the cavity's orientation as it rotates past the limb – and possibly also evolution of the structure – leads to the loss of a clearly viewed cavity, lagomorph, and velocity rings.

We found that almost half of the analyzed cavities have a width of about  $0.2\text{--}0.25 R_{\odot}$  (**Figure 5**, left). Detailed inspection of CoMP images and the intensity and velocity profiles indicate that flows are localized within the cavity (**Figures 2–4**). A histogram comparing the position of the strongest flow to the position of the cavity center is presented in **Figure 5** (right). In most cases this difference is within  $0.05 R_{\odot}$  of the cavity center which suggest that central flows are the strongest ones. In cases where the strongest flows are not observed in the center, a weaker central flow is often still present. We note that the errors in our method for finding the cavity center from AIA data are on the order  $.01 R_{\odot}$ , and that there are errors in alignment between AIA and CoMP of similar or somewhat larger size. These alignment errors may have a systematic component, which could also contribute to the skew in the distribution.

In most cases the range of velocities observed within a cavity is between 4 and 8 km/s (see **Figure 6**, left), which is consistent with previous reports (Schmit et al., 2009), but larger ranges ( $> 10$  km/s) are also sometimes observed. **Figure 6** (right) shows the relation between velocity range and cavity width. The strongest ranges in velocities are observed in the widest and largest cavities.

Because of the uncertainty in the zero point of the velocity, it is still not clear if flows are truly counterstreaming, however, velocity gradients are clearly observed. Even if concentric rings in velocity (**Figure 3**) do not imply a change in flow direction, each ring may be an indicator of a discontinuity in LOS-directed velocity. The number of loops (or whole rings for higher cavities) is thus of interest. Taking the derivative of the velocity profile we obtain the number of velocity gradient changes (if the structure were symmetric about the center, the number of loops would be half the number of gradient changes). Most cavities indicate 6 – 12 such gradient changes (see **Figure 7**, left), but this number changes with smoothing of the velocity profile (see error bars in the **Figure 7**, right). This number of changes is well correlated with the cavity width (**Figure 7**, right).

In all but three cases, we observed prominences in AIA 304 Å associated with the cavities. We analyzed the relation between cavity center height and the heights of these prominences. A histogram of the difference between the two values is presented in **Figure 8**, left. In all but two cases, the prominence top was below the cavity center and central flows (in the two cases, the prominence was only slightly higher). The prominence top heights are also correlated with the cavity height: for higher cavities, higher prominences were observed. Sample images for two cavities are presented in **Figure 9**.

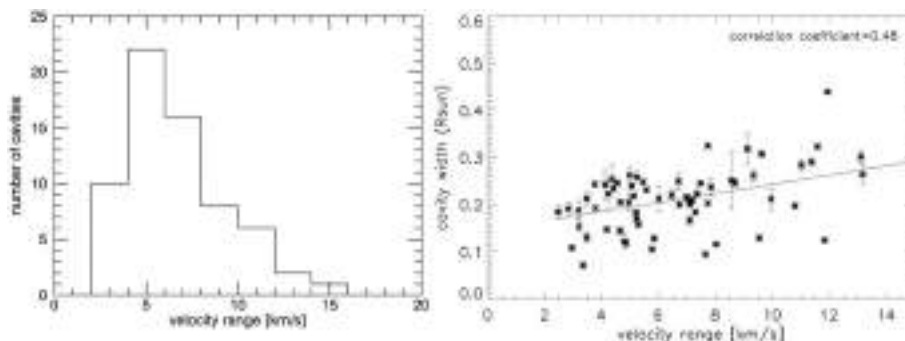


**FIGURE 6 | Left:** Histogram of velocity ranges, **Right:** Relation between velocity range and cavity width. Correlation coefficient is equal to 0.48.

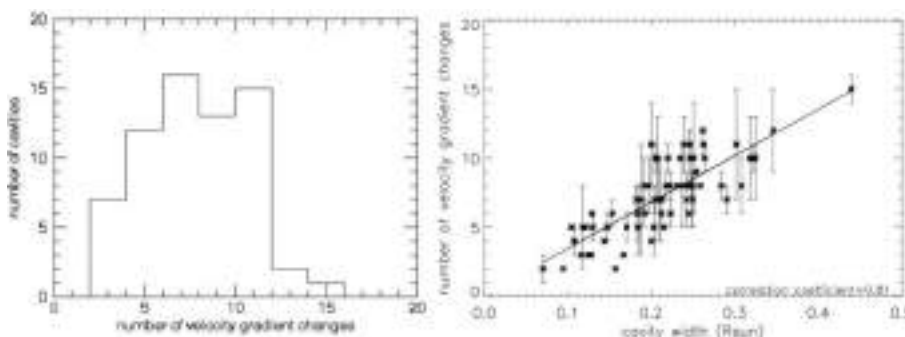


**FIGURE 7 | Left:** Histogram of number of velocity gradient changes. **Right:** Cavity width vs. number of velocity gradient changes. Correlation coefficient is equal to 0.81.

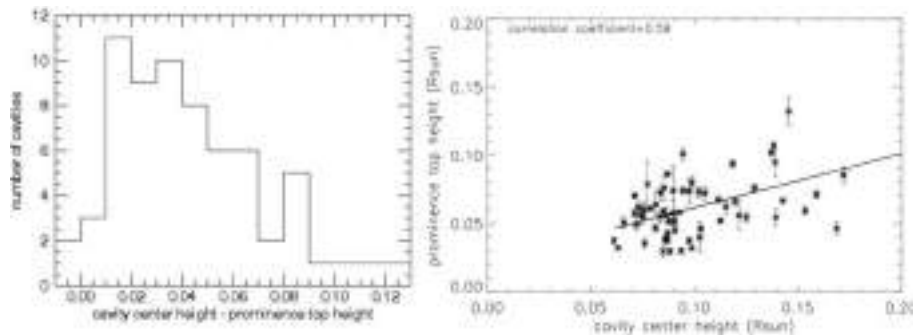


**FIGURE 8 | Left:** Histogram of difference between cavity center height and prominence top height, **Right:** Cavity center height vs. prominence top height. Correlation coefficient is equal to 0.59.

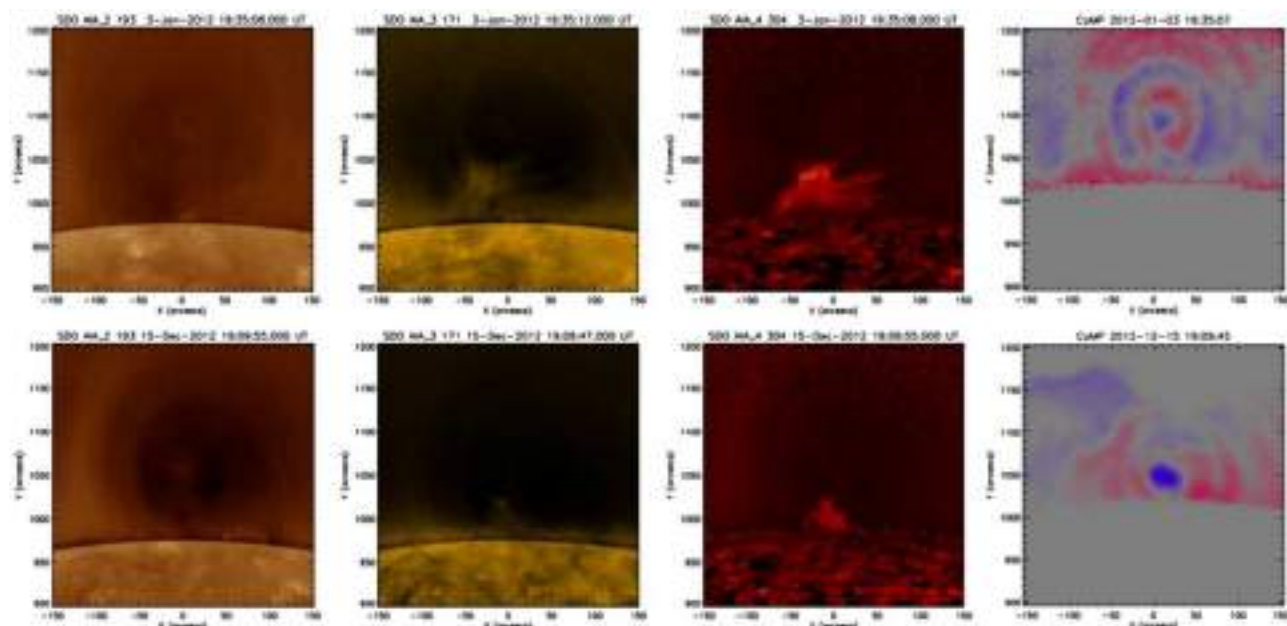


**FIGURE 9 |** Cavities observed on 2012 January 03 and 2012 December 15 by SDO/AIA 193, 171, 304 Å, and CoMP. Those images show that central flows are systematically located above the prominences and they are spatially correlated with the cavity center.

For two of the cavities we calculated DEM maps and profiles and estimated the average temperature using Equation 1. Maps characterizing the overall temperature are presented in Figures 10, 11 (middle). In both cases, at least the central portion of the cavity seems to be filled with hotter material than its surroundings, which is consistent with results of Habbal et al. (2010). We found that the temperature in the center of these cavities were 2.3 and 2.1 MK for 2012 March 19 and 2015 June 05, respectively. The position of these hot cores is spatially correlated within the cavity seen in AIA 193 Å (Figures 10, 11, top panels, left) and flows (Figures 10, 11, top panels, right). In the second example, the position of the hot core is strongly correlated with the position of the part of the cavity with the lowest density and the strongest central flow observed by CoMP. DEM maps are presented in Figures 10, 11 (bottom panels).

## 4. CONCLUSIONS

We have found that LOS-flow structure within coronal cavities is clearly related both to cavity morphology and to cool (prominence) and hot (corona) plasma distribution. Because the corona is magnetically dominated, these relations must ultimately derive from the magnetic field. The fact that prominences systematically lie below the center of cavities and the peak LOS coronal flow, indicates an association of the cavity center with a LOS-oriented, axial magnetic field. This, in combination with the concentric rings of flows surrounding this axis implies toroidal flux surfaces consistent with a magnetic flux rope topology. These observations thus provide complementary evidence toward conclusions based on previously discovered linear-polarization lagomorph signatures

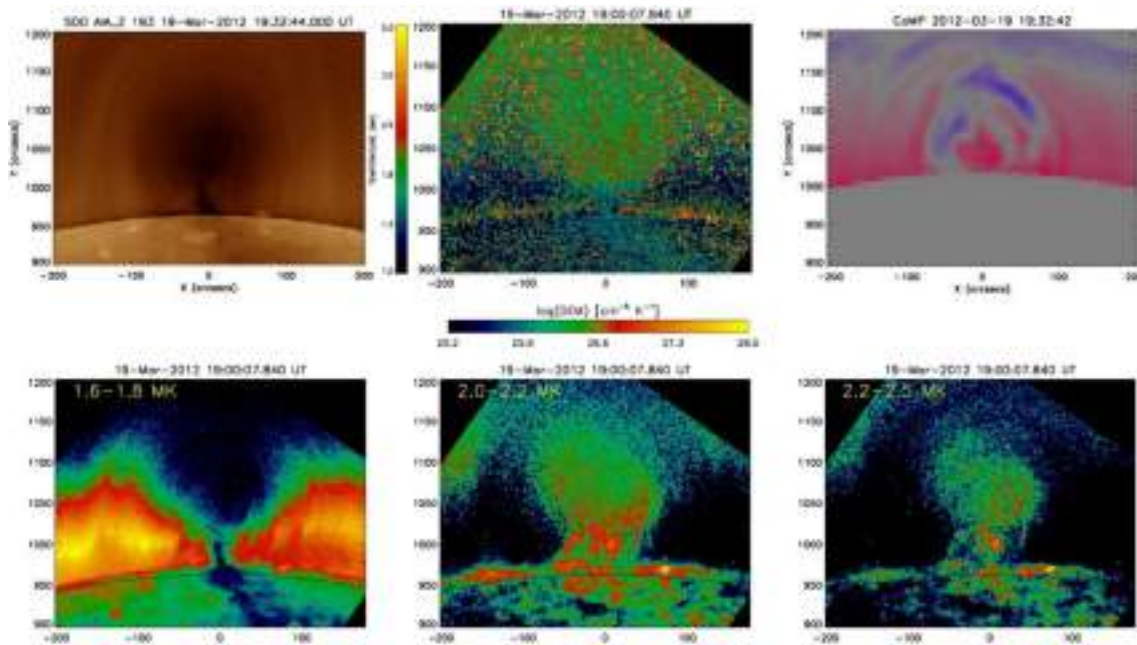


**FIGURE 10 | Top:Left:** Cavity observed on 2012 March 19 by SDO/AIA 193 Å. **Middle:** Maps of the DEM-weighted average temperature (calculated from Equation1). The position of the hot core is spatially correlated with the cavity and flows. **Right:** Doppler velocity from CoMP observations. **Bottom:** Emission measure in different temperature ranges.

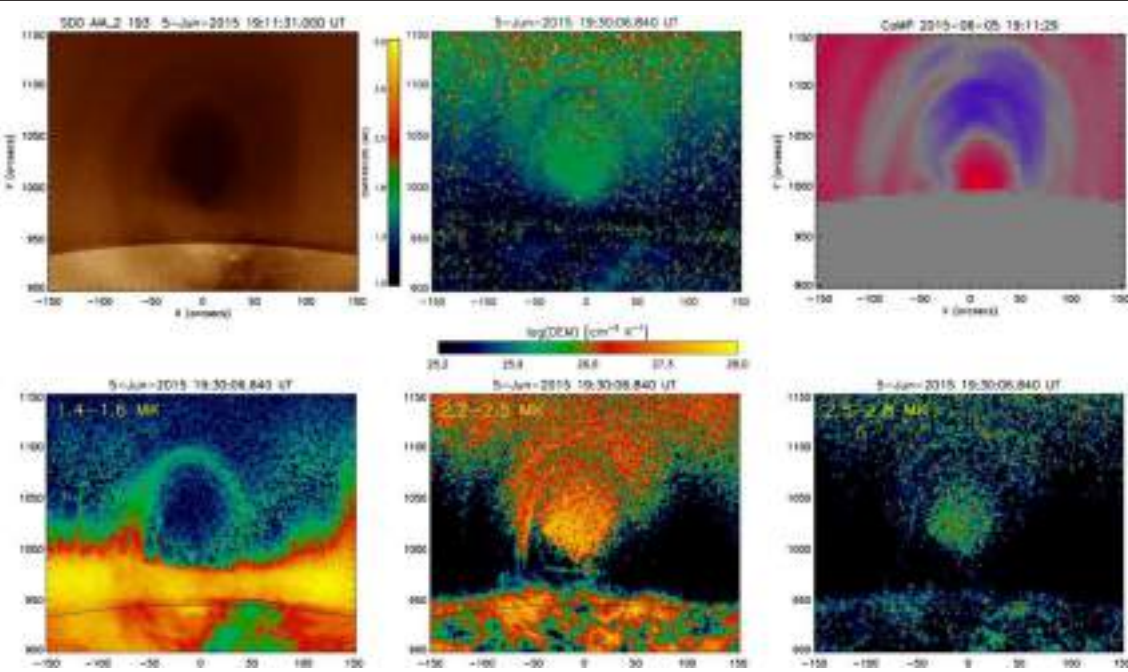


**FIGURE 11 |** The same as in Figure 10 but for the 2015 June 05 cavity.

within cavities. They also motivate efforts to obtain large-aperture telescope measurements of circular polarization [see further discussion in Gibson (2015)]. The details of how

these field-aligned flows originate remain uncertain, however, and represent a challenge to magnetohydrodynamic models of prominence and cavity formation.

## AUTHOR CONTRIBUTIONS

UBS led the design and carried out the statistical analysis, and led the interpretation and writing of the paper. SG contributed to the design and interpretation of the analysis, and to the writing of the paper. EC did the DEM analysis. All authors read and critically revised the paper, approved the final version, and agreed to be accountable for all aspects of the work.

## FUNDING

UBS and EC acknowledge financial support from the Polish National Science Centre grant 2011/03/B/ST9/00104. SG acknowledges support from the Air Force Office of Space

Research, FA9550-15-1-0030. NCAR is supported by the National Science Foundation.

## ACKNOWLEDGMENTS

This work was enabled by participation of UBS and SG in the International Space Science Institute (ISSI) working group on coronal magnetism (2013–2014). AIA data were courtesy of NASA/SDO and the AIA, EVE, and HMI science teams. The CoMP data was provided courtesy of the MLSO, operated by the HAO, as part of the NCAR. We thank Giuliana de Toma and Steve Tomczyk in particular for assistance with these data, and Giuliana de Toma for internal HAO review.

## REFERENCES

- Bąk-Stęślicka, U., Gibson, S. E., Fan, Y., Bethge, C., Forland, B., and Rachmeler, L. A. (2013). The magnetic structure of solar prominence cavities: new observational signature revealed by coronal magnetometry. *Astrophys. J.* 770, 28. doi: 10.1088/2041-8205/770/2/L28
- Bąk-Stęślicka, U., Gibson, S. E., Fan, Y., Bethge, C., Forland, B., and Rachmeler, L. A. (2014). “The spatial relation between EUV cavities and linear polarization signatures,” in *Nature of Prominences and their role in Space Weather. Proceedings of the International Astronomical Union, IAU Symposium*, Vol. 300, eds B. Schmieder, J.-M. Malherbe, and S. T. Wu (Cambridge, UK: Cambridge University Press), 395–396.
- Berger, T. E., Liu, W., and Low, B. C. (2012). SDO/AIA detection of solar prominence formation within a coronal cavity. *Astrophys. J.* 758, 37. doi: 10.1088/2041-8205/758/2/L37
- Cheng, X., Zhang, J., Saar, S. H., and Ding, M. D. (2012). Differential emission measure analysis of multiple structural components of coronal mass ejections in the inner corona. *Astrophys. J.* 761, 62. doi: 10.1088/0004-637X/761/1/62
- Dere, K. P., Landi, E., Mason, H. E., Monsignori Fossi, B. C., and Young, P. R. (1997). CHIANTI - an atomic database for emission lines. *Astron. Astrophys. Suppl.* 125, 149. doi: 10.1051/aa:1997368
- Forland, B. C., Gibson, S. E., Dove, J. B., Rachmeler L. A., and Fan, Y., (2013). Coronal cavity survey: morphological clues to eruptive magnetic topologies. *Sol. Phys.* 288, 603. doi: 10.1007/s11207-013-0361-1
- Fuller, J., Gibson, S. E., de Toma, G., and Fan, Y. (2008). Observing the unobservable? Modeling coronal cavity densities. *Astrophys. J.* 678, 515. doi: 10.1086/533527
- Fuller, J., and Gibson, S. E. (2009). A survey of coronal cavity density profiles. *Astrophys. J.* 700, 1205. doi: 10.1088/0004-637X/700/2/1205
- Gibson, S. E. (2015). “Coronal cavities: observations and implications for the magnetic environment of prominences,” in *Solar Prominences, Astrophysics and Space Science Library*, Vol. 415, eds J.-C. Vial and O. Engvold (Springer International Publishing Switzerland), 323.
- Gibson, S. E., Foster, D., Burkepile, J., de Toma, G., and Stanger, A. (2006). The calm before the storm: the link between quiescent cavities and coronal mass ejections. *Astrophys. J.* 641, 590. doi: 10.1088/0004-637X/641/2/590
- Gibson, S. E., Kucera, T. A., Rastawicki, D., Dove, J., and de Toma, G. (2010). Three-dimensional morphology of a coronal prominence cavity. *Astrophys. J.* 724, 1133. doi: 10.1088/0004-637X/724/2/1133
- Gibson, S. E., Kucera, T., White, S. M., Dove, J., Fan, Y., Forland, B. et al. (2016). FORWARD: A toolset for multiwavelength coronal magnetometry. *Front. Astron. Space Sci.* 3:8. doi: 10.3389/fspas.2016.00008
- Habbal, S. R., Druckmueller, M., Morgan, H., Scholl, I., Rusin, V., Daw, A., et al. (2010). Total solar eclipse observations of hot prominence shrouds. *Astrophys. J.* 719, 1362. doi: 10.1088/0004-637X/719/2/1362
- Heizel, P., Schmieder, B., Fárník, F., Schwartz, P., Labrosse, N., Kotrč, P. et al. (2008). Hinode, TRACE, SOHO, and ground-based observations of a quiescent prominence. *Astrophys. J.* 686, 1383. doi: 10.1086/591018
- Hudson, H. S., Acton, L. W., Harvey, K. A., and McKenzie, D. M. (1999). A stable filament cavity with a hot core. *Astrophys. J.* 513, 83. doi: 10.1086/311892
- Hudson, H. S., and Schwenn, R. (2000). Hot cores in coronal filament cavities. *Adv. Space Res.* 25, 1859. doi: 10.1016/S0273-1177(99)00618-3
- Illing, R. M., and Hundhausen, J. R. (1986). Disruption of a coronal streamer by an eruptive prominence and coronal mass ejection. *J. Geophys. Res.* 91, 10951.
- Jibben, P. R., Reeves, K. K., and Su, Y. (2016). Evidence for a magnetic flux rope in observations of a solar prominence-cavity system. *Front. Astron. Space Sci.* 3:10. doi: 10.3389/fspas.2016.00010
- Lemen, J. R., Title, A. M., Akin, D. J., Boerner, P. F., Chou, C., Drake, J. F., et al. (2012). The Atmospheric Imaging Assembly (AIA) on the Solar Dynamics Observatory (SDO). *Sol. Phys.* 275, 17. doi: 10.1007/s11207-011-9776-8
- Low, B. C. (1994). Magnetohydrodynamic processes in the solar corona: flares, coronal mass ejections, and magnetic helicity. *Phys. Plasmas* 1, 1684. doi: 10.1063/1.870671
- Low, B. C., and Hundhausen, J. R. (1995). Magnetostatic structures of the solar corona. 2: the magnetic topology of quiescent prominences. *Astrophys. J.* 443, 818.
- Marićić, D., Vršnak, B., Stanger, A. L., and Veronig, A. M. (2004). Coronal mass ejection of 15 may 2001: I. evolution of morphological features of the eruption. *Sol. Phys.* 225, 337. doi: 10.1007/s11207-004-3748-1
- Marqué, C. (2004). Radio metric observations of quiescent filament cavities. *Astrophys. J.* 602, 1037. doi: 10.1086/381085
- Marqué, C., Lantos, P., and Delaboudinère, J.-P. (2002). Multi wavelength investigation of the eruption of a sigmoidal quiescent filament. *Astron. Astrophys.* 387, 317. doi: 10.1051/0004-6361:20020309
- McCauley, P. I., Su, Y. N., Schanche, N., Evans, K. E., Su, C., McKillop, S., et al. (2015). Prominence and filament eruptions observed by the solar dynamics observatory: statistical properties, kinematics, and online catalog. *Sol. Phys.* 290, 1703. doi: 10.1007/s11207-015-0699-7
- Pesnell, W. D., Thompson, B. J., and Chamberlin, P. C. (2012). The Solar Dynamics Observatory (SDO). *Sol. Phys.* 275, 3. doi: 10.1007/s11207-011-9841-3
- Reeves, K. K., Gibson, S. E., Kucera, T. A., Hudson, H. S., and Kano, R. (2012). Thermal properties of a solar coronal cavity observed with the X-ray telescope on Hinode. *Astrophys. J.* 746, 146. doi: 10.1088/0004-637X/746/2/146
- Régnier, S., Walsh, R. W., and Alexander, C. E. (2011). A new look at a polar crown cavity as observed by SDO/AIA. Structure and dynamics. *Astron. Astrophys.* 533, L1. doi: 10.1051/0004-6361/20117381
- Schmit, D. J., Gibson, S. E., Tomczyk, S., Reeves, K. K., Sterling, A. C., Brooks, D. H., et al (2009). Large-scale flows in prominence cavities. *Astrophys. J.* 700:L96. doi: 10.1088/0004-637X/700/2/L96
- Su, Y., van Ballegooijen, A., McCauley, P., Ji, H., Reeves, K. K., and DeLuca, E. E. (2015). Magnetic structure and dynamics of the erupting solar polar crown prominence on 2012 march 12. *Astrophys. J.* 807, 144. doi: 10.1088/0004-637X/807/2/144
- Tandberg-Hanssen, E. (1995). *The Nature of Solar Prominences*, 2nd Edn. Dordrecht: Kluwer.

- Tian, H., Tomczyk, S., McIntosh, S. W., Bethge, C., de Toma, G., and Gibson, S. E. (2013). Observations of coronal mass ejections with the coronal multichannel polarimeter. *Sol. Phys.* 288, 637. doi: 10.1007/s11207-013-0317-5
- Tomczyk, S., Card, G. L., Darnell, T., Elmores, D. F., Lull, R., Nelson, P. G. et al (2008). An instrument to measure coronal emission line polarization. *Sol. Phys.* 247, 411. doi: 10.1007/s11207-007-9103-6
- Vaiana, G. S., Davis, J. M., Giacconi, R., Krieger, A. S., Silk, J. K., Timothy, A. F., et al. (1973a). Identification and analysis of structures in the corona from X-ray photography. *Sol. Phys.* 32, 81. doi: 10.1007/BF00152731
- Vaiana, G. S., Krieger, A. S., and Timothy, A. F. (1973b). X-Ray observations of characteristic structures and time variations from the solar corona: preliminary results from SKYLAB. *Astrophys. J.* 185, 47. doi: 10.1086/181318
- Vršnak, B., Maričić, D., Stanger, A. L., and Veronig, A. M. (2004). Coronal mass ejection of 15 may 2001: II. Coupling of the Cme acceleration and the flare energy release. *Sol. Phys.* 225, 355. doi: 10.1007/s11207-004-4995-x
- von Kluber, H. (1961). Photometric investigation of the inner solar corona using an eclipse plate of 1927 June 29. *Monthly Notices R. Astron. Soc.* 123, 61. doi: 10.1093/mnras/123.1.61
- Waldmeier, M. (1941). *Ergebnisse und Probleme der Sonnenforschung*. Leipzig: Becker & Erler kom.-ges.
- Waldmeier, M. (1970). The structure of the monochromatic corona in the surroundings of prominences. *Sol. Phys.* 15, 167.
- Weber, M. A., DeLuca, E. E., Golub, L., and Sette, A. L. (2004). "Temperature diagnostics with multichannel imaging telescopes," in *Multi-Wavelength Investigations of Solar Activity, IAU Symposium*, Vol. 223, eds A. V. Stepanov, E. E. Benevolenskaya, and A. G. Kosovichev (Cambridge, UK: Cambridge University Press), 312–328.
- Wesley, W. H. (1927). *Memoirs of the British Astronomical Association*, Vol. 64, Appendix.
- Williamson, N. K., Fullerton, C. M., and Billings, D. E. (1961). Coronal emission in the vicinity of quiescent prominences. *Astrophys. J.* 133, 973. doi: 10.1086/147102

**Conflict of Interest Statement:** The authors declare that the research was conducted in the absence of any commercial or financial relationships that could be construed as a potential conflict of interest.

The reviewer CJ and handling Editor declared a past collaboration and the handling Editor states that the process nevertheless met the standards of a fair and objective review.

Copyright © 2016 Bąk-Stęślicka, Gibson and Chmielewska. This is an open-access article distributed under the terms of the Creative Commons Attribution License (CC BY). The use, distribution or reproduction in other forums is permitted, provided the original author(s) or licensor are credited and that the original publication in this journal is cited, in accordance with accepted academic practice. No use, distribution or reproduction is permitted which does not comply with these terms.



# Evidence for a Magnetic Flux Rope in Observations of a Solar Prominence-Cavity System

**Patricia R. Jibben** <sup>1\*</sup>, **Katharine K. Reeves** <sup>1</sup> and **Yingna Su** <sup>2</sup>

<sup>1</sup> Harvard-Smithsonian Center for Astrophysics, Cambridge, MA, USA, <sup>2</sup> Key Laboratory for Dark Matter and Space Science, Purple Mountain Observatory, Chinese Academy of Sciences, Nanjing, China

## OPEN ACCESS

### Edited by:

Stephen M. White,  
Air Force Research Laboratory, USA

### Reviewed by:

Gordon James Duncan Petrie,  
National Solar Observatory, USA

Meng Jin,  
University Corporation for  
Atmospheric Research/Lockheed  
Martin Solar and Astrophysics  
Laboratory, USA

### \*Correspondence:

Patricia R. Jibben  
[pjibben@cfa.harvard.edu](mailto:pjibben@cfa.harvard.edu)

### Specialty section:

This article was submitted to  
Stellar and Solar Physics,  
a section of the journal

Frontiers in Astronomy and Space  
Sciences

**Received:** 04 January 2016

**Accepted:** 11 March 2016

**Published:** 31 March 2016

### Citation:

Jibben PR, Reeves KK and Su Y (2016) Evidence for a Magnetic Flux Rope in Observations of a Solar Prominence-Cavity System. *Front. Astron. Space Sci.* 3:10. doi: 10.3389/fspas.2016.00010

Coronal cavities are regions of low coronal emission that usually sit above solar prominences. These systems can exist for days or months before erupting. The magnetic structure of the prominence-cavity system during the quiescent period is important to understanding the pre-eruption phase. We describe observations of a coronal cavity situated above a solar prominence observed on the western limb as part of an Interface Region Imaging Spectrograph (IRIS) and Hinode coordinated Observation Program (IHOP 264). During the observation run, an inflow of hot plasma observed by the Hinode X-Ray Telescope (XRT) envelopes the coronal cavity and triggers an eruption of chromospheric plasma near the base of the prominence. During and after the eruption, bright X-ray emission forms within the cavity and above the prominence. IRIS and the Hinode EUV Imaging Spectrometer (EIS) show strong blue shifts in both chromospheric and coronal lines during the eruption. The Hinode Solar Optical Telescope (SOT) Ca II H-line data show bright emission during the ejection with complex, turbulent, flows near the prominence and along the cavity wall. These observations suggest a cylindrical flux rope best represents the cavity structure with the ejected material flowing along magnetic field lines supporting the cavity. We also find evidence for heating of the plasma inside the cavity after the flows. A model of the magnetic structure of the cavity comprised of a weakly twisted flux rope can explain the observed loops in the X-ray and EUV data. Observations from the Coronal Multichannel Polarimeter (CoMP) are compared to predicted models and are inconclusive. We find that more sensitive measurements of the magnetic field strength along the line-of-sight are needed to verify this configuration.

**Keywords:** sun, prominence, coronal cavity, magnetic field modeling, magnetic field

## 1. INTRODUCTION

Solar prominences are sheets of cool dense plasma suspended in the solar corona observed on the limb. Their formation and stability require several mechanisms working in tandem. It is widely accepted that the magnetic field provides the structural support of the prominence but direct observations of the magnetic field in the corona are not currently available. Comprehensive reviews of prominence systems and their dynamics are provided by Martin (1990), Mackay et al. (2010), Parenti (2014), Priest (2014), and Vial and Engvold (2015) and we will provide a brief review here. Prominences only form between regions of opposite magnetic field polarity. In other words, along the polarity inversion line (PIL; Smith, 1968; Martin, 1973). But not all PILs will exhibit prominence

formation; another condition required is a predominant transverse magnetic field aligned with the long axis of the prominence. The path in the chromosphere where this happens is referred to as a filament channel (Martin, 1990). Along filament channels, there is a significant decrease in the number of observed spicules compared to the surrounding area (Martin, 1990). Reduced spicule activity indicates weak radial magnetic fields and quiescent prominences may form along giant cell boundaries that separate unipolar magnetic field regions (Malherbe and Priest, 1983; Schröter et al., 1987). Bipoles within the filament channel are often characterized by a bald-patch topology (Titov and Démoulin, 1999) where the magnetic field at the photosphere is largely horizontal and points from negative to positive polarity (López Ariste et al., 2006). The long-term converging patches of opposite polarity flow into juxtaposition along the PIL and as they encounter one another, they disappear concurrently at their boundaries (Martin, 1990). Finally, prominences will quickly dissipate unless there is a closed arcade of magnetic field lines overlying and connecting regions of opposite polarity. The closed loops not only hold down the prominence material but they also create a magnetically stable system in which the cool prominence material interacts with the hot plasmas in the corona.

Under the arcade, a region of reduced coronal emission (the coronal cavity) can develop above quiescent prominences (Vaiana et al., 1973). Despite their reduced coronal emissions, these cavities are filled with complex, twisted structures when observed in white light eclipse data and are distinct from the magnetic structures defining the rest of the overlying arcade that forms the base of streamers as well as the boundaries of streamers (Habbal et al., 2010). This suggests the overlying arcade and underlying prominence are independent magnetic structures that can interact via magnetic reconnection at their boundaries. Therefore, the magnetic structure of the cavity and prominence system prior to an eruption is important to understanding how instabilities form.

A magnetic flux rope is often used to model the prominence and cavity system (Priest et al., 1989; Rust and Kumar, 1994; van Ballegooijen, 2004), with much of the prominence material sitting in the dips of the magnetic field lines (Kuperus and Raadu, 1974; Pneuman, 1983; Priest et al., 1989; van Ballegooijen and Martens, 1989; Rust and Kumar, 1994; Low and Hundhausen, 1995; Aulanier et al., 1998; Chae et al., 2001; van Ballegooijen, 2004; Gibson et al., 2006; Dudík et al., 2008). Fan and Gibson (2006) modeled a prominence as a twisted flux rope and found that a current sheet forms within the flux rope cavity along a bald-patch separatrix surface (BPSS), composed of the field lines that graze the anchoring lower boundary, enclosing the detached helical field that supports the prominence. They further show that resistive dissipation of the current sheet would produce a hot sheath surrounding the prominence material in the cavity, which could provide an explanation for the observed development of X-ray bright cores within a coronal cavity (Hudson et al., 1999; Hudson and Schwenn, 2000; Reeves et al., 2012). Su et al. (2015) constructed a series of magnetic field models with different configurations based on the observed photospheric magnetogram for a polar crown prominence, and they found that the model with a twisted flux rope best matches the observations.

Coronal magnetic fields provide the structure and support for the coronal cavity, but measuring coronal magnetic fields is difficult to do (Lin et al., 2004). Fortunately, some information about the coronal magnetic fields making up coronal cavities has been achieved with the Coronal Multi-Channel Polarimeter (Tomczyk et al., 2008; CoMP). A recent statistical study by Bąk-Stęślicka et al. (2013) found that quiescent prominence cavities consistently posses a “lagomorphic” signature in linear polarization indicating twist or shear extending up into the cavity above the PIL. They also compared the CoMP observations with synthetic CoMP-like data created using a forward magnetohydrodynamics (MHD) model and concluded that a cylindrical magnetic flux rope better represents polar-crown prominence cavities.

In this paper, we present chromospheric and coronal observations of a prominence-cavity system observed on the west limb. We develop a magnetic field model of the system based on these observations. We utilize data from Hinode (Kosugi et al., 2007), Interface Region Imaging Spectrograph (IRIS; De Pontieu et al., 2014), and the Solar Dynamics Observatory’s Atmospheric Imaging Assembly (AIA; Lemen et al., 2012) and Helioseismic and Magnetic Imager (HMI; Schou et al., 2012). Together, these instruments provide near simultaneous multithermal observations of the prominence-cavity system and its surroundings. The X-Ray Telescope (XRT; Golub et al., 2007) observes some of the hottest coronal temperatures between 2 and 10 MK. The EUV Imaging Spectrometer (EIS; Culhane et al., 2007) takes spectral data from the transition region to coronal temperatures. Finally, the Solar Optical Telescope (SOT; Tsuneta et al., 2008) and IRIS image chromospheric and transition region plasmas. We use photospheric line-of-sight (LOS) magnetic field data to derive a model of the structure of the system with the assumption it is a magnetic flux rope under an arcade. We vary the axial and poloidal fluxes of the model to best fit the observations and then we compare the coronal features predicted by the model with CoMP observations. We find evidence of heating within the cavity during an eruption and we find evidence that magnetic bipoles within the filament channel exhibit a bald-patch topology. Therefore, we conclude that a weakly twisted magnetic flux rope best represents the prominence-cavity system but further instrumentation is needed to resolve coronal magnetic signatures of a quiescent flux rope within the corona.

## 2. MATERIALS AND METHODS

The observations we use were part of an IRIS and Hinode Joint Observation Program (IHOP 264<sup>1</sup>) that included observations from all three Hinode instruments. The IHOP was run three times pointing at the same prominence on the west limb between 9 and 10 October 2014. We present the data taken between 18 and 22 UT on 9 October because CoMP was also observing at this time. We do not use the other two data sets because they either do not have corresponding CoMP observations or in the case of the 10 October data, a non-related filament erupted.

<sup>1</sup>[http://www.isas.jaxa.jp/home/solar/hinode\\_op/hop.php?hop=0264](http://www.isas.jaxa.jp/home/solar/hinode_op/hop.php?hop=0264).

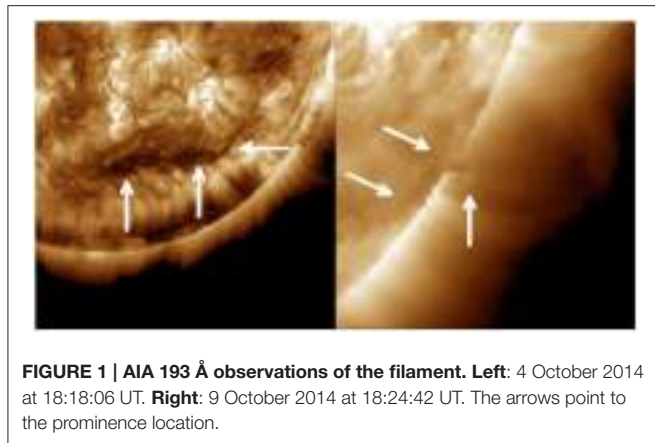


**FIGURE 1 | AIA 193 Å observations of the filament. Left:** 4 October 2014

**at 18:18:06 UT. Right:** 9 October 2014 at 18:24:42 UT. The arrows point to the prominence location.

## 2.1. Hinode XRT, EIS, and SOT Data Reduction

The XRT observations used in this study include 8 s thin-Be exposures at 60 s cadence. The field of view is  $\approx 790'' \times 790''$  and the images are binned  $2 \times 2$  giving a resolution of  $2''.0572$  per pixel. Observations were paused during times when Hinode passed through the South Atlantic Anomaly (SAA) causing 20–30 min gaps in the data. The data is processed using standard data reduction routines provided by the XRT team (Kobelski et al., 2014) and aligned using the database developed by Yoshimura and McKenzie (2015) distributed in SolarSoft (Freeland and Handy, 1998). Either individual or 5 min averaged data were spatially enhanced using the *à trous* wavelet transform with a cubic spline scaling function. See page 29, and Appendix A in Stark and Murtagh (2002) for a complete description of the routine. This method separates the image into different spatial scales based on pixel size along with a residual image containing the portion of the image outside of the spatial scales. We display the data without the residual image using a log-like scale so that only bright features with intensity gradients that vary over 1–3 pixels remain. Regions that do not change rapidly are threshold to white or are set to be transparent.

The EIS data utilize the  $2''$  slit with 50 s exposures, 75 raster positions with binning along the  $x$ -direction giving a  $300'' \times 512''$  FOV. Two raster scans are used in this study. The two scans were taken between 18:16–19:21 UT and 19:21–20:26 UT. The scans are processed in IDL using software provided by the EIS team and a thorough discussion of the routines is provided in the EIS data analysis guide<sup>2</sup>. A brief overview is given here.

The data are calibrated using EIS\_PREP with the default parameters outlined in the analysis guide. We use three coronal lines for this study, Fe XII 195.12 Å, Fe XIII 202.04 Å, and Fe XV 284.16 Å. The Fe XV 284.16 Å spectra is imaged on a different camera resulting in a slightly different field of view. The lines are fit with a Gaussian profile using EIS\_AUTO\_FIT routine (Young, 2013). From this, intensity, LOS Doppler velocity maps and line width maps are created.

The default velocity scale used in the data reduction software is derived using the Kamio method (Kamio et al., 2010). We

<sup>2</sup><http://solarb.mssl.ucl.ac.uk:8080/eiswiki/Wiki.jsp?page=EISAnalysisGuide>.

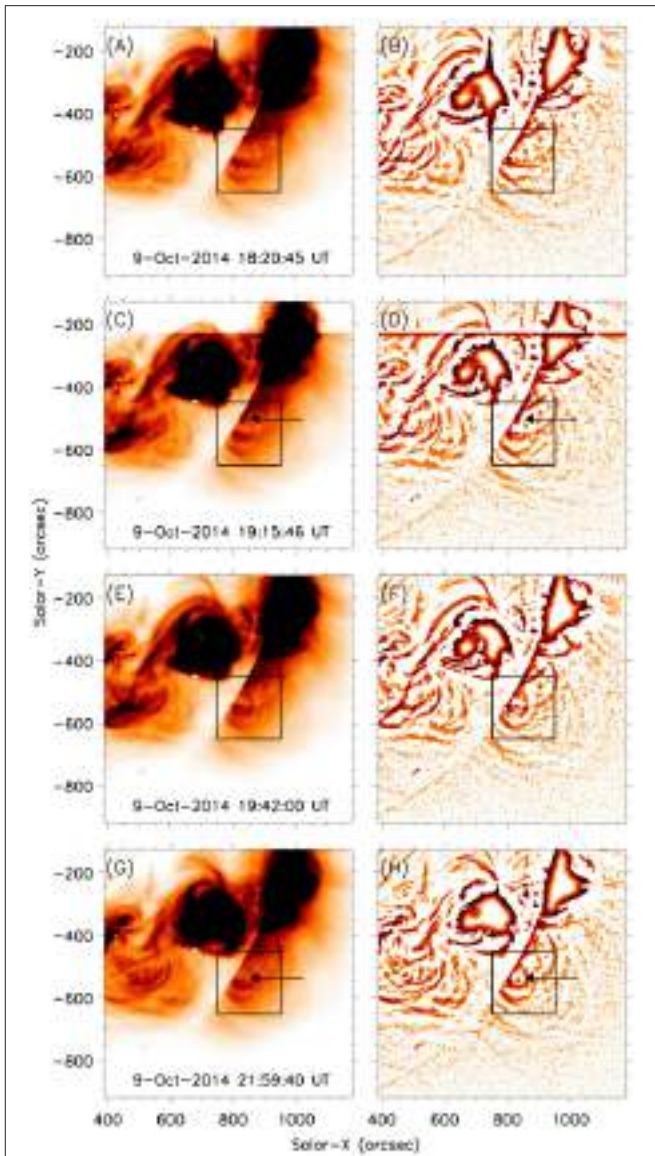


**FIGURE 2 | Left column:** Hinode XRT thin-Be (inverse log) intensity (5 min average) observations of the coronal cavity. **Right column:** Spatially enhanced image with the background emission threshold to white. Panels **(A,B)** shows the cavity prior to the eruption. Panels **(C,D)** shows the initial phase of the eruption with an arrow pointing to an increase in X-ray emission. Panels **(E–H)** show the cavity during and after the eruption with the arrows pointing to an increase in X-ray emission within the cavity.

update the velocity scale using a patch of quiet sun. We assume that the LOS velocities will average to zero in this region for each of the spectral lines (Warren et al., 2011). The off limb patch contains 120 pixels in the  $y$ -direction and we bin the data by 20 pixels at each raster position, a Gaussian profile is fit to the average of the bottom 6 binned pixels, thus defining the reference wavelength. We perform this procedure for each line separately because an absolute velocity scale cannot be derived for the Fe XV 284.16 Å line with respect to the other two since it is on a separate camera. The error in the

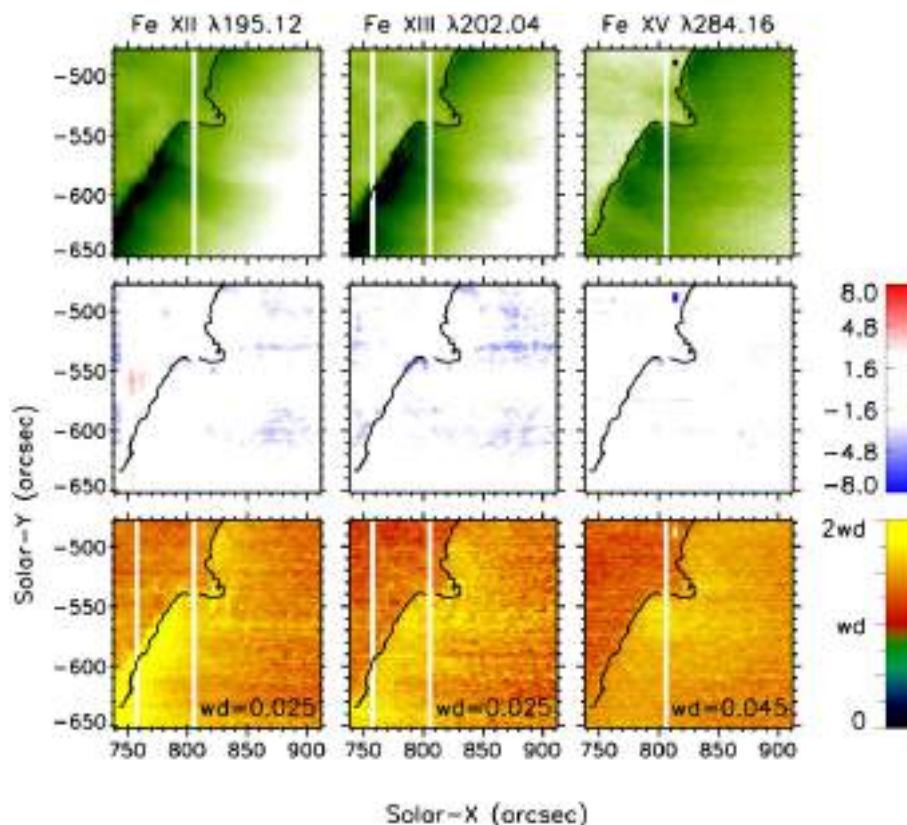


**FIGURE 3 | A subfield of the EIS raster scan starting from the left at 18:16 UT and finishing at 19:21 UT. Top row:** EIS intensity (inverse log) for Fe XII 195.12 Å, Fe XIII 202.04 Å, and Fe XV 284.16 Å. **Middle row:** Doppler velocity maps for the three lines. **Bottom row:** Line widths of the given lines with the median line width (wd) given in each window. The white stripes are regions of missing data.

velocity is provided from the routines used to generate the velocities.

The SOT data consists of  $\approx 112'' \times 112''$  Ca II H-line images taken at 30 s cadence between 18 and 20 UT and then 60 s cadence from 20 to 22 UT. The data are calibrated using routines provided in SolarSoft. In addition, the images are spatially enhanced using the same method used on the XRT data except the residual image is preserved. Small scale features are enhanced before recombining the image, which acts to sharpen the image while preserving information about the enhancement. After the images are spatially enhanced, a radial density filter is applied to reduce the intensity of the disk and spicule regions. The radial density filter applied is similar to the one described in Berger et al. (2010). After the images are scaled and sharpened they are aligned using the SolarSoft routine `fg_rigidalign.pro`. There was a shift in the SOT pointing between the 21:07 and 21:08 frames. The images after 21:08 UT are aligned manually by aligning features visible in both images. Features in SOT are compared with features in AIA 211 Å to coaligned SOT with other instruments.

## 2.2. IRIS Data Reduction

IRIS performed a 16-step coarse raster from 18:24 UT to 21:58 UT. The telescope was pointed on the west limb at  $803'', -546''$

capturing most of the prominence. The raster field of view was  $30'' \times 119''$  with a raster step cadence of 9.4 s making a raster cadence of 150 s with 8 s exposures. Two broadband filter (2796 and 1400 Å) slit-jaw images (SJI) were taken at a cadence of 19 s with a  $119'' \times 119''$  field of view. The calibrated level 2 data were used in this study and downloaded from the IRIS website<sup>3</sup>. The prominence material is significantly dimmer than on-disk regions for the chosen lines. To simultaneously observe both regions, we apply an intensity filter to the Si IV 1400 Å images decreasing the on-disk and spicule intensities. The on-disk intensity is decreased by 90% of its original intensity. The intensity of the spicule region is linearly increased from 10 to 100% at the edge of the spicule region. The intensity of the prominence and off limb features do not have their intensity altered. The resultant images are displayed using a square-root inverse intensity scaling.

We use the Mg II 2796 Å and Si IV 1394 Å spectra for this study. The Mg II h and k lines are formed at chromospheric temperature ( $10^4$  K). Emission from the Si IV 1394 Å line form in the prominence transition region (PCTR). The UV continuum at 1400 Å formed in the lower chromosphere is not present for a

<sup>3</sup><https://iris.lmsal.com/index.html>

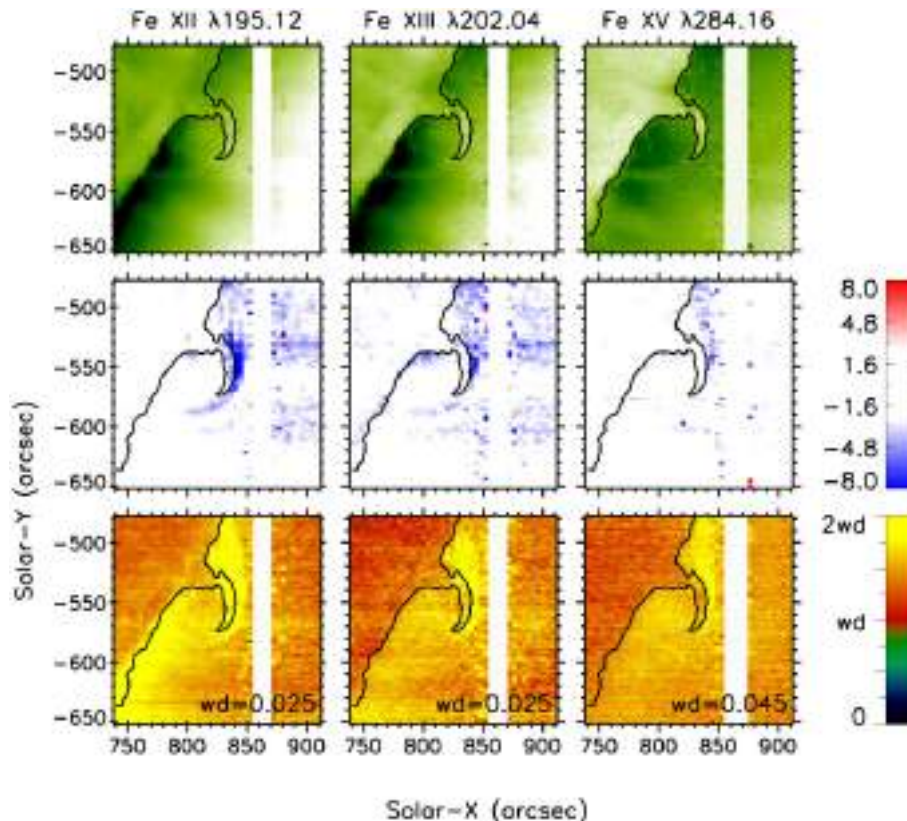


**FIGURE 4 | A subfield of the EIS raster scan starting from the left at 19:22 UT and finishing at 20:27 UT. Top row:** EIS intensity (inverse log) for Fe XII 195.12 Å, Fe XIII 202.04 Å, and Fe XV 284.16 Å. **Middle row:** Doppler velocity maps for the three lines. **Bottom row:** Line widths of the given lines with the median line width (wd) given in each window. The white stripes are regions of missing data.

prominence observed at the limb contrary to observations on the disk (Schmieder et al., 2014).

We perform a relative wavelength calibration to measure the Doppler velocities of the eruption. The reference wavelength for each spectral line window is selected at the centroid of the line profile averaged over the on-disk scan positions for each raster scan. Therefore, the relative Doppler velocities are measured with respect to the quiet Sun regions. The absolute uncertainty of the relative wavelength calibration is estimated to be  $4 \text{ km s}^{-1}$  by Liu et al. (2015). Their estimates include a wavelength shift, 20 mÅ from disk center to the limb and the IRIS orbital thermal variation of  $3 \text{ km s}^{-1}$ . In that paper, portions of the IRIS slit were on the disk throughout the observations.

### 2.3. CoMP Data Reduction

CoMP makes daily polarimetric (Stokes  $I$ ,  $Q$ ,  $U$ ,  $V$ ) of the forbidden lines of Fe XIII at 1074.4 nm and 1078.9 nm with a FOV of  $1.4\text{--}2 R_\odot$ . The degree of linear polarization ( $L/I$ ) constrains the direction of the plane-of-sky (POS) magnetic field. The amount of circular polarization ( $V/I$ ) provides information about the strength of the magnetic field along the LOS. The CoMP data consists of QuickInvert data of the Fe XIII 1074.7 nm coronal emission line. The data were downloaded from the High

Altitude Observatory/Mauna Loa Solar Observatory website<sup>4</sup>. The Quick Invert files contain five images: Stokes  $I$ ,  $Q$ ,  $U$ , linear polarization ( $L$ ), and magnetic field azimuth. The file is read into the FORWARD (Gibson et al., 2016) toolset where  $L/I$  is calculated and used for this study.

### 2.4. Magnetic Model of Prominence-Cavity System

A three-dimensional magnetic model of the prominence-cavity system is constructed using the Coronal Modeling System (CMS) developed by van Ballegooijen (2004). The CMS model assumes the prominence material is supported against gravity by a helical flux rope. The model utilizes SDO/HMI magnetograms to establish the magnetic field strength and topology at the photosphere where it is assumed to be radial. The model is constructed by inserting a flux rope along the PIL under a potential field representing the overlying coronal arcade. The axial flux (in Mx) and the poloidal flux per unit length (in Mx/cm) along the filament are set to an initial value and then magnetofrictional relaxation is used to drive the system to a nonlinear force free state. Detailed description of the methodology can be found in the

<sup>4</sup><http://www2.hao.ucar.edu/mlso/mlso-home-page>.

literature and references therein (Su et al., 2009, 2011; Su and van Ballegooijen, 2012) and we describe the method briefly below.

First, the potential field is computed from the observed magnetic maps. Then, by appropriate modifications of the vector potentials a “cavity” is created above the selected path, and a thin flux bundle, representing the axial flux of the flux rope, is inserted into the cavity with the footpoints of the flux rope embedded in regions near the PIL. The footpoints are chosen so that the flux rope begins and ends in a patch of positive and negative polarity, respectively. To preserve the radial component of the inner boundary, the patch representing the footpoints is removed/added from the photospheric flux distribution and is equal to the axial flux of the inserted flux rope. The poloidal flux is inserted by adding circular loops around the flux bundle (Su et al., 2015). The inserted flux rope is not in force-free equilibrium. We use magneto-frictional relaxation to drive the field toward a force-free state. This method is an iterative relaxation method (van Ballegooijen et al., 2000) specifically designed for use with vector potentials. Magnetofriction has the effect of expanding the flux rope until its magnetic pressure balances the magnetic tension applied by the surrounding potential arcade. Significant magnetic reconnection between the inserted flux rope and the ambient flux may occur during the relaxation process.

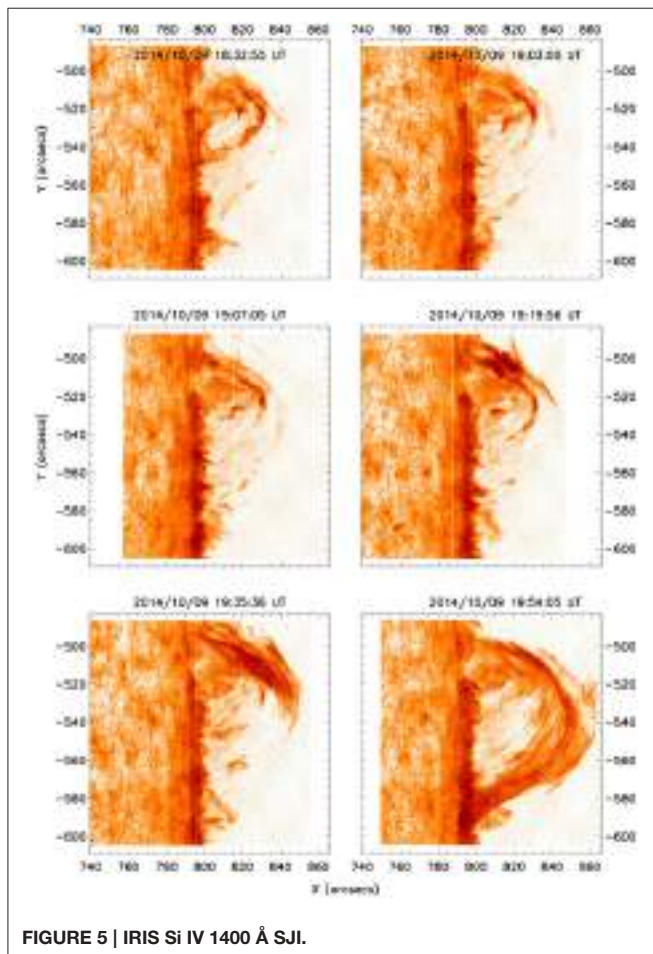


**FIGURE 5 |** IRIS Si IV 1400 Å SJI.

Therefore, the end points of the flux rope in the relaxed model may be different from that in the original model (Su et al., 2015).

The region around the filament is modeled with high spatial resolution (HIRES) on a variable grid, while more distant regions have a lower resolution on a uniform grid. The HIRES region may contain electric currents, whereas the global model is a current-free potential field. The lower boundary condition for the HIRES region is derived by combining several LOS photospheric magnetograms obtained with the SDO/HMI as these provide better signal to noise than vector magnetograms in quiet sun regions. Since the prominence is observed near the west limb, we use magnetograms that are taken several days before the prominence reaches the limb. We combine four magnetograms, each taken at 19:00 UT, between 2014 October 2–5 to construct a high-resolution map of the radial component  $B_r$  of the magnetic field as a function of longitude and latitude at the lower boundary of the HIRES region ( $0.002 R_\odot$ ) (Su et al., 2015). The high-resolution computational domain extends about  $117^\circ$  in longitude,  $36^\circ$  in latitude, and up to  $2.05 R_\odot$  from the Sun. We use the corresponding HMI synoptic map of  $B_r$  to compute a low-resolution ( $1^\circ$ ) global potential field, which provides the side boundary conditions for the HIRES domain, and allows us to trace field lines that pass through the side boundaries of the HIRES region (Su et al., 2015).

We construct a series of models with different combinations of axial and poloidal fluxes of the inserted flux rope. We compare each model with the size, location, and shape of the filament channel and cavity, including the emission structure on the two sides of the filament channel as well as the trajectory of plasma motions. We require the best-fit model to have an overall structure consistent with the observed LOS velocities observed by IRIS and EIS.

#### 2.4.1. Forward Modeling of Stokes Profiles

To compare the models with the CoMP we calculate what the expected  $L/I$  would be for our models. To calculate the Stokes vector produced along a given LOS for the magnetic field models, we use the forward models developed by Judge and Casini (2001) and implemented in the FORWARD (Gibson et al., 2016) suite of IDL codes. The FORWARD database is available to the public<sup>5</sup> and details are provided at the website and in the literature including Rachmeler et al. (2013). A brief summary is provided here.

The forward code uses the magnetic field, temperature, density, and velocity along the LOS to calculate the level population and emitted polarization profile for the Fe XIII 1074.7 nm transition. For our model, we assume an exponential isothermal atmosphere with a temperature of 1.5 MK and use HYDROCALC.pro to calculate the remaining parameters required for the forward calculations. It outputs Stokes I, Q, U, V and for the purpose of this study we use the relative linear polarization ( $L/I$ ) and relative circular polarization ( $V/I$ ). The models were based on SDO/HMI magnetograms and were

<sup>5</sup><http://www.hao.ucar.edu/FORWARD/>.

initially rotated to the 2014-10-04 23:59 UT. To compare with the CoMP observations, the models were rotated to the limb so that they match the observation time of the CoMP QuickInvert data, at 21:13 UT.

## 3. RESULTS

### 3.1. Observations

The prominence is composed of two linear structures with a N-S oriented component and an E-W component with a southern pitch. **Figure 1** shows what the prominence looked like in AIA 193 Å on 4 October 2014 at 18:18 UT (left) and at the beginning of the observation campaign at 18:24 UT on October 9 (right). It is sandwiched between several active regions to the north and the polar coronal hole to the south. The Sun is active during this period with small scale flares and coronal mass ejections associated with the active regions and numerous filaments on the disk.

The X-ray data displayed in **Figure 2** shows a small coronal cavity associated with the prominence. **Figures 2A,B** demonstrate how the region (inside black box) looked near the beginning of the observation run. There are several bright formations and it is not apparent which structures, if any, are associated with the prominence. The region remains stable until at 19:09 UT when there is an increase in X-ray emission just above the limb. The black arrows in **Figures 2C,D** point to this

region of increased X-ray emission in the 19:15 UT image. This is the last image XRT took until 19:42 UT, **Figures 2E,F**. At this time, the X-ray emission has increased around a circular structure which we identify as the cavity. Furthermore, there is now X-ray emission near the center of the cavity that persists throughout the remainder of the observations. **Figures 2G,H** shows the cavity near the end of the observation run. Black arrows point to the bright X-ray emission near the center of the cavity.

The coronal cavity and overlying arcade are also well sampled with EIS. **Figures 3, 4** compare raster scans before and during the eruption. The top row of **Figure 3** relates the intensity map (inverse log) for the three Fe lines of the prominence system prior to the eruption. The vertical white stripes represent missing data. The outline of the prominence as seen in Fe XV is overlaid for each image. The southern edge of the cavity is seen in the Fe XII 195.12 Å and Fe XIII 202.04 Å lines as a sharp decrease in intensity just south of the prominence starting from the limb at  $(770'', -570'')$  extending radially out to the edge of the field of view. Interestingly, the Fe XV 284.16 Å line does not show this trend. The Doppler velocity map (middle row) shows a quiet region lacking large-scale LOS flows. Velocities that fall within the error for the measurements are scaled to white. The images showing line widths (bottom row) exhibit some regions around the prominence with higher than average widths, especially in the Fe XV 284.16 Å line. These elevated line widths could indicate that turbulent motions are present.

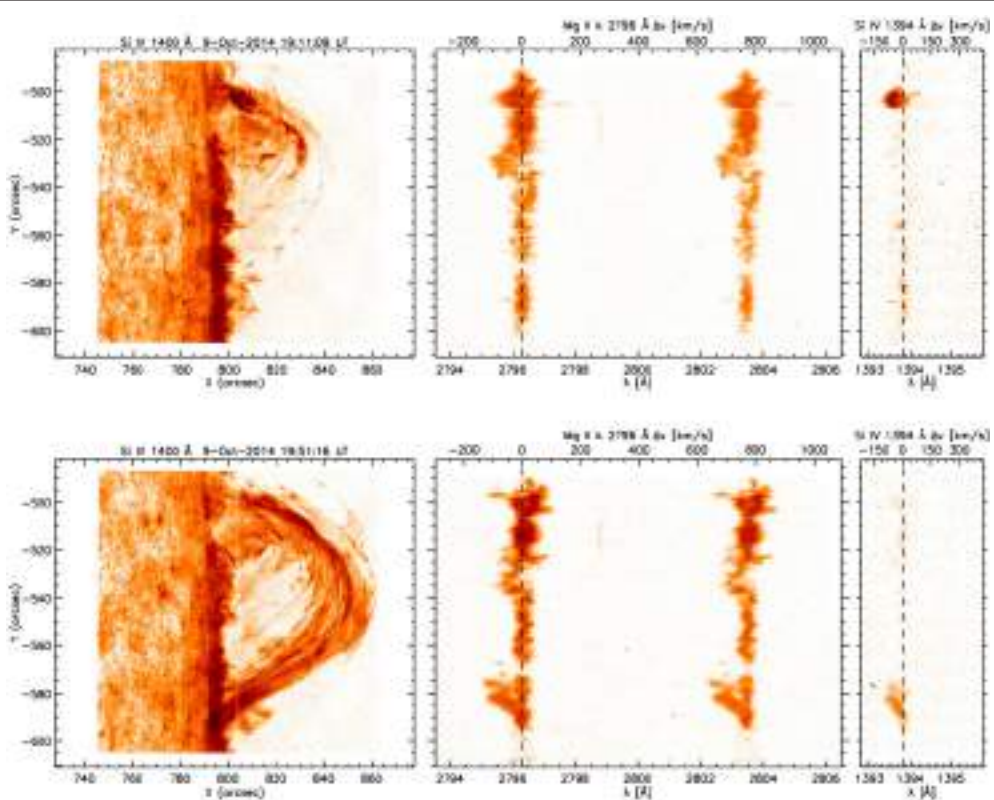


**FIGURE 6 | Left:** IRIS Si IV 1400 Å. **Middle:** Mg II 2796 Å spectra. **Right:** Si IV 1394 Å spectra. In each spectra panel, the top axis x-axis is the Doppler velocity whose reference wavelength is marked by a dashed line.

The top row of **Figure 4** shows the region during the eruption. Cool plasma is now present along an arc as an absorption feature in the Fe XV 284.16 Å. The Doppler velocity maps show the eruption is strongly blue shifted for all three Fe lines throughout the eruption site as well as the region just north of the prominence. Additionally, the line widths for these regions are large compared to the pre-eruptive state. There is flowing material around the cavity but the structure of the cavity and prominence remain stable. During and after the eruption there is evidence for turbulence and heating within the cavity.

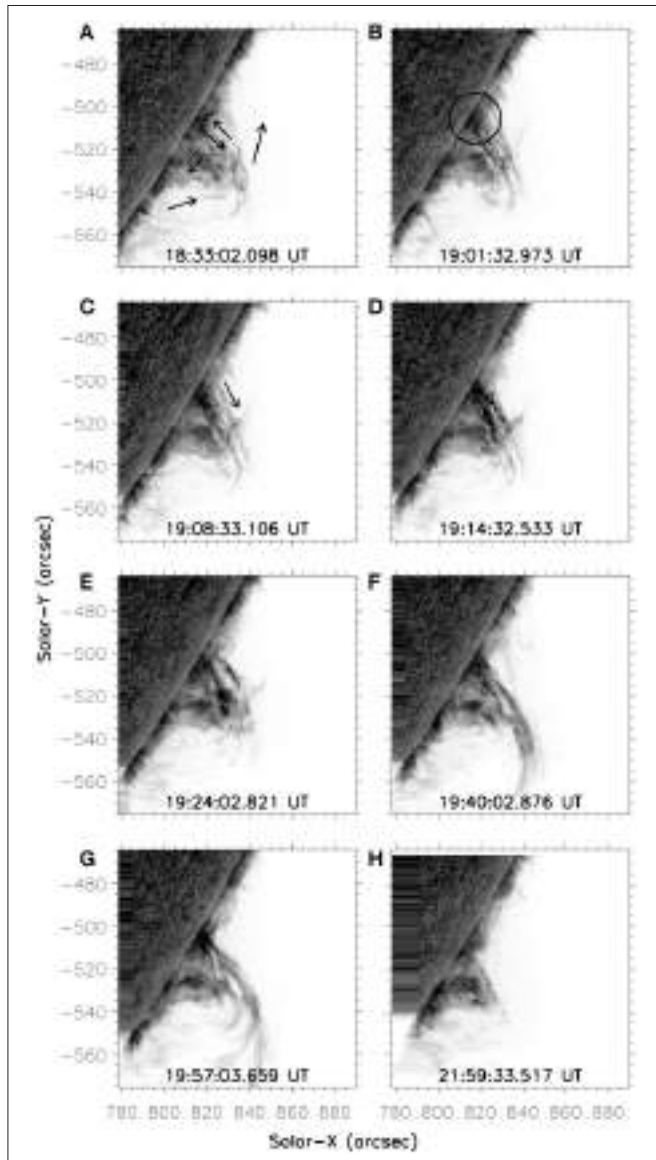


**FIGURE 7 |** Hinode SOT Ca II H-line observations (inverse intensity) of the prominence during the eruption. Panels (A,B) shows the prominence prior to the eruption with the arrows (A) indicating plasma motions and the base of the eruption is circled in (B). Panels (C–E) show the initial phase of the eruption. The arrow points in the direction of the eruption. Panels (F,G) show the trajectory of the eruption and Panel (H) shows the prominence after the eruption.

The chromospheric observations provide clues about the structure of the coronal cavity and overlying arcade when an eruption forces chromospheric plasma to flow over the cavity. **Figure 5** provides an overview of the evolution of the eruption as observed in the IRIS Si IV 1400 Å SJI. The observations start with a prominence that appears in a stable configuration exhibiting minor plasma flows (top row). At 19:07 UT, the northern edge of the prominence brightens (middle row) and the bright plasma travels up and out along the outer edge of the prominence. Once the plasma reaches a certain height it cascades back toward the limb (bottom row). The cool plasma flows along an arc that mimics the shape of the prominence. The eruption is over by 21 UT when the system returns to its original state. Doppler velocity measurements of the chromospheric plasmas also show a predominantly blue-shifted flow. **Figure 6** presents Si IV 1400 Å SJI with simultaneous spectra of Mg II 2796 Å and Si IV 1394 Å when the slit is just above the spicule region near the beginning of the eruption (top row) and near the end of the eruption (bottom row).

**Figure 7** and Supplementary Video 1 present high resolution SOT data showing striking details of the prominence and eruption. Initially, the prominence appears in a stable configuration with bi-directional plasma flows along the northern edge. This part of the prominence is highly stratified with the flows divided by regions with scant emission. **Figures 7A,B** show the prominence prior to the eruption with arrows pointing in the directions of plasma flow and a circle around the region where an intensity enhancement is seen in the minutes before the eruption. **Figure 7C** shows the time when the eruption starts. At this time, the bulk motion is in the direction of the arrow. As the eruption evolves, two bright ridges are prominent with regions of decreased intensity on either side. **Figures 7D,E** show that despite the upward bulk motion, the plasma does not move beyond the linear extrusion at the top of the prominence. In fact, the plasma flow is stalled as it encounters this barrier and the prominence experiences oscillatory motions in the regions around the two bright ridges. Eventually, the barrier is breached **Figure 7F** and plasma flows up along an arc, over the spine, exiting the FOV. Motions in the central regions of the prominence do not significantly change during or after the eruption. The motion slows and the plasma falls back down along the original trajectory path with some of the plasma flowing northward leaving the upper FOV **Figure 7G**. By the end of the observation run, the prominence is noticeably smaller **Figure 7H**.

Composite images of the X-ray emission with the SOT data are shown in **Figure 8** and Supplementary Video 2. The X-ray data is scaled using an orange color table while the SOT image is a grayscale image. The time differences between the XRT images and nearest SOT image range from 1 to 30 s. Regions with low X-ray emission are set to be transparent with respect to the SOT data. Prior to the eruption, the prominence sits in a region with little X-ray emission. An arrow points to the eruption site where the X-ray emission increases just off the limb and the chromospheric plasma is ejected. After the pause in observations, the X-ray emission is strongest just outside the chromospheric plasma flows. A circle encompasses the bright X-ray emission that forms near the top of the prominence in

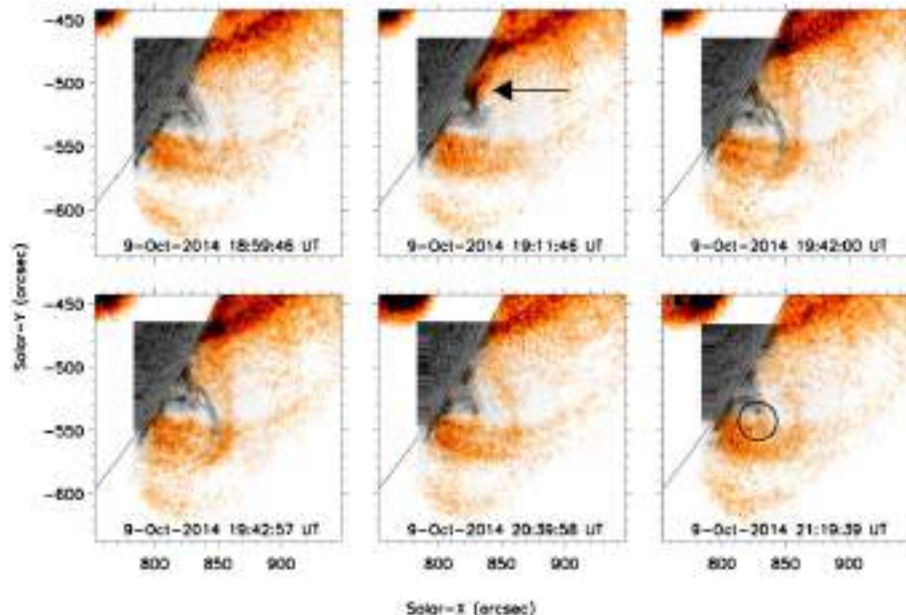


**FIGURE 8 | SOT inverse intensity (black and white) with XRT inverse intensity overlay (orange) of the prominence and cavity system.** The arrow points to the increased X-ray emission at the start of the eruption. The circle outlines a region of increased X-ray emission after the eruption.

**Figure 8.** These observations indicate that the eruption of the cool plasma observed by SOT was initiated by the incursion of hot plasma observed by XRT.

### 3.2. Model Results and Comparison to Observations

We construct several models with varying axial and poloidal fields and compare them with the observations. The model that best fit the observations has the correct magnetic field orientation to account for the observed plasma motions, Doppler velocities, and structures seen in XRT and the EUV data. **Figure 9** presents the best model (Model 1) along with the potential field model and a highly twisted flux rope model (Model 2). The initial inserted flux rope for Model 1 has axial and poloidal fluxes of  $2e20$  Mx and  $0$  Mx/cm, respectively. Model 2 has the same initial axial flux and  $-2e10$  Mx/cm poloidal flux. Both flux rope models have left helical twist and dextral chirality. After a 30,000-iteration relaxation, the models relax toward a force-free state.

**Figure 9A** shows a grayscale map of the LOS magnetic field with positive fields scaled white and negative fields black. The blue line shows the path of the inserted flux rope and the circles at the ends represent the footpoints of that flux rope. The path is selected to be along the PIL and the footpoints of the flux rope are embedded within patches of strong magnetic fields near the PIL. The same path is utilized for all of the models and a comparison of selected magnetic field lines (colored lines) for the three models are shown in **Figures 9 D,G,J** with an AIA 193 Å background image taken on 4 October 2014 at 23:59 UT. White arrows point to field lines that represent the orientation of the magnetic field.

The middle column of **Figure 9** compares the three models rotated to the limb. The background image is an AIA 171 Å taken at 20:00 UT on 9 October 2014. **Figure 9B** shows the prominence with white arrows pointing to regions of plasma flow around the cavity. The right column compares the models with the background image as XRT thin-Be taken at 19:42 UT. **Figure 9C** shows the cavity with white arrows pointing to the regions of increased X-ray intensity around the coronal cavity. The bottom three rows of **Figure 9** show selected field lines from the models in comparison to the Hinode/XRT and SDO/AIA observations.

**Figure 9** shows that the observed arc-like filament structure is corresponding to the overlying magnetic field lines in the models, which are more sheared in Model 1 (**Figure 9G**) and nearly perpendicular to the filament channel for Model 2 (**Figure 9J**). Model 1 exhibits a weakly twisted flux rope structure after the relaxation, although the initial inserted flux bundle has no twist. This twist may be produced during the relaxation due to reconnection between the inserted sheared flux bundle and the overlying arcade. Model 1, shows magnetic field lines oriented in a way that could produce the observed Doppler velocities but the highly twisted flux rope, has magnetic field lines in the wrong orientation to account for the observed LOS Doppler velocities. The sheared overlying field lines can account for the aforementioned observed blue-shift flow in the overlying arcade. Therefore, we think that the weakly twisted flux rope fit the observations better. In comparison to the potential field model, and Model 2, the weakly twisted flux rope clearly shows a much better match to both the on-disk filament channel and the cavity observed on the limb by XRT.

One feature in the IRIS Si IV 1394 Å spectra is a persistent region with no emission on a portion of the on-disk scans. This

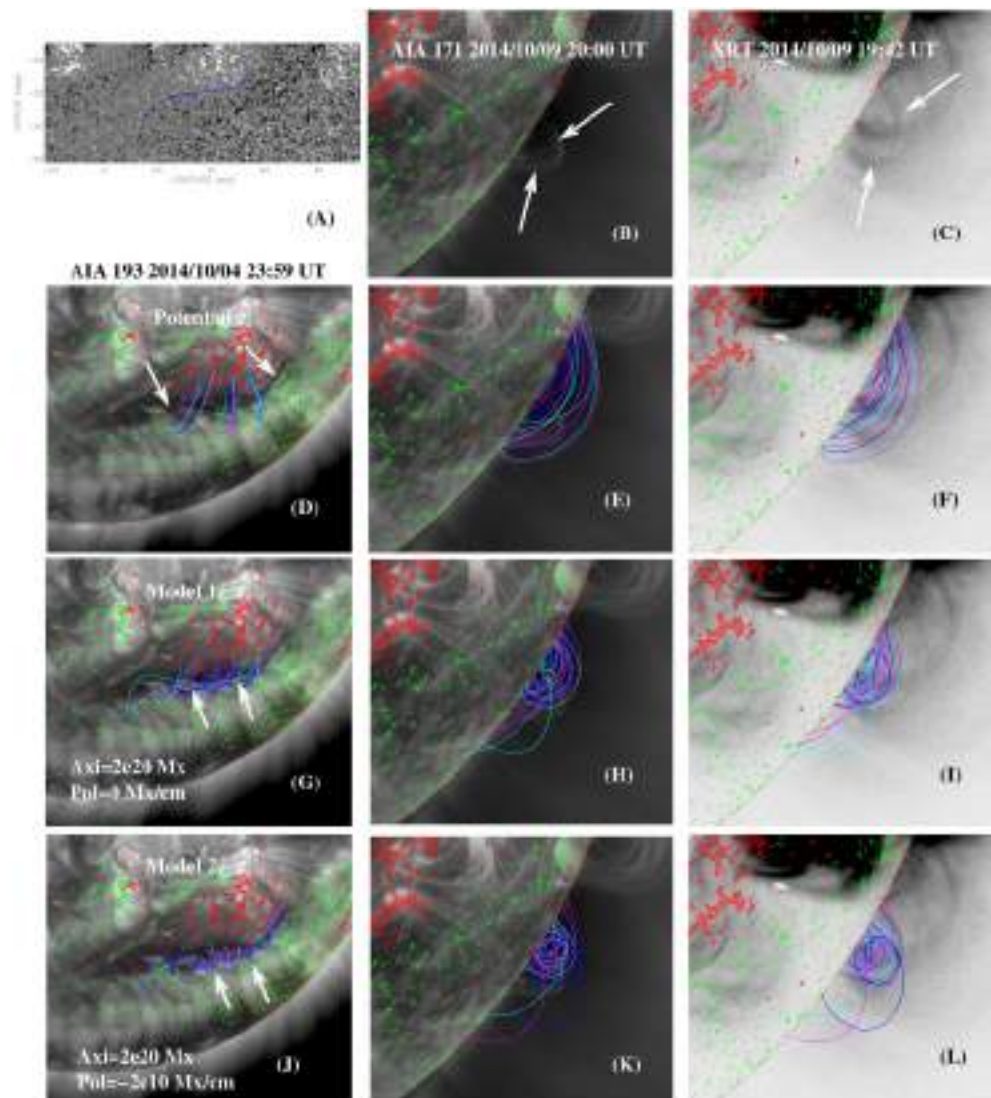


**FIGURE 9 | Magnetic field models constructed using the flux rope insertion method in comparison to observations.** The models use combined LOS magnetograms observed by SDO/HMI from 2014 October 2 to October 5 at 19:00 UT. Panel **(A)** grayscale map of the LOS magnetic field with positive (white) and negative (black). The blue curve is the path of the flux rope and the circles indicate the footpoints of the flux tube. The bottom three rows show color contours of the magnetogram as positive (red) and negative (green) overlay on AIA 193 Å taken at 23:59 UT on October 4 (**left**), AIA 171 Å taken at 20:00 UT on October 9 (**middle**), and Hinode/XRT Be-thin taken at 19:42 UT on October 9 (**right**) with the color lines referring to selected magnetic field lines. Panels **(B,C)** AIA 171 Å observations and XRT Be-thin observations with arrows pointing out plasma motions and the coronal cavity. The color lines in the bottom rows refer to selected magnetic field lines from the potential field **(D–F)**, Model 1 **(G–I)**, and Model 2 **(J–L)**.

region is outlined by two dotted lines in the top and bottom rows of **Figure 10**. This region persists throughout the observations but its location depends on the slit position. As the slit moves toward the limb, the region with no emission shifts northward until the slit reaches the limb. The Si IV emission just above the horizontal lines is also red-shifted relative to the average line centroid. The middle row of **Figure 10** shows one of two slit positions that are almost exactly on the solar limb. The emission is strong in this region throughout the entire slit length. Once the slit clears the limb, the region of reduced emission is located over the prominence (bottom row) and the region continues to

exhibit a redshift relative to the line average. There is also a noticeable decrease in the number of spicules near the base of the prominence. The orientation of the spicules in the peripheral regions of the prominence suggest they are curved away from the prominence.

We compare the location of the depleted region observed in the IRIS Si IV 1394 Å spectra with the location of the PIL in Model 1. **Figure 11** shows an IRIS Si IV 1400 Å SJ image, with the correct prominence orientation, along with contours (green/negative; red/positive) of the SDO/HMI LOS magnetic field model data. The region of reduced emission is located

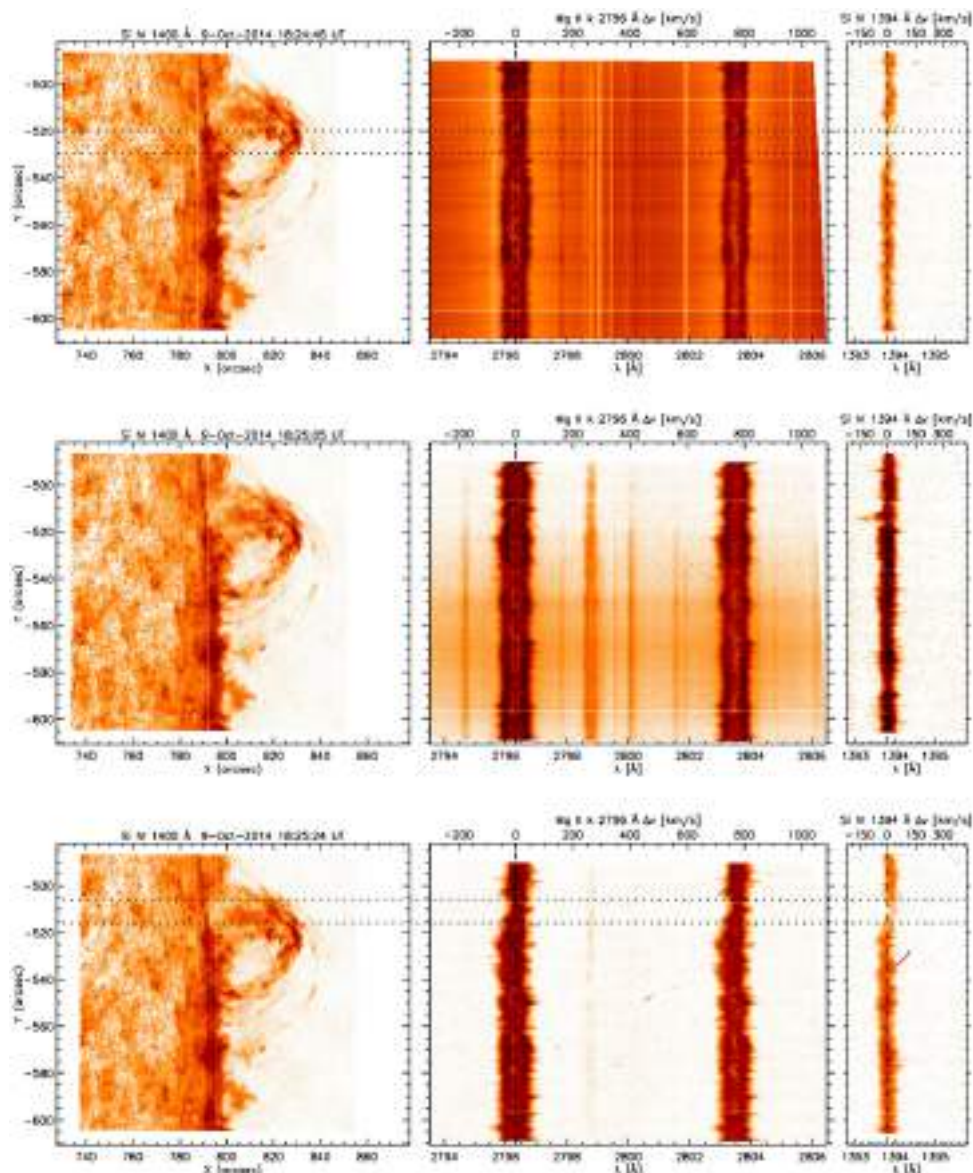


**FIGURE 10 | Left:** IRIS Si IV 1400 Å with corresponding spectra for the Mg II 2796 Å (**middle**) and Si IV 1394 Å (**right**). The vertical dashed lines represent the rest wavelength. The horizontal dotted lines outline a region of decreased Si IV 1394 Å line intensity in the right image.

between the two white dotted lines. These are at the same location of the horizontal lines in the top row of **Figure 10**. A bipole sits near the region of reduced emission. The pink line is a small field line from Model 1 that crosses the PIL indicating its location. The right image shows the same location on the model data before it was rotated to the limb.

To potentially constrain the model parameters we compare theoretical  $L/I$  measurements of Model 1 and the potential arcade with  $L/I$  CoMP measurements in **Figure 12**. The left image is CoMP  $L/I$  (log scale) observations of the prominence region. The prominence sits just above the limb (below  $1.3 R_{\odot}$ ) so we cannot directly observe the prominence-cavity system in the CoMP data. However, some elements of the structure could still

be present. The CoMP data does exhibit a linear decrease in intensity in a similar location to the potential arcade (middle panel) and Model 1 (right panel). The bright feature in the CoMP data is not seen in either of the models. The models do not contain information about other structures near the region so it is possible that the bright feature is not associated with the prominence. There are also minor differences between the potential arcade model and Model 1 far away from the disk. However, the CoMP data alone is not different enough to truly distinguish between the two models. Model 1 is a small flux rope embedded in a potential arcade, so at distances far from the flux rope, the  $L/I$  signatures are very similar to those of the potential arcade.

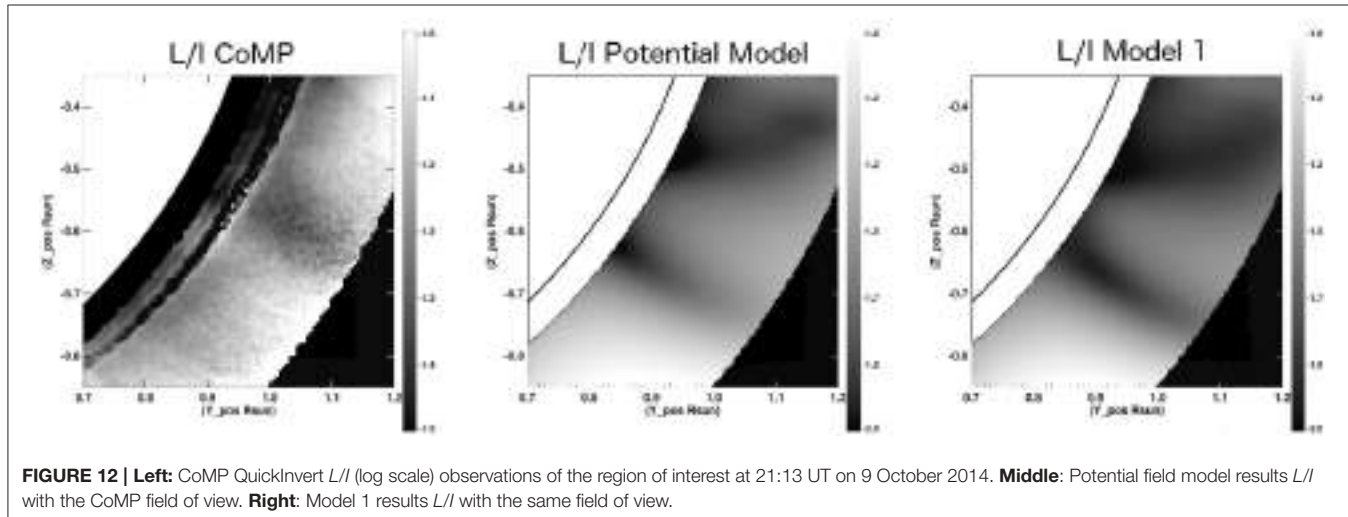
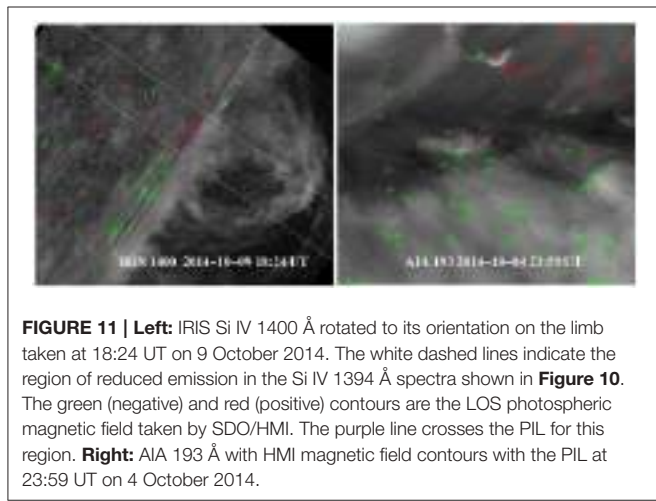
## 4. DISCUSSION

We present observations of a prominence and cavity system with an ensuing ancillary eruption that serves to highlight some of the topological features of the system. We find the prominence-cavity system maintains its structure during the event but heating is observed as an increase in X-ray emission around the coronal cavity and just above the prominence. Previous observational studies of bright X-ray emission within coronal cavities observed long-lived polar crown prominences where the bright core had already formed (Hudson et al., 1999; Reeves et al., 2012). The X-ray bright core always sits directly above the prominence although temperature structures found using EUV data (Schmit et al., 2009; Kucera et al., 2012) and white light studies find dynamic structures throughout the cavity (Habbal et al., 2010). The longevity of polar crown prominences, sometimes lasting several solar rotations, suggest a continuous heating process is needed to maintain the bright central emissions. Our observations suggest the heating inside the cavity is from a current sheet formed at a BPSS (Fan and

Gibson, 2006). The BPSS forms a sheath or tunnel enclosing the dipped prominence field lines extending from the prominence footpoints in the photosphere, up into the cavity and would appear to be central to the cavity when viewed edge on. The BPSS can explain the steady-state X-ray emissions observed in long-lived polar crown prominences and it can explain the rapid increase in X-ray emission when a stable prominence system is disturbed.

The eruption causes oscillatory motions in the prominence near the eruption site but plasma motions within the central regions of the prominence do not change suggesting the inner prominence is structurally isolated from the eruption site. We model the prominence-cavity system as a flux rope situated under a coronal arcade. After testing several combinations of axial and poloidal fluxes we found the model that fit the observations best was that of a weakly twisted flux rope with dextral chirality.

The flux rope has opposite chirality than we would expect for a southern prominence Martin et al. (1994). The active regions north of the prominence have a positive (red) leading polarity whereas the prominence has the opposite (Figure 9). The dextral chirality is based on the comparison with the AIA emissions on the two sides of the filament channel. Through a statistical study Su et al. (2010) found that the emission on the two sides of the filament channel are asymmetric with one side showing bright and curved loops and the other side faint and straight emissions. They proposed that the bright curve features (on the southern side of filament channel for our case) are corresponding to the field lines that turn into the flux rope, and the straight faint features to the north, are the legs of the large overlying arcade. This idea was also confirmed by the magnetic field modeling in Su and van Ballegooijen (2012). The dextral flux rope model matches the direction of the observed bright curved feature on the southern side for our prominence, Figure 9G. The configuration also explains the trajectory of the erupting plasma as it flowed along magnetic field lines within the overlying arcade. The orientation of the arcade is such that any plasma flowing within the arcade would exhibit a predominantly blue-shifted LOS velocity when viewed on the limb.



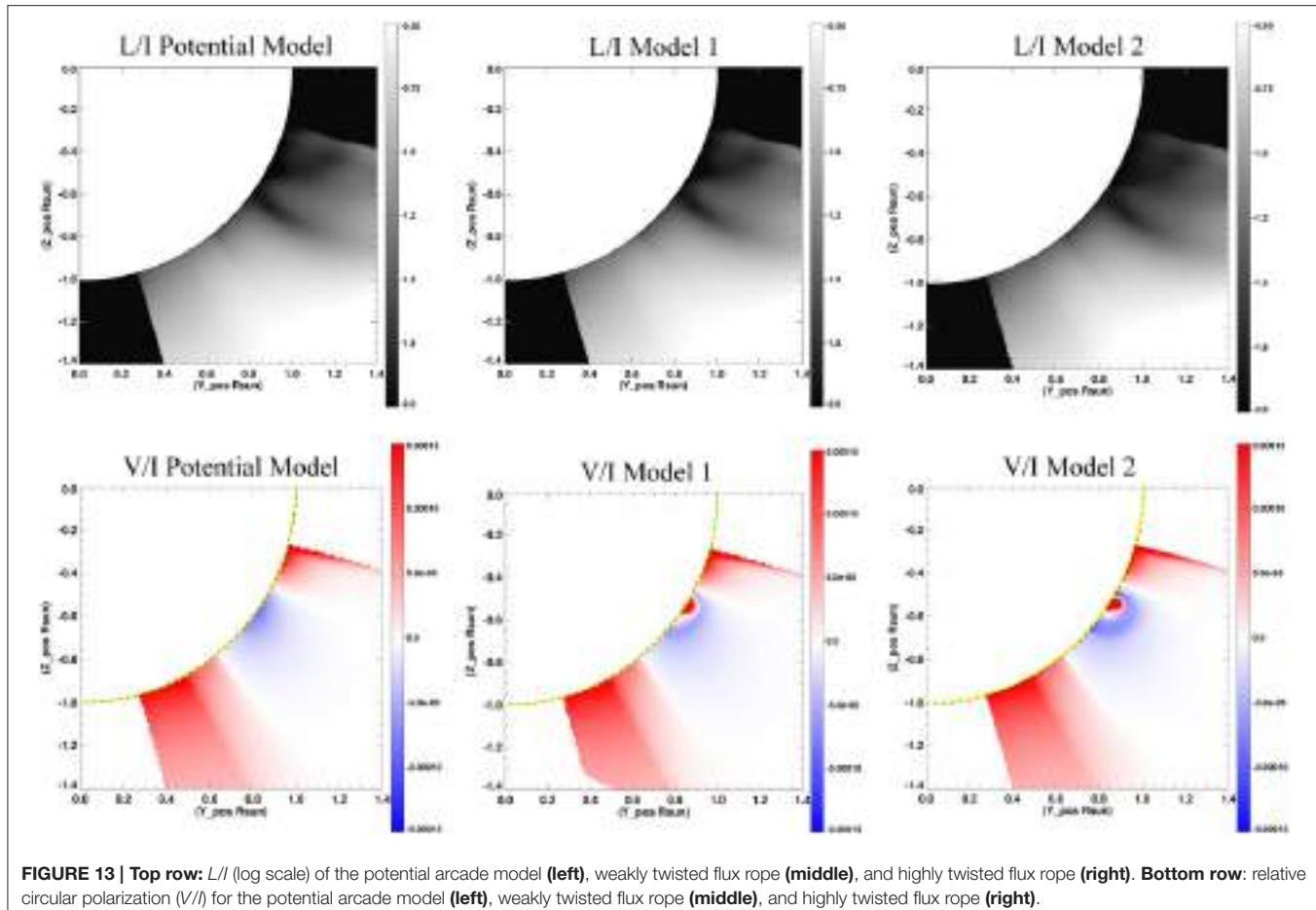


**FIGURE 13 | Top row:**  $L/I$  (log scale) of the potential arcade model (**left**), weakly twisted flux rope (**middle**), and highly twisted flux rope (**right**). **Bottom row:** relative circular polarization  $V/I$  for the potential arcade model (**left**), weakly twisted flux rope (**middle**), and highly twisted flux rope (**right**).

The decreased emission of the Si IV 1394 Å spectra on the disk and in close proximity to the prominence coincides with the location of a bipole within the PIL of the model and thus we interpret it as evidence for a bald-patch underneath the prominence. A study by López Ariste et al. (2006) used vector magnetic fields to analyze bipolar regions within a filament channel. They found that at least four of the six bipolar regions exhibited a bald-patch topology forming photospheric dips where the horizontal component of the magnetic field points from a negative toward positive polarity. They concluded the observed magnetic field topology in the photosphere tends to support models of prominence based on magnetic dips located within weakly twisted flux tubes. Their underlying and lateral extensions form photospheric dips both within the channel and below barbs.

A comparison of the model with CoMP  $L/I$  observations were inconclusive as the prominence structure lies just above the limb but below the CoMP FOV. The flux rope for this model is small and embedded in a potential arcade. Far from the flux rope, the linear polarization will be similar to that of the overlying arcade. Bąk-Stęślicka et al. (2016) performed a statistical study of quiescent coronal cavities observed with CoMP and found that coherent, often, ring-shaped, LOS Doppler velocity flows are common within cavities that possess a

“lagomorphic” signature in the  $L/I$  polarization. The portion of the prominence we are studying is not oriented in the E-W direction and may not be in the best orientation to observe these signatures. Another reason that could account for the differences between the CoMP data and models is that our model only considers the local fields around the prominence. Differences observed in CoMP could be from other coronal structures.

Even if we could make linear polarization measurements up to the solar disk we would still have a difficult time distinguishing the  $L/I$  signatures of small flux ropes from those of the overlying potential arcade. The top row of Figure 13 compares the  $L/I$  signatures of a potential arcade model, Model 1 and Model 2. The linear polarization signatures are similar with varying differences in intensity. To observe the differences between the models we need to have  $V/I$  polarization measurements closer to the limb. The bottom row Figure 13 shows the  $V/I$  polarization measurements for the three models. The  $V/I$  can distinguish between the three models. Currently,  $V/I$  measurements are not practical as they require hours long integration times. However, an observatory that would be capable of making high resolution polarization measurements close to the solar limb is the proposed COronal Solar Magnetism Observatory (COSMO) (de Wijn et al., 2014). Future measurements from COSMO would clearly be very

useful in determining magnetic structures of prominence-cavity systems.

## AUTHOR CONTRIBUTIONS

PJ performed the data analysis and document preparation. KR analyzed and interpreted the data. YS provided the NLFF models and documentation thereof.

## FUNDING

PJ and KR are supported by under contract 80111112705 from Lockheed-Martin to SAO, contract NNM07AB07C from NASA to SAO, grant number NNX12AI30G from NASA to SAO, and contract Z15-12504 from HAO to SAO under a grant from AFOSR. YS is supported by the Youth Fund of Jiangsu No. BK20141043, the NSFC No. 11473071, and the “One Hundred Talent Program” of the Chinese Academy of Sciences.

## REFERENCES

- Aulanier, G., Demoulin, P., van Driel-Gesztelyi, L., Mein, P., and Deforest, C. (1998). 3-D magnetic configurations supporting prominences. II. The lateral feet as a perturbation of a twisted flux-tube. *Astron. Astrophys.* 335, 309–322.
- Bąk-Stęlicka, U., Gibson, S. E., and Chmielewska, E. (2016). Line-of-sight velocity as a tracer of coronal cavity magnetic structure. *Front. Astron. Space Sci.* 3:7. doi: 10.3389/fspas.2016.00007
- Bąk-Stęlicka, U., Gibson, S. E., Fan, Y., Bethge, C., Forland, B., and Rachmeler, L. A. (2013). The magnetic structure of solar prominence cavities: new observational signature revealed by coronal magnetometry. *Astrophys. J. Lett.* 770:L28. doi: 10.1088/2041-8205/770/2/L28
- Berger, T. E., Slater, G., Hurlburt, N., Shine, R., Tarbell, T., Title, A., et al. (2010). Quiescent prominence dynamics observed with the hinode solar optical telescope. I. Turbulent upflow plumes. *Astrophys. J.* 716, 1288–1307. doi: 10.1088/0004-637X/716/2/1288
- Chae, J., Wang, H., Qiu, J., Goode, P. R., Strous, L., and Yun, H. S. (2001). The formation of a prominence in active region NOAA 8668. I. SOHO/MDI observations of magnetic field evolution. *Astrophys. J.* 560, 476–489. doi: 10.1086/322491
- Culhane, J. L., Harra, L. K., James, A. M., Al-Janabi, K., Bradley, L. J., Chaudry, R. A., et al. (2007). The EUV imaging spectrometer for hinode. *Solar Phys.* 243, 19–61. doi: 10.1007/s1007-007-0293-1
- De Pontieu, B., Title, A. M., Lemen, J. R., Kushner, G. D., Akin, D. J., Allard, B., et al. (2014). The Interface Region Imaging Spectrograph (IRIS). *Solar Phys.* 289, 2733–2779. doi: 10.1007/s11207-014-0485-y
- de Wijn, A. G., Tomczyk, S., and Burkepile, J. (2014). “A progress update for the coronal solar magnetism observatory for coronal and chromospheric polarimetry,” in *Solar Polarization 7*, Vol. 489 of *Astronomical Society of the Pacific Conference Series*, eds K. N. Nagendra, J. O. Stenflo, Q. Qu, and M. Samooprana (San Francisco), 323.
- Dudik, J., Aulanier, G., Schmieder, B., Bommier, V., and Roudier, T. (2008). Topological departures from translational invariance along a filament observed by THEMIS. *Solar Phys.* 248, 29–50. doi: 10.1007/s11207-008-9155-2
- Fan, Y., and Gibson, S. E. (2006). On the nature of the X-ray bright core in a stable filament channel. *Astrophys. J. Lett.* 641, L149–L152. doi: 10.1086/504107
- Freeland, S. L., and Handy, B. N. (1998). Data analysis with the solarsoft system. *Solar Phys.* 182, 497–500. doi: 10.1023/A:1005038224881
- Gibson, S. E., Foster, D., Burkepile, J., de Toma, G., and Stanger, A. (2006). The calm before the storm: the link between quiescent cavities and coronal mass ejections. *Astrophys. J.* 641, 590–605. doi: 10.1086/500446
- Gibson, S. E., Kucera, T. A., White, S. M., Dove, J. B., Fan, Y., Forland, B. C., et al. (2016). FORWARD: a toolset for multiwavelength coronal magnetometry. *Front. Astron. Space Sci.* 3:8. doi: 10.3389/fspas.2016.00008
- Golub, L., Deluca, E., Austin, G., Bookbinder, J., Caldwell, D., Cheimets, P., et al. (2007). The X-Ray Telescope (XRT) for the hinode mission. *Solar Phys.* 243, 63–86. doi: 10.1007/s11207-007-0182-1
- Habbal, S. R., Druckmüller, M., Morgan, H., Scholl, I., Rušin, V., Daw, A., et al. (2010). Total solar eclipse observations of hot prominence shrouds. *Astrophys. J.* 719, 1362–1369. doi: 10.1088/0004-637X/719/2/1362
- Hudson, H., and Schwenn, R. (2000). Hot cores in coronal filament cavities. *Adv. Space Res.* 25, 1859–1861. doi: 10.1016/S0273-1177(99)00618-3
- Hudson, H. S., Acton, L. W., Harvey, K. L., and McKenzie, D. E. (1999). A stable filament cavity with a hot core. *Astrophys. J. Lett.* 513, L83–L86. doi: 10.1086/311892
- Judge, P. G., and Casini, R. (2001). “A synthesis code for forbidden coronal lines,” in *Advanced Solar Polarimetry – Theory, Observation, and Instrumentation*, volume 236 of *Astronomical Society of the Pacific Conference Series*, ed M. Sigwarth (San Francisco), 503.
- Kamio, S., Hara, H., Watanabe, T., Fredrik, T., and Hansteen, V. H. (2010). Modeling of EIS spectrum drift from instrumental temperatures. *Solar Phys.* 266, 209–223. doi: 10.1007/s11207-010-9603-7
- Kobelski, A. R., Saar, S. H., Weber, M. A., McKenzie, D. E., and Reeves, K. K. (2014). Calibrating data from the hinode/X-ray telescope and associated uncertainties. *Solar Phys.* 289, 2781–2802. doi: 10.1007/s11207-014-0487-9
- Kosugi, T., Matsuzaki, K., Sakao, T., Shimizu, T., Sone, Y., Tachikawa, S., et al. (2007). The hinode (solar-B) mission: an overview. *Solar Phys.* 243, 3–17. doi: 10.1007/s11207-007-9014-6
- Kucera, T. A., Gibson, S. E., Schmit, D. J., Landi, E., and Tripathi, D. (2012). Temperature and extreme-ultraviolet intensity in a coronal prominence cavity and streamer. *Astrophys. J.* 757, 73. doi: 10.1088/0004-637X/757/1/73
- Kuperus, M., and Raadu, M. A. (1974). The support of prominences formed in neutral sheets. *Astron. Astrophys.* 31:189.
- Lemen, J. R., Title, A. M., Akin, D. J., Boerner, P. F., Chou, C., Drake, J. F., et al. (2012). The Atmospheric Imaging Assembly (AIA) on the Solar Dynamics Observatory (SDO). *Solar Phys.* 275, 17–40. doi: 10.1007/s11207-011-9776-8
- Lin, H., Kuhn, J. R., and Coulter, R. (2004). Coronal magnetic field measurements. *Astrophys. J.* 613, L177–L180. doi: 10.1086/425217
- Liu, W., De Pontieu, B., Vial, J.-C., Title, A. M., Carlsson, M., Uitenbroek, H., et al. (2015). First high-resolution spectroscopic observations of an erupting prominence within a coronal mass ejection by the Interface Region Imaging Spectrograph (IRIS). *Astrophys. Lett.* 803, 85. doi: 10.1088/0004-637X/803/2/85
- López Ariste, A., Aulanier, G., Schmieder, B., and Sainz Dalda, A. (2006). First observation of bald patches in a filament channel and at a barb endpoint. *Astron. Astrophys.* 456, 725–735. doi: 10.1051/0004-6361:20064923
- Low, B. C., and Hundhausen, J. R. (1995). Magnetostatic structures of the solar corona. 2: The magnetic topology of quiescent prominences. *Astrophys. Lett.* 443, 818–836. doi: 10.1086/175572

## ACKNOWLEDGMENTS

*IRIS* is a NASA small explorer mission developed and operated by LMSAL with mission operations executed at NASA Ames Research center and major contributions to downlink communications funded by ESA and the Norwegian Space Centre. *Hinode* is a Japanese mission developed and launched by ISAS/JAXA, with NAOJ as domestic partner and NASA and STFC (UK) as international partners. It is operated by these agencies in co-operation with ESA and NSC (Norway). The authors acknowledge Dr. Adriaan van Ballegooijen for his valuable suggestions on the magnetic field modeling.

## SUPPLEMENTARY MATERIAL

The Supplementary Material for this article can be found online at: <http://journal.frontiersin.org/article/10.3389/fspas.2016.00010>

- Mackay, D. H., Karpen, J. T., Ballester, J. L., Schmieder, B., and Aulanier, G. (2010). Physics of solar prominences: II-magnetic structure and dynamics. *Space Sci. Rev.* 151, 333–399. doi: 10.1007/s11214-010-9628-0
- Malherbe, J. M., and Priest, E. R. (1983). Current sheet models for solar prominences. I Magnetohydrostatics of support and evolution through quasi-static models. *Astron. Astrophys.* 123, 80–88.
- Martin, S. F. (1973). The evolution of prominences and their relationship to active centers (a review). *Solar Phys.* 31, 3–21. doi: 10.1007/BF00156070
- Martin, S. F. (1990). “Conditions for the formation of prominences as inferred from optical observations,” in *IAU Colloq. 117: Dynamics of Quiescent Prominences*, Vol. 363 of *Lecture Notes in Physics*, eds V. Ruzdjak and E. Tandberg-Hanssen (Berlin: Springer Verlag), 1–44.
- Martin, S. F., Bilmoria, R., and Tracadas, P. W. (1994). “Magnetic field configurations basic to filament channels and filaments,” in *NATO Advanced Science Institutes (ASI) Series C*, Vol. 433 of *NATO Advanced Science Institutes (ASI) Series C*, eds R. J. Rutten and C. J. Schrijver (Dordrecht), 303.
- Parenti, S. (2014). Solar prominences: observations. *Living Rev. Solar Phys.* 11, 1. doi: 10.12942/lrsp-2014-1
- Pneuman, G. W. (1983). The formation of solar prominences by magnetic reconnection and condensation. *Solar Phys.* 88, 219–239. doi: 10.1007/BF00196189
- Priest, E. (2014). *Magnetohydrodynamics of the Sun*. Cambridge, MA: Cambridge University Press.
- Priest, E. R., Hood, A. W., and Anzer, U. (1989). A twisted flux-tube model for solar prominences. I - General properties. *Astrophys. Lett.* 344, 1010–1025. doi: 10.1086/167868
- Rachmeler, L. A., Gibson, S. E., Dove, J. B., DeVore, C. R., and Fan, Y. (2013). Polarimetric properties of flux ropes and sheared arcades in coronal prominence cavities. *Solar Phys.* 288, 617–636. doi: 10.1007/s11207-013-0325-5
- Reeves, K. K., Gibson, S. E., Kucera, T. A., Hudson, H. S., and Kano, R. (2012). Thermal properties of a solar coronal cavity observed with the X-ray telescope on hinode. *Astrophys. J.* 746, 146. doi: 10.1088/0004-637X/746/2/146
- Rust, D. M., and Kumar, A. (1994). Helical magnetic fields in filaments. *Solar Phys.* 155, 69–97. doi: 10.1007/BF00670732
- Schmieder, B., Tian, H., Kucera, T., López Ariste, A., Mein, N., Mein, P., et al. (2014). Open questions on prominences from coordinated observations by IRIS, Hinode, SDO/AIA, THEMIS, and the Meudon/MSDP. *Astron. Astrophys.* 569:A85. doi: 10.1051/0004-6361/201423922
- Schmitt, D. J., Gibson, S. E., Tomczyk, S., Reeves, K. K., Sterling, A. C., Brooks, D. H., et al. (2009). Large-scale flows in prominence cavities. *Astrophys. J.* 700, L96–L98. doi: 10.1088/0004-637X/700/2/L96
- Schou, J., Scherrer, P. H., Bush, R. I., Wachter, R., Couvidat, S., Rabello-Soares, M. C., et al. (2012). Design and ground calibration of the Helioseismic and Magnetic Imager (HMI) instrument on the Solar Dynamics Observatory (SDO). *Solar Phys.* 275, 229–259. doi: 10.1007/s11207-011-9842-2
- Schröter, E.-H., Vázquez, M., and Wyller, A. A. (eds.). (1987). *The Role of Fine-Scale Magnetic Fields on the Structure of the Solar Atmosphere*. Cambridge: Cambridge University Press.
- Smith, S. F. (1968). “The formation, structure and changes in filaments in active regions,” in *Structure and Development of Solar Active Regions*, Vol. 35 of *IAU Symposium*, ed K. O. Kiepenheuer, 267. doi: 10.1007/978-94-011-6815-1\_42
- Stark, J.-L., and Murtagh, F. (2002). *Astronomical Image and Data Analysis*. Berlin: Springer.
- Su, Y., Surges, V., van Ballegooijen, A., DeLuca, E., and Golub, L. (2011). Observations and magnetic field modeling of the flare/coronal mass ejection event on 2010 april 8. *Astrophys. J.* 734, 53. doi: 10.1088/0004-637X/734/1/53
- Su, Y., and van Ballegooijen, A. (2012). Observations and magnetic field modeling of a solar polar crown prominence. *Astrophys. J.* 757, 168. doi: 10.1088/0004-637X/757/2/168
- Su, Y., van Ballegooijen, A., and Golub, L. (2010). Structure and dynamics of quiescent filament channels observed by hinode/XRT and STEREO/EUVI. *Astrophys. J.* 721, 901–910. doi: 10.1088/0004-637X/721/1/901
- Su, Y., van Ballegooijen, A., Lites, B. W., Deluca, E. E., Golub, L., Grigis, P. C., et al. (2009). Observations and nonlinear force-free field modeling of active region 10953. *Astrophys. J.* 691, 105–114. doi: 10.1088/0004-637X/691/1/105
- Su, Y., van Ballegooijen, A., McCauley, P., Ji, H., Reeves, K. K., and DeLuca, E. E. (2015). Magnetic structure and dynamics of the erupting solar polar crown prominence on 2012 march 12. *Astrophys. J.* 807, 144. doi: 10.1088/0004-637X/807/2/144
- Titov, V. S., and Démoulin, P. (1999). Basic topology of twisted magnetic configurations in solar flares. *Astron. Astrophys.* 351, 707–720.
- Tomczyk, S., Card, G. L., Darnell, T., Elmore, D. F., Lull, R., Nelson, P. G., et al. (2008). An instrument to measure coronal emission line polarization. *Solar Phys.* 247, 411–428. doi: 10.1007/s11207-007-9103-6
- Tsuneta, S., Ichimoto, K., Katsukawa, Y., Nagata, S., Otsubo, M., Shimizu, T., et al. (2008). The solar optical telescope for the hinode mission: an overview. *Solar Phys.* 249, 167–196. doi: 10.1007/s11207-008-9174-z
- Vaiana, G. S., Krieger, A. S., and Timothy, A. F. (1973). Identification and analysis of structures in the corona from X-Ray photography. *Solar Phys.* 32, 81–116. doi: 10.1007/BF00152731
- van Ballegooijen, A. A. (2004). Observations and modeling of a filament on the sun. *Astrophys. J.* 612, 519–529. doi: 10.1086/422512
- van Ballegooijen, A. A., and Martens, P. C. H. (1989). Formation and eruption of solar prominences. *Atmosph. J.* 343, 971–984. doi: 10.1086/167766
- van Ballegooijen, A. A., Priest, E. R., and Mackay, D. H. (2000). Mean field model for the formation of filament channels on the sun. *Astrophys. J.* 539, 983–994. doi: 10.1086/309265
- Vial, J.-C., and Engvold, O. (eds.). (2015). *Solar Prominences*, Vol. 415 of *Astrophysics and Space Science Library*. Springer International Publishing Switzerland.
- Warren, H. P., Ugarte-Urra, I., Young, P. R., and Stenborg, G. (2011). The temperature dependence of solar active region outflows. *Astrophys. J.* 727, 58. doi: 10.1088/0004-637X/727/1/58
- Yoshimura, K., and McKenzie, D. E. (2015). Calibration of hinode/XRT for coalignment. *Solar Phys.* 290, 2355–2372. doi: 10.1007/s11207-015-0746-4
- Young, P. (2013). *EIS Software Note No. 16*, ver. 2.5. Available online at: <http://solarb.mssl.ucl.ac.uk:8080/eiswiki/Wiki.jsp?page=EISAnalysisGuide>

**Conflict of Interest Statement:** The authors declare that the research was conducted in the absence of any commercial or financial relationships that could be construed as a potential conflict of interest.

Copyright © 2016 Jibben, Reeves and Su. This is an open-access article distributed under the terms of the Creative Commons Attribution License (CC BY). The use, distribution or reproduction in other forums is permitted, provided the original author(s) or licensor are credited and that the original publication in this journal is cited, in accordance with accepted academic practice. No use, distribution or reproduction is permitted which does not comply with these terms.



# Lifecycle of a Large-Scale Polar Coronal Pseudostreamer/Cavity System

**Chloé Guennou<sup>1\*</sup>, Laurel A. Rachmeler<sup>2</sup>, Daniel B. Seaton<sup>2,3,4</sup> and Frédéric Auchère<sup>5</sup>**

<sup>1</sup> Departamento de Astrofísica, Instituto de Astrofísica de Canarias, La Laguna, Universidad de La Laguna, La Laguna, Spain,

<sup>2</sup> Royal Observatory of Belgium, Uccle, Belgium, <sup>3</sup> Cooperative Institute for Research in Environmental Sciences, University of Colorado Boulder, Boulder, CO, USA, <sup>4</sup> National Centers for Environmental Information, National Oceanic and Atmospheric Administration, Boulder, CO, USA, <sup>5</sup> Stellar and Solar Physics, Institut d’Astrophysique Spatiale, Orsay, France

We report on an exceptional large-scale coronal pseudostreamer/cavity system in the southern polar region of the solar corona that was visible for approximately a year starting in February 2014. It is unusual to see such a large closed-field structure embedded within the open polar coronal hole. We investigate this structure to document its formation, evolution and eventually its shrinking process using data from both the PROBA2/SWAP and SDO/AIA EUV imagers. In particular, we used EUV tomography to find the overall shape and internal structure of the pseudostreamer and to determine its 3D temperature and density structure using DEM analysis. We found that the cavity temperature is extremely stable with time and is essentially at a similar or slightly hotter temperature than the surrounding pseudostreamer. Two regimes in cavity thermal properties were observed: during the first 5 months of observation, we found lower density depletion and highly multi-thermal plasma, while after the pseudostreamer became stable and slowly shrank, the depletion was more pronounced and the plasma was less multithermal. As the thermodynamic properties are strongly correlated with the magnetic structure, these results provide constraints on both the trigger of CMEs and the processes that maintain cavities stability for such a long lifetime.

## OPEN ACCESS

### Edited by:

Valery M. Nakariakov,  
University of Warwick, UK

### Reviewed by:

Dipankar Banerjee,  
Indian Institute of Astrophysics, India  
Gordon James Duncan Petrie,  
National Solar Observatory, USA

### \*Correspondence:

Chloé Guennou  
chloe.guennou@obspm.fr

### Specialty section:

This article was submitted to  
Stellar and Solar Physics,  
a section of the journal  
*Frontiers in Astronomy and Space  
Sciences*

**Received:** 03 January 2016

**Accepted:** 06 April 2016

**Published:** 03 May 2016

### Citation:

Guennou C, Rachmeler LA,  
Seaton DB and Auchère F (2016)  
Lifecycle of a Large-Scale Polar  
Coronal Pseudostreamer/Cavity  
System.  
*Front. Astron. Space Sci.* 3:14.  
doi: 10.3389/fspas.2016.00014

**Keywords:** Sun, corona, UV radiation, tomography, pseudostreamers, cavity

## 1. INTRODUCTION

Streamers are large, quiescent structures in the corona which lie at and under the interface of open magnetic field domains. Streamers generally fall into two categories: “helmet” streamers and pseudostreamers, which are topologically distinct (Wang et al., 2007). Helmet, or bipolar, streamers separate regions of open opposite magnetic polarity, while pseudostreamers, also called unipolar streamers, separate open magnetic domains of the same polarity. The fundamental difference between the two types of streamers is their magnetic topology (Wang et al., 2007; Rachmeler et al., 2014). While this topological difference is well understood, it is not clear if they share similar plasma properties.

The magnetic field configurations of unipolar and bipolar streamers have been shown to have a significant role in the dynamics of the solar wind, especially in the slow component. Moreover, it has been shown that streamers and pseudostreamers are closely related to Coronal Mass Ejections (CMEs), huge releases of coronal material and energies into the interplanetary space (Howard et al., 1985; Eselevich and Tong, 1997; Zhao and Webb, 2003; Wang, 2015). They are also

important tracers of the magnetic field in the heliosphere; the heliospheric current sheet extends from the top of a helmet streamer (see e.g., Borrini et al., 1981).

Streamers were first described in details in solar data much earlier than pseudostreamers (Sturrock and Smith, 1968). To date, pseudostreamer research mainly focused on their magnetic configurations and their role in both solar wind and space weather, while their thermal and density properties are poorly known. Borovsky and Denton (2013) showed that magnetic storms driven by pseudostreamers have systematically different phenomenologies than those driven from streamers. Zhao et al. (2013) proposed that pseudostreamers are associated with extreme-proton-flux slow solar wind measured by the Ulysses mission. Lynch and Edmondson (2013) showed that the pseudostreamer magnetic configuration is favorable for the breakout CME initiation mechanism. However, there are only a few studies about their thermodynamic properties (Abbo et al., 2015).

Both streamers and pseudostreamers can also contain coronal cavities, tunnel-like areas of rarefied density, which possess an elliptical cross-section (Gibson and Fan, 2006). A number of multi-wavelength studies demonstrated that cavities are depleted in density, with a typical depletion of about 30% relative to the surrounding streamers (see e.g., Marqué, 2004; Schmit and Gibson, 2011). Studies have shown that both the cavity and the streamer have temperatures in the range of 1.4–1.7 MK, though there is evidence of internal temperature variation and a hot core near the center of the cavity (Gibson et al., 2010; Schmit and Gibson, 2011; Kucera et al., 2012; Reeves et al., 2012). However, there is still no clear evidence of whether or not the cavities are typically hotter than the surrounding pseudostreamer/streamer.

Coronal cavities, often characterized by their croissant-like morphology in three dimensions (3D), provide important information about the magnetic structures that support prominences. The magnetic energy is stored through the non-potentiality of the twisted or sheared magnetic field associated with the prominences. This energy is ultimately released through CMEs. To be able to forecast these energetic releases of material and prevent potential terrestrial consequences, the understanding of its three dimensional morphology and its magnetic field is essential. The prominences embedded in the cavity only trace a small part of the magnetic field, whereas the much larger cavity provides more information about the magnetic field morphology. As a result, a clear understanding of the coronal volume of the cavity significantly advances our understanding of both the pre-eruption equilibrium and the triggers of such eruptions.

Determining both morphological and thermodynamical coronal structures is difficult due to the optically thin nature of the plasma. UV and visible observations are subject to integration along the line-of-sight (LOS). This effect can strongly complicate both the derivation and the interpretation of important physical quantities. The background and foreground emission can easily overwhelm the signal of interest, leading to a loss of information about the 3D geometry.

One way to deduce the 3D structure is with solar rotational tomography (SRT). In general terms, tomography

is a technique used to determine the 3D structure of an object. Many different areas of science—such as medicine, geophysics, and astrophysics—use this class of technique. For the particular case of SRT, the plasma emissivity is estimated from EUV/white light images taken from different viewpoints, mathematically corresponding to the inversion of the LOS-integration. Physical properties can be then derived from these multi-wavelength emissivities. Tomography is a highly under-determined problem (Aschwanden, 2011), and the intrinsic difficulties of non-robustness and non-uniqueness of the solution have to be overcome. SRT in particular is further complicated by the lack of simultaneous viewpoints, which is limited by the number and location of available spacecraft. Multi-spacecraft observations in the optimal position when possible, coupling with the natural solar rotation provides the necessary multiple points of view. Tomographic inversion generally assumes that the structure to be inverted is not time-varying, complicating the inversion process. The reconstruction is further complicated by the fact that the Sun rotates differentially and coronal features can change during a rotation. As a result, the inverse-problem is further ill-posed. In practice, the inversion codes assume rigid rotation and non-evolving structures, although some authors developed techniques to overcome the time variability (e.g., Barbey et al., 2008; Butala et al., 2010; Barbey et al., 2013). In this work, we propose a simple alternative to these challenges using a technique of sliding time-windows.

Due to rapid progress in inversion algorithms, faster computation facilities, and the availability of new data, SRT has been recently used for the study of a variety of coronal structures observed in EUV. Nuevo et al. (2015) used a technique similar to the one used in this work in order to determine the 3D thermal structure of the corona. Their measurements revealed the omnipresence of bi-modal DEM within the quiet corona, with clearly distinct cool and hot components. Huang et al. (2012) and Nuevo et al. (2013) used a combination of tomography and magnetic field extrapolation (the Michigan Loop Diagnostic Technique - MLDT) to determine the temperature along quiet-Sun coronal loops. Morphological properties of polar plumes have also been investigated by de Patoul et al. (2013), and using Hough-wavelet transform and filtered-back projection tomography, the authors determined the plumes temporal variation and cross-sectional shape. Vásquez et al. (2009) presented tomographic measurements of polar-crown cavities using the DEMT method of (Frazin et al., 2005b). They found density-depleted cavities (about one-third) and broader thermal distribution shifted toward higher temperatures, relative to the surroundings streamers. For an exhaustive review about general solar tomography, the reader is referred to Aschwanden (2011).

In this paper, we report the observation of an exceptional large-scale coronal pseudostreamer/cavity system in the southern polar region of the solar corona, which was visible for approximately a year starting in February 2014. It is unusual to see such a large closed-field structure embedded within the usually open polar region. We tracked the formation, evolution and disappearance of the pseudostreamer/cavity system using SRT. To our knowledge this is the first time that SRT has been applied specifically to a pseudostreamer system. We tracked

the 3D plasma parameters and their evolution over the whole life-cycle of the pseudostreamer, using a combination of both tomography and DEM inversions. The technique of SRT is complementary to coronal magnetometry, as different domains of plasma parameters correlate with the magnetic structure. Used together, they can provide a powerful diagnostic of not only the magnetic structure of the corona, but also the feedback between the plasma and the field.

## 2. METHODS : MEASURING THE 3D THERMAL STRUCTURE

To derive the plasma properties of the structure and evolution thereof, we couple SRT and differential emission (DEM) analysis. We first use SRT to determine the three-dimensional emission of the plasma in multiple EUV wavelength bands. For each location in space, we then use the emissivity in a differential emission analysis (Pottasch, 1963) which calculates the plasma density and temperature at that location.

### 2.1. Solar Rotational Tomography

The first step in our analysis is to estimate the three-dimensional distribution of the coronal plasma emissivity. We used the SRT software TomograPy, described in Barbey et al. (2013), an open-source program freely available in the Python Package Index<sup>1</sup>. The software performs fast tomographic inversions using one of several parallelized-projection algorithms. Various types of solar image data can be used as input including multiple UV wavelengths and white-light observations.

In the case of optically thin plasma, the intensity  $I_b$ , produced by collisional emission lines and continua in a given UV or EUV waveband  $b$ , integrated along the LOS  $l$ , can be expressed as

$$I_b = \int_{-\infty}^{\infty} R_b(n_e, T_e) n_e^2 dl \quad (1)$$

where  $R_b$  is the response function to a unit volume of plasma of electron temperature  $T_e$  and density  $n_e$  of the instrument. This temperature response function takes into account the intensity produced by each emission line, the contribution of the continuum, and the spectral sensitivity of the instrument band  $b$ . The function  $R_b$  accounts for all of the physics of the radiation emission process (see e.g., Mason and Fossi, 1994). Given a simple case where the input is EUV images from a single spacecraft, and assuming that the Sun does not change during the observation window, SRT inverts the integration along the LOS and solves for

$$e_{b,i} = R_b(n_e, T_e) n_e^2, \quad (2)$$

the local emissivity of the coronal plasma. In this case, we can easily discretize Equation (2), assuming that the reconstructed object-map is a cubic regular grid centered on the Sun

$$I_j = \sum_i P_{i,j} e_i + n_j \quad (3)$$

<sup>1</sup><https://pypi.python.org>

where  $I_j$  is the intensity in the image pixel  $j$ ,  $e_i$  is the local emissivity in the voxel number  $i$  along the LOS,  $P_{i,j}$  is the length of the portion of the LOS  $j$  passing through the voxel  $i$ , i.e., the volume element of the 3D reconstruction grid, and  $n_j$  is the noise associated with the image pixel  $j$ . Equation (3) can then be rewritten in matrix notation

$$\mathbf{I} = \mathbf{P} \mathbf{e} + \mathbf{n} \quad (4)$$

where  $\mathbf{I}$  contains all the pixels of every image of size  $N$  and  $\mathbf{e}$  the reconstruction cube of size  $M$ . The projection matrix  $\mathbf{P}$ , called the *projector* in TomograPy, takes into account the position and the orientation of the spacecraft for each pixel of each image used in the reconstruction. To compute the exact path of each LOS through the various voxels, the software uses a parallelized implementation of the Siddon algorithm (Siddon, 1985) in C. Designed for Cartesian grid, this algorithm computes the projection or back-projection operations very quickly, and the huge projection matrix of size  $M \times N$  does not need to be stored in memory.

The tomographic inversion process is likely to be under-determined and highly ill-conditioned, and thus the direct inversion of Equation (4) is not feasible. The TomograPy software uses Baye's formalism to solve this tomographic linear inverse problem, fully equivalent to classical regularization methods (see e.g., Frazin et al., 2005b; Barbey et al., 2008, 2013). In this approach, we define a prior model which encompasses all the *a priori* available information on the unknown true solution,  $\mathbf{e}$ . Usually, the prior is chosen to be the finite-difference operator, which favors a smoother solution, and thus suppresses noise. Using the following minimization process, we calculate the our estimated local emissivity cube,  $\hat{\mathbf{e}}$ :

$$\hat{\mathbf{e}} = \arg \min_{\mathbf{e}} \{ ||\mathbf{y} - \mathbf{P} \mathbf{e}||^2 + \lambda ||\mathbf{DRe}||^2 \} \quad (5)$$

where the first term relies on a simple least-square inversion. The *a priori* information is given by the second term, where  $\mathbf{D}$  is the finite-difference operator,  $\lambda \geq 0$  is a free parameter controlling the smoothness, and  $\mathbf{R}^2$  is a diagonal smoothing prior, increasing with height. Solar image data becomes noisier with height, as the true signal strength drops off. The  $\mathbf{R}^2$  serves to suppress the influence of this noise in the tomographic solution. Additionally, as other SRT methods use spherical grids,  $\mathbf{R}^2$  improves the similarity of solutions between the cartesian and spherical grid implementations. This is because the voxel size grows with height in spherical grids, increasing the signal-to-noise ratio there.

Our tomographic reconstruction technique is closely related to the method of Frazin et al. (2005b), except for some technical aspects. The main differences are their use of a spherical grid and their imposition of positive-only solutions; we use a Cartesian grid and allow negative values of the emissivity. Negative values in tomographic reconstructions are obviously not physical, but their presence reveals temporal evolution in the solution. Static tomography assumes that the emissivity in each voxel is constant over time. But when temporal evolution is present, as it is in the Sun on rotational timescales, this assumption is not strictly valid, and our algorithm compensates for this behavior by introducing

negative values, which allow us to identify areas that are subject to evolution.

## 2.2. Coupling DEM Analysis and Tomography

While tomography is used to alleviate the ambiguity imposed by LOS integration through an optically thin plasma, the DEM analysis quantifies the temperature distribution of the plasma along the LOS, without regard for its morphological properties. Introduced by Pottasch (1963) for elemental abundance measurements, the DEM is now widely used in the solar community, for all types of coronal structures. The DEM provides a measure of the amount of emitting material along the LOS as a function of the electron temperature  $T_e$ . Recasting Equation (1) as a function of the temperature, the intensity observed in an UV band is given by

$$I_b = \int_0^\infty R_b(n_e, T_e) \xi(T_e) d\log T_e. \quad (6)$$

The DEM  $\xi$  is defined as

$$\xi(T_e) = \overline{n_e^2}(T_e) dp/d\log T_e \quad [\text{m}^{-5} \cdot \text{K}^{-1}] \quad (7)$$

where  $\overline{n_e^2}$  is the square electron density averaged over the portions  $dp$  of the LOS at temperature  $T_e$  (see Craig and Brown, 1976, for details). Nevertheless, reliably inferring the DEM from observations is a genuine challenge, due to the inverse nature of the problem. The fundamental limitations of DEM inversion have been discussed in e.g., Jefferies et al. (1972); Craig and Brown (1976); Brown et al. (1991); Judge et al. (1997) and more recently by Testa et al. (2012); Guennou et al. (2012a,b), including issues due to noise in the input measurements, systematic uncertainties, the width and the shape of the temperature response functions, and the associated consequences of multiple solutions.

These two techniques are linear inverse problems and the coupling of the both leads to the estimation of the three-dimensional distribution in temperature and density of the coronal plasma. Frazin et al. (2005b, 2009) were the first to propose such a combination of these two techniques, in a procedure called Differential Emission Measure Tomography (DEMT), demonstrating the ability of such a diagnostic to distinguish plasma of different temperatures from multi-waveband EUV observations. Tomography mitigates the integration along the LOS, but the temperature is still unlikely to be constant within a given voxel volume, as the typical voxel volume is  $\sim 8000 \text{ km}^3$ . We can thus define a local DEM by recasting Equation (2) as

$$e_{b,i} = \int_0^\infty R_b(T_e, n_e) \xi_{loc,i}(T_e) d\log T_e, \quad (8)$$

with  $\xi_{loc}$  the local DEM of the  $i$ th voxel, defined over the volume voxel  $V_i$  rather than a portion of the LOS as

$$\xi_{loc,i} = \overline{n_e^2}(T_e) dV_i / d\log T_e \quad [\text{m}^{-3} \cdot \text{K}^{-1}] \quad (9)$$

assuming that the density  $n_e$  is constant over the voxel volume (see Brown et al., 1991, for a rigorous definition of the volumetric DEM). Analogous to the classical DEM, the local DEM describes the temperature distribution of the plasma within the voxel, therefore at a smaller scale than the grid itself. Because the integration volume is significantly smaller for the local DEM than for the classical DEM formalism, the temperature variation within the voxel should be substantially reduced.

Once we have estimated the local plasma emissivity cubes,  $\hat{e}_b$ , estimated independently for each waveband by solving Equation (4), we are then able to determine the local DEM for each voxel. A variety of classical DEM algorithms have been proposed (e.g., Kashyap and Drake, 1998; Hannah and Kontar, 2012; Cheung et al., 2015, and references therein), easily adjustable to plasma emissivity rather than intensity. However, we only have at maximum the six coronal channels available in this work, and therefore the complexity of the reconstructed local DEMs is limited. We chose to limit the possible local DEM solutions to Gaussian distributions defined by three parameters, central temperature  $T_c$ , amplitude  $n_e$  and width  $\sigma$ , as

$$\begin{aligned} \xi_{loc,i} &= n_e^2(T_c) \mathcal{N}(\log T_e - \log T_c) \\ \text{with } \mathcal{N}(x) &= \frac{1}{\sigma \sqrt{2\pi}} \exp\left(-\frac{x^2}{2\sigma^2}\right). \end{aligned} \quad (10)$$

There is no physical reason the temperature distributions within a voxel should follow a Gaussian. Nonetheless, this formalism is able to describe a great variety of plasma conditions, and is simple enough to allow easy computation of the local DEMs for a large number of voxels. Additionally, Gaussian local DEM inversions have been fully analyzed and calibrated by Guennou et al. (2012a,b), allowing us to identify possible secondary solutions.

We determine the local DEM  $\xi_{loc,i}$  for each voxel, using a simple least-square criterion

$$\chi^2 = \min \left[ \sum_{b=1}^{N_b} \left( \frac{e_{b,i}^{\text{tomo}} - e_b^{\text{synth}}(T_c, n_e, \sigma)}{\sigma_{b,u}^2} \right)^2 \right], \quad (11)$$

where  $N_b$  denotes the number of wavebands (6 for AIA), and  $\sigma_{b,u}^2$  are the uncertainties related to calibration, atomic physics, and instrumental noise, estimated to be 35%, according to Guennou et al. (2012a). For each waveband the synthetic emissivities  $e_b^{\text{synth}}$  are calculated through

$$\begin{aligned} e_b^{\text{synth}}(T_c, n_e, \sigma) &= n_e^2 \int_0^\infty R_b(T_e, n_e) \mathcal{N}(\log T_e - \log T_c) d\log T_e \\ &= n_e^2 (R_b * \mathcal{N})(T_c, \sigma). \end{aligned} \quad (12)$$

We note that the synthetic emissivities are equal to the convolution product of the temperature response function by the Gaussian local DEM. They correspond to the expected emissivity values for all possible combinations of the three local DEM parameters  $n_e$ ,  $T_c$ , and  $\sigma$ . The response temperature  $R_b(T_e)$  of the six AIA coronal bands have been computed using version 7.1

of the CHIANTI atomic database (Dere et al., 1997; Landi et al., 2013). The temperature varies from  $\log T_e = 5$  to  $\log T_e = 7$  in steps of 0.0025  $\log T_e$ , whereas the density covers the range from  $10^7$  to  $10^{10} \text{ cm}^{-3}$  in steps of 0.01  $\log n_e$ . The local DEM width varies linearly in 80 steps from  $\sigma = 0$  to  $\sigma = 0.8 \log T_e$ . This choice of sampling leads to pre-computed emissivity cubes with  $\sim 2 \times 10^7$  elements for each AIA band, which are easily manageable data cubes.

The final result of our analysis gives us the emissivity in each bandpass for each voxel location, as well as the local DEM obtained from these emissivities. From the local DEM analysis, we extract the temperature (i.e., the central temperature of the Gaussian local DEM), the density, and the Gaussian local DEM width, which corresponds the thermal width of the plasma, for each voxel. Thus, in conjunction with the time analysis described in the next section, we can track the evolution of both morphological and thermal properties of our observed large-scale polar pseudostreamer.

### 2.3. Tracking the Time Evolution

A common source of error in SRT is the dynamic nature of the corona during rotational timescales. Even using multiple simultaneous points of view when possible, we still need a few days of data acquisition to generate a tomographic map. Auchère et al. (2012) reduced this to 5 days of data using three separate spacecrafts: STEREO/EUVIA, STEREO/EUVIB (Wuelser et al., 2004), and PROBA2/SWAP (PProject for Onboard Autonomy 2/Sun Watcher using Active Pixel system detector and image processing Seaton et al., 2013). Some authors have developed methods attempting to overcome this issue, which take into account the temporal variation of coronal structures. Barbey et al. (2008) developed a 3D model for plumes, in which plumes are considered to be static objects—but objects whose intensity is allowed to vary. This method is especially tailored for plumes as they can sporadically appear and disappear at the same place. Barbey et al. (2008)'s results show a great improvement of the quality of plume reconstructions. Smooth temporal SRT, providing global 4D reconstructed cubes, have been developed by Frazin et al. (2005a) and Butala et al. (2010) using Kalman filtering, and later by Barbey et al. (2013), showing that allowing temporal variation leads to qualitatively better reconstructions.

In this work, we chose to adopt a different approach to combat this issue. Instead of seeking to model the temporal evolution of the whole corona, and thus increasing the degree of under-determination of the inverse problem, we instead search for the stable structures within our reconstructions. To achieve this, we use sliding-windows in time to reconstruct the corona. We compute a reconstruction of the corona using a 17 day window, which is then shifted by 1 day at a time for a total time coverage of approximately a year. If a structure is completely stable over a long period of time, it will be detected at the same location in successive reconstructions. On the other hand, the artifacts created by temporal evolution or other projection effects (see Sections 5 and 4 for more details) will change significantly between successive reconstructions. In this way, we can differentiate between static structures and artifacts and ensure that certain observed structures are real.

The differential rotation of the Sun is another issue of concern for coronal tomography. On the photosphere, the rotation rate varies with latitude, with faster velocities close to the equator. However, the rotation rate of the corona is still uncertain, many studies have shown that the differential rotation in the corona is weaker than on the photosphere. Altrock (2003) suggest that structures with lower temperatures rotate at a slower rate. Polar coronal holes for example, show rotation rates close to rigid body, according to the study of Wang et al. (1988). Given the difficulties and uncertainties mentioned above, we do not currently take differential rotation into account in SRT. The photospheric rotation rate close to the pole is about  $10.53^\circ$  per day. This is the reason why we used 17 days of data for each reconstruction, to ensure over  $180^\circ$  of coverage in longitude (only half a rotation is needed at the poles since the plasma is optically thin), in the extreme case that some structures could be subject to different rotation rates.

## 3. OBSERVATIONS

The large scale pseudostreamer that is the subject of this paper lasted around 1 year, beginning in February 2014. We used the SWAP 174 Å and AIA 94, 131, 171, 193, 211, 335 Å UV coronal images to follow its evolution and produce the tomographic and local DEM inversions. To observe the formation process of this long-lived pseudostreamer, the SWAP data time series begins on 2013 December 19, about 2 months before its formation. We tracked its evolution until 2015 March 31. For AIA, we used observations from 2014 January 1 until 2015 February 28. In March 2015 two gaps in the AIA data prevent us from computing accurate tomographic reconstructions: from March 1 to March 5 and from March 8 to March 14.

The SWAP data were fully calibrated using the SolarSoft IDL p2sc\_prep routine which removes dark current, corrects for the flat field, deconvolves the point spread function, and corrects the image so that the Sun is round, centered, and solar north is up. To create high signal-to-noise images, 100 min of data were median-stacked to create a single frame for input into TomograPy. The processing steps and the median-stacking of the images was described in more detail by Halain et al. (2013) and Seaton et al. (2013). The median-stacking suppresses short-time-scale dynamics of the Sun, which improves the tomographic inversion accuracy. For each tomographic inversion, 17 days of data at a cadence of 100 min (totalling  $\sim 240$  median-stacked frames) were used.

To examine the thermal distribution of the corona, we used AIA images from the six coronal waveband channels. For each waveband, the data were first rotated, translated, scaled and normalized, using a Python function equivalent to the SSW routine aia\_prep.pro. Then, 10 images (1 frame per minute) were averaged together to create a single frame with high signal-to-noise ratio. For each tomographic inversion, 17 days of data at a cadence of 2 h (totalling  $\sim 204$  averaged frames) were used.

**Figure 1** depicts the evolution of the streamer over time, as shown by SWAP in the 174 Å waveband using a linear and inverted intensity scaling. The full lifecycle is shown from

pre-formation to post-disappearance; the images in **Figure 1** depict data from 2014, January 15, February 23, July 11, October 05, December 19, and 2015, March 17. An animation showing the entire 15 months of SWAP data is available in the online material. Additionally, **Figure 2** shows the schematic view of the evolution of the streamer/pseudostreamer magnetic field configuration.

The magnetic field configuration and evolution, jointly with the corresponding magnetograms, will be discussed in more details in a follow-up paper (Rachmeler et al., in preparation).

Before the pseudostreamer forms, a streamer encircles the entire pole, as seen in **Figure 1A**. The neutral line, corresponding to the filament channel, and base of the cavity (Vial and

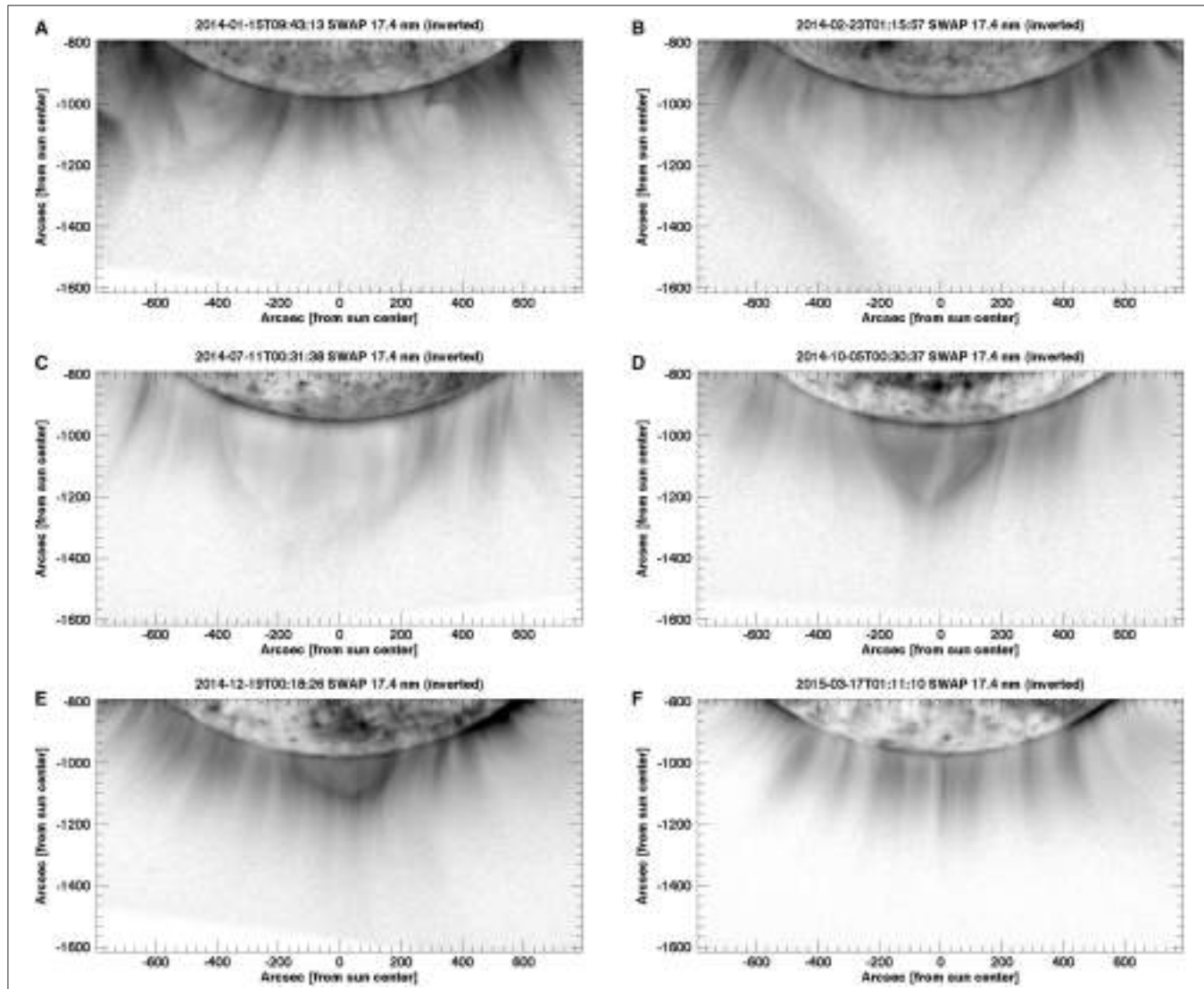


**FIGURE 1 | Evolution of the pseudostreamer observed with SWAP 174 Å waveband.** Color scale is inverted, so black corresponds to the higher intensity values.

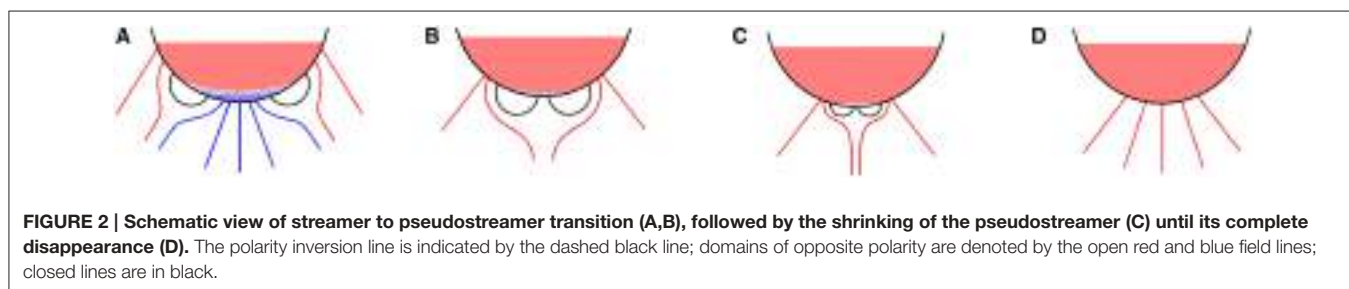


**FIGURE 2 | Schematic view of streamer to pseudostreamer transition (A,B), followed by the shrinking of the pseudostreamer (C) until its complete disappearance (D).** The polarity inversion line is indicated by the dashed black line; domains of opposite polarity are denoted by the open red and blue field lines; closed lines are in black.

Engvold, 2015), surrounds the pole (highlighted by a dashed line in **Figure 2A**), and the corresponding polar-crown cavity is apparent as two cavity lobes in the plane of the sky, with suppressed EUV emission (lighter gray in the inverted SWAP images). Open field at the pole has a positive polarity, which was the dominant polarity of the previous coronal hole (blue in **Figure 2**), separated by the streamer from regions with negative polarity (red in **Figure 2**).

The polarity inversion line then drifts toward the pole, reducing the area of open field lines at the pole. By dint of this gradual displacement, the remains of the old polar coronal hole shrink until the open field disappears completely at which time the structure transitions from a 360° steamer to a topologically different pseudostreamer, as shown in **Figure 2B**. This transition first occurs on 2014 February 22. Subsequently a pseudostreamer can be seen at intervals during a period of about 2 month, suggesting irregular oscillations between streamer/pseudostreamer configurations. Afterwards, the pseudostreamer is definitively established, and observable until 2015 March 11. This new pseudostreamer magnetic field configuration is illustrated schematically in **Figure 2B**. All open field lines now have the new (that is, negative/red) polarity, except photospheric regions south of the polarity inversion line which still have the old (positive/blue) polarity. At this point, the corona and the heliosphere have reversed their polarity, but the photospheric polar field has not. **Figure 1B** shows the newly formed pseudostreamer, as bright strands (i.e., darker area) above the pole, surrounding the closed loops. A cusp-shape void can be observed at the top of the pseudostreamer, likely corresponding to plasma at hotter temperature than the SWAP 174 Å waveband.

Afterwards, the polarity inversion line continues to move toward the pole, and the pseudostreamer shrinks (see **Figure 2C**). The gradual shrinking can be observed in **Figures 1B–E**, where the pseudostreamer apex decreases from about 1.6 R<sub>☉</sub> (*b*) to about 1.1 R<sub>☉</sub>. The bright ray emanating from the top of the pseudostreamer corresponds to the separatrix between distinct magnetic domains (Rachmeler et al., 2014). Once the pseudostreamer and the associated polarity inversion line completely disappears, the south pole magnetic field has fully reversed.

## 4. TOMOGRAPHY : MORPHOLOGICAL PROPERTIES

In order to further increase the signal-to-noise ratio for SWAP data, we performed the daily tomographic reconstructions using images spatially binned by a factor of 4, resulting in 256 × 256 pixel images. The reconstruction cubes are centered on the Sun with a size of 256 × 256 × 256 voxels and with a width, height, and depth of 3.5 R<sub>☉</sub> each. To compute the solution, we minimize Equation (5) using a hyper-parameter, corresponding to the parameter of the prior distribution,  $\lambda = 0.45$ , estimated empirically by the authors using simulations, although some methods exist to evaluate it automatically (see e.g., Higdon et al., 1997; Frazin, 2000; Frazin and Janzen, 2002). For AIA data, the same parameters were used, except for the spatial binning of

the images by a factor of 16 due to AIAs higher initial spatial resolution.

**Figures 3, 4** show the SWAP local emissivity, in units of Digital Numbers (DN) as a function of solar radii, in selected reconstruction cubes at a constant altitude of 1.05 and 1.10 R<sub>☉</sub>, respectively. A gnomonic projection is used, and longitude and latitude (assuming that the origin 0° is at the equator) are reported accordingly. Negative values are highlighted in gray. Movies showing the all of the reconstruction cubes with polar views at 1.05, 1.10, and 1.15 R<sub>☉</sub>, and the corresponding time standard deviation maps (described in Section 5) covering the whole 15 month period are available in the electronic version of this journal.

The reconstruction cubes in **Figures 3, 4** correspond to a time window centered on the SWAP images in **Figure 1**. For each polar view, the black plus sign represents the position of the cavity center, measured at a constant height of 1.05 R<sub>☉</sub>. This was done by tracing the latitudinal emissivity profile in our data cubes for the longitude corresponding to the central meridian of the time centered image of the SWAP data used. The central position of the cavity was chosen to be the local minimum of the profile, closest to the emissivity peak associated with the pseudostreamer.

In both **Figures 3, 4** (see also the movie online), a part of the projections, in the longitude area opposite to the marked cavity position, is smoother and presents lower emissivity. This artifact, which is more pronounced at higher altitudes, is due to the fact that we used 17 days of data (approximately half a solar rotation), as opposed to a full rotation. In the Siddon algorithm, the LOS are stopped once they hit the photosphere, and therefore some parts of the pole are poorly constrained in the reconstruction process. Because we used a 1 day time sliding window for our reconstructions, a low emissivity structure can be seen in the online movies, always located on the other side of the sun from the marked cavity positions. The choice of using only 17 days of data instead of a full rotation is valid as we are mainly interested in the volume above the pole that is never blocked by the solar limb, but it still results in reduced emissivity in the back side of the Sun. In order to obtain a better estimation of these locations, ~7 more days of data can be added to each reconstruction, but this would in turn exacerbate the artifacts due to temporal variations, inducing negatives values in the reconstructions. Because the reconstructions maintain a fixed central meridian, the viewing angle of the solar images rotates around the pole. Thus, the region of lower emissivity appears to rotate or swirl with time in the movies. This rotation is purely due to the low-emissivity artifact, and is not associated with solar differential rotation.

The polar views of **Figures 3, 4** clearly show the three dimensional morphology of the pseudostreamer. A distinct decrease of the mean emissivity over time is clearly visible in successive frames of the figure, indicating that the activity at the pole slightly decreases as the pseudostreamer shrinks. At first, in January 2014 (top left), when the pseudostreamer is not formed yet, the cavity, corresponding to regions of lower emissivity (i.e., in green and blue), encircles the entire pole and is mostly circular, tilted by about 7° relative to the Carrington frame, and located between -60 and -70° in latitude. The bright streamer

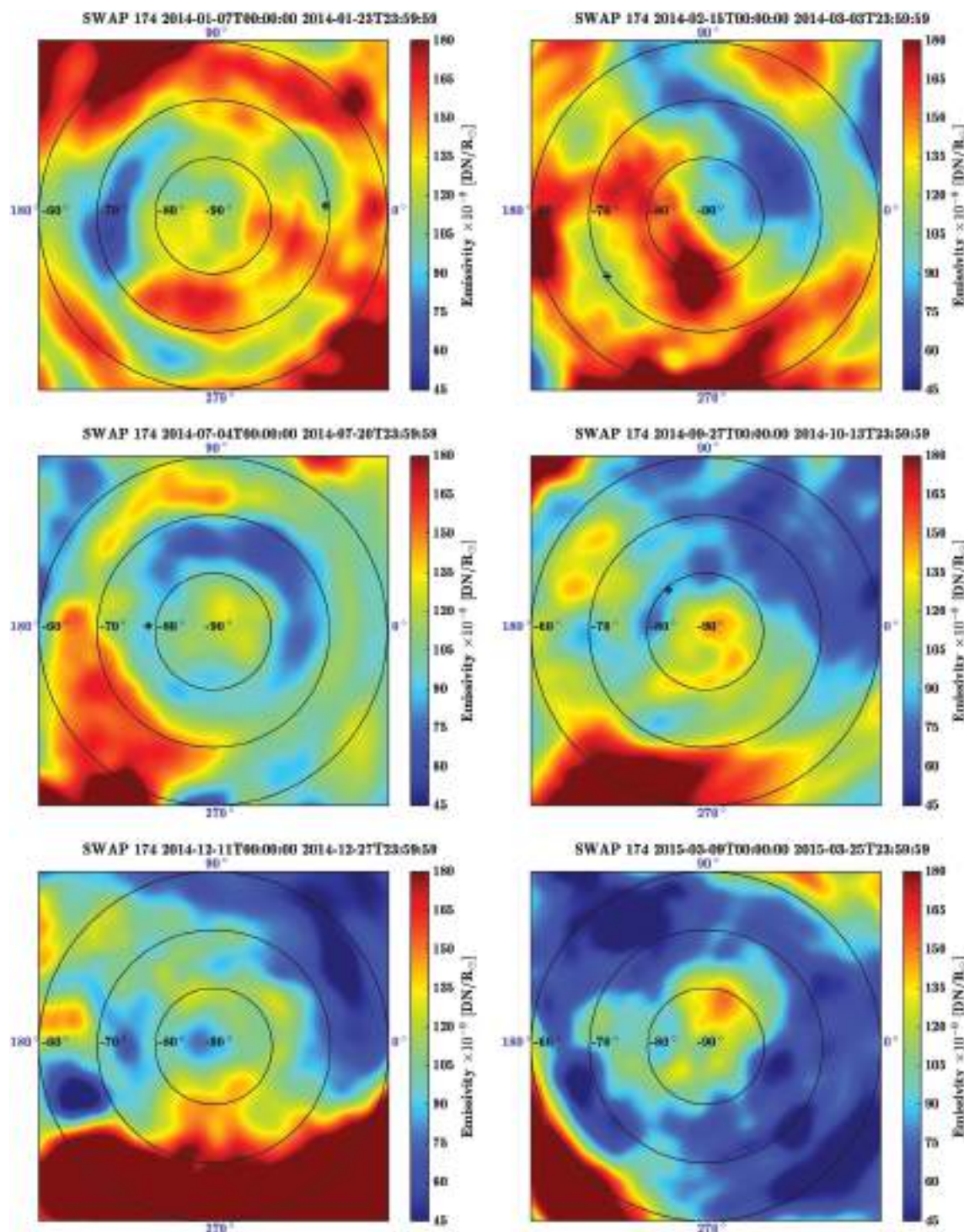
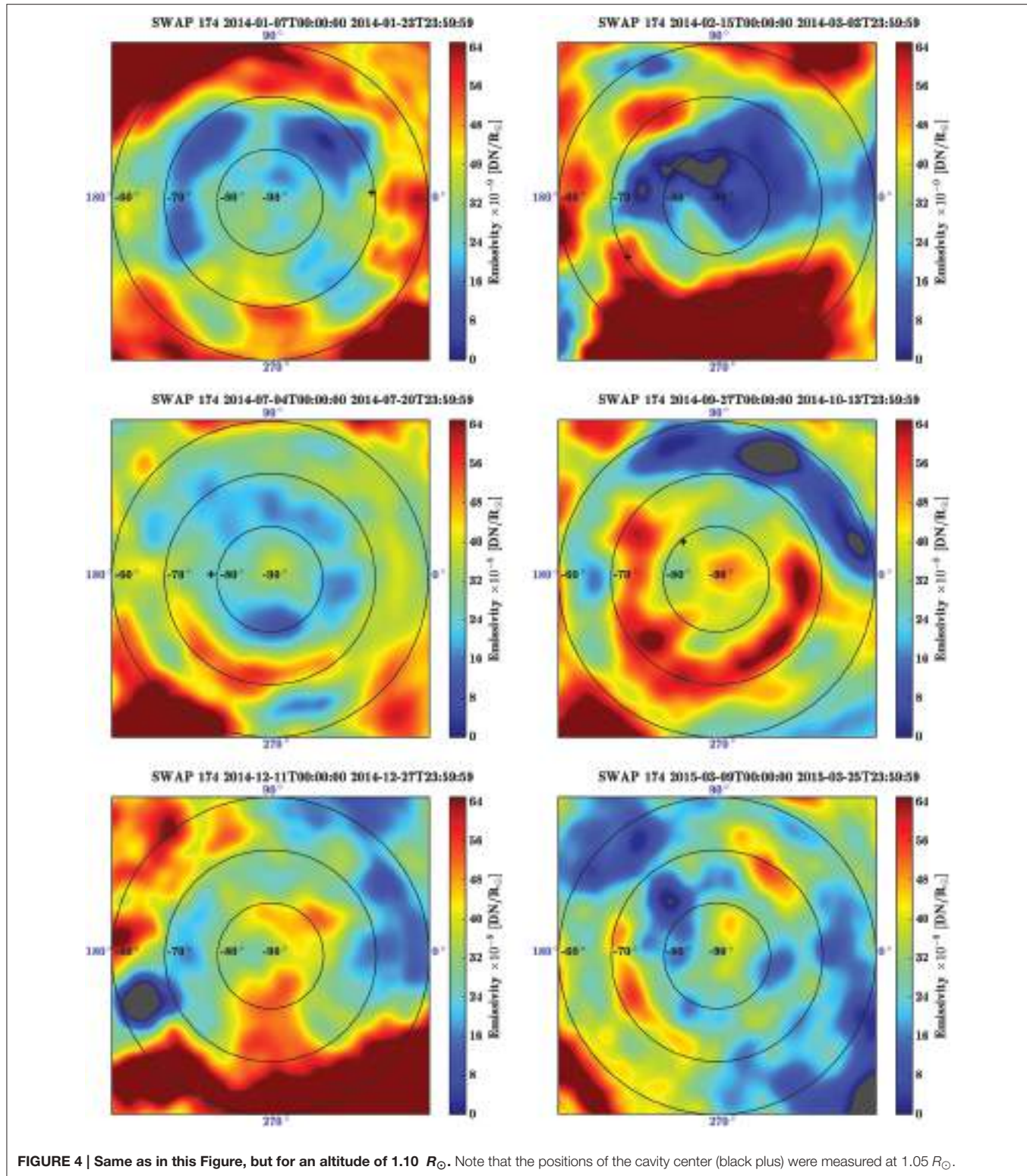


**FIGURE 3 |** SWAP polar view of the south pole at  $1.05 R_{\odot}$  for select tomographic reconstructions corresponding to the images in Figure 1. The black plus represents the position of the cavity center (see text for details).

material (in red) equatorward of the cavity also encircles the pole, and is located around  $-60^{\circ}$  in latitude, although it does dip closer to  $-70^{\circ}$  latitude near  $90^{\circ}$  longitude. In February (top right), once the pseudostreamer is formed, structures are more

complex, as can be seen in Figure 1B and there is no longer clear circular symmetry. The pseudostreamer is visible in the half of the pole centered around the marked cavity position. The cavity—and thus the neutral line as well—is not obviously



continuous, and only located between  $210$  and  $40^{\circ}$  longitude. Nonetheless it is still located around  $-60^{\circ}$  in latitude, as it was in January. The following frame shows the well-established and stable pseudostreamer (see the online movie of SWAP data), and

its shrinking can be observed in the subsequent polar projections. The pseudostreamer exhibits a clear circular symmetry, with an embedded circular cavity. In July (middle left) and October (middle right), the pseudostreamer, and thus polar crown cavity,

slowly move toward the pole, with cavity positions at about  $-78$  and  $-81^\circ$  latitude, respectively, fully in agreement with the cavity position measured in the SWAP images (**Figure 5**). In December (bottom left), the suppressed emissivity region is very small and centered on the pole. Finally, in March (bottom right), the pseudostreamer has disappeared completely, and the coronal hole covers the whole pole. Some remnant structures are observable within the coronal hole, identified as bright nodules that are associated with the plumes observed in **Figure 1F**.

In order to compare our long-term tomographic reconstructions with the series of 15 months of SWAP data, we compare the cavity position measured both in the cubes and in the initial data, reported in **Figure 5**. The position of the cavity in the tomographic reconstructions was made as described above in this section. In the images, this was done by eye, by selecting at  $1.05 R_\odot$  the center of the cavity (i.e., with lower intensity) in the plane of the sky on both western and eastern edge (Rachmeler et al., in preparation). Latitudinal cavity positions were then de-rotated by a quarter-rotation to be able to compare both measurements. **Figure 5** shows that there is an excellent agreement between tomographic measurements (black dots) and the SWAP cavity positions (gray circles), indicating clear consistency between images and tomographic reconstructions. The periodic shape of the curves is due to an offset between the Sun's rotation axis and the cavity's symmetry axes. Some tomographic measurement points in late March and early May are far away the curves. The first period occurred when the structure oscillated between a streamer and a pseudostreamer, while the second period contained many dynamic events.

The pseudostreamer is particularly steady and thus very well reconstructed from early June to mid-October, 2014. In the rest of this section, we discuss a single reconstruction using data from July 14 to 30, which we will call the July 14th reconstruction. **Figure 6** shows the reconstructed polar view at  $1.05 R_\odot$  using the six coronal channels of AIA at  $94, 131, 171, 193, 211, 335 \text{ \AA}$  (from left to right, top to bottom). Images are saturated in order

to enhance the contrast between dark and bright structures, and the SWAP cavity position is also superposed as a black plus-sign on each image. The cavity is strongest in the  $131$  (top right),  $171$  (middle left), and  $335 \text{ \AA}$  (bottom right) wavebands, but still visible in the other channels. In the  $171 \text{ \AA}$  waveband (middle left), the cavity exhibits a quasi-circular shape, between  $-70$  and  $-80^\circ$  in latitude. The polar crown cavity is less visible in the  $193$  and  $211 \text{ \AA}$  channels, corresponding to temperatures of around  $1.2 \times 10^6 - 2 \times 10^7$  and  $2 \times 10^6 \text{ K}$ , respectively. However, the cavity is clearly discernible in the  $131 \text{ \AA}$  waveband, which is sensitive to very hot plasma temperatures around  $10 - 15 \text{ MK}$ . Note that the low signal region in the bottom left corner of each image is the artifact due to the lack of data covering that longitudinal area, as described above. The cavity is embedded in the polar crown pseudostreamer, the outer edge of which is clearly visible in each image as a bright ring just equatorward of the cavity. Using these six reconstruction cubes, we present in the next Section, 5, the corresponding DEM inversion and time analysis.

## 5. COUPLING THE DEM : THERMAL PROPERTIES

Following the method described in Section 2.2, we obtained the local DEM associated with each spatial location of our reconstruction cubes, for the whole period considered. Full results for the entire time interval studied here are available on the online version of this journal and are discussed in Section 5.2.

### 5.1. Example: The July 14th Tomographic/DEM Reconstruction

The Gaussian DEM inversion results corresponding to the AIA reconstructions presented in **Figure 6** are displayed in **Figures 7, 8**, showing a collection of polar views at  $1.05$  and  $1.10 R_\odot$ , respectively. The corresponding SWAP reconstruction is shown on the top left panel, with the cavity position

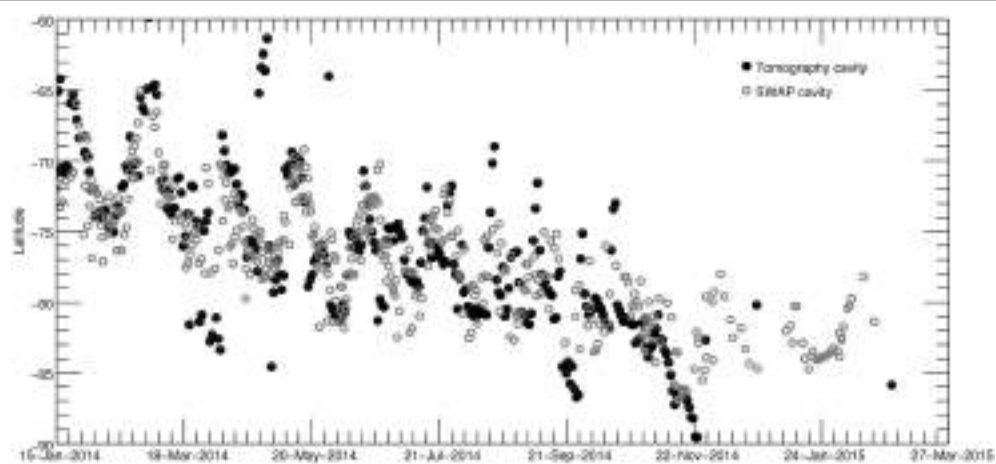


**FIGURE 5 | Cavity positions in both tomographic reconstructions (black dots) and images (gray circles), as a function of time.** The periodic variations are due to the tilt of the polar crown cavity with respect to the solar rotation axis. On average, there is a very good agreement between the two measurements, demonstrating the consistency of the tomographic reconstructions.

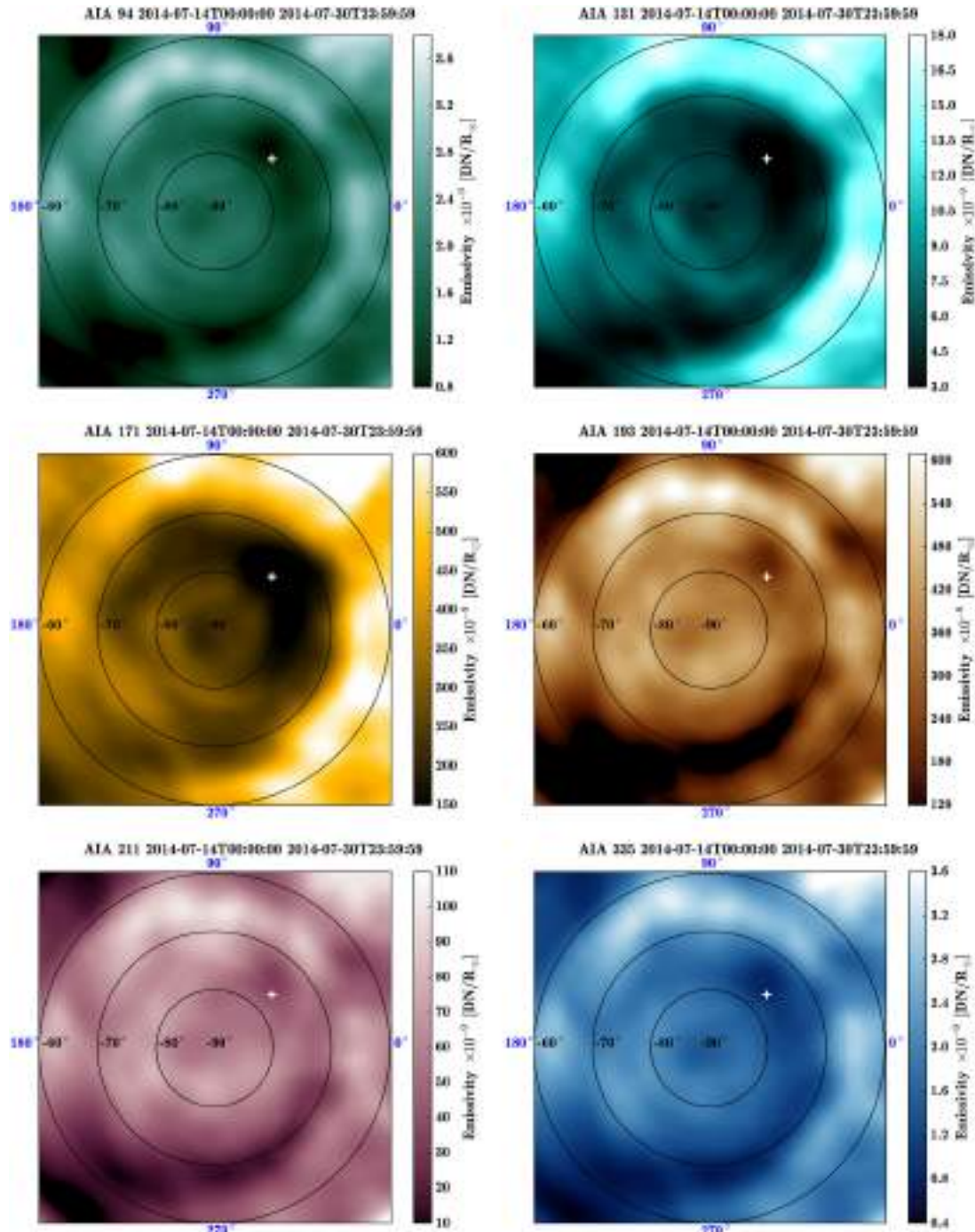


**FIGURE 6 |** AIA polar view for each coronal channel (94, 131, 171, 193, 211, 335 Å, from top to bottom, left to right), at a constant altitude of  $1.05 R_{\odot}$  for an AIA data window covering July 14–30, 2014. The position of the cavity center (white plus) measured in the SWAP reconstruction (174 Å) is indicated on each figure.

marked by a black plus sign, which is also indicated on each subsequent image in the figure. The 3 Gaussian DEM parameters, i.e., the central temperature  $T_c$ , the density  $n_e$  and the thermal width  $\sigma$  (see Equation 10) are displayed on the top right, middle left and middle right panels, while the

corresponding  $\chi^2$  residual (see Equation 11) is shown on the bottom left panel. Note that the low signal region in the bottom left corner of each images is the artifact due to the lack of data covering that longitudinal area, as described in Section 4.

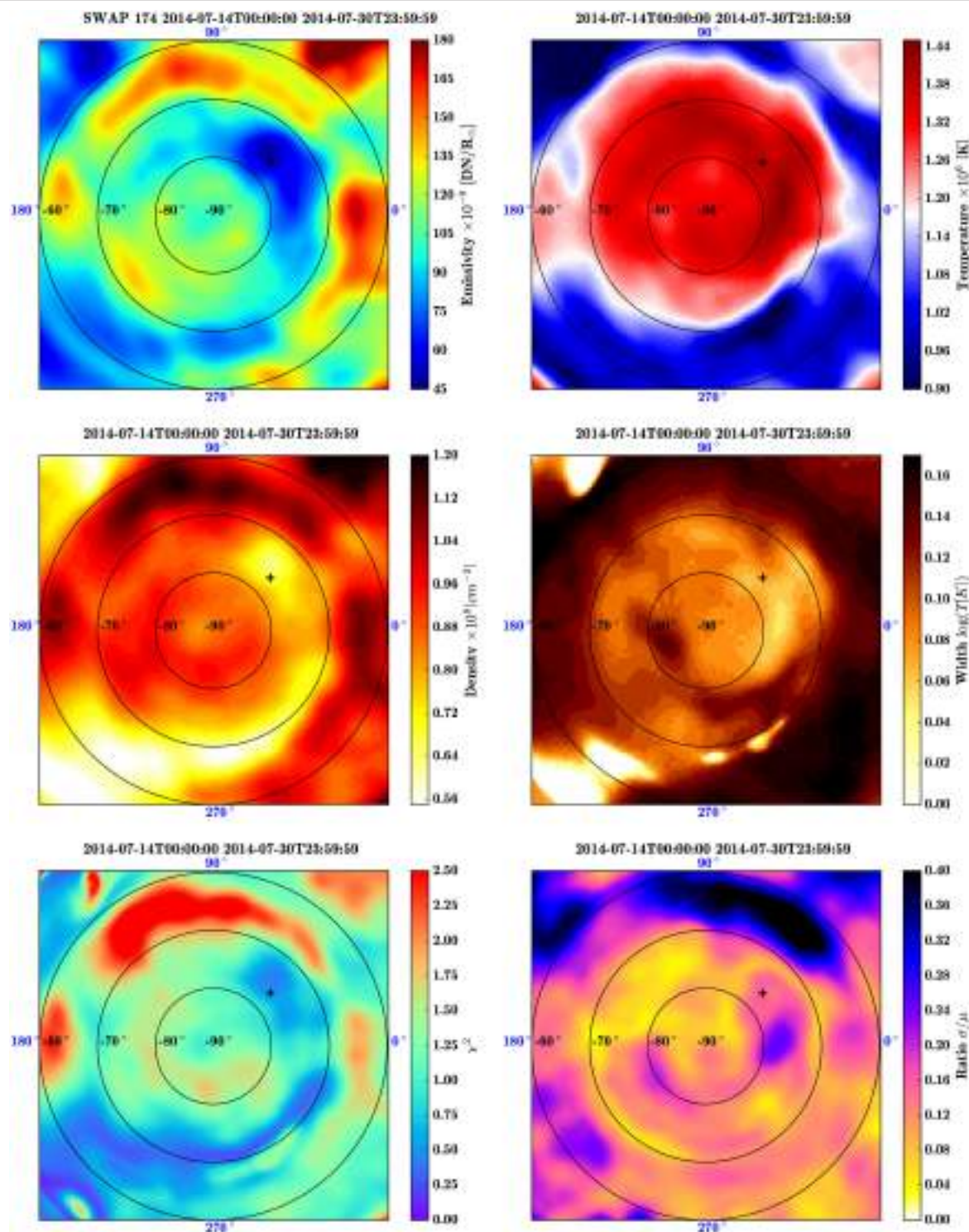


**FIGURE 7 | Example of full tomography/Gaussian DEM coupling analysis at  $1.05 R_\odot$  corresponding to the AIA polar view presented in Figure 6.** The black plus sign is the cavity position measured in the SWAP cubes at  $1.05 R_\odot$ . **Top left:** Corresponding SWAP polar view. **Top right:** Temperature [K], i.e., the central temperature  $T_c$  of the assumed Gaussian local DEMs. **Middle left:** Density, in units of  $\text{cm}^{-3}$ . **Middle right:** Thermal width, i.e., the Gaussian width of the assumed Gaussian DEM. **Bottom left:** Residual  $\chi^2$  of the Gaussian DEM inversion. **Bottom right:** Standard deviation of the 17 consecutive emissivity cubes computed using a 1-day time-sliding window, giving an indication of the temporal evolution of the system.

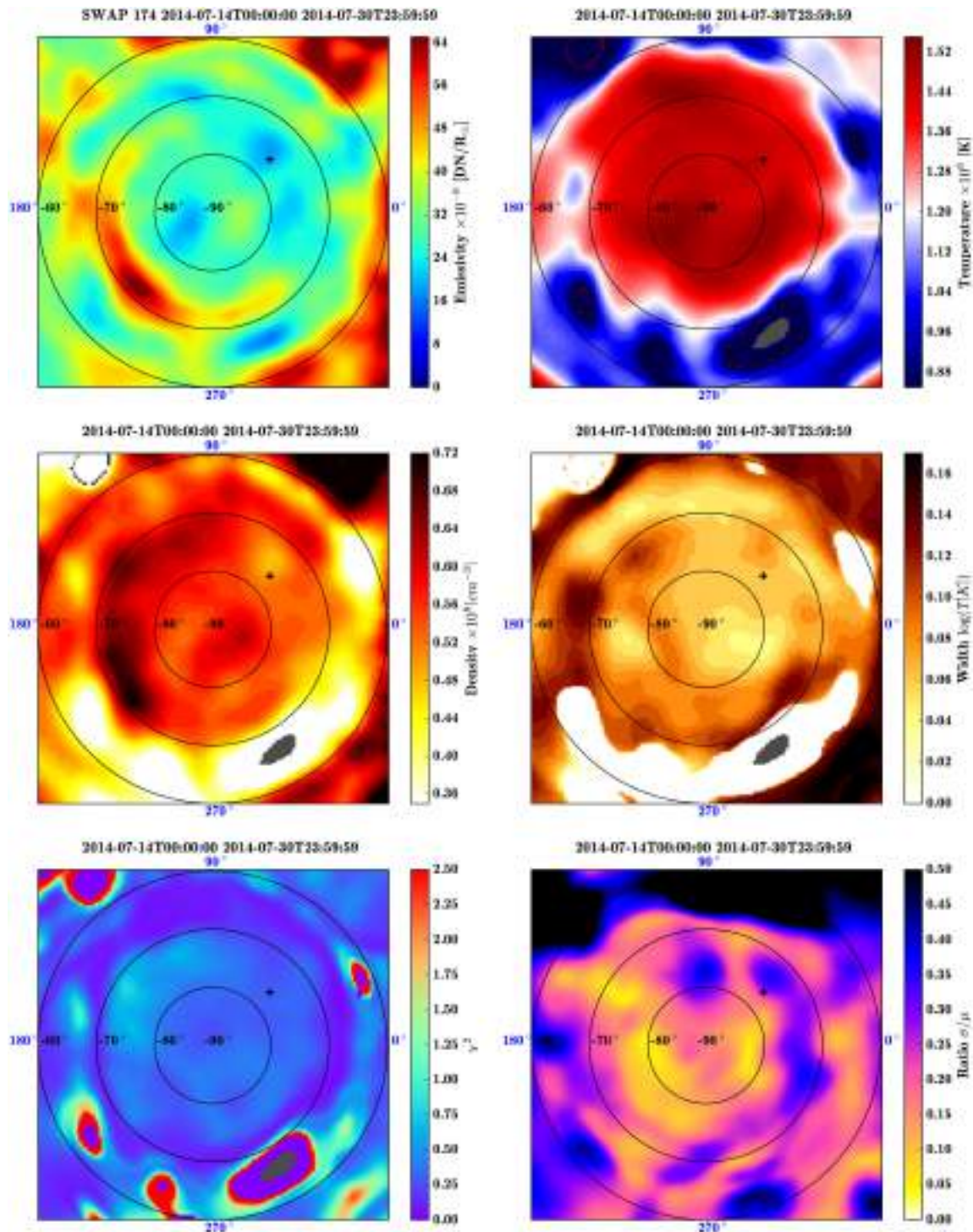


**FIGURE 8 |** Same as Figure 7 but for an altitude of  $1.10 R_{\odot}$ . Note that the position of the cavity center reported here (black plus sign) was measured at  $1.05 R_{\odot}$ .

The bottom right panel of Figures 7, 8 represents the SWAP standard deviation-to-mean ratio  $\sigma/\mu$  of the emissivity computed over the 17 consecutive tomographic reconstructions (see Section 2.3). Because a 17 days windows is used for

reconstructing the corona, if the cavity is completely stable in time, the standard deviation computed for each voxel at the same location, over the 17 consecutive reconstruction cubes should be small, while the artifacts and dynamic structures should

present a large one. Thus, for the 14th of July reconstruction, the standard deviation and the mean have been computed through the 17 consecutive SWAP cubes spanning the observation time range from July 14 to August 16, 2014. The emissivity standard deviation-to-mean maps give us indications of the time evolution of the structures, and therefore which structures are stable in the reconstruction series. They can also be used as a way of providing uncertainties on emissivity tomographic reconstruction. This will be discussed in more details in Section 5.3.

At the height of  $1.05 R_{\odot}$ , the emissivity map on top left panel of **Figure 7** shows that the cavity is embedded in the quasi circular pseudostreamer observable between  $-70^{\circ}$  and  $-60^{\circ}$  in latitude (corresponding to orange-red structures). This is confirmed by the corresponding map of measured density (middle left panel) which is evaluated  $\sim 6.6 \times 10^7 \text{ cm}^{-3}$  at the longitude corresponding to the central meridian of the time-centered SWAP image. In the whole cavity, the density fluctuates between  $\sim 6.4 \times 10^7$  and  $\sim 8.8 \times 10^7 \text{ cm}^{-3}$ , while the density computed for the pseudostreamer is in the  $1-1.1 \times 10^8 \text{ cm}^{-3}$  range. This corresponds to a density depletion of about 20–40 %.

The corresponding temperature map is shown on top right panel of **Figure 7**. The area embedded within the pseudostreamer clearly exhibits higher temperatures, in the range between 1.20–1.40 MK. In particular, besides the low emissivity artifact mentioned above, the regions with lower density (see the middle left panel), are correlated with the higher temperatures, corresponding to the observable part of the cavity. Outside the closed field regions the temperature delineated by the external edge of the pseudostreamer are systematically below 1 MK, with a mean value about 0.95 MK. The internal portion of the pseudostreamer exhibits temperatures slightly lower than the center of the cavity, with respective temperature about 1.2 and 1.35 MK, consistent with the previous AIA observations of **Figure 6**, discussed in Section 4. The thermal width, equivalent to the degree of multi-thermality of the voxel plasma, is lower in the cavity than in the pseudostreamer (clear areas in the middle right map of **Figure 7**). The pseudostreamer presents a thermal width in the range  $\sigma = 0.12 - 0.14 \log T_e$ , while the cavity has much smaller values, around  $0.04 - 0.06 \log T_e$ . This result suggests a different heating process in both structures, with a continuous injection of energy in the cavity supplying the radiative losses, and a more sporadic heating in the pseudostreamer.

The associated normalized  $\chi^2$ , evaluating the pertinence of the Gaussian DEM model (see Equation 11), is presented in the bottom left panel of **Figure 7**. The  $\chi^2$  values for the whole polar map are mainly concentrated around 0 and 2.50, indicating a satisfactory DEM inversion for most of the voxels. Assuming that the inferred DEMs are only affected by normally distributed random errors, the  $\chi^2$  DEM inversion should be equivalent to a statistical chi-squared with  $3^{\circ}$  of freedom, since we solve for the three parameters  $T_e$ ,  $n_e$ , and  $\sigma$ . For a theoretical chi-squared  $3^{\circ}$  of freedom, the most probable value is  $\sim 1.4$ , which is close to the mean value of the observed map, while 95% of them are comprised between 0 and 12. This indicates that the Gaussian DEM is consistent with the observations, but this does not imply, however, that this model is the only or the best possible interpretation of the data (see Guennou et al., 2012b). It

is worth noting that since the six residual  $\chi^2$  corresponding to the minimization process in each waveband are not completely independent, the actual chi-squared distribution will be slightly different from the expected chi-squared  $3^{\circ}$  of freedom Guennou et al. (2012a).

The corresponding emissivity standard deviation-to-mean ratio is shown in the bottom left panel of **Figure 7**. As can be observed, in the center of the cavity (i.e., in the neighborhood of the black plus sign) the  $\sigma/\mu$  ratio is between 12–16%, whereas some portions of the cavity, between  $80^{\circ}$  and  $180^{\circ}$  in longitude for example, are notably steadier, with a  $\sigma/\mu$  ratio close to 4%. For the pseudostreamer, the standard deviation-to-mean ratio is really high, about 40% or more, in the area comprised between  $40^{\circ}$  and  $95^{\circ}$  in longitude and  $-60^{\circ}$  and  $-70^{\circ}$  in latitude. This means that this part of the pseudostreamer is not stable in time, and that the signal is quite different from a reconstruction to another. Thus, these part of the map can be considered as highly uncertain.

At higher altitude, as presented in **Figure 8**, the pseudostreamer can still be well-observed in the SWAP emissivity map, with a quasi-circular shape, mostly located in the  $-70^{\circ}$  latitude area. The cavity is identifiable as before, correlated with area of lower density embedded in the pseudostreamer. As height increases, the density decreases accordingly, both in the pseudostreamer and the cavity, with respective typical values about  $6.5 \times 10^7$  and  $4.5 \times 10^7 \text{ cm}^{-3}$ , corresponding to a cavity depletion of about 30%. On the other hand, the temperature increases with height in the whole map; the cavity here has a temperature about 1.45 MK whereas the external edge of the pseudostreamer is colder, with temperature around 1.2 MK. The residuals are still mostly distributed in the 0–2.5 range, with a smaller mean value than at  $1.05 R_{\odot}$ , indicating, as above, a good consistency between the Gaussian DEM model and the data. The Gaussian width is also in average smaller than at lower heights, and even smaller in average in the cavity areas. However, the standard deviation is in average higher than at low heights, meaning that some temporal variations or artifacts are present. Indeed, as the height increases, strong geometrical artifacts, preventing from analyzing the structures for altitude higher than  $1.15 R_{\odot}$ . They are also visible using simulations, and are geometrical effects caused by the B-angle, corresponding to the tilt of the ecliptic with respect to the solar equatorial plane (see also Barbey, 2008). Using simulations, we determined that at  $1.10 R_{\odot}$ , they produce an additional error around 10–15 % in the reconstructions. This is consistent with the increase of the  $\sigma/\mu$  ratio of about 15% in average observed on the bottom right panel of **Figure 8**.

Radial properties of both the cavity and streamer are presented in **Figure 9**. The top and bottom panels show the temperature and density variations with respect to the altitude for both the cavity (red solid line) and the pseudostreamer (blue solid line). The measurements are made from the constant longitude corresponding to the central meridian of the central SWAP image of the data series used for the July 14th reconstruction. The cavity center is defined as the local minimum of the latitudinal emissivity profile in the SWAP 174 Å channel (indicated by the black plus sign), while the pseudostreamer edge is defined as the emissivity peak just equatorward of the cavity. The temperature in the cavity is slightly hotter than at the

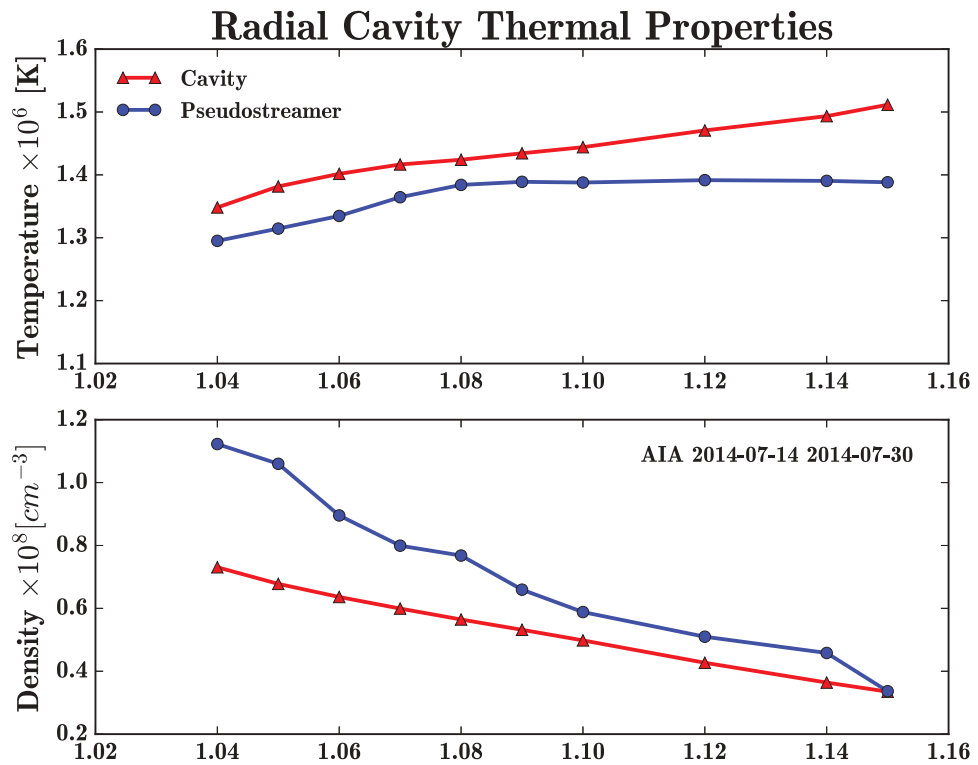


**FIGURE 9 | Radial evolution of the temperature and density with respect to the altitude in both the cavity and the pseudostreamer for the July 14th reconstruction.** The temperatures are slightly higher in the cavity, while the density is clearly lower, especially at low heights.

pseudostreamer edge, as the maps in **Figures 7, 8** show. The density is clearly smaller in the cavity at low heights, and becomes more similar to that of the pseudostreamer at altitudes higher than  $1.10 R_{\odot}$ , suggesting that the cavity extends to  $1.15 R_{\odot}$ .

## 5.2. Evolution of the Thermal Properties

**Figure 10** summarizes the evolution of the local DEM parameters over the year-long lifetime of the cavity. Central temperature  $T_c$  (top panel), density  $n_e$  (second panel), thermal width  $\sigma$  and the  $\chi^2$  residuals are shown as a function of time for three different heights, at  $1.05$ ,  $1.10$ , and  $1.15 R_{\odot}$  (using red, blue, and green solid lines, respectively). The electronic version of this journal, also contains movies corresponding to **Figures 7, 8** showing the evolution of each parameter over the entire period. The reported cavity measurements in **Figure 10** were made at the cavity position indicated by the black plus sign in the movie (see Section 4 for more details).

Clearly, the cavity is not well-defined at large heights until early May 2014. In **Figure 10**, many points for this time period are undefined, except at  $1.05 R_{\odot}$  altitude. For larger heights, strong artifacts with negative values appear in the tomographic reconstructions. This is the result of the strong dynamics of the polar structures at this period, discussed in Section 3, when irregular oscillations between streamer/pseudostreamer configurations were observed. The high values of the B-angle at this period also contribute to the uncertainty. The standard deviation-to-mean ratio is particularly high at altitudes higher

than  $1.10 R_{\odot}$  during this period, confirming the presence of these artifacts (see bottom third panel in the online movies). However, it is still clear that the mean temperature and density for this period are higher than during the shrinking phase of the pseudostreamers life. Most of the south pole has a temperature above  $1.1$  MK, and the highest temperatures are correlated with lowest density area (see top second and third panels of the online movie). The thermal width measured for this period of time is generally greater than that measured in the pseudostreamer.

Following this period, the pseudostreamer is well established and starts to shrink. As can be observed on the online movies, the pseudostreamer volume systematically presents temperatures higher than  $1.15$ ,  $1.20$ , and  $1.35$  MK for the respective altitudes of  $1.05$ ,  $1.10$ , and  $1.15 R_{\odot}$ . Outside the pseudostreamer, the temperature is always below  $1$  MK, corresponding to typical temperatures measured in the open field coronal holes. Inside the pseudostreamer volume, higher temperatures are observed. The cavity itself has the highest temperature, and the lowest local density measurements. The shrinking of the pseudostreamer is well observable in each of the local DEM parameters. The high-temperature quasi-circular region corresponding to the pseudostreamer system is clearly reduced with time, corresponding to the pseudostreamer morphology observed in the SWAP emissivity map. The mean density of the whole south pole slowly decreases with time, and the cavity is easily identifiable as the lowest density central area, slowly drifting toward the pole. While the pseudostreamer shrinks, the

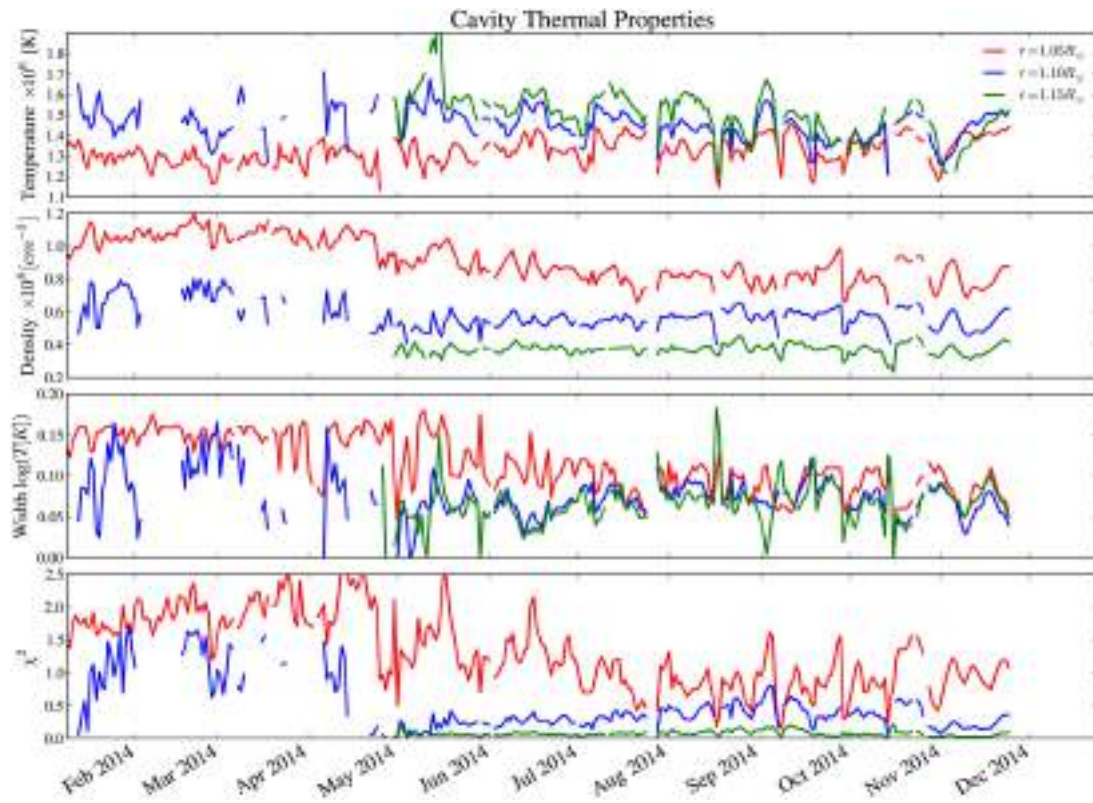


**FIGURE 10 |** Evolution of the cavity Gaussian DEM parameters over the ~1-year lifetime of the cavity.

mean thermal width of the whole south pole slowly decreases. The  $\chi^2$  residuals exhibit smaller values than the early 2014 reconstructions, indicating a better agreement between the Gaussian DEM model and the data. This is consistent with the increased stability of the pseudostreamer for this period, leading to better reconstruction quality. Accordingly, the  $\sigma/\mu$  ratio is, on average, smaller for this time interval.

According to **Figure 10**, two regimes can be observed within the cavity, at least at low height. During the first 5 months before the pseudostreamer starts to shrink, the cavity temperature, density and thermal width measured at  $1.05 R_\odot$  (red solid line) are quite stable, with respective values of about 1.25 MK,  $1 \times 10^8 \text{ cm}^{-3}$  and  $0.14 \log T_e$ . However, once the pseudostreamer shrinks, the density, thermal width and the  $\chi^2$  slowly decrease until July, 2014, while the temperature stays stable. At  $1.05 R_\odot$ , the mean density settles at about  $0.8 \times 10^8 \text{ cm}^{-3}$ , the thermal width about  $0.08 \log T_e$  and the  $\chi^2$  decreases from the 1.5–2.5 to the 0.4–1.4 range. At greater heights, the first regime is not observable due to the lack of data during the January–May interval. Nevertheless, the second regime, during the shrinking process of the pseudostreamer, i.e., after May 2014, is well-observable and the density, thermal width and  $\chi^2$  remains mostly stable. This stability is likely a result of the fact that, except when the pseudostreamer is very large early in its lifetime, the location at  $1.15 R_\odot$  is in the open field polar coronal hole. The temperature, especially at  $1.15 R_\odot$  fluctuates

somewhat, most probably due to the artifacts generated at large heights.

### 5.3. Uncertainties

There are a number of uncertainties affecting the results. SWAP and AIA observations are mostly subject to random errors, caused by both Poisson photon noise and detection noises, such as dark current-induced electron shot noise and read noise. This noise can be reduced by the median- and average-stacking done on the individual frames used in each reconstruction. The reconstructed emissivities are then affected by the errors involved in the reconstruction process, such as the temporal variation of the corona, or the geometrical artifacts discussed in the Section 5 like differential rotation. TomograPy uses the Baye's formalism, assuming a statistical Gaussian noise affecting the data. In this framework, the uncertainties associated with the observational noises are provided by the covariance matrix. Unfortunately, in most practical case, the covariance is too big to be kept in memory (see Barbey et al., 2013, for more details). Comparatively, the random errors involved in the SWAP and AIA data are more likely to be smaller than in comparison to the uncertainties associated with the tomographic reconstruction process, and can be neglected.

Quantifying how much the time variation of the corona affects the reconstruction is not trivial and is beyond the scope of this paper. However, the standard deviation-to-mean

ratio,  $\sigma/\mu$  described in Section 5 can give us an estimate of the degree of temporal variation. Inspecting the online movie showing the SWAP polar caps and the associated  $\sigma/\mu$  ratio, we can derive an upper limit on the emissivity uncertainty, at least for the steady lifetime of the pseudostreamer system (i.e., from May to December 2015). For the altitudes of 1.05, 1.10, 1.15  $R_{\odot}$ , the standard deviation-to-mean ratio generally does not exceed—except in some rare cases—values of about 15, 20, and 25%, respectively. These values will be considered as the upper limit of the emissivity uncertainties in the following discussion.

The local DEM is estimated from the AIA multi-wavelength emissivities computed using a second inversion process. Aside from the classical difficulties inherent to inverse problems, the systematic errors involved in the AIA instrument calibration and in the atomic physics systematically skew the interpretation of the measured emissivity in the same direction. The calibration involves a complex chain of measurements, from which the uncertainties are difficult to deduce. Initially estimated to 25%, the AIA calibration error was reduced to 10% by Boerner et al. (2014) after applying the cross-calibration. Errors associated with atomic physics are a major source of uncertainty the DEM inversion problem. Missing atomic transitions, especially for the 94 and 131 Å observations, underestimate the signal observed. The assumption of ionization equilibrium can also be invalid in some cases, affecting the calculated transition rates. Abundances uncertainties, and variations along the LOS also impact the interpretation of the observations, particularly in the corona where the first ionization effect (FIP) takes place in some structures.

Effects of both calibration and atomic physics uncertainties on the robustness of the AIA Gaussian DEM inversion have been studied in detail by Guennou et al. (2012a) and Guennou et al. (2012b). Based on a Bayesian interpretation of Monte-Carlo simulations, the authors determined how much the AIA Gaussian DEM inversion is affected by the uncertainties. In these previous studies, both types of errors are estimated at 25%, and detection noise is considered, although the latter are mostly negligible in comparison with the systematics. From the probability distributions computed by the authors, the uncertainties associated to the measured DEM parameters can be derived (see Guennou et al., 2013, for a practical example). Authors showed that it is possible to reconstruct simple DEMs with AIA data, but that the accuracy of the results decreases with respect to the thermal width of the plasma.

In this present work, we assume the following: 10% error for the calibration, 25% error for atomic physics, and a reconstruction noise that varies between 15 and 25% depending on altitude. This leads to a total uncertainty between 30 and 36% in the present DEM inversions, which is quite similar to the total 35% uncertainty reported by Guennou et al. (2012b). The thermal width at the south pole never exceeds  $0.2 \log T_e$ , in the results presented here. Moreover, during the stable lifetime of the pseudostreamer, the thermal width is typically in the range of  $0.06$ – $0.09 \log T_e$ . For these characteristic intervals of the thermal width, Guennou et al. (2012b) showed that the AIA Gaussian inversion is robust, although some secondary solutions, can appear with low probability. For isothermal plasma

in the temperature range of about 1 MK, authors found that the temperature resolution is proportional to the total uncertainty level  $\sigma_{unc}$  as  $\Delta T_c^P \sim 0.15\sigma_{unc}$ . Using the probability maps, given a maximum thermal width of  $\sigma = 0.02 \log T_e$  and taking  $\sigma_{unc} = 35\%$ , we find an upper limit on the temperature resolution of  $\Delta T_c = 0.075 \log T_e$ . The density is better constrained, with an upper limit estimated at  $\Delta n_e = 0.055 \log n_e$ . These estimations have been made by adopting a rigorous approach to uncertainties in the DEM inversion problem. However, the emissivity uncertainties, given by the standard deviation-to-mean ratio can be higher locally, especially when artifacts are present.

## 6. DISCUSSION

### 6.1. Pseudostreamer and Cavity Density

In our results, the cavity is clearly less dense than the surrounding pseudostreamer. The cavity depletion, relative to the surrounding pseudostreamer varies in the range of 20–40% at  $1.05 R_{\odot}$ , depending on the period studied. These results are consistent with previous EUV and white-light studies, which have unambiguously established the presence of density depletion within cavity (see e.g., Gibson and Fan, 2006; Fuller and Gibson, 2009; Kucera et al., 2012, and references therein). Our observations reveal that the density depletion decreases with height, as shown by the density profile in Figure 9. These results are also in agreement with the density profiles measured by Fuller et al. (2008), where the density depletion in a white-light cavity is maximum at low altitude and decreases to practically nothing at the cavity top.

Lower density in cavities can be expected in the case that the magnetic field dramatically changes at the cavity boundaries due to a current sheet or layer. The conservation of the total pressure leads to a reduction in thermal pressure to counter the magnetic pressure increase within the cavity. If the temperature is not significantly different between the cavity and its surroundings, as this is the case in our results (see Section 6.2), the pressure change leads to a density depletion. According to Gibson and Fan (2006), even if the axial field change at the cavity boundaries is very small, it still results in a strong jump in thermal pressure and a current sheet does form, a scenario consistent with the generally distinct elliptical boundaries of cavities. The density depletion observed in the center of the cavity is still not fully understood, though some compelling hypotheses exist (Gibson et al., 2010; Schmit et al., 2013).

The magnetic structure, and in particular the magnetic field length, induces some thermodynamic variations, which in turn lead to density depletion within the cavity. For a flux rope cavity model, the integration along the LOS of longer field line, carrying more particles than the shorter one, results in higher observed density (Krall and Chen, 2005). By resolving the hydrostatic equilibrium along the flux rope magnetic field lines, Schmit and Gibson (2011) show that short axial field lines would be depleted by a factor about 35%. Significant thermal non-equilibrium effects can also take place for the longer field line (Klimchuk et al., 2010). Additionally, the degree of twist of the flux rope is an important parameter controlling the amount of density

depletion within the cavity (Gibson et al., 2010). Therefore, our measurements of the cavities 3D morphology, together with the density and temperature profiles can help to constrain the flux rope twist and arch.

## 6.2. Pseudostreamer and Cavity Temperature

Our results clearly show that the volume enclosed within the pseudostreamer is systematically hotter than the plasma outside of it, a feature which is observed during the entire pseudostreamer lifetime. This volume systematically presents temperatures higher than 1.15, 1.20, and 1.35 MK for the respective altitudes of 1.05, 1.10, and 1.15  $R_{\odot}$ . The outermost temperature is always below 1 MK, corresponding to typical temperatures measured in the open field coronal holes. Examining the fine temperature distribution of the internal portion of the pseudostreamer, we found that the area corresponding to the lowest local density are correlated with the hottest temperature. The difference is small though, with 1.2 MK in most of the pseudostreamer vs. 1.35 MK within the cavity at 1.05  $R_{\odot}$  for the July 14th reconstruction presented in Section 5.

However, taking the upper limit temperature uncertainties to be about  $0.075 \log T_e$  as discussed in Section 5.3, the pseudostreamer/cavity temperatures become  $1.2^{+0.22}_{-0.19}$  and  $1.35^{+0.25}_{-0.21}$  MK, and the difference is within the error bars. In spite of that, given the predominantly systematic nature of the source of the uncertainties, the results are likely to be pushed all together in the same direction. Therefore, the difference is most probably to be significant, even though a formal conclusion is not possible. Efforts are needed to reduce the uncertainty sources, which will be a significant task in and of itself.

The temperature profile of coronal cavities is still an open question. Previous analyses resulted in conflicting results, some authors arguing that cavities are hotter (Fuller et al., 2008; Vásquez et al., 2009; Habbal et al., 2010), whereas Guhathakurta et al. (1992) found them cooler. Using a combination of Hinode/EIS and M4K coronameter data, Kucera et al. (2012) concluded that streamer and cavity have essentially the same temperature. They found a temperature profile of about 1.4 MK at  $1.04 R_{\odot}$  to about 1.6 MK at  $1.14\text{--}1.16 R_{\odot}$  in both the surrounding streamer and the cavity. This is, given the uncertainties, consistent with our temperature profiles presented in Figure 9.

The hot central core of the cavities, referred as the “chewy nougat” can sometimes be observed in soft X-rays (Hudson et al., 1999) and persist for the lifetime of the cavity. The hot core has a roughly tube-like shape, suspended above the base of the cavity (Reeves et al., 2012). They are suspected to be the result of current sheet formation and associated reconnection at the flux rope base. We do not observe any similar temperature increase in our reconstructions, even in the AIA channels sensible to high temperatures (94, 131, and 193 Å). It could be due to the transitory nature of these “chewy nougat” events, for which the tomography timescale is too extensive to resolve. However, this is consistent with Vial and Engvold (2015), mentioning in their cavity review that there is not, generally, a corresponding signature to the hot core in EUV wavelengths.

Temperature variations in the cavity are most likely correlated with the magnetic structure. Temperature measurements are thus improved by knowledge of the 3D morphology, to separate potential projection effects. Therefore, our results, in combination with cavity models and simulations, can be very useful in providing strong constraints on the processes that maintain cavity stability for long periods of time.

## 6.3. Evolution of the Pseudostreamer/Cavity System

Two regimes in the pseudostreamer/cavity system are clearly discernible—at least at low heights. During the January–May 2014 interval, the pseudostreamer seems to oscillate between streamer/pseudostreamer configuration, making the tomographic reconstructions more difficult to achieve, highlighted by the higher values of both the  $\chi^2$  and standard deviation to mean ratio higher values. However, we can clearly note that, the density and the thermal width are higher for this time period, and that the entire south pole is at temperature higher than 1.1 MK, indicating that no open field lines configuration are present. The thermal width is, on average, higher in the low density areas, corresponding to the cavity, than it is in the pseudostreamer features.

Once the pseudostreamer is clearly established and therefore in a more steady state, it starts to slowly shrink. The temperature of the pseudostreamer/cavity system, remains, on average, stable meanwhile the shrinking is occurring. By contrast, the density slowly decreases with time within the pseudostreamer/cavity system. At  $1.05 R_{\odot}$ , the cavity density is around  $1.1 \times 10^8 \text{ cm}^{-3}$  in January 2014 and  $0.8 \times 10^8 \text{ cm}^{-3}$  in December 2015. At higher altitudes, a similar trend can be noted, even though both the intense pseudostreamer dynamics and geometric artifacts highly limits the tomographic reconstructions interpretation in the first 5 months of 2014. The thermal width is distinctly smaller than in the first semester 2014, with values decreasing from about 0.15 to about  $0.07 \times \log T_e$ . On the other hand, the cavity thermal width exhibits lower values in average than that of the pseudostreamer, an opposite behavior to that observed in the first part of 2014.

If previous studies did not converge toward a non-ambiguous answer to the cavity temperature question, most authors found more thermal variability in the cavity plasma than in the surrounding corona. In our results, this occurs only during the first half lifetime of the cavity. As we mentioned previously, the thermodynamic properties of the plasma can vary significantly, depending on the magnetic field line length and curvature. Therefore, this change could be related to a reorganization in the magnetic configuration in the south pole. This investigation is beyond the scope of the present paper, but comparison between magnetic field extrapolation and our tomographic reconstructions are planned in a future work.

## 7. SUMMARY

In this work, we present a full analysis of an exceptional long-lived pseudostreamer/cavity system, observable for almost a year, starting in February 2014. We used SWAP data and 6 AIA coronal wavebands to study its evolution, examining both

its 3D morphology and thermodynamical properties. At first, a streamer encircles the entire pole, associated with a polar-crown cavity. By dint of a gradual displacement toward the south pole, a pseudostreamer is formed above the south pole in February 2014, which remains visible for approximately a year. Following that, the pseudostreamer gradually shrink until its disappearance in March 2015, at which point the southern polar coronal hole once again dominates the pole.

We used a combination of tomography and DEM analysis to track the evolution of the 3D thermodynamical properties of this unusually long-lived pseudostreamer/cavity system. Tomography is used to recover the three-dimensional emission of the plasma using multiple EUV wavelengths, allowing us to determine the south pole morphology. From these multi-wavelength 3D observations, we then derive the plasma density, temperature and thermal distribution for each location in space, using the DEM formalism.

The dynamic nature of the corona, as cavity swirling motions (Wang and Stenborg, 2010) or rising bubbles, plumes and flows in prominences (Schmit et al., 2013) may complicate our tomographic analyses, which assume no time variations during the 17 days of acquisition. In this work, we chose to only focus on the stable coronal structures in our reconstructions, instead dynamic and eruptive events which in turn increase the degree of under-determination of the inverse problem. For our time-analysis we used a 1 day sliding-window in time, and then constructed standard deviation-to-mean ratio over successive reconstructions. This allow us to discriminate static structures from the temporal and geometrical artifacts, and ensure that the observed features in our reconstructions are real. To our knowledge, this is the first time that this kind of approach has been used to analyze tomographic reconstructions.

Our results are summarized as follows:

- The cavity depletion, relative to the surrounding pseudostreamer varies in the range of 20–40% depending on height,
- The cavity density depletion decreases with height, from a maximum of about 40% at the cavity lower boundary to  $\sim 0\%$  at the cavity top,
- The cavity density slowly decreases with time as the pseudostreamer shrinks,
- The volume enclosed within the pseudostreamer is systematically hotter than the surrounding open-field plasma,
- The cavity temperature is essentially at similar or slightly higher temperatures than the pseudostreamer,
- No cavity hot cores were observed in our dataset,

## REFERENCES

- Abbo, L., Lionello, R., Riley, P., and Wang, Y.-M. (2015). Coronal pseudo-streamer and bipolar streamer observed by SOHO/UVCS in March 2008. *Sol. Phys.* 290, 2043–2054. doi: 10.1007/s11207-015-0723-y
- Altrock, R. C. (2003). A study of the rotation of the solar corona. *Sol. Phys.* 213, 23–37. doi: 10.1023/A:1023204814099

- Two regimes in cavity density and thermal distribution are observable during the pseudostreamer lifetime. The January–June 2014 interval corresponds to the highest cavity density values, while the thermal distribution is higher in cavity than in the pseudostreamer. Afterwards, the cavity density and the thermal width both decrease.

These results, used in combination with pseudostreamer/cavity models, can give us important information about magnetic configuration, a meaningful parameter to understand both the origin of CMEs and the processes that maintain cavity stability for such long periods of time. Thermodynamic properties being strongly correlated to the magnetic structure, our measurements of the cavities 3D morphology, together with the density and temperature profiles can help to constrain the flux rope twist and arch.

## AUTHOR CONTRIBUTIONS

The works was mainly done by CG. CG performed all the tomographic reconstructions, the local DEM inversions, prepared the AIA data, and analyzed and interpreted the results. LR analyzed the SWAP, compared with magnetograms, and interpret the data from the magnetic point of view. DS prepared the SWAP data and helped during the writing process. FA participated to the tomographic reconstructions, and helped in their interpretation, in particular for the understanding of the geometric artifacts.

## ACKNOWLEDGMENTS

CG acknowledges financial support from the Spanish Ministry of Economy and Competitiveness (MINECO) under the 2011 Severo Ochoa Program MINECO SEV-2011-0187. The authors would like to thank the technical staff at the Computer Science Department of the Institut d’Astrophysique Spatiale, Orsay, France, for allowing us to use their computational facilities. CG would like to thank in particular Claude Mercier and Elie soubrié for helpful suggestions in the DEM inversion code parallelization. The Atmospheric Imaging Assembly on the Solar Dynamics Observatory is part of NASA’s Living with a Star program. CHIANTI is a collaborative project involving the NRL (USA), the Universities of Florence (Italy) and Cambridge (UK), and George Mason University (USA). LR and DS acknowledge support from the Belgian Federal Science Policy Office (BELSPO) through the ESA-PRODEX program, grant No. 4000103240. SWAP is a project of the Centre Spatial de Liege and the Royal Observatory of Belgium funded by BELSPO.

- Aschwanden, M. J. (2011). Solar stereoscopy and tomography. *Living Rev. Sol. Phys.* 8:5. doi: 10.12942/lrsp-2011-5
- Auchère, F., Guennou, C., and Barbey, N. (2012). “Tomographic reconstruction of polar plumes,” in *EAS Publications Series, Volume 55 of EAS Publications Series*, eds M. Faurobert, C. Fang, and T. Corbard, 207–211. Available online at: <http://cdsads.u-strasbg.fr/abs/2012EAS....55..207A>

- Barbey, N. (2008). *Determination of the Tridimensional Structures of the Solar Corona Using Data from the SoHO and STEREO missions*. Theses, Université Paris Sud - Paris XI.
- Barbey, N., Auchère, F., Rodet, T., and Vial, J.-C. (2008). A time-evolving 3D method dedicated to the reconstruction of solar plumes and results using extreme ultraviolet data. *Sol. Phys.* 248, 409–423. doi: 10.1007/s11207-008-9151-6
- Barbey, N., Guennou, C., and Auchère, F. (2013). TomograPy: a fast, instrument-independent, solar tomography software. *Sol. Phys.* 283, 227–245. doi: 10.1007/s11207-011-9792-8
- Boerner, P. F., Testa, P., Warren, H., Weber, M. A., and Schrijver, C. J. (2014). Photometric and thermal cross-calibration of solar EUV instruments. *Sol. Phys.* 289, 2377–2397. doi: 10.1007/s11207-013-0452-z
- Borovsky, J. E., and Denton, M. H. (2013). The differences between storms driven by helmet streamer CIRs and storms driven by pseudostreamer CIRs. *J. Geophys. Res. Space Phys.*, 118, 5506–5521. doi: 10.1002/jgra.50524
- Borrini, G., Wilcox, J. M., Gosling, J. T., Bame, S. J., and Feldman, W. C. (1981). Solar wind helium and hydrogen structure near the heliospheric current sheet - A signal of coronal streamers at 1 AU. *J. Geophys. Res.* 86, 4565–4573. doi: 10.1029/JA086iA06p04565
- Brown, J. C., Dwivedi, B. N., Sweet, P. A., and Almleaky, Y. M. (1991). The interpretation of density sensitive line diagnostics from inhomogeneous plasmas. II - Non-isothermal plasmas. *Astron. Astrophys.* 249, 277–283.
- Butala, M. D., Hewett, R. J., Frazin, R. A., and Kamalabadi, F. (2010). Dynamic three-dimensional tomography of the solar corona. *Sol. Phys.* 262, 495–509. doi: 10.1007/s11207-010-9536-1
- Cheung, M. C. M., Boerner, P., Schrijver, C. J., Testa, P., Chen, F., Peter, H. et al. (2015). Thermal diagnostics with the atmospheric imaging assembly on board the solar dynamics observatory: a validated method for differential emission measure inversions. *Astrophys. J.* 807, 143. doi: 10.1088/0004-637X/807/2/143
- Craig, I. J. D., and Brown, J. C. (1976). Fundamental limitations of X-ray spectra as diagnostics of plasma temperature structure. *Astron. Astrophys.* 49, 239–250.
- de Patoul, J., Inhester, B., Feng, L., and Wiegelmann, T. (2013). 2D and 3D polar plume analysis from the three vantage positions of STEREO/EUVI A, B, and SOHO/EIT. *Sol. Phys.* 283, 207–225. doi: 10.1007/s11207-011-9902-7
- Dere, K. P., Landi, E., Mason, H. E., Monsignori Fossi, B. C., and Young, P. R. (1997). CHIANTI - an atomic database for emission lines. *Astron. Astrophys. Suppl. Ser.* 125, 149–173. doi: 10.1051/aas:1997368
- Eselevich, V. G., and Tong, Y. (1997). New results on the site of initiation of coronal mass ejections and an interpretation of observation of their interaction with streamers. *J. Geophys. Res.* 102, 4681–4690. doi: 10.1029/96JA02875
- Frazin, R. A. (2000). Tomography of the solar corona. I. A robust, regularized, positive estimation method. *Astrophys. J.* 530, 1026–1035. doi: 10.1086/308412
- Frazin, R. A., Butala, M. D., Kemball, A., and Kamalabadi, F. (2005a). Time-dependent reconstruction of nonstationary objects with tomographic or interferometric measurements. *Astrophys. J. Lett.* 635, L197–L200. doi: 10.1086/499431
- Frazin, R. A., and Janzen, P. (2002). Tomography of the solar corona. II. Robust, regularized, positive estimation of the three-dimensional electron density distribution from LASCO-C2 polarized white-light images. *Astrophys. J.* 570, 408–422. doi: 10.1086/339572
- Frazin, R. A., Kamalabadi, F., and Weber, M. A. (2005b). On the combination of differential emission measure analysis and rotational tomography for three-dimensional solar EUV imaging. *Astrophys. J.* 628, 1070–1080. doi: 10.1086/431295
- Frazin, R. A., Vásquez, A. M., and Kamalabadi, F. (2009). Quantitative, three-dimensional analysis of the global corona with multi-spacecraft differential emission measure tomography. *Astrophys. J.* 701, 547–560. doi: 10.1088/0004-637X/701/1/547
- Fuller, J., and Gibson, S. E. (2009). A survey of coronal cavity density profiles. *Astrophys. J.* 700, 1205–1215. doi: 10.1088/0004-637X/700/2/1205
- Fuller, J., Gibson, S. E., de Toma, G., and Fan, Y. (2008). Observing the unobservable? Modeling coronal cavity densities. *Astrophys. J.* 678, 515–530. doi: 10.1086/533527
- Gibson, S. E., and Fan, Y. (2006). Coronal prominence structure and dynamics: a magnetic flux rope interpretation. *J. Geophys. Res. Space Phys.* 111, 12103. doi: 10.1029/2006ja011871
- Gibson, S. E., Kucera, T. A., Rastawicki, D., Dove, J., de Toma, G., Hao, J., et al. (2010). Three-dimensional morphology of a coronal prominence cavity. *Astrophys. J.* 724, 1133–1146. doi: 10.1088/0004-637X/724/2/1133
- Guennou, C., Auchère, F., Klimchuk, J. A., Bocchialini, K., and Parenti, S. (2013). Can the differential emission measure constrain the timescale of energy deposition in the corona? *Astrophys. J.* 774, 31. doi: 10.1088/0004-637X/774/1/31
- Guennou, C., Auchère, F., Soubrié, E., Bocchialini, K., Parenti, S., and Barbey, N. (2012a). On the accuracy of the differential emission measure diagnostics of solar plasmas. Application to SDO/AIA. I. Isothermal plasmas. *Astrophys. J. Suppl. Ser.* 203, 25. doi: 10.1088/0067-0049/203/2/25
- Guennou, C., Auchère, F., Soubrié, E., Bocchialini, K., Parenti, S., and Barbey, N. (2012b). On the accuracy of the differential emission measure diagnostics of solar plasmas. Application to SDO/AIA. II. Multithermal plasmas. *Astrophys. J. Suppl. Ser.* 203, 26. doi: 10.1088/0067-0049/203/2/26
- Guhathakurta, M., Rottman, G. J., Fisher, R. R., Orrall, F. Q., and Altrock, R. C. (1992). Coronal density and temperature structure from coordinated observations associated with the total solar eclipse of 1988 March 18. *Astrophys. J.* 388, 633–643. doi: 10.1086/171180
- Habbal, S. R., Druckmüller, M., Morgan, H., Scholl, I., Rušin, V., Daw, A., et al. (2010). Total solar eclipse observations of hot prominence shrouds. *Astrophys. J.* 719, 1362–1369. doi: 10.1088/0004-637X/719/2/1362
- Halain, J.-P., Berghmans, D., Seaton, D. B., Nicula, B., De Groof, A., Mierla, M., et al. (2013). The SWAP EUV imaging telescope. Part II: in-flight performance and calibration. *Sol. Phys.* 286, 67–91. doi: 10.1007/s11207-012-0183-6
- Hannah, I. G., and Kontar, E. P. (2012). Differential emission measures from the regularized inversion of Hinode and SDO data. *Astron. Astrophys.* 539:A146. doi: 10.1051/0004-6361/201117576
- Higdon, D. M., Bowsher, J. E., Johnson, V. E., Turkington, T. G., Gilland, D. R., and Jaszcza, R. J. (1997). Fully bayesian estimation of Gibbs hyperparameters for emission computed tomography data. *IEEE Trans. Med. Imaging* 16, 516–526. doi: 10.1109/42.640741
- Howard, R. A., Sheeley, Jr. N. R., Michels, D. J., and Koomen, M. J. (1985). Coronal mass ejections - 1979-1981. *J. Geophys. Res.* 90, 8173–8191. doi: 10.1029/JA090iA09p08173
- Huang, Z., Frazin, R. A., Landi, E., Manchester, W. B., Vásquez, A. M., and Gombosi, T. I. (2012). Newly discovered global temperature structures in the quiet sun at solar minimum. *Astrophys. J.* 755, 86. doi: 10.1088/0004-637X/755/2/86
- Hudson, H. S., Acton, L. W., Harvey, K. L., and McKenzie, D. E. (1999). A stable filament cavity with a hot core. *Astrophys. J. Lett.* 513, L83–L86. doi: 10.1086/311892
- Jefferies, J. T., Orrall, F. Q., and Zirker, J. B. (1972). The interpretation of total line intensities from optically thin gases. I: a general method. *Sol. Phys.* 22, 307–316. doi: 10.1007/BF00148698
- Judge, P. G., Hubeny, V., and Brown, J. C. (1997). Fundamental limitations of emission-line spectra as diagnostics of plasma temperature and density structure. *Astrophys. J.* 475, 275–290. doi: 10.1086/303511
- Kashyap, V., and Drake, J. J. (1998). Markov-Chain Monte Carlo reconstruction of emission measure distributions: application to solar extreme-ultraviolet spectra. *Astrophys. J.* 503, 450–466. doi: 10.1086/305964
- Klimchuk, J. A., Karpen, J. T., and Antiochos, S. K. (2010). Can thermal nonequilibrium explain coronal loops? *Astrophys. J.* 714, 1239–1248. doi: 10.1088/0004-637X/714/2/1239
- Krall, J., and Chen, J. (2005). Density structure of a preeruption coronal flux rope. *Astrophys. J.* 628, 1046–1055. doi: 10.1086/430810
- Kucera, T. A., Gibson, S. E., Schmit, D. J., Landi, E., and Tripathi, D. (2012). Temperature and extreme-ultraviolet intensity in a coronal prominence cavity and streamer. *Astrophys. J.* 757:73. doi: 10.1088/0004-637X/757/1/73
- Landi, E., Young, P. R., Dere, K. P., Del Zanna, G., and Mason, H. E. (2013). CHIANTI - an atomic database for emission lines. XIII. soft X-Ray improvements and other changes. *Astrophys. J.* 763:86. doi: 10.1088/0004-637X/763/2/86
- Lynch, B. J., and Edmondson, J. K. (2013). Sympathetic magnetic breakout coronal mass ejections from pseudostreamers. *Astrophys. J.* 764:87. doi: 10.1088/0004-637X/764/1/87
- Marqué, C. (2004). Radio metric observations of quiescent filament cavities. *Astrophys. J.* 602, 1037–1050. doi: 10.1086/381085

- Mason, H. E., and Fossi, B. C. M. (1994). Spectroscopic diagnostics in the UV for solar and stellar plasmas. *Astron. Astrophys. Rev.* 6, 123–179. doi: 10.1007/BF01208253
- Nuevo, F. A., Huang, Z., Frazin, R., Manchester, IV, W. B., Jin, M., and Vásquez, A. M. (2013). Evolution of the global temperature structure of the solar corona during the minimum between solar cycles 23 and 24. *Astrophys. J.* 773:9. doi: 10.1088/0004-637X/773/1/9
- Nuevo, F. A., Vásquez, A. M., Landi, E., and Frazin, R. (2015). Multimodal differential emission measure in the solar corona. *Astrophys. J.* 811:128. doi: 10.1088/0004-637X/811/2/128
- Pottasch, S. R. (1963). The lower solar corona: interpretation of the ultraviolet spectrum. *Astrophys. J.* 137:945. doi: 10.1086/147569
- Rachmeler, L. A., Platten, S. J., Bethge, C., Seaton, D. B., and Yeates, A. R. (2014). Observations of a hybrid double-streamer/pseudostreamer in the solar corona. *Astrophys. J. Lett.* 787:L3. doi: 10.1088/2041-8205/787/1/L3
- Reeves, K. K., Gibson, S. E., Kucera, T. A., Hudson, H. S., and Kano, R. (2012). Thermal properties of a solar coronal cavity observed with the X-Ray telescope on hinode. *Astrophys. J.* 746:146. doi: 10.1088/0004-637X/746/2/146
- Schmit, D. J., Gibson, S., Luna, M., Karpen, J., and Innes, D. (2013). Prominence mass supply and the cavity. *Astrophys. J.* 779:156. doi: 10.1088/0004-637X/779/2/156
- Schmit, D. J., and Gibson, S. E. (2011). Forward modeling cavity density: a multi-instrument diagnostic. *Astrophys. J.* 733:1. doi: 10.1088/0004-637X/733/1/1
- Seaton, D. B., Berghmans, D., Nicula, B., Halain, J.-P., De Groof, A., Thibert, T., et al. (2013). The SWAP EUV imaging telescope part I: instrument overview and pre-flight testing. *Sol. Phys.* 286, 43–65. doi: 10.1007/s11207-012-0114-6
- Siddon, R. L. (1985). Prism representation: a 3D ray-tracing algorithm for radiotherapy applications. *Phys. Med. Biol.* 30, 817–824. doi: 10.1088/0031-9155/30/8/005
- Sturrock, P. A., and Smith, S. M. (1968). Magnetic-field structure associated with coronal streamers. *Sol. Phys.* 5, 87–101. doi: 10.1007/BF00147122
- Testa, P., De Pontieu, B., Martínez-Sykora, J., Hansteen, V., and Carlsson, M. (2012). Investigating the reliability of coronal emission measure distribution diagnostics using three-dimensional radiative magnetohydrodynamic simulations. *Astrophys. J.* 758:54. doi: 10.1088/0004-637X/758/1/54
- Vásquez, A. M., Frazin, R. A., and Kamalabadi, F. (2009). 3D temperatures and densities of the solar corona via multi-spacecraft EUV tomography: analysis of prominence cavities. *Sol. Phys.* 256, 73–85. doi: 10.1007/s11207-009-9321-1
- Vial, J.-C., and Engvold, O. (eds.). (2015). *Solar Prominences, Vol. 415 of Astrophysics and Space Science Library*. Springer International Publishing. Available online at: <http://www.springer.com/us/book/9783319104157>
- Wang, Y.-M. (2015). Pseudostreamers as the source of a separate class of solar coronal mass ejections. *Astrophys. J. Lett.* 803:L12. doi: 10.1088/2041-8205/803/1/L12
- Wang, Y.-M., Sheeley, Jr. N. R., Nash, A. G., and Shampine, L. R. (1988). The quasi-rigid rotation of coronal magnetic fields. *Astrophys. J.* 327, 427–450. doi: 10.1086/166205
- Wang, Y.-M., Sheeley, Jr. N. R., and Rich, N. B. (2007). Coronal Pseudostreamers. *Astrophys. J.* 658, 1340–1348. doi: 10.1086/511416
- Wang, Y.-M., and Stenborg, G. (2010). Spinning motions in coronal cavities. *Astrophys. J.* 719, L181–L184. doi: 10.1088/2041-8205/719/2/L181
- Wuelser, J.-P., Lemen, J. R., Tarbell, T. D., Wolfson, C. J., Cannon, J. C., Carpenter, B. A., et al. (2004). “EUVI: the STEREO-SECCHI extreme ultraviolet imager,” in *Telescopes and Instrumentation for Solar Astrophysics, Volume 5171 of Proceedings of the SPIE*, eds S. Fineschi and M. A. Gummin, 111–122. Available online at: <http://cdsads.u-strasbg.fr/abs/2004SPIE.5171..111W>
- Zhao, L., Gibson, S. E., and Fisk, L. A. (2013). Association of solar wind proton flux extremes with pseudostreamers. *J. Geophys. Res. Space Phys.* 118, 2834–2841. doi: 10.1002/jgra.50335
- Zhao, X. P., and Webb, D. F. (2003). Source regions and storm effectiveness of frontside full halo coronal mass ejections. *J. Geophys. Res. Space Phys.* 108:1234. doi: 10.1029/2002JA009606

**Conflict of Interest Statement:** The authors declare that the research was conducted in the absence of any commercial or financial relationships that could be construed as a potential conflict of interest.

Copyright © 2016 Guennou, Rachmeler, Seaton and Auchère. This is an open-access article distributed under the terms of the Creative Commons Attribution License (CC BY). The use, distribution or reproduction in other forums is permitted, provided the original author(s) or licensor are credited and that the original publication in this journal is cited, in accordance with accepted academic practice. No use, distribution or reproduction is permitted which does not comply with these terms.



# 3D Global Coronal Density Structure and Associated Magnetic Field near Solar Maximum

Maxim Kramar<sup>1</sup>, Vladimir Airapetian<sup>2,3\*</sup> and Haosheng Lin<sup>4</sup>

<sup>1</sup> Physics Department, The Catholic University of America, Washington, DC, USA, <sup>2</sup> Department of Physics and Astronomy, George Mason University, Fairfax, VA, USA, <sup>3</sup> NASA/Goddard Space Flight Center, Code 671, Greenbelt, MD, USA, <sup>4</sup> College of Natural Sciences, Institute for Astronomy, University of Hawaii at Manoa, Pukalani, HI, USA

## OPEN ACCESS

### Edited by:

Valery M. Nakariakov,  
University of Warwick, UK

### Reviewed by:

Gordon James Duncan Petrie,  
National Solar Observatory, USA  
Keiji Hayashi,  
Nagoya University, Japan

### \*Correspondence:

Vladimir Airapetian  
vladimir.airapetian@nasa.gov

### Specialty section:

This article was submitted to  
Stellar and Solar Physics,  
a section of the journal  
*Frontiers in Astronomy and Space  
Sciences*

Received: 16 March 2016

Accepted: 26 July 2016

Published: 09 August 2016

### Citation:

Kramar M, Airapetian V and Lin H (2016) 3D Global Coronal Density Structure and Associated Magnetic Field near Solar Maximum. *Front. Astron. Space Sci.* 3:25. doi: 10.3389/fspas.2016.00025

Measurement of the coronal magnetic field is a crucial ingredient in understanding the nature of solar coronal dynamic phenomena at all scales. We employ STEREO/COR1 data obtained near maximum of solar activity in December 2012 (Carrington rotation, CR 2131) to retrieve and analyze the three-dimensional (3D) coronal electron density in the range of heights from 1.5 to 4  $R_{\odot}$  using a tomography method and qualitatively deduce structures of the coronal magnetic field. The 3D electron density analysis is complemented by the 3D STEREO/EUVI emissivity in 195 Å band obtained by tomography for the same CR period. We find that the magnetic field configuration during CR 2131 has a tendency to become radially open at heliocentric distances below  $\sim 2.5 R_{\odot}$ . We compared the reconstructed 3D coronal structures over the CR near the solar maximum to the one at deep solar minimum. Results of our 3D density reconstruction will help to constrain solar coronal field models and test the accuracy of the magnetic field approximations for coronal modeling.

**Keywords:** Sun, corona, electron density, magnetic field, tomography

## 1. INTRODUCTION

Solar coronal magnetic field is a major source of dynamics and thermodynamics of global coronal corona and transient coronal events including the coronal heating, solar flares, coronal mass ejections, and the solar wind. Its dynamics affects space weather processes that may impact Earth's magnetosphere and atmosphere and affect life on our planet. Thus, the knowledge of coronal magnetic field strength and topology represents one of major goals of the solar physics. Currently, coronal magnetic fields cannot directly measured. The major techniques that are currently used to derive the global magnetic structures of the solar corona represent indirect methods including potential field source surface (PFSS) models, non-linear force-free field (NLFFF) models and multi-dimensional magnetohydrodynamic (MHD) models of the global solar corona. These methods use solar photospheric scalar or vector magnetic field as input directly derived from photospheric magnetograms. However, as we discussed in Kramar et al. (2014), all these methods cannot adequately describe the dynamics of magnetic fields observed in the solar corona driven by current carrying structures. Moreover, they do not provide accurate information about the coronal thermodynamics, and thus cannot be used for modeling the coronal emission measures derived from extreme ultraviolet (EUV) observations. The MHD modeling of the solar corona provides a self-consistent time-dependent treatment of the plasma pressure, gravitational and magnetic forces, but are limited by approximations used for describing the coronal heating, and the uncertainties

in the boundary conditions that are deduced from synoptic data. Thus, direct measurements of the coronal magnetic field remains one of the most reliable and challenging ways for characterization of solar coronal processes.

Direct measurement of the coronal magnetic field is the most challenging problem in observational solar physics. A major progress here was reached with the deployment of the Coronal Multichannel Polarimeter (CoMP) (Tomczyk et al., 2007, 2008). In order to interpret such type of data, a vector tomography method has been developed for 3D reconstruction of the global coronal magnetic field (Kramar et al., 2006, 2013), and recently, first 3D reconstruction of the global coronal magnetic field has been performed based on the CoMP data (Kramar et al., 2016).

Another, thought implicit but also based on coronal observations, way to reconstruct some global coronal magnetic field structures was investigated in Kramar et al. (2014). There we applied the tomography method that employs STEREO data to reconstruct 3D density of global solar corona and related it to the coronal magnetic field structure. This method was applied to characterize the solar corona over the Carrington rotation 2066 occurred during deep solar minimum for the range of coronal heights from 1.5 to  $4 R_{\odot}$  and provided description of the open/close magnetic field boundaries in the solar corona.

In this paper, we apply this method to study global solar coronal structures for the period of over the half of Carrington rotation 2131, which represents the case of solar maximum. Specifically, we use the STEREO/COR1 coronagraph data for half a solar rotation period during CR 2131 as input for the tomographic reconstruction of the 3D coronal electron density and the configuration of magnetic field associated with them. Our results are complemented by the 3D emissivity obtained by tomography method applied for the the STEREO *Extreme Ultraviolet Imager* (EUVI) data in the 195 Å band. We also compared the reconstructed 3D coronal structures with those implied by the PFSS model. In Section 4, we present the comparison of the 3D coronal structure near the solar maximum to those at deep solar minimum (CR 2066).

Two of the addressed problems we have analyzed are at which distance the global coronal magnetic field lines become radially directed and where are boundaries between closed and open magnetic field structures. An answer to this question is particularly important for predictions of the slow/fast solar wind and CME. Thus, it has been found that once erupted CME does not follow straight path but deflects according the global 3D coronal magnetic field (Xie et al., 2009; Kay et al., 2015). This complicates prediction of when and whether a CME encounter the Earth.

## 2. METHODS

Because the solar corona is optically thin at visible and EUVI wavelengths, the observed flux in these spectral ranges is an integral of the emissivity along any line of sight (LOS). To our knowledge, tomography is the most effective method for three-dimensional (3D) reconstruction of optically thin objects based *only* on the LOS measurements made from

multiple observing directions. The nice property of the method is that in its basic form it does not require any *a priori* knowledge about 3D properties of the object (except that it is optically thin) and its accuracy is generally depends on the quantity of measurements (number and coverage), their accuracy, a physical effect used in the LOS signal (i.e., diffraction limit, relation of emitting/absorbed light to the local property of the object, etc.), numerical inversion scheme (Natterer, 2001). This makes the method to be effectively used in many fields such as medical imaging, material structure research, geophysics, heliophysics and astrophysics (Boffin et al., 2001).

In this study, we apply the tomography method that employs STEREO data to reconstruct 3D density and EUVI emissivity of global solar corona. The method has been extensively described in Kramar et al. (2009, 2014). One of the most distinctive feature of this method is that it uses preconditioning which allows us to account for a large dynamical range of the coronal density values.

The relation of the 3D global coronal density and EUVI 195 Å emissivity to the properties of the coronal magnetic field has been investigated in Kramar et al. (2014). Particularly, it has been found that the position of maximal gradient of the density and 195 Å emissivity can be an indicator for the position of boundary between closed and open magnetic structures. In this study, we apply these methods to study 3D global solar coronal structures near maximum of the solar activity cycle and compare the reconstructed 3D corona with PFSS models.

Thought potential field models do not accurately describe the solar corona structure, they are very robust. One of the main adjustable parameters in PFSS models is location of the source surface after which the magnetic field becomes radially directed. There are several recent studies about consistency of PFSS model for various source surface distances with EUVI synoptic map and interplanetary magnetic field (Lee et al., 2011; Arden et al., 2014). Our approach on this matter is different. We compare PFSS models with 3D coronal electron density and related to it magnetic properties (open/closed magnetic field lines boundary).

For boundary conditions for the PFSS model (Altschuler and Newkirk, 1969), we used Carrington Rotation spherical harmonic transform coefficients from the National Solar Observatory (NSO) GONG data<sup>1</sup>. We restricted the spherical harmonic polynomial coefficients in the PFSS model to 20th order which is sufficient for the extrapolation of the global corona.

## 3. 3D CORONAL STRUCTURE DURING CR 2131

CR 2131 represents the period near maximum of solar activity cycle. In this study, we performed two types of tomographic reconstructions: 3D reconstruction of the electron density based on STEREO/COR1 data and 3D reconstruction for the EUVI

<sup>1</sup><http://gong.nso.edu/data/magmap/QR/mqc/>

195 Å emissivity [units of photons s<sup>-1</sup> sr<sup>-1</sup> cm<sup>-3</sup>] based on STEREO/EUVI data.

In order to demonstrate a general structure of the coronal streamer belt for CR 2131, **Figure 1** shows a spherical cross-section of the electron density at the heliocentric distance of  $2 R_{\odot}$  and **Figure 2** shows a spherical cross-section of the EUVI 195 Å emissivity at the heliocentric distance of  $1.1 R_{\odot}$ . Solid black and dashed red lines indicate the magnetic neutral line at corresponding heights for PFSS model with source surface located at  $1.5 R_{\odot}$  and  $2 R_{\odot}$ , respectively. It was demonstrated earlier in Kramar et al. (2014) that the density maximum locations can serve as an indicator of current sheet position which is characterized by the magnetic neutral line. We can see in the Figures that coincidence of the derived from the PFSS models positions of the magnetic neutral line with the density concentrations is far from ideal.

**Figure 3** shows several meridional cross-sections of the electron density (range from  $1.5$  to  $4 R_{\odot}$ ) and EUVI 195 Å emissivity (range from  $1.05$  to  $1.29 R_{\odot}$ ). The figure with a set of all cross-sections is available in the Electronic Supplementary Material.

The black contour lines in **Figure 3** show boundaries between open and closed magnetic-field structures in two PFSS models with Source Surface heliocentric distances [ $R_{ss}$ ] at  $1.5$  and  $2.0 R_{\odot}$ . The PFSS model with  $R_{ss} = 2.0 R_{\odot}$  does not coincide with the

derived positions of the streamer and pseudo-streamer as well as with the coronal hole positions indicated by the STEREO/EUVI 195 Å emissivity 3D reconstruction. The PFSS model with  $R_{ss} = 1.5 R_{\odot}$  appears to fit the latter structures better.

It was previously demonstrated that the position of maximal gradient of the density and 195 Å emissivity can be an indicator for the position of boundary between closed and open magnetic structures Kramar et al. (2014). Therefore, in order to exhibit the possible real boundary positions, **Figure 4** shows gradient of electron density and EUVI 195 emissivity,  $\partial N_e / \partial \theta$  and  $\partial \varepsilon_{195} / \partial \theta$ , for CR 2131 and for the same longitudinal cross-sections as in **Figure 3**. Both **Figures 3, 4** demonstrate that the magnetic field configuration during CR 2131 has a tendency to become radially open at heliocentric distances below  $\sim 2.5 R_{\odot}$ . This is lower than corresponding distance during the deep solar minimum near CR 2066 (Kramar et al., 2014).

Also, it should be noted that in **Figures 3, 4** reconstructed streamers sometimes appear to slightly inclined toward the solar north. This could be because of stronger southern polar field. In fact, averaged over northern and southern hemispheres absolute values of magnetic field strength at  $1.2 R_{\odot}$  in the PFSS model with source surface at  $2.0 R_{\odot}$  are  $0.59$  and  $1.04$ , respectively. The prevailing strength of the southern over the northern fields extends to higher distances. For example, the respective values at  $1.9 R_{\odot}$  are  $0.06$  and  $0.11$ .

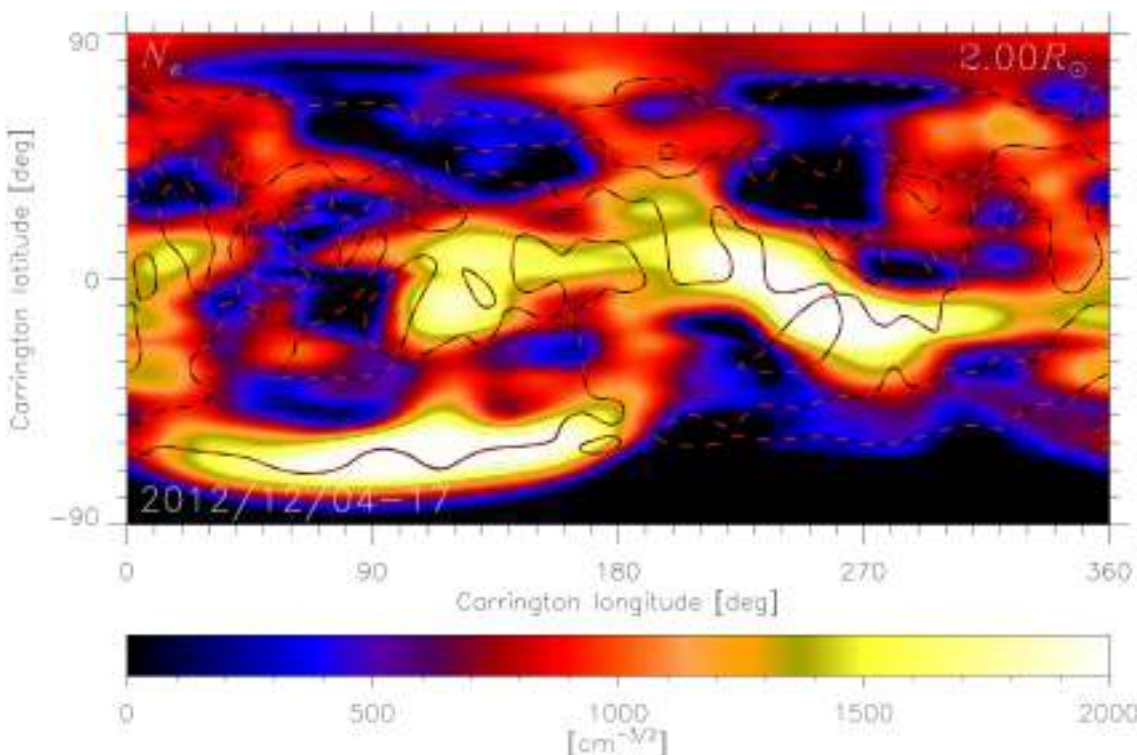


**FIGURE 1 | Spherical cross-section of the reconstructed electron density in square root scale at heliocentric distance of  $2 R_{\odot}$ .** The reconstruction is obtained by tomography based on COR-1 data obtained during December 4–17, 2012 (CR 2131). Solid black and dashed red lines indicate the magnetic neutral line in PFSS model with source surface located at  $1.5 R_{\odot}$  and  $2 R_{\odot}$ , respectively.

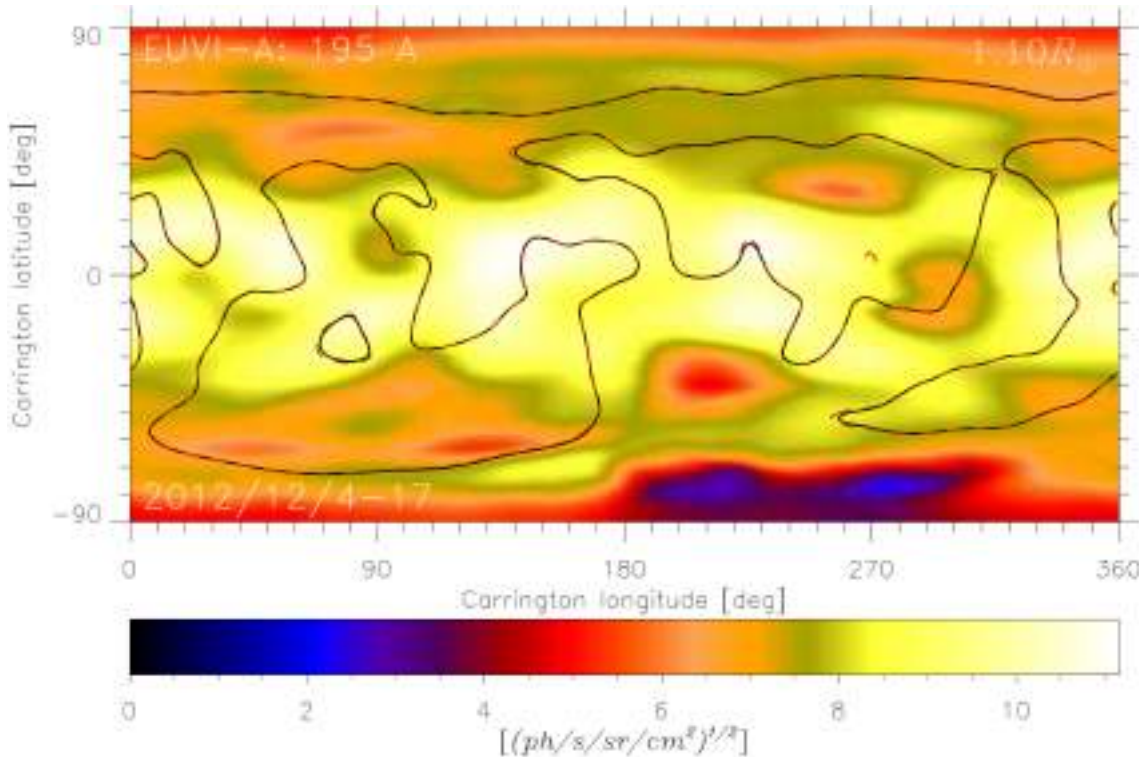


**FIGURE 2 | Spherical cross-section of the reconstructed 3D EUVI 195 Å emissivity in square root scale at heliocentric distances of  $1.1 R_{\odot}$ .** The reconstruction is obtained by tomography based on COR-1 data obtained during December 4–17, 2012 (CR 2131). Solid black and dashed red lines indicate the magnetic neutral line in PFSS model with source surface located at  $1.5 R_{\odot}$  and  $2 R_{\odot}$ , respectively.

**Figure 5** shows the radial profiles of the maximum (left panel) and average (right panel) electron density values at different heliocentric distances for CR 2066 (dashed green), 2112 (solid red), and 2131 (solid black). CR 2066 corresponds to deep solar minimum, while CR 2131 corresponds to period near solar maximum. The maximum values of coronal density mostly reflect the closed magnetic field structures represented by solar active regions, while average values include contributions from both open and closed field regions. The plot suggests that the maximum coronal density at the solar maximum is larger than the coronal density at two Carrington rotations representing the periods of lower magnetic activity. Specifically, at the lower boundary (at  $1.8 R_{\odot}$ ) of the reconstruction region the maximum density at solar maximum is more than twice greater than the maximum coronal density at solar minimum represented by CR 2066. This reflects the fact that the total unsigned magnetic flux that is structured in the form of coronal active regions during solar maximum is a factor of 2–3 greater than the emerging magnetic flux during solar minimum (Solanki et al., 2002). The average coronal density is a factor of 1.6 greater during solar maximum as compared to solar minimum, because it reflects the contribution of plasma emission formed in the diffuse corona as well as coronal active regions.

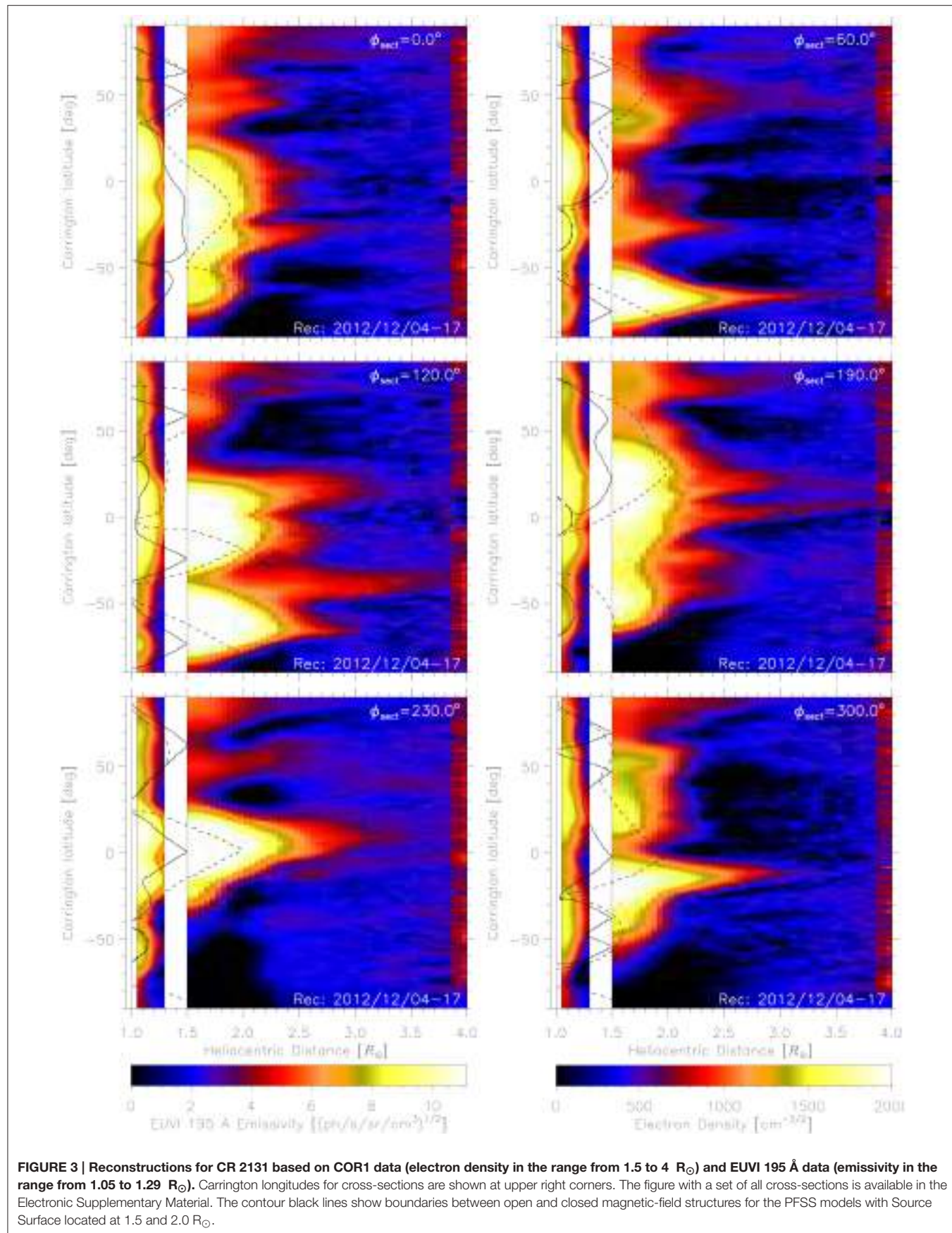
**Figure 6** shows the snapshot of the isosurface of coronal electron density value of  $10^6 \text{ cm}^{-3}$  (in blue) for CR 2066 occurred at solar minimum (left) and CR 2131 at solar maximum

(right). The corresponding movie showing the density isosurface over these two Carrington rotations are available provided in online version of the paper. The figure and the movie clearly demonstrate that the volume filling factor of the plasma with the density of  $10^6 \text{ cm}^{-3}$  increases at solar maximum, which is consistent with **Figure 5**.

## 4. CONCLUSION AND OUTLOOK

We applied the tomography method to STEREO-B/COR1 data to derive the reconstructions of the 3D global coronal electron density and EUVI 195 Å emissivity based on STEREO/COR1 and STEREO/EUVI observations near solar maximum represented by Carrington rotation CR 2131 (December 2012). We complemented the tomography with MHD simulations to obtain the open/closed magnetic field boundaries in the solar corona. Because the 3D reconstructions are based entirely on *coronal* data, these results could serve as an independent test and/or as an additional constraint for the models of the solar corona. Specifically, we used the PFSS model with different source surface distances as a test case for the reconstructed 3D electron density and EUVI 195 emissivity structures.

We have shown that magnetic field structures deviate significantly from the PFSS approximation as evident from the



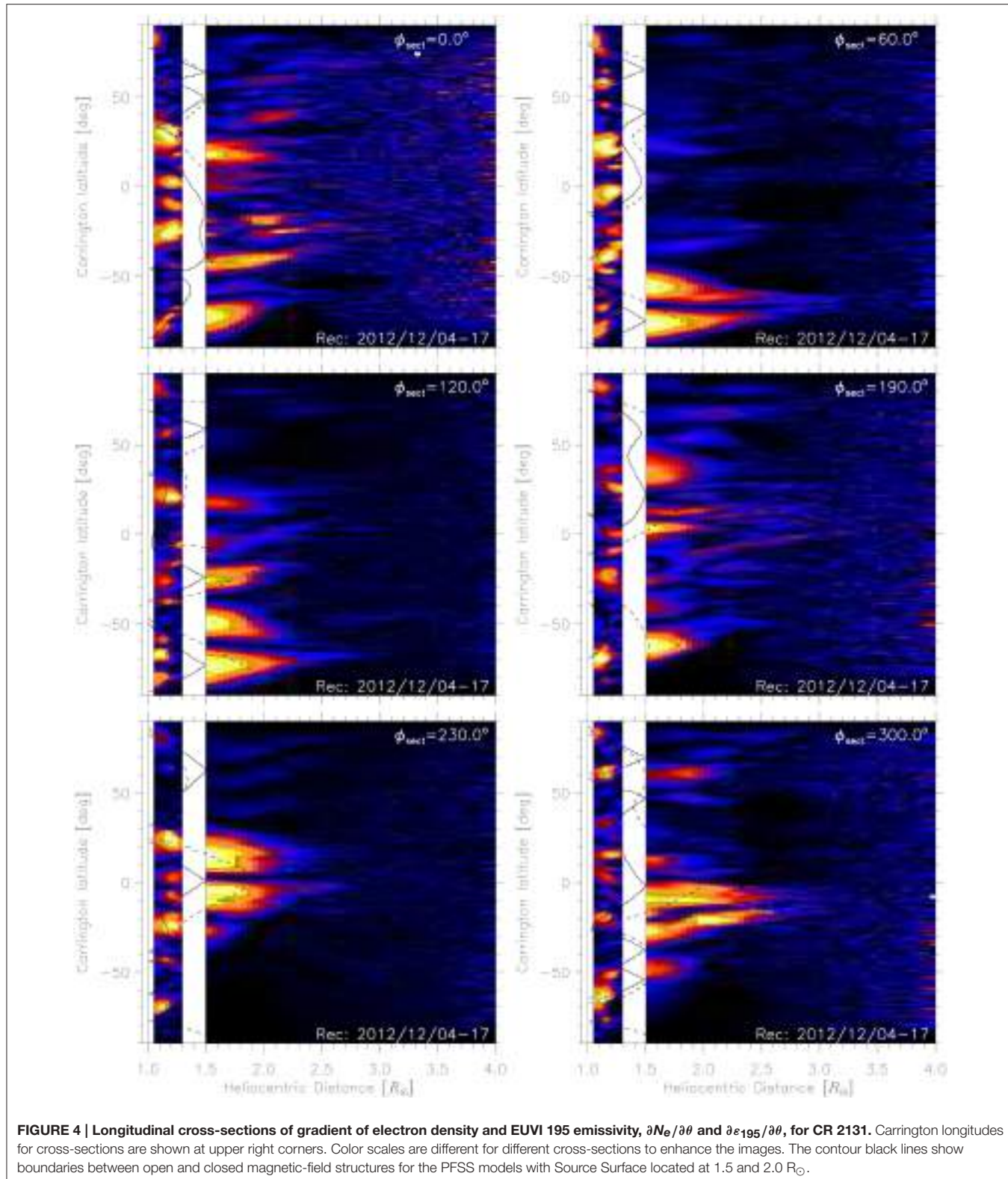


**FIGURE 4 |** Longitudinal cross-sections of gradient of electron density and EUVI 195 emissivity,  $\partial N_e / \partial \theta$  and  $\partial e_{195} / \partial \theta$ , for CR 2131. Carrington longitudes for cross-sections are shown at upper right corners. Color scales are different for different cross-sections to enhance the images. The contour black lines show boundaries between open and closed magnetic-field structures for the PFSS models with Source Surface located at 1.5 and 2.0  $R_\odot$ .

derived boundaries of open/closed field for both solar minimum (Kramar et al., 2014) and solar maximum. This suggests that potential field approximation for the low corona is not valid

approximation when describing its large-scale structures. This discrepancy is most probably due to non-potential character of the solar coronal magnetic field. Although the fact that PFSS uses

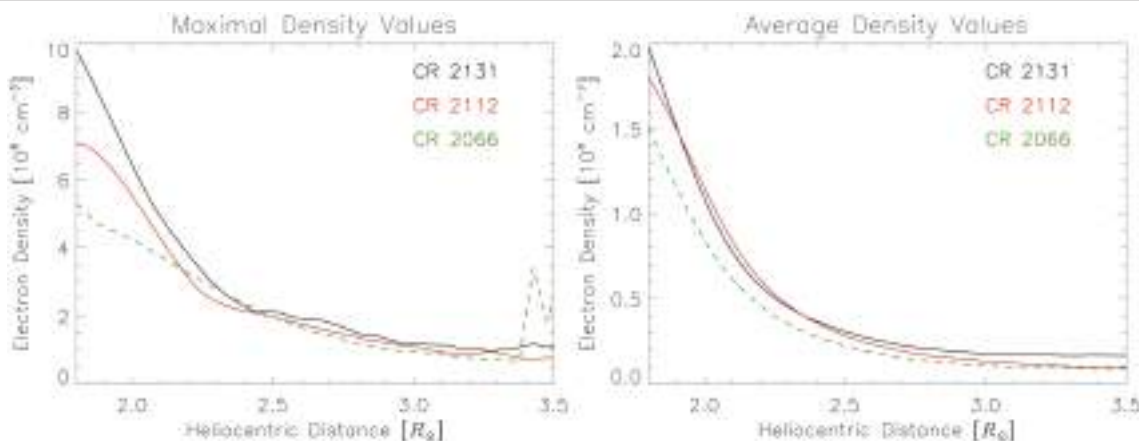


**FIGURE 5 |** Maximal (left panel) and average over a spherical surface area (right panel) electron density values at different heliocentric distances for CR 2066 (dashed green), 2112 (solid red), and 2131 (solid black). CR 2066 corresponds to deep solar minimum, while CR 2131 corresponds to period near solar maximum.

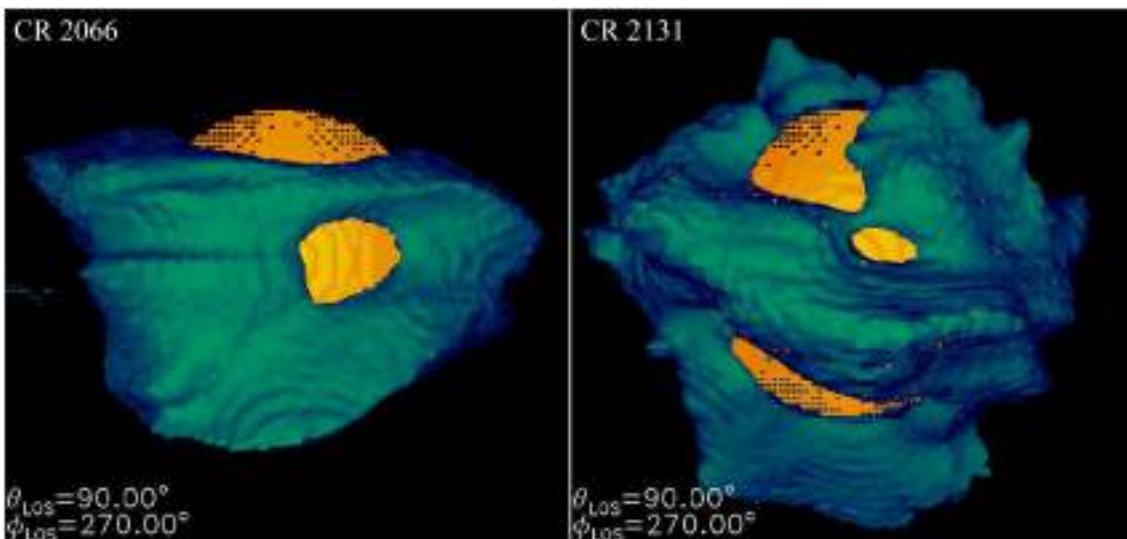


**FIGURE 6 |** Isosurface of coronal electron density value of  $10^6 \text{ cm}^{-3}$  (in blue) for CR 2066 (left) and 2131 (right). The orange sphere is located at  $1.5R_\odot$  just for scaling purpose. The movie demonstrating the isosurfaces for the whole longitudinal projection range is provided in online version of the paper.

magnetograms collected over about a whole CR period while the tomographic reconstructions require observations over only half a CR period, the tomography provides more accurate description of the solar corona.

It is important to note that the magnetic field becomes radial at heights greater than  $2.5R_\odot$  during solar minimum, while its open up at heights below  $\sim 2.5R_\odot$  during solar maximum.

Our studies also show that the average and the maximum electron densities in the low solar corona at heights  $\sim 1.8R_\odot$  are about 2 times greater than that obtained during solar minimum. This is an important result that can be extrapolated to coronal densities of active and young solar-like stars. These

stars show much greater levels of stellar activity in terms of at  $> 10$  times greater surface magnetic flux, up to 1000 times more luminous in X-rays and at least 10 times denser and hotter corona. These results open up an interesting opportunity to provide scaling of the electron density of the solar corona with different levels of magnetic activity traced by its X-ray luminosity and average surface magnetic flux. These scaling laws can be then used for characterization of stellar corona of active stars, which may provide insights on the nature of stellar coronal heating at various phases of their evolution.

Applied in this study method can also be used for verification of 3D global coronal vector magnetic field obtained by vector

tomography based on coronal polarimetric observations (Kramar et al., 2016).

## AUTHOR CONTRIBUTIONS

MK developed the methods and wrote the codes. Also, MK led the calculations and contributed to the analysis of the results and writing the article. VA and HL assisted in calculations

and contributed to the analysis of the results and writing the article.

## SUPPLEMENTARY MATERIAL

The Supplementary Material for this article can be found online at: <http://journal.frontiersin.org/article/10.3389/fspas.2016.00025>

## REFERENCES

- Altschuler, M. D., and Newkirk, G. (1969). Magnetic fields and the structure of the solar corona. I: methods of calculating coronal fields. *Solar Phys.* 9, 131–149. doi: 10.1007/BF00145734
- Arden, W. M., Norton, A. A., and Sun, X. (2014). A “breathing” source surface for cycles 23 and 24. *J. Geophys. Res. (Space Phys.)* 119, 1476–1485. doi: 10.1002/2013JA019464
- Boffin, H. M. J., Steeghs, D., and Cuypers, J., (eds.). (2001). *Astro tomography, Volume 573 of Lecture Notes in Physics*. Berlin: Springer Verlag.
- Kay, C., Opher, M., and Evans, R. M. (2015). Global trends of CME deflections based on CME and solar parameters. *Astrophys. J.* 805:168. doi: 10.1088/0004-637X/805/2/168
- Kramar, M., Airapetian, V., Mikić, Z., and Davila, J. (2014). 3D coronal density reconstruction and retrieving the magnetic field structure during solar minimum. *Solar Phys.* 289, 2927–2944. doi: 10.1007/s11207-014-0525-7
- Kramar, M., Inhester, B., Lin, H., and Davila, J. (2013). Vector tomography for the coronal magnetic field. II. Hanle effect measurements. *Astrophys. J.* 775:25. doi: 10.1088/0004-637X/775/1/25
- Kramar, M., Inhester, B., and Solanki, S. K. (2006). Vector tomography for the coronal magnetic field. I. Longitudinal Zeeman effect measurements. *Astron. Astrophys.* 456, 665–673. doi: 10.1051/0004-6361:20064865
- Kramar, M., Jones, S., Davila, J., Inhester, B., and Mierla, M. (2009). On the tomographic reconstruction of the 3D electron density for the solar corona from STEREO COR1 data. *Solar Phys.* 259, 109–121. doi: 10.1007/s11207-009-9401-2
- Kramar, M., Lin, H., and Tomczyk, S. (2016). Direct observation of solar coronal magnetic fields by vector tomography of the coronal emission line polarizations. *Astrophys. J. Lett.* 819:L36. doi: 10.3847/2041-8205/819/2/L36
- Lee, C. O., Luhmann, J. G., Hoeksema, J. T., Sun, X., Arge, C. N., and de Pater, I. (2011). Coronal field opens at lower height during the solar cycles 22 and 23 minimum periods: IMF comparison suggests the source surface should be lowered. *Solar Phys.* 269, 367–388. doi: 10.3847/2041-8205/819/2/L36
- Natterer, F. (2001). *The Mathematics of Computerized Tomography*. Classics in Applied Mathematics. Philadelphia, PA: Society for Industrial and Applied Mathematics, SIAM monographs on mathematical modeling and computation.
- Solanki, S. K., Schüssler, M., and Fligge, M. (2002). Secular variation of the Sun’s magnetic flux. *Astron. Astrophys.* 383, 706–712. doi: 10.1051/0004-6361:200111790
- Tomczyk, S., Card, G. L., Darnell, T., Elmore, D. F., Lull, R., Nelson, P. G., et al. (2008). An instrument to measure coronal emission line polarization. *Solar Phys.* 247, 411–428. doi: 10.1007/s11207-007-9103-6
- Tomczyk, S., McIntosh, S. W., Keil, S. L., Judge, P. G., Schad, T., Seeley, D. H., et al. (2007). Alfvén waves in the solar corona. *Science* 317:1192. doi: 10.1126/science.1143304
- Xie, H., St. Cyr, O. C., Gopalswamy, N., Yashiro, S., Krall, J., Kramar, M., et al. (2009). On the origin, 3D structure and dynamic evolution of CMEs near solar minimum. *Solar Phys.* 259, 143–161. doi: 10.1007/s11207-009-9422-x

**Conflict of Interest Statement:** The authors declare that the research was conducted in the absence of any commercial or financial relationships that could be construed as a potential conflict of interest.

Copyright © 2016 Kramar, Airapetian and Lin. This is an open-access article distributed under the terms of the Creative Commons Attribution License (CC BY). The use, distribution or reproduction in other forums is permitted, provided the original author(s) or licensor are credited and that the original publication in this journal is cited, in accordance with accepted academic practice. No use, distribution or reproduction is permitted which does not comply with these terms.



# Analyses of the Photospheric Magnetic Dynamics in Solar Active Region 11117 Using an Advanced CESE-MHD Model

Chaowei Jiang<sup>1,2\*</sup>, Shi T. Wu<sup>2,3\*</sup> and Xueshang Feng<sup>1</sup>

<sup>1</sup> SIGMA Weather Group, State Key Laboratory for Space Weather, National Space Science Center, Chinese Academy of Sciences, Beijing, China, <sup>2</sup> Center for Space Plasma and Aeronomics Research, The University of Alabama in Huntsville, Huntsville, AL, USA, <sup>3</sup> Department of Mechanical and Aerospace Engineering, The University of Alabama in Huntsville, AL, USA

## OPEN ACCESS

### Edited by:

Sarah Gibson,  
National Center for Atmospheric Research/High Altitude Observatory,  
USA

### Reviewed by:

Gordon James Duncan Petrie,  
National Solar Observatory, USA  
Satoshi Inoue,  
Max-Planck Institute for Solar System Research, Germany  
**\*Correspondence:**  
Chaowei Jiang  
cwjiang@spaceweather.ac.cn;  
Shi T. Wu  
wus@uah.edu

### Specialty section:

This article was submitted to  
Stellar and Solar Physics,  
a section of the journal  
Frontiers in Astronomy and Space  
Sciences

**Received:** 22 October 2015

**Accepted:** 19 April 2016

**Published:** 10 May 2016

### Citation:

Jiang C, Wu ST and Feng X (2016)  
Analyses of the Photospheric Magnetic Dynamics in Solar Active Region 11117 Using an Advanced CESE-MHD Model.  
Front. Astron. Space Sci. 3:16.  
doi: 10.3389/fspas.2016.00016

In this study, the photospheric vector magnetograms obtained by Helioseismic and Magnetic Imager on-board the Solar Dynamics Observatory are used as boundary conditions for a CESE-MHD model to investigate some photosphere characteristics around the time of a confined flare in solar active region NOAA AR 11117. We report our attempt of characterizing a more realistic solar atmosphere by including a plasma with temperature stratified from the photosphere to the corona in the CESE-MHD model. The resulted photospheric transverse flow is comparable to the apparent movements of the magnetic flux features that demonstrates shearing and rotations. We calculated the relevant parameters such as the magnetic energy flux and helicity flux, and with analysis of these parameters, we find that magnetic non-potentiality is transported across the photosphere into the corona in the simulated time interval, which might provide a favorable condition for producing the flare.

**Keywords:** sun: corona, flares, magnetic fields, magnetohydrodynamics (MHD)

## INTRODUCTION

It is well known that the magnetic evolution of solar active regions (ARs) holds the key to understanding solar eruptive events such as flares, filament eruptions, and coronal mass ejections. Particularly, the evolution of the three-dimensional (3D) magnetic configuration should be able to give us the crucial information for the initiation of solar eruptive events as suggested by Schrijver (2011). In recent years, many magnetic parameters have been used with the intention to predict the initiation of solar eruptive events, such as the surface magnetic free energy (Leka and Barnes, 2003; Falconer et al., 2006; Wu et al., 2009), the unsigned magnetic fluxes and electric currents (Falconer, 2001; Falconer et al., 2003; Schrijver, 2007; Georgoulis and Rust, 2007), as well as magnetic shear (Falconer, 2001; Falconer et al., 2003). However, all these parameters are directly derived from the magnetic field measurements confined on the solar surface (i.e., the photosphere). To measure the 3D coronal magnetic field is still beyond our reach, thus it leads us to seek numerical modeling (simulation) to fulfill the void region of measurements, namely to deduce the magnetic field topology and strength in the higher layers of solar atmosphere from the measured photospheric magnetic field.

Recently, there are studies using nonlinear force-free field (NLFFF) extrapolations to investigate the structures and evolution of the coronal magnetic field in solar active regions. For example, Tadesse et al. (2012) have used a NLFFF code to investigate NOAA AR 11117 (which is also the target AR of the present study) to determine the sources of flare activity and temporal evolution between pre- and post-flare stages using measured vector magnetic fields from Synoptic Optical Long-term Investigation on the Sun (SOLIS). We have also demonstrated that analyses based on NLFFF modeling can shed important lights for the understanding the physics of the solar eruptive events (Jiang et al., 2014). However, in the NLFFF modeling, the effect due to interaction of magnetic field with plasma is totally omitted, which seems to be not realistic because the coronal plasma  $\beta$  (ratio of plasma thermal pressure to magnetic pressure) is actually larger than what can be negligible (Peter et al., 2015). Also the photospheric magnetic field is far from force-free, which conflicts with the assumption of force-freeness. Consequently, the NLFFF model regards the bottom of extrapolation as the base of corona rather than the photosphere, and some kind of pre-processing of the original magnetogram is required to mitigate the problem. The limitations of the NLFFF model are also pointed by Wang and Liu (2015), who have given a comprehensive review concerning the evolution of the active region magnetic field associated with solar eruptions. They pointed out that a magnetohydrodynamic (MHD) model driven by data can provide a step forward in understanding the evolution of magnetic fields associated with flares.

We are already on the way of developing such a data-driven MHD model aimed for studying the dynamics of solar ARs (Wu et al., 2006; Jiang et al., 2012, 2013). In our previous CESE-MHD model (Jiang et al., 2012), we have used the SDO/HMI vector magnetogram as the bottom boundary conditions to calculate a time-sequence of 3D MHD equilibria for mimic the AR evolution. But that model is designed for simulating only the corona, since the bottom boundary of the model is also assumed to be the coronal base, similarly as in the NLFFF models. Here we report our first attempt of characterizing a more realistic solar atmosphere by including in the model a plasma with temperature stratified from the photosphere to the corona. In this way, the solution can be used to simulate the MHD equilibrium for solar atmosphere of the full domain from the thin layers of photosphere, chromosphere and transition region until to the corona. We then apply our new model to AR 11117 in a time interval around a C-class confined flare, and in particular, here we limit our study at the photosphere surface while an analysis of the coronal field dynamics will be left for another paper. We calculated the relevant parameters such as plasma flow, magnetic energy flux and helicity flux, which are important information of how the non-potentiality is transported from below the photosphere into the corona. The paper is structured as follows: we first describe the mathematical model and procedures of the simulation in Section The Data-Driven CESE-MHD Model, then the results of application to AR 11117 in Section Results, and we conclude in Sections Concluding Remarks.

## THE DATA-DRIVEN CESE-MHD MODEL

This model is developed similar to the data-driven active region evolution MHD model given by Wu et al. (2006) with a different numerical scheme. We solve a set of 3D, time-dependent, compressible MHD equations, and take into consideration of the highly-stratified atmosphere from the photosphere to the corona in a simplified way. In comparison to our previous action region evolution model (Wu et al., 2005, 2006), the effects of differential rotation and meridional flow together with the higher order transport (i.e., effective diffusion due to random motion of granules or supergranules, and cyclonic turbulence effects) are not included. It will improve the efficiency of the computation and as our focus is on the coronal field evolution which could lead to eruption, those higher order transport effects have limited importance on the magnetic field topology and its related properties for short term evolution study.

The initial setup of the model consists of constructing hydrostatic equilibrium of solar atmosphere and a potential field model based on the vertical component ( $B_z$ ) of the vector magnetogram, and then we input the vector magnetogram (including the transverse field) at the bottom boundary to driven the evolution of the model, which can then be regarded as a way of modeling the realistic and dynamical corona. However, a real dynamical simulation by continuously inputting a time-series observed vector magnetograms (for example, Wu et al., 2009) has not been done here because of the limitations of the numerical procedure. Instead, we perform on each set of magnetogram via a relaxation process to a new MHD equilibrium solution which is then used to approximately represent a single snapshot of the solar atmosphere evolution, i.e., the physical conditions at a specific time. In the following we present more details of the model.

### Model Equations

The set of governing equations are the conservation laws and magnetic induction equation as follows:

$$\frac{\partial \rho}{\partial t} + \nabla \cdot (\rho \mathbf{v}) = 0, \quad \rho \frac{D\mathbf{v}}{Dt} = -\nabla p + \mathbf{J} \times \mathbf{B} + \rho \mathbf{g} + \nabla \cdot (\mathbf{v} \mathbf{v} \rho \nabla \mathbf{v}),$$

$$\frac{\partial \mathbf{B}}{\partial t} = \nabla \times (\mathbf{v} \times \mathbf{B}), \quad \frac{\partial T}{\partial t} + \nabla \cdot (T \mathbf{v}) = (2 - \gamma) T \nabla \cdot \mathbf{v} + Q. \quad (1)$$

In these equations:  $\rho$ ,  $\mathbf{v}$ ,  $\mathbf{B}$ ,  $T$  denote the plasma density, flow velocity, magnetic field and temperature, respectively;  $\mathbf{J}$  is the electric current;  $p$  is the gas pressure given by  $p = \rho R T$  with the gas constant  $R = 1.65 \times 10^4 \text{ m}^2 \text{ s}^{-2}$ ;  $\gamma$  is the specific heat ratio with value of 5/3;  $\mathbf{g}$  is the solar gravity and is assumed to be constant as its photospheric value since we simulate from the photosphere to low corona with height less than 100 Mm. A small kinematic viscosity  $\nu$  with a value of  $\sim \Delta x^2 / \Delta t$  ( $\Delta x$  is the grid space and  $\Delta t$  is the time step in the numerical computation) is added for consideration of numerical stability. In this work we do not try to incorporate the complicated thermodynamic processes of the real corona, such as the thermal conduction and radiative losses [e.g., see numerical works by Abbott (2007), Fang et al.

(2010)], which are difficult to be simulated directly and is not our focus. Instead, we simply use an ad-hoc heating function  $Q$  to preserve the highly-stratified temperature structure from the photosphere to the corona. Following the work of Abbott and Fisher (2003) and Leake and Arber (2006), this can be done by simply setting a Newton-cooling equation of the temperature

$$Q = -\frac{T - T(t=0)}{\tau} \quad (2)$$

which can force the local temperature back to its pre-defined value (initial)  $T(t=0)$  when it deviates from  $T(t=0)$  on a time-scale  $\tau$ . This is also reasonable since we are interested in only the nonlinear dynamic interactions between the plasma flow field and magnetic field. We use the typical values of photospheric parameters to normalize the equations, which are given in **Table 1**. Especially the length unit  $H_0 = RT_0/g_p$  is the pressure scale height at the photosphere.

The above equation system (1) is solved by our CESE-MHD code (Feng et al., 2007; Jiang et al., 2010). The CESE (Conservation Element and Solution Element) method deals with three-dimensional governing equations in a substantially different way that is unlike traditional numerical methods (e.g., the finite-difference or finite-volume schemes). The key principle, also a conceptual leap of the CESE method, is treating space and time as one entity. By introducing the CESEs as the vehicles for calculating the space-time flux, the CESE method can enforce conservation laws both locally and globally in their natural space-time unity form. Compared with many other numerical schemes, the CESE method can achieve higher accuracy with the same mesh resolution and provide simple mathematics and coding free of any type of Riemann solver or eigen-decomposition. For more detailed descriptions of the CESE method for MHD simulations including the multi-method control of the  $\nabla \cdot \mathbf{B}$  numerical errors, see our previous work, e.g., Feng et al. (2006, 2007) and (Jiang et al., 2010, 2011).

## Initial Conditions

The initial configuration of the magnetic field simulation consists of a potential field matching the vertical component of the

**TABLE 1 | Reference Values for Nondimensionalization.**

Quantity	Reference	Value
$\rho$	$\rho_0$	$3 \times 10^{-7} \text{ g cm}^{-3}$
$T$	$T_0$	5100 K
$P$	$P_0 = \rho_0 RT_0$	$2.52 \times 10^5 \text{ dyn cm}^{-2}$
$r$	$H_0 = RT_0/g_p$	307 Km
$v$	$v_0 = \sqrt{\rho_0/\rho_0} = \sqrt{RT_0}$	$9.17 \text{ km s}^{-1}$
$t$	$T_0 = H_0/v_0$	33.5 s
$g$	$g_0 = \frac{t_0}{H_0^2} = g_p$	$274 \text{ m s}^{-2}$
$B$	$B_0 = \sqrt{\mu_0 P_0}$	1781 G

$g_p$  is the gravity at the level of photosphere and  $R$  is gas constant with value of  $1.65 \times 10^4 \text{ m}^2 \text{ s}^{-2}$ .

observed magnetogram and temperature-stratified plasma in hydrostatic equilibrium in the solar gravitational field. The potential field is obtained by a Green's function method (Metcalfe et al., 2008). Because the magnetic field is measured on the photosphere surface, we also set the simulation volume extending from this very surface all the way to the corona, which can then describe self-consistently the behavior of the magnetic field in a highly stratified plasma with  $\beta$  from  $> 1$  to  $<< 1$  (Gary, 2001). This differs from the NLFFF model. To simulate a continuous temperature distribution from the photosphere ( $\sim 5000$  K) to the corona ( $\sim 1$  MK) in the solar atmosphere, we use a simple normalized stratified temperature model similar to those given by Wu et al. (2005),

$$T(z) = 1 + \frac{T_{\text{cor}} - 1}{2} \left[ \tanh \left( \frac{z - z_{tr}}{w_{tr}} \right) + 1 \right] \quad (3)$$

where  $z$  is the height from the photosphere, e.g.,  $z = 0$  represents the photosphere surface, the coronal temperature  $T_{\text{cor}} = 1 \times 10^6 \text{ K}/T_0$ , and  $z_{tr}$  and  $w_{tr}$  represent the height and width of the transition region with  $z_{tr} = 3.75 \text{ Mm}/H_0$  and  $w_{tr} = 0.75 \text{ Mm}/H_0$ . The density and gas pressure on the photosphere are assumed to be uniform. According to the hydrostatic equilibrium equation

$$\frac{dp}{dz} = -\rho = -\frac{p}{T} \quad (4)$$

we have

$$p(z) = \exp \left[ - \int_0^z \frac{1}{T(z')} dz' \right] = \left[ \left( \frac{T(z)}{T(0)} \right)^{1-1/T_{\text{cor}}} \left( \frac{T(0)-1}{T(z)-1} \right) \left( \frac{T_{\text{cor}}-T(z)}{T_{\text{cor}}-T(0)} \right)^{1/T_{\text{cor}}} \right]^{w_{tr}/2}. \quad (5)$$

**Figure 1** shows the typical configuration of the parameters along a vertical line through the computation volume.

## Computation Grid

In order to obtain optimal resolution of the computed physical properties, a special grid system is adopted. The horizontal grid is uniform with resolution as that of the magnetogram. In the vertical direction a non-uniform mesh is designed to both resolve the large gradient of the plasma parameters near the photosphere and meanwhile avoid too much computational overhead. We take advantage of our CESE-MHD code that can deal with general curvilinear grid by mapping a non-uniform physical grid onto a uniform reference grid. Here the mapping is defined as  $dx/d\xi = dy/d\eta = H_m$  (normalized) and

$$\frac{dz}{d\xi} = \begin{cases} k & \text{if } \xi_1 < \xi_1 \\ k + \frac{H_m - k}{2} \left[ 1 - \cos \left( \frac{\pi(\xi - \xi_1)}{w_\xi} \right) \right] & \text{if } \xi_1 \leq \xi \leq \xi_1 + w_\xi \\ H_m & \text{if } \xi_1 < \xi_1 + w_\xi \end{cases} \quad (6)$$

with  $H_m$  is the pixel size of the magnetogram. For the present work we choose  $H_m = 2.4$ ,  $k = 0.25$ ,  $\xi_1 = 80$ ,  $w_\xi = 80$ . In the reference space we use uniform grid  $d_\xi = d_\eta = d_\zeta = 1$ . In this

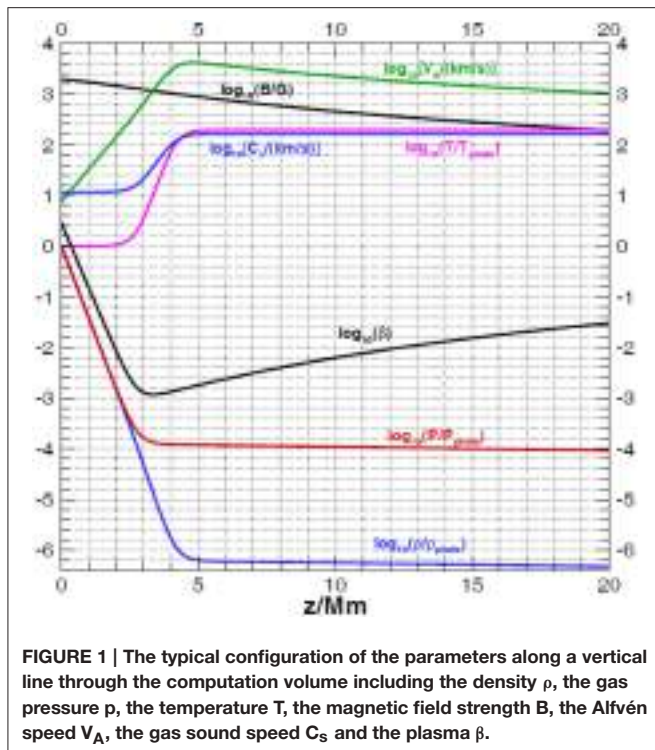


**FIGURE 1 |** The typical configuration of the parameters along a vertical line through the computation volume including the density  $\rho$ , the gas pressure  $p$ , the temperature  $T$ , the magnetic field strength  $B$ , the Alfvén speed  $v_A$ , the gas sound speed  $C_s$  and the plasma  $\beta$ .

way the photosphere and the whole transition region  $z \in [0, 0.5]$  Mm is resolved with a grid spacing of 0.25 times the scale height  $H_0$  on the photosphere surface.

Besides the setup of spatial grid, we also need careful consideration for the time step. According to the CESE method, the numerical viscosity will become very large if the ratio of the actual time step to the local time step is small, especially when this ratio is smaller than 0.1 (Zhang et al., 2004). As shown in **Figure 1**, the Alfvén speed  $v_A$  increases from several km/s to  $10^3$  km/s within the height of 5 Mm which is covered by a nearly uniform grid of  $\Delta z = 0.25H_0 \approx 70$  km. Thus the sharply increased Alfvén speed gives a sharply decreased local time step according to the Courant-Friedrichs-Lowy (CFL) stable condition  $\Delta t \propto \Delta z/v_A$ . If an uniform time step is used, the ratio to the local time step near the photosphere, e.g.,  $z \leq 1$  Mm can be smaller than 0.01. This will result a very large numerical viscosity to the near-photosphere region, making the information difficult to pass through the high- $\beta$  layer to the corona. Thus it is necessary to use a variable time step algorithm and here we use the time step directly according to the local time step. The detailed algorithm of using variable time step proportioned to the local grid spacing is described in Jiang et al. (2010) and here the only difference with the previous code is also to allow the time step variable according to the local wave speed.

## Boundary Conditions

The computational domain includes six planes (i.e., four sided planes, top, and bottom). The boundary conditions used for the four sides and top plane are non-reflective. In order to accommodate the observation at the bottom boundary, the

evolutionary boundary conditions must be used; thus, the method of projected characteristics, originated by Nakagawa (1981a,b) and implemented by Wu and Wang (1987) is used for the derivation of such boundary conditions. The briefly described derivation and its resulting time-dependent boundary conditions are given in the Appendix of Wu et al. (2006) and thus will not be repeated here.

## RESULTS

Here we apply the model to study AR 11117 around the time of a small flare. Since a rather full description of AR 11117 has been given in our previous paper (Jiang et al., 2012), we only briefly summarize some of the highlights here for completeness. During the Carrington Rotation (CR) 2101, the HMI on-board SDO has measured the 3 magnetic field components on the Sun's surface from October 20 – November 2, 2010. On the 25th of October 2010, this region became active with several small B-class flares being observed and near the end of the day, a C2.3-class flare occurred. GOES (Geostationary Operational Environmental Satellite) 15 recorded a soft x-ray event which began at 22:06UT, reaching a peak at 22:12UT and ending at 22:18UT as shown in the **Figure 2**. From observations recorded by AIA/SDO, it shows that only the central part of the active region is associated with the flare as shown in **Figure 2**. It indicates that the flare is confined to a low altitude without inducing significant changes to cause eruption of these coronal loops.

We have chosen a sequence of vector magnetograms measured by HMI/SDO close to the C-class flare. Specifically the sequence of magnetograms was taken at 21:00, 21:36, 22:00, 22:12, 22:36, and 23:00 UT. By input of the measured vector magnetograms for a specific time at the lower boundary of the model, we obtain the MHD equilibrium solution for each of the input of vector magnetic field. Those solutions are used to approximately represent the snapshot of the solar atmosphere at that specific time.

**Figure 3** shows the coronal magnetic field configuration and its comparison with the AIA-171 observations at 21:00 UT as an example. Overall the morphology of the simulated magnetic resembles the EUV observations. Especially, the traced coronal loops are matched well by the magnetic field lines. When examining the change of the magnetic field configuration in the different times, we find it is not easy to recognize. This is because the flare is a confined flare without eruption and the basic coronal-loop system as observed from AIA-171 shows very small changes, but reconnection at a magnetic topology surface might cause the flare, as suggested by Jiang et al. (2012).

The flaring loop system appears to be connected with the polarities at the southwest of the AR (see **Figure 2**). There, the apparent movement of the photospheric magnetic flux clearly show shearing and rotation, as can be seen in a movie of the HMI magnetogram (see the Supplementary Video 1). The small positive polarity (denoted by P in the movie) moves to the east (i.e., left of the field of view) with respect to its neighboring negative polarities. The negative polarity that has a circular shape (denoted by N in the movie) seems to rotate clockwise, and

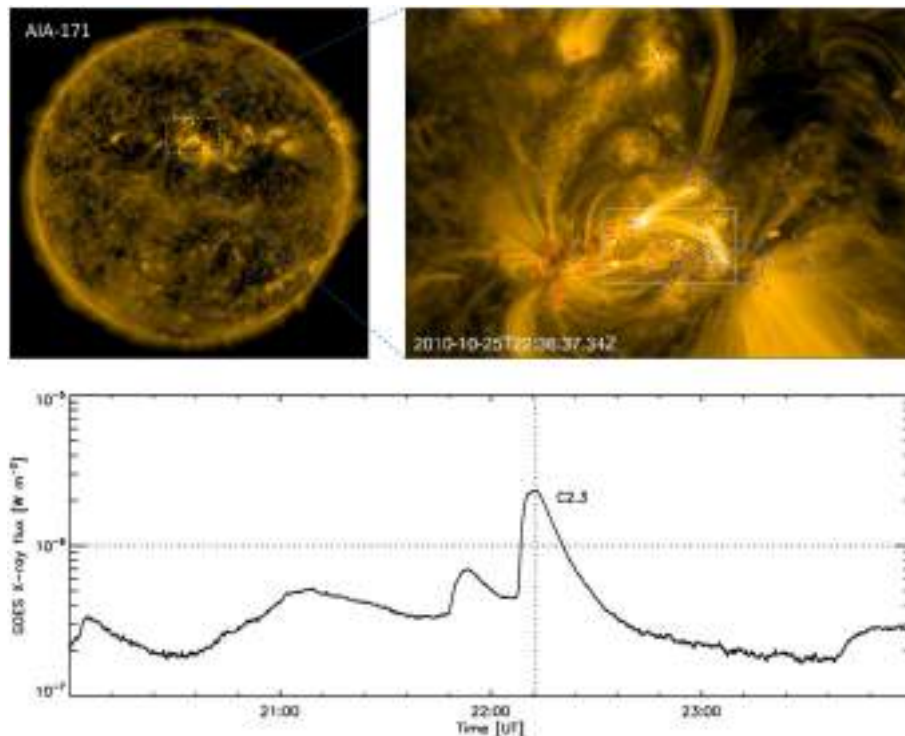


**FIGURE 2 | Top left:** a full-disk SDO/AIA 171  $\text{\AA}$  image showing the location of AR 11117. **Top right:** AIA-171 image of the post-flare loops about 20 min after the flare peak time. The contour lines for the photospheric field  $B_r$  of  $-500 \text{ G}$  (blue) and  $500 \text{ G}$  (red) are overlaid. Supplementary Video 1 shows the evolution of  $B_r$  from 21:00 to 23:00 UT of the same field of view. The boxed region denotes the field of view shown in **Figure 4**. **Bottom:** GOES soft-X ray flux from 20:00 UT to 24:00 UT on 2010 October 25 in the wavelength range of 1–8  $\text{\AA}$ . The horizontal dotted line indicates the C-minor flare class and the vertical dotted line indicates the peak time of the flux.

at the same time, moves to the west, squeezing the negative polarities in its west. Such features of photospheric motion is captured by our model to some extent. As can be seen in the top left panel of **Figure 4**, which shows the transverse velocity field obtained from the simulation at time 22:00 UT, shearing of the polarities is clear, and there is distinctly a clockwise vortex pattern of the velocity for the circular negative polarity (results for the other simulated times are similar and are not repeated here). Thus, both the observation and our simulation indicate a build-up of magnetic stress, which drives the coronal field further away from a potential-field state. The results based our previous model did not reproduce such a plasma flow at its bottom surface, likely because of its over-simplification of the plasma model.

To further quantify the transport of magnetic non-potentiality across the photosphere, we calculated parameters including the Poynting flux, the magnetic helicity flux, and the current helicity at the surface, which are defined in the following, respectively:

Poynting flux, i.e., the amount of magnetic energy flux across the lower boundary (photosphere) to the corona can be expressed as (Démoulin and Berger, 2003);

$$\left( \frac{dE}{dt} \right) = \frac{1}{4\pi} \int_{photo} (\mathbf{B}_t \cdot \mathbf{v}_t) B_n dS + \frac{1}{4\pi} \int_{photo} B_t^2 \cdot v_n dS \quad (7)$$

where the  $\mathbf{B}_t$  and  $\mathbf{v}_t$  are the transverse magnetic field and velocity, respectively, and  $B_n$  and  $v_n$  are the normal components of magnetic field and velocity, respectively. On the right side of Equation (9), the first term represents the surface flow effect and the second term is due to direct flux emergence from below the photosphere.

Magnetic helicity flux, i.e., the injection rate of relative helicity across the photosphere, can be expressed similarly as (Démoulin and Berger, 2003)

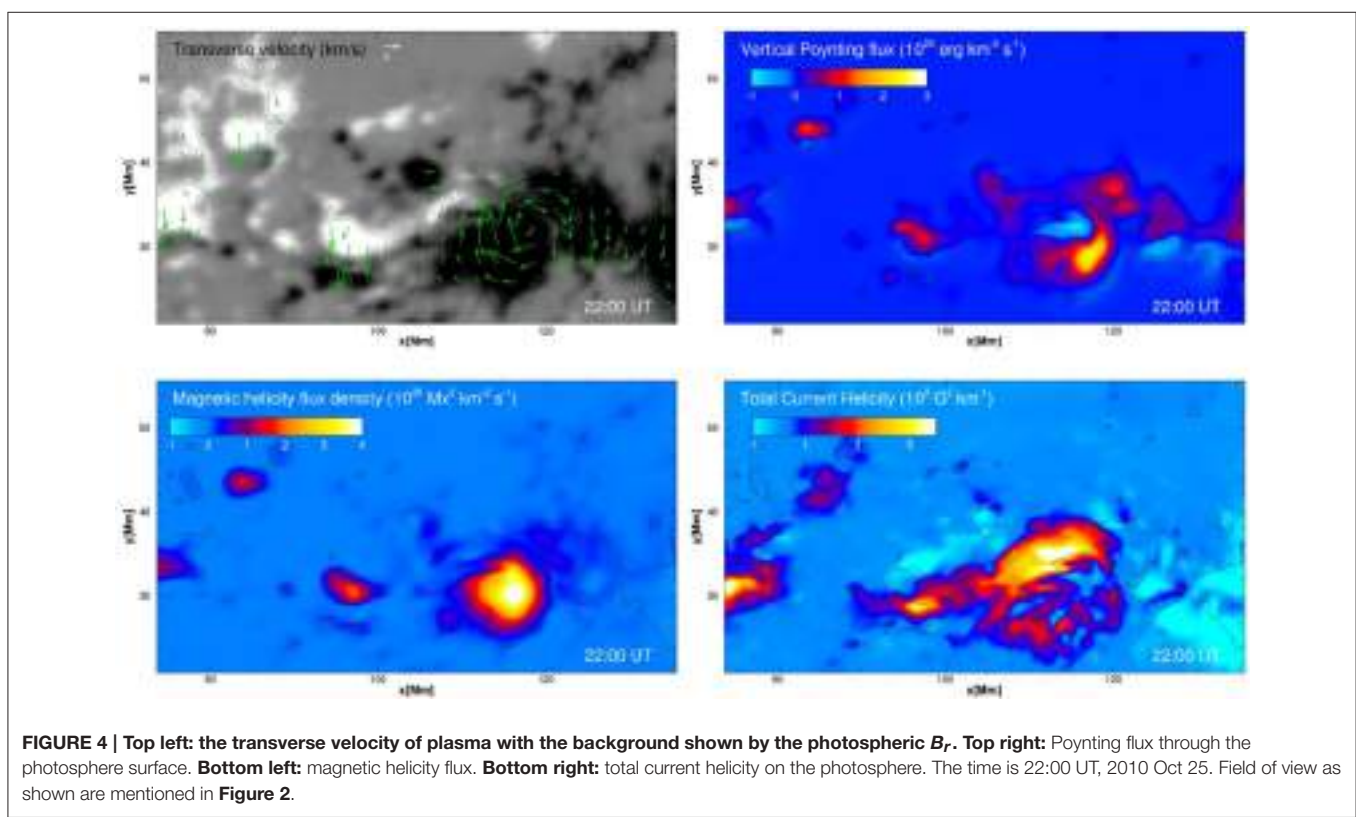
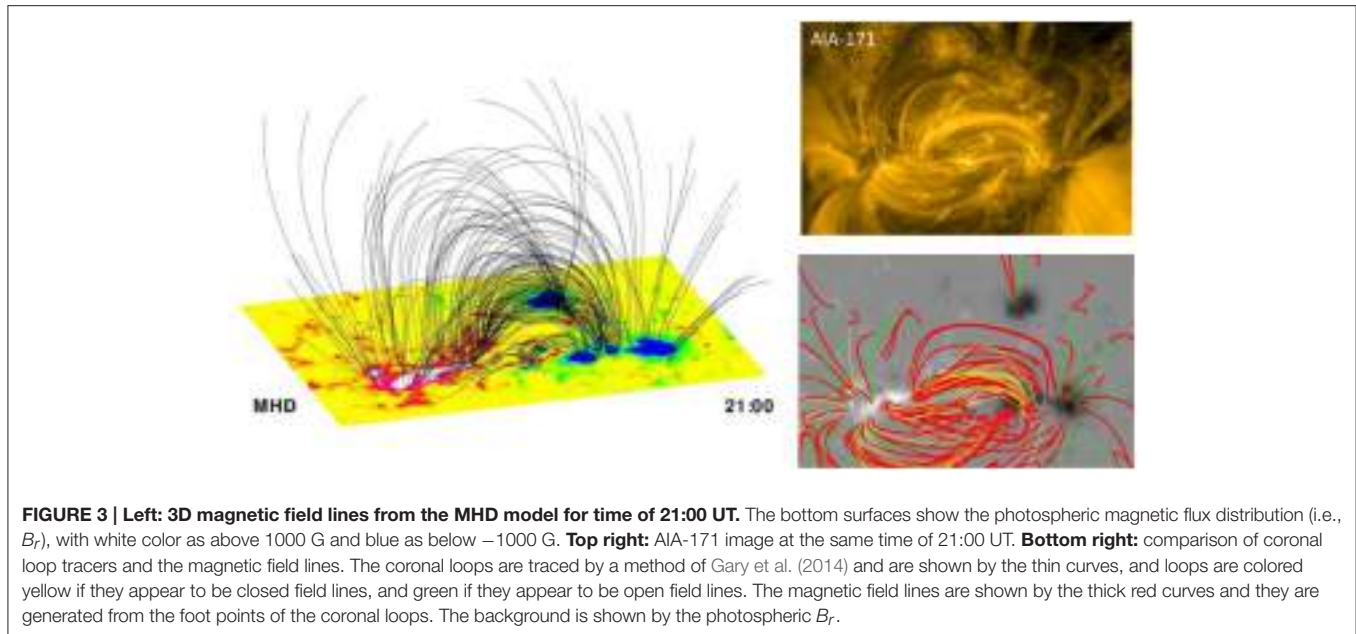
$$\left( \frac{dH}{dt} \right) = -2 \int_{photo} (\mathbf{A}_p \cdot \mathbf{v}_t) B_n dS + 2 \int_{photo} (\mathbf{A}_p \cdot \mathbf{B}_t) \cdot v_n dS \quad (8)$$

where  $\mathbf{A}_p$  is the vector potential of a potential field specified by the observed flux distribution  $B_n$  on the surface.

The current helicity is defined as (Bao and Zhang, 1998)

$$H_c = \mathbf{B} \cdot (\nabla \times \mathbf{B}) = B_n \cdot (\nabla \times \mathbf{B})_n + \mathbf{B}_t \cdot (\nabla \times \mathbf{B})_t \quad (9)$$

which show that the current helicity can also be separated into two parts, one related to the parallel component in the direction of the line of sight to the observer and the other to the vertical one. From photospheric vector magnetograms, only the first term



can be inferred, while with the MHD solutions, we can calculate fully the two terms, so we refer to our results as the total current helicity.

Again in Figure 4, we show the distributions of these parameters on the surface, at 22:00 UT as an example, since the changes of these distributions within the modeled time interval is not significant. The distribution of the flux means that the flux

density is calculated for each pixel on the surface. By examining these results, we recognize that there is net positive injection of energy in the studied area (a sum of the total flux density within the area, see also Figure 5), although mixed signs of flux density can be seen. The results are consistent with the flow pattern of strong shearing and rotation. Considering that the magnetic flux content does not changed significantly in the

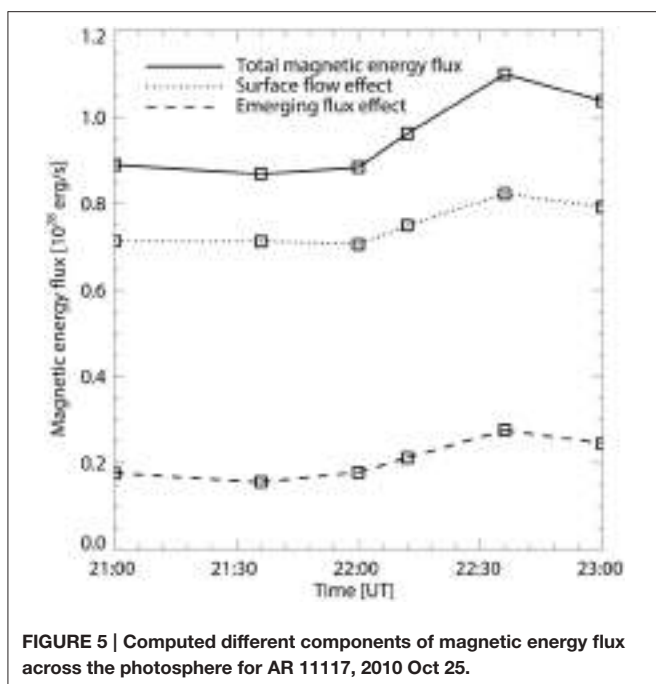


**FIGURE 5 |** Computed different components of magnetic energy flux across the photosphere for AR 11117, 2010 Oct 25.

studied duration, such injection of energy should mostly go to the non-potential energy. **Figure 5** shows the total magnetic energy flux as a function of time, and its two components separately [i.e., the two terms of Equation (9)]. It is clearly seen that the majority of energy flux results from the first term of Equation (9), which is caused by transverse flow effect (i.e., shearing and rotation). Our analysis is further supported by the results of the relative helicity injection flux, which is directly correlated with the twisting motion of the flux. The current helicity, as a more direct indicator of the non-potentiality, again speaks for the same conclusion.

## CONCLUDING REMARKS

In the present study, we present a modified CESE-MHD model constrained by the SDO/HMI vector magnetograms. By including a more realistic stratified atmosphere with a suitable grid design in both space and time, we are able to more closely

mimic the MHD structures with behavior of  $\beta$  changing abruptly from  $> 1$  (at the photosphere) to  $<< 1$  (in the corona). For a specific AR around the time of a flare, we apply this model to study the photospheric surface dynamics which are thought to play an important role in the cause of energetic events in the solar corona. This advanced model calculates a coronal field matching the EUV coronal loops, and at the same time, recover the photospheric plasma flow field in reasonable agreement with the apparent motion of the magnetic polarities. By quantifying a set of physical properties such as the transverse velocity, Poynting flux, the relative helicity flux as well as the current helicity, we conclude that magnetic non-potentiality is injected into the corona in the simulated time interval, which might provide a favorable condition for producing the flare. The present work is a step forward in developing a realistic MHD model for simulating structure and evolution of solar AR's magnetic fields associated with solar eruptions. In a future work, we will pursue a data-driven MHD analyses by input of a sequence of magnetic maps to study the true dynamics of the magnetic evolution leading to the flare.

## AUTHOR CONTRIBUTIONS

CJ and SW worked to put the paper together with the assistance of XF.

## ACKNOWLEDGMENTS

This work is supported by the 973 program under grant 2012CB825601, the Chinese Academy of Sciences (KZZD-EW-01-4), the National Natural Science Foundation of China (41574170, 41231068, 41274192, 41031066, and 41374176), and the Specialized Research Fund for State Key Laboratories, and Youth Innovation Promotion Association of CAS (2015122). CJ and SW are also supported by NSF-AGS1153323. Data are courtesy of NASA/SDO and the HMI science teams.

## SUPPLEMENTARY MATERIAL

The Supplementary Material for this article can be found online at: <http://journal.frontiersin.org/article/10.3389/fspas.2016.00016>

## REFERENCES

- Abbott, W. P. (2007). The magnetic connection between the convection zone and corona in the quiet Sun. *Astrophys. J.* 665, 1469–1448. doi: 10.1086/519788
- Abbott, W. P., and Fisher, G. H. (2003). A coupled model for the emergence of active region magnetic flux into the solar corona. *Astrophys. J.* 582, 475–483. doi: 10.1086/344613
- Bao, S. D., and Zhang, H. Q. (1998). Patterns of current helicity for solar cycle 22. *Astrophys. J.* 496, L43–L46. doi: 10.1086/311232
- Démoulin, P., and Berger, M. A. (2003). Magnetic energy and helicity fluxes at the photospheric level. *Solar Phys.* 251, 203–215. doi: 10.1023/A:1025679813955
- Falconer, D. A. (2001). A prospective method for predicting coronal mass ejections from vector magnetograms. *J. Geophys. Res. Space Phys.* 106, 25185–25190. doi: 10.1029/2000JA004005
- Falconer, D. A., Moore, R. L., and Gary, G. A. (2003). A measure from line-of-sight magnetograms for prediction of coronal mass ejections. *J. Geophys. Res. Space Phys.* 108, 1380. doi: 10.1029/2003JA010030
- Falconer, D. A., Moore, R. L., and Gary, G. A. (2006). Magnetic causes of solar coronal mass ejections: dominance of the free magnetic energy over the magnetic twist alone. *Astrophys. J.* 644, 1258. doi: 10.1086/503699
- Fang, F., Manchester, W., Abbott, W. P., and van der Holst, B. (2010). Simulation of flux emergence from the convection zone to the corona. *Astrophys. J.* 714, 1649–1657. doi: 10.1088/0004-637X/714/2/1649
- Feng, X. S., Hu, Y. Q., and Wei, F. S. (2006). Modeling the resistive MHD by the CESE method. *Solar Phys.* 235, 235–257. doi: 10.1007/s11207-006-0040-6
- Feng, X. S., Zhou, Y. F., and Wu, S. T. (2007). A novel numerical implementation for solar wind modeling by the modified conservation element/solution element method. *Astrophys. J.* 655:1110. doi: 10.1086/510121

- Gary, G. A. (2001). Plasma beta above a solar active region: rethinking the paradigm. *Solar Phys.* 203, 71–86. doi: 10.1023/A:1012722021820
- Gary, G. A., Hu, Q., and Lee, J. K. (2014). A rapid, manual method to map coronal-loop structures of an active region using Cubic Bézier Curves and its applications to misalignment angle analysis. *Solar Phys.* 289, 847–865. doi: 10.1007/s11207-013-0359-8
- Georgoulis, M. K., and Rust, D. M. (2007). Quantitative forecasting of major solar flares. *Astrophys. J. Lett.* 661, L109. doi: 10.1086/518718
- Jiang, C. W., Feng, X. S., Fan, Y., and Xiang, C. (2011). Reconstruction of the coronal magnetic field using the CESE-MHD method. *Astrophys. J.* 727:101. doi: 10.1088/0004-637X/727/2/101
- Jiang, C. W., Feng, X. S., Wu, S. T., and Hu, Q. (2012). Study of the three-dimensional coronal magnetic field of active region 11117 around the time of a confined flare using a data-driven CESE-MHD model. *Astrophys. J.* 759:85. doi: 10.1088/0004-637X/759/2/85
- Jiang, C. W., Feng, X. S., Wu, S. T., and Hu, Q. (2013). Magnetohydrodynamic simulation of a sigmoid eruption of active region 11283. *Astrophys. J. Lett.* 771:L30. doi: 10.1088/2041-8205/771/2/L30
- Jiang, C. W., Feng, X. S., Zhang, J., and Zhong, D. K. (2010). AMR simulations of magnetohydrodynamic problems by the CESE method in curvilinear coordinates. *Solar Phys.* 267, 463–491. doi: 10.1007/s11207-010-9649-6
- Jiang, C. W., Wu, S. T., Feng, X. S., and Hu, Q. (2014). Formation and Eruption of an Active Region Sigmoid. I. A study by nonlinear force-free field modeling. *Astrophys. J.* 780:55. doi: 10.1088/0004-637X/780/1/55
- Leake, J. E., and Arber, T. D. (2006). The emergence of magnetic flux through a partially ionised solar atmosphere. *Astron. Astrophys.* 450, 805–818. doi: 10.1051/0004-6361:20054099
- Leka, K. D., and Barnes, G. (2003). Photospheric magnetic field properties of flaring versus flare-quiet active regions. I. Data, general approach, and sample results. *Astrophys. J.* 595:1277. doi: 10.1086/377511
- Metcalf, T. R., DeRosa, M. L., Schrijver, C. J., Barnes, G., van Ballegooijen, A. A., Wiegelmann, T., et al. (2008). Nonlinear force-free modeling of coronal magnetic fields. II. Modeling a filament arcade and simulated chromospheric and photospheric vector fields. *Solar Phys.* 247, 269–299. doi: 10.1007/s11207-007-9110-7
- Nakagawa, Y. (1981a). Evolution of magnetic field and atmospheric response. I-Three-dimensional formulation by the method of projected characteristics. II-Formulation of proper boundary equations. *Astrophys. J.* 247:707. doi: 10.1086/159082
- Nakagawa, Y. (1981b). Evolution of magnetic field and atmospheric responses-part two-formulation of proper boundary equations. *Astrophys. J.* 247:719. doi: 10.1086/159083
- Peter, H., Warnecke, J., Chitta, L. P., and Cameron, R. H. (2015). Limitations of force-free magnetic field extrapolations: revisiting basic assumptions. *Astron. Astrophys.* 584, A68. doi: 10.1051/0004-6361/201527057
- Schrijver, C. J. (2007). A characteristic magnetic field pattern associated with all major solar flares and its use in flare forecasting. *Astrophys. J. Lett.* 655:L117. doi: 10.1086/511857
- Schrijver, C. J. (2011). Long-range magnetic couplings between solar flares and coronal mass ejections observed by SDO and STEREO. *J. Geophys. Res. Space Phys.* 116, 2156–2202. doi: 10.1029/2010JA016224
- Tadesse, T., Wiegelmann, T., Inhester, B., and Pevtsov, A. (2012). Coronal magnetic field structure and evolution for flaring AR 11117 and its surroundings. *Solar Phys.* 281, 53–65. doi: 10.1007/s11207-012-9961-4
- Wang, H. M., and Liu, C. (2015). Structure and evolution of magnetic fields associated with solar eruptions. *Res. Astron. Astrophys.* 15, 145–174. doi: 10.1088/1674-4527/15/2/001
- Wu, S. T., Wang, A. H., and Falconer, D. A. (2005). *IAU Symposium 226 on Coronal and Stellar Mass Ejections*, eds K. P. Dere and J. X. Wang (Cambridge: Cambridge Univ. Press), 291.
- Wu, S. T., Wang, A. H., Gary, G. A., Kucera, A., Rybak, J., Liu, Y., et al. (2009). Analyses of magnetic field structures for active region 10720 using a data-driven 3D MHD model. *Advances Space Res.* 44, 46–53. doi: 10.1016/j.asr.2009.03.020
- Wu, S. T., Wang, A. H., Liu, Y., and Hoeksema, J. T. (2006). Data-driven magnetohydrodynamic model for active region evolution. *Astrophys. J.* 652:800. doi: 10.1086/507864
- Wu, S. T., and Wang, J. F. (1987). Numerical tests of a modified full implicit continuous Eulerian (FICE) scheme with projected normal characteristic boundary conditions for MHD flows. *Comput. Methods Appl. Mechanics Eng.* 64, 267–282. doi: 10.1016/0045-7825(87)90043-0
- Zhang, M. J., Yu, S. T. J., and Chang, S. C. (2004). Solving magnetohydrodynamic equations without special treatment for divergence-free magnetic field. *AIAA J.* 42, 2605–2608. doi: 10.2514/1.8512

**Conflict of Interest Statement:** The authors declare that the research was conducted in the absence of any commercial or financial relationships that could be construed as a potential conflict of interest.

Copyright © 2016 Jiang, Wu and Feng. This is an open-access article distributed under the terms of the Creative Commons Attribution License (CC BY). The use, distribution or reproduction in other forums is permitted, provided the original author(s) or licensor are credited and that the original publication in this journal is cited, in accordance with accepted academic practice. No use, distribution or reproduction is permitted which does not comply with these terms.



# A Comparative Study of Divergence Cleaning Methods of Magnetic Field in the Solar Coronal Numerical Simulation

Man Zhang and Xueshang Feng \*

SIGMA Weather Group, State Key Laboratory for Space Weather, National Space Science Center, Chinese Academy of Sciences, Beijing, China

## OPEN ACCESS

### Edited by:

Sarah Gibson,  
National Center for Atmospheric Research, USA

### Reviewed by:

Pete Riley,  
Predictive Science, USA  
Antonia Stefnova Savcheva,  
Smithsonian Astrophysical Observatory, USA

### \*Correspondence:

Xueshang Feng  
[fengx@spaceweather.ac.cn](mailto:fengx@spaceweather.ac.cn)

### Specialty section:

This article was submitted to  
Stellar and Solar Physics,  
a section of the journal  
Frontiers in Astronomy and Space Sciences

Received: 19 October 2015

Accepted: 11 February 2016

Published: 03 March 2016

### Citation:

Zhang M and Feng X (2016) A Comparative Study of Divergence Cleaning Methods of Magnetic Field in the Solar Coronal Numerical Simulation. *Front. Astron. Space Sci.* 3:6. doi: 10.3389/fspas.2016.00006

This paper presents a comparative study of divergence cleaning methods of magnetic field in the solar coronal three-dimensional numerical simulation. For such purpose, the diffusive method, projection method, generalized Lagrange multiplier method and constrained-transport method are used. All these methods are combined with a finite-volume scheme in spherical coordinates. In order to see the performance between the four divergence cleaning methods, solar coronal numerical simulation for Carrington rotation 2056 has been studied. Numerical results show that the average relative divergence error is around  $10^{-4.5}$  for the constrained-transport method, while about  $10^{-3.1} - 10^{-3.6}$  for the other three methods. Although there exist some differences in the average relative divergence errors for the four employed methods, our tests show they can all produce basic structured solar wind.

**Keywords:** magnetic field divergence cleaning, three-dimensional MHD, solar corona, numerical simulation, solar wind

## 1. INTRODUCTION

Magnetohydrodynamics (MHD) equations are presently the only system available to self-consistently describe large-scale dynamics of space plasmas, and numerical MHD simulations have enabled us to capture the basic structures of the solar wind plasma flow and transient phenomena. The modern MHD codes can successfully solve both in time accurate and steady state problems involving all kinds of discontinuities. Different from the usual computational fluid mechanics, the MHD scheme has to be designed so as to guarantee the divergence free constraint of the magnetic field in two or three-dimensional MHD calculations. It is well-known that simply transferring conservation law methods for the Euler to the MHD equations can not be supposed to work at default in maintaining the divergence-free of magnetic field. The  $\nabla \cdot \mathbf{B}$  error accumulated during the calculation may grow in an uncontrolled fashion, which can result in unphysical forces and numerical instability (Tóth, 2000; Jiang et al., 2012a).

Several methods have been proposed to satisfy the  $\nabla \cdot \mathbf{B} = 0$  constraint in MHD calculations. The eight-wave formulation approach, suggested by Powell et al. (1993, 1999), is to solve the MHD equations with the additional source terms that are proportional to  $\nabla \cdot \mathbf{B}$  without modifying the MHD solver. In this approach, divergence of the magnetic can be controlled to a truncation error and the robustness of a MHD code can be improved (Hayashi, 2005; Jiang et al., 2012a,b). The projection method was first proposed by Brackbill and Barnes (1980). In the projection method,

the magnetic field  $\mathbf{B}^*$  provided by the base scheme in the new time step  $n + 1$  is projected onto the subspace of zero divergence solutions by a linear operator, and the magnetic field in the new time step  $n + 1$  is completed by this projected magnetic field solution (Brackbill and Barnes, 1980; Tóth, 2000; Balsara and Kim, 2004; Hayashi, 2005; Feng et al., 2010). Some authors (e.g., Brandenburg et al., 2008; Manabu et al., 2009) modify the MHD equations with the help of vector potential  $\mathbf{A}$  instead of the magnetic field  $\mathbf{B} = \nabla \times \mathbf{A}$  to keep divergence cleaning

condition. In this case,  $\nabla \cdot (\nabla \times \mathbf{A}) = 0$  is guaranteed mathematically, such that solving the time evolution of the vector potential  $\mathbf{A}$  maintains the magnetic field divergence-free during the time evolution. The diffusive method is to add a source term  $\eta \nabla(\nabla \cdot \mathbf{B})$  in the induction equation to reduce the numerical error of  $\nabla \cdot \mathbf{B}$ , so that the numerically generated divergence can be diffused away at the maximal rate limited by the CFL condition (van der Holst and Keppens, 2007; Feng et al., 2011; Shen et al., 2014). To guarantee the divergence

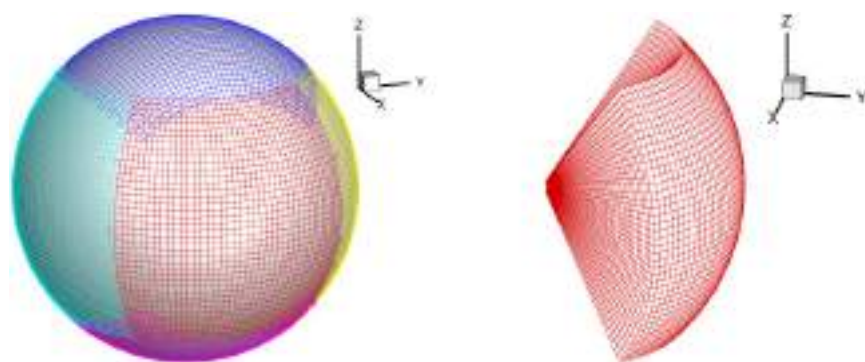


**FIGURE 1 |** Partition of a sphere into six identical components with partial overlap (left) and one-component mesh stacked in the  $r$  direction (right).

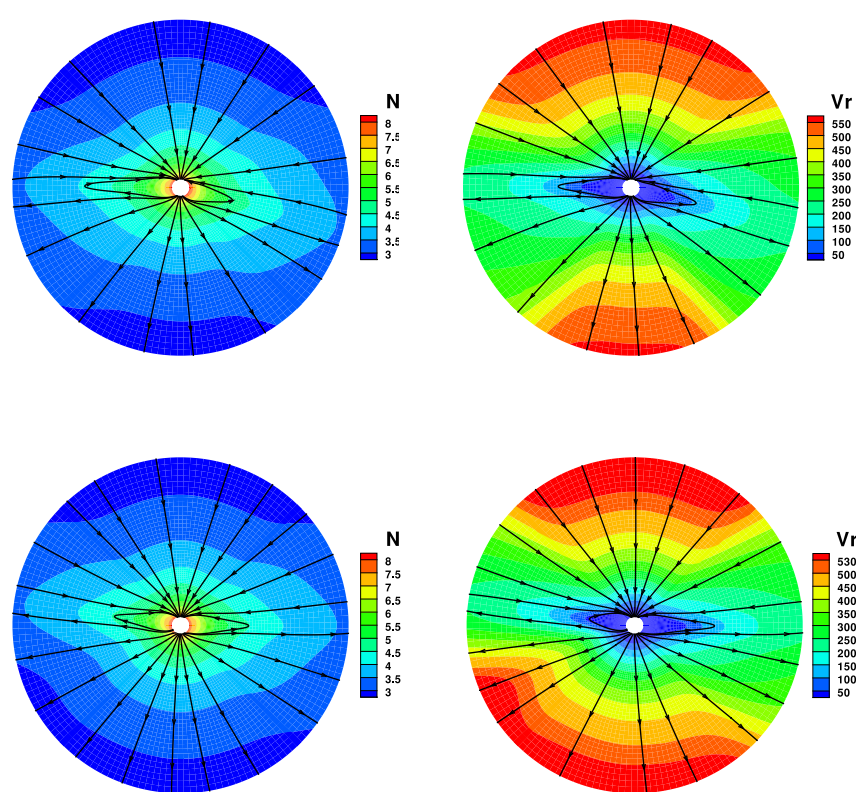


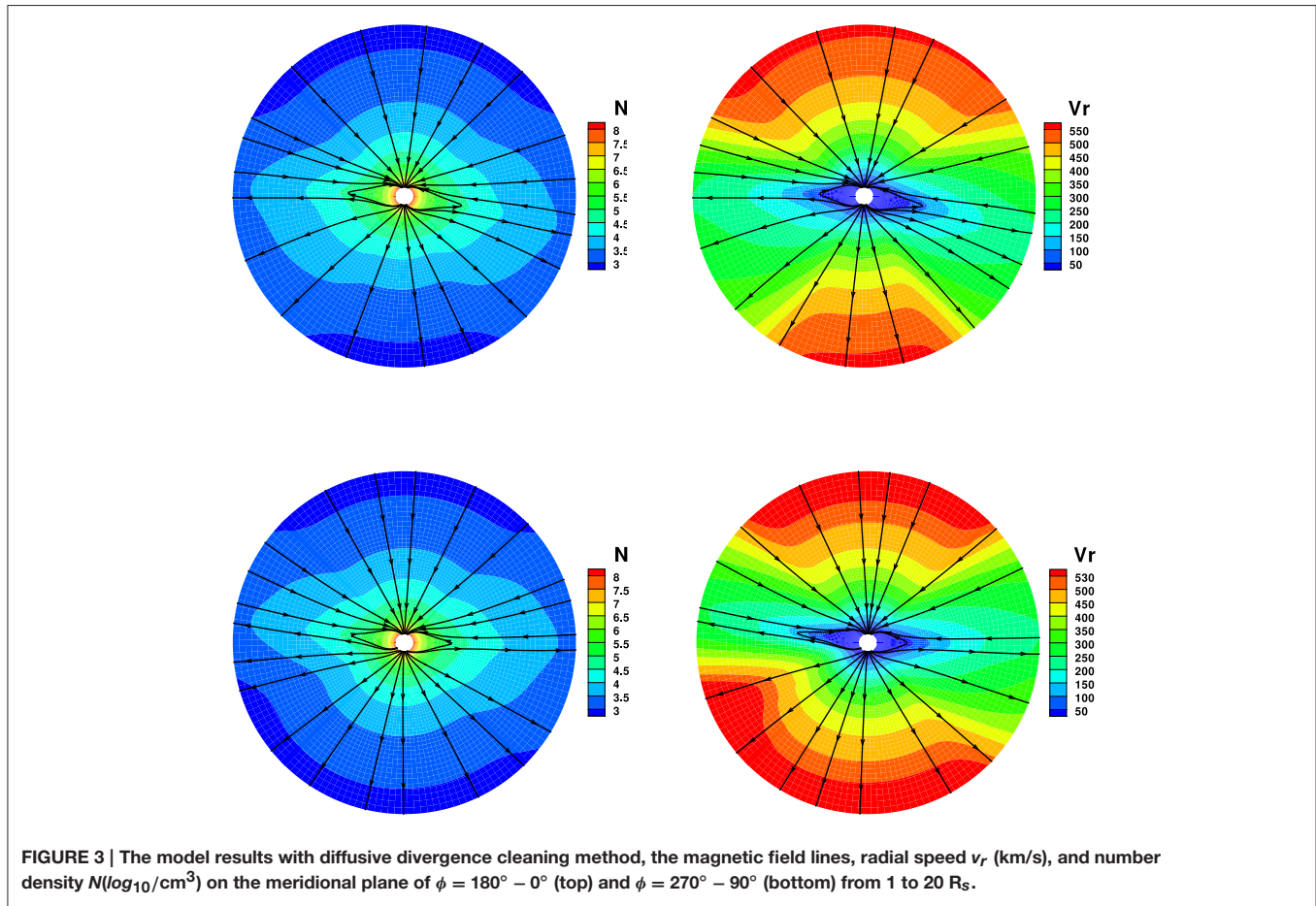
**FIGURE 2 |** The model results with CT divergence cleaning method, the magnetic field lines, radial speed  $v_r$  (km/s), and number density  $N(\log_{10}/\text{cm}^3)$  on the meridional plane of  $\phi = 180^\circ - 0^\circ$  (top) and  $\phi = 270^\circ - 90^\circ$  (bottom) from 1 to  $20 R_s$ .

cleaning of the magnetic fields, Dedner et al. (2002) proposed the hyperbolic divergence cleaning approach by introducing a generalized Lagrange multiplier (GLM). In the GLM method, a newly transport variable  $\psi$  is introduced to the MHD system, which plays the role of convecting the local divergence error out of the computational domain (Dedner et al., 2002, 2003; Mignone and Tzeferacos, 2010; Mignone et al., 2010; Jiang et al., 2012a,b; Susanto et al., 2013). The constrained transport (CT) method is a different strategy to control  $\nabla \cdot \mathbf{B}$  originally devised by Evans and Hawley (1988), in which the magnetic field is defined at face centers and the remaining fluid variables are provided at cell centers. In this approach, the electric field along the cell edges defining the boundary of the corresponding face is used to calculate the magnetic flux at cell faces. The CT method sustains a specified discretization of the magnetic field divergence around the machine round off error as long as the boundary and initial conditions are compatible with the constraints (Ziegler, 2011, 2012; Feng et al., 2014).

Since magnetic fields with a non-zero divergence can lead to severe artifacts in numerical simulations, keeping the magnetic field divergence-free is a curial problem in space plasma physics of solar and interplanetary phenomena. To say a few without exhausting, Linker et al. (1999) used the vector potential method to maintain the  $\nabla \cdot \mathbf{B}$  constraint for global solar corona

simulations. Hayashi (2005) simulate the solar corona and solar wind using the eight-wave method and the projection method to reduce the nonphysical effects of  $\nabla \cdot \mathbf{B}$ . Jiang et al. (2012a,b) simulated the coronal and chromospheric microflares by adopting the eight-wave method and the extended generalized Lagrange multiplier (EGLM) method to clean the divergence error. The GLM method was used in a nonlinear force-free field (NLFFF) study for the dynamics of solar active region (Inoue et al., 2015). The eight-wave method, the projection method, the CT method and the GLM method were implemented (Tóth, 2000; Tóth et al., 2005, 2012; Feng et al., 2010, 2011, 2014; Shen et al., 2014) for solar coronal and heliospheric studies, so as to maintain the solenoidal constraint.

In this paper, we give a comparative study of divergence cleaning methods of magnetic field in the solar coronal numerical simulation. The CT method, the diffusive method, the projection method and the GLM method are used to maintain divergence constraint respectively. The 3D solar wind model (Feng et al., 2014) is used for the experiments. The code employed a semi-discrete central scheme, designed by Ziegler (2011, 2012) within an finite volume (FV) framework without a Riemann solver or characteristic decomposition, and a composite grid system in spherical coordinates without polar singularities (Feng et al., 2010, 2011, 2014).



This paper proceeds as follows. In Section 2, model equations and grid system for solar wind plasma in spherical coordinates are described. Section 3 introduces the four methods to maintain the divergence cleaning constraint on the magnetic field. Section 4 gives the initial and boundary conditions in the code. Section 5 presents the numerical results for the steady-state solar wind structure of Carrington rotation (CR) 2056. Finally, we present some conclusions in Section 6.

## 2. GOVERNING EQUATIONS AND MESH GRID SYSTEM

### 2.1. Governing Equations

The magnetic field  $\mathbf{B} = \mathbf{B}_1 + \mathbf{B}_0$  is splitted as a sum of a time-independent potential magnetic field  $\mathbf{B}_0$  and a time-dependent deviation  $\mathbf{B}_1$  (Feng et al., 2010, 2014). The MHD equations are splitted into the fluid and the magnetic parts. The governing equations have the same form as Feng et al. (2014). The fluid part of the vector  $\mathbf{U} = (\rho, \rho v_r, \rho v_\theta, \rho v_\phi r \sin \theta, e)^T$  reads as follows:

$$\frac{\partial \mathbf{U}}{\partial t} + \frac{1}{r^2} \frac{\partial}{\partial r} r^2 \mathbf{F} + \frac{1}{r \sin \theta} \frac{\partial}{\partial \theta} \sin \theta \mathbf{G} + \frac{1}{r \sin \theta} \frac{\partial}{\partial \phi} \mathbf{H} = \mathbf{S} \quad (1)$$

The magnetic induction equation runs as follows:

$$\begin{aligned} \frac{\partial B_{1r}}{\partial t} + \frac{1}{r \sin \theta} \frac{\partial}{\partial \theta} (\sin \theta (v_\theta B_r - v_r B_\theta)) - \frac{1}{r \sin \theta} \frac{\partial}{\partial \phi} (v_r B_\phi - v_\phi B_r) = 0 \\ (v_r B_\phi - v_\phi B_r) = 0 \end{aligned} \quad (2)$$

$$\begin{aligned} \frac{\partial B_{1\theta}}{\partial t} - \frac{1}{r} \frac{\partial}{\partial r} (r(v_\theta B_r - v_r B_\theta)) + \frac{1}{r \sin \theta} \frac{\partial}{\partial \phi} (v_\phi B_\theta - v_\theta B_\phi) = 0 \\ \frac{\partial B_{1\phi}}{\partial t} + \frac{1}{r} \frac{\partial}{\partial r} (r(v_r B_\phi - v_\phi B_r)) - \frac{1}{r} \frac{\partial}{\partial \theta} (v_\phi B_\theta - v_\theta B_\phi) = 0 \end{aligned} \quad (3)$$

$$\frac{\partial B_{1\phi}}{\partial t} + \frac{1}{r} \frac{\partial}{\partial r} (r(v_r B_\phi - v_\phi B_r)) - \frac{1}{r} \frac{\partial}{\partial \theta} (v_\phi B_\theta - v_\theta B_\phi) = 0 \quad (4)$$

Here,  $\rho$  is the mass density,  $\mathbf{v} = (v_r, v_\theta, v_\phi)$  are the flow velocities in the frame rotating with the Sun,  $p$  is the thermal pressure.  $e$  stands for the modified total energy density consisting of the kinetic, thermal, and magnetic energy densities (written in terms of  $\mathbf{B}_1$ ).

### 2.2. Mesh Grid System

Following Feng et al. (2010, 2012a,b,c), the computational domain is divided into a composite mesh consisting of six identical component meshes designed to envelop a spherical surface with partial overlap on their boundaries (**Figure 1**).

In the present work, the parallel implementation over the whole computational domain from 1  $R_s$  to 26  $R_s$  is realized

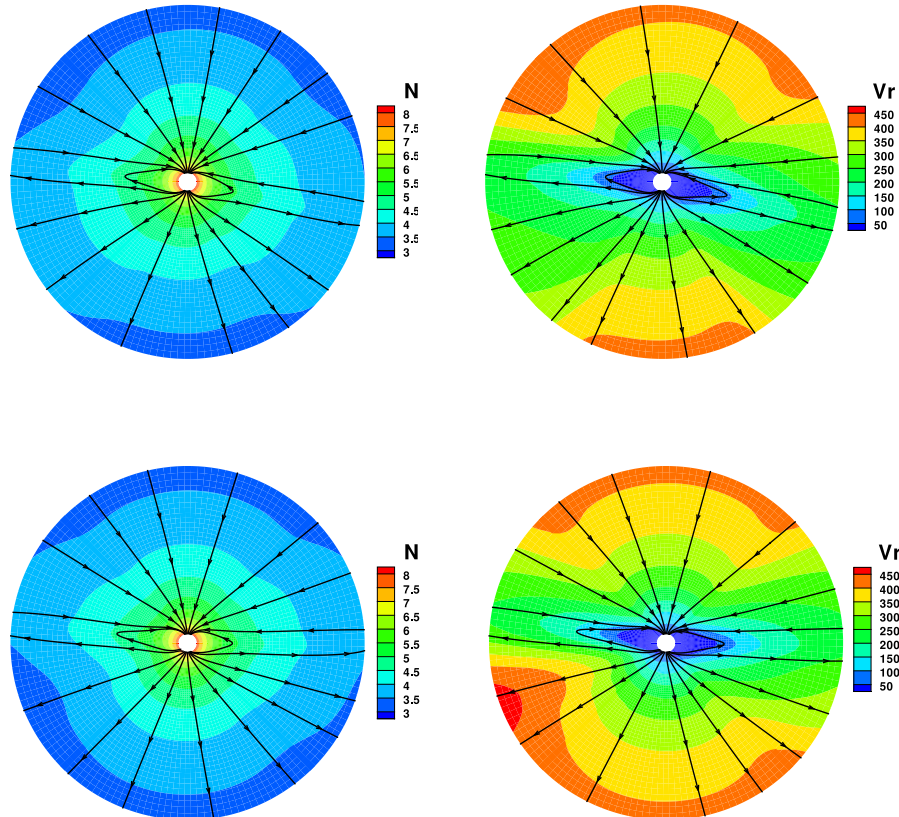


**FIGURE 4 |** The model results with projection divergence cleaning method, the magnetic field lines, radial speed  $v_r$  (km/s), and number density  $N(\log_{10}/\text{cm}^3)$  on the meridional plane of  $\phi = 180^\circ - 0^\circ$  (top) and  $\phi = 270^\circ - 90^\circ$  (bottom) from 1 to 20  $R_s$ .

by domain decomposition of six-component grids based on the spherical surface and radial direction partition. The following grid partitions are employed:  $N_\theta = N_\phi = 42$ .  $\Delta r(i) = 0.01 R_s$  if  $r(i) < 1.1 R_s$ ;  $\Delta r(i) = \min(A \times \log_{10}(r(i-1)), \Delta\theta \times r(i-1))$  with  $A = 0.01/\log_{10}(1.09)$  if  $r(i) < 3.5 R_s$ ;  $\Delta r(i) = \Delta\theta \times r(i-1)$  if  $r(i) > 3.5 R_s$ .

### 3. NUMERICAL SCHEME FORMULATION

The following four subsections are devoted to the introduction of four methods to maintain the divergence cleaning constraint on the magnetic field.

#### 3.1. CT Method

By the usage of a special discretization of the magnetic field Equations (2)–(4), CT technique imitates the analytical fact that  $\frac{\partial \nabla \cdot \mathbf{B}}{\partial t} = \nabla \cdot \nabla \times (\mathbf{v} \times \mathbf{B}) = 0$ . This discretization is routinely made on a particular stencil, therefore employs a staggered mesh, over which the solenoidal constraint up to the machine accuracy is satisfied on condition that initially  $\nabla \cdot \mathbf{B} = 0$  is met in the whole computational domain. The hydrodynamic state variables are evaluated at the cell center, whereas magnetic field is evaluated at the cell faces and the electric field is at the cell edges. The origin of this technique is attributed to the staggered

divergence-free scheme formulated for electromagnetism by Yee (1966). For spatial discretization of our numerical scheme formulation, we strictly follow those of Feng et al. (2014) by using the FV discretization of Equation (1), and by averaging Equations (2)–(4) over facial areas to obtain the semi-integral forms of magnetic induction equations. Second-order accurate linear ansatz reconstruction are adopted.

#### 3.2. Diffusive Method

The diffusive method in maintaining the divergence-free constraint runs as follows. As usual, regarding the coupling of fluids and magnetic fields as a whole system, then we have

$$\begin{aligned} \mathbf{U} &= (\rho, \rho v_r, \rho v_\theta, \rho v_\phi r \sin \theta, e, B_{1r}, B_{1\theta}, B_{1\phi})^T \\ \frac{\partial \mathbf{U}}{\partial t} + \frac{1}{r^2} \frac{\partial}{\partial r} r^2 \mathbf{F} + \frac{1}{r \sin \theta} \frac{\partial}{\partial \theta} \sin \theta \mathbf{G} + \frac{1}{r \sin \theta} \frac{\partial}{\partial \phi} \mathbf{H} &= \mathbf{S} \quad (5) \end{aligned}$$

with the symbols having their routine meanings, three variables added into Equation (1), and the first five variables keeping the same.

We use the diffusive method proposed to handle the  $\nabla \cdot \mathbf{B}$  constraint. A source term  $\eta \nabla(\nabla \cdot \mathbf{B})$  is introduced in the induction equation to reduce the numerical error of  $\nabla \cdot \mathbf{B}$ . The  $\nabla \cdot \mathbf{B}$  error

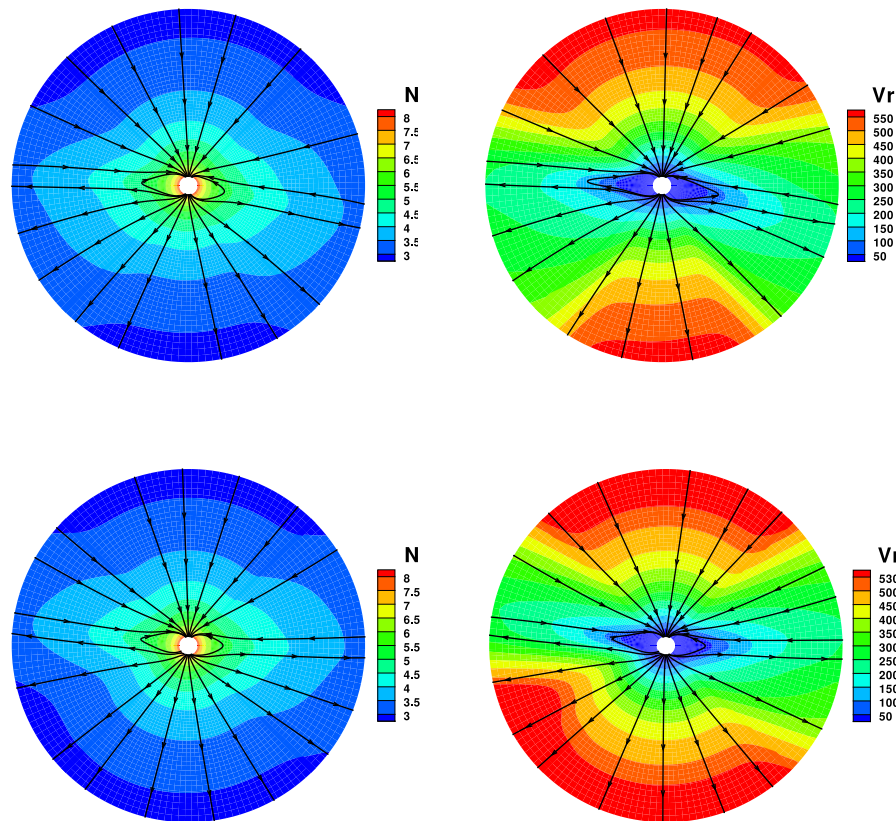


**FIGURE 5 |** The model results with GLM divergence cleaning method, the magnetic field lines, radial speed  $v_r$  (km/s), and number density  $N$ ( $\log_{10}/\text{cm}^3$ ) on the meridional plane of  $\phi = 180^\circ - 0^\circ$  (top) and  $\phi = 270^\circ - 90^\circ$  (bottom) from 1 to  $20 R_s$ .

produced by the diffusive method is controlled by iterating

$$\mathbf{B}^{n+1} = \mathbf{B}^{n+1} + \eta \Delta t \nabla (\nabla \cdot \mathbf{B}^{n+1})$$

$\eta \Delta t \leq C_d \left( \frac{1}{(\Delta r)^2} + \frac{1}{(r \Delta \theta)^2} + \frac{1}{(r \sin \theta \Delta \phi)^2} \right)^{-1}$ , where  $\Delta r$ ,  $\Delta \theta$ ,  $\Delta \phi$  are grid spacings in spherical coordinates. Here, we set  $C_d = 1.3$  (van der Holst and Keppens, 2007; Rempel et al., 2009; Feng et al., 2011; Shen et al., 2014). This artificial diffusivity does not violate shock capturing property or second-order accuracy at least in smooth regions, but higher order accuracy may depend on the slope limiter used.

### 3.3. Projection Method

In the projection method formulation, the magnetic field  $\mathbf{B}^*$  obtained by the base scheme using Equation (5) is projected onto the subspace of zero divergence solutions by a linear operator, and the magnetic field in the new time step  $n+1$  is completed by this projected magnetic field solution  $\mathbf{B}^{n+1}$ . That is, the magnetic field can be decomposed by the sum of a curl and a gradient

$$\mathbf{B}^* = \nabla \times A + \nabla \phi$$

After taking the divergence of both sides one can achieve a Poisson equation

$$\nabla^2 \phi = \nabla \cdot \mathbf{B}^* \quad (6)$$

Then the magnetic field is corrected by

$$\mathbf{B}^{n+1} = \mathbf{B}^* - \nabla \phi \quad (7)$$

The numerical divergence of  $\mathbf{B}^{n+1}$  can be exactly zero if the  $\nabla^2 \phi$  in Equation (4) is evaluated as a divergence of the gradient with the same difference operators as used for calculating  $\nabla \cdot \mathbf{B}^*$ . In order to solve Equation (4), a pseudo-time derivative is introduced to the equation (Hayashi, 2005)

$$\frac{\partial \phi}{\partial \tau} = \nabla^2 \phi - \nabla \cdot \mathbf{B}^*$$

We adopt a first-order backward finite difference scheme for the pseudo-time derivative with the pseudo-time step  $\Delta \tau$  ( $< \Delta t$ ). If we want obtain an accurate transient solution, the pseudo-time (sub-iterations) must get converged at each physical time step. But this is too costly to make the sub-iteration procedure performed until convergence to machine precision. In this paper, besides setting up convergence criterion  $\frac{\Delta \phi}{\Delta \tau} \leq 10^{-6}$  of the pseudo-time (sub-iterations), we also set up maximal sub-iterations 10 to avoid infinite iterations.

### 3.4. GLM Method

Using the GLM (Dedner et al., 2002), the divergence constraint is coupled with the conservation laws by introducing a newly

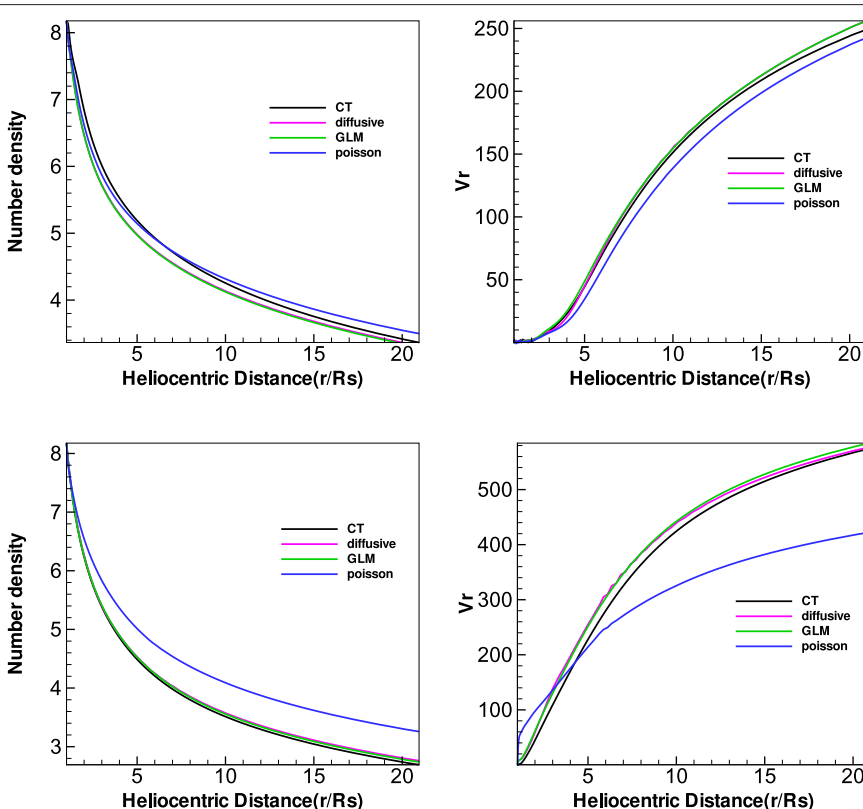


**FIGURE 6 |** The number density  $N(\log_{10}/\text{cm}^3)$  and radial speed  $v_r$  (km/s) distribution along heliocentric distance with different latitudes  $\theta = 100^\circ$  (top) and  $\theta = 174^\circ$  (bottom) at the same longitude  $\phi = 0^\circ$  from the four divergence cleaning methods.

variable  $\psi$ . Now, the governing Equations (5) contain nine equations with the ninth equation written in the following form

$$\frac{\partial \psi}{\partial t} + c_h^2 \nabla \cdot \mathbf{B} = -\frac{c_h^2}{c_p^2} \psi$$

The fluxes for magnetic field have following forms  $F_6 = c_h^2$ ,  $G_7 = c_h^2$ ,  $H_8 = c_h^2$ ,  $S_6 = \frac{2\psi}{r}$ ,  $S_7 = \frac{1}{r}(B_\theta v_r - B_r v_\theta) + \frac{\psi \cot \theta}{r}$ . The  $c_h$  is often chosen to be the largest eigenvalue in the computational domain

$$c_h = \max_{i,j,k} (|v_r| + c_{fr}, |v_\theta| + c_{f\theta}, |v_\phi| + c_{f\phi})$$

Here,  $c_{fr}$ ,  $c_{f\theta}$ , and  $c_{f\phi}$  are the fast magnetosonic speeds in the  $(r, \theta, \phi)$  directions, defined respectively by  $c_{fr} = \frac{1}{\sqrt{2}} \sqrt{c_s^2 + c_A^2 + ((c_s^2 + c_A^2)^2 - 4c_s^2 \frac{B_\theta^2}{\mu\rho})^{\frac{1}{2}}}$ ,  $c_{f\theta} = \frac{1}{\sqrt{2}} \sqrt{c_s^2 + c_A^2 + ((c_s^2 + c_A^2)^2 - 4c_s^2 \frac{B_\theta^2}{\mu\rho})^{\frac{1}{2}}}$ ,  $c_{f\phi} = \frac{1}{\sqrt{2}} \sqrt{c_s^2 + c_A^2 + ((c_s^2 + c_A^2)^2 - 4c_s^2 \frac{B_\phi^2}{\mu\rho})^{\frac{1}{2}}}$ , where  $c_s = \sqrt{\frac{\gamma p}{\rho}}$

and  $c_A = \sqrt{\frac{B_r^2 + B_\theta^2 + B_\phi^2}{\mu\rho}}$  are the sound and Alfvénic speeds. As for  $c_p$ , we follow Mignone and Tzeferacos (2010) and Mignone et al. (2010) by setting the parameter  $\alpha = \Delta h c_h / c_p^2$ ,

$\Delta h = \min(\Delta r, r\Delta\theta, r \sin \theta \Delta\phi)$  and we choose  $\alpha = 0.1$  in our code. Initially,  $\psi$  is set to 0. The  $\phi$  at the inner and outer boundaries is fixed.

### 3.5. Time Integration

Time integration for the full system is implemented over time with a second-order Runge-Kutta scheme (Ziegler, 2004; Fuchs et al., 2009; Feng et al., 2014).

$$\bar{\mathbf{U}}^* = \bar{\mathbf{U}}^n + \Delta t \mathcal{R}_{\mathbf{U}}[\bar{\mathbf{U}}^n, \bar{\mathbf{B}}^n]$$

$$\bar{\mathbf{B}}^* = \bar{\mathbf{B}}^n + \Delta t \mathcal{R}_{\mathbf{B}}[\bar{\mathbf{U}}^n, \bar{\mathbf{B}}^n]$$

$$\bar{\mathbf{U}}^{n+1} = \frac{1}{2} \bar{\mathbf{U}}^n + \frac{1}{2} (\bar{\mathbf{U}}^* + \Delta t \mathcal{R}_{\mathbf{U}}[\bar{\mathbf{U}}^*, \bar{\mathbf{B}}^*]) \quad (8)$$

$$\bar{\mathbf{B}}^{n+1} = \frac{1}{2} \bar{\mathbf{B}}^n + \frac{1}{2} (\bar{\mathbf{B}}^* + \Delta t \mathcal{R}_{\mathbf{B}}[\bar{\mathbf{U}}^*, \bar{\mathbf{B}}^*]) \quad (9)$$

As usual, the time step length is limited by the Courant-Friedrichs-Lowy (CFL) stability condition:

$$\Delta t = \text{CFL} / \max \left( \sqrt{\left( \frac{|v_r| + c_{fr}}{\Delta r} \right)^2 + \left( \frac{|v_\theta| + c_{f\theta}}{r \Delta \theta} \right)^2 + \left( \frac{|v_\phi| + c_{f\phi}}{r \sin \theta \Delta \phi} \right)^2} \right)$$

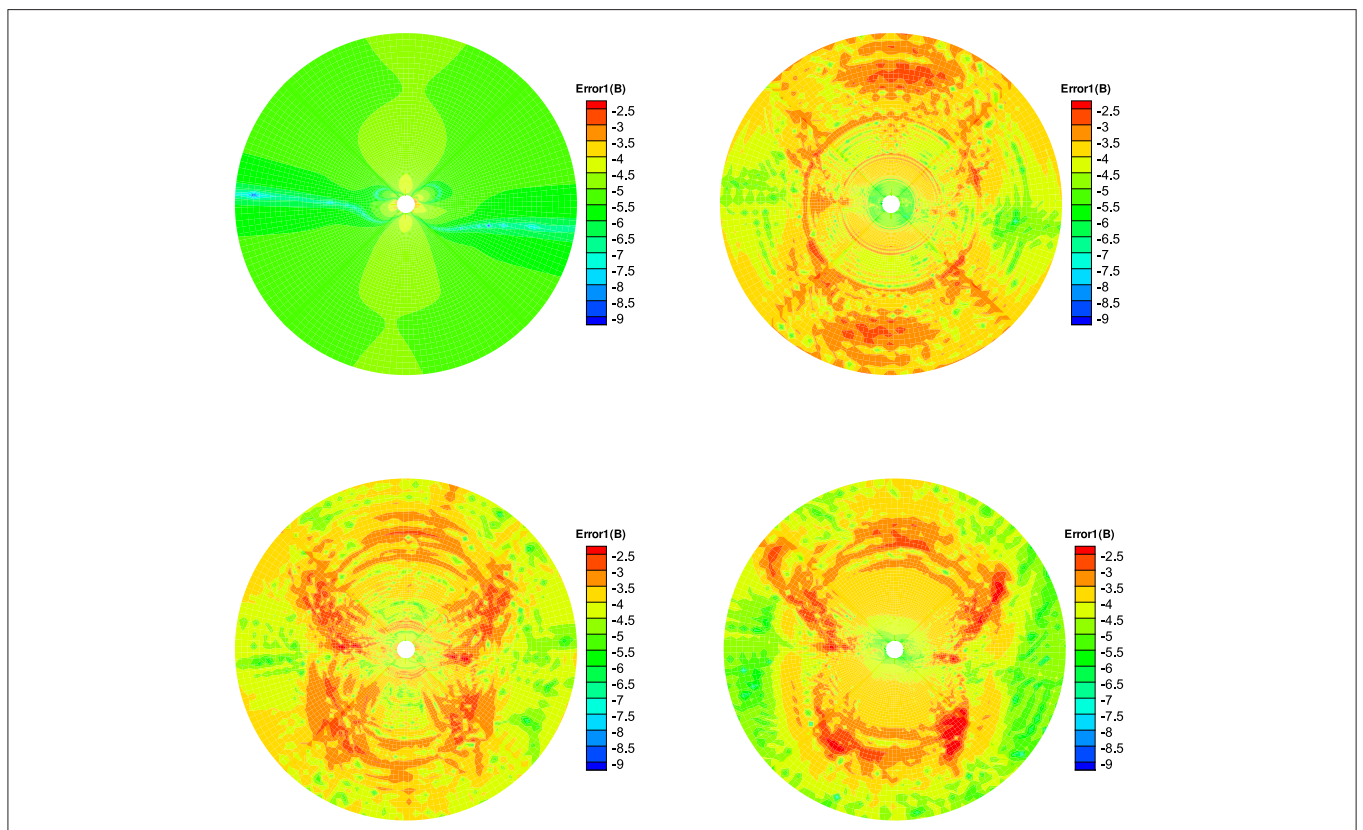


**FIGURE 7 |** The  $\log_{10}\text{Error1}(\mathbf{B})$  in the calculation at  $t = 5$  h on the meridional plane of  $\phi = 180^\circ - 0^\circ$  from 1 to 20  $R_s$ , the results from CT method (left) and diffusive method (right) are displayed in the top row, the bottom row is from the projection method (left) and GLM method (right).

Here,  $\mathcal{R}_U[\bar{\mathbf{U}}, \bar{\mathbf{B}}]$  and  $\mathcal{R}_B[\bar{\mathbf{U}}, \bar{\mathbf{B}}]$ , denote the discretized fluxes moved to the right-hand sides of the governing Equations (1)–(4) and their corresponding source terms. In the following run we employ a simultaneous time integration with  $CFL = 0.5$ .

## 4. INITIAL-BOUNDARY VALUE CONDITIONS

Initially, the magnetic field is specified by using the potential field source surface (PFSS) model to produce a 3D global magnetic field in the computational domain with the line-of-sight photospheric magnetic data from the Wilcox Solar Observatory.  $\mathbf{B}$  calculated by PFSS model inevitably can have a very small but non-zero  $\nabla \cdot \mathbf{B}$  when evaluated in the discretized space. The initial profiles of flow parameters such as plasma density  $\rho$ , pressure  $p$ , and velocity  $\mathbf{v}$  are given by Parker's solar wind flow solution (Parker, 1963).

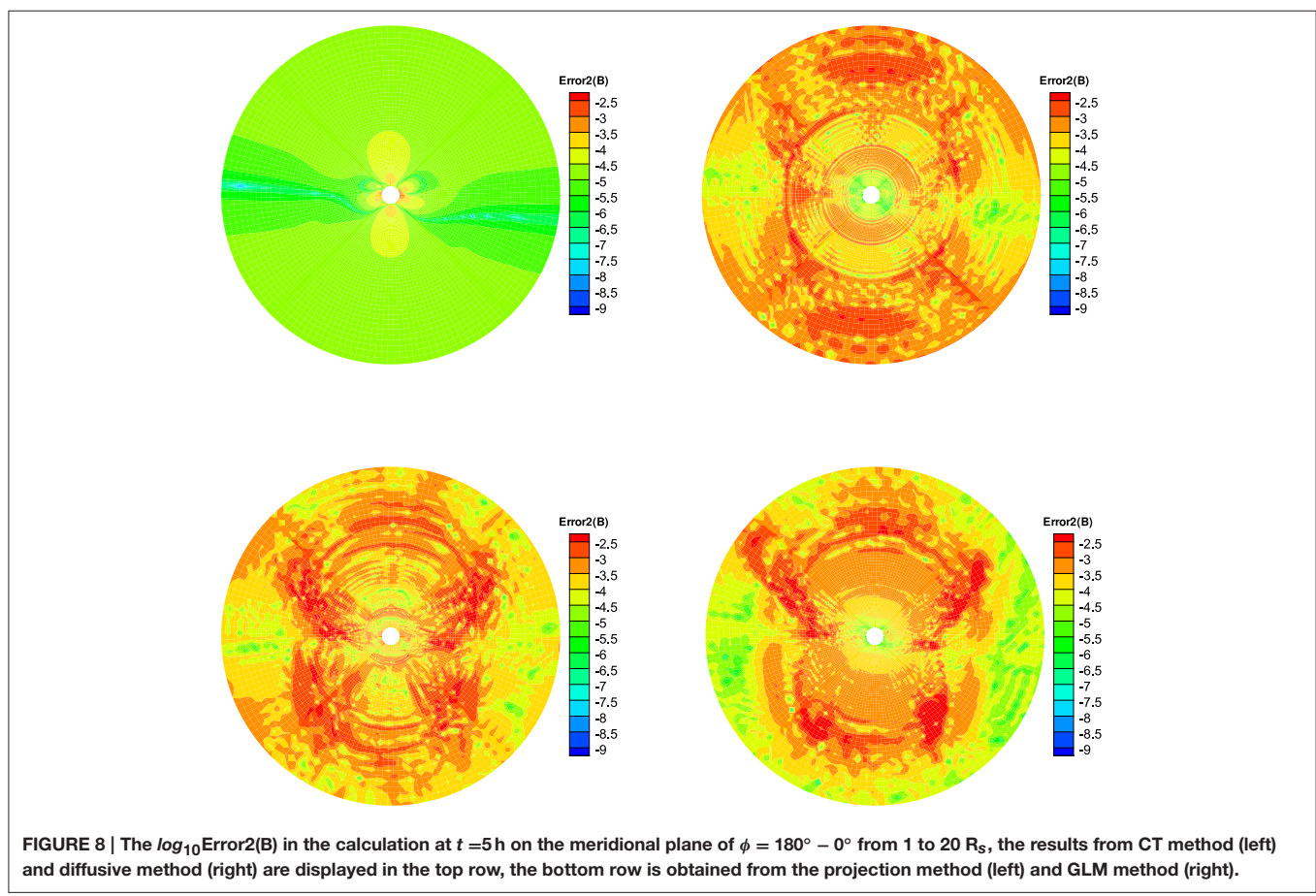
In this paper, the inner boundary at  $1 R_s$  is fixed for simplicity. The solar wind parameters at the outer boundary are imposed by linear extrapolation across the relevant boundary to the ghost node. The horizontal boundary values of each component grid in the  $(\theta, \phi)$  directions in the overlapping parts of the six-component system are determined by interpolation from the neighbor stencils lying in its neighboring component grid, which has been detailed (Feng et al., 2010, 2014).

## 5. NUMERICAL RESULTS

In this section, we present the numerical results from CR 2056 for the solar coronal numerical simulation with these four methods to maintain the divergence-free constraint.

To see the differences with the four divergence cleaning methods in solar corona simulation, Figures 2–5 show the magnetic field lines, radial speed  $v_r$ , and number density  $N$  on two different meridional planes at  $\phi = 180^\circ - 0^\circ$  and  $\phi = 270^\circ - 90^\circ$  from 1 to  $20 R_s$ , where the arrowheads on the black lines stand for the magnetic field directions. The four divergence cleaning methods can all produce structured solar wind. At high latitudes, the magnetic field lines extend into interplanetary space and the solar wind in this region has a faster speed and lower density. On the contrary, the slow solar wind and high density are located at lower latitudes around the Heliospheric current sheet (HCS). We can also see a helmet streamer stretched by the solar wind in this region. Above the streamer, a thin current sheet exists between different magnetic polarities.

Figure 6 presents the variation of number density  $N$  and radial speed  $v_r$  from  $1 R_s$  to  $20 R_s$  with the four divergence cleaning methods at different latitudes  $\theta = 174^\circ$  and  $\theta = 100^\circ$ , where  $\theta = 174^\circ$  corresponds to the open field region while  $\theta = 100^\circ$  corresponds to the HCS region. Reasonably, the speed is larger in the open field region holding the fast solar wind, while the



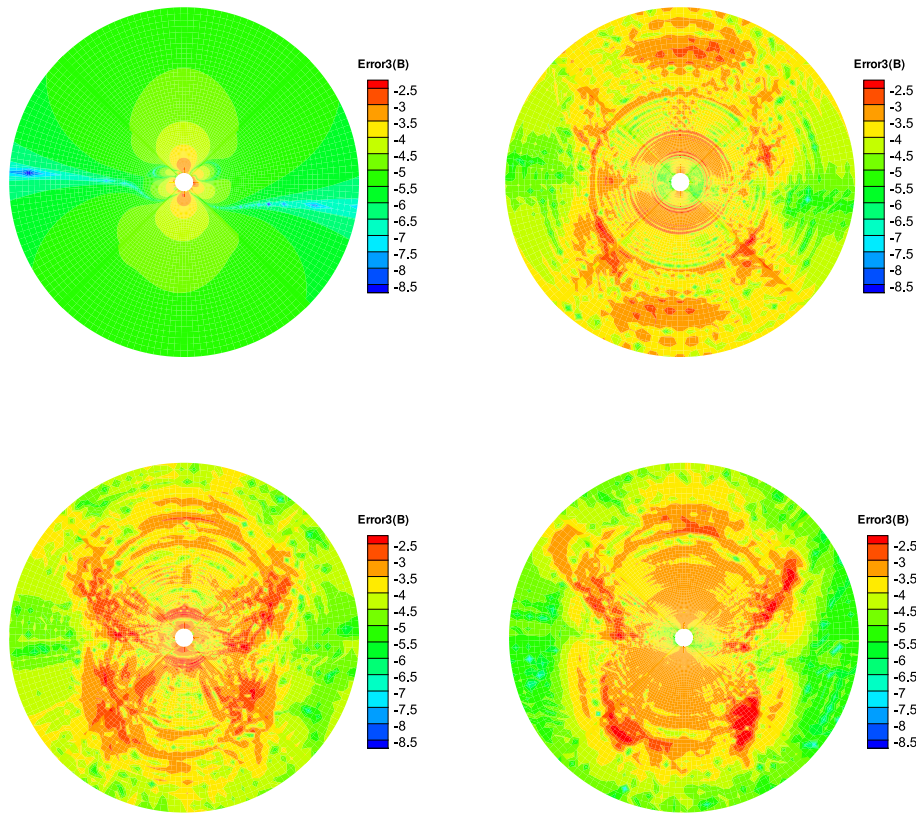


**FIGURE 9 |** The  $\log_{10}\text{Error3}(\mathbf{B})$  in the calculation at  $t = 5\text{ h}$  on the meridional plane of  $\phi = 180^\circ - 0^\circ$  from 1 to  $20 R_S$ , the results from CT method (left) and diffusive method (right) are displayed in the top row, the bottom row follows from the projection method (left) and GLM method (right).

speed is smaller in the HCS region for the slow solar wind, and the number density changes contrarily to that of the speed. Overall, the four divergence cleaning methods can all produce large-scale solar wind.

To quantitatively see how  $\nabla \cdot \mathbf{B}$  evolves, we define three relative divergence errors of the cell as  $\text{Error1}(\mathbf{B}) = \frac{\left| \int_{V_k} \nabla \cdot \mathbf{B} dV \right|}{\int_{S_k} |\mathbf{B}| dS}$ ,  $\text{Error2}(\mathbf{B}) = \frac{|\nabla \cdot \mathbf{B}| \cdot |R|}{|\mathbf{B}|}$ , and  $\text{Error3}(\mathbf{B}) = \frac{|\nabla \cdot \mathbf{B}| \cdot |R|}{\sqrt{2\rho}}$  (Powell et al., 1999; Pakmor and Springel, 2013; Mocz et al., 2014), where  $V_k$  is the  $k$ th sliding volume cell involved with the mesh grids, and  $S_k$  is the surface areas involved with  $V_k$ , and  $R = \sqrt{\frac{3}{(\Delta r)^2 + (\Delta \theta)^2 + (\sin \theta \Delta \phi)^2}}$  is the characteristic size of the cell.

**Figures 7–9** show the  $\text{Error1}(\mathbf{B})$  and  $\text{Error2}(\mathbf{B})$  and  $\text{Error3}(\mathbf{B})$  of the four divergence cleaning methods at  $t = 5\text{ h}$  on the meridional plane of  $\phi = 180^\circ - 0^\circ$ . From these figures we can see that all the divergence cleaning methods can keep the  $\nabla \cdot \mathbf{B}$  related errors under control, however, there are some differences in the relative magnitude of the resulting divergence errors. As is clearly visible in these figures, the divergence error is larger in the inner boundary for CT method compared to the other three methods, as to the outer region, that is on the contrary. That is because the local divergence error can be convected out of the domain using the diffusive method, the projection method or the GLM

method, and the CT method maintain the initial divergence error unchanged in computation.

**Figures 10–12** show the  $\text{Error1}(\mathbf{B})$ ,  $\text{Error2}(\mathbf{B})$ , and  $\text{Error3}(\mathbf{B})$  of the four divergence cleaning methods at  $t = 20\text{ h}$  on the meridional plane of  $\phi = 180^\circ - 0^\circ$ . Compared to **Figures 7–9**, there have small difference of the four methods, which verify that these methods keeping the divergence error small and no obvious large error appears in computation. The divergence error for CT method stays almost the same after  $t = 5\text{ h}$ . As for GLM method, the divergence error is convected out of the domain. Overall, the spatial distribution of the errors for these four methods are very similar and the relative divergence errors are around  $10^{-3} - 10^{-8}$ .

**Figure 13** gives the evolution of the average relative divergence errors as a function of time from the four methods in the calculation. The average relative divergence errors defined as  $\text{Error1}(\mathbf{B})^{ave} = \sum_{k=1}^M \frac{\left| \int_{V_k} \nabla \cdot \mathbf{B} dV \right|}{\int_{S_k} |\mathbf{B}| dS} / M$ ,  $\text{Error2}(\mathbf{B})^{ave} = \sum_{k=1}^M \frac{|\nabla \cdot \mathbf{B}| \cdot |R|}{|\mathbf{B}|} / M$ ,  $\text{Error3}(\mathbf{B})^{ave} = \sum_{k=1}^M \frac{|\nabla \cdot \mathbf{B}| \cdot |R|}{\sqrt{2\rho}} / M$ , where  $M$  is the total number of cells in the computational domain. From this figure we can see that  $\text{Error1}(\mathbf{B})^{ave}$  for CT method is around  $10^{-4.6}$ , for diffusive method is around  $10^{-3.7}$ , for GLM method is around  $10^{-3.6}$  and for projection method is around  $10^{-3.2}$ . The  $\text{Error2}(\mathbf{B})^{ave}$  is larger than  $\text{Error1}(\mathbf{B})^{ave}$  and  $\text{Error3}(\mathbf{B})^{ave}$ . The average relative divergence errors stay the

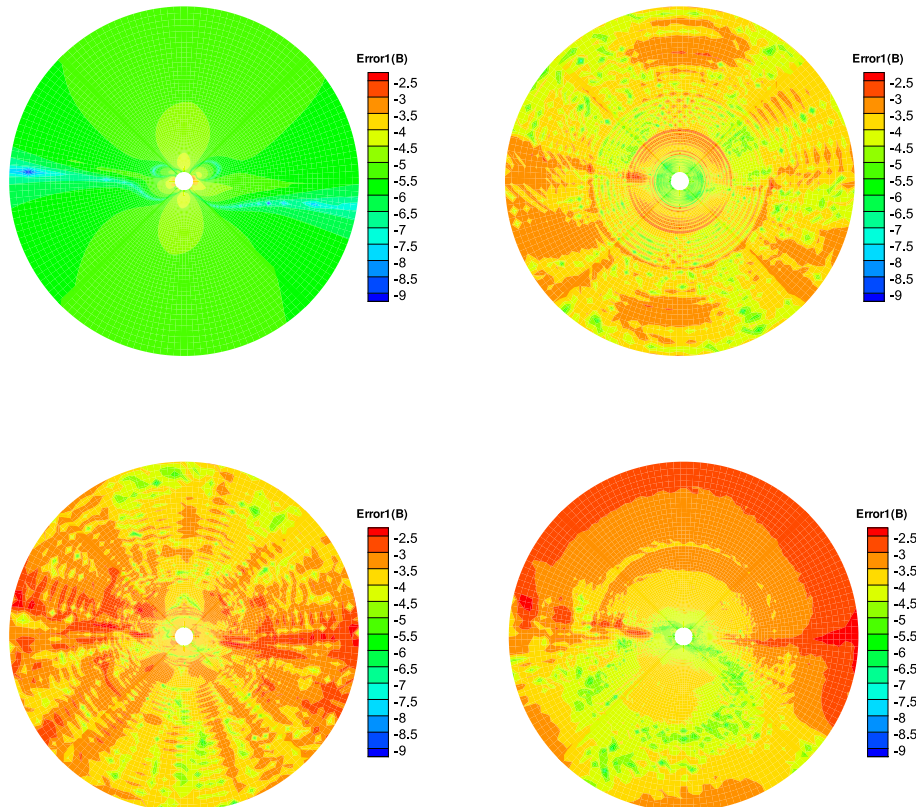


**FIGURE 10 |** The  $\log_{10} \text{Error1}(\mathbf{B})$  in the calculation at  $t = 20$  h on the meridional plane of  $\phi = 180^\circ - 0^\circ$  from 1 to  $20 R_S$ , the results from CT method (left) and diffusive method (right) are displayed in the top row, the bottom row is provided by the projection method (left) and GLM method (right).

same after 10 h and no obvious large error appears after a long run time. This verifies that the numerical error for the magnetic field divergence can continue to be acceptable during calculation. The CT method has the smallest average relative divergence errors compared to the other three methods and the errors stay the same as initial in calculation, the initial magnetic fields evaluated in the discretized space contributes significantly to the average relative divergence errors. The average relative divergence errors for diffusive method are smaller than GLM method or projection method. The relative divergence errors of diffusive method and projection method are affected by maximal sub-iterations, increasing maximal sub-iterations will make the relative divergence errors decrease but is time-consuming. Figures 14, 15 shows the average relative divergence errors for diffusive method and projection method using maximal sub-iterations 30. The  $\text{Error1}(\mathbf{B})^{\text{ave}}$  for diffusive method is about  $10^{-4.3}$ , and for projection method is about  $10^{-3.3}$ , the errors become small compared to Figure 13. Since increasing the maximal sub-iterations will decrease the computation efficiency, and Figure 13 also shows the results are acceptable without increasing the maximal sub-iterations. So we use sub-iteration 1 for diffusive method and maximal sub-iterations 10 for projection method in our code.

It is important to note that for all methods the average relative divergence errors are small, the spatial distribution of the errors

are very similar for them. Although the employed approach to limit divergence errors are significantly different and there have some differences in the average relative divergence errors as a function of time, there are excellent agreement for them in solar corona simulation, they can all produce structured solar wind.

## 6. CONCLUSIONS AND DISCUSSIONS

In this study, we employ four methods to maintain divergence cleaning constraint of magnetic field and compared the differences between them in solar corona simulation. All these algorithms are combined with a finite-volume scheme based on a six-component grid system in spherical coordinates (Ziegler, 2011, 2012; Feng et al., 2014), numerical results show that they can all produce large-scale solar wind though the relative divergence errors are different for them.

The CT method maintain the  $\nabla \cdot \mathbf{B} = 0$  constraint by utilizing a special discretization on a staggered grid. This method evolves area-averaged magnetic field components at the cell faces rather than volume-averaged quantities as fluid part, and electric field components on cell edges are needed. The CT method is attractive from a physical point of view, however, requires the magnetic field variables to be treated differently from the fluid variables, which may be inconvenient

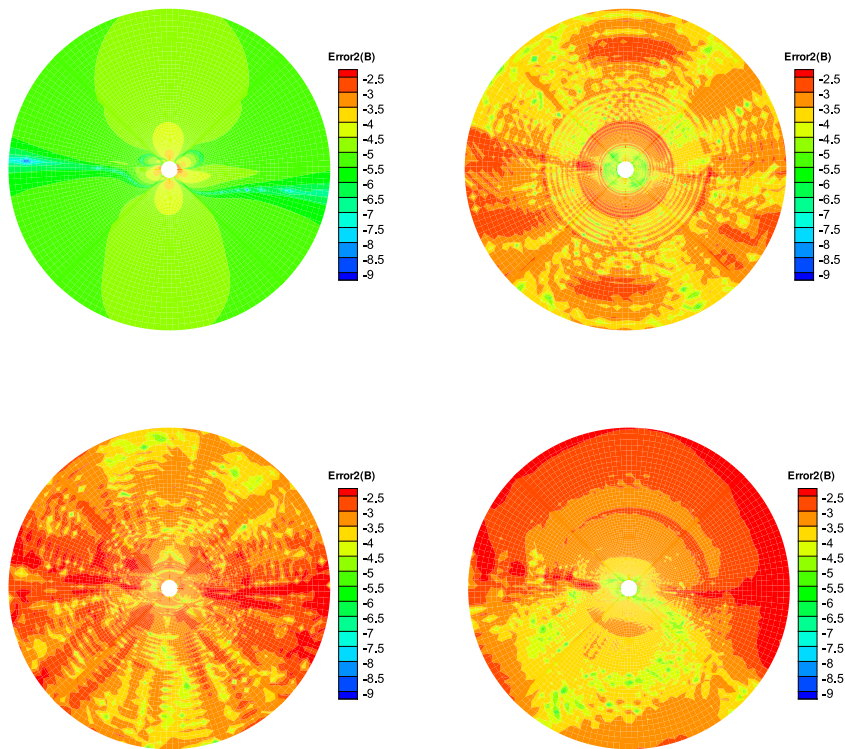


**FIGURE 11 |** The  $\log_{10}\text{Error2}(B)$  in the calculation at  $t = 20$  h on the meridional plane of  $\phi = 180^\circ - 0^\circ$  from 1 to  $20 R_s$ , the results from CT method (left) and diffusive method (right) are displayed in the top row, the bottom row is produced from the projection method (left) and GLM method (right).

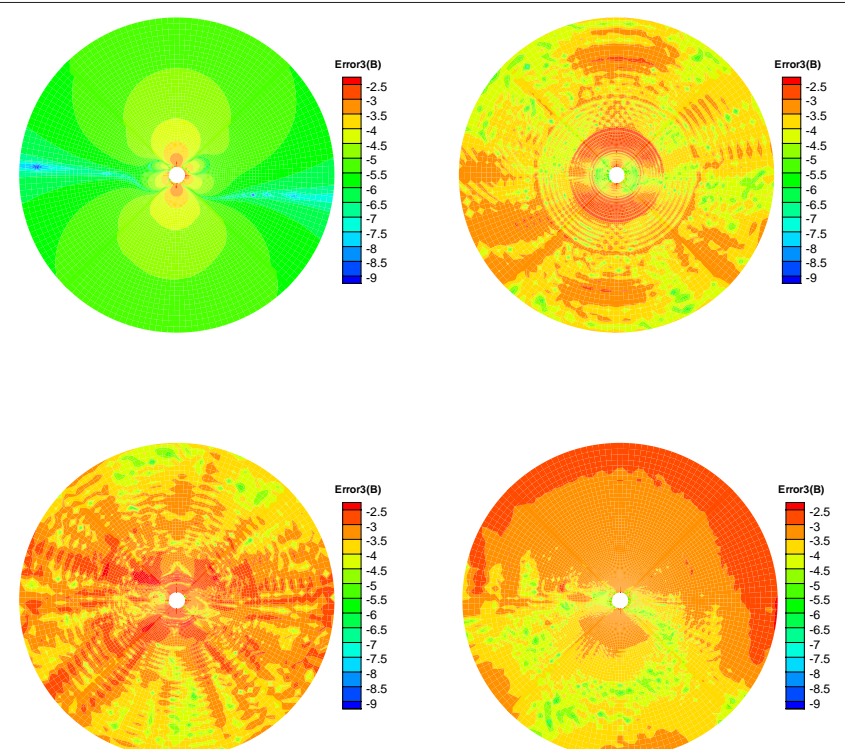


**FIGURE 12 |** The  $\log_{10}\text{Error3}(B)$  in the calculation at  $t = 20$  h on the meridional plane of  $\phi = 180^\circ - 0^\circ$  from 1 to  $20 R_s$ , the results from CT method (left) and diffusive method (right) are displayed in the top row, the bottom row is produced from the projection method (left) and GLM method (right).

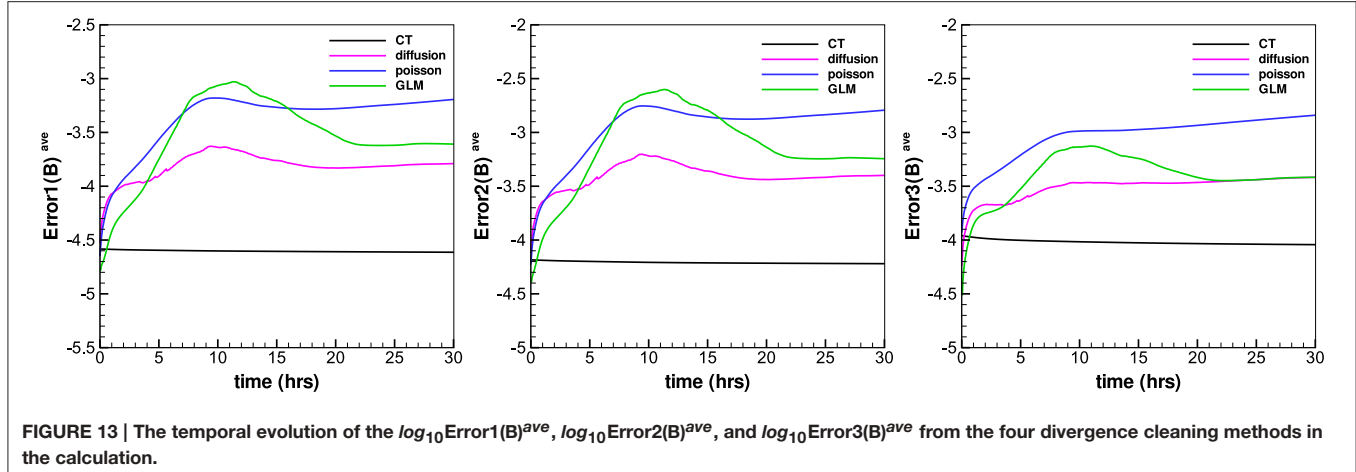


**FIGURE 13 |** The temporal evolution of the  $\log_{10}\text{Error1}(\mathbf{B})^{\text{ave}}$ ,  $\log_{10}\text{Error2}(\mathbf{B})^{\text{ave}}$ , and  $\log_{10}\text{Error3}(\mathbf{B})^{\text{ave}}$  from the four divergence cleaning methods in the calculation.

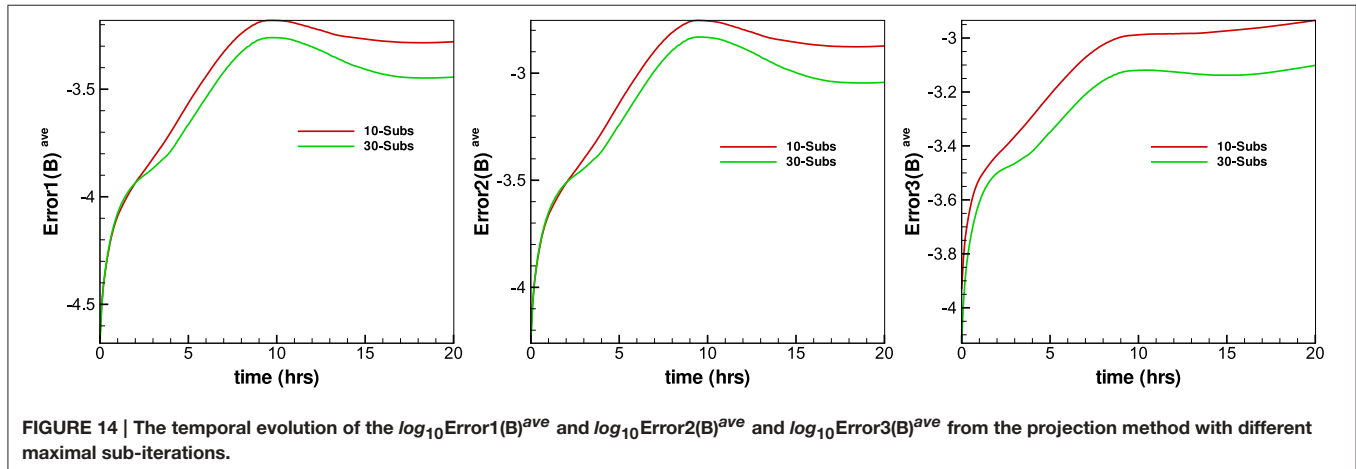


**FIGURE 14 |** The temporal evolution of the  $\log_{10}\text{Error1}(\mathbf{B})^{\text{ave}}$  and  $\log_{10}\text{Error2}(\mathbf{B})^{\text{ave}}$  and  $\log_{10}\text{Error3}(\mathbf{B})^{\text{ave}}$  from the projection method with different maximal sub-iterations.

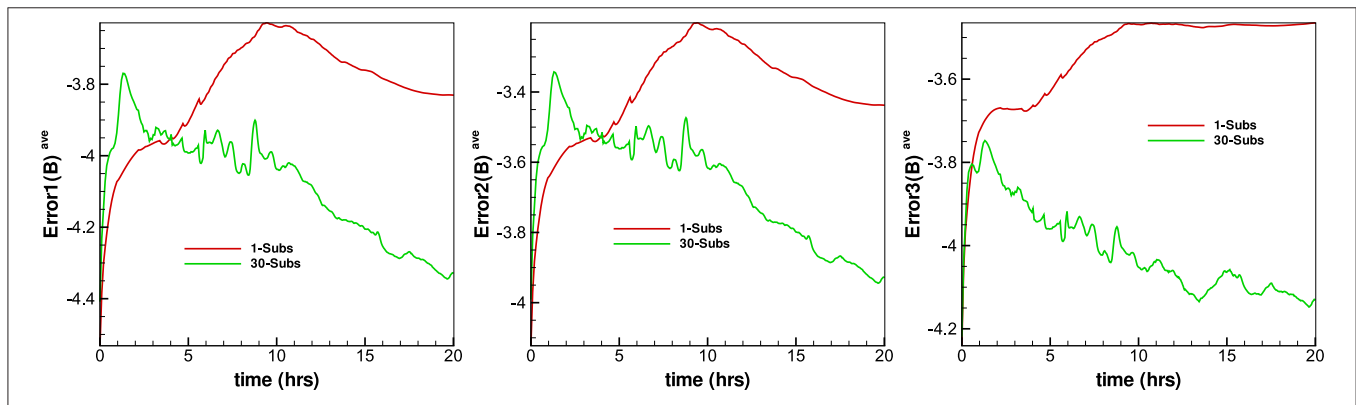


**FIGURE 15 |** The temporal evolution of the  $\log_{10}\text{Error1}(\mathbf{B})^{\text{ave}}$  and  $\log_{10}\text{Error2}(\mathbf{B})^{\text{ave}}$  and  $\log_{10}\text{Error3}(\mathbf{B})^{\text{ave}}$  from the diffusive method with different maximal sub-iterations.

for implementation. The diffusive method reduce the numerical error of  $\nabla \cdot \mathbf{B}$  by adding a source term in the induction equation. The projection method involves the solution of a poisson equation after every time step to correct errors of  $\nabla \cdot \mathbf{B}$ , and thus can be coupled with any numerical scheme, but solving the additional Poisson equation can significantly increase the

computational cost. The GLM method maintain the  $\nabla \cdot \mathbf{B} = 0$  constraint by introducing a newly transport variable  $\psi$  to the MHD system. The GLM method is fully conservative in mass, momentum, magnetic induction and energy, it is effective in controlling divergence error and can easily be applied on general grids. Our numerical results showed the CT method can

maintain the average relative divergence error around  $10^{-4.5}$ . The diffusive method can maintain the average relative divergence error about  $10^{-3.6}$ , and we only use sub-iteration 1 in this paper, increasing maximal sub-iterations will decrease the relative divergence error. The average relative divergence error for GLM method is about  $10^{-3.3}$  and for projection method is  $10^{-3.1}$ . So the CT method and the diffusive approach can maintain divergence cleaning constraint better, the diffusive method is a good choice by considering simplicity, and the CT method should be considered while we want to capture the discontinuity structure. The projection method in our paper is a preliminary try and we think the result can be better if we use multigrid in the future.

Although there have some differences in the average relative divergence errors for the four employed methods, the differences dose't effect the large-scale solar wind structure and they can all produce structured solar wind. They all produce many typical properties of the solar wind, such as an obvious slow speed area near the slightly tilted HCS plane and a fast speed area near the poles, and high density in the slow speed area and vice versa in both poles. Overall, our model can produce all

the physical parameters everywhere within the computation domain.

## AUTHOR CONTRIBUTIONS

MZ run the cases and plotted all the figures. Both MZ and XF are involved in the development of the three-dimensional MHD code, the analysis numerical results, the writing of the manuscript.

## ACKNOWLEDGMENTS

The work is jointly supported by the National Basic Research Program of China (Grant No. 2012CB825601), the National Natural Science Foundation of China (Grant Nos. 41231068, 41504132, 41274192, and 41531073), the Knowledge Innovation Program of the Chinese Academy of Sciences (Grant No. KZZD-EW-01-4), and the Specialized Research Fund for State Key Laboratories. The numerical calculation has been completed on our SIGMA Cluster computing system. The Wilcox Solar Observatory is currently supported by NASA.

## REFERENCES

- Balsara, D. S., and Kim, J. (2004). A comparison between divergence-cleaning and staggered-mesh formulations for numerical magnetohydrodynamics. *Astrophys. J.* 602, 1079–1090. doi: 10.1086/381051
- Brackbill, J. U., and Barnes, D. C. (1980). The effect of nonzero  $\nabla \cdot \mathbf{B}$  on the numerical solution of the magnetohydrodynamic equations. *J. Comput. Phys.* 35, 426–430. doi: 10.1016/0021-9991(80)90079-0
- Brandenburg, A., Rädler, K. H., Rheinhardt, M., and Käpylä, P. J. (2008). Magnetic diffusivity tensor and dynamo effects in rotating and shearing turbulence. *Astrophys. J.* 676, 740–751. doi: 10.1086/527373
- Dedner, A., Kemm, F., Kröner, D., Munz, C. D., Schnitzer, T., and Wesenberg, W. (2002). Hyperbolic divergence cleaning for the MHD equations. *J. Comput. Phys.* 175, 645–673. doi: 10.1006/jcph.2001.6961
- Dedner, A., Rohde, C., and Wesenberg, M. (2003). “A new approach to divergence cleaning in magnetohydrodynamic simulations,” in *Hyperbolic Problems: Theory, Numerics, Applications*, eds T. Y. Hou and E. Tadmor (Berlin; Heidelberg: Springer-Verlag), 509–518. doi: 10.1007/978-3-642-55711-8-47
- Evans, C. R., and Hawley, J. F. (1988). Simulation of magnetohydrodynamic flows-a constrained transport method. *Astrophys. J.* 332, 659–677. doi: 10.1086/166684
- Feng, X., Zhang, M., and Zhou, Y. (2014). A new three-dimensional solar wind model in spherical coordinates with a six-component grid. *Astrophys. J. Suppl. Ser.* 214, 6. doi: 10.1088/0067-0049/214/1/6
- Feng, X. S., Jiang, C. W., Xiang, C. Q., Zhao, X. P., and Wu, S. T. (2012a). A data-driven model for the global coronal evolution. *Astrophys. J.* 758, 62. doi: 10.1088/0004-637X/758/1/62
- Feng, X. S., Yang, L. P., Xiang, C. Q., Jiang, C. W., Ma, X. P., Wu, S. T., et al. (2012b). Validation of the 3D AMR SIP-CESE solar wind model for four Carrington rotations. *Solar Phys.* 279, 207–229. doi: 10.1007/s11207-012-9969-9
- Feng, X. S., Yang, L. P., Xiang, C. Q., Liu, Y., Zhao, X. P., and Wu, S. T. (2012c). “Numerical study of the global corona for CR 2055 driven by daily updated synoptic magnetic field,” in *Astronomical Society of the Pacific Conference Series*, Vol. 459 (San Francisco, CA), 202–208.
- Feng, X. S., Yang, L. P., Xiang, C. Q., Wu, S. T., Zhou, Y. F., and Zhong, D. K. (2010). Three-dimensional solar wind modeling from the Sun to Earth by a SIP-CESE MHD model with a six-component grid. *Astrophys. J.* 723, 300–319. doi: 10.1088/0004-637X/723/1/300
- Feng, X. S., Zhang, S. H., Xiang, C. Q., Yang, L. P., Jiang, C. W., and Wu, S. T. (2011). A hybrid solar wind model of the CESE+HLL method with a Yin-Yang overset grid and an AMR grid. *Astrophys. J.* 734, 50. doi: 10.1088/0004-637X/734/1/50
- Fuchs, F. G., Mishra, S., and Risebro, N. H. (2009). Splitting based finite volume schemes for ideal MHD equations. *J. Comput. Phys.* 228, 641–660. doi: 10.1016/j.jcp.2008.09.027
- Hayashi, K. (2005). Magnetohydrodynamic simulations of the solar corona and solar wind using a boundary treatment to limit solar wind mass flux. *Astrophys. J. Suppl. Ser.* 161, 480–494. doi: 10.1086/491791
- Inoue, S., Hayashi, K., Magara, T., Choe, G. S., and Park, Y. D. (2015). Magnetohydrodynamic Simulation of the X2.2 Solar Flare on 2011 February 15. II. Dynamics Connecting the Solar Flare and the Coronal Mass Ejection. *Solar Stell. Astrophys.* 803, 73. doi: 10.1088/0004-637X/803/2/73
- Jiang, R. L., Fang, C., and Chen, P. F. (2012a). A new MHD code with adaptive mesh refinement and parallelization for astrophysics. *Comput. Phys. Commun.* 183, 1617–1633. doi: 10.1016/j.cpc.2012.02.030
- Jiang, R. L., Fang, C., and Chen, P. F. (2012b). Numerical simulation of solar microflares in a canopy-type magnetic configuration. *Astrophys. J.* 751, 152. doi: 10.1088/0004-637X/751/2/152
- Linker, J. A., Mikić, Z., Biesecker, D. A., Forsyth, R. J., Gibson, S. E., Lazarus, A. J., et al. (1999). Magnetohydrodynamic modeling of the solar corona during whole Sun month. *J. Geophys. Res.* 104, 9809–9830. doi: 10.1029/1998JA900159
- Manabu, Y., Kanako, S., and Yosuke, M. (2009). Development of a magnetohydrodynamic simulation code satisfying the solenoidal magnetic field condition. *Comput. Phys. Commun.* 180, 1550–1557. doi: 10.1016/j.cpc.2009.04.010
- Mignone, A., and Tzeferacos, P. (2010). A second-order unsplit Godunov scheme for cell-centered MHD: the CTU-GLM scheme. *J. Comput. Phys.* 229, 2117–2138. doi: 10.1016/j.jcp.2009.11.026
- Mignone, A., Tzeferacos, P., and Bodo, G. (2010). High-order conservative finite difference GLM-MHD schemes for cell-centered MHD. *J. Comput. Phys.* 229, 5896–5920. doi: 10.1016/j.jcp.2010.04.013
- Mocz, P., Vogelsberger, M., and Hernquist, L. (2014). A constrained transport scheme for mhd on unstructured static and moving meshes. *Month. Notices R. Astron. Soc.* 442, 43–55. doi: 10.1093/mnras/stu865
- Pakmor, R., and Springel, V. (2013). Simulations of magnetic fields in isolated disc galaxies. *Month. Notices R. Astron. Soc.* 432, 176–193. doi: 10.1093/mnras/stt428

- Parker, E. N. (1963). *Interplanetary Dynamical Processes*. New York, NY: Interscience Publishers.
- Powell, K. G., Roe, P. L., Linde, T. J., Gombosi, T. I., and De Zeeuw, D. L. (1999). A solution-adaptive upwind scheme for ideal magnetohydrodynamics. *J. Comput. Phys.* 154, 284–309. doi: 10.1006/jcph.1999.6299
- Powell, K. G., Roe, P. L., and Quirk, J. (1993). “Adaptive-mesh algorithms for computational fluid dynamics,” in *Algorithmic Trends in Computational Fluid Dynamics*, eds M. Y. Hussaini, A. Kumar and M. D. Salas (New York, NY: Springer), 303–337. doi: 10.1007/978-1-4612-2708-3-18
- Rempel, M., Schüssler, M., and Knölker, M. (2009). Radiative magnetohydrodynamic simulation of sunspot structure. *Astrophys. J.* 691, 640–649. doi: 10.1088/0004-637X/691/1/640
- Shen, F., Shen, C. L., Zhang, J., Hess, P., Wang, Y. M., Feng, X. S., et al. (2014). Evolution of the 12 July 2012 CME from the sun to the earth: data-constrained three-dimensional MHD simulations. *J. Geophys. Res. Space Phys.* 119, 7128–7141. doi: 10.1002/2014JA020365
- Susanto, A., Ivan, L., Sterck, H. D., and Groth, C. P. T. (2013). High-order central ENO finite-volume scheme for ideal MHD. *J. Comput. Phys.* 250, 141–164. doi: 10.1016/j.jcp.2013.04.040
- Tóth, G. (2000). The  $\nabla \cdot \mathbf{B} = 0$  constraint in shock-capturing magnetohydrodynamics codes. *J. Comput. Phys.* 161, 605–652. doi: 10.1006/jcph.2000.6519
- Tóth, G., Sokolov, I. V., Gombosi, T. I., Chesney, D. R., Clauer, C. R., Zeeuw, D. L. D., et al. (2005). Space weather modeling framework: a new tool for the space science community. *J. Geophys. Res.* 110, A12226. doi: 10.1029/2005JA011126
- Tóth, G., van der Holst, B., Sokolov, I. V., De Zeeuw, D. L., Gombosi, T. I., Fang, F., et al. (2012). Adaptive numerical algorithms in space weather modeling. *J. Comput. Phys.* 231, 870–903. doi: 10.1016/j.jcp.2011.02.006
- van der Holst, B., and Keppens, R. (2007). Hybrid block-AMR in Cartesian and curvilinear coordinates: MHD applications. *J. Comput. Phys.* 226, 925–946. doi: 10.1016/j.jcp.2007.05.007
- Yee, K. (1966). Numerical solution of initial boundary value problems involving Maxwell's equations in isotropic media. *IEEE Trans. Anten. Propagat.* 14, 302–307. doi: 10.1109/TAP.1966.11138693
- Ziegler, U. (2004). A central-constrained transport scheme for ideal magnetohydrodynamics. *J. Comput. Phys.* 196, 393–416. doi: 10.1016/j.jcp.2003.11.003
- Ziegler, U. (2011). A semi-discrete central scheme for magnetohydrodynamics on orthogonal-curvilinear grids. *J. Comput. Phys.* 230, 1035–1063. doi: 10.1016/j.jcp.2010.10.022
- Ziegler, U. (2012). Block-structured adaptive mesh refinement on curvilinear-orthogonal grids. *SIAM J. Sci. Comput.* 34, C102–C121. doi: 10.1137/110843940

**Conflict of Interest Statement:** The authors declare that the research was conducted in the absence of any commercial or financial relationships that could be construed as a potential conflict of interest.

Copyright © 2016 Zhang and Feng. This is an open-access article distributed under the terms of the Creative Commons Attribution License (CC BY). The use, distribution or reproduction in other forums is permitted, provided the original author(s) or licensor are credited and that the original publication in this journal is cited, in accordance with accepted academic practice. No use, distribution or reproduction is permitted which does not comply with these terms.



# FORWARD: A Toolset for Multiwavelength Coronal Magnetometry

**Sarah E. Gibson<sup>1\*</sup>, Therese A. Kucera<sup>2</sup>, Stephen M. White<sup>3</sup>, James B. Dove<sup>4</sup>, Yuhong Fan<sup>1</sup>, Blake C. Forland<sup>5</sup>, Laurel A. Rachmeler<sup>6,7</sup>, Cooper Downs<sup>8</sup> and Katharine K. Reeves<sup>9</sup>**

<sup>1</sup> High Altitude Observatory, National Center for Atmospheric Research, Boulder, CO, USA, <sup>2</sup> Goddard Space Flight Center, National Aeronautics and Space Administration (NASA), Greenbelt, MD, USA, <sup>3</sup> Air Force Research Labs, Kirtland Air Force Base, Albuquerque, NM, USA, <sup>4</sup> Department of Physics, Metro State University Denver, Denver, CO, USA, <sup>5</sup> Department of Physics, Indiana University, Bloomington, IN, USA, <sup>6</sup> Royal Observatory of Belgium, Brussels, Belgium, <sup>7</sup> Marshall Space Flight Center, National Aeronautics and Space Administration (NASA), Huntsville, AL, USA, <sup>8</sup> Predictive Science Inc., San Diego, CA, USA, <sup>9</sup> Department of High Energy Astrophysics, Harvard-Smithsonian Center for Astrophysics, Cambridge, MA, USA

## OPEN ACCESS

### Edited by:

Xueshang Feng,

National Space Science Center, China

### Reviewed by:

Satoshi Inoue,

Max-Planck Institute for Solar System Research, Germany

Jiansen He,

Peking University, China

### \*Correspondence:

Sarah E. Gibson

sgibson@ucar.edu

### Specialty section:

This article was submitted to

Stellar and Solar Physics,

a section of the journal

Frontiers in Astronomy and Space

Sciences

**Received:** 06 January 2016

**Accepted:** 24 February 2016

**Published:** 15 March 2016

### Citation:

Gibson SE, Kucera TA, White SM, Dove JB, Fan Y, Forland BC, Rachmeler LA, Downs C and Reeves KK (2016) FORWARD: A Toolset for Multiwavelength Coronal Magnetometry. *Front. Astron. Space Sci.* 3:8. doi: 10.3389/fspas.2016.00008

Determining the 3D coronal magnetic field is a critical, but extremely difficult problem to solve. Since different types of multiwavelength coronal data probe different aspects of the coronal magnetic field, ideally these data should be used together to validate and constrain specifications of that field. Such a task requires the ability to create observable quantities at a range of wavelengths from a distribution of magnetic field and associated plasma—i.e., to perform forward calculations. In this paper we describe the capabilities of the FORWARD SolarSoft IDL package, a uniquely comprehensive toolset for coronal magnetometry. FORWARD is a community resource that may be used both to synthesize a broad range of coronal observables, and to access and compare synthetic observables to existing data. It enables forward fitting of specific observations, and helps to build intuition into how the physical properties of coronal magnetic structures translate to observable properties. FORWARD can also be used to generate synthetic test beds from MHD simulations in order to facilitate the development of coronal magnetometric inversion methods, and to prepare for the analysis of future large solar telescope data.

**Keywords:** sun: corona, sun: magnetic fields, sun: x-rays, sun: radio, sun: infrared, sun: EUV

## 1. INTRODUCTION

In essence, the goal of coronal magnetometry is to solve an inverse problem. Given magnetically-sensitive coronal observations (including, but not limited to polarimetry), the challenge is to determine the magnetic field distribution that generates them. Solving such an inverse problem requires three things: a means of specifying the physical state (e.g., the distribution of density, temperature, velocity, and magnetic field), a well-defined forward calculation (i.e., the physical process relating the physical state and the observations), and the observations themselves.

FORWARD is a set of more than 200 IDL procedures and functions that form a SolarSoft (Freeland and Handy, 1998) package for synthesizing observables and comparing them to coronal data from EUV/Xray imagers, UV/EUV spectrometers, visible/IR/UV polarimeters, white-light coronagraphs, and radio telescopes. It may be called from the command line (i.e., `for_drive`), or via a widget interface (i.e., `for_widget`; Forland et al., 2014). The standard output product is a 2D plane-of-sky map, 2D latitude-longitude (Carrington) map, or user-specified spatial sampling

(**Figure 1**). Image field of view and resolution is user-controlled, as is “viewer” position and line-of-sight (LOS) integration spacing and limits. Details on how to run and install FORWARD are available at <http://www.hao.ucar.edu/FORWARD/>.

This paper describes how FORWARD addresses all three of the requirements for coronal magnetometric inversion and gives examples of how it may be used. Section 2 demonstrates how the physical state may be defined through analytic or numerical models, either user-inputted or generated by FORWARD through included codes or via its interface with online coronal simulations. Section 3 describes the multiwavelength forward calculations that predict observational manifestations of physical processes such as *Thomson scattering*, *collisional excitation*, *continuum absorption*, *resonance scattering*, *Zeeman and Hanle effects*, *Doppler shift*, *thermal bremsstrahlung*, *gyroresonance*, and *Faraday rotation*, and discusses the magnetic diagnostic potential of each. Section 4 describes how FORWARD enables the access and manipulation of observations and converts them to a format directly comparable to the predictions of forward calculations. Section 5 shows how FORWARD may be applied to validate models, build intuition regarding coronal magnetic signatures, tune models to match data, and generally guide the development of multiwavelength magnetometric inversion techniques. Finally, in Section 6 we present our conclusions.

## 2. THE PHYSICAL STATE

When discussing solar-coronal forward analysis, it is important to differentiate between the model of the *physical state* of the

corona, which addresses the distribution of magnetic fields and plasma throughout 3D space, and the model of how these fields and plasma operate in the presence of a *physical process*, which enables the synthesis of an observed quantity. We will treat the latter in Section 3 as the heart of the forward calculation.

Models of the physical state essentially create synthetic Suns—generally through solutions of the MHD equations. FORWARD includes several analytic models in its distribution (i.e., Low and Hundhausen, 1995; Lites and Low, 1997; Gibson et al., 2010; **Figure 1**; Gibson and Low, 1998; **Figure 2**). It is straightforward to expand it to incorporate other analytic models. Alternatively, a user may input a numerical data cube describing the 3D distribution of plasma and fields. If the data cube is not global, options are provided regarding what to do outside the cube (e.g., zero, constant, or dipolar field, and hydrostatic atmospheres—either isothermal-exponential or power-law). If the data cube only provides a magnetic field, hydrostatic atmospheres can be applied throughout space. (See [http://www.hao.ucar.edu/FORWARD/FOR\\_SSW/idl/MODELS/NUMCUBE/make\\_my\\_cube.pro](http://www.hao.ucar.edu/FORWARD/FOR_SSW/idl/MODELS/NUMCUBE/make_my_cube.pro) for instructions on how to convert a numerical data cube to FORWARD format.) In addition to the forward-calculated observables discussed in Section 3, FORWARD allows easy display of the parameters of the physical state, e.g., density, temperature, magnetic field, velocity (see e.g., **Figure 2**).

Given a calendar date, FORWARD can also automatically interface with the SolarSoft Potential Field Source Surface (PFSS) package (<http://www.lmsal.com/~derosa/pfsspack/>) and

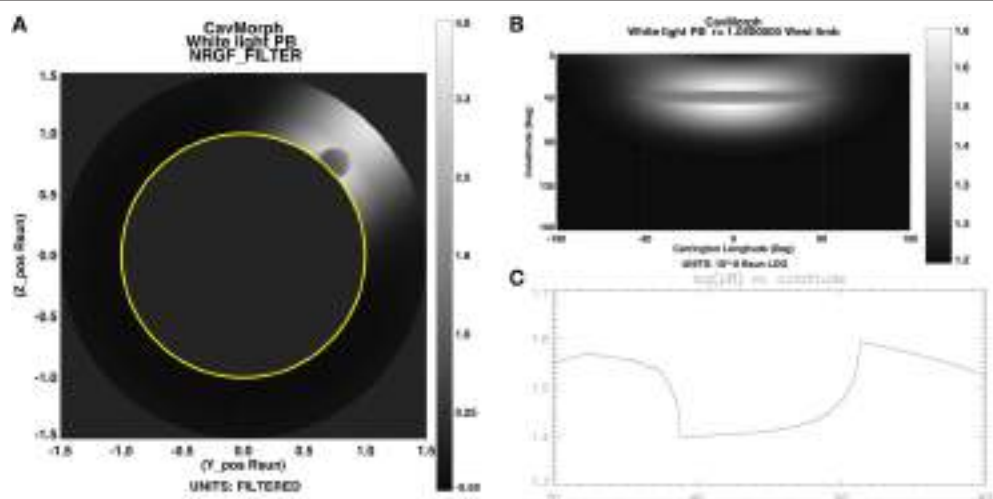
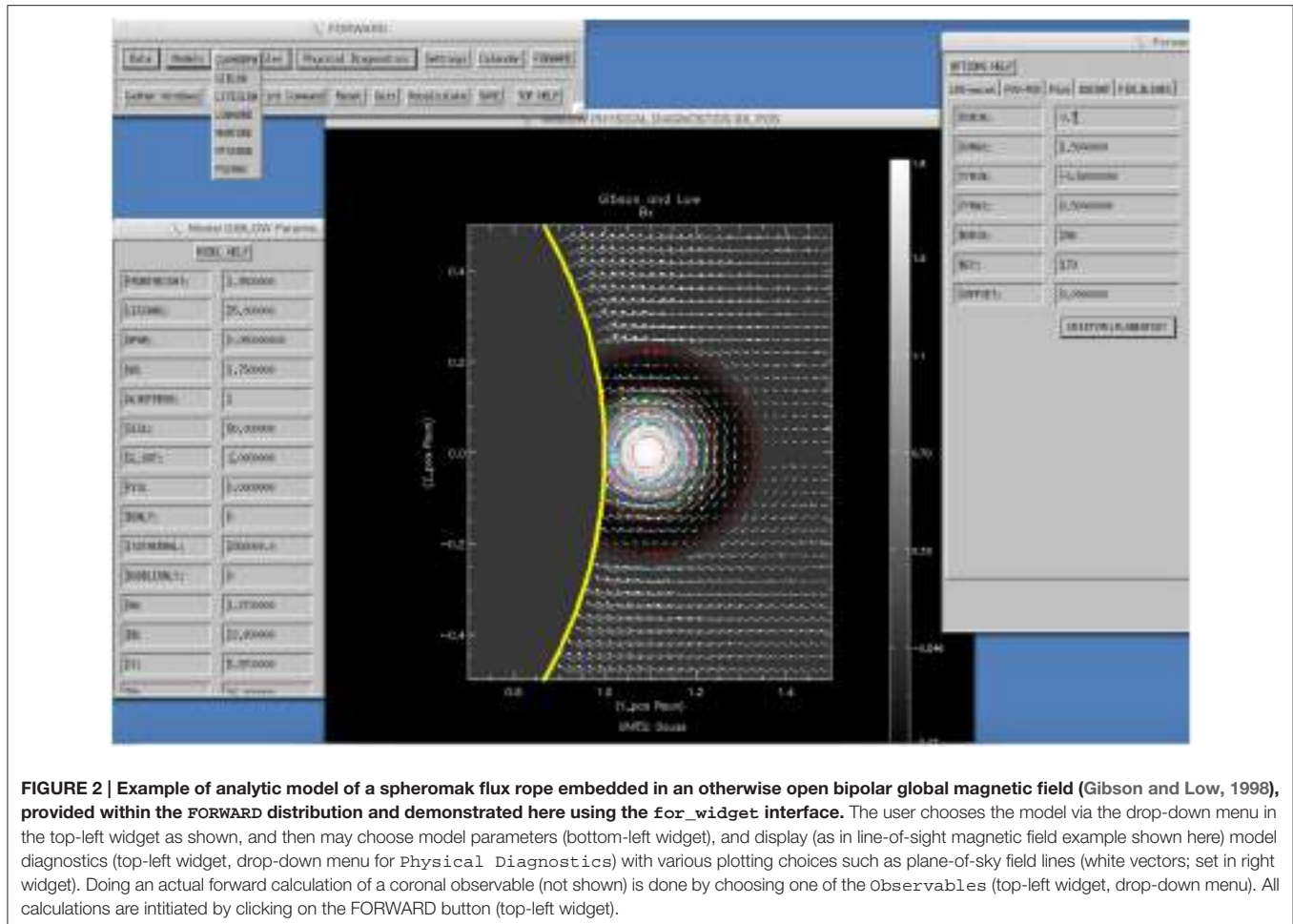


**FIGURE 1 | Examples of FORWARD output of LOS-integrated white-light polarized Brightness (pB) for a morphological model of a cavity embedded in a coronal streamer** (Gibson et al., 2010). **(A)** Cavity in plane of sky at limb (plotted with non-radial gradient filter Morgan et al., 2006). Plot obtained by FORWARD line command: `for_drive, 'cavmorph', inst='wl', line='pb', thcs=45, cavlength=150, rfILTER='NRGF_FILTER'`. **(B)** Cavity in latitude-longitude Carrington map. Plot obtained as for **(A)**, but without `rfILTER` keyword and with `,gridtype='Carrmap', cmer=0, charsize=.85` added. **(C)** Cavity in constant radius latitudinal cut. Plot obtained as for **(A)**, but with removal of `rfILTER` keyword and addition of keywords: `,gridtype='user', ruser=dblarr(201)+1.05, thuser=dindgen(201)*.15+30, phuser=dblarr(201)-30., quantmap=quantmap` and followed by command: `plot, dindgen(201)*.15+30, alog10(quantmap.data), yrangle=[1.3,1.7], xrange=[30.,60.], title='log(pB) vs. colatitude'`. Note that this and other IDL commands provided in figure captions below can be accessed via \$FORWARD\_DOCS/EXAMPLES/examples\_forwardpaper.html.



the web-served Magnetohydrodynamic Algorithm outside a Sphere (MAS)-corona MHD simulation data cubes ([http://www.predsci.com/hmi/data\\_access.php](http://www.predsci.com/hmi/data_access.php); **Figure 3**; Lionello et al., 2009). This enables global descriptions of the 3D coronal magnetic field, and for the MAS model also the plasma in MHD force balance, specific to a given time/day and viewer position.

FORWARD also allows the user to specify the physical state of two populations of plasma that may need to be treated independently in the forward calculation. For example, a user may specify a population of plasma at a coronal temperature, and another population of cooler, chromospheric plasma subject to continuum absorption in EUV images (see Section 3.3). This provides capability, for example, for depicting models where cool solar prominences exist in the context of surrounding coronal temperature material, such as those produced by Luna et al. (2012) or Xia et al. (2014) (see also the cavity-prominence test-bed simulation shown in Section 5). Another application would be to allow models where two different coronal populations lie along the line of sight, each with different abundance properties. It is also possible to set a filling factor for one or both populations. This capability allows exploitation of the diagnostic potential of comparing emissions which may have different dependencies on density (as we discuss in Section 3).

### 3. THE FORWARD CALCULATION: PHYSICAL PROCESSES

Given a modeled physical state, i.e., a specification of the distribution of density, temperature, magnetic field and velocity in the corona, FORWARD is able to produce many different synthetic observables. These observables arise from various physical processes manifesting at different wavelengths of light in the corona. They depend upon the viewer's line of sight, along which (for example) optically-thin emission must be integrated. FORWARD establishes these lines of sight either through keyword definition of an observer's heliographic latitude and longitude, or through keyword setting of a calendar date from which the position of the Earth (or STEREO spacecraft) can be determined. In this section, we will discuss a range of physical processes relevant to the corona, describe how they translate to observables that FORWARD synthesizes, and consider their potential for coronal magnetometry. **Table 1** provides a summary.

#### 3.1. Thomson Scattering

Thomson scattering is the main physical process responsible for illuminating the continuum, or "K" corona. Photospheric

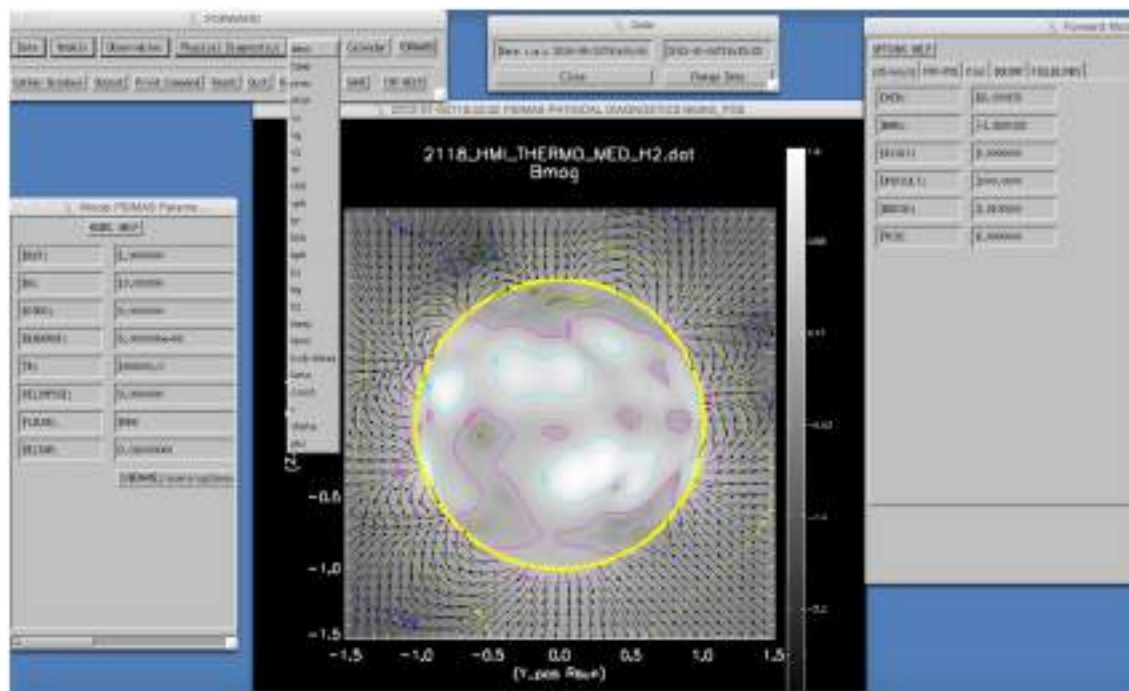


**FIGURE 3 | Example of MAS model data cube loaded into FORWARD by date, and displaying magnetic field strength (contours) and field lines (black arrows) in the plane of the sky.** As with the analytic model of Figure 2, display options and model parameters can be set through the widgets. Descriptions of the model parameters and other options are found via the TOP HELP, MODEL HELP, and OPTIONS HELP buttons at the top of the three main widget windows. See Section 3 for further discussion and Figures 4, 6 for examples of forward calculation using the MAS and PFSS models.

**TABLE 1 | Physical processes as defined in Section 3, highlighting dependency on attributes of the physical state, which observations are sensitive to them, and diagnostic sensitivity to the 3D coronal magnetic field.**

Process	Physical-state dependency	Observation	Magnetic quantity probed
Thomson scattering	Electron density	White-light pB, TB	Plasma structured by field (e.g., closed vs. open field boundaries, flux surfaces)
Collisional excitation	Electron density, temperature	IR/Visible/EUV/SXR emission	Plasma structured by field (incl. loops, closed/open boundaries, flux surfaces)
Continuum absorption	Chromospheric population density, electron density, temperature	EUV absorption features	Can indicate magnetic geometry suitable for prominence formation
Resonance scattering; polarization	Electron density, temperature, vector magnetic field	Visible/IR spectra	$B_{los}$ from Stokes V; Magnetic field direction from Stokes Q, U
Doppler shift	Electron density, temperature, velocity	Visible/IR spectra	$B_{los}$ and field line direction from waves; flux surfaces from bulk flows
Thermal bremsstrahlung	Electron density, temperature, vector magnetic field	Radio emission (intensity and circular polarization) as a function of frequency	$B_{los}$ from Stokes V
Gyroresonance	Electron density, temperature, vector magnetic field	Radio emission (intensity and circular polarization) as a function of frequency	Surfaces of constant magnetic field strength at each frequency
Faraday rotation	Electron density, temperature, vector magnetic field	Rotation of plane of polarization	$B_{los}$ from rotation measure

light scatters off of free coronal electrons and results in both unpolarized and linearly polarized emission. Both the total brightness ( $TB$ ) and polarized brightness ( $pB$ ) of white light are proportional to  $n_e$  and to a scattering function that depends upon radial distance from the photosphere (Billings, 1966). They are also integrated along the line of sight in the optically-thin corona.

Given a distribution of electron density, FORWARD can synthesize images of  $TB$ ,  $pB$ , and degree of polarization  $p$  (Figures 4A, 5A), comparable to observations from white light coronagraphs such as SOHO/LASCO, STEREO/SECCHI, and MLSO/KCOR. If keyword *fcor* is set, FORWARD will call upon SolarSoft function *fcorpol\_KL.pro* in order to add a model

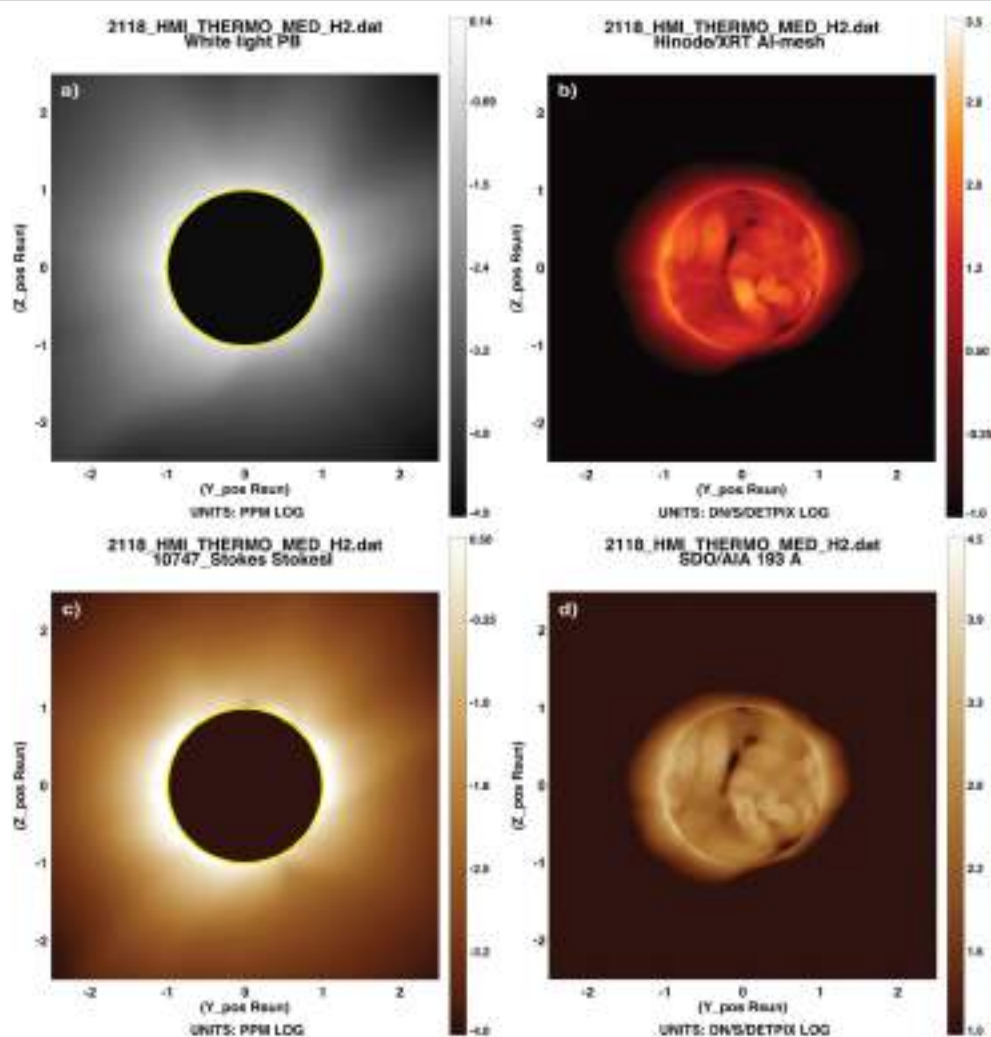


**FIGURE 4 | Figure showing MAS synthetic data. (A)** pB (see Section 3.1). Plot obtained via widget as in **Figure 2** but selecting pB via the observables menu, or alternatively via FORWARD line command `for_drive,'psimas',date='2012-01-04',xxmin=-2.5,xxmax=2.5,yymin=-2.5,ymax=2.5,units='PPM'`. **(B)** XRT Al-Mesh line (see Section 3.2). Plot obtained as in **(A)** with removal of units keyword and addition of `/xrt, line='AL-MESH', usecolor=3`. **(C)** (infrared) Fe XIII 1074.7 Å intensity (see Section 3.4). Plot obtained as in **(A)** with additional keyword `/comp, ngrid=256, ngy=256`. **(D)** (EUV) Fe XIII 193 Å intensity (see Section 3.2). Plot obtained as in **(A)** with removal of units keyword and addition of `/aia`. Note that **(A,C)** are in units of  $10^{-6}$  solar Brightness (log), or parts per million (PPM). **(B,D)** are in instrument detector units per second with default intensity ranges chosen to match expectations of XRT and AIA telescopes.

distribution of F-coronal brightness (Koutchmy and Lamy, 1985). This arises from light diffracting through interplanetary particles in the plane of the ecliptic, and is also known as the zodiacal light. It is essentially unpolarized in the first few solar radii (Mann, 1992).

Thomson scattering has no direct dependency on magnetic field, but there is sensitivity to magnetic topology through its dependence on density. For example, bright (dense) coronal streamers generally correspond to closed magnetic fields, and dark (sparse) coronal holes generally correspond to open magnetic fields. For this reason, white light coronagraph data have been used to qualitatively validate features of coronal magnetic models (Newkirk and Altschuler, 1970), and more quantitatively, to define the average nonradial expansion of

magnetic fields in coronal holes (Kopp and Holzer, 1976; Munro and Jackson, 1977). Magnetic flux surfaces also may be delineated by white light structures, such as three-part CME features (Low and Hundhausen, 1995), and prominence cavities (e.g., **Figure 5A**; see also Gibson and Fan, 2006).

### 3.2. Collisional Excitation

Solar coronal radiation in the extreme ultraviolet (EUV) and soft X-ray (SXR) is produced by collisionally-excited atoms in thermal and ionization equilibrium. The intensity of this emission is proportional to  $n_e^2$  and the temperature response of the line(s). For spectrographs, FORWARD calculates the integrated intensities of lines in physical units to be compared with processed spectral data. For waveband imagers, FORWARD

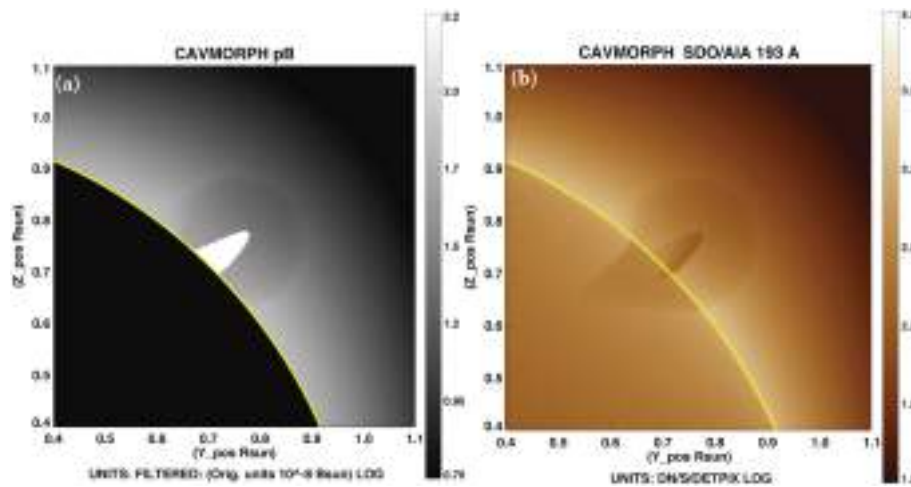


**FIGURE 5 | A simplified cavity and prominence produced using the Gibson et al. (2010) model. (A)** synthesized white light polarized brightness (see Section 3.1), with high-density prominence appearing as enhanced intensity. Plot obtained by FORWARD line command: `for_drive,'cavmorph',/nougat,thcs=45,cdens=1e10,cff_noug=[.2,8.,0,0,0,0],nougwidth=.025,nougtop_r=.9,pop2T=2,xxmin=0.4,yymin=0.4,ymax=1.1,xxmax=1.1.` **(B)** SDO/AIA 193 Å emission, with dark prominence because of continuum absorption (see Sections 3.2–3.3). Plot obtained by above command with the addition of keyword `/aia`.

incorporates the wavelength-response function of the instrument into its calculated intensities. The emission is integrated along the line of sight in the optically-thin corona.

FORWARD synthesizes images comparable to those produced by numerous EUV and Soft X-ray imagers and also many spectral line intensities in these wave bands. Currently simulated imagers include SOHO/EIT, STEREO/EUVI, Hinode/XRT (e.g., **Figure 4B**), ProbA-2/SWAP, and SDO/AIA (e.g., **Figures 4D, 5B**). Adding new imagers is straightforward if the wavelength response function is available. Count rates for imagers are calculated by convolving the wavelength response function of the imager with pre-calculated spectra at various temperatures and densities, produced using the Chianti atomic data base and related software (Dere et al., 1997; Del Zanna et al., 2015). For the imagers, users may select from pre-calculated abundance options; current selections include coronal abundances determined by Feldman et al. (1992) or Schmelz et al. (2012) or photospheric abundances of Caffau et al. (2011). The code uses the Chianti ionization equilibrium calculations (Dere et al., 2009).

Spectral line intensities can be calculated for any line between 1 and 1410 Å, again under the assumption that the coronal plasma is collisionally excited and in thermal and ionization equilibrium. Based on a user-specified instrumental line-width, the code includes any blended lines included in the Chianti spectral line calculations. For spectral lines, users may specify any abundance or ionization table in the Chianti database format. Default line widths are provided for particular instruments like Hinode/EIS, IRIS, and SoHO/CDS, but the code is not limited to lines observed by these instruments. The wavelength range covers the IRIS far ultraviolet (FUV) range, but not the near ultraviolet (NUV) range, which does not include lines that can be modeled by FORWARD.

As with Thomson scattering, radiation from collisional excitation does not have a direct dependence on magnetic fields. However, the suppression of conductivity across magnetic field lines means that magnetic field lines are essentially traced out in coronal emission. EUV and SXR structures thus often provide a diagnostic of local magnetic field geometry—for example when coronal loops are lit up in active regions (see e.g., Savcheva et al., 2013; Malanushenko et al., 2014; also Savcheva and Malanushenko, in preparation). Magnetic boundaries or flux surfaces are also often delineated due to sharp density/temperature gradients, as in the case of open vs. closed fields (e.g., **Figures 4B,D**), and prominence cavities (e.g., **Figure 5B**).

### 3.3. Continuum Absorption

Relatively cool, chromospheric temperature material suspended in the corona (e.g., a prominence) results in Lyman continuum absorption by neutral hydrogen and by neutral and once-ionized helium (see Kucera, 2015 for further details).

The observed intensity is

$$I = I_f + I_b e^{-\tau} \quad (1)$$

where  $I_f$  is the foreground radiation,  $I_b$  is the background radiation, and  $\tau$  is the continuum absorption summed over the three absorbing species:

$$\tau = \sum_i \sigma_i \int n_i dh \quad (2)$$

where  $h$  is the distance along the line of sight,  $n_i$  is the number density of each species, and  $\sigma_i$  is the absorbing cross section as a function of wavelength (values calculated with the formulation of Keady and Kilcrease, 2000).

Through the definition of a second population of low-temperature plasma with a specified density distinct from the primary coronal population, FORWARD calculates the effect of continuum absorption on the total intensity in EUV. **Figure 5B** shows a model of a simple prominence inside a cavity in the 193 Å band of SDO/AIA. The cavity is darker than its surroundings because it has a lower density, but the central prominence is darker because of continuum absorption of background emission.

Again, continuum absorption has no direct dependence on magnetic fields. However, magnetic field geometry (e.g., dipped or flat field lines) is expected to play an important role in establishing where prominences form (see Karpen, 2014 and references therein).

### 3.4. Resonance Scattering and Polarization

Emission from the coronal forbidden lines arises both from collisional excitation as described above in Section 3.2, and also from resonance scattering. In resonance scattering, anisotropic radiation from the underlying photosphere excites coronal ions and leads to reemitted light with a characteristic polarization signature (Casini and Judge, 1999). This emission depends linearly upon ion density (and thus electron density), as opposed to quadratically as in collisional excitation. **Figure 4C** vs. **Figure 4D** illustrates the difference between the collisionally-excited/resonantly-scattered infrared Fe XIII line and the predominantly collisionally-excited EUV Fe XIII line. Intensity of the latter drops off quickly, while the former shows similarity in the outer field of view to the Thomson-scattered white light (**Figure 4A**), which is also linearly-dependent upon electron density at these heights (see Habbal et al., 2011 for further discussion).

FORWARD employs the Coronal Line Emission (CLE) Fortran-77 polarimetry code developed by Judge and Casini (2001) to synthesize Stokes ( $I$ ,  $Q$ ,  $U$ ,  $V$ ) line profiles for the visible and infrared forbidden lines including Fe XIII 1074.7 and 1079.8 nm (currently observed by MLSO/CoMP as discussed in Section 4), Fe XIV 530.3 nm, Si IX 393.4 nm, and Si X 1430.5 nm. Stokes  $I$  indicates the total intensity of the line,  $Q$  and  $U$  together constitute its linearly polarized intensity, and  $V$  is the circularly polarized intensity. The CLE code models the lines under the combined influence of resonance scattering and particle collisions in the presence of coronal magnetic fields.

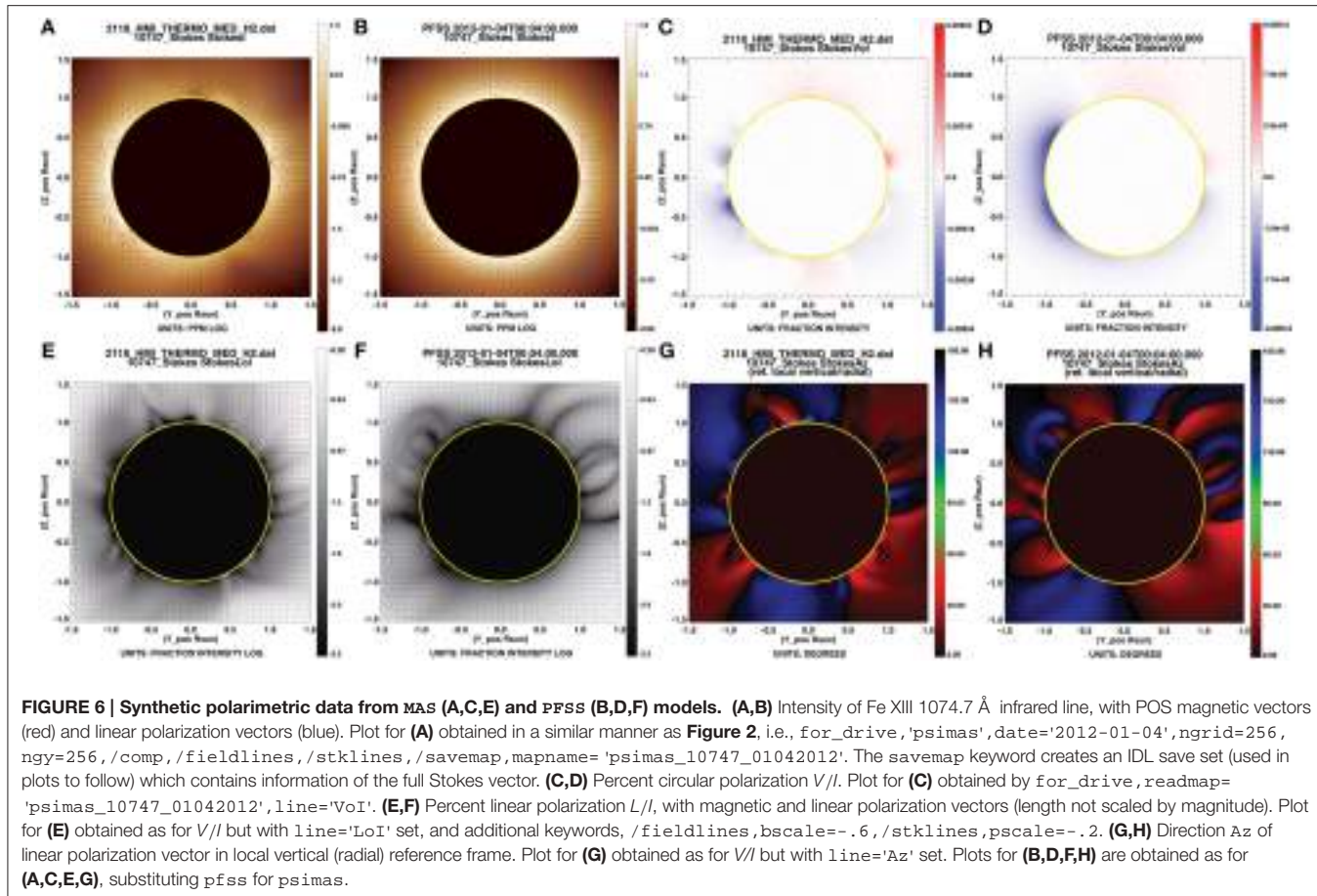
Because of its sensitivity to magnetic fields, the Stokes  $I$ ,  $Q$ ,  $U$ ,  $V$  polarization vector can be used as a direct diagnostic of coronal magnetism (subject to intensity-weighted line-of-sight integration). For example, the Zeeman effect generates circularly polarized light (Stokes  $V$ ) proportional to line-of-sight-oriented magnetic field  $B_{los}$ . Since the coronal visible/infrared forbidden lines treated by CLE have a Larmor frequency  $\nu_L \approx \mu_B B/h$  that is much larger than the inverse lifetime of the atomic transitions being modeled, they lie in the strong field (or saturation) limit of the Hanle effect (see Raouafi et al., submitted; Dima et al., submitted) for discussion of magnetometry in the UV “unsaturated” Hanle regime). In the saturated regime, linear polarization provides a probe of the direction of the magnetic

field in the plane-of-sky (POS), but not its strength. In particular, the direction of the linear polarization vector [or azimuth,  $Az = -0.5 * atan(U/Q)$ ] is parallel to the POS component of the magnetic field, as long as the local magnetic vector field has an angle relative to the solar radial direction ( $\vartheta_B$ ) less than the critical “van Vleck” angle, at which point the azimuth becomes perpendicular to the POS field. This occurs because the atomic alignment upon which the linear polarization depends goes through zero (and changes sign) when  $3cos^2(\vartheta_B) = 1$ , i.e., when  $\vartheta_B = 54.74^\circ$  (van Vleck, 1925). The location of van Vleck nulls in linear polarization  $L = \sqrt(Q^2 + U^2)$  thus also acts as a diagnostic of magnetic field direction (see Section 5.1 for further discussion).

**Figures 6A,C,E,G** shows  $I$ ,  $V/I$ ,  $Az$  and  $L/I$  calculated from the MAS coronal model. From this it is clear that, despite the line-of-sight superposition of optically-thin coronal plasma, Stokes polarimetry can provide a quantitative measure of coronal magnetic field strength and direction. The Stokes  $V/I$  (**Figure 6C**) represents a line-of-sight intensity-weighted average of  $B_{los}$ . The dark linear-polarization features shown in **Figure 6E** are generally signatures of magnetic fields oriented at the van Vleck angle (although note that the presence of strong  $B_{los}$  field can also result in linear polarization nulls; see Section 5.1 for further discussion). Even with LOS integration, the linear polarization vectors (blue) are largely aligned with the POS magnetic field vectors (red) (see **Figures 6A,E**), except when at the van Vleck angle they flip 90°. **Figure 6G** also illustrates this sensitivity to POS magnetic field direction, showing magnitude of departure from radial-orientation in  $Az$  (red = counterclockwise, blue = clockwise). The coronal hole in the south/southwest is evident as a broad blue/red interface in  $Az$ , indicative of diverging magnetic fields, while closed field structures exhibit a red-black-blue interface (e.g., south/southeast) which indicates converging fields.

Strongly nonradial azimuths (represented as green in the local-vertical reference frame of **Figure 6G**) are rare. They can occur if the local magnetic vector  $> 54.74^\circ$  as measured from the solar radial direction but the POS projection is close to radial, as in the case of magnetic fields that are oriented largely along the LOS. In order for such a nearly-perpendicular azimuth to survive LOS integration, either the plasma must be localized to a magnetic structure oriented in this manner, or a larger-scale magnetic structure must possess a symmetry along the LOS. Such symmetries are fairly common in large-scale POS-oriented fields extended along the LOS, e.g., arcade fields or coronal holes, and because such structures are POS-oriented, they possess a strong linear-polarization signal and so the azimuth survives LOS integration (see further discussion in Section 5.1). Even if LOS-oriented fields are localized or exist with orientation extended along the LOS, however, because they do not possess a strong linear polarization signal they are likely to be obscured by any POS-oriented fields lying along their integration path.

**Figures 6B,D,F,H** shows the polarization for a potential field model extrapolation for the same day and using similar (although not identical) photospheric magnetic boundary data as the MAS model of **Figures 6A,C,E,G**. The differences between MAS and



PFSS predictions for circular and linear polarization result from differences at the lower boundary, from the non-potentiality of the MAS model magnetic field, and also to some degree from differences in intensity-weighting along the line of sight (the PFSS solution requires a density/temperature distribution that is spherically-symmetric). The significance of intensity weighting is also evident in **Figure 7**, where the LOS-integrated Stokes V differs depending on the wavelength used to observe it (visible, IR, radio). Since the same (MAS) model is used for all four forward calculations, variation must be due to the different sensitivities to temperature and density for the four wavelength regimes, which in turn means that different distributions of plasma are contributing to the integrals along the line of sight. In Section 5 we will discuss the importance of making full use of such multiwavelength magnetic dependencies in choosing between models.

### 3.5. Doppler Shift

If light-emitting plasma is moving, spectral lines are subject to a Doppler shift proportional to the line-of-sight component of the plasma velocity ( $v_{los}$ ). For optically-thin plasma, this  $v_{los}$  is further weighted by the distribution of intensity along the line of sight. From the line profiles in the visible and IR generated by CLE (see Section 3.4), FORWARD determines Doppler shift and integrates

along the line of sight to get a synthetic observable comparable to observations.

Doppler velocity observations in the IR by the MLSO/CoMP telescope have proved to be a good resource for measuring ubiquitous waves in the corona (Tomczyk et al., 2007). The phase speeds of these waves are expected to be proportional to the plane-of-sky component of the magnetic field strength, and the direction of propagation of the waves will be aligned with the magnetic field direction. In general, the flux-freezing condition forces plasma flows to follow the direction of the magnetic field, so bulk velocity flows also can act as a probe of magnetic structure (**Figure 10C**; Bąk-Stęślicka et al., 2013, also Bąk-Stęślicka et al., submitted).

### 3.6. Radio Emission: Thermal Bremsstrahlung and Gyroresonance

The two thermal emission mechanisms that dominate non-flaring solar radio emission are bremsstrahlung (also known as “free–free emission”) and gyroresonance emission. Bremsstrahlung is produced by all plasma in the solar atmosphere and is strongest in dense regions, while gyroresonance emission requires strong magnetic fields in the corona and is usually confined to locations above sunspots. The Jansky Very Large Array, the Expanded Owens Valley Solar Array, the

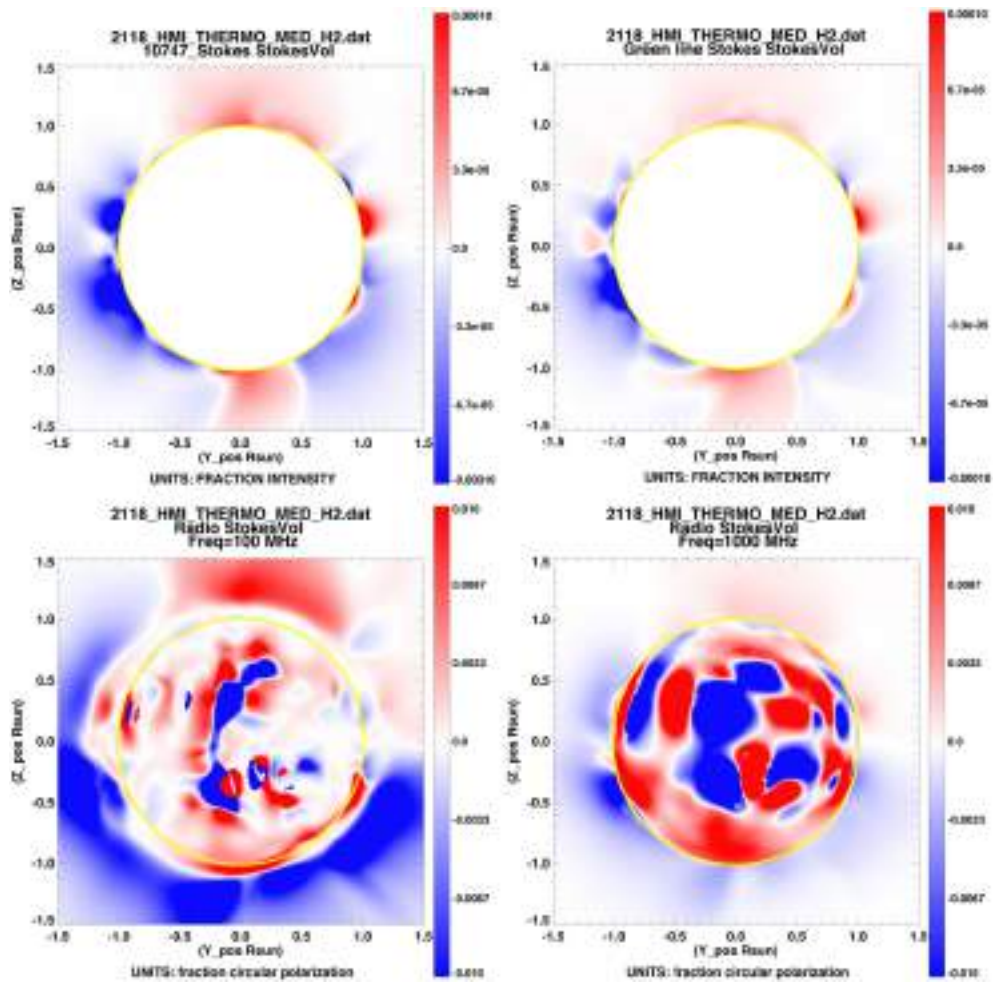


**FIGURE 7 |** Because of different dependencies on plasma along the line of sight, the representation of integrated circular polarization (dependent upon line-of-sight magnetic field strength) appears differently at different wavelengths. (Top left) MAS model  $V/I$  for Fe XIII 1074.7. Plot obtained as in **Figure 6**, with additional keywords `imin=-0.00001`, `imax=0.00001`. (Top right) Same for Fe XIV green line. Plot obtained by following the process outlined in **Figure 6**, but substituting `/greencomp` for `/comp`. (Bottom left) Same for radio bremsstrahlung, at a frequency of 100 MHz. Plot obtained as in **Figure 6**, but with `/radio` instead of `/comp` and `frequency_MHz=100`, `imin=-0.001`, `imax=0.001`. (Bottom right) Same, but substituting `frequency_MHz=1000`. Unlike the visible and IR lines, radio frequencies can be observed above the solar disk as well as at the limb.

Nobeyama Radioheliograph and the Mingantu Ultrawide Spectral Radioheliograph are examples of radio telescopes capable of high-resolution, high-dynamic-range imaging, including circular polarization imaging, in the frequency range (1–20 GHz) where these two mechanisms are important diagnostics of the magnetic field in the solar atmosphere.

Optical depths are generally significant in the solar atmosphere at radio wavelengths and in order to calculate the radio emission arising from either of these physical processes one must carry out a radiative transfer calculation (as for continuum absorption in Section 3.3). It is convenient to do the calculation in terms of brightness temperature,  $T_B$ , because radio emission takes place in the Rayleigh–Jeans limit where the effective radiative temperature of an optically thick source is the physical temperature of that source. Brightness temperature may be converted to flux density  $S$  via the relation

$$S = k_B \frac{f^2}{c^2} \int T_B d\Omega \quad (3)$$

where  $k_B$  is Boltzmann's constant,  $c$  is the speed of light and the integral is over the solid angle  $\Omega$  of interest. Note that brightness temperature is a local quantity whereas flux density is integrated over a source area.

The radiative transfer calculation for radio emission in FORWARD follows standard methods: the brightness temperature transfer is governed by the differential equation (e.g., Dulk, 1985):

$$\frac{dT_B}{ds} = \kappa (T_e - T_B) \quad (4)$$

where  $\kappa$  is the opacity per unit distance  $s$  along the line of sight and  $T_e$  is the local electron temperature. We solve radiative

transfer by determining  $\kappa$  and  $T_e$  in each pixel along the line of sight and integrate Equation 4 across each pixel as follows:

$$T_B' = T_B e^{-d\tau} + T_e (1 - e^{-d\tau}) \quad (5)$$

where  $T_B$  is the incident brightness temperature, and  $T_B'$  is the emergent brightness temperature—integrated across the line-of-sight pixel and serving as the incident brightness temperature to the next pixel.  $d\tau = \kappa ds$  is the opacity change across the pixel.

Radio emission from the solar atmosphere is strongly influenced by the magnetic field in the emitting regions and provides valuable diagnostics of solar magnetic fields that complement other techniques. The magnetic field plays a role in the absorption coefficients  $\kappa$ : electrons interact more strongly with the sense of circular polarization that matches the sense of rotation of an electron as it spirals along magnetic field lines under Larmor motion. The polarization that interacts more strongly with electrons is the *extraordinary* or *x* mode, with the other polarization being labeled the *ordinary* (*o*) mode. Under most conditions in the solar corona, and following propagation to terrestrial observers, the *x* and *o* modes are 100% circularly polarized with opposite sense of polarization. FORWARD solves the radiative transfer equations as described above for each of the circular polarizations separately. The difference between the *x* and *o* modes is then Stokes V (modulo a sign), while the sum is the total intensity, Stokes I (For radio emission from the solar atmosphere, we may ignore any weak linear polarization present due to the fact that the large Faraday rotation in the solar atmosphere wipes out linear polarization over a finite observing bandwidth, see below).

For thermal bremsstrahlung, which is always included in a FORWARD radio emission calculation, opacity results from collisions between electrons and ions. We use the simple expression (Dulk, 1985; Gelfreikh, 2004)

$$\kappa = 0.2 \frac{n_e^2}{T_e^{1.5} (f \pm f_B |\cos \theta|)^2} \quad (6)$$

which is appropriate for coronal temperatures, where  $f_B = 2.8 \times 10^6 B_{\text{gauss}} \text{ Hz}$  is the electron gyrofrequency and the factor in parentheses deals with polarization (with the assumption that  $f \gg f_B$ ):  $\theta$  is the angle between the magnetic field direction and the line of sight, and the minus sign refers to the *x* mode while the plus sign refers to the *o* mode. Thus, the magnetic field information present in bremsstrahlung emission resides in the circular polarization and represents the line-of-sight component of  $B$ .

The dependencies in Equation 6 mean that bremsstrahlung is strongly favored in dense regions of the atmosphere and weighted toward cooler material (since in Equation 4,  $\kappa T_e \propto T_e^{-0.5}$ , e.g., White, 2000). The  $f^{-2}$  dependence of bremsstrahlung opacity also means that optical depth decreases rapidly as frequency increases, and at low frequencies one is likely to be optically thick such that the lower the frequency, the higher in the atmosphere one sees. This is evident in Figure 8, where polarization extends much higher above the photosphere at 100 MHz (lower left panel) than at 1000 MHz (lower right panel). When optically thick,

the circular polarization produced by bremsstrahlung emission actually depends on the presence of a temperature gradient. If one has well-calibrated brightness temperature measurements across a continuous frequency range, one can in fact determine both the temperature gradient and the magnetic field from the data (Grebinskij et al., 2000, disproving a comment in White, 2000). In Figure 7 the lower degrees of polarization over much of the disk at 100 MHz reflect the fact that the temperature gradient is weaker higher in the corona.

The gyroresonance calculation is more complex. Gyroresonance opacity results from the acceleration of electrons in a magnetic field under the Lorentz force, and is only significant in narrow layers where the observing frequency  $f$  is a low integer multiple  $s$  of the electron gyrofrequency  $f_B$  (e.g., White and Kundu, 1997). The optical depth  $\tau$  of a thermal gyroresonance layer (the absorption coefficient integrated through the layer) is

$$\tau_{x,o}(s, f, \theta) \propto \frac{n_e L_B(\theta)}{f} \frac{s^2}{s!} \left( \frac{s^2 \sin^2 \theta}{2\mu} \right)^{s-1} F_{x,o}(\theta) \quad (7)$$

where  $L_B(\theta)$  is the scale length of the magnetic field ( $B/\partial l$ ) evaluated along the line of sight and  $\mu = m_e c^2/k_B T_e$ . For coronal conditions  $\mu \approx 2000$ , and the  $\mu^{-s}$  dependence in Equation 7 produces a dramatic change in opacity as harmonic number  $s$  changes.  $F_{x,o}(\theta)$  is a function of angle which is of order unity for the *x* mode near  $\theta = 90^\circ$ , but decreases sharply at smaller  $\theta$ , and is smaller in the *o* mode than in the *x* mode. FORWARD uses a more exact approximation for  $\tau_{x,o}$  due to Robinson and Melrose (1984) which requires a careful calculation of the cold plasma properties of the electromagnetic modes under the conditions that apply in the gyroresonance layer. FORWARD incorporates gyroresonance emission by testing for harmonic layer crossings along the line of sight in the range  $s = 1$  to 5, and calculating the resulting opacity as shown above: significant gyroresonance opacity at higher harmonics generally requires mildly relativistic electrons which puts emission in the gyrosynchrotron limit in which harmonics are much broader and Equation 7 is no longer valid [Note the simulation package *GX\_Simulator* can handle gyrosynchrotron emission (Nita et al., 2015)].

Gyroresonance emission is most commonly seen in the strong magnetic fields above solar active regions. At frequencies above a few GHz, bremsstrahlung does not produce enough opacity to make the corona optically thick, while the large change in gyroresonance opacity as  $s$  decreases (typically a factor of order 1000) means that a given harmonic layer is usually either very optically thick or very optically thin. When optically thick, gyroresonance produces million-K coronal brightness temperature features in radio images. In practice, we see down to the highest optically thick layer (usually  $s = 3$  in *x* mode and  $s = 2$  in *o* mode), and the brightness temperature variations across the surface (of constant field strength for a given frequency) represent actual temperature variations across that surface. Thus, for this mechanism the magnetic field information contained in the emission morphology is somewhat complex and does not simply reside in the polarization (White and Kundu, 1997).

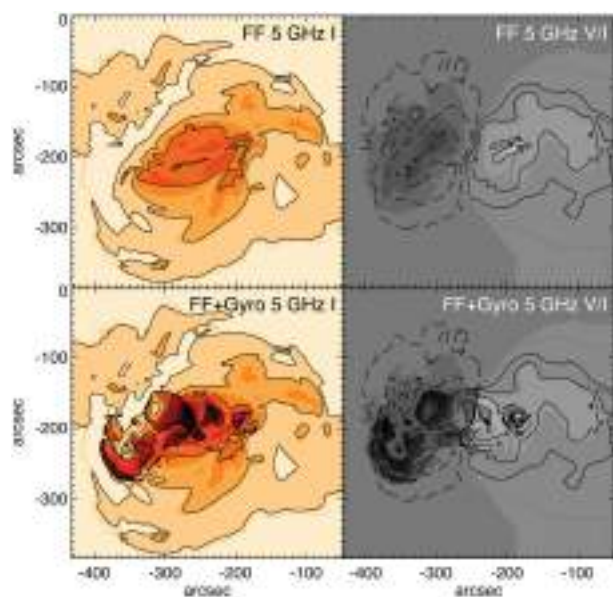


**FIGURE 8 | Radio emission from a model active region comparing calculations with and without gyroresonance emission.** Thermal bremsstrahlung or free-free emission ("FF") is included in both cases. Total intensity (Stokes  $I$ ) is plotted in the left panels and degree of polarization ( $V/I$ , scaled from  $-1$  to  $1$ ) is plotted in the grayscale in the right panels, with contours showing Stokes  $V$ . The brightness temperature display range in the left-hand panels is  $0$  to  $2.5 \times 10^6$  K. Contour levels are at  $16, 32, 64, 128$ , and  $256 \times 10^4$  K in the Stokes  $I$  panels, and  $1, 4, 16$ , and  $64 \times 10^4$  K in the  $V/I$  images. The pixel size is  $1.5$  arcsec.

Internally, FORWARD carries out radiative transfer for radio emission in the  $x$  and  $o$  modes by summing the requested absorption coefficients in each pixel: bremsstrahlung is the default opacity and gyroresonance opacity may be turned on or off. The brightness temperatures in the two modes are summed and differenced to report Stokes  $I$  and  $V$ , or one can display  $V/I$ , the degree of circular polarization, as in Figures 7, 8. Mode coupling between the  $x$  and  $o$  modes, which can result in reversal in the sense of circular polarization at points where the magnetic field direction along the line of sight reverses (e.g., White et al., 1992), is not yet included in the FORWARD calculation but will be in future releases. Figure 8 shows an example of a FORWARD radio emission calculation using a three-dimensional hydrodynamic active region model (density, vector magnetic field and temperature) with thermal conduction and radiative cooling (Lionello et al., 2013). The upper panels show the model radio emission obtained with just bremsstrahlung opacity included, while the lower panels include gyroresonance opacity. The brightness temperatures are much higher when gyroresonance opacity is included, and the polarization structure becomes more complex.

FORWARD does not currently include plasma emission: this is the dominant emission in low-frequency solar radio bursts (e.g., Kundu, 1965), but it is a coherent emission mechanism and there is no simple way to calculate it (e.g., see Schmidt and Cairns, 2012a,b, for a detailed calculation). In addition, fundamental plasma emission occurs at frequencies where the

refractive index may be significantly different from unity and refraction can play a major role in determining ray paths. FORWARD assumes linear ray paths along lines of sight and does not currently handle refraction at low radio frequencies which will produce curved ray paths in a realistic solar atmosphere.

### 3.7. Faraday Rotation

In general radio emission can be elliptically polarized. Electromagnetic radiation in a magnetized plasma can be decomposed into two natural modes with orthogonal polarizations, and as radiation propagates the two intrinsic polarizations have different refractive indices and slightly different phase speeds. This effect causes the plane of linear polarization to rotate, with the amount of rotation being a function of frequency. In the lower regions of the solar atmosphere the rotation is so large that, as mentioned in the previous subsection, when averaged across a finite observing bandwidth the linear polarization is washed out. However, further out in the solar wind where the magnetic field is lower, Faraday rotation can be measured as a function of frequency, and such measurements are one of the few techniques that can be used as a remote probe of the magnetic field in the solar wind. This technique has been applied to both communication transmissions from satellites (e.g., Bird et al., 1985; Jensen et al., 2005, 2013) as well as polarized background cosmic sources (e.g., Bird et al., 1980; Mancuso and Spangler, 2000; Ord et al., 2007; You et al., 2012; Kooi et al., 2014). In FORWARD it can be used to simulate the contributions of CME and solar wind plasma to an observable diagnostic of the magnetic field.

The expression for Faraday rotation is relatively straightforward: the angle of rotation  $FR$  (in radians) at wavelength  $\lambda$  is

$$FR = RM \lambda^2 \quad (8)$$

where the rotation measure  $RM$  (measured in radians per square meter) is the wavelength-independent measure of Faraday rotation, calculated from the integral of the product of electron density and line-of-sight magnetic field along the ray path:

$$RM = 2.6 \times 10^{-13} \int n_e B \cos \theta ds \text{ (rad m}^{-2}\text{)} \quad (9)$$

with  $B$  measured in Gauss and electron density in  $\text{cm}^{-3}$ . FORWARD carries out this integral and will report either  $FR$  at a specific frequency or  $RM$ .

A related and useful quantity that is obtained in conjunction with Faraday rotation measurements of pulsars is dispersion measure,

$$DM = \int n_e ds \quad (10)$$

which in radio astronomy is usually measured in units of  $\text{cm}^{-3}$  parsecs. The dispersion measure is used to remove the frequency-dependent delay of pulsar pulses introduced by the variation of refractive index in the interstellar and interplanetary media with

frequency, so that pulses can be aligned across the full observing bandwidth, a necessary step in measuring the rotation of the plane of polarization vs. frequency. FORWARD provides the same quantity but referred to as a column density (accessed via keyword `/colden` or in the Physical Diagnostics drop-down menu of the widget, in units of  $\text{cm}^{-2}$ ). Variations in  $DM$  on timescales of tens of minutes to hours are dominated by density variations in the solar wind, and knowledge of  $DM$  is valuable when trying to assess the relative roles of density and magnetic field in observed  $RM$  variability.

## 4. OBSERVATIONS

As described above in Section 3 and summarized in **Table 1**, multiple physical processes operating in the corona have sensitivities to the coronal magnetic field and manifest observable signatures from radio to soft-Xray emission. There is thus clear value in obtaining observations at a broad range of wavelengths for intercomparison and use in constraining and defining models.

To facilitate model-data comparisons, FORWARD enables the access and manipulation of observations in a form designed to match the output of forward calculations. To this end, FORWARD extracts SolarSoft IDL maps from FITS-format observational data files, and preserves these along with associated structures in a standard format. Observational data are accessed either “by date” or “by file”—via keywords if using the command-line version of FORWARD, or a calendar/directory search if

using the widget interface (see **Figure 9**). Note that FORWARD looks first in a user-defined working directory for existing FORWARD-formatted maps or fits files before downloading or processing new files.

Since the focus of this paper is magnetometry, we first describe how FORWARD enables access and manipulation of Stokes polarimetric data. The Mauna Loa Solar Observatory (MLSO) Coronal Multi-channel Polarimeter (CoMP) on Hawaii (Tomczyk et al., 2008) is a 20-cm aperture coronagraph with a full field of view of the corona from 1.05 to 1.38 solar radii. It utilizes a narrow-band imaging polarimeter to observe the Fe XIII coronal line at 1074.7 and 1079.8 nm and the chromospheric HeI line at 1083 nm. Data products currently served include intensity, Doppler velocity, line width, and Stokes linear polarization [ $Q$ ,  $U$  as well as  $L = (Q^2 + U^2)^{\frac{1}{2}}$  and  $Az = 0.5 * \text{atan}(\frac{U}{Q})$ ]. CoMP linear polarization is currently the only direct magnetic diagnostic of the corona publicly available on a near-daily basis (subject to weather, etc.). These data are available online, beginning from May 2011, and can be downloaded in FITS or image format via the MLSO web pages (<http://www2.hao.ucar.edu/mlso>).

FORWARD offers another means of downloading CoMP data, and moreover acts as a tool for its display and analysis (see Gibson, 2015b for further details). **Figures 10B,D** illustrate FORWARD linear polarization output given a specified calendar date and field of view. In this case, CoMP standard “Quick Invert” data file for that date is automatically accessed, which represents an averaged image and may not include all CoMP data products.

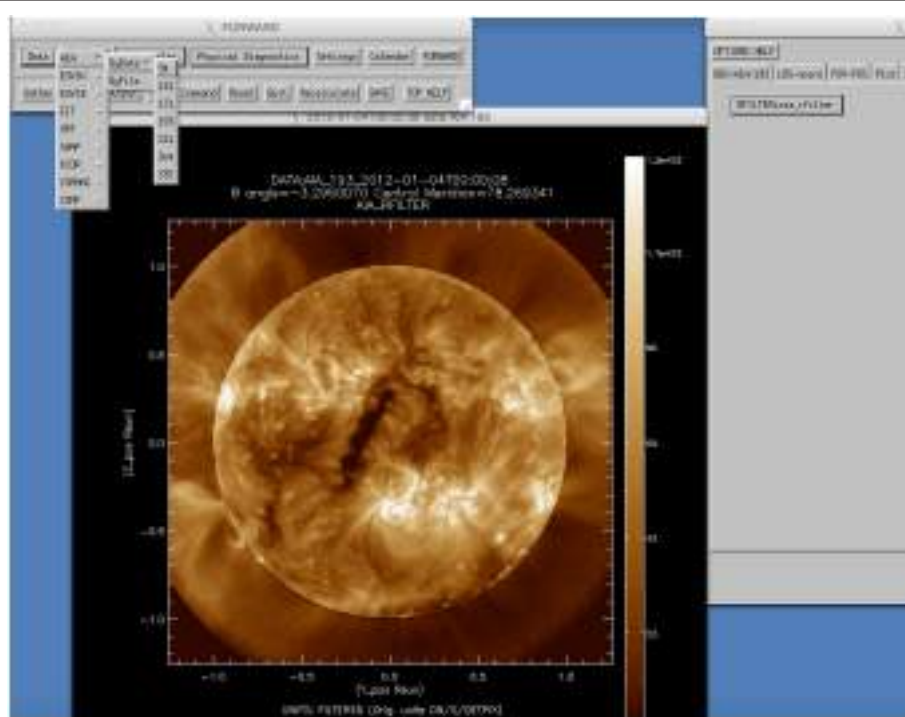


**FIGURE 9 | Example of automatically uploading SDO/AIA data via FORWARD widget by date access.** Data are accessed via either the Virtual Solar Observatory SolarSoft interface, or an observatory's own web interface. Data may also be uploaded by file from locally stored FITS files, and in some cases (e.g., the CorMag telescope—Fineschi et al., in preparation), this is currently the only available choice.

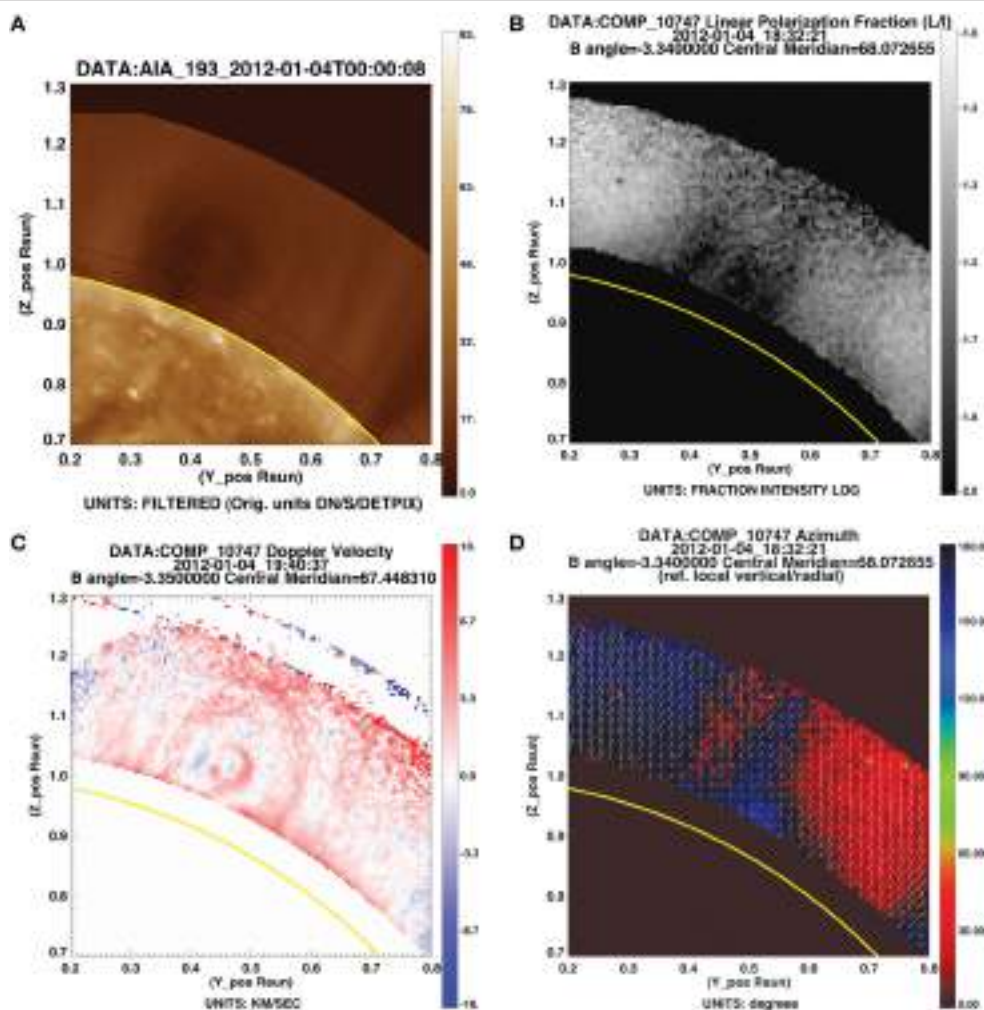


**FIGURE 10 | Example of FORWARD-displayed data products for a coronal cavity.** **(A)** SDO/AIA 193 Angstrom. Plot obtained via widget as described in the text, or through IDL line command `for_plotfits, date='2012-01-04', /aia, xxmin=-.2, xxmax=.8, yymin=.7, yymax=1.3, occult=-1.05, up occult=1.29`. **(B)** CoMP fraction of linearly-polarized light  $L/I$ . Plot obtained via widget and utilizing `moreplots` option as described in the text, or command as in **(A)** substituting `/comp` for `/aia`, removing `occult` and `up occult` keywords, and adding `line='LoI', imin=-2., imax=-1.` **(C)** CoMP Doppler velocity (partially corrected for solar rotation Tian et al., 2013). Plot displays data from CoMP Dynamics fits file downloaded from MLSO web page (<http://www2.hao.ucar.edu/mlso>), through widget “By File” option or command as in **(A)** substituting `/comp`, removing `date` and `occult`, `up occult` keywords, and adding `filename='20120104.194037.comp.1074.dynamics.3.fts', line='DOPPLERVLOS'.` **(D)** CoMP linear polarization azimuth. Plot obtained by widget or command line as in **(A)**, but substituting `/comp`, and adding `line='Az'.`

Comprehensive, non-averaged data are available in the “Daily Dynamics” and “Daily Polarization” FITS archives on the MLSO web pages, and once these are downloaded to a local directory they may be displayed “by file” using FORWARD. This has been done to show the CoMP Doppler velocity image of **Figure 10C**. White light data from the MLSO K-coronagraph (KCOR) can similarly be downloaded and displayed through the FORWARD widget tools.

A range of extreme ultraviolet (EUV) and soft X-ray (SXR) imager data is available through the Virtual Solar Observatory (VSO; Hill et al., 2009) and accessed by FORWARD. These include data from the currently operating Solar Dynamics Observatory Atmospheric Imaging Assembly (SDO/AIA) and Hinode X-ray Telescope (XRT), along with prior data from the

Solar and Heliospheric Observatory Extreme ultraviolet Imaging Telescope (SOHO/EIT) and Transition Region and Coronal Explorer (TRACE), which provide observations at wavelengths spanning coronal and transition region temperatures. Data from the ProbA-2 “Sun Watcher using APS and Image Processing” (SWAP) EUV imager (Halain et al., 2013; Seaton et al., 2013) provide an extended (54 arcminute) field of view (FOV), and the Solar-Terrestrial Relations Observatory Extreme Ultraviolet Imagers (STEREO/EUVIA and EUVIB) provide additional viewing options for EUV coronal structures.

It is particularly simple to intercompare observations using the widget interface. For example, AIA data may be loaded by date as in **Figure 9**, and then a particular structure such as the cavity shown in **Figure 10A** may be zoomed in on using the field

of view (FOV-POS) tab of the right-hand widget. By switching on the keyword `moreplots` (located in the Output tab of the top-left widget), the zoomed-in FOV is retained and closest date/time sought in subsequent loading of CoMP data (b-d). This capability extends to forward-modeled synthetic data: if the `moreplots` option is turned on and followed by choice of a model and a click on the FORWARD button (top left widget), the field of view, viewer's position, and observable (instrument and line) are all preserved in subsequent forward calculations unless explicitly changed. In this manner, as demonstrated by Figures 11, 12 and discussed in the next section, model predictions may be directly compared to observations.

## 5. MULTIWAVELENGTH MAGNETOMETRY

Having described how FORWARD incorporates the three essential components of physical state, physical process, and observation, we now discuss how it may be used to further

multiwavelength magnetometry. FORWARD can be applied to validating models, to building intuition into how magnetic fields manifest in observations, to forward-fitting models to data, and ultimately, to developing coronal magnetic inversion methods that take full advantage of multiwavelength observations.

### 5.1. Comparing Models and Data

Figure 11 shows the CoMP observations for the day profiled in most of the Figures so far, allowing validation of the predictions of the MAS model. Inspection shows that while some regions match very well, others do not. For example, Figure 12 illustrates that for the southeast quadrant, the open region of diverging field (just below the equator) is well-captured by the model. Some of the details south of this are not captured, but the red-black-blue interface characteristic of a large-scale closed structure is reproduced. In contrast, the northwest quadrant shows considerably more structure in linear polarization observations (Figure 11A) than in the model (Figure 11C). Figure 10 further

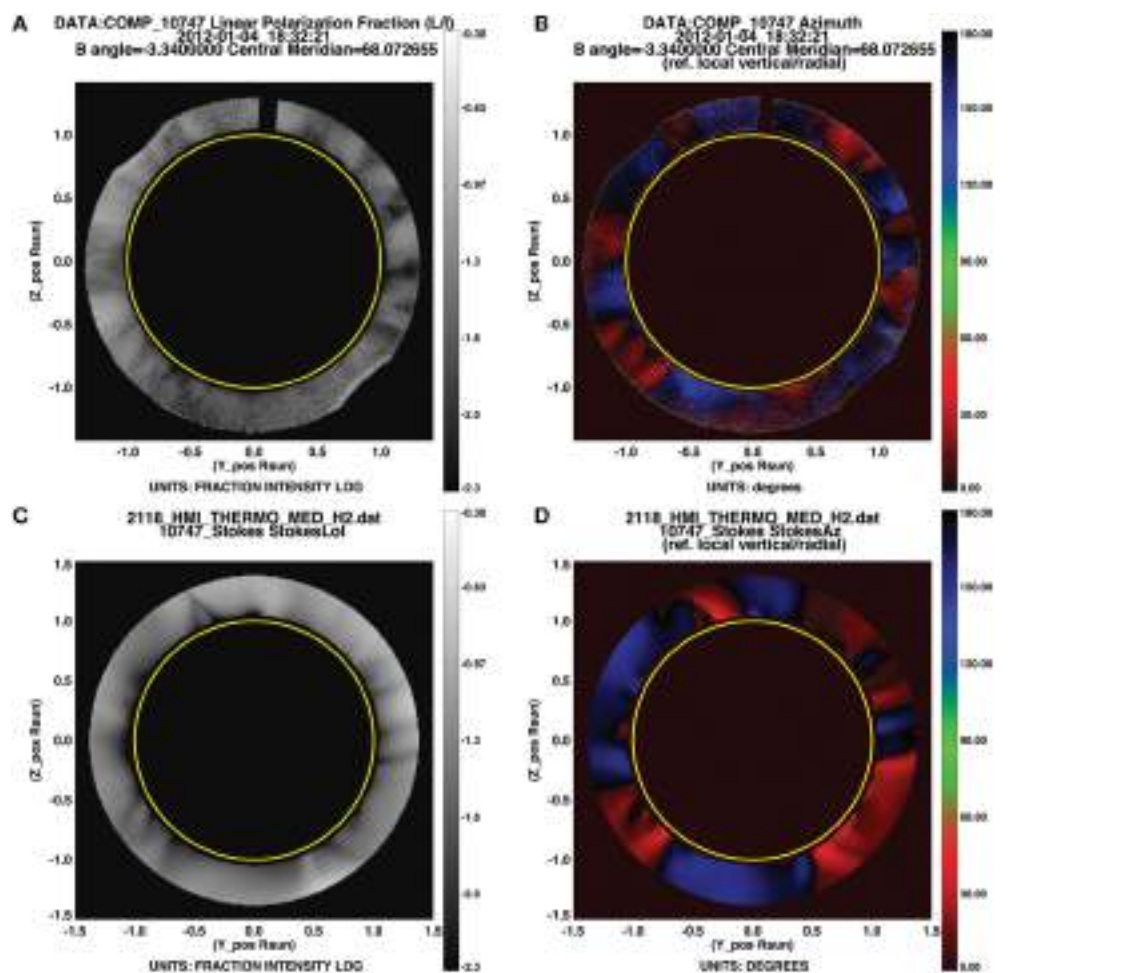


**FIGURE 11 | Linear polarization: observations vs. model. (A,B)** Fraction and direction of linear polarization. Plots obtained from widget or IDL line commands as in Figures 10B,D, but without the `xxmin`, `xxmax` keywords set. **(C,D)** Same from forward calculation of MAS model. Plots obtained as in Figures 6E,G, with addition of keywords `occult=1.05`, `upocult=1.29`. Alternatively, **(C,D)** may be obtained by loading **(A,B)** from the widget, choosing the PSIMAS model from the drop-down menu, and clicking FORWARD.

magnifies the data in this region, and demonstrates that the northern-most of these linear polarization structures is associated with a coronal cavity. The difference between model and data in this region likely arises because, although the MAS simulation we have shown is non-potential, it does not capture all coronal currents. In particular, currents that slowly build up over time are not reproduced. Such a buildup of currents is expected in polar crown regions (Yeates and Mackay, 2012), and is thus likely in the region of the cavity of **Figure 10**.

The linear polarization observations of the CoMP telescope represent a unique observational resource, and one that has benefited greatly from the intuition built via forward modeling. In advance of CoMP's synoptic operation at MLSO, the CLE code was used to demonstrate that the presence of currents in the corona should be observable in Fe XIII linear polarization (Judge et al., 2006). Indeed, this has proved the case, and comparisons of CoMP data to FORWARD-generated images have shown linear polarization to be a useful diagnostic of magnetic topologies, including spheromaks (Dove et al., 2011),

pseudostreamers (Rachmeler et al., 2014), and cylindrical flux ropes (Bąk-Stęślicka et al., 2013; Rachmeler et al., 2013). The CoMP linear polarization structure shown in **Figure 10B** is an example of a "lagomorph" (named for its rabbit's-head shape). Bąk-Stęślicka et al. (2013, 2014) studied dozens of examples of CoMP lagomorphs, and showed clear correlation with the size and location of associated EUV prominence cavities (e.g., **Figure 10A** vs. **Figure 10B**). The authors also used forward modeling to demonstrate that a magnetic flux rope model results in a lagomorph: the van Vleck angles within the outer portions of the flux rope and the overlying arcade creates a dark structure framing the rabbit's ears and the sides of its head, and sheared or twisted fields at the flux rope's axis, being oriented perpendicular to the plane of sky, are also relatively dark in linear polarization and form the center of the head.

The presence of a wide V shape is expected even for a potential field arcade. Using an analytic model of a flux rope included in FORWARD (Low and Hundhausen, 1995), **Figure 13** shows how the addition of coronal currents above the magnetic neutral

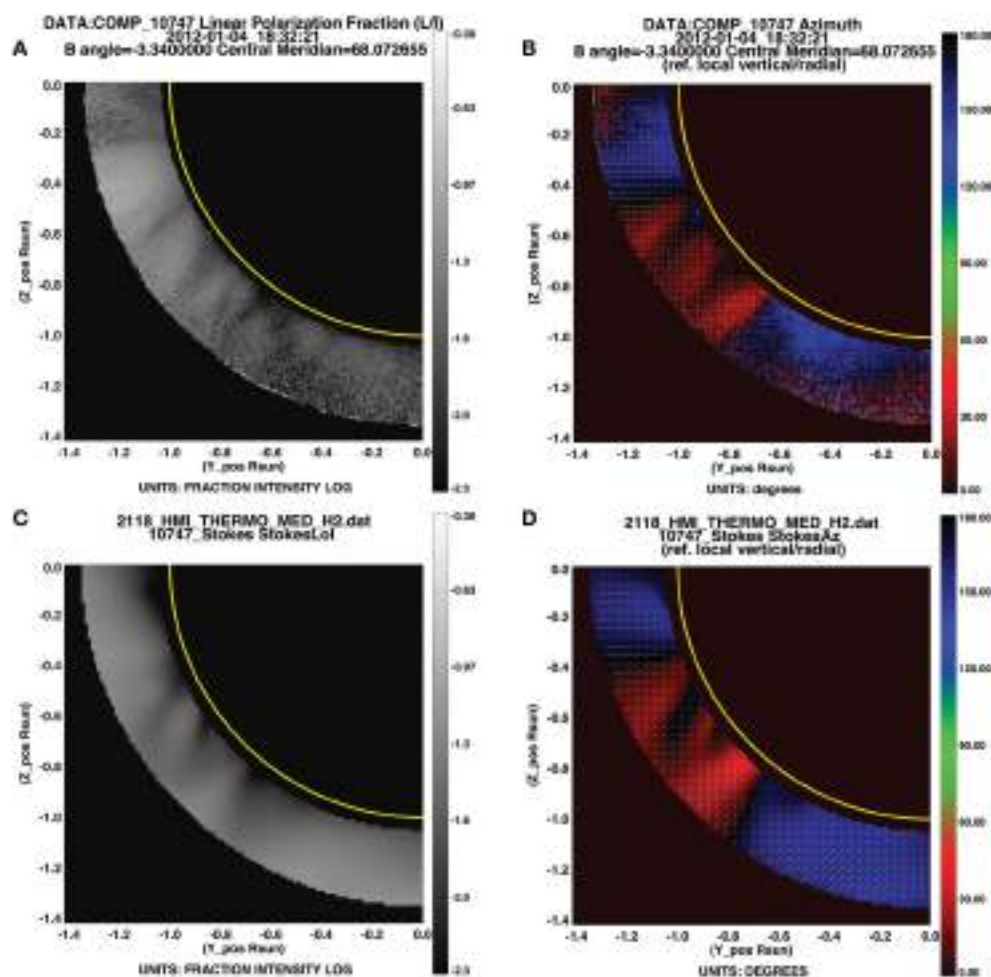


**FIGURE 12 |** Linear polarization: observations vs. model (A–D) as in Figure 11, but zoomed in to southeast quadrant (keywords set: `xxmax=0.`, `yymax=0.`).

line narrows this V and introduces a dark central structure. The bottom row of **Figure 13** may be compared to **Figure 10**, noting that the top of the cavity/flux rope is near the top of the CoMP field of view, so that the ears are not captured in this case.

As we have discussed above, there are a range of multiwavelength observations that can be used to constrain coronal magnetic fields. Indeed, coronal-cavity white light and emission observations have been interpreted as largely independent indicators of a flux-rope magnetic structure (see

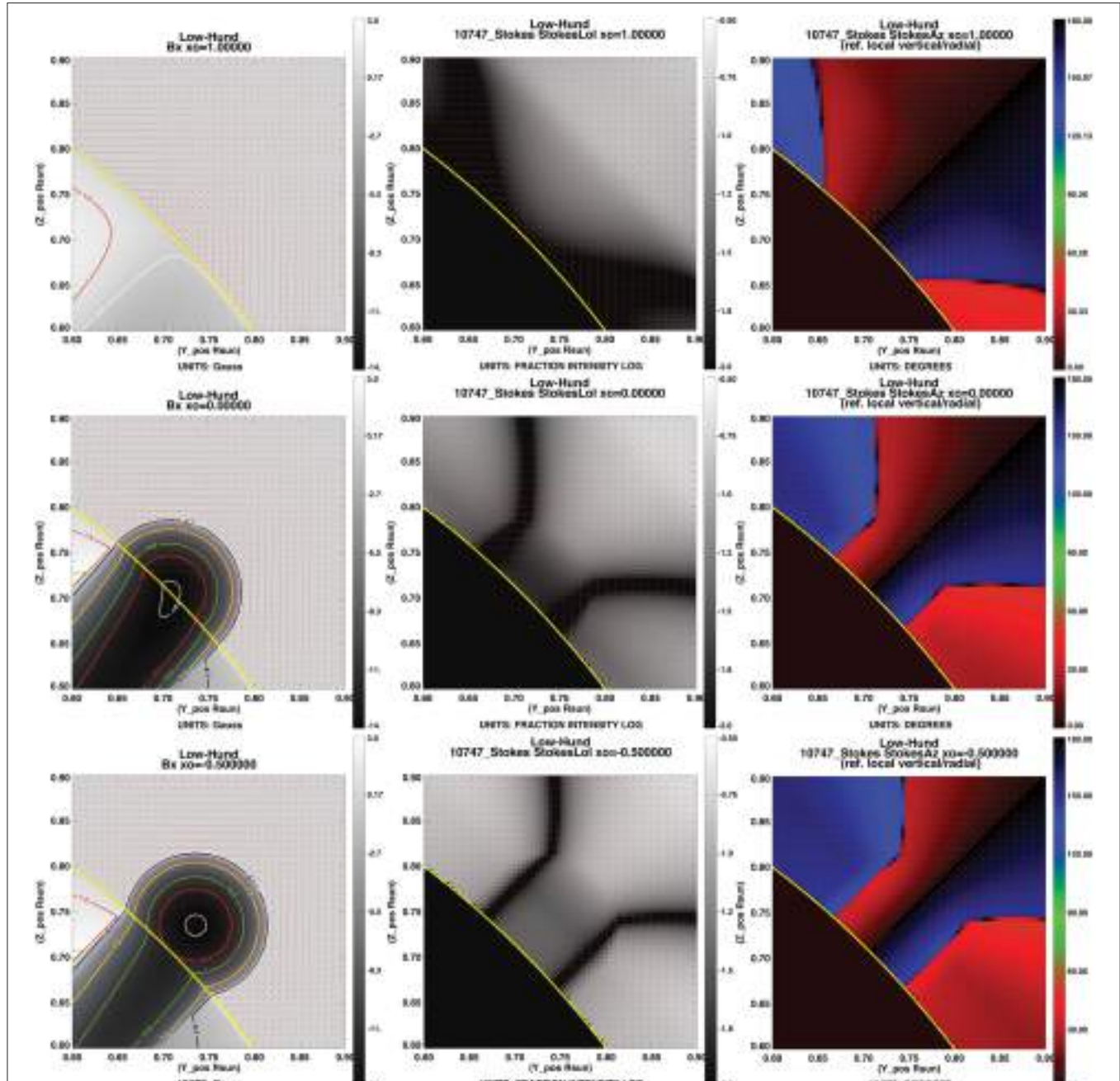


**FIGURE 13 |** Using an analytic flux-rope model (Low and Hundhausen, 1995), we see that the presence of currents above the underlying neutral line narrows the ears and introduces the dark central head structure to a linear polarization lagomorph. Left column: LOS-oriented magnetic field strength. Plots obtained through commands `for_drive,'lwhund',line='bx',thetao=45.,x_oinput=xo,xxmin=0.6,xxmax=0.9,yymin=0.6,ymax=0.9,/fieldlines,imin=-14,imax=3` for values of  $x_0 = 1.0, 0., -0.5$ . Middle column: LOS-integrated linear polarization fraction. Plots obtained from same commands, substituting `line='LoI',imax=-.5,imin=-2.` and adding keyword `/comp`. Right column: LOS-integrated linear polarization direction (azimuth). Plots obtained as for  $L/I$ , but substituting `line='Az'`.

discussion in Gibson, 2014, 2015a; see also Bąk-Stęślicka et al., in preparation for discussion of LOS flows as indications of magnetic-flux-rope topology). Quantification of the three-dimensional morphology, substructure, and plasma properties of cavities have served to justify such interpretations. These quantifications were obtained by fitting the “CAVMORPH” analytic model included within the FORWARD distribution to observations of cavities in white light, EUV, and SXR (Gibson et al., 2010; Schmit and Gibson, 2011; Kucera et al., 2012; Reeves et al., 2012).

Such “forward fitting” goes beyond intuition building, and in fact is a means of inverting observations to quantify properties of the physical state. It does require specification of a parameterized model, such that through iteration best-fit parameters are determined. Dalmasse et al. (in preparation) provides an example

of a statistical method applied to forward fitting a flux-rope model to visible/IR polarimetric data, including both linear and circular polarization (see also Jibben et al., submitted). Other inversion methods applicable to these data are also under development (Kramar et al., 2006, 2013, 2014; Plowman, 2014; also Kramar et al., in preparation).

## 5.2. Synthetic Testbeds and Beyond

The method described in Dalmasse et al. (in preparation) employs synthetic Fe XIII linear polarization data generated using FORWARD. This work represents an area of active development for FORWARD, i.e., the creation of multiwavelength synthetic data for coronal magnetic structures ranging from active regions (e.g., M. Rempel, private communication), to polar crown prominence/cavity systems

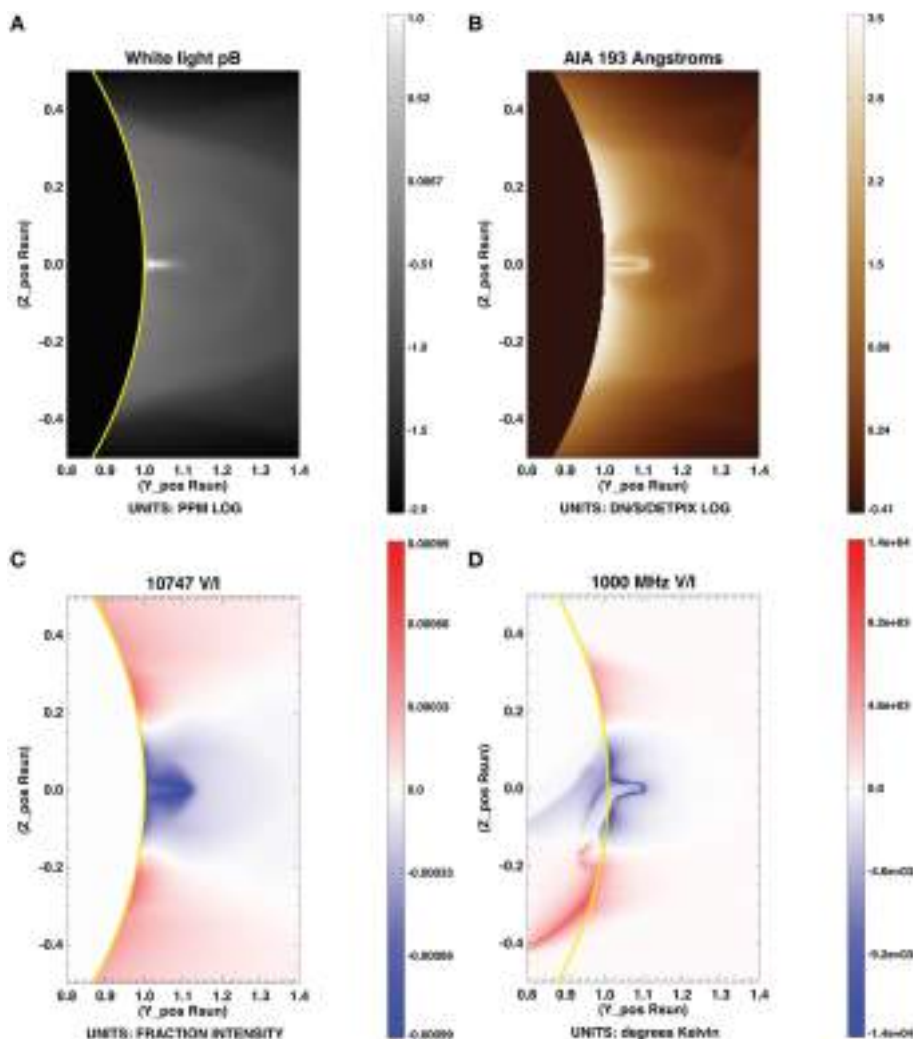


**FIGURE 14 |** Synthetic data including (A) visible and (B) EUV intensity, and (C) IR and (D) radio circular polarization, generated for simulated prominence-cavity system (Fan, personal communication). Plot (A) obtained by FORWARD line command: `for_drive, 'numcube', cubename='$FORWARD_DB/TESTBEDS/fullthermodynamic_erupting_qp_mhd_Fan', xxmin=0.8, xxmax=1.4, yymin=-.5, yymax=.5, units='PPM', cuberot=-25., colortable=0`. Plot (B) obtained with addition of keyword /aia. Plot (C) added with addition of keyword /comp, line='VOI', and (D) with addition of /radio, line='VOI'.

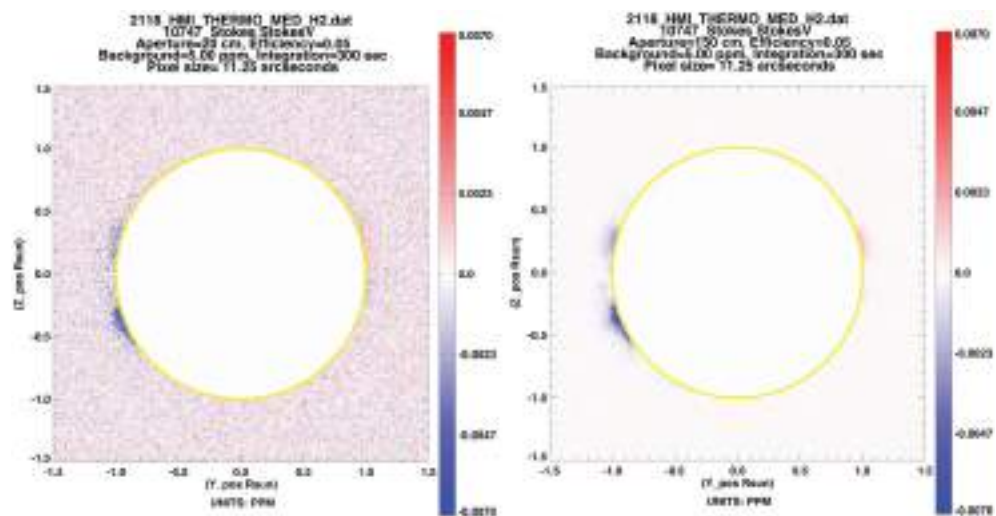


**FIGURE 15 | Stokes V/I for MAS model as in Figure 6C, with the addition of photon noise expected for 5 min integration for a 20 cm (e.g., MLSO/CoMP) vs. a 150 cm (e.g., proposed COSMO) telescope.** Note systematic errors are not included. Plots obtained by (left) for \_drive, readmap='psimas\_10747\_01042012', line='V', /donoise and (right) same, with addition of aperture=150.

(e.g., Fan, personal communication; see **Figure 14**, to a global corona containing a variety of currents, e.g., D. Mackay, private communication). These numerical simulations will be included in future FORWARD SolarSoft distributions, and from them synthetic data ranging from radio to SXR wavelengths can be generated as community testbeds to aid in the development of inversion methods and in analyses of the sensitivity of different types of observations to physical parameters.

The images shown in **Figures 1–14** are idealized. Real data has noise, and inversions must take this into account. Sensitivity, field of view and spatial resolution of the telescope used to obtain the data may all contribute to noise. For polarimetry, sensitivity is usually a constraining factor because (at least at optical, IR and UV wavelengths) the polarized signals are much weaker than the total intensities and subject to cross-talk that requires careful time-consuming calibration to ensure robust measurements. With modern telescopes one is also often trading large fields of view for high spatial resolution, and for the observation of spatially extended features this can be a problem.

At radio wavelengths, one has to deal with the fact that spatial resolution is always frequency dependent: for a fixed effective aperture dimension, the size of a resolution element is inversely proportional to frequency, and for typical modern radio observations taken over a wide frequency range, the spatial resolution can vary by factors of several from high to low frequencies. For the purpose of measuring coronal magnetic fields with gyroresonance emission where field strength is proportional to frequency, this means that one generally has poorer spatial resolution for the study of weak fields than for strong fields. Fortunately this is in the right direction since strong-field regions are usually smaller, but it does limit our ability to study three-dimensional fields with uniform resolution.

At the moment, FORWARD only implements noise for visible/IR spectropolarimetry (Section 3.4), and then only photon

noise (see **Figure 15**). Efforts are underway to allow “instrument personality profiles” in which a loss of resolution appropriate to a particular observation could be overlaid on the forward calculation, given details of a telescope and its observing configuration. This capability would enable the design and use of future large telescopes such as the Daniel K. Inouye Solar Telescope (DKIST), the Frequency Agile Solar Telescope (FASR), and the Coronal Solar Magnetism Observatory (COSMO; e.g., **Figure 15**; see also Lin, 2016).

## 6. CONCLUSIONS

Our primary motivation in developing FORWARD has been to enable multiwavelength coronal magnetometry. The coronal magnetic field lies at the heart of many of the mysteries of solar physics, including coronal heating, solar wind acceleration, and flare and coronal mass ejection onset and evolution. It holds the key to progress in predictive capability for space-weather events: in particular, the direction of the magnetic field at 1 AU depends crucially on the magnetic field at its coronal source, and on the context of this source in both time and space. In this paper we have demonstrated how different physical processes effectively highlight different aspects of the coronal magnetic field, and how these manifest in observations at different wavelengths. Because the photospheric magnetic field is not force-free, our ability to find a meaningful solution to coronal magnetic field through extrapolations from this boundary is limited (De Rosa et al., 2009). We therefore *must* make use of multiwavelength observations of the solar atmosphere to further constrain the global coronal magnetic field.

FORWARD represents a community effort to design and gather a library of codes for the synthesis of multiwavelength coronal data from physical models. Our philosophy has been

to incorporate as many existing resources as possible, and to make use of the comprehensive and ever-growing resources available via SolarSoft IDL. We note complementary capabilities available for forward modeling in radio wavelengths, i.e., the *GX\_Simulator* package referred to above in Section 3.6 (Nita et al., 2015), and for forward modeling coronal waves, i.e., the *FoMo* codes described in van Doorsselaere et al. (2016).

FORWARD continues to be developed. New subroutines for ultraviolet spectropolarimetry in the unsaturated Hanle regime are being tested (Fineschi, 2001; see also Raouafi et al., submitted; Dima et al., submitted). We are also expanding our numerical interface to allow varied-grid models (currently numerical datacubes must be on a regular grid). A future goal will be to add capability for synthesizing heliospheric images, which would complement current capability for Faraday rotation, and enable connections between imaging and *in situ* observations during the era of Solar Probe and Solar Orbiter. The wide variety of multiwavelength data currently and soon to be available, in combination with ongoing efforts to develop comprehensive and efficient inversion methods, makes us confident that ultimately the goal of quantifying the coronal magnetic field will be achieved.

## AUTHOR CONTRIBUTIONS

SG was primary author of this paper, wrote or contributed to most of the subroutines in FORWARD, and is responsible for the oversight of its ongoing development. TK wrote Sections 3.2, 3.3, and contributed to Sections 5, 6. She wrote or otherwise coordinated all FORWARD codes and databases related to EUV/SXR imaging and spectroscopy, and contributed to several other FORWARD subroutines. SW wrote Sections 3.6, 3.7, and contributed to Section 5, 6. He wrote or otherwise coordinated all FORWARD codes related to radio spectropolarimetry. JD was the main author of the integration of CLE into FORWARD, and the initial developer of several of the backbone subroutines of FORWARD as well as the analytic model interface. LR developed the numerical interface and incorporated the PFSS model into FORWARD, and contributed to the data-download interface codes and other FORWARD subroutines. YF contributed to the numerical interface effort, provided an axisymmetric flux rope model to the FORWARD package for demonstration purposes, and is providing numerical simulations for synthetic test-beds as discussed in Section 5. BF was the initial developer of the *for\_widget* interface. CD contributed a subroutine for interfacing with the PSI MAS model and assisted with its

implementation. KR contributed the XRT response subroutine. All authors read and critically revised the paper, approved the final version, and agreed to be accountable for all aspects of the work.

## FUNDING

NCAR is supported by the National Science Foundation. SG acknowledges support from the Air Force Office of Space Research, FA9550-15-1-0030. TK acknowledges support from NASA. LR acknowledges support from the Belgian Federal Science Policy Office (BELSPO) through the ESA-PRODEX program, grant No. 4000103240. KR acknowledges support from contract NNM07AB07C from NASA to SAO.

## ACKNOWLEDGMENTS

We thank Phil Judge and Roberto Casini for their assistance with the utilization and interpretation of the FORTRAN CLE code incorporated within FORWARD, and Roberto Casini for his internal review of this paper. We thank the International Space Science Institute (ISSI) teams on coronal cavities (2008–2010) and coronal magnetism (2013–2014) who were key to initiating and guiding FORWARD development efforts. In particular, we thank Tim Bastian for contributions to the radio codes within FORWARD, and Jeff Kuhn for interesting discussions pertaining to instrument personality profiles (currently under development). We acknowledge Matthias Rempel and Duncan Mackay for contributions of synthetic test-beds for FORWARD. We also acknowledge the Data-Optimized Coronal Field Model (DOC-FM) team and especially Kevin Dalmasse, Silvano Fineschi, Natasha Flyer, Nathaniel Mathews, and Doug Nychka for current engagement in FORWARD development, and Haosheng Lin, Don Schmit, and Chris Bethge for past code contributions. In addition, we acknowledge Enrico Landi for assistance with CHIANTI interfacing, Dominic Zarro for assistance with VSO interfacing, and Sam Freeland for assistance with SolarSoft interfacing. FORWARD makes use of a range of SolarSoft codes developed by others—we are grateful to Marc de Rosa for his PFSS SolarSoft codes, and Andrew Hayes for his routines for the F corona. We acknowledge Leonard Sitongia for initial help with MLSO data access, and Joan Burkepile, Giuliana de Toma, and Steve Tomczyk for ongoing assistance. MLSO is operated by the High Altitude Observatory, as part of the National Center for Atmospheric Research (NCAR). AIA data are courtesy of NASA/SDO and the AIA, EVE, and HMI science teams.

## REFERENCES

- Bąk-Stęślicka, U., Gibson, S. E., Fan, Y., Bethge, C., Forland, B., and Rachmeler, L. A. (2013). The magnetic structure of solar prominence cavities: new observational signature revealed by coronal magnetometry. *Astrophys. J.* 770:28. doi: 10.1088/2041-8205/770/2/L28
- Bąk-Stęślicka, U., Gibson, S. E., Fan, Y., Bethge, C., Forland, B., and Rachmeler, L. A. (2014). The spatial relation between EUV cavities and linear polarization signatures. *Proc. Int. Astronom. Union* 300, 395–396. doi: 10.1017/S1743921313011253
- Billings, D. E. (1966). *A Guide to the Solar Corona*. New York, NY: Academic Press.
- Bird, M. K., Schruefer, E., Volland, H., and Sieber, W. (1980). Coronal faraday rotation during solar occultation of PSR0525 + 21. *Nature* 283, 459. doi: 10.1038/283459a0
- Bird, M. K., Volland, H., Howard, R. A., Koomen, M. J., Michels, D. J., Sheeley, Jr., N. R., et al. (1985). White-light and radio sounding observations

- of coronal transients. *Solar Phys.* 98, 341–368. doi: 10.1007/BF00152465
- Caffau, E., Ludwig, H.-G., Steffen, M., Freytag, B., and Bonifacio, P. (2011). Solar chemical abundances determined with CO5BOLD 3D model atmosphere. *Solar Phys.* 268, 255–269. doi: 10.1007/s11207-010-9541-4
- Casini, R., and Judge, P. G. (1999). Spectral Lines for Polarization Measurements of the Coronal Magnetic Field. II. Consistent Treatment of the Stokes Vector for Magnetic-Dipole Transitions. *Astrophys. J.* 522, 524. doi: 10.1086/307629
- De Rosa, M. L., Schrijver, C. J., Barnes, G., Leka, K. D., Lites, B. W., Aschwanden, M. J., et al. (2009). A critical assessment of nonlinear force-free field modeling of the solar corona for active region 10953. *Astrophys. J.* 696, 1780–1791. doi: 10.1088/0004-637X/696/2/1780
- Del Zanna, G., Dere, K. P., Young, P. R., Landi, E., and Mason, H. E. (2015). CHIANTI - An atomic database for emission lines. Version 8. *Astron. Astrophys.* 582:A56. doi: 10.1051/0004-6361/201526827
- Dere, K. P., Landi, E., Mason, H. E., Monsignori Fossi, B. C., and Young, P. R. (1997). CHIANTI - an atomic database for emission lines. *Astron. Astrophys. Suppl.* 125, 149–173. doi: 10.1051/aas:1997368
- Dere, K. P., Landi, E., Young, P. R., Del Zanna, G., Landini, M., and Mason, H. E. (2009). CHIANTI - an atomic database for emission lines. IX. Ionization rates, recombination rates, ionization equilibria for the elements hydrogen through zinc and updated atomic data. *Astron. Astrophys.* 498, 915–929. doi: 10.1051/0004-6361/200911712
- Dove, J., Gibson, S., Rachmeler, L. A., Tomczyk, S., and Judge, P. (2011). A ring of polarized light: evidence for twisted coronal magnetism in cavities. *Astrophys. J. Lett.* 731:L1. doi: 10.1088/2041-8205/731/1/L1
- Dulk, G. A. (1985). Radio emission from the sun and stars. *Ann. Rev. Astron. Astrophys.* 23:169. doi: 10.1146/annurev.aa.23.090185.001125
- Feldman, U., Mandelbaum, P., Seely, J. F., Doschek, G. A., and Gursky, H. (1992). The potential for plasma diagnostics from stellar extreme-ultraviolet observations. *Astrophys. J. Suppl.* 81, 387–408. doi: 10.1086/191698
- Fineschi, S. (2001). “Space-based instrumentation for magnetic field studies of solar and stellar atmospheres,” in *Magnetic Fields Across the Hertzsprung-Russell Diagram, ASP Conference Proceedings*, Vol. 248, eds G. Mathys, S. K. Solanki, and D. T. Wickramasinghe (San Francisco, CA: Astronomical Society of the Pacific), 597.
- Forland, B. F., Gibson, S. E., Dove, J. B., and Kucera, T. A. (2014). The solar physics forward codes: now with widgets. *Proc. Int. Astronom. Union* 300, 414–415. doi: 10.1017/S1743921313011332
- Freeland, S. L., and Handy, B. N. (1998). Data analysis with the solarSoft system. *Solar Phys.* 182, 497–500. doi: 10.1023/A:1005038224881
- Gelfreikh, G. B. (2004). “Coronal magnetic field measurements through bremsstrahlung emission,” in *Solar and Space Weather Radiophysics*, eds D. E. Gary and C. U. Keller (Dordrecht: Kluwer Academic Publishers), 115–133. doi: 10.1007/1-4020-2814-8\_6
- Gibson, S. E. (2014). “Magnetism and the invisible man: the mysteries of coronal cavities,” in *IAU Symposium, Volume 300 of IAU Symposium*, eds B. Schmieder, J.-M. Malherbe, and S. T. Wu, 139–146.
- Gibson, S. (2015a). “Coronal cavities: observations and implications for the magnetic environment of prominences,” in *Astrophysics and Space Science Library, Vol. 415 of Astrophysics and Space Science Library*, eds J.-C. Vial and O. Engvold (Springer), 323–353. doi: 10.1007/978-3-319-10416-4\_13
- Gibson, S. (2015b). Data-model comparison using FORWARD and CoMP. *Proc. Int. Astronom. Union* 305, 245–250. doi: 10.1017/S1743921315004846
- Gibson, S. E., and Fan, Y. (2006). Coronal prominence structure and dynamics: a magnetic flux rope interpretation. *J. Geophys. Res.* 111:A12103. doi: 10.1029/2006ja011871
- Gibson, S. E., Kucera, T. A., Rastawicki, D., Dove, J., de Toma, G., Hao, J., et al. (2010). Three-dimensional morphology of a coronal prominence cavity. *Astrophys. J.* 723:1133. doi: 10.1088/0004-637X/724/2/1133
- Gibson, S. E., and Low, B. C. (1998). A time-dependent three-dimensional magnetohydrodynamic model of the coronal mass ejection. *Astrophys. J.* 493, 460. doi: 10.1086/305107
- Grebinskij, A., Bogod, V., Gelfreikh, G., Urpo, S., Pohjolainen, S., and Shibasaki, K. (2000). Microwave tomography of solar magnetic fields. *Astron. Astrophys. Suppl.* 144:169. doi: 10.1051/aas:2000202
- Habbal, S. R., Morgan, H., and Druckmüller, M. (2011). “A new view of coronal structures: implications for the source and acceleration of the solar wind,” in *Astronomical Society of India Conference Series, Vol. 2 of Astronomical Society of India Conference Series*, eds A. R., Choudhuri and D. Banerjee, 259–269.
- Halain, J.-P., Berghmans, D., Seaton, D. B., Nicula, B., De Groof, A., Mierla, M., et al. (2013). The SWAP EUV imaging telescope. Part II: in-flight performance and calibration. *solarphys* 286, 67–91. doi: 10.1007/s11207-012-0183-6
- Hill, F., Martens, P., Yoshimura, K., Gurman, J., Hourcle, J., Dimitoglou, G., et al. (2009). The virtual solar observatory - a resource for international heliophysics research. *Earth Moon Plan.* 104, 315–330. doi: 10.1007/s11038-008-9274-7
- Jensen, E. A., Bird, M. K., Asmar, S. W., Iess, L., Anderson, J. D., and Russell, C. T. (2005). The cassini solar faraday rotation experiment. *Adv. Space Res.* 36, 1587–1594. doi: 10.1016/j.asr.2005.09.039
- Jensen, E. A., Bisi, M. M., Breen, A. R., Heiles, C., Minter, T., and Vilas, F. (2013). Measurements of faraday rotation through the solar corona during the 2009 solar minimum with the MESSENGER spacecraft. *Solar Phys.* 285, 83–95. doi: 10.1007/s11207-012-0213-4
- Judge, P. G., and Casini, R. (2001). “A synthesis code for forbidden coronal lines,” in *Advanced Solar Polarimetry—Theory, Observation, and Instrumentation, 20TH NSO/Sac Summer Workshop, ASP Conference Proceedings*, Vol. 236, of *Astronomical Society of the Pacific Conference Series* (San Francisco, CA: Astronomical Society of the Pacific), 503.
- Judge, P. G., Low, B. C., and Casini, R. (2006). Spectral lines for polarization measurements of the coronal magnetic field. iv. stokes signals in current-carrying fields. *Astrophys. J.* 651:1229. doi: 10.1086/507982
- Karpen, J. (2014). “Plasma structure and dynamics,” in *Solar Prominences, Vol. 415, of Astrophysics and Space Science Library*, eds O. Engvold and J. C. Vial (Springer), 237–257. doi: 10.1007/978-3-319-10416-4\_10
- Keady, J. J., and Kilcrease, D. P. (2000). “Radiation,” in *Allens Astrophysical Quantities*, ed A. N. Cox (New York, NY: AIP), 95–120.
- Kooi, J. E., Fischer, P. D., Buffo, J. J., and Spangler, S. R. (2014). Measurements of coronal faraday rotation at 4.6 R<sub>sun</sub>. *Astrophys. J.* 784:68. doi: 10.1088/0004-637X/784/1/68
- Kopp, R. A., and Holzer, T. E. (1976). Dynamics of coronal hole regions. I - Steady polytropic flows with multiple critical points. *Solar Phys.* 49, 43–56.
- Koutchmy, S., and Lamy, P. L. (1985). “The F-corona and the circum-solar dust evidences and properties,” in *IAU Colloq. 85: Properties and Interactions of Interplanetary Dust, Vol. 119 of Astrophysics and Space Science Library*, eds R. H. Giese and P. Lamy (Springer), 63–74.
- Kramar, M., Airapetian, V., Mikić, Z., and Davila, J. (2014). 3D coronal density reconstruction and retrieving the magnetic field structure during solar minimum. *Solar Phys.* 289, 2927–2944. doi: 10.1007/s11207-014-0525-7
- Kramar, M., Inhester, B., Lin, H., and Davila, J. (2013). Vector tomography for the coronal magnetic field. II. Hanle effect measurements. *Astron. Astrophys.* 775, 25. doi: 10.1088/0004-637X/775/1/25
- Kramar, M., Inhester, B., and Solanki, S. K. (2006). Vector tomography for the coronal magnetic field. I. Longitudinal Zeeman effect measurements. *Astron. Astrophys.* 456, 665–673. doi: 10.1051/0004-6361:20064865
- Kucera, T. (2015). *Solar Prominences, Astrophysics and Space Science Library, Vol. 415*, eds O. Engvold and J. C. Vial (Switzerland: Springer International Publishing Switzerland), 79. doi: 10.1007/978-3-319-10416-4\_4
- Kucera, T. A., Gibson, S. E., Schmit, D. J., Landi, E., and Tripathi, D. (2012). Temperature and euv intensity in a coronal prominence cavity. *Astrophys. J.* 757:73. doi: 10.1088/0004-637X/757/1/73
- Kundu, M. R. (1965). *Solar Radio Astronomy*. New York, NY: Interscience Publishers.
- Lin, H. (2016). mxCSM: A 100-slit, 6-wavelength wide-field coronal spectropolarimeter for the study of the dynamics and the magnetic fields of the solar corona. *Front. Astron. Space Sci.* 3:9. doi: 10.3389/fspas.2016.00009
- Lionello, R., Linker, J. A., and Mikic, Z. (2009). Multispectral emission of the sun during the first whole sun month. *Astrophys. J.* 690:902. doi: 10.1088/0004-637X/690/1/902
- Lionello, R., Winebarger, A. R., Mok, Y., Linker, J. A., and Mikić, Z. (2013). Thermal non-equilibrium revisited: a heating model for coronal loops. *Astrophys. J.* 773:134. doi: 10.1088/0004-637X/773/2/134
- Lites, B. W., and Low, B. C. (1997). Flux emergence and prominences: a new scenario for 3-dimensional field geometry based on observations with the advanced stokes polarimeter. *Solar Phys.* 174, 91. doi: 10.1023/A:1004936204808

- Low, B. C., and Hundhausen, J. R. (1995). Magnetostatic structures of the solar corona. ii. the magnetic topology of quiescent prominences. *Astrophys. J.* 443, 818. doi: 10.1086/175572
- Luna, M., Karpen, J. T., and DeVore, C. R. (2012). Formation and evolution of a multi-threaded solar prominence. *Astrophys. J.* 746, 30. doi: 10.1088/0004-637X/746/1/30
- Malanushenko, A., Schrijver, C. J., DeRosa, M. L., and Wheatland, M. S. (2014). Using coronal loops to reconstruct the magnetic field of an active region before and after a major flare. *Solar Stell. Astrophys.* 783, 102. doi: 10.1088/0004-637X/783/2/102
- Mancuso, S., and Spangler, S. R. (2000). Faraday rotation and models for the plasma structure of the solar corona. *Astrophys. J.* 539, 480–491. doi: 10.1086/309205
- Mann, I. (1992). The solar F-corona - calculations of the optical and infrared brightness of circumsolar dust. *Solar Phys.* 261, 329–335.
- Morgan, H., Habbal, S. R., and Woo, R. (2006). The depiction of coronal structure in white-light images. *Astrophysics* 236, 263–272. doi: 10.1007/s11207-006-0113-6
- Munro, R. H., and Jackson, B. V. (1977). Physical properties of a polar coronal hole from 2 to 5 solar radii. *Astrophys. J.* 213, 874. doi: 10.1086/155220
- Newkirk, G., and Altschuler, M. D. (1970). Magnetic fields and the solar corona. III: the observed connection between magnetic fields and the density structure of the corona. *Solar Phys.* 13, 131–152. doi: 10.1007/BF00963948
- Nita, G. M., Fleishman, G. D., Kuznetsov, A. A., Kontar, E. P., and Gary, D. E. (2015). Three-dimensional radio and X-ray modeling and data analysis software: revealing flare complexity. *Astrophys. J.* 799, 236. doi: 10.1088/0004-637X/799/2/236
- Ord, S. M., Johnston, S., and Sarkissian, J. (2007). The magnetic field of the solar corona from pulsar observations. *Solar Phys.* 245, 109–120. doi: 10.1007/s11207-007-9030-6
- Plowman, J. (2014). Single-point inversion of the coronal magnetic field. *Astrophys. J.* 792, 23. doi: 10.1088/0004-637X/792/1/23
- Rachmeler, L. A., Gibson, S. E., Dove, J. B., DeVore, C. R., and Fan, Y. (2013). Polarimetric properties of flux ropes and sheared arcades in coronal prominence cavities. *Solar. Phys.* 288, 617–636. doi: 10.1007/s11207-013-0325-5
- Rachmeler, L. A., Platten, S. J., Bethge, C., Seaton, D. B., and Yeates, A. R. (2014). Observations of a hybrid double-streamer/pseudostreamer in the solar corona. *Solar Stell. Astrophys.* 787, L3. doi: 10.1088/2041-8205/787/1/l3
- Reeves, K. K., Gibson, S. E., Kucera, T. A., and Hudson, H. S. (2012). Thermal properties of coronal cavities observed with the X-ray telescope on Hinode. *Astrophys. J.* 746:146. doi: 10.1088/0004-637X/746/2/146
- Robinson, P. A., and Melrose, D. B. (1984). Gyromagnetic emission and absorption: approximate formulas of wide validity. *Aust. J. Phys.* 37, 675. doi: 10.1071/PH840675
- Savcheva, A. A., McKillop, S. C., McCauley, P. I., Hanson, E. M., and DeLuca, E. E. (2013). A new sigmoid catalog from hinode and the solar dynamics observatory: statistical properties and evolutionary histories. *Solar Phys.* 289, 3297–3311. doi: 10.1007/s11207-013-0469-3
- Schmelz, J. T., Reames, D. V., von Steiger, R., and Basu, S. (2012). Composition of the solar corona, solar wind, and solar energetic particles. *Astrophys. J.* 755, 33. doi: 10.1088/0004-637X/755/1/33
- Schmidt, J. M., and Cairns, I. H. (2012a). Type II radio bursts: 1. New entirely analytic formalism for the electron beams, Langmuir waves, and radio emission. *J. Geophys. Res.* 117, 4106. doi: 10.1029/2011ja017318
- Schmidt, J. M., and Cairns, I. H. (2012b). Type II radio bursts: 2. Application of the new analytic formalism. *J. Geophys. Res.* 117, 11104. doi: 10.1029/2012JA017932
- Schmit, D. J., and Gibson, S. E. (2011). Forward modeling cavity density: a multi-instrument diagnostic. *Astrophys. J.* 733:1. doi: 10.1088/0004-637X/733/1/1
- Seaton, D. B., Berghmans, D., Nicula, B., Halain, J.-P., De Groof, A., Thibert, T., et al. (2013). The SWAP EUV imaging telescope part I: instrument overview and pre-flight testing. *Solar. Phys.* 286, 43–65. doi: 10.1007/s11207-012-0114-6
- Tian, H., Tomczyk, S., McIntosh, S. W., Bethge, C., de Toma, G., and Gibson, S. (2013). Observations of coronal mass ejections with the coronal multichannel polarimeter. *Solar Phys.* 288, 637–650. doi: 10.1007/s11207-013-0317-5
- Tomczyk, S., Card, G. L., Darnell, T., Elmore, D. F., Lull, R., Nelson, P. G., et al. (2008). An instrument to measure coronal emission line polarization. *Solar Phys.* 247:411. doi: 10.1007/s11207-007-9103-6
- Tomczyk, S., McIntosh, S. W., Keil, S. L., and Judge, P. G. (2007). Alfven waves in the solar corona. *Science* 317:1192. doi: 10.1126/science.1143304
- van Doorsselaere, T., Antolin, P., Yuan, D., Reznikova, V., and Magyar, N. (2016). Forward modeling of EUV and gyrosynchrotron emission from coronal plasmas with FoMo. *Front. Astron. Space Sci.* 3:4. doi: 10.3389/fspas.2016.00004
- van Vleck, J. H. (1925). On the quantum theory of the polarization of resonance radiation in magnetic fields. *Proc. Natl. Acad. Sci. U.S.A.* 11:612. doi: 10.1073/pnas.11.10.612
- White, S. M. (2000). Radio versus euv/x-ray observations of the solar atmosphere. *Solar Phys.* 190, 309. doi: 10.1023/A:1005253501584
- White, S. M., and Kundu, M. R. (1997). Radio observations of gyroresonance emission from coronal magnetic fields. *Solar Phys.* 174, 31. doi: 10.1023/A:1004975528106
- White, S. M., Thejappa, G., and Kundu, M. R. (1992). Mode coupling in the solar corona and bipolar noise storms. *Solar Phys.* 138, 163. doi: 10.1007/BF00146202
- Xia, C., Keppens, R., Antolin, P., and Porth, O. (2014). Simulating the *in situ* condensation process of solar prominences. *Solar Stell. Astrophys.* 792, L38. doi: 10.1088/2041-8205/792/2/l38
- Yeates, A. R., and Mackay, D. H. (2012). Chirality of high-latitude filaments over solar cycle 23. *Solar Stell. Astrophys.* 753, L34. doi: 10.1088/2041-8205/753/2/l34
- You, X. P., Coles, W. A., Hobbs, G. B., and Manchester, R. N. (2012). Measurement of the electron density and magnetic field of the solar wind using millisecond pulsars. *Monthly Notices R. Astron. Soc.* 422, 1160–1165. doi: 10.1111/j.1365-2966.2012.20688.x

**Conflict of Interest Statement:** The authors declare that the research was conducted in the absence of any commercial or financial relationships that could be construed as a potential conflict of interest.

Copyright © 2016 Gibson, Kucera, White, Dove, Fan, Forland, Rachmeler, Downs and Reeves. This is an open-access article distributed under the terms of the Creative Commons Attribution License (CC BY). The use, distribution or reproduction in other forums is permitted, provided the original author(s) or licensor are credited and that the original publication in this journal is cited, in accordance with accepted academic practice. No use, distribution or reproduction is permitted which does not comply with these terms.



# Forward Modeling of EUV and Gyrosynchrotron Emission from Coronal Plasmas with FoMo

**Tom Van Doorsselaere<sup>1\*</sup>, Patrick Antolin<sup>2</sup>, Ding Yuan<sup>1†</sup>, Veronika Reznikova<sup>1,3</sup> and Norbert Magyar<sup>1</sup>**

<sup>1</sup> Centre for mathematical Plasma Astrophysics, Department of Mathematics, KU Leuven, Leuven, Belgium, <sup>2</sup> National Astronomical Observatory of Japan, Mitaka, Japan, <sup>3</sup> Radiophysical Research Institute (NIRFI), Nizhny Novgorod, Russia

## OPEN ACCESS

### Edited by:

Laurel Anne Rachmeler,  
National Aeronautics and Space  
Administration, USA

### Reviewed by:

Therese Kucera,  
National Aeronautics and Space  
Administration, USA  
Cooper Downs,  
Predictive Science Incorporated, USA

### \*Correspondence:

Tom Van Doorsselaere  
tom.vandoorsselaere@wis.kuleuven.be

### †Present Address:

Ding Yuan,  
Jeremiah Horrocks Institute, University  
of Central Lancashire, Preston, UK

### Specialty section:

This article was submitted to  
Stellar and Solar Physics,  
a section of the journal  
*Frontiers in Astronomy and Space  
Sciences*

**Received:** 28 October 2015

**Accepted:** 08 February 2016

**Published:** 26 February 2016

### Citation:

Van Doorsselaere T, Antolin P, Yuan D,  
Reznikova V and Magyar N (2016)  
Forward Modeling of EUV and  
Gyrosynchrotron Emission from  
Coronal Plasmas with FoMo.  
*Front. Astron. Space Sci.* 3:4.  
doi: 10.3389/fspas.2016.00004

The FoMo code was developed to calculate the EUV and UV emission from optically thin coronal plasmas. The input data for FoMo consists of the plasma density, temperature and velocity on a 3D grid. This is translated to emissivity on the 3D grid, using CHIANTI data. Then, the emissivity is integrated along the line-of-sight (LOS) to calculate the emergent spectral line for synthetic spectrometer observations. The code also generates the emission channels for synthetic AIA imaging observations. Moreover, the code has been extended to model also the gyrosynchrotron emission from plasmas with a population of non-thermal particles. In this case, also optically thick plasmas may be modeled. The radio spectrum is calculated over a large wavelength range, allowing for the comparison with data from a wide range of radio telescopes.

**Keywords:** solar physics, solar corona, EUV emission, radio emission, forward modeling

## 1. INTRODUCTION

The mean free path of photons becomes increasingly long when going up from the solar photosphere, into the solar corona. Thus, the solar corona is typically optically thin. As a result, observations are 2D projections of a 3D configuration in the solar corona. This makes interpreting observations rather difficult, because the precise position of the plasma along the line-of-sight (LOS) is unavailable. One exception is stereoscopy with the STEREO space mission (e.g., Marsh et al., 2009; Verwichte et al., 2009; Aschwanden, 2011), where one uses multiple vantage points to infer the 3D structure of the observations.

The lack of 3D information in observations also makes the comparison of simulation or model data to observations difficult. Typically, simulations output physical quantities in the plasma that cannot be measured directly (e.g., density, temperature), while observations only show spectral line profiles (integrated over space, time and wavelength, depending on the instrument). Thus, to allow for a direct comparison, a conversion from model data to emission is necessary by creating artificial observations. This technique is called forward modeling.

In solar coronal physics, several tools are available for forward modeling. Perhaps the most prominent one is FORWARD, which computes EUV emission and polarimetric signals from a given coronal model (Gibson, 2015; Gibson et al., 2016). Besides that, there is the GX\_SIMULATOR (Nita et al., 2015), which computes radio and X-ray emission and is mainly aimed at forward modeling flares. In this article, we will describe the technical aspects of the FOMO tool, another possibility for calculating coronal emission, mainly developed at the KU Leuven (Belgium).

The development of the FOMO tool was mainly motivated by the desire to perform forward modeling of coronal wave models. It had become clear that the connection between wave properties and the expected emission was less straightforward than expected. For instance, Gruszecki et al. (2012) used a naive forward modeling method (i.e., putting the emission in each simulation point proportional to  $n_e^2$ , where  $n_e$  is the electron density) to show that the intensity modulation of sausage waves (e.g., Vasheghani Farahani et al., 2014) is second order in the wave amplitude, because the density depletion is compensated in first order by the increased LOS. FOMO was thus first used by Antolin and Van Doorsselaere (2013) to calculate the emission from numerical and analytical models of the sausage mode, in a self-consistent way using atomic data from the CHIANTI database (Dere et al., 1997; Landi et al., 2013). Antolin and Van Doorsselaere (2013) showed that the sausage mode causes EUV intensity variations, but that the level of variation is highly dependent on the temperature of the emitting loop and the spectral line, the observational setup and instrument (LOS angle and instrument resolution).

After extending FOMO in order to compute gyrosynchrotron emission, Reznikova et al. (2014) compared the full, integrated emission from sausage modes in a cylindrical model to the analytical predictions and found that the predicted phase was not valid (e.g., Mossessian and Fleishman, 2012), although only a uniform distribution of non-thermal particles in the loop was considered. Kuznetsov et al. (2015) extended the model to a 3D semi-torus loop, and Reznikova et al. (2015) computed the expected polarization variations for sausage modes.

The FOMO code was also used for modeling the emission from propagating slow waves. On the one hand, it was used to model the emission features of slow waves and periodic upflow (if such a thing exists in MHD) by De Moortel et al. (2015). It was found that these two physical behaviors are almost impossible to distinguish observationally. On the other hand, FOMO was used to model the damping behavior of slow waves. Previously, it had been found that omnipresent slow waves (Krishna Prasad et al., 2012) had a peculiar dependence of the damping length on the period (Krishna Prasad et al., 2014). With FOMO, it was shown that this behavior could be explained by damping with thermal conduction (Mandal et al., 2016). Furthermore, the propagating slow waves in hot coronal loops (Kumar et al., 2013, 2015) were modeled successfully with FOMO (Fang et al., 2015). Additionally, FOMO was used for the modeling of standing slow waves in hot coronal loops (Wang, 2011; Yuan et al., 2015).

Last but not least, we mention the modeling of standing kink waves in coronal loops performed with FOMO. Antolin et al. (2014, 2015) have calculated the emission from a 3D simulation of a transversally oscillating coronal loop and prominence. In the former work, it was argued that the Kelvin-Helmholtz instability in the resonant layer around the loop could lead to the formation of apparently stranded loops. The simulations in the latter work were used to compare to observational results (Okamoto et al., 2015). The excellent agreement and the direct comparison between the observational signatures and forward model from the simulation allowed to identify the observations as a signature of resonant absorption.

It is clear from the above description that FOMO is ideally situated to improve the current coronal seismology techniques. Coronal seismology compares observations of coronal waves to their models, in order to obtain extra information on the plasma background (such as a coronal loop). For a review on coronal seismology, please see e.g., Nakariakov and Verwichte (2005); De Moortel and Nakariakov (2012); Liu and Ofman (2014). In particular, coronal seismology may be used for the measurement of the magnetic field (e.g., Nakariakov and Ofman, 2001; Van Doorsselaere et al., 2007) and, in general, Alfvén travel times (Arregui et al., 2007; Goossens et al., 2008; Asensio Ramos and Arregui, 2013). Thus, by allowing a direct comparison between the observations and the forward modeling, FOMO improves the magnetometry by waves in the solar corona (i.e., by coronal seismology).

Furthermore, while FOMO is targeted at modeling emission from coronal plasma, its use can be extended to the calculation of emission from any optically thin medium.

## 2. FORWARD MODELING WITH FoMo

### 2.1. General Approach

In what follows, three numerical implementations of the forward modeling procedure will be described: FoMo-C, FoMo-IDL, FoMo-GS. First, FoMo-IDL was developed to model the EUV emission of the solar corona. A little while later, FoMo-GS was written to extend its application to the gyrosynchrotron radiation. It became clear that IDL is not widely available on clusters, and therefore it was decided to also implement the procedure in C++ (FoMo-C), immediately also giving access to parallelization. In this paragraph, we first describe what is common in all three implementations.

The corona is optically thin, and thus the specific intensity  $I(\lambda, x', y')$  (in ergs  $\text{cm}^{-2} \text{s}^{-1} \text{sr}^{-1} \text{\AA}^{-1}$ ) at a wavelength  $\lambda$  is the integral of the monochromatic emissivity  $\epsilon(\lambda, x, y, z)$  at each point along the LOS. Let us assume that the LOS is along a given  $z'$  axis, that may not be aligned to any of the numerical axes.

$$I(\lambda, x', y') = \int \epsilon(\lambda, x(z'), y(z'), z(z')) dz'. \quad (1)$$

Here  $(x, y, z)$  are the coordinates in the original simulation, and  $(x', y', z')$  are the coordinates in the rotated frame of reference of the observation.  $(x', y')$  are the coordinates in the image plane (also known as the plane-of-the-sky, or POS), and  $z'$  is the direction along the LOS. The two coordinate systems are connected by two rotations, first an angle  $l$  around the  $z$ -axis, then around an angle  $-b$  around the  $y$ -axis:

$$\begin{pmatrix} x' \\ y' \\ z' \end{pmatrix} = \begin{pmatrix} \cos b & 0 & -\sin b \\ 0 & 1 & 0 \\ \sin b & 0 & \cos b \end{pmatrix} \begin{pmatrix} \cos l & -\sin l & 0 \\ \sin l & \cos l & 0 \\ 0 & 0 & 1 \end{pmatrix} \begin{pmatrix} x \\ y \\ z \end{pmatrix}. \quad (2)$$

The simulation box with grid  $(x, y, z)$  is considered as the input for FOMO, and is the data for which the forward model needs to be computed. FoMo-C and FoMo-IDL calculate the optically thin EUV emission in spectral lines or AIA passbands. There the input model needs to contain the  $x$ -,  $y$ -,  $z$ -coordinates

of each data point, and specify the number density  $n_e$ , the temperature  $T$  and three velocity components ( $v_x$ ,  $v_y$ ,  $v_z$ ) at these data points. For the necessary input of the FOMO-GS code, please see Section 2.4.

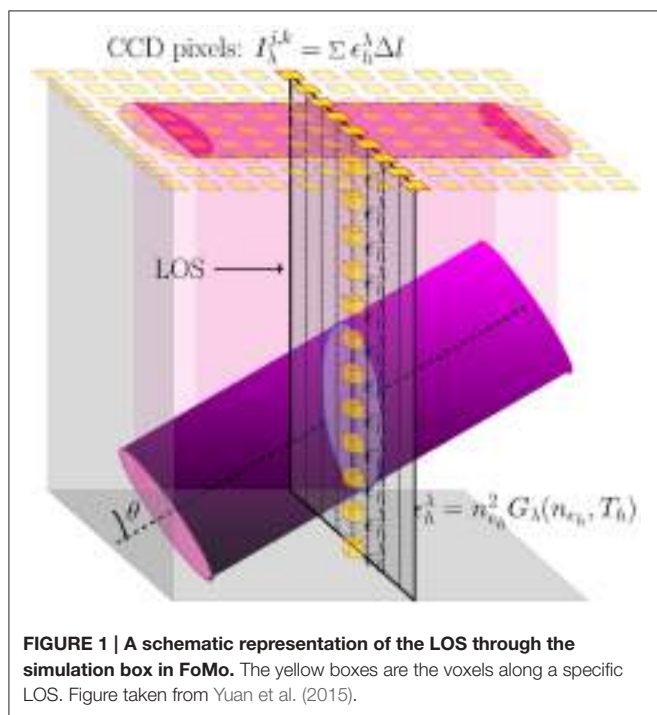
Then, a new grid is generated in the observation reference frame ( $x'$ ,  $y'$ ,  $z'$ ). The grid points in this new, “observational” grid are called *voxels*. The resolution of the new grid is set by the user in FOMO-C, and determined from the simulation grid in FOMO-IDL and FOMO-GS. In FOMO-C, the choice for the resolution in the  $z'$ -direction ( $\Delta l$ ) should be close to the numerical resolution of the input model, as otherwise emission features may be missed in the forward models.

The numerical resolution of the forward model is not related to the instrument resolution. The numerical resolution is necessary to capture the fine emission features that may be present in the numerical model. The instrument resolution should be simulated by post-processing the forward model with a point spread function (or simply summing pixels to degrade the image).

At each voxel  $(x'_i, y'_j, z'_k)$ , the emissivity is interpolated from the nearest grid point in the  $(x, y, z)$ -space and then the LOS integration is performed. The configuration is schematically shown in **Figure 1**. The integral in Equation (1) is then discretised as follows

$$I(\lambda, x'_i, y'_j) = \sum_k \epsilon(\lambda, x'_i, y'_j, z'_k) \Delta l, \quad (3)$$

which converges to the true emission for  $\Delta l \rightarrow 0$ , thus stressing the need for a high resolution in the  $z'$ -direction in FOMO-C. The FOMO-GS code additionally computes the radiative



transfer along the LOS because it is optically thick, and thus the computation is more complicated (see Section 2.4).

For calculation of monochromatic emission with FOMO-C and FOMO-IDL, we first convert the physical variables  $n_e$ ,  $T$  to the emissivity  $\tilde{\epsilon}(x, y, z)$  (in ergs  $\text{cm}^{-3} \text{s}^{-1} \text{sr}^{-1}$ ) of the spectral line at rest wavelength  $\lambda_0$  at each grid point by

$$\tilde{\epsilon}(x, y, z) = \frac{A_b}{4\pi} n_e^2(x, y, z) G_{\lambda_0}(n_e(x, y, z), T(x, y, z)), \quad (4)$$

where  $A_b$  is the abundance of the emitting element (with respect to hydrogen) and  $G_{\lambda_0}$  the contribution function for that specific spectral line (including the Gaunt factor and oscillator strength for the spectral line). The abundance  $A_b$  is taken to be constant along the LOS. The abundance  $A_b$  is read from a CHIANTI abundance file. As a standard sun\_coronal.abund is used in FOMO-C and FOMO-IDL, but it may be swapped with another file if needed.

The  $G_{\lambda_0}$  is calculated by a look-up table. The look-up table was generated for a range of temperatures and densities using g\_of\_t.pro in the CHIANTI database (Dere et al., 1997; Landi et al., 2013). This routine assumes that the plasma satisfies the coronal approximation, in particular, that electrons and protons have the same temperature and that the plasma is in ionization equilibrium. For the latter, the chianti.ioneq is used by default. Moreover, the emission tables are generated with the assumption that the spectral lines are collisionally excited.

At the moment, FOMO contains tabulated contribution functions  $G_{\lambda_0}$  for a number of emission lines. These are listed in **Table 1**. For the addition of extra spectral lines, first the element and ionization number for the spectral line should be known. Then the CHIANTI line identification may be found with the routine emiss\_calc and finding the correct line in the routine output. It is important to know that the line identification may change from one CHIANTI version to the next. With the CHIANTI identification, it is straightforward to generate the extra emission table with the routines included in the FOMO package. Instructions for this can be found at <https://wiki.esat.kuleuven.be/FoMo/GeneratingTables>.

Some included line emission (such as He II, Mg II) is often observed to be optically thick. The users of the code need to ensure that the considered model (and its expected emission) is in the optically thin regime for these spectral lines, and the assumption of ionization equilibrium is not too stringent for the modeled environment.

We compute the full-width half-maximum of the spectral line  $\lambda_w$  (or width of Gaussian  $\sigma_w$ ) from the temperature by

$$\lambda_w = 2\sqrt{2 \ln 2} \frac{v_{\text{th}}}{c} \lambda_0 = 2\sqrt{2 \ln 2} \sqrt{\frac{kT}{\mu_{\lambda_0} m_p}} \frac{\lambda_0}{c},$$

equivalent to taking  $\sigma_w = \frac{v_{\text{th}}}{c} \frac{\lambda_0}{\sqrt{2}}$ ,

(5)

where  $k$  is the Boltzmann constant,  $c$  is the speed of light,  $m_p$  is the mass of a proton,  $\mu_{\lambda_0}$  is the atomic weight (in proton masses) of the emitting element and  $v_{\text{th}} = \sqrt{\frac{2kT}{\mu_{\lambda_0} m_p}}$  is the thermal

**TABLE 1 | List of tabulated emission in FoMo.**

Spectral lines			
Element	log(T)	Wavelength (Å)	
C II	4.74	1334.53	
	4.62	1335.71	
C III	4.93	977.02	
		1174.93	
C IV	5.04	1548.19	
		1550.78	
Fe IX	5.93	171.073	
Fe XII	6.19	186.88	
		193.509	
		195.12	
Fe XIX	6.95	1118.1	
He II	4.92	303.781	
Mg II	4.22	2796.35	
		2803.53	
Ne VIII	5.8	770.41	
O IV	5.17	1399.77	
		1401.16	
		1404.78	
Si IV	4.89	1393.76	
		1402.77	
Si VII	5.8	197.768	

List of spectral lines for which the tabulated emission  $G_{\lambda_0}$  is incorporated in FoMo-C and FoMo-IDL (left). List of instrument response functions in FoMo-C and FoMo-IDL (right).

velocity. This is done at each voxel in FoMo-C, but only for each histogram bin in FoMo-IDL (see Section 2.3).

Thus, in this first step of the computation, the physical variables  $n_e$ ,  $T$  are converted to  $\tilde{\epsilon}$ ,  $\lambda_w$ .

In the second step, the integration along the LOS is performed. At each voxel, the emissivity, spectral line width and velocity  $\tilde{\epsilon}$ ,  $\lambda_w$ ,  $\vec{v}$  are interpolated from its nearest neighbor in the  $(x, y, z)$  grid. Then the wavelength dependence of the monochromatic emissivity is calculated by taking a Gaussian shaped spectral line with the correct thermal line width (Equation 5) and the local Doppler shift.

$$\epsilon(\lambda, x', y', z') = \frac{2\sqrt{2\ln 2}}{\sqrt{2\pi}\lambda_w} \tilde{\epsilon}(x', y', z') \exp\left(-\frac{4\ln 2}{\lambda_w^2} \left(\lambda - \lambda_0 \left(1 - \vec{z}' \cdot \vec{v}/c\right)\right)^2\right) \quad (6)$$

$$= \frac{1}{\sigma_w \sqrt{2\pi}} \tilde{\epsilon}(x', y', z') \exp\left(-\frac{1}{2\sigma_w^2} \left(\lambda - \lambda_0 \left(1 - \vec{z}' \cdot \vec{v}/c\right)\right)^2\right) \quad (7)$$

The local Doppler shift is calculated by projecting the local velocity  $\vec{v}(x, y, z)$  onto a unit vector  $\vec{z}'$  along the LOS, given by

$$\vec{z}' = \begin{pmatrix} \sin b \cos l \\ -\sin b \sin l \\ \cos b \end{pmatrix}, \quad (8)$$

as can be readily derived from Equation (2). The velocity projection is done in each grid point, and then the value is interpolated to the forward modeling grid.

After summation with Equation (3), the specific intensity  $I(\lambda, x'_i, y'_j)$  is returned as a result of the second step in the code. This specific intensity can then be fitted with a Gaussian in order to obtain intensity, Doppler shift and line width. An example of this is shown in Figure 2.

For the calculation of emission in the imaging telescopes of SDO/AIA, we have computed instrument response functions  $\kappa_\alpha(n_e, T)$  for bandpass  $\alpha$  on a grid of densities  $n_e$  and temperatures  $T$ . For this we have used the AIA temperature response functions (obtained with `aia_get_resp.pro`, Boerner et al., 2012) and the contribution function  $G(\lambda, n_e, T)$  with the CHIANTI `isothermal.pro` routine (and also includes the continuum emission), following the procedure detailed in Del Zanna et al. (2011). The instrument response is then computed by

$$\kappa_\alpha(n_e, T) = \int_{\lambda_\alpha} G(\lambda_\alpha, n_e, T) R_\alpha(\lambda_\alpha) d\lambda_\alpha, \quad (9)$$

where  $R_\alpha$  is the wavelength-dependent response function of bandpass  $\alpha$ , and where the wavelength integration is done over all spectral lines with wavelengths contained in the bandpass (the wavelength range is roughly centered on the dominant spectral line and has a width largely covering the FWHM given by the response function). The available instrument responses are listed in Table 1, and have been computed with both coronal and photospheric abundances.

The instrument response in the image plane of the forward model is then obtained through integrating  $\kappa_\alpha$  over the LOS. Thus, the equivalent for Equation (3) for the imaging telescope is

$$I(x'_i, y'_j) = \sum_k \kappa_\alpha(x'_i, y'_j, z'_k) \Delta l, \quad (10)$$

in which the emissivity was replaced by the instrument response function.

The above features are common in at least FoMo-C and FoMo-IDL. In the following subsection, we will outline the specific methods used for applying the above derivation, and which optimizations have been implemented. FoMo-GS is rather different than the above procedure, since it calculates the gyrosynchrotron emission with 1D radiative transfer. It is described separately in Section 2.4.

## 2.2. FoMo-C v3.2

The FoMo-C code is written as shared object library, against which the user can link the code for the specific problem at hand. In the library an object `FoMoObject` is defined. It has several members defined:

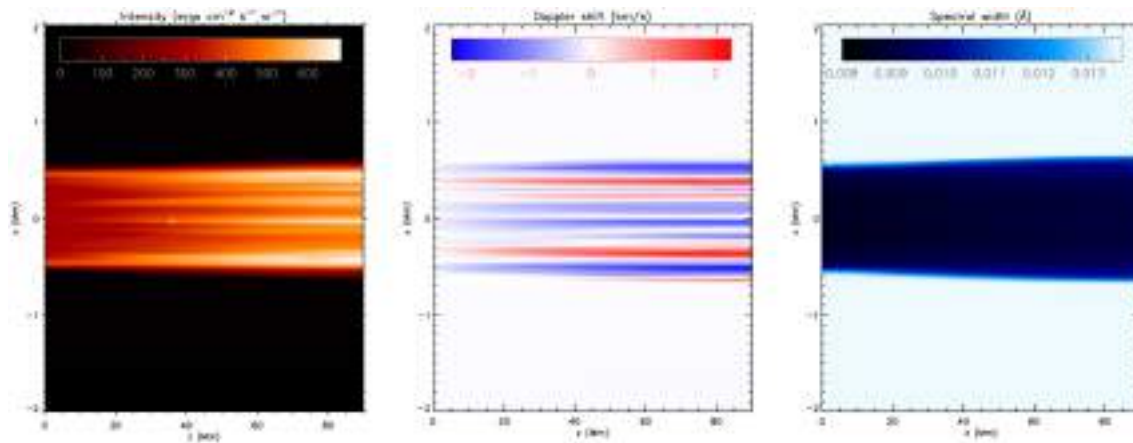


**FIGURE 2 | The typical data products from FoMo.** The left panel shows the intensity, the middle panel the Doppler shift, and the right panel the line width. This rendering has been performed for the data used for the code validation in Section 2.6. The white “+” shows the position for the spectral line comparison in **Figure 3**.

- `push_back_datapoint({x,y,z},{rho,T,vx,vy,vz})`: This adds data points of the simulation to the `FoMoObject`.
- `setresolution(nx,ny,nz,nlambda,lambdawidth)`: This sets the resolution of the rendering. The resolution should more or less match the resolution of the simulation.
- `render(l,b)`: The member performing the actual rendering of the data cube, for angle  $l$  and  $b$ . The result will be written out to hard disk, for post-processing and analysis.

For more information on the members of the `FoMoObject` and example for the practical usage, please consult the FOMO wikipage at <https://wiki.esat.kuleuven.be/FoMo/>, or the documentation provided through *doxygen* in the source files of the code.

Interpolations in FOMO-C are performed with the CGAL library (The CGAL Project, 2015). This happens on two occasions in the code:

1. The first usage of the CGAL library occurs for the interpolation of  $G_{\lambda_0}$  [for using in Equation (4)] on the simulation grid  $(x, y, z)$  in the conversion from  $n_e, T$  to  $\tilde{\epsilon}$ . First the data is read in from the tabulated CHIANTI file [as a function  $\tilde{\epsilon}(n_e, T)$ ], then a 2D triangulation is constructed of this function. Then, at each simulation point, the pair of  $(n_e, T)$  is located in the triangulation, and a linear interpolation between neighboring points is performed.
2. The second interpolation in the CGAL library is for the interpolation of the voxels into the 3D grid of the original simulation. A 3D triangulation is constructed for the grid of the simulation (using the parallel triangulation algorithm of CGAL, based on Intel’s Thread Building Blocks). Thus, FOMO-C does not rely on a regular grid, and allows for the use of general grids in the simulation (including adaptive mesh refinement, and even unstructured grids). Then, each voxel is located within the 3D triangulation, and the emissivity of the nearest grid point is used as the interpolated value.

The integration along the LOS is parallelized through OpenMP tasks. Each pixel in the imaging plane is independent from other pixels, and thus constitutes a task. In the task, the processor walks along the LOS, gradually adding the (wavelength-dependent) emission to obtain the intensity in that respective pixel.

The main attraction of FOMO-C is that (1) it is built in a modular fashion, and adding of new rendering algorithms is easy, (2) it allows for having irregular grids (such as adaptive mesh refinement, or unstructured grids), (3) it is parallelized with OpenMP and Intel’s Thread Building Blocks, (4) it is written and built in C++ with the GNU autotools and should thus work on a variety of systems.

The current version of FOMO-C (v3.2) contains documentation written in *doxygen*. Moreover, examples are provided on how to read in data and render it, including examples on the processing of HDF5 output from the FLASH code (Fryxell et al., 2000; Lee et al., 2009). Routines are also provided in order to import the FOMO-C output into IDL, where the output can be post-processed (e.g., Gaussian fitting of the spectral lines and visualization).

### 2.3. FoMo-IDL

FOMO-IDL has been written taking into account the numerical limitations encountered when using IDL, namely, limits on memory management, CPU speed and parallelization, all of which can make the computations significantly slower than in C++. Nevertheless, the implementations performed in the programming of the IDL version make the computations highly efficient and comparable (to some extent) to the C++ counterpart.

As mentioned in Section 2.1 the main idea behind our forward modeling is to convert the physical variables  $n_e, T$  in the numerical model to the observables  $\tilde{\epsilon}, \lambda_w$ . For dealing with this conversion in an efficient manner in IDL we construct histograms of the velocity and emissivity and work with the resulting bins as groups of pixels instead of individual pixels. The constructed bins are then representations sampling the entire velocity -

emissivity space. Doppler shifts and thermal width calculations are therefore applied to the groups of pixels within single bins “simultaneously” instead of pixel by pixel. Let us explain this binning procedure in more detail.

With the help of IDL’s histogram function we first generate bins of the velocity space from the numerical box with a given velocity width (set by default to  $0.5 \text{ km s}^{-1}$ ). Let the set of velocity bins be  $\{V_i\}_{i=1,\dots,n}$ . The group of pixels within a bin  $V_i$  forms a set of emissivities  $\epsilon(V_i)$ , given by Equation (4). We then generate a second histogram, now of emissivities, for each set  $\{\epsilon(V_i)\}_{i=1,\dots,n}$ , each leading to a binning of the emissivities corresponding to a velocity  $v_i$  of the bin  $V_i$ . Let the group of emissivity bins linked to the velocity bin  $V_i$  be  $\{\epsilon_{V_i}\}_{j=1,m}$ . Now, consider a bin  $\epsilon_{V_{ij}}$  of this second set of bins. We calculate the average temperature  $T_{i,j}^{\text{av}} \equiv \overline{T(\epsilon_{V_{ij}})}$  of the pixels within this bin. The average line width  $\overline{\lambda_{w,T_{i,j}^{\text{av}}}}$  for this bin will then be given by Equation (5), replacing the temperature by this average temperature in the bin. The emissivity for all pixels within this bin is then set to the corresponding emissivity bin value  $\epsilon_{V_{ij}}$ . A Gaussian function is then constructed for all pixels within this emissivity bin linked to the velocity bin  $V_i$ , having a total emissivity  $\epsilon_{V_{ij}}$ , Doppler shifted by a velocity  $v_i$ , and with a FWHM  $\overline{\lambda_{w,T_{i,j}^{\text{av}}}}$ .

FOMO-IDL requires the numerical box to have uniform grids (although it will be extended to non-uniform grids in the future). Based on given numerical grids new grids are constructed for the voxels. The resolution in the new grids is set based on the original numerical resolution and the LOS, aiming at making the forward modeling as precise as possible. For instance, assuming that the LOS is in the  $(x, y)$  plane and that the resolution elements of the original grids are  $dx$  and  $dy$ , then the resolution step of pixels along the LOS is given by  $\min\{dy, \sqrt{((dx \cos(\theta))^2 + (dy \sin(\theta))^2)}\}$  for  $dx < dy$  and  $\min\{dx, \sqrt{((dx \cos(\theta))^2 + (dy \sin(\theta))^2)}\}$  for  $dy < dx$  (and is set equal to  $dx$  when  $dx = dy$ ). Here  $\theta$  is the angle in **Figure 1** and the plane of the image corresponds to the  $(x, y)$  plane.

Interpolations in FOMO-IDL, as in FOMO-C, are linear and occur twice per run. The first time is for calculating the emissivity values (Equation 4) corresponding to the physical variables  $n_e$ ,  $T$  in the numerical box from the look-up table of the contribution function. The second time is for the integration along the LOS in the new (uniform) grid, where, before summing, the set of Doppler shifted emissivity pixels calculated from the binning step is interpolated into the new grid along the LOS.

More details about FOMO-IDL, especially on the practical use, can be found in the online wiki of the FOMO project at <https://wiki.esat.kuleuven.be/FoMo/>.

## 2.4. FoMo-GS

FOMO-GS is an alternative version of the FOMO code in which the radio emission is computed, instead of the EUV emission (as in FOMO-C and FOMO-IDL). For EUV emission, the local density, temperature and velocity is the required information for the computation of the emission. However, for radio emission entirely different quantities are important. A first approximation for the gyrosynchrotron emission for coronal plasmas is given

by Dulk and Marsh (1982). In their formulae, it is apparent that rather the magnitude and direction of the magnetic field, the number density of non-thermal particles, and the power law index of the particle distribution are important parameters for the gyrosynchrotron emission.

Thus, prior to running FOMO-GS, it is essential for the user to choose a distribution of non-thermal particles in the simulation domain. One possibility is to take the number density proportional to the total number of electrons in each simulation cell (as was done in Reznikova et al., 2014, 2015; Kuznetsov et al., 2015, although computing the density with energetic tracer particles may be more accurate). Moreover, the user needs to make a choice on the power law of non-thermal particles (which may differ from point to point in the simulation). Finally, a pitch-angle distribution for the non-thermal electrons needs to be fixed.

For the projection along the LOS, FOMO-GS follows the implementation of FOMO-IDL, using an angle  $l$  and  $b$  to rotate the simulation data cube (following Equation 2). The angle  $\theta$  of the magnetic field with the LOS is computed from the simulation by

$$\cos \theta = \frac{\vec{z} \cdot \vec{B}}{B}, \quad (11)$$

where  $B$  is the magnitude of the magnetic field and the unit vector  $\vec{z}$  along the LOS was defined in Equation (8). Then, the necessary information along the LOS is extracted by doing a nearest-neighbor interpolation of the LOS voxels into the original simulation grid.

Subsequently, the physical quantities on the LOS voxels are fed into the fast gyrosynchrotron code by Fleishman and Kuznetsov (2010). This code computes for each voxel the emissivity and absorption coefficient. It is based on the formulae given in Ramaty (1969), but implements several optimizations to speed up the computation time drastically. Then, the fast gyrosynchrotron code performs a 1D radiative transfer calculation along the LOS (see Equation 25 in Ramaty, 1969). As a result, the intensity in left- and right-polarized radio waves is obtained in each observational pixel, which allows for the computation of the intensity and polarization.

Once again, for the practical usage of FOMO-GS we refer to the webpage of the FOMO project at <https://wiki.esat.kuleuven.be/FoMo/>.

## 2.5. Data Handling

Often the simulation data are very large. It is thus not trivial to fit all the simulation data into the computer memory, let alone the triangulation and forward model. Therefore, a clever choice of a subset of the simulation is often necessary for all three flavors of FOMO.

Alternatively, it may be possible to split the simulation in several 2D slices or 3D subsets (that contain the LOS rays), and to perform the rendering on those. Afterwards the partial artificial simulations may be rejoined. The user can write a program to do this in an automated fashion.

Such a splitting approach may also lead to further parallelization over multiple computers (e.g., with MPI),

since rendering all subsets of the simulation data is independent from the other subsets and is thus massively parallel, both in computational power and memory.

## 2.6. Validation

For performing the code validation and performance analysis, we have taken a snapshot from simulations similar to the one in Antolin et al. (2014). In the simulation, an overdense coronal loop was simulated subjected to an initial transverse velocity. The loop starts to oscillate, and generates turbulence-like Kelvin-Helmholtz vortices at the edge. The simulation is performed for a quarter of the loop (given the symmetry of the transverse mode) with a numerical resolution of  $512 \times 256 \times 50$  points (with the smallest number of points along the magnetic field,  $z$  in **Figure 2**). The datacube that is fed into the forward modeling is  $512 \times 512 \times 50$ , and has now also the data mirrored with respect to the mid-plane of the loop. For more details, the reader is referred to Antolin et al. (2014).

For the validation, we render the simulation at snapshot 251 in the Fe XII 193.509 Å spectral line, both with FoMo-C and FoMo-IDL. The resolution for both renderings is chosen as  $724 \times 50 \times 100$  ( $x'y'x\lambda$ ), and with 724 points along the LOS direction. The simulation is viewed with an angle of  $45^\circ$  with respect to the direction of the initial velocity perturbation. We choose a quasi-random position ( $x'_s, y'_s$ ) in the resulting data-cube, within the loop (i.e., where the emission is higher), indicated with a white “+” in **Figure 2**. In the left panel of **Figure 3**, we show the specific intensity  $I(\lambda, x'_s, y'_s)$  at this position, for both FoMo-C (with pluses) and FoMo-IDL (with diamonds). It is clear that the results from both codes are very close to each other.

To quantify the discrepancy between the two codes better, we have displayed a histogram of the difference between the specific intensity in both codes ( $|I_{FoMo-C} - I_{FoMo-IDL}|$ ) in the right panel of **Figure 3**. Here as well, the majority of the simulation point lie within  $10 \text{ ergs cm}^{-2} \text{ s}^{-1} \text{ sr}^{-1} \text{ Å}^{-1}$  from each other, compared to a maximum specific intensity of  $3 \times 10^4 \text{ ergs cm}^{-2} \text{ s}^{-1} \text{ sr}^{-1} \text{ Å}^{-1}$ .

## 2.7. Performance

We have compared the performance of the FOMO-IDL and FOMO-C codes using the same rendering as described in Section 2.6. The performance tests were done on a machine with two Intel Xeon E5-2630 v3 CPUs, each with eight cores (and thus 16 threads) running at 2.40 GHz. The machine has 128 GB memory. The results of the performance test are shown in **Table 2**.

FOMO-C generally uses a lot of memory (as also shown in the table). This is mainly because of the memory-intensive computation of the triangulation by CGAL. It is clear from the table that FOMO-IDL outperforms FOMO-C. This is no surprise, because the FOMO-IDL code has been optimized for the forward modeling of regularly gridded data. Moreover, when a favorable angle is chosen along an axis of the simulation ( $0$  or  $90^\circ$ ), the computation time of FOMO-IDL is more than halved.

This also indicates in which direction FOMO-C could improve in future releases.

One of the advantages of FOMO-C is that it allows for easy parallelization via OpenMP. In **Table 2**, we have studied the computation times for FOMO-C when running with 1, 16, or 32 threads on a 16 core machine. Going from the non-parallel run to 16 threads, the code is sped up by roughly a factor 10. The non-perfect speed-up is mainly because the construction of the CGAL triangulation is not happening in parallel and the read-in and write-out times of the large data files. Adding more threads does not benefit strongly the efficiency of the computation.

**TABLE 2 | Performance of the FoMo-C and FoMo-IDL code.**

Code and usage	Duration (s)	Maximum memory (MB)
FoMo-IDL	1048	382
FoMo-C with OpenMP (32 threads on 16 cores)	1481	15,591
FoMo-C with OpenMP (16 threads on 16 cores)	1653	15,589
FoMo-C without OpenMP	16,814	15,587

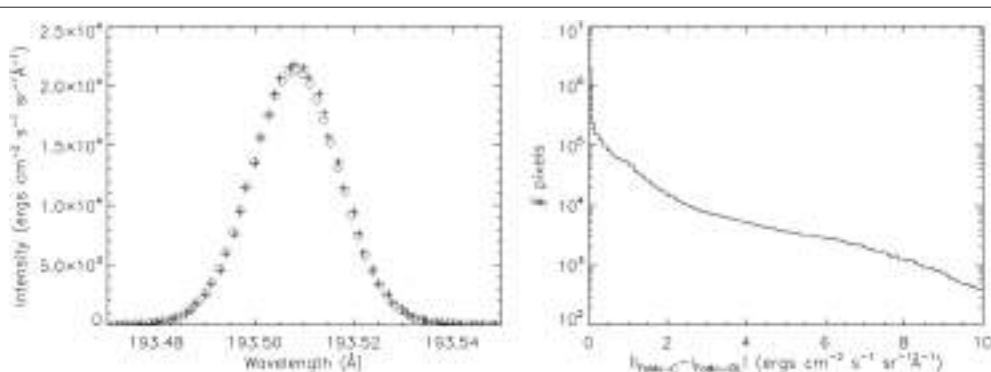


**FIGURE 3 |** The left panel shows the specific intensity as a function of the wavelength, for a pixel in the center of the numerical domain. The pluses show the results from FoMo-C, while the diamonds show the results from FoMo-IDL. The right panel displays a histogram of the differences of specific intensity  $|I_{FoMo-C} - I_{FoMo-IDL}|$  between the results of FoMo-C and FoMo-IDL. The vertical axis shows the number of pixels with the deviation indicated on the horizontal axis (in  $\text{ergs cm}^{-2} \text{ s}^{-1} \text{ sr}^{-1} \text{ Å}^{-1}$ ).

In principle, it is possible to parallelize the code using MPI [chopping up the “observation” plane in roughly equal parts, and doing parallel interpolation of the emissivity  $\tilde{\epsilon}$  in Equation (7)], but we have not tested this in practice.

### 3. CONCLUSIONS

In this article, we have given an overview of the techniques used in the FOMO code. FOMO is a numerical code for the forward modeling of emission from coronal plasmas. There are three versions of FOMO. The purpose of FOMO-C and FOMO-IDL is equivalent, and they compute the EUV emission from optically thin coronal plasmas by direct integration of the emissivity along the LOS. To this end, they both use CHIANTI emissivity tables. They both have the option to compute the emission in imaging telescopes (in particular SDO/AIA) and spectrometers (such as Hinode/EIS). FOMO-C has more features than FOMO-IDL: it also has parallelism and can perform forward modeling for non-regular grids (adaptive mesh or unstructured), although the usage of FOMO-IDL will be extended to non-uniform grids as well.

The third part of FOMO is the FOMO-GS code. FOMO-GS computes gyrosynchrotron emission from coronal plasmas. It uses the fast gyrosynchrotron codes (Fleishman and Kuznetsov, 2010) as backend to perform the 1D radiative transfer along the LOS. It thus also computes the gyrosynchrotron emission from optically thick plasmas.

FOMO was developed with the aim of performing forward modeling of coronal wave models. It has been previously used for the modeling of sausage waves (Antolin and Van Doorsselaere,

2013; Reznikova et al., 2014, 2015; Kuznetsov et al., 2015), kink waves (Antolin et al., 2014, 2015), and slow waves (De Moortel et al., 2015; Yuan et al., 2015). However, the code has a much wider applicability.

### AUTHOR CONTRIBUTIONS

TVD initiated the development of FoMo through his Odysseus grant and is the main developer for FoMo-C. PA is the main developer of FoMo-IDL. DY is a major contributor of FoMo-C. VR has written the FoMo-GS code. NM has developed the FLASH example for FoMo-C. TVD has written the first draft of the current paper, and received input from all co-authors.

### FUNDING

Odysseus funding (FWO-Vlaanderen), IAP P7/08 CHARM (Belspo), GOA-2015-014 (KU Leuven), NAOJ Visiting Fellows Program. NM is a PhD student of the FWO-Vlaanderen.

### ACKNOWLEDGMENTS

TVD thanks the hospitality of PA and the National Astronomical Observatory of Japan during a visit in which part of the coding on FOMO was done. Discussion at the ISSI and ISSI-BJ also contributed in the development of the code. Numerical computations were carried out on Cray XC30 at the Center for Computational Astrophysics, National Astronomical Observatory of Japan.

### REFERENCES

- Antolin, P., Okamoto, T. J., De Pontieu, B., Uitenbroek, H., Van Doorsselaere, T., and Yokoyama, T. (2015). Resonant absorption of transverse oscillations and associated heating in a solar prominence. II. Numerical aspects. *Astrophys. J.* 809:72. doi: 10.1088/0004-637X/809/1/72
- Antolin, P., and Van Doorsselaere, T. (2013). Line-of-sight geometrical and instrumental resolution effects on intensity perturbations by sausage modes. *Astron. Astrophys.* 555:A74. doi: 10.1051/0004-6361/201220784
- Antolin, P., Yokoyama, T., and Van Doorsselaere, T. (2014). Fine strand-like structure in the solar corona from magnetohydrodynamic transverse oscillations. *Astrophys. J. Lett.* 787:L22. doi: 10.1088/2041-8205/787/2/L22
- Arregui, I., Andries, J., Van Doorsselaere, T., Goossens, M., and Poedts, S. (2007). MHD seismology of coronal loops using the period and damping of quasi-mode kink oscillations. *Astron. Astrophys.* 463, 333–338. doi: 10.1051/0004-6361:20065863
- Aschwanden, M. J. (2011). Solar stereoscopy and tomography. *Living Rev. Solar Phys.* 8:5. doi: 10.12942/lrsp-2011-5
- Asensio Ramos, A., and Arregui, I. (2013). Coronal loop physical parameters from the analysis of multiple observed transverse oscillations. *Astron. Astrophys.* 554:A7. doi: 10.1051/0004-6361/201321428
- Berner, P., Edwards, C., Lemen, J., Rausch, A., Schrijver, C., Shine, R., et al. (2012). Initial calibration of the Atmospheric Imaging Assembly (AIA) on the Solar Dynamics Observatory (SDO). *Solar Phys.* 275, 41–66. doi: 10.1007/s11207-011-9804-8
- De Moortel, I., Antolin, P., and Van Doorsselaere, T. (2015). Observational signatures of waves and flows in the solar corona. *Solar Phys.* 290, 399–421. doi: 10.1007/s11207-014-0610-y
- De Moortel, I., and Nakariakov, V. M. (2012). Magnetohydrodynamic waves and coronal seismology: an overview of recent results. *R. Soc. Lond. Philos. Trans. A* 370, 3193–3216. doi: 10.1098/rsta.2011.0640
- Del Zanna, G., O’Dwyer, B., and Mason, H. E. (2011). SDO AIA and Hinode EIS observations of “warm” loops. *A&A* 535:A46. doi: 10.1051/0004-6361/201117470
- Dere, K. P., Landi, E., Mason, H. E., Monsignori Fossi, B. C., and Young, P. R. (1997). CHIANTI - an atomic database for emission lines. *Astron. Astrophys. Suppl.* 125, 149–173. doi: 10.1051/aas:1997368
- Dulk, G. A., and Marsh, K. A. (1982). Simplified expressions for the gyrosynchrotron radiation from mildly relativistic, nonthermal and thermal electrons. *Astrophys. J.* 259, 350–358. doi: 10.1086/160171
- Fang, X., Yuan, D., Van Doorsselaere, T., Keppens, R., and Xia, C. (2015). Modeling of reflective propagating slow-mode wave in a flaring loop. *Astrophys. J.* 813:33. doi: 10.1088/0004-637X/813/1/33
- Fleishman, G. D., and Kuznetsov, A. A. (2010). Fast gyrosynchrotron codes. *Astrophys. J.* 721, 1127–1141. doi: 10.1088/0004-637X/721/2/1127
- Fryxell, B., Olson, K., Ricker, P., Timmes, F. X., Zingale, M., Lamb, D. Q., et al. (2000). FLASH: an adaptive mesh hydrodynamics code for modeling astrophysical thermonuclear flashes. *Astrophys. J. Suppl.* 131, 273–334. doi: 10.1086/317361
- Gibson, S. E. (2015). Data-model comparison using FORWARD and CoMP. *Proc. Int. Astron. Union* 305, 245–250. doi: 10.1017/S1743921315004846
- Gibson, S., Kucera, T., White, S. M., Dove, J., Fan, Y., Forland, B., et al. (2016). FORWARD: A toolset for multiwavelength coronal magnetometry. *Front. Astron. Space Sci.* 3:8. doi: 10.3389/fspas.2016.00008
- Goossens, M., Arregui, I., Ballester, J. L., and Wang, T. J. (2008). Analytic approximate seismology of transversely oscillating coronal loops. *Astron. Astrophys.* 484, 851–857. doi: 10.1051/0004-6361:200809728

- Gruszecki, M., Nakariakov, V. M., and Van Doorsselaere, T. (2012). Intensity variations associated with fast sausage modes. *Astron. Astrophys.* 543:A12. doi: 10.1051/0004-6361/201118168
- Krishna Prasad, S., Banerjee, D., and Van Doorsselaere, T. (2014). Frequency-dependent damping in propagating slow magneto-acoustic waves. *Astrophys. J.* 789:118. doi: 10.1088/0004-637X/789/2/118
- Krishna Prasad, S., Banerjee, D., Van Doorsselaere, T., and Singh, J. (2012). Omnipresent long-period intensity oscillations in open coronal structures. *Astron. Astrophys.* 546:A50. doi: 10.1051/0004-6361/201219885
- Kumar, P., Innes, D. E., and Inhester, B. (2013). Solar dynamics observatory/atmospheric imaging assembly observations of a reflecting longitudinal wave in a coronal loop. *Astrophys. J. Lett.* 779:L7. doi: 10.1088/2041-8205/779/1/L7
- Kumar, P., Nakariakov, V. M., and Cho, K.-S. (2015). X-Ray and EUV observations of simultaneous short and long period oscillations in hot coronal arcade loops. *Astrophys. J.* 804:4. doi: 10.1088/0004-637X/804/1/4
- Kuznetsov, A. A., Van Doorsselaere, T., and Reznikova, V. E. (2015). Simulations of gyrosynchrotron microwave emission from an oscillating 3D magnetic loop. *Solar Phys.* 290, 1173–1194. doi: 10.1007/s11207-015-0662-7
- Landi, E., Young, P. R., Dere, K. P., Del Zanna, G., and Mason, H. E. (2013). CHIANTI-an atomic database for emission lines. XIII. Soft X-Ray improvements and other changes. *Astrophys. J.* 763:86. doi: 10.1088/0004-637X/763/2/86
- Lee, D., Deane, A. E., and Federrath, C. (2009). “A new multidimensional unsplit MHD solver in FLASH3,” in *Numerical Modeling of Space Plasma Flows: ASTRONUM-2008, volume 406 of Astronomical Society of the Pacific Conference Series*, eds N. V. Pogorelov, E. Audit, P. Colella, and G. P. Zank (San Francisco, CA), 243.
- Liu, W., and Ofman, L. (2014). Advances in observing various coronal EUV waves in the SDO era and their seismological applications (invited review). *Solar Phys.* 289, 3233–3277. doi: 10.1007/s11207-014-0528-4
- Mandal, S., Magyar, N., Yuan, D., Banerjee, D., and Van Doorsselaere, T. (2016). Forward modeling of propagating slow waves in coronal loops and its frequency-dependent damping. *Astrophys. J.* doi: 10.1088/0004-637X/789/2/118. Available online at: <http://adsabs.harvard.edu/abs/2016arXiv160200787M>
- Marsh, M. S., Walsh, R. W., and Plunkett, S. (2009). Three-dimensional coronal slow modes: toward three-dimensional seismology. *Astrophys. J.* 697, 1674–1680. doi: 10.1088/0004-637X/697/2/1674
- Mossessian, G., and Fleishman, G. D. (2012). Modeling of gyrosynchrotron radio emission pulsations produced by magnetohydrodynamic loop oscillations in solar flares. *Astrophys. J.* 748:140. doi: 10.1088/0004-637X/748/2/140
- Nakariakov, V. M., and Ofman, L. (2001). Determination of the coronal magnetic field by coronal loop oscillations. *Astron. Astrophys.* 372, L53–L56. doi: 10.1051/0004-6361:20010607
- Nakariakov, V. M., and Verwichte, E. (2005). Coronal waves and oscillations. *Living Rev. Solar Phys.* 2:3. doi: 10.12942/lrsp-2005-3
- Nita, G. M., Fleishman, G. D., Kuznetsov, A. A., Kontar, E. P., and Gary, D. E. (2015). Three-dimensional radio and X-Ray modeling and data analysis software: revealing flare complexity. *Astrophys. J.* 799:236. doi: 10.1088/0004-637X/799/2/236
- Okamoto, T. J., Antolin, P., De Pontieu, B., Uitenbroek, H., Van Doorsselaere, T., and Yokoyama, T. (2015). Resonant absorption of transverse oscillations and associated heating in a solar prominence. I. Observational aspects. *Astrophys. J.* 809:71. doi: 10.1088/0004-637X/809/1/71
- Ramaty, R. (1969). Gyrosynchrotron emission and absorption in a magnetoactive plasma. *Astrophys. J.* 158:753. doi: 10.1086/150235
- Reznikova, V. E., Antolin, P., and Van Doorsselaere, T. (2014). Forward modeling of gyrosynchrotron intensity perturbations by sausage modes. *Astrophys. J.* 785:86. doi: 10.1088/0004-637X/785/2/86
- Reznikova, V. E., Van Doorsselaere, T., and Kuznetsov, A. A. (2015). Perturbations of gyrosynchrotron emission polarization from solar flares by sausage modes: forward modeling. *Astron. Astrophys.* 575:A47. doi: 10.1051/0004-6361/201424548
- The CGAL Project (2015). *CGAL User and Reference Manual, 4.6.2 Edn.* CGAL Editorial Board.
- Van Doorsselaere, T., Nakariakov, V. M., and Verwichte, E. (2007). Coronal loop seismology using multiple transverse loop oscillation harmonics. *Astron. Astrophys.* 473, 959–966. doi: 10.1051/0004-6361:20077783
- Vasheghani Farahani, S., Hornsey, C., Van Doorsselaere, T., and Goossens, M. (2014). Frequency and damping rate of fast sausage waves. *Astrophys. J.* 781:92. doi: 10.1088/0004-637X/781/2/92
- Verwichte, E., Aschwanden, M. J., Van Doorsselaere, T., Foullon, C., and Nakariakov, V. M. (2009). Seismology of a large solar coronal loop from EUVI/STEREO observations of its transverse oscillation. *Astrophys. J.* 698:397. doi: 10.1088/0004-637X/698/1/397
- Wang, T. (2011). Standing slow-mode waves in hot coronal loops: observations, modeling, and coronal seismology. *Space Sci. Rev.* 158, 397–419. doi: 10.1007/s11214-010-9716-1
- Yuan, D., Van Doorsselaere, T., Banerjee, D., and Antolin, P. (2015). Forward modeling of standing slow modes in flaring coronal loops. *Astrophys. J.* 807:98. doi: 10.1088/0004-637X/807/1/98

**Conflict of Interest Statement:** The authors declare that the research was conducted in the absence of any commercial or financial relationships that could be construed as a potential conflict of interest.

Copyright © 2016 Van Doorsselaere, Antolin, Yuan, Reznikova and Magyar. This is an open-access article distributed under the terms of the Creative Commons Attribution License (CC BY). The use, distribution or reproduction in other forums is permitted, provided the original author(s) or licensor are credited and that the original publication in this journal is cited, in accordance with accepted academic practice. No use, distribution or reproduction is permitted which does not comply with these terms.



# ROAM: A Radial-Basis-Function Optimization Approximation Method for Diagnosing the Three-Dimensional Coronal Magnetic Field

**Kevin Dalmasse<sup>1\*</sup>, Douglas W. Nychka<sup>2</sup>, Sarah E. Gibson<sup>3</sup>, Yuhong Fan<sup>3</sup> and Natasha Flyer<sup>2</sup>**

<sup>1</sup> CISL/HAO, National Center for Atmospheric Research, Boulder, CO, USA, <sup>2</sup> CISL, National Center for Atmospheric Research, Boulder, CO, USA, <sup>3</sup> HAO, National Center for Atmospheric Research, Boulder, CO, USA

## OPEN ACCESS

### Edited by:

Xueshang Feng,  
State Key Laboratory of Space Weather, China

### Reviewed by:

Gordon James Duncan Petrie,  
National Solar Observatory, USA  
Keiji Hayashi,  
Nagoya University, Japan

### \*Correspondence:

Kevin Dalmasse  
dalmasse@ucar.edu

### Specialty section:

This article was submitted to  
Stellar and Solar Physics,  
a section of the journal  
*Frontiers in Astronomy and Space Sciences*

**Received:** 27 May 2016

**Accepted:** 08 July 2016

**Published:** 26 July 2016

### Citation:

Dalmasse K, Nychka DW, Gibson SE, Fan Y and Flyer N (2016) ROAM: A Radial-Basis-Function Optimization Approximation Method for Diagnosing the Three-Dimensional Coronal Magnetic Field. *Front. Astron. Space Sci.* 3:24. doi: 10.3389/fspas.2016.00024

The Coronal Multichannel Polarimeter (CoMP) routinely performs coronal polarimetric measurements using the Fe XIII 10747 and 10798 lines, which are sensitive to the coronal magnetic field. However, inverting such polarimetric measurements into magnetic field data is a difficult task because the corona is optically thin at these wavelengths and the observed signal is therefore the integrated emission of all the plasma along the line of sight. To overcome this difficulty, we take on a new approach that combines a parameterized 3D magnetic field model with forward modeling of the polarization signal. For that purpose, we develop a new, fast and efficient, optimization method for model-data fitting: the Radial-basis-functions Optimization Approximation Method (ROAM). Model-data fitting is achieved by optimizing a user-specified log-likelihood function that quantifies the differences between the observed polarization signal and its synthetic/predicted analog. Speed and efficiency are obtained by combining sparse evaluation of the magnetic model with radial-basis-function (RBF) decomposition of the log-likelihood function. The RBF decomposition provides an analytical expression for the log-likelihood function that is used to inexpensively estimate the set of parameter values optimizing it. We test and validate ROAM on a synthetic test bed of a coronal magnetic flux rope and show that it performs well with a significantly sparse sample of the parameter space. We conclude that our optimization method is well-suited for fast and efficient model-data fitting and can be exploited for converting coronal polarimetric measurements, such as the ones provided by CoMP, into coronal magnetic field data.

**Keywords:** Sun: corona, Sun: magnetic fields, Sun: infrared, methods: statistical, methods: radial basis functions

## 1. INTRODUCTION

Modification to the polarization of light is one of the many signatures of a non-zero magnetic field in the solar corona, and more generally, in the solar atmosphere (e.g., Stenflo, 2015, and references therein). Several mechanisms producing or modifying the polarization of light have been observed and studied in the solar corona at different wavelengths including, but not limited to, the Zeeman

and Hanle effects (see e.g., Hale, 1908; Hanle, 1924; Bird et al., 1985; White and Kundu, 1997; Casini and Judge, 1999; Lin et al., 2004; Gibson et al., 2016, and references therein). The former induces a frequency-modulated polarization while the latter induces a depolarization of scattered light (e.g., Sahal-Brechot et al., 1977; Bommier and Sahal-Brechot, 1982; Rachmeler et al., 2013; López Ariste, 2015). Both mechanisms allow us to probe the strength and direction of the coronal magnetic field. Coronal polarization associated with these two mechanisms is currently measured above the solar limb by the Coronal Multichannel Polarimeter from forbidden coronal lines such as the Fe XIII lines (10747 Å and 10798 Å; Tomczyk et al., 2008). For these two lines, the circular polarization signal is dominated by the Zeeman effect while the linear polarization signal is dominated by the Hanle effect (e.g., Judge et al., 2006).

Translating the polarization maps of CoMP into magnetic field maps is a challenging task. The main difficulty is that the solar corona is optically thin at these wavelengths (e.g., Rachmeler et al., 2012; Plowman, 2014). The observed signal is therefore the integrated emission of all the plasma along the line of sight (LOS). Hence, the polarization maps cannot, in general, be directly inverted into 2D maps of the plane-of-sky (POS) magnetic field. On the other hand, extracting individual magnetic information at specific positions along the LOS is extremely difficult without stereoscopic observations (e.g., Kramar et al., 2014). Another limitation is that the Hanle effect associated with the aforementioned forbidden infrared lines operates in the saturated regime (e.g., Casini and Judge, 1999; Tomczyk et al., 2008). Accordingly the linear polarization signal measured by CoMP is sensitive to the direction of the magnetic field but not its strength. Deriving the magnetic field associated with the polarization maps of CoMP therefore requires a different approach than the single point inversion that can be done with, e.g., photospheric polarimetric measurements.

The alternate approach we propose to follow is to combine a parameterized 3D magnetic field model with forward modeling of the polarization signal observed by CoMP. For that purpose, we take advantage of the Coronal Line Emission (CLE) polarimetry code developed by Casini and Judge (1999) and integrated into the FORWARD package. FORWARD<sup>1</sup> is a Solar Soft<sup>2</sup> IDL package designed to perform forward modeling of various observables including, e.g., visible/IR/UV polarimetry, EUV/X-ray/radio imaging, and white-light coronagraphic observations (Gibson et al., 2016). The goal is then to optimize a user-specified likelihood function comparing the polarization signal predicted by FORWARD to the real one and find the parameters of the magnetic field model such that the predicted signal fits the real data.

In the present paper, we develop and test a new method for performing fast and efficient optimization in a  $d$ -dimensional parameter space that may be used for converting the polarization observations of CoMP into magnetic field data. The optimization

method, called ROAM (Radial-basis-functions Optimization Approximation Method) is designed to be general enough so that it can be applied independently of the dimension and size of the parameter space, the 3D magnetic field model, the type of observables (provided that one can forward model them), and the form of the likelihood function used for comparing the predicted signal to the real one. ROAM is introduced in Section 2. Section 3 describes the results of multiple applications of ROAM to a synthetic test bed as validation of the optimization method. Our conclusions are then summarized in Section 4.

## 2. METHODS

The goal of this paper is to propose a model-data fitting method to be used for *near-real-time* 3D reconstruction of the solar coronal magnetic field. This requires developing a fast and efficient method for searching for the set of values of the model parameters that optimize a pre-defined function quantifying the differences between the predicted (or forward-modeled) and real data. Although similar approaches are standard in engineering (e.g., Jones et al., 1998), we propose a simplified version and tailored to the context of solar physics. The proposed method, ROAM, combines the computation of a log-likelihood function on a sparse sample of the parameter space with function approximation and is based on the five following steps:

1. Sparse sampling of the parameter space is performed using *Latin Hypercube Sampling* (LHS; McKay et al., 1979; Iman et al., 1981). LHS is a statistical method for generating a random sample of the parameter values in a  $d$ -dimensional space. For a  $d$ -dimensional space of  $n^d$  points ( $n$  is the number of points for each dimension), LHS creates a set,  $\{x_i\}$ , of  $n$  independent points or  $d$ -vectors of the parameter space (an example is given **Figure 1**) that will be referred to as the *design* in the following.
2. The model is computed for each point,  $x_i$ , of the design and used to generate the corresponding predicted observation,  $y(x_i)$ , to be compared with the ground truth,  $y_{gt}$  (which is either an actual observation or a synthetic one for test beds using analytical models or numerical simulations).
3. The set of predicted observations,  $\{y(x_i)\}$ , is then compared to the ground truth by means of a user-specified log-likelihood function

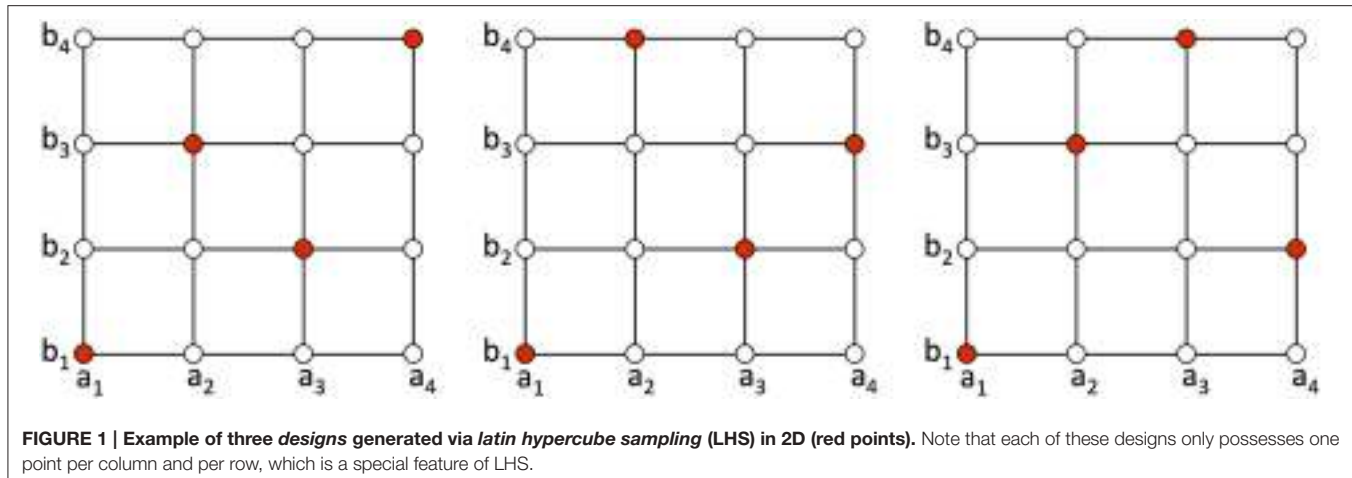
$$\ell(x_i) = \log \mathcal{L} = f(y(x_i) - y_{gt}), \quad (1)$$

where  $\mathcal{L}$  is the likelihood function,  $x_i$  is a  $d$ -vector of the design and  $f$  is a general, user-specified, well-behaved, scalar function. Typically, the likelihood function simplifies to depend on the difference between the observations and the predicted values and function  $f$  reflects that. An explicit expression of  $f$  is given in the section of each test considered in this paper (see Section 3).

4. This log-likelihood function is then approximated using radial-basis-function (RBF) decomposition (see e.g., Powell,

<sup>1</sup><http://www.hao.ucar.edu/FORWARD/>

<sup>2</sup><http://www.lmsal.com/solarsoft/>



1977; Broomhead and Lowe, 1988; Buhmann, 2003; Nychka et al., 2015)

$$\ell(x) \approx \hat{\ell}(x) = \sum_{j=1}^n a_j \varphi_j(\|x - x_j\|) + \sum_{j=1}^{\binom{p+d}{p}} b_j \psi_j(x), \quad (2)$$

$$\begin{aligned} \varphi_j(\|x - x_j\|) &= \|x - x_j\|^{2m-d} \log(\|x - x_j\|), \\ &\text{if } d \text{ is even,} \\ &= \|x - x_j\|^{2m-d}, \text{ if } d \text{ is odd,} \end{aligned} \quad (3) \quad (4)$$

where  $\varphi_j$  is the  $j$ -th RBF centered at point  $x_j$  of the design,  $\|\cdot\|$  is the usual Euclidean norm,  $m \in \mathbb{N}$  is such that  $2m - d > 1$ , and  $\{\psi_j\}$  is a set of polynomials up to degree  $p$  in the dimension  $d$  of the problem with the constraint  $p \leq m - 1$ . In the following, we always use  $p = m - 1$ . When periodic components of the  $d$ -space exist, the value of  $d$  must be modified for the RBF decomposition to take the periodicities into account (an example and further details on handling periodic components are provided in Appendix 2 of Supplementary Material). Note that the particular choice of RBFs,  $\varphi_j$ , in Equations (3) and (4) is called a *Polyharmonic Spline* (see e.g., Duchon, 1977; Madych and Nelson, 1990) and that the polynomial term in Equation (2) is not a regularization term but an additional term that directly comes from the definition of Polyharmonic Splines as minimizers of the energy functional  $\int_{V \subset \mathbb{R}^d} |\nabla^m g|^2 dx$  (which is not modified by adding polynomials of order  $p \leq m - 1$  to  $g$ ). Although required from the definition of Polyharmonic Splines, this polynomial term is particularly beneficial for improving the fitting accuracy and extrapolation away from the RBF centers  $x_j$ , while also ensuring polynomial reproducibility. Note also that the  $a_j$  and  $b_j$  are coefficients determined from the set of  $n$  equations provided by the constraint (the detailed derivation of the coefficients is given in Appendix 1 of Supplementary Material)

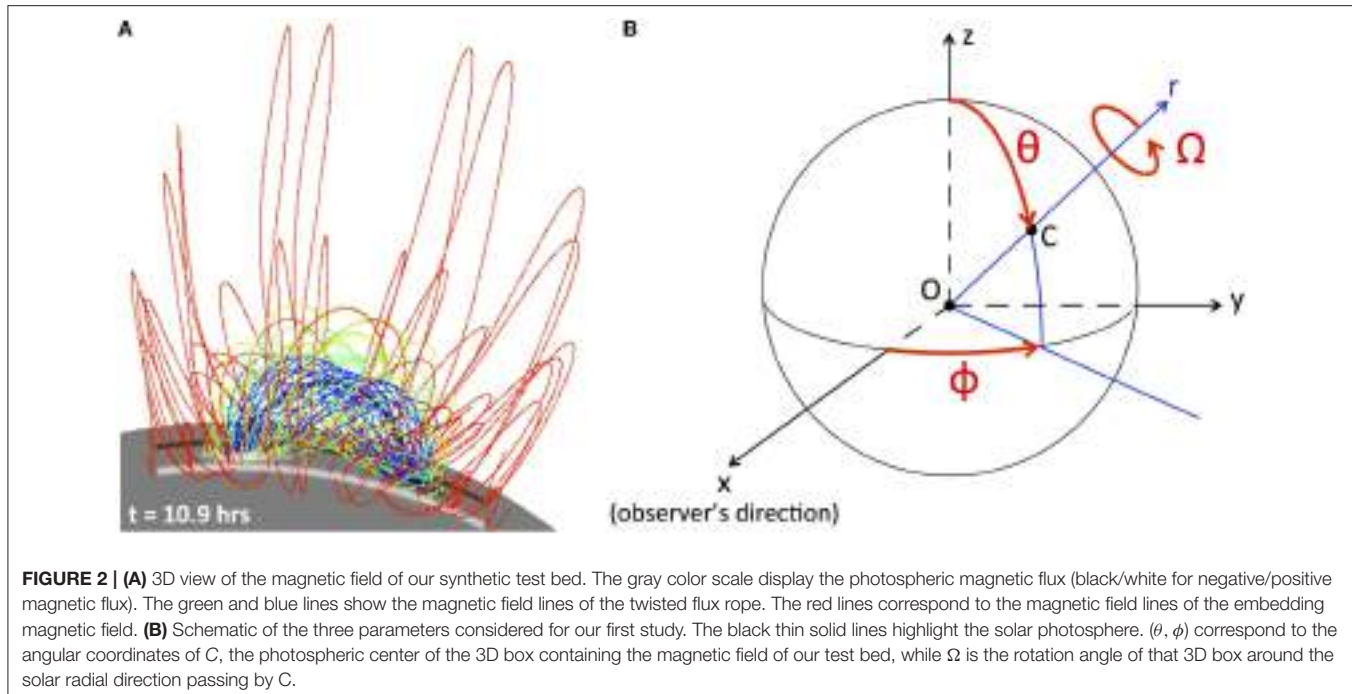
$$\hat{\ell}(x_i) = \ell(x_i). \quad (5)$$

5. Finally, we compute the set of values of the model parameters optimizing the approximated log-likelihood function using

the DFPMIN IDL routine and take it as the maximum-likelihood estimator of the set of values optimizing the exact log-likelihood function. To ensure the reliability of the maximum likelihood estimator (MLE; see Section 3.2) obtained with DFPMIN, we apply the latter from (i) the point of the design that possesses the largest likelihood function value prior to step (4), (ii)  $N^d$  points spanning the entire parameter space and where  $N (\neq n)$  is a relatively low number of points (typically  $N \lesssim 10$ ), and (iii) the likelihood-weighted average position of these  $N^d$  points (i.e., their center of mass). Starting from these  $N^d + 2$  points ensures that at least one of them will lead DFPMIN to converge toward the global maximum when the approximated log-likelihood function contains multiple global and local maxima.

An RBF is a real-valued function that only depends on the Euclidean distance to a center whose location can be set arbitrarily. RBFs provide a class of functions that possess particularly interesting properties such as continuity, smoothness, and infinite differentiability. Their use is widely spread in various branches of applied mathematics and computer science including, e.g., function approximation (Powell, 1993; Buhmann, 2003), data mining and interpolation (Harder and Desmarais, 1972; Lam, 1983; Nychka et al., 2015), numerical analysis with meshfree methods for, e.g., solving partial differential equations in numerical simulations (Fasshauer, 2007; Flyer and Fornberg, 2011; Fornberg and Flyer, 2015; Flyer et al., 2016), computer graphics and machine learning (Broomhead and Lowe, 1988; Boser et al., 1992). Polyharmonic Splines (PHS) are a type of infinitely smooth RBFs that does not possess any free parameter requiring a manual tuning. PHS can therefore be easily implemented for automated calculations.

As previously stated, the goal behind combining sparse calculations of a log-likelihood with an RBF decomposition is to limit the number of model evaluations / forward calculations ( $n$ ) to reduce the computational cost while maintaining a good accuracy on retrieving the exact maximum likelihood. Through low number of model evaluations, we mean to keep  $n \lesssim 100 - 300$  regardless of the dimension of the parameter



space, such that all model evaluations can easily be performed at once in parallel on a high-performance computing cluster. This provides us with a significant advantage as compared with more traditional sequential optimization methods since the effective computational time of our optimization method would only correspond to the computational time of *one* model evaluation (because steps 4 and 5 of the method only take up to  $\lesssim 30$  s as long as  $n \lesssim 500$ ). The optimization method we propose would, in general, also be more advantageous than a full grid search. Indeed, an accurate full grid search would typically require to sample each parameter of the  $d$ -space with about 50 – 100 points at the least. This rapidly leads to a number of model evaluations that is not practical even when using parallel computing. Finally, ROAM should be competitive with genetic algorithms. Genetic algorithms applied to small population samples, e.g.,  $\lesssim$  a few 100 points, typically require on the order of hundred generations to converge (e.g., Louis and Rawlins, 1993; Gibson and Charbonneau, 1998, and references therein), while faster convergence would require larger population sets. For ROAM, the equivalent of a population sample is a design of the parameter space and the equivalent of a generation would be an iteration of ROAM on a smaller parameter space region. For a population/design of  $n$ -points, ROAM should, in principle, be able to converge toward the solution without the need for iterations and, hence, we estimate would be at least 50–100 times faster than a genetic algorithm with the same population/design. In practice, preliminary tests of an iterative implementation of ROAM, which will be published in a subsequent paper, show robust and accurate convergence of ROAM within a few iterations (typically  $< 10$ ).

### 3. RESULTS

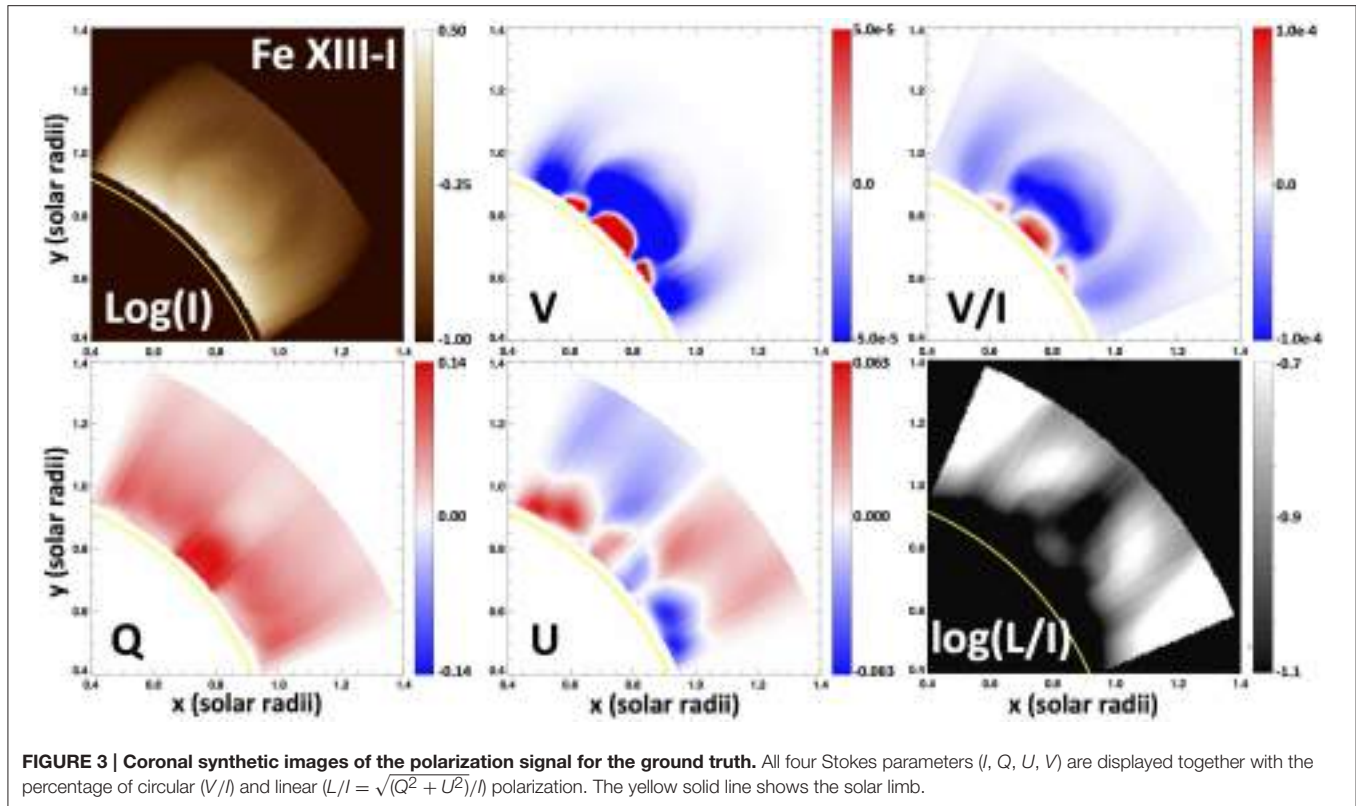
In this section, we present a set of test cases performed on a synthetic test bed to validate ROAM (Section 2) prior to any observational application. The set of test cases aims at assessing the performance of our method in different circumstances and defining a framework of application that will make use of its strengths.

#### 3.1. Numerical Setup for the Forward Calculations

Our goal is to use the proposed optimization method for data-constrained modeling of the solar coronal magnetic field using, in particular, coronal polarimetric observations (i.e., the four Stokes parameters,  $(I, Q, U, V)$ , where Stokes  $I$  is the total line intensity, Stokes  $V$  is the circular polarization, and Stokes  $Q$  and  $U$  are the two components of the linear polarization). All our test cases are therefore applied to a 3D model of magnetic fields chosen to represent scenarios typically observed in the solar atmosphere. The considered magnetic model is that of a 3D coronal magnetic flux rope generated from a 3D MHD numerical simulation of the emergence of twisted magnetic fields in the solar corona (Figure 2A; Fan, 2012).

For the test cases, this magnetic field is assumed to depend on four parameters, i.e., height in the corona ( $h$ ; monotonically depends on the time of the MHD simulation, though not linearly), co-latitude ( $\theta$ ), longitude ( $\phi$ ), and rotation angle<sup>3</sup>

<sup>3</sup>Note that  $(\theta; \phi; \Omega)$  are the co-latitude, longitude, and rotation angle of the numerical box—containing the magnetic field of the MHD simulation—around the Sun, while  $h$  is the actual height of the flux rope in that numerical box (inside of which the solar photosphere is located at  $h = 0$ ).



( $\Omega$ ; of **Figure 2B**). A series of synthetic polarimetric data, referred to as the ground truth (GT) in the following, is generated for the flux rope associated with  $(h; \theta; \phi; \Omega) = (0.16 R_\odot; 45^\circ; 90^\circ; 30^\circ)$  (see **Figure 3**; note that both Stokes  $Q$  and  $U$  are presented in a frame of reference relative to the local vertical, or radial coordinate). All synthetic data are computed using the FORWARD Solar Soft IDL package with a field-of-view (FOV) set to  $y \times z = [0 R_\odot; 1.5 R_\odot]^2$  (where  $y$  and  $z$  are the POS coordinates) and  $x = [-0.79; 0.79] R_\odot$  for the LOS. We use 192 points along both directions for the POS and 80 points for each LOS, leading to spatial resolutions of  $7.6''$  and  $19.3''$  respectively. We limit the forward calculations of the polarization signals to a radial range of  $[1.03; 1.5] R_\odot$ , i.e., the FOV of CoMP. Although the spatial resolution of CoMP is  $4.5''$ , we restrict ourselves to a spatial resolution of  $7.6''$  to allow for relatively fast (about 4–5 min on a MacBook Pro with a 2.7 GHz Intel Core i7 processor) calculations of the polarization signals while maintaining a quasi-CoMP resolution. We impose this FOV and POS spatial resolution to show that CoMP data currently carry meaningful information that can be used to constrain 3D reconstructions of the solar coronal magnetic field.

Finally, it should be emphasized that the considered flux rope possesses a strong degree of symmetry, such that  $B(\theta; \phi = 90; \Omega \pm 180^\circ) = -B(\theta; \phi = 90; \Omega)$ . We will exploit these symmetry properties to test ROAM when faced with a log-likelihood function containing multiple maxima.

### 3.2. Likelihood Function with a Single Maximum

We first apply ROAM in the context of a 3D likelihood function possessing a single maximum. The parameters considered for this study are the co-latitude, longitude, and rotation angle, i.e.,  $(\theta; \phi; \Omega)$ . We then build a likelihood function that takes into account all four Stokes parameters, i.e.,  $I$ ,  $Q$ ,  $U$ , and  $V$ . For the set  $\{x_i\}$  of a design, we first define the log-likelihood function for a given Stokes parameter,  $S = \{I, Q, U, V\}$ , up to a constant, as

$$\ell_S(x_i) = f(S(x_i) - S_{gt}) = - \sum_k \left( S_k(x_i) - S_k^{gt} \right)^2, \quad (6)$$

where  $k$  is the  $k$ -th pixel of the Stokes,  $S$ , image. The final log-likelihood function is then constructed as

$$\ell(x_i) = w_I \ell_I(x_i) + w_Q \ell_Q(x_i) + w_U \ell_U(x_i) + w_V \ell_V(x_i), \quad (7)$$

where the weighting coefficients  $w_S$  were chosen to ensure that  $I$ ,  $Q$ ,  $U$ , and  $V$  similarly contribute to the log-likelihood function, which behavior would otherwise be dominated by the quantity possessing the largest values (here, Stokes  $I$ ). We use  $(w_I; w_Q; w_U; w_V) = (1.3 \times 10^{-4}; 1.9 \times 10^{-2}; 9.2 \times 10^{-2}; 1.2 \times 10^4)$ .

With the log-likelihood function defined in Equation (7), we consider three test cases referred to as 3DN31, 3DN301, and 3DN31ZOOM (see **Table 1**). These three test cases each contain

**TABLE 1 | Characteristics of the test with a likelihood function possessing a single maximum.**

	<i>n</i>	<i>t<sub>elapsed</sub></i> (hrs)	<i>t<sub>full</sub></i> (hrs)	<i>h</i> ( $R_{\odot}$ )	$\theta$ (°)	$\phi$ (°)	$\Omega$ (°)
3DN31	31	2.6	$2.5 \times 10^3$	0.16	[24; 66]	[60; 120]	[0; 90]
3DN301	301	25	$2.3 \times 10^6$	0.16	[24; 66]	[60; 120]	[0; 90]
3DN31ZOOM	31	2.6	$2.5 \times 10^3$	0.16	[42; 48]	[75; 105]	[15; 45]

*n* is the number of points per design. *t<sub>elapsed</sub>* is the elapsed time for forwarding the Stokes images associated with the *n* points of a design in series, while *t<sub>full</sub>* is the total elapsed time that would be required to compute Stokes images for the  $n^3$  points of the 3D parameter space in series. Each test case contains 100 randomly-chosen different designs. The naming convention is such that “xD” indicates the dimension of the parameter space and “Nx” indicates the number of points per design (*n*). The polarimetric data for the ground-truth are associated with  $(h; \theta; \phi; \Omega) = (0.16 R_{\odot}; 45^{\circ}; 90^{\circ}; 30^{\circ})$ .

100 different designs and differ by the number of points in the designs (31 or 301) as well as by the size of the parameter space to allow us to investigate their role on the performances of ROAM. These test cases are designed to allow us to determine the criteria required for the method to ensure robustness and reliability of the results, i.e., such that the method provides a maximum likelihood estimator (MLE) that gives a good approximation of the parameters of the maximum of the exact likelihood function independently of the design and number of points used.

For each test case, the parameters of the RBF decomposition are  $d = 3$ ,  $m = 3$  and  $p = m - 1 = 2$ . We choose the minimum  $m$  satisfying the condition  $2m - d > 1$  (see Section 2). Although  $\theta$ ,  $\phi$ , and  $\Omega$  all are periodic parameters, their corresponding range is smaller than half the associated period and, hence, no periodic effect is expected. As explained Appendix 2 in Supplementary Material, disregarding the periodicity and curvature of the  $d$ -space should not significantly affect the results in such circumstances. We therefore ignore the periodicity of  $\theta$ ,  $\phi$ , and  $\Omega$  in all 3D cases considered in this section, but return to the issue of periodicity in Section 3.3.

**Figure 4** presents 2D dispersion plots of the MLEs obtained for each one of the 100 randomly-chosen designs of the 3DN31 (red), 3DN301 (blue), and 3DN31ZOOM (yellow) cases. For the 3DN31, the MLEs are fairly weakly dispersed for the  $\theta$  parameter, spanning a range of roughly  $10^{\circ}$ . As summarized in **Table 2**, the root mean square (hereafter, rms) of the MLEs,  $\theta_{\text{MLEs}}$ , is  $\approx 47.1^{\circ}$ , which is only  $\approx 2.1^{\circ}$  different from  $\theta_{\text{GT}} = 45^{\circ}$ . This suggests that  $\theta_{\text{MLEs}}$  is not overly sensitive to the design used for the RBF decomposition. These conclusions contrast with both the  $\phi$  and  $\Omega$  parameters. Although  $\phi_{\text{rms}} \approx 92.8^{\circ}$  is very close to the ground-truth,  $\phi_{\text{GT}} = 90^{\circ}$ , the ensemble of solutions,  $\phi_{\text{MLEs}}$ , spans the entire  $\phi$ -range considered for the 3DN31. Similarly poor results are obtained for the set of  $\Omega_{\text{MLEs}}$ , whose rms is  $\approx 21^{\circ}$  off from the ground-truth,  $\Omega_{\text{GT}} = 30^{\circ}$  (see **Table 2**). **Figure 4** further shows that there is a strong coupling between  $\phi$  and  $\Omega$ . In particular, we find that  $\Omega_{\text{MLEs}}$  provide a poor estimation of  $\Omega_{\text{GT}}$  whenever  $\phi_{\text{MLEs}}$  are themselves a poor estimation of  $\phi_{\text{GT}}$  (and vice-versa). Such results trace very poor performances of our optimization method for the chosen setup of the 3DN31 case. The MLE strongly depends on the design used to perform the RBF decomposition. Hence, the MLE obtained from applying

**TABLE 2 | Optimization results for a likelihood function with a single maximum.**

	$\theta_{\text{rms}}$	$\phi_{\text{rms}}$	$\Omega_{\text{rms}}$
3DN31	47.1	92.8	51.0
3DN301	45.2	90.0	30.2
3DN31ZOOM	45.0	89.8	29.7

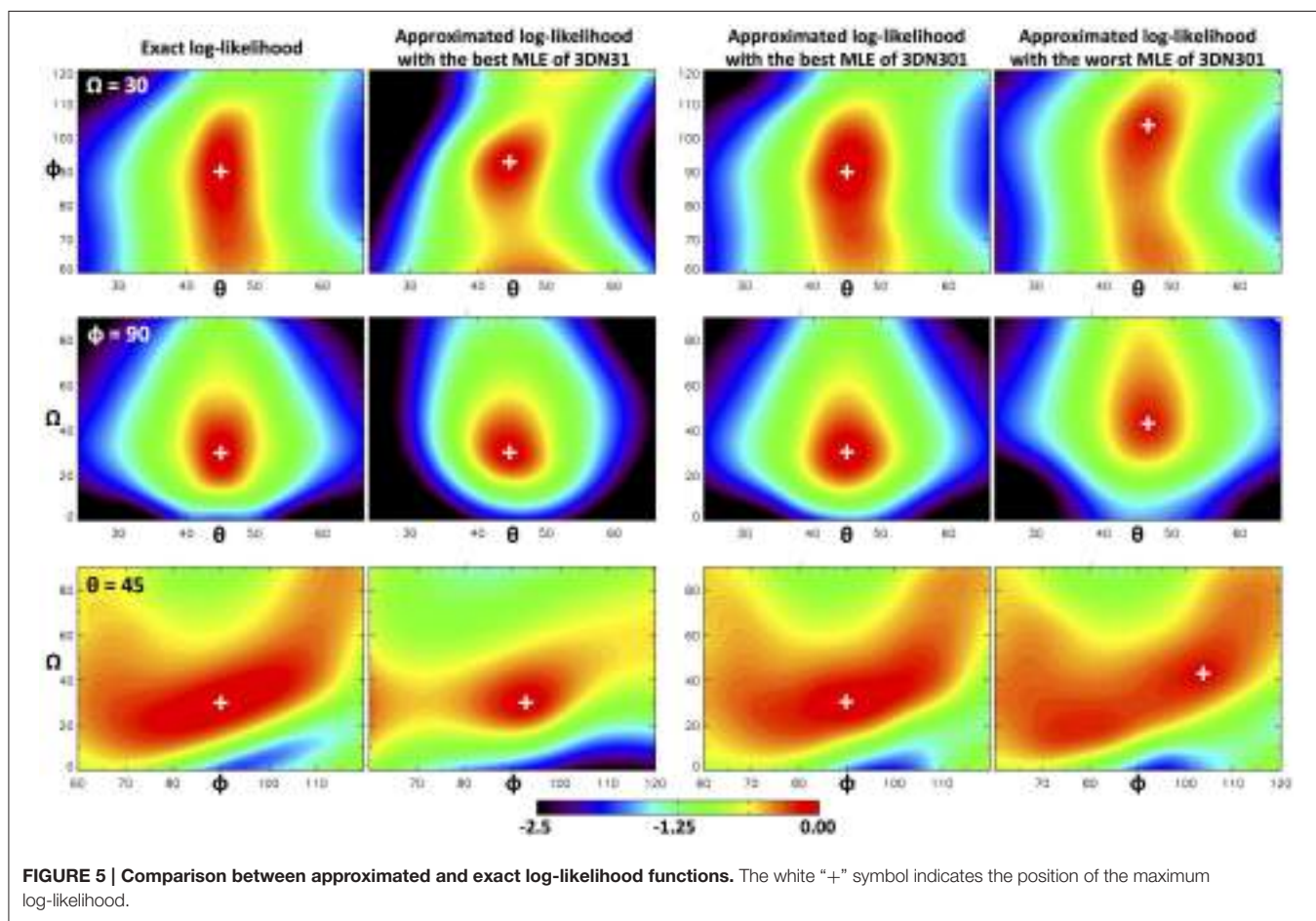
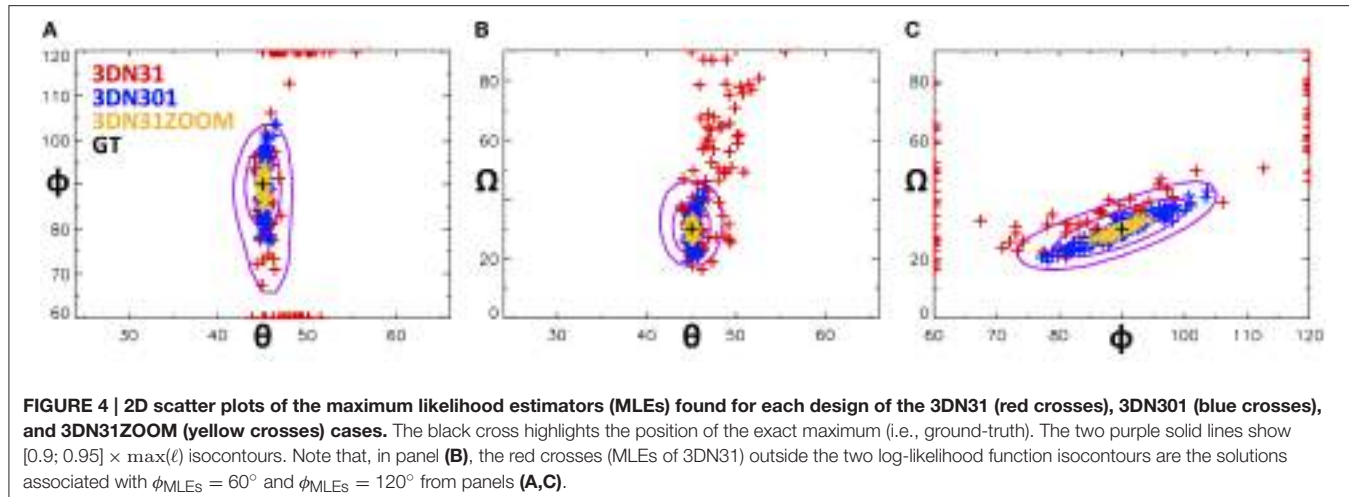
The ground-truth parameters are  $(\theta; \phi; \Omega) = (45^{\circ}; 90^{\circ}; 30^{\circ})$ . All angles are in degrees.

our method to a single design is not reliable for the setup of the 3DN31 case.

When comparing 3DN31 to 3DN301 in **Figure 4**, we can see that increasing the number of points significantly improves the performances of ROAM (see dark blue crosses). For all three parameters, the rms is only  $\approx 0.2^{\circ}$  off the ground-truth for 3DN301. The range spanned by the ensemble of solutions is relatively smaller than for 3DN31,  $\approx 5$  times smaller for  $\theta_{\text{MLEs}}$  and  $\approx 3$  times smaller for both  $\phi_{\text{MLEs}}$  and  $\Omega_{\text{MLEs}}$ . Again, the strong coupling between  $\phi$  and  $\Omega$  is still present but its effect on their uncertainties is strongly reduced as compared with the case 3DN31. Such results are not yet perfect since the set of solutions for both  $\phi$  and  $\Omega$  is spread over  $20^{\circ}$ , which is relatively significant considering the range of their values. However, they do show that increasing the number of points per design strongly helps in reducing (a) the dependence of the MLE on the design used for the RBF decomposition, and (b) the effect of (even strong) coupling of parameters on their uncertainty. Increasing the number of points per design therefore strongly helps in improving the reliability and robustness of the proposed optimization method.

Compared with 3DN31, the 3DN31ZOOM case is used to investigate the effect of focusing the parameter space around a region closer to the exact maximum while keeping the number of points per design constant. **Figure 4** shows that reducing the size of the parameter space is also beneficial for reducing the MLEs dispersion (see yellow crosses). The rms values for all three parameters are as close to the ground-truth as for 3DN301 (see **Table 2**) and the solutions are spanning a range that is  $\approx 4$  times smaller than for 3DN301 and  $\approx 12$  times smaller than for 3DN31. The MLEs are now independent of the design used for the RBF decomposition for  $\theta$  and very weakly dependent on that design for both  $\phi$  and  $\Omega$ . The effect of the strong  $\phi - \Omega$  coupling on their uncertainty is again strongly reduced and even smaller than for the 3DN301 case. These very good results prove that ROAM can perform very well and provide an accurate estimation of the ground-truth parameters when the setup is suitably defined.

**Figure 5** displays 2D cuts of the exact log-likelihood function and the approximated ones associated with the designs of 3DN31 and 3DN301 giving the best MLEs (referred to as *best cases* in the following), as well as the approximated log-likelihood function associated with the design of 3DN301 giving the worst MLEs (referred to as *worst case*). Here, the best (worst) MLE is defined as the MLE minimizing (maximizing) the distance to the ground truth in the parameter space. The best MLE from 3DN31 is  $(\theta; \phi; \Omega)_{\text{best-MLE}} = (44.6^{\circ}; 92.9^{\circ}; 30.1^{\circ})$  while the best MLE from 3DN301 is



$(\theta; \phi; \Omega)_{\text{best-MLE}} = (45.0^\circ; 89.9^\circ; 30.3^\circ)$ . The worst MLE from 3DN301 is  $(\theta; \phi; \Omega)_{\text{best-MLE}} = (46.5^\circ; 103.7^\circ; 43.0^\circ)$ . The figure shows that the approximated log-likelihood function of the best case from 3DN31 gives an overall rough approximation of the exact one both in terms of values and shape. Note, though, that the rms error on the log-likelihood is 0.24, which is rather small

given that  $\max(|\ell(x)|) \approx 3.5$  for the considered parameter space. For the log-likelihood function of the best case from 3DN301, the results are very much better. The approximated log-likelihood function is able to accurately capture both the values and shape of the exact log-likelihood function; the rms error is 0.05, i.e.,  $\approx 5$  times smaller than for the best case of 3DN31. For the

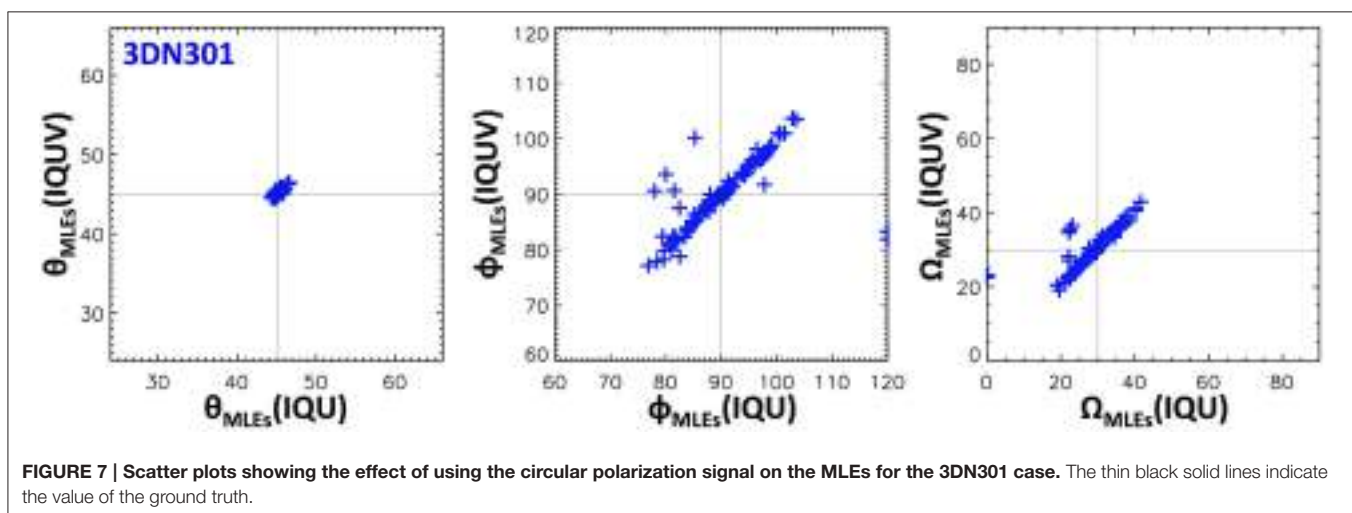
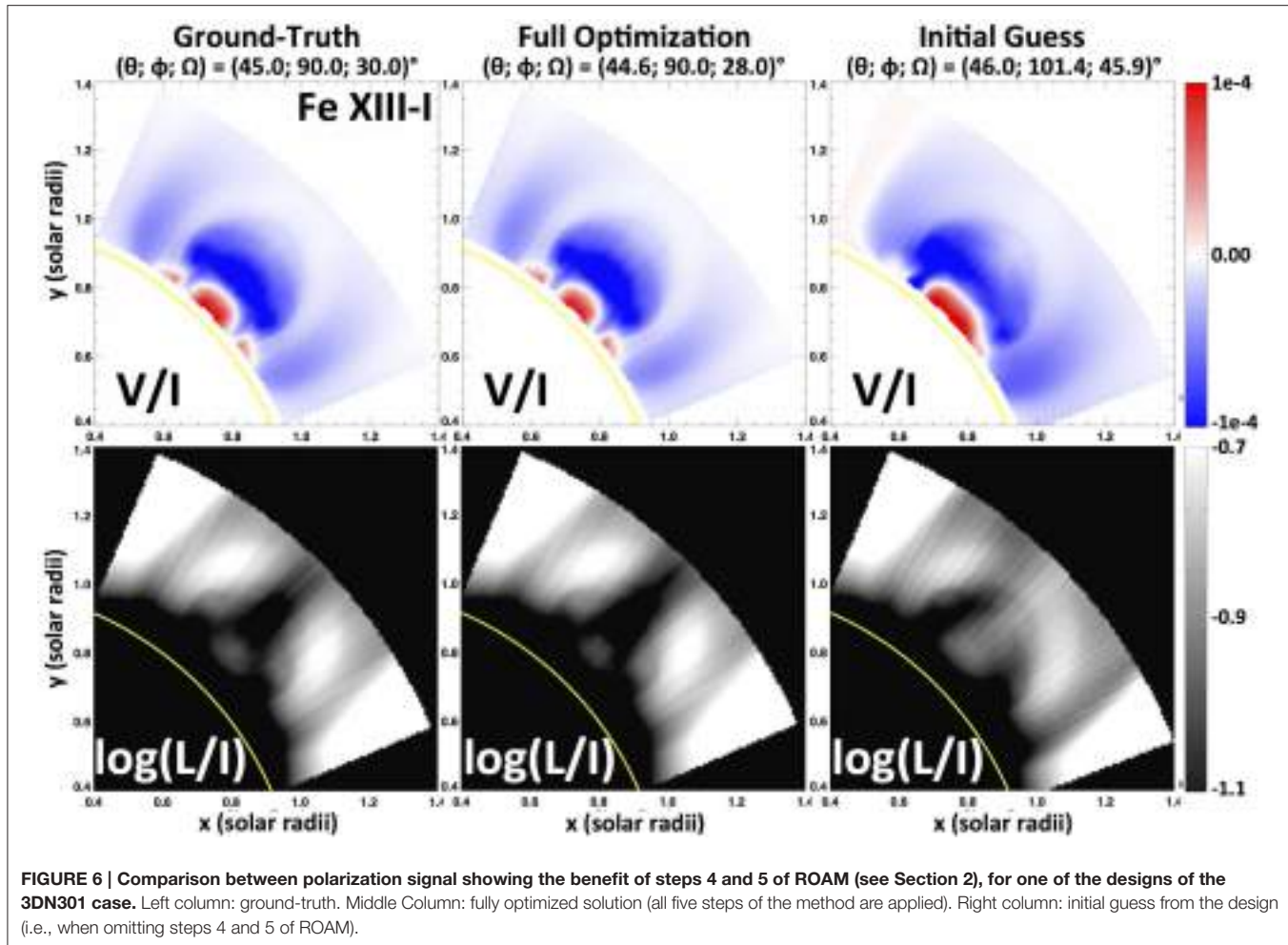
worst case of 3DN301, the rms error on the log-likelihood is 0.25, which is very similar to that of the best case of 3DN31, and the MLE is far from the ground truth for both  $\phi$  and  $\Omega$ . However, we find that the worst case from 3DN301 provides a more accurate RBF decomposition of the exact log-likelihood function than the best case of 3DN31; the log-likelihood function surfaces display a similar pattern as for the best case of 3DN301 but shifted in the  $\Omega$  direction. The difference with the 3DN31 lies in the density of points in the entire design, and in the vicinity of the exact maximum, with regard to the structuring, or gradients, of the exact log-likelihood function. This is because the goodness of the approximation is determined by that of the RBF decomposition, which depends on the number of constraints—and hence, points—brought by the design. In other words, the more structured the exact log-likelihood function, the stronger the effect of point density on the goodness of the RBF decomposition / log-likelihood function approximation, similar to what one would expect when discretizing a continuous functions that contains strong gradients. While not shown here, the combined effect of point density and log-likelihood function structuring on the quality of the RBF decomposition is further supported and illustrated by the best case of 3DN31ZOOM that provides the best approximation of the exact log-likelihood function in the vicinity of the exact maximum even though the corresponding design only includes 31 points.

The aforementioned results show that the RBF decomposition performed well from a sparse sampling of the parameter space, and hence ROAM, is able to capture both the values and variations of the exact log-likelihood function when suitable conditions are met, namely, when the design contains a high enough density of points in the surroundings of the exact maximum and in areas where the exact log-likelihood function is strongly structured. They further demonstrate that ROAM can perform well even with a very low number of points per design although not as robustly. The combined results from 3DN31 and 3DN31ZOOM indicate that an iterative application of ROAM with a smaller and smaller parameter space would be an interesting way to improve its robustness when used with a very sparse design. Such a robust approach has been successfully tested but is beyond the scope of this work and will be presented in a subsequent paper. In particular, the iterative implementation of ROAM strongly improves  $\phi_{\text{MLEs}}$  and  $\Omega_{\text{MLEs}}$ , leading to a better than  $0.5^\circ$  accuracy on both of these parameters in typically 4–5 iterations with designs of 31 points. The solution is quasi-independent of the design used for the RBF decomposition and the strong  $\phi - \Omega$  coupling (previously mentioned and visible in **Figure 4C** and in the  $\phi - \Omega$  cut of the exact log-likelihood function shown in **Figure 5**) is comfortably reduced and overcome [note that such coupling could also be overcome by separately optimizing one of the coupled parameters, e.g.,  $\Omega$ , and apply ROAM to the 2D parameter space  $(\theta; \phi)$ ].

Note that, with the goal of increasing speed, and considering our previous comments on the acceptable degree of roughness in the log-likelihood function approximation and an iterative implementation of ROAM, a less sophisticated approach might be conceived. For instance, one could first go through steps 1 to 3 of the method (see Section 2). Then, step 4 (i.e., the

RBF decomposition) would be replaced by taking the point of the design associated with the highest log-likelihood function value as a temporary MLE and one would iterate the procedure by defining a smaller design centered around the temporary MLE until a convergence criterion is reached. There are several reasons for not making such a choice. The main reason is that such an initial guess can be far from the exact maximum likelihood, which would likely slow down the convergence by requiring unnecessary iterations and would make the final result more sensitive to local maxima. In addition, applying the RBF decomposition and the search for the maximum from the approximated log-likelihood function is computationally cheap when the number of RBFs is as small as for the cases considered in this study, i.e., typically takes  $<10$  s for the designs of the 3DN301 case. The benefits of applying steps 4 and 5 of ROAM as proposed in Section 2 (i.e., the RBF decomposition and the search for the MLE from the RBFs approximated log-likelihood function) are illustrated in **Figure 6**. The figure displays Stokes images for the ground truth, the MLE obtained from fully applying our optimization method to one design of the 3DN301, and for the initial guess from that design. As one can see, the initial MLE guess from the design,  $(\theta; \phi; \Omega)_{\text{IG}} = (46.0^\circ; 101.4^\circ; 45.9^\circ)$ , has a  $\phi_{\text{IG}}$  and  $\Omega_{\text{IG}}$  that are far off both the ground truth  $[(\theta; \phi; \Omega)_{\text{GT}} = (45.0^\circ; 90.0^\circ; 30.0^\circ)]$  and the MLE obtained from the RBF decomposition [full application of ROAM;  $(\theta; \phi; \Omega)_{\text{MLEs}} = (44.6^\circ; 90.0^\circ; 28.0^\circ)$ ]. These strong differences in  $\phi$  and  $\Omega$  result in significantly different Stokes profiles. Iterations would then be needed for the results to be as close to the ground truth as the MLE from the full optimization, which (1) gives a very good estimation of the parameters of the exact maximum likelihood without any real need for iterations, and (2) only takes a few more seconds of calculations.

In practice, the current capabilities of the CoMP instrument and calibration software do not allow routine measurements of Stokes  $V$  since the signal-to-noise ratio is too small. We therefore perform an additional test to show that the current linear polarization signal from CoMP is sufficient to constrain the parameters of a magnetic model using ROAM. The log-likelihood function is defined as in Equation (7) keeping  $w_I$ ,  $w_Q$ ,  $w_U$  as before, but now setting  $w_V = 0$ . The results of that study are displayed in **Figure 7** for 3DN301. The figure presents scatter plots of the MLEs of a design obtained when using all four Stokes vs. obtained when using Stokes  $I$ ,  $Q$ , and  $U$  only. In such plots, the points should form a line of equation  $y = x$  whenever the solutions obtained one way or the other remain the same. As one can see from **Figure 7**, this is exactly the case for  $\theta_{\text{MLEs}}$ . Most of the points are also forming a straight line,  $y = x$ , for both  $\phi_{\text{MLEs}}$  and  $\Omega_{\text{MLEs}}$ , with only about 7–8 points (out of 100) being off the line. Such results indicate that a log-likelihood function built from Stokes  $I$ ,  $Q$ , and  $U$  contains sufficient information to constrain the three spatial location and orientation parameters considered here. We therefore conclude that the current linear polarization measurements from CoMP contain sufficient observational information to constrain *some* of the parameters of a given magnetic model.



### 3.3. Likelihood Function with Multiple Maxima

In this section, we test ROAM in the case of a log-likelihood function with multiple maxima having similar values. For that

purpose, we only build the log-likelihood function with Stokes  $Q$  and  $U$ , setting the weight coefficients of Equation (7) to  $(w_I; w_Q, w_U, w_V) = (0.; 2.0 \times 10^{-2}; 6.9 \times 10^{-2}; 0.)$ . Only the height of the flux rope in the corona,  $h$ , and the tilt angle,  $\Omega$ ,

**TABLE 3 | Characteristics of the test with a likelihood function possessing multiple maxima.**

<i>n</i>	<i>t<sub>elapsed</sub></i> (hrs)	<i>t<sub>full</sub></i> (hrs)	<i>h</i> ( $R_{\odot}$ )	$\theta$ (°)	$\phi$ (°)	$\Omega$ (°)	
2DN120	120	10	$1.2 \times 10^3$	[0.04; 0.52]	45	90	[0; 357]

The test case contains 100 different designs.  $t_{full}$  is the total elapsed time that would be required to compute the Stokes images for the  $n^2$  points of the 2D parameter space in series. The polarimetric data for the ground-truth are associated with  $(h; \theta; \phi; \Omega) = (0.16 R_{\odot}; 45^\circ; 90^\circ; 30^\circ)$ .

are considered for this test (see **Table 3** for the range of values considered for each parameter).

Stokes *Q* and *U* signals are associated with the transverse magnetic field, i.e., the component of a magnetic field perpendicular to the LOS. For a single point in the solar corona, the transverse magnetic field diagnosed from either the Hanle or Zeeman effect is subject to a  $180^\circ$  ambiguity (e.g., Casini and Judge, 1999; Judge, 2007). In terms of the parameters considered in our tests, it means that a single point magnetic field set with a rotation angle,  $\Omega_{SP}$ , will give the same Stokes *Q* and *U* signals as when set with  $\Omega_{SP} \pm 180^\circ$ . Considering that  $\phi_{GT} = 90^\circ$  (that is, the flux rope is centered at the solar limb) and the strong symmetry of our flux rope (see Section 3.1), we expect the LOS integrated Stokes *Q* and *U* to be the same for  $\Omega$  and  $\Omega \pm 180^\circ$ , resulting in a log-likelihood function with two maxima respectively located at  $\Omega_{GT}$  and  $\Omega_{GT} \pm 180^\circ$ ; note that the symmetry of Stokes *Q* and *U* would be broken if the flux rope were not centered on the solar limb. This is indeed the case as shown **Figure 8B** where a maximum region can be observed at  $\Omega = 30^\circ$  and  $\Omega = 210^\circ$ . **Figure 8B** further shows the presence of two additional maximum regions located at  $\Omega = 150$  and  $330^\circ$ . These two solutions suggest a symmetry with regard to the plane  $\Omega = 0^\circ$  that is not expected. We find that the corresponding Stokes *Q* and *U* images are, as expected, different from those of the ground truth. However, the differences are small as compared with other values of  $\Omega$ , resulting in a local maximum in those two regions. Note, though, that these four maximum regions are only possible because  $\phi = 90^\circ$ , whereas any other value of  $\phi$  would break the symmetry of the Stokes *Q* and *U* images.

In the present test case, the periodic parameter  $\Omega$  varies on a range of values larger than half its period. In such circumstances, we must consider its periodicity for the RBF decomposition (see Appendix 2 in Supplementary Material). Accordingly, the parameters of the RBF decomposition are  $d' = 3$ ,  $m = 3$  and  $p = m - 1 = 2$ . As in Section 3.2, we run our optimization method on 100 different designs whose properties are given in **Table 3**. The results are summarized in a 2D dispersion plot in **Figure 8A**. The figure shows that the 100 MLEs are mainly, and almost equally, clustering around the two global  $\Omega$  maximum regions, corresponding to the ground truth and its counterpart at  $180^\circ$ . We further find that, out of these 100 solutions, only four are associated with one of the two local maximum regions, here  $\Omega \approx 150^\circ$ . As for the height of the MLEs, we find an average value of  $1.6 \times 10^{-1} R_{\odot}$  with a  $2\sigma$  dispersion level of  $0.5 \times 10^{-1} R_{\odot}$ , meaning that the height is well constrained even from using Stokes *Q* and *U* only. The dispersion plot from

**Figure 8A** therefore indicates that our optimization method is strongly sensitive to multiple global maxima and *can* be sensitive to local maxima. Note that the sensitivity to local maxima depends upon both the number of points used in the design and the value of these local maxima relatively to that of the global maxima.

**Figure 8C** displays a surface plot of the log-likelihood function from the best case of 2DN120. As one can see, the RBF decomposition is able to capture both the values and shapes of the exact log-likelihood function. We find an rms error of 0.04 on the log-likelihood. The RBF decomposition can therefore provide a good approximation of the exact log-likelihood function even with a periodic space and the presence of multiple maxima.

Finally, we show in **Figure 9** that using the Stokes *V* signal to build the log-likelihood function removes the  $\Omega$  ambiguities that were observed in the log-likelihood function constructed from Stokes *Q* and *U* only. When using Stokes *V*, the optimization leads to  $\Omega_{rms} \approx 28.8^\circ$ . This means that some additional observables might be worth considering to remove ambiguities in parameters when they exist. Another alternative to remove ambiguities is to reduce the parameter space to regions having a single maximum. Then, one can either study each region separately or use prior constraints to eliminate regions that are very unlikely. For instance, one can use the photospheric magnetograms, or H $\alpha$  observations, prior to or after the passage of the flux rope at a limb to estimate the rotation angle (i.e.,  $\Omega$ ) and put strong constraints on the values of rotation angle to consider for the parameter space.

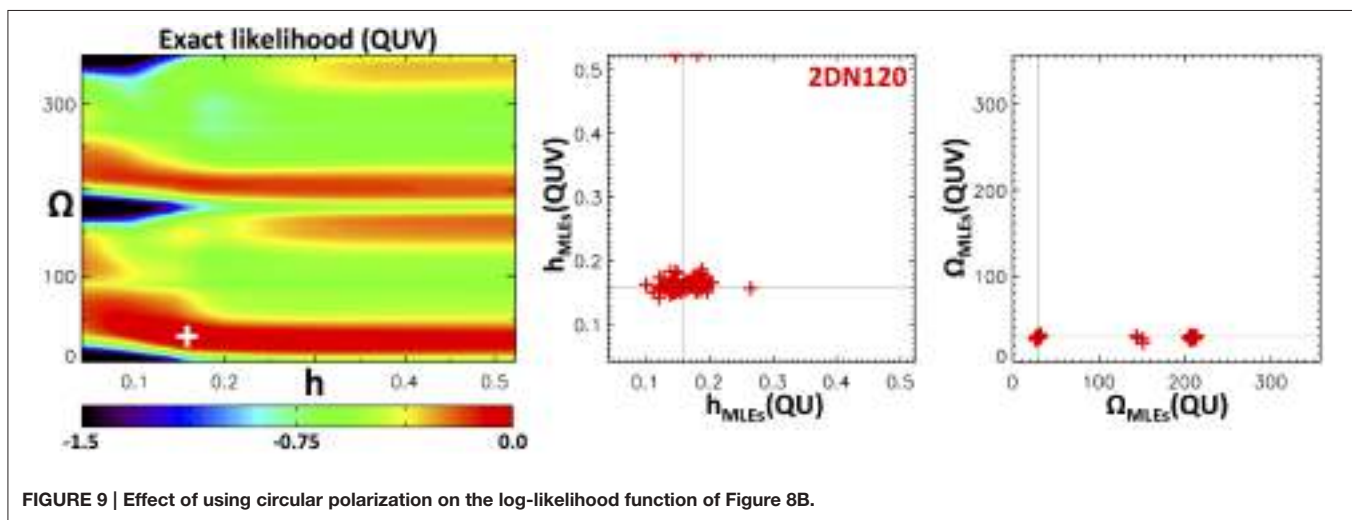
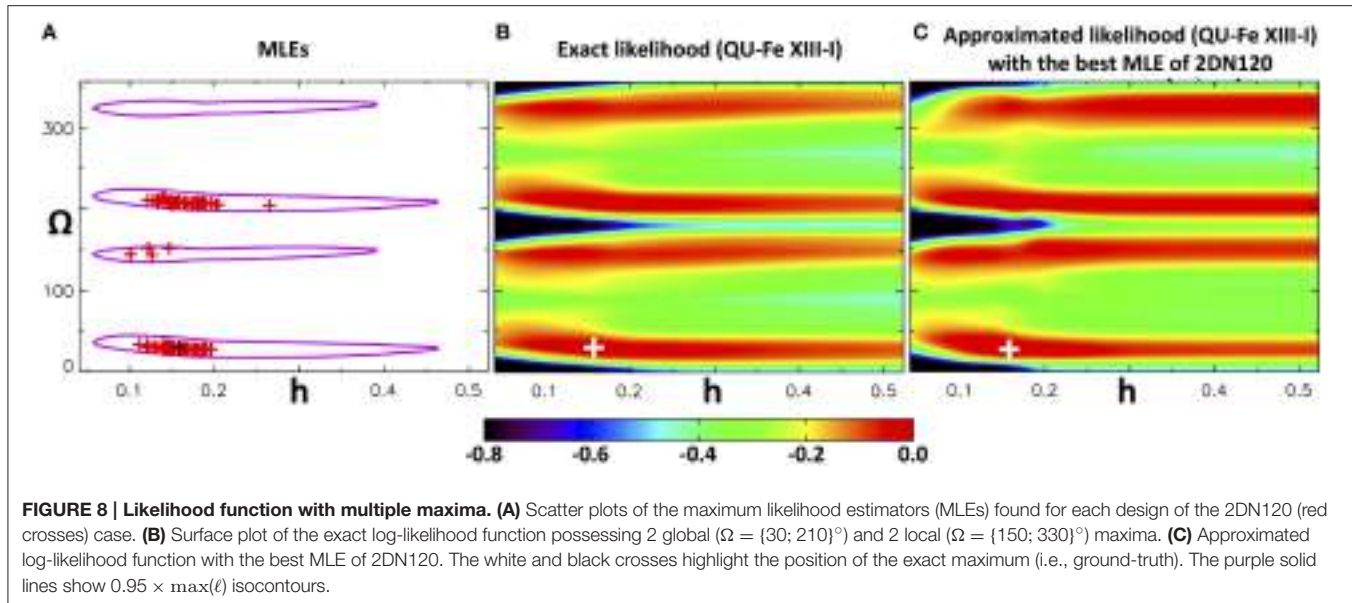
### 3.4. Stability with Regard to Noise in the Data

In practice, any real data is subject to measurement errors. Such errors may prevent the retrieval of any meaningful information about the polarization, and hence, the magnetic field in regions of weak signals and/or when the signal-to-noise ratio is weak. The results of ROAM might be sensitive to such noise and we therefore need to investigate that sensitivity. For that reason, we now test our method when the synthetic observations associated with the ground truth contain some noise. In this regard, we build the log-likelihood function with Stokes *U* images only

$$\ell(x_i) = \frac{\ell_U(x_i)}{\sigma_U^2}, \quad (8)$$

where  $\sigma_U$  is the root mean square of the noise in the synthetic Stokes *U* signal of the ground truth.

For a given value of photon noise,  $\sigma_I$ ,  $\sigma_Q$ ,  $\sigma_U$ ,  $\sigma_V$  are all different. As a consequence, if one uses more than one Stokes component, then varying the noise further changes the relative contribution of each Stokes parameter to the log-likelihood function due to the weighting by  $1/\sigma_S$ . We need to be free of the variation of relative contribution of the different Stokes in order to isolate the sole effect of noise on the robustness of our optimization method, which then implies using only one Stokes parameter to define the log-likelihood function. Considering CoMP capabilities and the current magnetic model and ground truth, we performed several tests with different levels of noise



(which can be added using FORWARD) and found that (1) Stokes  $V$  cannot be used for realistic exposure times because its values for our test bed are too weak and would require an unrealistic 4 days exposure time to reach a moderate level of noise for the particular choices of ground-truth parameters and pixel sizes (see corresponding values in Section 3.1), (2) Stokes  $I$  cannot be used because it is not sensitive enough to noise (even a 1 s exposure time leads to a very weak level of noise), and (3) Stokes  $Q$  and  $U$  are better suited for the noise test with exposure times of the order of 1–100 s. From this analysis, we chose Stokes  $U$  because it was slightly more sensitive to noise than Stokes  $Q$  for the setup considered in this paper (note that both  $Q$  and  $U$  are presented in a frame of reference relative to the local vertical, or radial coordinate).

FORWARD already implements a photon noise calculation for the infra-red lines under consideration (see e.g., Gibson et al.,

2016). The noise is calculated according to the specifications of the instrument considered (telescope aperture, detector efficiency), the background photon level, and the exposure time to obtain a forward calculation that includes the noise. For CoMP, the aperture is 20 cm, the efficiency is 0.05 throughput and the background is five parts per million of solar brightness. We perform three tests with different exposure time,  $t_{\text{exp}}$ , hence noise level, i.e.,  $t_{\text{exp}} = (1; 10; 300)$  seconds that respectively correspond to strong, moderate, and weak noise cases for the considered setup. The synthetic Stokes  $U$  images of the ground truth for these noise levels are displayed in Figure 10. These synthetic ground truth are used with all designs of the 3DN31, 3DN301, and 3DN31ZOOM cases.

Figure 11 presents scatter plots of the error on the MLEs obtained when noise is included in the ground truth Stokes  $U$  images as compared with the case when no noise is considered.

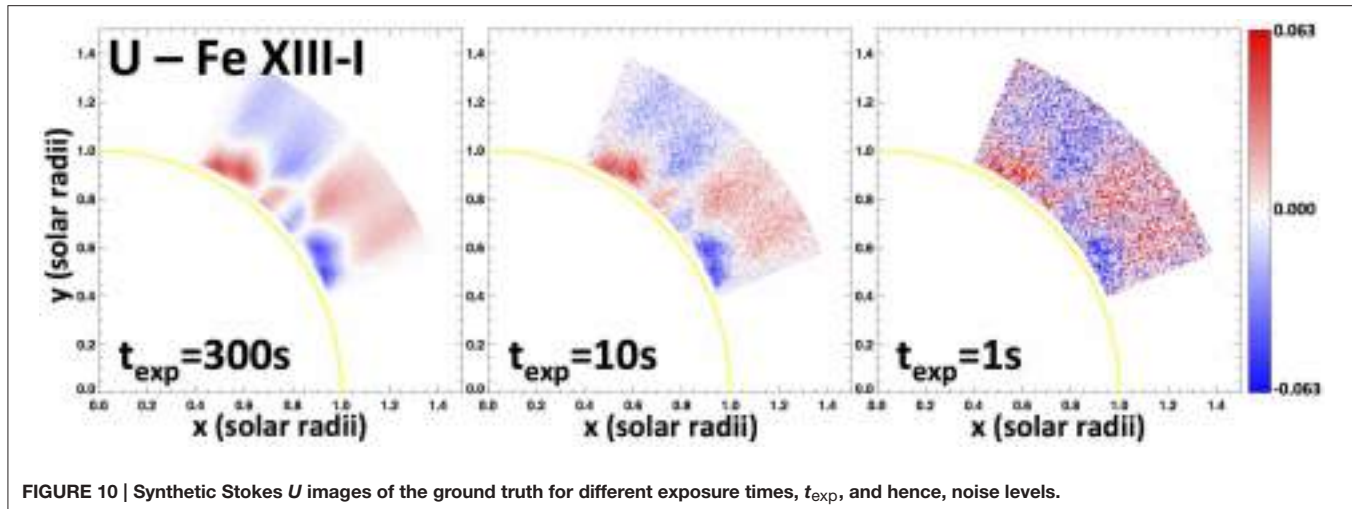


**FIGURE 10 |** Synthetic Stokes  $U$  images of the ground truth for different exposure times,  $t_{\text{exp}}$ , and hence, noise levels.

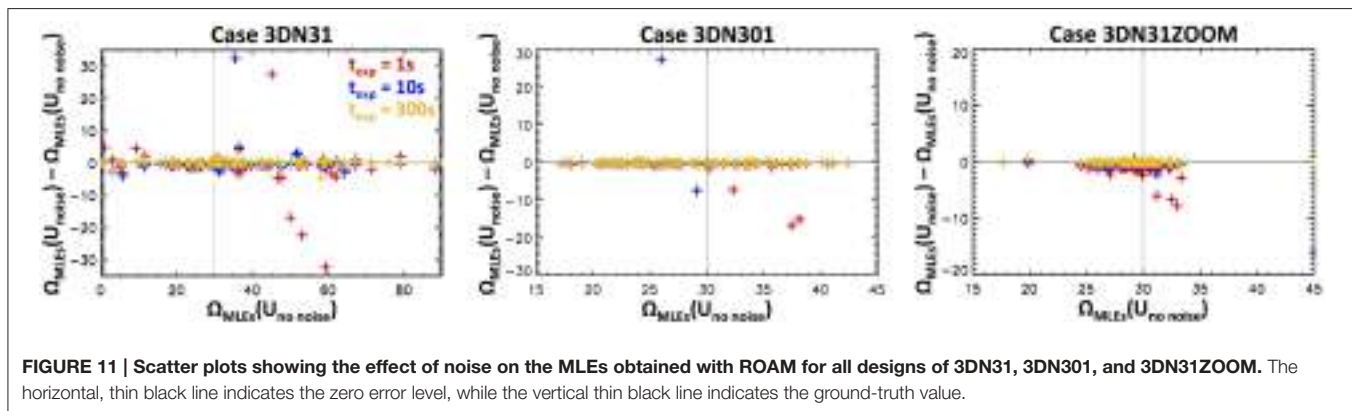


**FIGURE 11 |** Scatter plots showing the effect of noise on the MLEs obtained with ROAM for all designs of 3DN31, 3DN301, and 3DN31ZOOM. The horizontal, thin black line indicates the zero error level, while the vertical thin black line indicates the ground-truth value.

The plots are only shown for the  $\Omega$  parameter because all three parameters  $\theta$ ,  $\phi$ , and  $\Omega$  display very similar results. In **Figure 11**, one can see a nearly perfect horizontal line at  $y = 0$  for  $\Omega_{\text{MLE}}$  obtained with an exposure time of 300 s (yellow crosses) for all test cases (3DN31, 3DN301, and 3DN31ZOOM). This means that the  $t_{\text{exp}} = 300$  s case is equivalent to the no-noise case. For cases  $t_{\text{exp}} = 10$  and  $t_{\text{exp}} = 1$  s, the plots show some departure from the  $y = 0$  line, which increases with the level of noise. The figure also shows that the noise effect on the robustness of the MLEs depends on the density of points in the designs, i.e., 3DN31 is the most affected by the noise while 3DN31ZOOM is the least affected. That being said, we find that only less than  $\approx 10 - 15$  points (out of 100) of 3DN31 exhibit a strong sensitivity to noise for the  $t_{\text{exp}} = 1$  second case, i.e., with an error  $>5^\circ$ . This number drops to  $\approx 5$  when  $t_{\text{exp}} = 10$  s. For the  $t_{\text{exp}} = 1$  s, **Figure 10** shows that the noise strongly masks the real Stokes  $U$  signal, although not entirely. We therefore deduce that our optimization method is very stable against the presence of noise in the data as long as the noise does not entirely mask the real signal. Considering that Stokes  $Q$  is similarly sensitive to noise as Stokes  $U$  and that Stokes  $I$  is much less sensitive to the noise, we conclude that our method can be robustly used with the Stokes  $I$ ,  $Q$ , and  $U$  data provided by the CoMP.

## 4. CONCLUSIONS

In this paper, we introduced and validated a new optimization method for model-data fitting, ROAM (Radial-basis-functions Optimization Approximation Method). Our primary motivation for this work has been to develop a novel approach for diagnosing the solar coronal magnetic field by combining a parameterized 3D magnetic field model with forward modeling of coronal polarization. From various tests applied to the synthetic test bed of a coronal magnetic flux rope, we showed that ROAM allows for fast, efficient, and accurate model-data fitting in a  $d$ -dimensional parameter space. These test cases further enabled us to analyze and specify a framework for an optimal application of ROAM.

Applying our method with forward modeling of IR coronal polarimetry, we demonstrated that ROAM can be exploited for converting coronal polarimetric measurements into magnetic field data. The use of our model-data fitting method therefore opens new perspectives for the development and exploitation of coronal polarimetric measurements such as the ones routinely performed by CoMP (Tomczyk et al., 2008) and future telescopes such as the Daniel K. Inoue Solar Telescope<sup>4</sup> and the Coronal Solar Magnetism Observatory (Tomczyk et al., 2016), but also for

<sup>4</sup><http://www.ifa.hawaii.edu/~schad/dlnirsp/>

a wider range of coronal observations including, e.g., UV (see e.g., Fineschi, 2001; Raouafi et al., 2009) and radio polarimetry (e.g., White and Kundu, 1997; Gelfreikh, 2004; see also Gibson et al., 2016, for discussion of multiwavelength magnetometry).

Beyond the analysis of coronal polarimetric measurements, ROAM offers interesting perspectives for magnetic field reconstruction models. Most of the current 3D diagnostics of the coronal magnetic field of solar active regions (ARs) are derived from the analysis of magnetic field reconstruction models including, e.g., force-free field extrapolations of the photospheric magnetic field (see e.g., Alissandrakis, 1981; Demoulin et al., 1989; Wheatland et al., 2000; Yan and Sakurai, 2000; Wiegelmann, 2004; Amari et al., 2006; Malanushenko et al., 2012, and references therein), and magneto-frictional methods (see e.g., van Ballegooijen, 2004; Valori et al., 2005, 2007; Jiang et al., 2011; Inoue et al., 2012; Titov et al., 2014, and references therein). ROAM could, in principle, be used to perform model-data fitting with such reconstruction models that either already are (i.e., through the poloidal and axial flux for the magneto-frictional methods with flux rope insertion) or could be (e.g., through the photospheric force-free parameter for both force-free field extrapolations and magneto-frictional methods without flux rope insertion) parameterized. The extensive work performed over the years in terms of forward modeling of various observables (see e.g., Gibson et al., 2016, and references therein) would then allow for using several types of different observations to constrain the parameters of the magnetic field reconstruction models. ROAM therefore opens new perspectives for including coronal polarimetric measurements into magnetic field reconstructions and, more generally, for data-optimized reconstruction of the solar coronal magnetic field. Such perspectives will be tackled in the framework of the Data Optimized Coronal Field Model<sup>5</sup> (DOCFM), a collaborative project that will make use of ROAM.

<sup>5</sup><http://www.hao.ucar.edu/DOCFM/>

## REFERENCES

- Alissandrakis, C. E. (1981). On the computation of constant alpha force-free magnetic field. *Astron. Astrophys.* 100, 197–200.
- Amari, T., Boulmezaoud, T. Z., and Aly, J. J. (2006). Well posed reconstruction of the solar coronal magnetic field. *Astron. Astrophys.* 446, 691–705. doi: 10.1051/0004-6361:20054076
- Bird, M. K., Volland, H., Howard, R. A., Koomen, M. J., Michels, D. J., Sheeley, N. R. Jr., et al. (1985). White-light and radio sounding observations of coronal transients. *Solar Phys.* 98, 341–368. doi: 10.1007/BF00152465
- Bommier, V., and Sahal-Brechot, S. (1982). The Hanle effect of the coronal L-alpha line of hydrogen - Theoretical investigation. *Solar Phys.* 78, 157–178. doi: 10.1007/BF00151151
- Boser, B. E., Guyon, I. M., and Vapnik, V. N. (1992). “A training algorithm for optimal margin classifiers,” in *Proceedings of the Fifth Annual Workshop on Computational Learning Theory*, COLT ’92, (New York, NY: ACM), 144–152. doi: 10.1145/130385.130401
- Broomhead, D. S. and Lowe, D. (1988). Multivariable functional interpolation and adaptive networks. *Complex Syst.* 2, 321–355.
- Buhmann, M. D. (2003). *Radial Basis Functions: Theory and Implementations*. Cambridge, UK: Cambridge Monographs on Applied and Computational Mathematics; Cambridge University Press.

Finally, we wish to mention that ROAM is not limited to coronal magnetic field diagnostics and could be used for other optimization problems. The method will be of particular interest for model-data fitting for which a model evaluation (here, the evaluation of the model itself and/or the forward modeling of an observable if applicable) is computationally expensive.

## AUTHOR CONTRIBUTIONS

All authors listed, have made substantial, direct and intellectual contribution to the work, and approved it for publication.

## FUNDING

KD acknowledges funding from the Computational and Information Systems Laboratory and from the High Altitude Observatory, and along with SG and YF acknowledges support from the Air Force Office of Scientific Research under award FA9550-15-1-0030.

## ACKNOWLEDGMENTS

We thank the two anonymous referees and Anna Malanushenko for a careful consideration of the manuscript and constructive comments. The National Center for Atmospheric Research is sponsored by the National Science Foundation.

## SUPPLEMENTARY MATERIAL

The Supplementary Material for this article can be found online at: <http://journal.frontiersin.org/article/10.3389/fspas.2016.00024>

- Casini, R., and Judge, P. G. (1999). Spectral lines for polarization measurements of the coronal magnetic field. II. Consistent treatment of the stokes vector for magnetic-dipole transitions. *Astrophys. J.* 522, 524–539. doi: 10.1086/307629
- Demoulin, P., Priest, E. R., and Anzer, U. (1989). A three-dimensional model for solar prominences. *Astron. Astrophys.* 221, 326–337.
- Duchon, J. (1977). *Constructive Theory of Functions of Several Variables: Proceedings of a Conference Held at Oberwolfach April 25 – May 1, 1976*. Berlin; Heidelberg: Springer Berlin Heidelberg. doi: 10.1007/BFb0086566
- Fan, Y. (2012). Thermal signatures of tether-cutting reconnections in pre-eruption coronal flux ropes: hot central voids in coronal cavities. *Astrophys. J.* 758:60. doi: 10.1088/0004-637X/758/1/60
- Fasshauer, G. E. (2007). *Meshfree Approximation Methods with MATLAB*, Vol. 6 of *Interdisciplinary Mathematical Sciences*. Singapore: World Scientific Publishing Company.
- Fineschi, S. (2001). “Space-based instrumentation for magnetic field studies of solar and stellar atmospheres,” in *Magnetic Fields Across the Hertzsprung-Russell Diagram*, Vol. 248 of *Astronomical Society of the Pacific Conference Series*, eds G. Mathys, S. K. Solanki, and D. T. Wickramasinghe (San Francisco, CA: Astronomical Society of the Pacific), 597.
- Flyer, N., Barnett, G. A., and Wicker, L. J. (2016). Enhancing finite differences with radial basis functions: experiments on the Navier-Stokes equations. *J. Comput. Phys.* 316, 39–62. doi: 10.1016/j.jcp.2016.02.078

- Flyer, N., and Fornberg, B. (2011). Radial basis functions: developments and applications to planetary scale flows. *Comput. Fluids* 46, 32. doi: 10.1016/j.compfluid.2010.08.005
- Fornberg, B. and Flyer, N. (2015). Solving PDEs with radial basis functions. *Acta Numerica* 24, 215–258. doi: 10.1017/S0962492914000130
- Gelfreikh, G. B. (2004). “Coronal magnetic field measurements through Bremsstrahlung emission,” in *Astrophysics and Space Science Library*, Vol. 314 of *Astrophysics and Space Science Library*, eds D. E. Gary and C. U. Keller (Dordrecht: Springer), 115. doi: 10.1007/1-4020-2814-8 6
- Gibson, S., Kucera, T., White, S. M., Dove, J., Fan, Y., Forland, B., et al. (2016). FORWARD: a toolset for multiwavelength coronal magnetometry. *Front. Astron. Space Sci.* 3:8. doi: 10.3389/fspas.2016.00008
- Gibson, S. E., and Charbonneau, P. (1998). Empirical modeling of the solar corona using genetic algorithms. *J. Geophys. Res.* 103, 14511–14522. doi: 10.1029/98JA00676
- Hale, G. E. (1908). On the probable existence of a magnetic field in sun-spots. *Astrophys. J.* 28, 315. doi: 10.1086/141602
- Hanle, W. (1924). Über magnetische Beeinflussung der Polarisation der Resonanzfluoreszenz. *Z. Phys.* 30, 93–105. doi: 10.1007/BF01331827
- Harder, R. L., and Desmarais, R. N. (1972). Interpolation using surface splines. *J. Aircraft* 9, 189–191. doi: 10.2514/3.44330
- Iman, R. L., Helton, J. C., and Campbell, J. E. (1981). An approach to sensitivity analysis of computer models, part 1. introduction, input variable selection and preliminary variable assessment. *J. Qual. Technol.* 13, 174–183.
- Inoue, S., Magara, T., Watari, S., and Choe, G. S. (2012). Nonlinear force-free modeling of a three-dimensional sigmoid observed on the sun. *Astrophys. J.* 747:65. doi: 10.1088/0004-637X/747/1/65
- Jiang, C., Feng, X., Fan, Y., and Xiang, C. (2011). Reconstruction of the coronal magnetic field using the CESE-MHD Method. *Astrophys. J.* 727:101. doi: 10.1088/0004-637X/727/2/101
- Jones, D. R., Schonlau, M., and Welch, W. J. (1998). Efficient global optimization of expensive black-box functions. *J. Glob. Optimization* 13, 455–492. doi: 10.1023/A:1008306431147
- Judge, P. G. (2007). Spectral lines for polarization measurements of the coronal magnetic field. V. Information content of magnetic dipole lines. *Astrophys. J.* 662, 677–690. doi: 10.1086/515433
- Judge, P. G., Low, B. C., and Casini, R. (2006). Spectral lines for polarization measurements of the coronal magnetic field. IV. Stokes signals in current-carrying fields. *Astrophys. J.* 651, 1229–1237. doi: 10.1086/507982
- Kramar, M., Airapetian, V., Mikić, Z., and Davila, J. (2014). 3D coronal density reconstruction and retrieving the magnetic field structure during solar minimum. *Solar Phys.* 289, 2927–2944. doi: 10.1007/s11207-014-0525-7
- Lam, N. S. N. (1983). Spatial interpolation methods: a review. *Am. Cartogr.* 10, 129–149.
- Lin, H., Kuhn, J. R., and Coulter, R. (2004). Coronal magnetic field measurements. *Astrophys. J.* 613, L177–L180. doi: 10.1086/425217
- López Ariste, A. (2015). “Magnetometry of prominences,” in *Solar Prominences*, Vol. 415 of *Astrophysics and Space Science Library*, eds J.-C. Vial and O. Engvold (Cham: Springer International Publishing), 179.
- Louis, S. J., and Rawlins, G. J. E. (1993). “Syntactic analysis of convergence in genetic algorithms,” in *Foundations of Genetic Algorithms - 2*, ed L. D. Whitley (San Mateo, CA: Morgan Kauffman), 141–152.
- Madych, W. R., and Nelson, S. A. (1990). Polyharmonic cardinal splines. *J. Approx. Theory* 60, 141–156. doi: 10.1016/0021-9045(90)90079-6
- Malanushenko, A., Schrijver, C. J., DeRosa, M. L., Wheatland, M. S., and Gilchrist, S. A. (2012). Guiding nonlinear force-free modeling using coronal observations: first results using a Quasi-Grad-Rubin scheme. *Astrophys. J.* 756:153. doi: 10.1088/0004-637X/756/2/153
- McKay, M. D., Beckman, R. J., and Conover, W. J. (1979). A comparison of three methods for selecting values of input variables in the analysis of output from a computer code. *Technometrics* 21, 239–245.
- Nychka, D., Bandyopadhyay, S., Hammerling, D., Lindgren, F., and Sain, S. (2015). A multiresolution gaussian process model for the analysis of large spatial datasets. *J. Comput. Graphical Stat.* 24, 579–599. doi: 10.1080/10618600.2014.914946
- Plowman, J. (2014). Single-point inversion of the coronal magnetic field. *Astrophys. J.* 792:23. doi: 10.1088/0004-637X/792/1/23
- Powell, M. J. D. (1977). Restart procedures for the conjugate gradient method. *Math. Programming* 12, 241–254. doi: 10.1007/BF01593790
- Powell, M. J. D. (1993). *Some Algorithms for Thin Plate Spline Interpolation to Functions of Two Variables*. Cambridge University Dept. of Applied Mathematics and Theoretical Physics technical report.
- Rachmeler, L. A., Casini, R., and Gibson, S. E. (2012). “Interpreting Coronal Polarization Observations,” in *Second ATST-EAST Meeting: Magnetic Fields from the Photosphere to the Corona*, Vol. 463 of *Astronomical Society of the Pacific Conference Series*, eds T. R. Rimmele, A. Tritschler, F. Wöger, M. Collados Vera, H. Socas-Navarro, R. Schlichenmaier, M. Carlsson, T. Berger, A. Cadavid, P. R. Gilbert, P. R. Goode, and M. Knölker (San Francisco, CA: Astronomical Society of the Pacific), 227.
- Rachmeler, L. A., Gibson, S. E., Dove, J. B., DeVore, C. R., and Fan, Y. (2013). Polarimetric properties of flux ropes and sheared arcades in coronal prominence cavities. *Solar Phys.* 288, 617–636. doi: 10.1007/s11207-013-0325-5
- Raouafi, N.-E., Solanki, S. K., and Wiegmann, T. (2009). “Hanle effect diagnostics of the coronal magnetic field: a test using realistic magnetic field configurations,” in *Solar Polarization 5: In Honor of Jan Stenflo*, Vol. 405 of *Astronomical Society of the Pacific Conference Series*, eds S. V. Berdyugina, K. N. Nagendra, and R. Ramelli (San Francisco, CA: Astronomical Society of the Pacific), 429.
- Sahal-Brechot, S., Bommier, V., and Leroy, J. L. (1977). The Hanle effect and the determination of magnetic fields in solar prominences. *Astron. Astrophys.* 59, 223–231.
- Stenflo, J. O. (2015). History of solar magnetic fields since George Ellery Hale. *Space Sci. Rev.* 1–31. doi: 10.1007/s11214-015-0198-z
- Titov, V. S., Török, T., Mikic, Z., and Linker, J. A. (2014). A method for embedding circular force-free flux ropes in potential magnetic fields. *Astrophys. J.* 790:163. doi: 10.1088/0004-637X/790/2/163
- Tomczyk, S., Card, G. L., Darnell, T., Elmore, D. F., Lull, R., Nelson, P. G., et al. (2008). An instrument to measure coronal emission line polarization. *Solar Phys.* 247, 411–428.
- Tomczyk, S., Landi, E., Burkepile, J. T., Casini, R., DeLuca, E. E., Fan, Y., et al. (2016). Scientific objectives and capabilities of the Coronal Solar Magnetism Observatory. *J. Geophys. Res. Space Phys.* doi: 10.1002/2016JA022871
- Valori, G., Kliem, B., and Fuhrmann, M. (2007). Magnetofrictional extrapolations of low and low's force-free equilibria. *Solar Phys.* 245, 263–285. doi: 10.1007/s11207-007-9046-y
- Valori, G., Kliem, B., and Keppens, R. (2005). Extrapolation of a nonlinear force-free field containing a highly twisted magnetic loop. *Astron. Astrophys.* 433, 335–347. doi: 10.1051/0004-6361:20042008
- van Ballegooijen, A. A. (2004). Observations and modeling of a filament on the Sun. *Astron. Astrophys.* 612, 519–529. doi: 10.1086/422512
- Wheatland, M. S., Sturrock, P. A., and Roumeliotis, G. (2000). An optimization approach to reconstructing force-free fields. *Astron. Astrophys.* 540, 1150–1155. doi: 10.1086/309355
- White, S. M., and Kundu, M. R. (1997). Radio observations of gyroresonance emission from coronal magnetic fields. *Solar Phys.* 174, 31–52. doi: 10.1023/A:1004975528106
- Wiegmann, T. (2004). Optimization code with weighting function for the reconstruction of coronal magnetic fields. *Solar Phys.* 219, 87–108.
- Yan, Y., and Sakurai, T. (2000). New boundary integral equation representation for finite energy force-free magnetic fields in open space above the Sun. *Solar Phys.* 195, 89–109. doi: 10.1023/A:1005248128673

**Conflict of Interest Statement:** The authors declare that the research was conducted in the absence of any commercial or financial relationships that could be construed as a potential conflict of interest.

Copyright © 2016 Dalmasse, Nychka, Gibson, Fan and Flyer. This is an open-access article distributed under the terms of the Creative Commons Attribution License (CC BY). The use, distribution or reproduction in other forums is permitted, provided the original author(s) or licensor are credited and that the original publication in this journal is cited, in accordance with accepted academic practice. No use, distribution or reproduction is permitted which does not comply with these terms.



# Waves and Magnetism in the Solar Atmosphere (WAMIS)

**Yuan-Kuen Ko<sup>1\*</sup>, John D. Moses<sup>2</sup>, John M. Laming<sup>1</sup>, Leonard Strachan<sup>1</sup>, Samuel Tun Beltran<sup>1</sup>, Steven Tomczyk<sup>3</sup>, Sarah E. Gibson<sup>3</sup>, Frédéric Auchère<sup>4</sup>, Roberto Casini<sup>3</sup>, Silvano Fineschi<sup>5</sup>, Michael Knoelker<sup>3</sup>, Clarence Korendyke<sup>1</sup>, Scott W. McIntosh<sup>3</sup>, Marco Romoli<sup>6</sup>, Jan Rybak<sup>7</sup>, Dennis G. Socker<sup>1</sup>, Angelos Vourlidas<sup>8</sup> and Qian Wu<sup>3</sup>**

<sup>1</sup> Space Science Division, Naval Research Laboratory, Washington, DC, USA, <sup>2</sup> Heliophysics Division, Science Mission Directorate, NASA, Washington, DC, USA, <sup>3</sup> High Altitude Observatory, Boulder, CO, USA, <sup>4</sup> Institut d'Astrophysique Spatiale, CNRS Université Paris-Sud, Orsay, France, <sup>5</sup> INAF - National Institute for Astrophysics, Astrophysical Observatory of Torino, Pino Torinese, Italy, <sup>6</sup> Department of Physics and Astronomy, University of Florence, Florence, Italy, <sup>7</sup> Astronomical Institute, Slovak Academy of Sciences, Tatranska Lomnica, Slovakia, <sup>8</sup> Applied Physics Laboratory, Johns Hopkins University, Laurel, MD, USA

## OPEN ACCESS

### Edited by:

Mario J. P. F. G. Monteiro,  
Institute of Astrophysics and Space  
Sciences, Portugal

### Reviewed by:

Gordon James Duncan Petrie,  
National Solar Observatory, USA  
Robertus Erdélyi,  
University of Sheffield, UK  
João José Graça Lima,  
Institute of Astrophysics and Space  
Sciences, Portugal

### \*Correspondence:

Yuan-Kuen Ko  
yuan-kuen.ko@nrl.navy.mil

### Specialty section:

This article was submitted to  
Stellar and Solar Physics,  
a section of the journal  
Frontiers in Astronomy and Space  
Sciences

**Received:** 02 November 2015

**Accepted:** 14 January 2016

**Published:** 16 February 2016

### Citation:

Ko Y-K, Moses JD, Laming JM,  
Strachan L, Tun Beltran S, Tomczyk S,  
Gibson SE, Auchère F, Casini R,  
Fineschi S, Knoelker M, Korendyke C,  
McIntosh SW, Romoli M, Rybak J,  
Socker DG, Vourlidas A and Wu Q  
(2016) Waves and Magnetism in the  
Solar Atmosphere (WAMIS).  
*Front. Astron. Space Sci.* 3:1.  
doi: 10.3389/fspas.2016.00001

Comprehensive measurements of magnetic fields in the solar corona have a long history as an important scientific goal. Besides being crucial to understanding coronal structures and the Sun's generation of space weather, direct measurements of their strength and direction are also crucial steps in understanding observed wave motions. In this regard, the remote sensing instrumentation used to make coronal magnetic field measurements is well suited to measuring the Doppler signature of waves in the solar structures. In this paper, we describe the design and scientific values of the Waves and Magnetism in the Solar Atmosphere (WAMIS) investigation. WAMIS, taking advantage of greatly improved infrared filters and detectors, forward models, advanced diagnostic tools and inversion codes, is a long-duration high-altitude balloon payload designed to obtain a breakthrough in the measurement of coronal magnetic fields and in advancing the understanding of the interaction of these fields with space plasmas. It consists of a 20 cm aperture coronagraph with a visible-IR spectro-polarimeter focal plane assembly. The balloon altitude would provide minimum sky background and atmospheric scattering at the wavelengths in which these observations are made. It would also enable continuous measurements of the strength and direction of coronal magnetic fields without interruptions from the day-night cycle and weather. These measurements will be made over a large field-of-view allowing one to distinguish the magnetic signatures of different coronal structures, and at the spatial and temporal resolutions required to address outstanding problems in coronal physics. Additionally, WAMIS could obtain near simultaneous observations of the electron scattered K-corona for context and to obtain the electron density. These comprehensive observations are not provided by any current single ground-based or space observatory. The fundamental advancements achieved by the near-space observations of WAMIS on coronal field would point the way for future ground based and orbital instrumentation.

**Keywords:** corona, magnetic field, MHD waves, spectroscopy, polarization

## INTRODUCTION

Since the advent of the Solar and Heliospheric Observatory (SOHO; Domingo et al., 1995) followed by the Transition Region and Coronal Explorer (TRACE; Handy et al., 1999; Schrijver et al., 1999) and the Solar Dynamics Observatory (SDO; Pesnell et al., 2012), the solar atmosphere has come to be increasingly appreciated as a dynamic and complex environment. The concept of a static quiescent atmosphere and corona has given way to an environment where waves play a much larger role in shaping the plasma properties than hitherto assumed, and can have non-negligible energy densities compared to the thermal gas in the low  $\beta$  corona. Periodic oscillations in the solar atmosphere have long been observed (e.g., Chapman et al., 1972; Roberts et al., 1983; Antonucci et al., 1984; Aschwanden, 1987; Harrison, 1987), and various oscillation modes of coronal loops have been identified (e.g., Aschwanden et al., 1999; Nakariakov et al., 1999; Wang et al., 2009). Compressive waves connected to slow mode or fast mode waves, or their analogs in inhomogeneous media, have been readily detected, but the non-compressive Alfvén wave has proven more elusive. Early claims of Alfvén wave detections (Cirtain et al., 2007; De Pontieu et al., 2007; Tomczyk et al., 2007) have been discussed (Erdélyi and Fedun, 2007; Van Doorsselaere et al., 2008), and as this last reference emphasizes, the realization that Alfvén or fast mode waves (loosely collectively referred to as “Alfvénic” when close to parallel propagation where magnetic tension is the dominant restoring force) are ubiquitous in the solar upper atmosphere (McIntosh et al., 2011) signifies an important new development with profound consequences for our understanding of the corona and solar wind. More recently Jess et al. (2009) have detected Alfvén waves lower in the solar atmosphere.

Comprehensive measurements of magnetic fields in the solar corona have a longer history as an important scientific goal (e.g., Dulk and McLean, 1978; House et al., 1982; Arnaud and Newkirk, 1987; Lin et al., 2004; Tomczyk et al., 2007). As well as being crucial to understanding coronal structures and the Sun’s generation of space weather which can affect communications, GPS systems, space flight, and power transmission (Hanslmeier, 2003; Lambour et al., 2003; Iucci et al., 2006), the measurement of its strength and direction is also a crucial step in understanding observed wave motions. Most forms of solar activity, including high energy electromagnetic radiation, solar energetic particles, flares, and coronal mass ejections (CMEs), derive their energy from magnetic fields. The corona is also the most plausible source of the solar wind with its embedded magnetic field that engulfs the Earth. The ability to measure coronal magnetic fields will lead to improved predictions of hazardous space weather effects on Earth because of further understanding of the underlying physical processes.

Magnetic fields in the corona have been extremely difficult to measure for three important reasons: (1) the magnetic fields in the corona are intrinsically weak compared to the rest of the sun; (2) coronal spectroscopic lines are dimmer than their photospheric counterparts; and (3) the optically thin corona requires interpretation of magnetic signatures integrated along extended path lengths. Most knowledge to date has been derived

from extrapolations from photospheric magnetograms (see e.g., the review by Wiegelm and Sakurai, 2012; Régner, 2013). Recently, the HAO-NCAR Coronal Multi-channel Polarimeter (CoMP) instrument (Tomczyk et al., 2008) made breakthrough measurements of the coronal magnetic field that lead to discoveries of coronal Alfvén waves (Tomczyk et al., 2007), as well as advancement in the magnetic structure in prominences and coronal cavities (Dove et al., 2011; Bak-Stęlicka et al., 2013). However, such ground observations are still limited by the sky background, atmospheric seeing effect and the day-night and weather related interruptions. With such observations from space still lacking and the prospect of such instrumentation on a space mission still uncertain, the most sensible way is to take the measurements from above the atmosphere with long-duration balloon flights.

In this paper, we describe the design and scientific values of the Waves and Magnetism in the Solar Atmosphere (WAMIS) investigation. In The Importance of Magnetic Field and Waves Measurements in the Corona we describe the importance of coronal magnetic field and waves measurements in answering current outstanding questions in solar physics. WAMIS Instrument Concept describes the observational requirements, methodology and the WAMIS Instrument Design for making breakthroughs in the coronal field measurements. Concluding remarks gives some concluding remarks.

## THE IMPORTANCE OF MAGNETIC FIELD AND WAVES MEASUREMENTS IN THE CORONA

In this section, we describe major outstanding questions in solar physics research that illustrate the importance of direct measurements of the coronal magnetic field in its strength, structure and dynamics.

### What Determines the Magnetic Structure of the Corona?

The large-scale coronal structure is a consequence of surface field advection, differential rotation, and photospheric flux emergence. Information on the evolution and interactions between magnetically closed and open regions could shed light into understanding the changing structure of the heliospheric magnetic field and how the slow solar wind is formed. The fast solar wind has been known for some time to originate in open field regions, i.e., coronal holes (e.g., Krieger et al., 1973). The origins of the slow wind are more obscure, but are thought to be at the interface between open and closed field where reconnection opens up previously closed regions (e.g., Fisk and Schwadron, 2001). This idea has been refined recently by Antiochos et al. (2011) in terms of the S-web (“S” stands for separatrix), where extensions from the polar coronal holes reach down to lower latitudes, allowing open field and closed field regions to interact.

Coronal magnetic field measurements would allow a reconstruction of magnetic field in the extended corona from which the topology of the S-web could be estimated. Also, turbulence in the slow wind is known to be more “balanced”

than in the fast wind (e.g., Bruno and Carbone, 2005), meaning that the amplitudes of waves propagating in opposite directions along the magnetic field are more nearly equal than in the fast wind. The existing claims for coronal Alfvén wave detections (Cirtain et al., 2007; De Pontieu et al., 2007; Tomczyk et al., 2007; Tomczyk and McIntosh, 2009; Okamoto and De Pontieu, 2011) often see a preponderance of waves propagating in one direction (i.e., upwards), more consistent with fast wind. More recently De Moortel et al. (2014) and Liu et al. (2014) have seen upward propagating waves at both loop footpoints meeting at the apex and generating higher frequency (presumably balanced) turbulence. In the likely case that this difference in turbulence has its origin in the solar wind source regions, measurement of waves in the corona has unique potential to distinguish between slow and fast wind in this way, and thus investigate their interface. Such investigations are ideally suited to solar minimum conditions when polar coronal holes are better defined and magnetic topology is less complex than at solar maximum.

Another distinction between fast and slow solar wind lies in their elemental compositions. The fast wind is relatively unfractionated, while the slow wind exhibits an enhancement in abundance of elements with first ionization potential (FIP) less than about 10 eV (the so-called “FIP Effect”; e.g., see von Steiger et al., 1995; Feldman and Laming, 2000). This effect is most convincingly explained in terms of the ponderomotive force in the chromosphere, resulting from the propagation through or reflection from the chromosphere of Alfvén waves (Laming, 2004, 2009, 2012, 2015; Rakowski and Laming, 2012) with peak amplitudes in the corona of  $25\text{--}100 \text{ km s}^{-1}$ , depending on the chromospheric model and coronal density. This amplitude is larger than that typically associated with nonthermal mass motions inferred from spectral line broadening by a factor of up to 4, but evidence for such motions has more recently been documented (e.g., Peter, 2001, 2010). CoMP sees much lower Doppler velocity amplitudes than these (Tomczyk et al., 2007), but McIntosh and De Pontieu (2012) argue that this is due to line of sight (LoS) superposition effects “hiding” the true coronal wave flux in enhanced non-thermal broadening. FIP fractionated closed loops should show more balanced waves than less fractionated open field regions, due to repeated Alfvén wave reflection from the chromosphere, consistent with presumed origin of the slow wind in a fractionated closed loop and the fast wind in a relatively unfractionated open field region. De Moortel et al. (2014) and Liu et al. (2014) see something like this in CoMP observations of coronal loops, though the balanced turbulence is restricted to the apex region, and is observed at higher frequencies possibly indicating an onset of turbulent cascade where upcoming waves from each footpoint meet. The interpretation of decreasing spectral line widths with height above a coronal hole in terms of Alfvén wave damping (Hahn et al., 2012; Hahn and Savin, 2013) would lead to the prediction of a similar phenomenon in open fields, if the Alfvén wave damping proceeds by turbulent cascade. Counter propagating Alfvénic waves have recently been detected in coronal holes (Morton et al., 2015), supporting this inference. Further, Alfvén and fast mode waves also behave differently around coronal null points, also represented by separatrices or quasi-separatrix layers. Fast

mode waves refract across field lines and accumulate at the null point, leading to increased wave heating, while Alfvén waves are confined to magnetic field lines (Thurgood and McLaughlin, 2013). Detecting these waves directly would provide valuable information for distinguishing the solar wind formation and acceleration mechanisms in both the fast and slow solar wind.

## How are Flux Ropes Formed, How Do they Evolve, and How are they Related to CMEs?

Opposing views exist regarding the nature of flux tubes in active regions. Some authors suggest that coronal loop must have twisted field, in order to give it a distinct identity, separate from other coronal magnetic field (e.g., Hood et al., 2009; Vasheghani Farahani et al., 2010), and to be sufficiently buoyant to emerge from the convection zone (e.g., Archontis, 2008). Others argue that newly emerged flux is untwisted, and the flux rope signatures seen in *in situ* observations of ICMEs arise due to reconnection of a sheared arcade during the CME eruption (e.g., Lynch et al., 2004) or a pre-CME flare (Patsourakos et al., 2013). Sakai et al. (2001) found that torsional waves in twisted high  $\beta$  ( $\approx 1$ ) loops propagate preferentially in a direction that unwinds the twist. Observations of constant cross sectional loops have been interpreted as being due to circular loops necessarily exhibiting significant twist (Klimchuk, 2000). More recent studies suggest that this is an observational selection effect, and that coronal magnetic field is asymmetric and untwisted (Malanushenko and Schrijver, 2013). The distinction is important, relating to the mechanisms by which flux emerges, CMEs erupt, and the nature of waves on such structures. Pure torsional Alfvén waves may only propagate on untwisted flux tubes (Vasheghani Farahani et al., 2010). The twist necessarily introduces mixing between Alfvén and kink modes, with consequences for the wave damping and coronal heating. The absence of intensity oscillations seen by CoMP (Tomczyk et al., 2007) suggests that any torsional waves in the solar corona must have been propagating on untwisted magnetic field.

Observing the magnetic structure of various loops, including prominences, and prominence flows, e.g., through He I 1083.0 nm, together with observations of the chromospheric magnetic fields under the same structure, once inverted (e.g., Orozco Suárez et al., 2014), could place constraints on prominence densities and determine how prominence and coronal magnetic fields interact, how and where magnetic energy is stored (e.g., flux and helicity transport) and how it is released (e.g., instabilities, reconnection, dissipative heating). In particular, measurements of prominence cavities obtained by the CoMP instrument indicate a characteristic “lagomorphic” signal (i.e., morphologically shaped like a rabbit’s ear) in linear polarization consistent with twisted magnetic flux tubes, or ropes. Bak-Steślicka et al. (2013) showed that coronal prominence cavities, for example as observed by SDO/AIA193 Å channel, are observed by CoMP to have such linear polarization signature in the Fe XIII 1074.7 nm line. This signature can be explained as arising from an arched magnetic flux rope with axis oriented along the LoS (e.g., Fan, 2010; Gibson et al., 2010). When

integrated along the LoS, a combination of linear polarization nulls occurring where the flux rope magnetic field is oriented at the van Vleck angle  $\theta$ , ( $\cos^2\theta = 1/3$ ), or where the axial magnetic field is oriented completely out of the plane of sky (PoS), leads to a forward-modeled signal of the same characteristic shape as observed. Linear polarization is sensitive to PoS magnetic field, so a “polarization ring” may occur when magnetic field winds around a central LoS-oriented axis. Indeed, early CoMP observations of a prominence cavity showed just such a structure (Dove et al., 2011). LoS effects play an important role so that such a pure ring may be rare, and may also indicate a different magnetic topology to the flux ropes in Bak-Steślicka et al. (2013). However, analysis of CoMP observations indicate a truly ubiquitous lagomorphic structure in linear polarization observed in Fe XIII associated with prominence cavities that matches expectations for the linear polarization signal of a forward-modeled, arched magnetic flux rope fully integrated along the LoS (e.g., Rachmeler et al., 2013). Analysis of the circular polarization of such structures would confirm the presence of a magnetic axis and quantify its field strength. Inside prominences, similar studies may be undertaken with the He I 1083.0 nm line, while outside a coronal line, such as Fe XIII 1074.7 nm, can be used.

## Where Do CME-Associated Shocks Form?

Particles accelerated by CME-driven shocks have the highest particle energies of all suprathermal species and pose the greatest space weather hazards to spaceborne instrumentation and humans. The very highest SEP energies arise when acceleration begins very close to the sun. Gopalswamy et al. (2001) and Mann et al. (2003) use model magnetic fields and density profiles for different solar regions, with particular attention to active regions, to estimate the heliocentric radius where a CME driven disturbance becomes a shock (i.e., Alfvén Mach number,  $M_A > 1$ ), and where it becomes supercritical ( $M_A > 2-3$ , depending on plasma  $\beta$  and shock obliquity). This last transition is crucial, because it determines where the shock begins to become turbulent and may begin to reflect and accelerate particles (Edmiston and Kennel, 1984), in the absence of pre-existing seed particles.

Measurements of the electron density and constraints on the magnetic field within about  $1.25 R_\odot$  (where the Fe XIII 1074.7 nm/1079.8 nm line pair is sensitive to electron density) would remove the ambiguities introduced in the model for these quantities entering in the calculation of the Alfvén speed. Further the magnetic field PoS direction allows inference of the CME shock obliquity. Such shocks are currently believed to propagate close to the Sun as quasi-perpendicular, evolving to quasi-parallel further out (Tylka and Lee, 2006; Rouillard et al., 2011). This has consequences for particle acceleration (Laming et al., 2013). More sophisticated current shock acceleration theories generally treat only the parallel case (e.g., Ng and Reames, 2008).

Coronal magnetic field measurements during the passage of a CME can detect compressions and distortions in the magnetic field as well as associated waves due to the formation and passage of a CME shock. Density compressions resulting from shock formation can be large enough to produce intensity enhancements in white light coronal images as well

(Vourlidas et al., 2003) that are complementary to coronal field measurement for understanding the CME shock and its role in producing SEPs.

## How is Energy Stored and Released by Reconnection in Coronal Heating, Flares and CMEs?

Most observations designed to detect signatures of magnetic reconnection in the solar corona to date have focused on observing high temperature plasma, specifically high electron temperatures. While observations of CME current sheets have been successful in this respect (e.g., Ciaravella et al., 2002; Ko et al., 2003; Ciaravella and Raymond, 2008; Savage et al., 2010), searches of the solar corona for evidence of nanoflare heating have been less clear (e.g., Brooks et al., 2009). Observations by Hi-C (Cirtain et al., 2013) suggest that both nanoflares (e.g., Testa et al., 2013) and steady heating (e.g., Warren et al., 2010; Peter et al., 2013), presumably associated with waves, are present. Such waves are often suggested to propagate up from the convection zone (e.g., Asgari-Targhi et al., 2013), although reconnection is also a potential source of waves (e.g., Sturrock, 1999; Longcope et al., 2009; Kigure et al., 2010; Liu et al., 2011), and offers another interpretation of the results of De Moortel et al. (2014). Hence it appears that the detection and identification of different modes of magneto-hydrodynamic (MHD) waves, combined with observations of magnetic topology, would be highly constraining on the nature and existence of magnetic reconnection at the heart of an active region. The magnetic free energy could be calculated from the non-potential field (e.g., extrapolated from photospheric or chromospheric magnetograms), and compared with energetics of the active region.

Direct experimental knowledge of LoS magnetic field strengths before and after a CME eruption would allow estimation of the magnetic energy released, for comparison with measurements of CME kinetic, thermal and gravitational energy. This would be complementary to the estimates derived from field extrapolations. It would also allow an assessment of the likely mechanism of CME eruption (see e.g., Ugarte-Urra et al., 2007) from the change in magnetic topology. The LoS field strength and PoS direction together provide diagnostics for magnetic topologies, including magnetic nulls and current sheets that can be compared to the location of high temperature emission.

## WAMIS INSTRUMENT CONCEPT

The Waves and Magnetism in the Solar Atmosphere (WAMIS) investigation is a long duration balloon (LDB) based 20 cm aperture coronagraph designed to meet challenges of answering these outstanding questions. WAMIS builds on the heritage of CoMP (Tomczyk et al., 2008), and could obtain continuous measurements over at least 2 weeks of the strength and direction of coronal magnetic fields within a large field-of-view (FOV) at the spatial and temporal resolutions required to address outstanding problems in coronal physics. The key WAMIS characteristics are summarized in **Table 1**. Additionally, the WAMIS investigation would make near simultaneous

**TABLE 1 | WAMIS long duration balloon instrument characteristics.**

Telescope type	Internally occulted Lyot coronagraph
Objective lens	f/10 singlet, aperture 20 cm, focal length 203.3 cm
Objective Stray Light	<0.2 $\mu$ B <sub>0</sub> goal, 1.2–2.8 R <sub>0</sub> (B <sub>0</sub> = 9.34 × 10 <sup>6</sup> erg/cm <sup>2</sup> /s/sr/nm)
Overall Throughput	≈5%
Plate Scale	4.5"/pixel low magnification mode; 1.5"/pixel high magnification mode
Fe XIII (1074.7 nm)	1 × 10 <sup>5</sup> photons/pixel/s @1.5"/pixel magnification
Count Rate @ 1.1 R <sub>0</sub>	
Detector	Goodrich Visible+SWIR camera, 15 micron pixels, 1280 × 1024 format
Inner FOV Limit	1.02 R <sub>0</sub>
Outer FOV	±2.8 R <sub>0</sub> @4.5"/pixel Sun Centered; 1.8 R <sub>0</sub> @1.5"/pixel Limb Centered
Primary Lines of Interest	Fe XIII (1074.7, 1079.8 nm); AR observations; Fe X (637.5 nm), Fe XI (789.2 nm); CH&CHB observations; He I (1083.0 nm); prominence/flux rope observations
Filter	Tunable Lyot filter, 3.8 cm aperture, 530–1100 nm range
Duration of Continuous Observational Sequence	2 weeks minimum; ≥4 weeks optimum

observations of the electron scattered K-corona for context and to establish electron density out to greater radial distances than those accessible with the Fe XIII 1074.7 nm/1079.8 nm intensity ratio ( $\sim 1.25$  R<sub>0</sub>; wavelengths given here and elsewhere are values in air). These comprehensive observations are not provided by any current single observatory. The visible-IR spectral range covers emission lines for understanding the magnetic field strength and structure in the active region (AR) and coronal hole (CH), the coronal hole boundary (CHB) region relevant for solar wind studies, as well as the prominence/flux rope structures. Observations of MHD waves would address fundamental issues in coronal heating and the sources and acceleration of the solar wind. In particular, the cross helicity of observed waves (from Fe XIII together with Fe X 637.5 or Fe XI 789.2 nm) should allow an empirical distinction between “balanced” turbulence in the slow wind, compared to more directed turbulence in the fast wind (e.g., Bruno and Carbone, 2005). Since coronal waves detected so far are ubiquitously “Alfvénic,” their direction of propagation indicates the magnetic field vector [either because of their natural properties (Alfvén mode), or because of refraction to high density that follows the magnetic field (fast mode)], and such observations obviously complement direct magnetic field measurements.

## Observational Requirements

The science questions in Section The Importance of Magnetic Field and Waves Measurements in the Corona could be addressed through observation of coronal magnetic fields and waves over a 1.02–1.8 R<sub>0</sub> FOV with high spatial resolution of 1.5" or an alternative 1.02–2.8 R<sub>0</sub> large-FOV mode with a spatial resolution of 4.5", at a temporal cadence of 5 min (see Section Advantages of Measurements Outside of the Atmosphere for more detail). At this cadence, WAMIS would be sensitive to magnetic field

strengths of <10 Gauss for the faintest detectable coronal structures and one Gauss for the brightest. A spatial resolution of 4.5" is sufficient to address many of the scientific questions pertaining to the global magnetic structure of the corona, while the 1.5" resolution allows a more detailed view of individual coronal features. The capability for the higher spatial resolution observations (1.5") over a more limited FOV would be achieved with interchangeable magnification lenses. This new capability of WAMIS is potentially important for observations of active region loops, and represents a significant improvement on the capabilities of CoMP. According to McIntosh and De Pontieu (2012), WAMIS should see correspondingly higher Alfvén wave amplitudes than CoMP, due to reduced confusion caused by spatial-averaging. The large FOV of WAMIS (up to 2.8 R<sub>0</sub> from Sun center) would be needed to observe the global properties of the corona and is required to address the science questions, concerned with tracking the outward motion and other basic properties of the solar wind, CMEs and prominences as they are ejected from the corona. It is also necessary to observe as low in the corona as possible to understand how the corona continually reacts to changes occurring in the photosphere and chromosphere. High temporal cadence is needed to capture the relentless dynamic evolution of the coronal plasma structure and explosive disturbances (e.g., MHD waves, shocks, prominence eruptions, CMEs). The physical properties of CMEs and eruptive prominences are best determined from the polarization signal of broadband filtered white-light observations because the scattered light from the corona is partially polarized. Furthermore, the absence of all atmospheric seeing effects (not just sky brightness) could prove to be a critical advantage to balloon-borne as opposed to ground-based instrumentation.

Note that a 5 min cadence for magnetic field measurement does not limit the minimum wave frequency WAMIS can measure, because wave observations (unpolarized) would not need the same accumulated exposure time for a given signal-to-noise ratio (S/N, see discussion of magnetic field S/N in Section Improved Sensitivity for Measurement of the Magnetic Field Strength). Depending upon the intensity of the target structure for wave observations, the image cadence could be as short as 2 s, thus detecting waves of period as low as 1 min. The images required for a wave investigation at this cadence would not necessarily require a different observational program from the magnetic field observing program. Thus the wave and magnetic field observing programs could run simultaneously, even though the cadence of the two measurements generated by post-flight analysis would be very different.

**Table 2** shows the science traceability matrix. There is a specific need to directly measure the magnetic field both in the corona and in the chromosphere. Recent observations suggest that MHD waves in the upper chromosphere have sufficient energy to accelerate the solar wind outside of active regions (Aschwanden et al., 2007; De Pontieu et al., 2007; McIntosh et al., 2011), if they can escape into the corona. WAMIS would provide routine magnetic field and wave measurements in this key region and would complement observations of activity lower in the solar atmosphere such as by the Interface Region Imaging Spectrograph (IRIS, De Pontieu et al., 2014)

and Chromosphere and Prominence Magnetometer (ChroMag, de Wijn et al., 2012), already under development, and planned for deployment at Mauna Loa Solar Observatory (MLSO) by 2016. These measurements altogether would provide critical information on the magnetic and plasma conditions to couple the coronal magnetic fields with those measured at photospheric heights.

### Advantages of Measurements Outside of the Atmosphere

#### *Improved sensitivity for measurement of the magnetic field strength*

In order to achieve such observational requirements, WAMIS would need to observe features down to a few millionths of the brightness of the solar disk ( $2 \times 10^{-6} B_{\odot}$  or  $2 \mu B_{\odot}$ ), which requires an effective sky background an order of magnitude lower (e.g.,  $0.2 \mu B_{\odot}$ ). For example, bright loops above active regions are typically of the order of  $20\text{--}25 \mu B_{\odot}$  while in coronal holes the brightness is typically  $1\text{--}2 \mu B_{\odot}$ . One objective of the WAMIS instrument would be to perform coronal magnetometry using the forbidden emission lines of Fe XIII at 1074.7 and 1079.8 nm and the He I emission line at 1083.0 nm. While coronal magnetometry would not be the only objective of WAMIS, it is instructive to consider the details of this measurement from outside the atmosphere.

Because the amplitude of the Zeeman-induced circular polarization (Stokes  $V$ ) signal is  $\approx 10^{-3}$  for a 10 G field for

the Fe XIII 1074.7 nm line [the linear polarization signal is typically 2 orders of magnitude higher (Lin et al., 2000; Tomczyk et al., 2008)], the S/N requirement for the circular polarization measurements drives the requirement for coronal magnetometry (such as by enlarging the aperture of the coronagraph or longer integration time to obtain better counting statistics). For ground-based observations, stray light in the form of sky brightness is usually the dominant noise source. The expected noise in the LoS component of the coronal field due to the combination of photon counting statistics in the signal and in the stray light background can be derived from consideration of the propagation of errors in the circular polarization measurements (Penn et al., 2004), and is given by

$$\sigma_B[G] = \frac{8500}{\sqrt{I_{\text{line}}}} \sqrt{1 + 2 \frac{I_{\text{sky}}}{I_{\text{line}}}} \quad (1)$$

where  $I_{\text{line}}$  and  $I_{\text{sky}}$  are the number of photons in the emission line and background, respectively. This equation assumes photon noise limited observations in the Fe XIII 1074.7 nm (Landé  $g$  factor = 1.5) emission line. Note this equation ignores all other atmospheric seeing effects generating noise in the polarization measurement except for atmospheric stray light (sky brightness). Equation (1) shows that the presence of sky background (including instrument scattered light) reduces the effective aperture of the telescope. That is the reason why long integration times are needed from the ground to achieve the desired polarimetric sensitivity. From MLSO, where CoMP is located, the sky brightness is nominally  $5.0 \mu B_{\odot}$ . However, for balloon-borne observations, internally generated stray light of the coronagraph dominates the sky background. For the internally occulted design of WAMIS a conservative estimate of the stray light-generated sky background is equivalent to  $I_{\text{sky}} = 0.2 \mu B_{\odot}$ . We can combine Equation (1) with a flux budget for the corona and compute the expected noise level as a function of coronagraph aperture size and coronal brightness. This is illustrated in Figure 1, assuming a system throughput of 5%, a pixel of  $5''$ , and an integration time of 5 min. On the left are balloon-borne observations where the stray light is strictly generated by the coronagraph (e.g.,  $0.2 \mu B_{\odot}$ ). On the right are

**TABLE 2 |** Science traceability matrix; see text for details.

Science Objective	FoV/Spatial Resolution	Physical Observable
1. Fast/Slow Wind, Coronal B	$1.02\text{--}1.8 R_{\odot}/1.5''$ pix.; Waves: Doppler velocity, plasma density, B-field direction structure	
2. Prominences, flux ropes	$1.02\text{--}1.8 R_{\odot}/1.5''$ pix	B-field magnitude & direction from He I and Fe XIII
3. CME Shocks	$1.02\text{--}2.8 R_{\odot}/4.5''$ pix.	B-field magnitude & direction, Waves: Doppler velocity, plasma density
4. Reconnection	$1.02\text{--}1.8 R_{\odot}/1.5''$ pix.	B-field magnitude & direction, Waves: Doppler velocity, plasma density

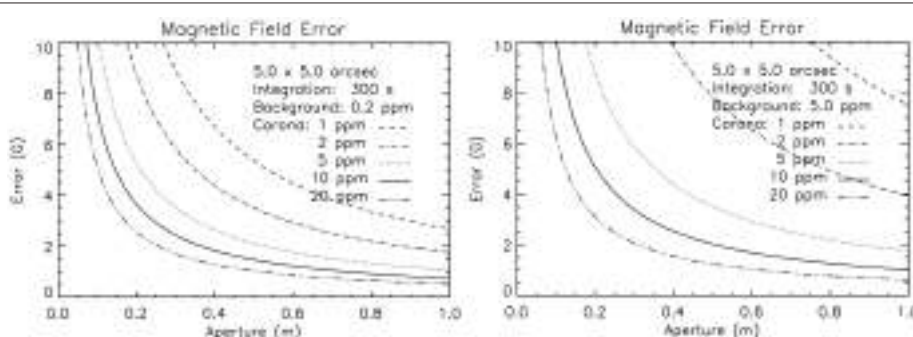


**FIGURE 1 |** These plots illustrate the impact of stray light on the relationship between LoS magnetic field strength sensitivity in Fe XIII 1074.7 nm and telescope aperture (see text for detail).

observations at MLSO where a typically good sky background is  $5.0 \mu\text{B}_\odot$ . The lines plotted correspond to various intensities of the corona in  $\mu\text{B}_\odot$  units. With balloon-borne observations, it is possible to achieve magnetic field sensitivities of 3.5 G in 5 min for coronal structures with brightness of  $10 \mu\text{B}_\odot$  using a 20 cm aperture telescope. From a similar instrument from the ground (i.e., CoMP at MLSO), with 5 min integration one achieves a sensitivity of 5 G. The needed integration time to reach comparable  $\sigma_B$  on the ground would be two times longer.

**Figure 2** compares the modeled Fe XIII 1074.7 nm Stokes V signal integrated for 1 h for the sky background expected for WAMIS vs. that for CoMP. The larger circular polarization signal of a balloon-borne WAMIS is obvious. For example, Rachmeler et al. (2013) modeled the linear and circular polarizations from a flux rope and a sheared arcade. They showed that the true disambiguator between the two magnetic models is the circular polarization. A flux rope will have a clearly defined magnetic axis, where the circular polarization (proportional to the LoS magnetic field) will peak. This demonstrates the importance and advantage of performing IR coronal magnetometry from a balloon-borne or space platform.

#### Eliminating seeing effect through the Earth's atmosphere

Near-space observations on a balloon platform would eliminate all polarization noise (variability) introduced by the Earth's atmosphere which is difficult to quantify for ground-based observations. This would provide a fundamental advantage in the interpretation of all coronal magnetometry observations, including observations with future larger aperture ground-based instruments, e.g., the Daniel K. Inouye Solar Telescope (DKIST), and the Coronal Solar Magnetism Observatory (COSMO). A second advantage would be to allow WAMIS

to forego simultaneous continuum observations required for ground-based instruments (such as the Wollaston prism on CoMP, Tomczyk et al., 2008). Therefore, the full imager plane can be used for the line image resulting in an increase in routine spatial resolution for a given detector format and FOV. While continuum images do not need to be obtained simultaneously with the line images, they could be obtained at appropriate intervals to provide reference background and K-corona imaging.

#### Enabling continuous observations

The continuity of balloon-borne observations (independent of atmospheric variation, and no day/night cycle and weather-related interruptions) could be used to integrate signals over extended periods of time and beat down the photon noise. Coronal cavities associated with polar crown prominences would be good candidates for such a study, since they tend to be dynamically stable and are extended along the LoS, so that they can be essentially unchanged for up to several days of limb observations. Since most coronal lines observed by WAMIS are optically thin plasma projected against the PoS, this advantage is critical in separating the 3-D structure of the corona from short-term evolution of the corona. Uninterrupted observations also increase the probability of detecting and following solar transient events. In addition, uninterrupted observations of over 2 weeks with the expected magnetic field sensitivity of WAMIS could in principle enable tomographic inversions for 3D magnetic field vector (Kramar et al., 2006, 2013; Judge et al., 2013).

#### Advantages of the Large Field-of-View

The FOV of WAMIS ( $1.02\text{--}2.8 R_\odot$ ) would enable analysis of the global magnetic topology of the corona. For example, Rachmeler

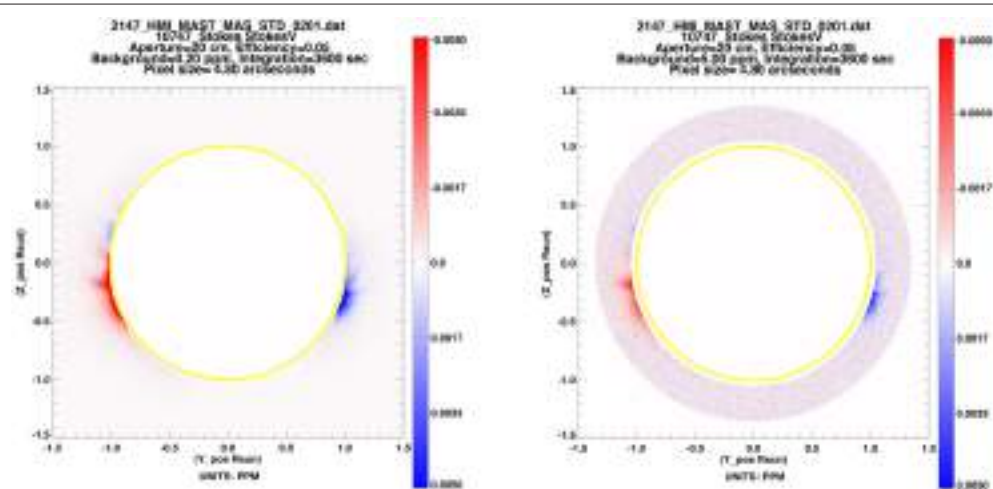


**FIGURE 2 | Comparison of forward-modeled circular polarization for a global coronal MHD model (Predictive Science Inc. MAS model for Carrington Rotation 2147, from [http://www.predsci.com/hmi/data\\_access.php](http://www.predsci.com/hmi/data_access.php)), and applying the FORWARD SolarSoft codes (<http://www.hao.ucar.edu/FORWARD>). Photon noise is added based on telescope aperture, efficiency, background, pixel size, and integration time. Left: Background = 0.2 PPM (i.e.,  $0.2 \mu\text{B}_\odot$ , appropriate for WAMIS), Right: Background = 5 PPM (appropriate for CoMP), all integrated for 1 h. WAMIS vs. CoMP FOVs are explicitly applied to these images as internal/external occulters (at  $1.02/1.05, 2.8/1.35 R_\odot$  respectively). Note that sources of systematic errors are not considered, but are expected to be significant since the signal shown here is on the order of 0.1% of intensity.**

et al. (2014) forward modeled Fe XIII signals for pseudostreamers vs. double streamers and found clear distinctions between these magnetic topologies arising from the null point lying above the pseudostreamer (at  $\sim 1.4 R_{\odot}$ ). Analysis of PROBA2 Sun Watcher using Active Pixel System Detector and Image Processing (SWAP) data yielded structures in EUV that aligned with the expected distinctions in morphology, but the Fe XIII 1074.7 nm linear polarization topological measurement was limited by the CoMP FOV. WAMIS will be able to unambiguously reveal the pseudostreamer topology. The large FOV would also allow better tracing of the evolution of the CME dynamics from the line intensity, Doppler shift and width (Tian et al., 2013). As a comparison, the up to 5 arcmin FOV of DKIST is not designed for studies of the global coronal structure and CMEs, and the 1.05–1.35  $R_{\odot}$  FOV of CoMP would miss a significant fraction of the null points in coronal structures and post-CME current sheet, as well as the likely formation of SEP-produced CME shocks above  $1.5 R_{\odot}$ .

## Coronal Magnetometry via Zeeman and Hanlé Effect

The Zeeman effect in forbidden coronal lines can provide information on coronal magnetic fields with strengths as low as a fraction of a Gauss and as high as several thousand Gauss. This is very important as it provides information on both the large-scale “quiet” coronal fields as well as the active region fields. The observations are restricted to off-limb observations obtained with coronagraphs (or at total solar eclipses) and in which LoS integration issues arise, because of the small optical depths in the corona. However, this is not an overwhelming issue as argued by Judge et al. (2013). To address the LoS confusion of coronagraph observations one can use coincident white-light and EUV observations such as those from the Solar Terrestrial Relations Observatory (STEREO), the Large Angle and Spectrometric Coronagraph Experiment (LASCO, Brueckner et al., 1995) on SOHO, and SDO observations to determine the distribution and the emission measure of material along the LoS. Also, persistent observations over at least 2 weeks under identical conditions can be used as rotational “tomography” on long-lived structures.

The Zeeman effect in circular polarization only gives information on the magnetic field projection along the LoS. Thus it provides a lower bound for the true magnetic strength. These measurements are challenging because the circular polarization signal is typically very small in the quiet corona (about 0.1% of the intensity for field strengths of 10 G). Thus a rigorous calibration of all possible sources of polarization noise is fundamental. The extended sequence of observations without atmospheric noise will allow an examination of the ultimate return that can be achieved by these techniques and guide the design and use of future large aperture ground based coronal magnetographs.

Using the saturated Hanlé effect (scattering polarization) applicable in coronal conditions, the PoS direction of the magnetic field can be determined from the linear polarization signal of the scattered radiation, subject in general to a  $90^{\circ}$  ambiguity (e.g., Lin and Casini, 2000). Where the Stokes

parameters  $U = 0$  and  $Q \neq 0$ , the field coincides with one of axes defined by  $Q$ . The ambiguity can be resolved due to the “Van Vleck” effect which causes nulls of linear polarization to occur at a specific angle  $\theta$ , where  $\cos^2\theta = 1/3$ , between the magnetic field and the solar vertical. On either side of the null, the polarization direction changes by  $90^{\circ}$ . Identification of nulls can then be used to tightly constrain the morphology of the magnetic structure. These measurements are much easier, because the linear polarization of the forbidden coronal lines is typically of a few percent. The Fe XIII 1074.7 nm line is chosen because its emission is dominated by scattered disk radiation, and depolarizing effects due to collisions and radiative cascades are insignificant (Judge, 1998). The Fe XIII 1079.8 nm line conversely is dominated by collisions, yielding the density sensitivity of the ratio to the 1074.7 nm line. WAMIS magnetic field observations would additionally be supplemented by the ChroMag full-disk measurements of the chromospheric vector magnetic field, and by measurements of wave propagation in the PoS. Thus the PoS Alfvén speed will be inferred, and with the density from the 1074.7/1079.8 nm intensity ratio, or from white light polarization brightness, the PoS magnetic field can also be calculated.

Measurements using both Zeeman effect and Hanlé effect can yield vector field information when the polarized light originates from a defined volume (Casini and Judge, 1999). In those cases constraints can be placed on the inclination of the magnetic field and therefore the total field strength and direction. In cases when a structure possesses substantial uniformity along the LoS (such as polar-crown-filaments and their cavities), magnetic field strength and structure may likewise be determined. **Table 3** lists key observables by WAMIS and the means to obtain them. See **Table 2** for connecting these observables to the science objectives.

## WAMIS Instrument Design

### CoMP as Heritage Instrumentation

The techniques described in Section Coronal Magnetometry via Zeeman and Hanlé Effect have been fully demonstrated with CoMP on the 20 cm aperture OneShot coronagraph originally at National Solar Observatory’s Sacramento Peak Observatory in New Mexico (Tomczyk et al., 2008), and later has been operating on a daily basis at MLSO since 2011. The CoMP instrument was designed to observe the coronal magnetic field with a FOV in the low corona ( $\sim 1.03$  to  $1.4 R_{\odot}$ ), as well as to obtain information about the plasma density and motion.

**TABLE 3 | Key WAMIS observables.**

Line-of-sight $B$ , field strength	Circular polarization	Longitudinal Zeeman effect
Plane-of-sky $B$ , field direction	Linear polarization	Resonance scattering effect (Hanlé effect)
Line of sight velocity	Intensity vs. wavelength	Doppler effect
Plasma density	Fe XIII 1074.7 nm/1079.8 nm intensity ratio, IR continuum	Atomic physics, radiation transfer

The CoMP instrument is a combination polarimeter and narrowband tunable filter that can measure the Doppler shift and complete polarization state of the Fe XIII infrared coronal emission lines at 1074.7 and 1079.8 nm and the chromospheric 1083 nm He I line. The polarimeter function is achieved by a pair of Liquid Crystal Variable Retarders (LCVRs) followed by a linear polarizer that allows the selection of a polarization state characterized by Stokes parameters ( $I$ ,  $Q$ ,  $U$ ,  $V$ ). The filter is a four-stage, wide-field calcite birefringent filter with a bandwidth of 0.14 nm at 1074.7 nm. It is tuned in wavelength by four additional LCVRs. Both the polarization and filter bandpass selections are accomplished electro-optically. The CoMP filter has a transmission to unpolarized light of about 30%. The camera for CoMP is a liquid nitrogen cooled Rockwell Scientific (now Teledyne) 1024  $\times$  1024 HgCdTe Infrared detector array. A filter wheel holding three order-blocking filters selects the emission line to be observed. See Tomczyk et al. (2008) for detailed descriptions.

The CoMP observations have a spatial sampling of 4.5'' per pixel and required 30 min of integration time to acquire a measure of the LoS magnetic field strength. As an example shown in Tomczyk et al. (2008), data were obtained in groups of 60 images in quick succession. For linear polarization, five images were taken at each of the four polarization states  $I+Q$ ,  $I-Q$ ,  $I+U$ ,  $I-U$ , and at the three wavelengths, 1074.52, 1074.65, and 1074.78 nm, across the line. For circular polarization, 10 images were taken in each of the two polarization states of  $I+V$  and  $I-V$  at the same three sample wavelengths. The exposure time for the individual images was 250 ms and the two image groups were each obtained at a cadence of  $\sim$ 15 s with a duty cycle of 52%. The driver of the number of image groups (thus integration time) required for a single observation set is the level of sky brightness at MLSO (typically  $5 \mu\text{B}_\odot$ ). The WAMIS coronal magnetometer will profit much more from the unique observation conditions obtained at long duration balloon altitudes, because of the absence of sky brightness background as well as seeing-induced polarization cross-talk and atmospheric-induced source intensity fluctuations (Section Advantages of Measurements Outside of the Atmosphere).

### WAMIS Filter/Polarimeter

In the time since the completion of the CoMP instrument, technological advances in broad-band polarizers and super-achromatic waveplates now present the possibility to construct a compact coronal polarimeter capable of observing coronal and prominence emission lines over a much wider wavelength range than the CoMP instrument. These advances have been incorporated into a filter/polarimeter called “CoMP-S” built by HAO for the Astronomical Institute of the Slovak Academy of Sciences (AISAS) coronagraph on Lomnický Peak. The CoMP-S filter has been operational on the Lomnický Peak Observatory 20 cm Zeiss coronagraph since April 2013. WAMIS filter will use the same CoMP-S filter/polarimeter design (Kucera et al., 2010; Koza et al., 2013; Rybak et al., 2013).

The CoMP-S design was primarily chosen to enable the WAMIS instrument to observe over the range between the Fe XIV coronal green line at 530.3 nm and the He I line at

1083 nm. While the target lines for WAMIS are the IR coronal emission lines 1074.7 nm Fe XIII and 1079.8 nm Fe XIII, and the IR prominence emission line 1083.0 nm He I, this filter will have the additional capability to observe corresponding visible lines - including 530.3 nm Fe XIV, 637.5 nm Fe X and 789.2 nm Fe XI in the corona and 587.6 nm He I and 656.3 nm H $\alpha$  in prominences—for context and additional diagnostics. One particularly important diagnostic achieved with this extension of the wavelength range is the capability to observe coronal waves at temperatures other than Fe XIII, e.g., wave observations in coronal hole and coronal hole boundary with Fe X and Fe XI to study the origin of the slow solar wind. Each line will require a pre-filter be inserted in the optical system with a bandpass that depends on the free spectral range of the birefringent filter at that wavelength.

A secondary motivation for using the CoMP-S design is the use of Ferroelectric Liquid Crystals (FLC) in the polarization modulation instead of the usual LCVR. The objective of using FLC is their faster response time, which will significantly increase the duty cycle of the WAMIS instrument. The polarization modulator will consist of two FLC retarders and a fixed retarder followed by a linear polarizer acting as an analyzer. As for CoMP, the polarizer will also act as the entrance polarizer to the birefringent filter. Note that neither the FLCs nor the fixed retarder are achromatic and the value of retardation and orientation must be selected to optimize the Stokes modulation efficiency over a very broad wavelength range.

For ground observations, simultaneous images in the emission line and continuum bandpasses is important in that it allows the instrument to be insensitive to variations in the intensity of the background caused by image motion and the passage of atmospheric aerosols through the FOV. For a balloon flight above the atmosphere, no such simultaneous observations are required. However, the K-corona can be sequentially imaged in the continuum at a variety of wavelengths to obtain the electron density information.

### WAMIS Coronagraph

The WAMIS coronagraph follows the classic internally occulted Lyot coronagraph design principles (Figure 3). The solar radiation is incident on the entrance aperture. A high quality solar image is produced at the occulter. Coronal radiation from heights of 1.02 to 2.8  $R_\odot$  passes through the coronagraph front end and is collimated before entering into the polarizer/filter assembly. A reimaging lens produces a high quality coronal image at the detector. A compensator plate located at the Lyot stop removes spherical aberration in the coronal image at the occulter plane. A polarization calibration optic will be incorporated in front of the instrument aperture to assure the instrumental polarization effects are understood to a level well under  $10^{-4}$ . Table 4 lists the optical design. The resulting plate scale is 4.5'' for low magnification mode, and 1.5'' for high magnification mode. The WAMIS coronagraph uses a 20 cm entrance aperture, f/10 objective which is sufficient to achieve the scientific requirements in Table 2. The diffraction limit corresponding to this aperture is 1.3'' at a wavelength of 1  $\mu\text{m}$ , so diffraction effects are below the plate scale.

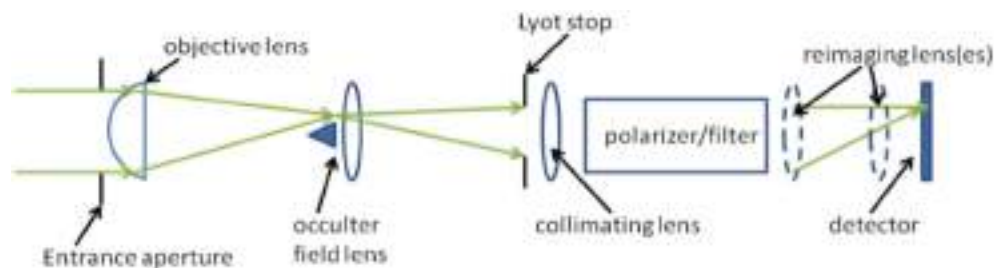


**FIGURE 3 | Optical elements of internally occulted Lyot coronagraph.** Solar radiation enters from left.

**TABLE 4 | Optical design.**

Objective	203.3 cm fl.
Field lens	31.0 cm fl.
Collimating lens	38.0 cm fl.
Re-imaging lens	High Mag. 38.0 cm fl. Low Mag. 12.9 cm fl.

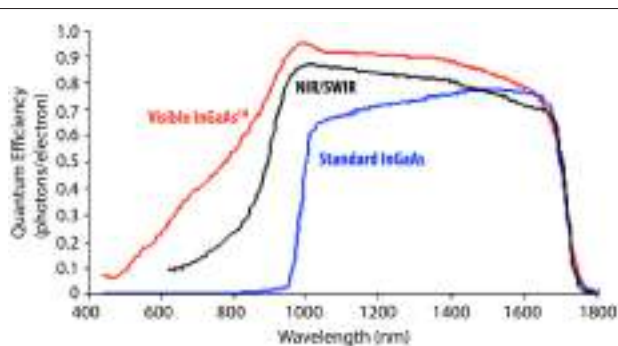


**FIGURE 4 | Detector quantum efficiency (red curve) of the Goodrich Corp. InGaAs High Resolution Visible + SWIR Camera for WAMIS, compared to other camera models (NIR/SWIR and standard InGaAs).**

## WAMIS Detector System

WAMIS will use the Goodrich Corp. InGaAs High Resolution Visible+SWIR (short wavelength infrared) Camera as the detector instead of the Teledyne HgCdTe hybrid camera used on CoMP. A single detector for the wide range of wavelength coverage is also beneficial over separate detectors for the visible and IR. The  $1280 \times 1024$  pixel array focal plane hybrid detector has a 15 micron pitch, achieves 80% quantum efficiency in the target wavelength regime (Figure 4).

## Gondola and Pointing Control

There are at least a couple of options to carry instrument under the balloon. An HAO-developed gondola system was successfully used for two Sunrise solar observations in 2009 and 2012 (Barthol et al., 2011). The NASA Wallops Flight Facility (WFF) Balloon

Program Office (BPO) recently has available a gondola system under the Columbia Science Balloon Facility (CSBF), successfully pioneered by the University of Colorado HyperSpectral Imager for Climate Science (HySICS) investigation in 2013. WAMIS high resolution imaging of  $1.5''$  requires a matching performance in the pointing control during the balloon flight. The NASA Wallops Arc Second Pointer (WASP) system has achieved a pointing performance of better than  $0.25''$  RMS error in both pitch and yaw. This will easily satisfy the WAMIS requirements.

## CONCLUDING REMARKS

The fundamental advance of the balloon-borne WAMIS beyond any ground-based coronal magnetograph will come from an effectively complete absence of variability in the polarization background and the extension of the duration of uninterrupted observing by over an order of magnitude. A good analogy for this advancement is the way the SOHO Michelson Doppler Imager (MDI, Scherrer et al., 1995) made fundamental discoveries on photospheric field even though it was preceded by decades of ground based observations by larger instruments. The freedom to explore different temporal regimes without seeing variability or day-night cycle interruptions was the key to these discoveries. Similarly, the fundamental advancements achieved by the near-space observations of WAMIS on coronal magnetic field and waves will point the way for future ground based and orbital instrumentation.

## AUTHOR CONTRIBUTIONS

All authors contributed to the science and design of the WAMIS instrument. The first seven authors contributed significantly to the write-up of this manuscript.

## ACKNOWLEDGMENTS

This research is supported by the Chief of Naval Research. NCAR is supported by the National Science Foundation.

## REFERENCES

- Antiochos, S. K., Mikić, Z., Titov, V. S., Lionello, R., and Linker, J. A. (2011). A model for the sources of the slow solar wind. *Astrophys. J.* 731, 112–122. doi: 10.1088/0004-637X/731/2/112
- Antonucci, E., Gabriel, A. H., and Patchett, B. E. (1984). Oscillations in EUV emission lines during a loop brightening. *Solar Phys.* 93, 85–94.
- Archontis, V. (2008). Magnetic Flux Emergence in the Sun. *J. Geophys. Res.* 113, A03S04. doi: 10.1029/2007ja012422
- Arnaud, J., and Newkirk, G. Jr. (1987). Mean properties of the polarization of the Fe XIII 10747 Å coronal emission line. *Astron. Astrophys.* 178, 263–268.
- Aschwanden, M. J. (1987). Theory of radio pulsations in coronal loops. *Solar Phys.* 111, 113–136. doi: 10.1007/BF00145445
- Aschwanden, M. J., Fletcher, L., Schrijver, C. J., and Alexander, D. (1999). Coronal loop oscillations observed with the transition region and coronal explorer. *Astrophys. J.* 520, 880–894. doi: 10.1086/307502
- Aschwanden, M. J., Winebarger, A., Tsiklauri, D., and Peter, H. (2007). The coronal heating paradox. *Astrophys. J.* 659, 1673–1681. doi: 10.1086/513070
- Asgari-Targhi, M., van Ballegooijen, A. A., Cranmer, S. R., and DeLuca, E. E. (2013). The spatial and temporal dependence of coronal heating by Alfvén wave turbulence. *Astrophys. J.* 773, 111–122. doi: 10.1088/0004-637X/773/2/111
- Bak-Steślicka, U., Gibson, S. E., Fan, Y., Bethge, C., Forland, B., and Rachmeler, L. A. (2013). The magnetic structure of solar prominence cavities: new observational signature revealed by coronal magnetometry. *Astrophys. J.* 770, L28–L32. doi: 10.1088/2041-8205/770/2/L28
- Barthol, P., Gandorfer, A., Solanki, S. K., Schüssler, M., Chares, B., Curdt, W., et al. (2011). The Sunrise mission. *Solar Phys.* 268, 1–34. doi: 10.1007/s11207-010-9662-9
- Brooks, D. H., Warren, H. P., Williams, D. R., and Watanabe, T. (2009). Hinode/Extreme ultraviolet imaging spectrometer observations of the temperature structure of the quiet corona. *Astrophys. J.* 705, 1522–1532. doi: 10.1088/0004-637X/705/2/1522
- Brueckner, G. E., Howard, R. A., Koomen, M. J., Korendyke, C. M., Michels, D. J., Moses, J. D., et al. (1995). The Large Angle Spectroscopic Coronagraph (LASCO): visible light coronal imaging and spectroscopy. *Solar Phys.* 162, 357–402. doi: 10.1007/BF00733434
- Bruno, R., and Carbone, V. (2005). The solar wind as a turbulence laboratory. *Living Rev. Solar Phys.* 2:4. doi: 10.12942/lrsp-2005-4
- Casini, R., and Judge, P. G. (1999). Spectral lines for polarization measurements of the coronal magnetic field. II. consistent treatment of the Stokes vector for magnetic-dipole transitions. *Astrophys. J.* 522, 524–539. doi: 10.1086/307629
- Chapman, R. D., Jordan, S. D., Neupert, W. M., and Thomas, R. J. (1972). Evidence for the 300-SECOND Oscillation from OSO-7 Extreme-Ultraviolet Observations. *Astrophys. J.* 174, L97–L99. doi: 10.1086/180957
- Ciaravella, A., and Raymond, J. C. (2008). The current sheet associated with the 2003 November 4 coronal mass ejection: density, temperature, thickness, and line width. *Astrophys. J.* 686, 1372–1382. doi: 10.1086/590655
- Ciaravella, A., Raymond, J. C., Li, J., Reiser, P., Gardner, L. D., Ko, Y.-K., et al. (2002). Elemental abundances and post-coronal mass ejection current sheet in a very hot active region. *Astrophys. J.* 575, 1116–1130. doi: 10.1086/341473
- Cirtain, J. W., Golub, L., Lundquist, L., van Ballegooijen, A., Savcheva, A., Shimojo, M., et al. (2007). Evidence for Alfvén Waves in Solar X-ray jets. *Science* 318, 1580–1582. doi: 10.1126/science.1147050
- Cirtain, J. W., Golub, L., Winebarger, A. R., de Pontieu, B., Kobayashi, K., Moore, R. L., et al. (2013). Energy Release in the solar corona from spatially resolved magnetic braids. *Nature* 493, 501–503. doi: 10.1038/nature11772
- De Moortel, I., McIntosh, S. W., Threlfall, J., Bethge, C., and Liu, J. (2014). Potential evidence for the onset of Alfvénic turbulence in trans-equatorial coronal loops. *Astrophys. J.* 782, L34–L39. doi: 10.1088/2041-8205/782/2/L34
- De Pontieu, B., Title, A. M., Lemen, J. R., Kushner, G. D., Akin, D. J., Allard, B., et al. (2014). The Interface Region Imaging Spectrograph (IRIS). *Solar Phys.* 289, 2733–2779. doi: 10.1007/s11207-014-0485-y
- De Pontieu, B., McIntosh, S. W., Carlsson, M., Hansteen, V. H., Tarbell, T. D., Schrijver, C. J., et al. (2007). Chromospheric Alfvénic waves strong enough to power the solar wind. *Science* 318, 1574–1577. doi: 10.1126/science.1151747
- de Wijn, A. G., Bethge, C., Tomczyk, S., and McIntosh, S. (2012). “The chromosphere and prominence magnetometer,” in *Proceedings of SPIE* 8446, 844678, eds I. S. McLean, S. K. Ramsey, and H. Takami (Amsterdam). doi: 10.1117/12.926395
- Domingo, V., Fleck, B., and Poland, A. I. (1995). The SOHO mission: an overview. *Solar Phys.* 162, 1–37. doi: 10.1007/BF00733425
- Dove, J. B., Gibson, S. E., Rachmeler, L. A., Tomczyk, S., and Judge, P. (2011). A ring of polarized light: evidence for twisted coronal magnetism in cavities. *Astrophys. J.* 731, L1–L5. doi: 10.1088/2041-8205/731/1/L1
- Dulk, G. A., and McLean, D. J. (1978). Coronal magnetic fields. *Solar Phys.* 57, 279–295. doi: 10.1007/BF00160102
- Edmiston, J. P., and Kennel, C. F. (1984). A parametric survey of the first critical mach number for a fast MHD shock. *J. Plasma Phys.* 32, 429–441. doi: 10.1017/S002237780000218X
- Erdélyi, R., and Fedun, V. (2007). Are there Alfvén waves in the solar atmosphere? *Science* 318, 1572–1574. doi: 10.1126/science.1153006
- Fan, Y. (2010). On the eruption of coronal flux ropes. *Astrophys. J.* 719, 728–736. doi: 10.1088/0004-637X/719/1/728
- Feldman, U., and Laming, J. M. (2000). Element abundances in the upper atmosphere of the sun and stars: update of observational results. *Phys. Scripta* 61, 222–252. doi: 10.1238/Physica.Regular.061a00222
- Fisk, L. A., and Schwadron, N. A. (2001). Origin of the solar wind: theory. *Space Sci. Rev.* 97, 21–33. doi: 10.1023/A:1011805606787
- Gibson, S. E., Kucera, T. A., Rastawicki, D., Dove, J., de Toma, G., Hao, J., et al. (2010). Three-dimensional morphology of a coronal prominence cavity. *Astrophys. J.* 724, 1133–1146. doi: 10.1088/0004-637X/724/2/1133
- Gopalswamy, N., Lara, A., Kaiser, M. L., and Bougeret, J.-L. (2001). Near-sun and near-Earth manifestations of solar eruptions. *J. Geophys. Res.* 106, 25261–25278. doi: 10.1029/2000JA004025
- Hahn, M., Landi, E., and Savin, D. W. (2012). Evidence of wave damping at low heights in a polar coronal hole. *Astrophys. J.* 753, 36–44. doi: 10.1088/0004-637X/753/1/36
- Hahn, M., and Savin, D. W. (2013). Observational quantification of the energy dissipated by Alfvén waves in a polar coronal hole: evidence that waves drive the fast solar wind. *Astrophys. J.* 776, 78–87. doi: 10.1088/0004-637X/776/2/78
- Handy, B. N., Acton, L. W., Kankelborg, C. C., Wolfson, C. J., Akin, D. J., Bruner, M. E., et al. (1999). The transition region and coronal explorer. *Solar Phys.* 187, 229–260. doi: 10.1023/A:1005166902804
- Hanslmeier, A. (2003). Space weather - effects of radiation on manned space missions. *Hvar Observatory Bull.* 27, 159–170.
- Harrison, R. A. (1987). Solar soft X-ray pulsations. *Astron. Astrophys.* 182, 337–347.
- Hood, A. W., Archontis, V., Galsgaard, K., and Moreno-Insertis, F. (2009). The emergence of toroidal flux tubes from beneath the solar photosphere. *Astron. Astrophys.* 503, 999–1011. doi: 10.1051/0004-6361/200912189
- House, L. L., Querfeld, C. W., and Rees, D. E. (1982). Coronal emission-line polarization from the statistical equilibrium of magnetic sublevels. II. Fe XIV 5303 Å. *Astrophys. J.* 255, 753–763. doi: 10.1086/159874
- Iucci, N., Dorman, L. I., Levitin, A. E., Belov, A. V., Eroshenko, E. A., Ptitsyna, N. G., et al. (2006). Spacecraft operational anomalies and space weather impact hazards. *Adv. Space Res.* 37, 184–190. doi: 10.1016/j.asr.2005.03.028
- Jess, D. B., Mathioudakis, M., Erdélyi, R., Crockett, P. J., Keenan, F. P., and Christian, D. J. (2009). Alfvén waves in the lower solar atmosphere. *Science* 323, 1582–1585. doi: 10.1126/science.1168680
- Judge, P. G. (1998). Spectral lines for polarization measurements of the coronal magnetic field. I. theoretical intensities. *Astrophys. J.* 500, 1009–1022. doi: 10.1086/305775
- Judge, P. G., Habbal, S., and Landi, E. (2013). From forbidden coronal lines to meaningful coronal magnetic fields. *Solar Phys.* 288, 467–480. doi: 10.1007/s11207-013-0309-5
- Kigure, H., Takahashi, K., Shibata, K., Yokoyama, T., and Nozawa, S. (2010). Generation of Alfvén waves by magnetic reconnection. *PASJ*, 62, 993–1004. doi: 10.1093/pasj/62.4.993
- Klimchuk, J. A. (2000). Cross-sectional properties of coronal loops. *Solar Phys.* 193, 53–75. doi: 10.1023/A:1005210127703
- Ko, Y.-K., Raymond, J. C., Lin, J., Lawrence, G., Li, J., and Fludra, A. (2003). Dynamical and physical properties of a post-coronal mass ejection current sheet. *Astrophys. J.* 594, 1068–1084. doi: 10.1086/376982
- Koza, J., Ambroz, J., Gomory, P., Habaj, P., Kozak, M., Kucera, A., et al. (2013). “The CoMP-S instrument at the Lomnický Peak Observatory and possible synergy aspects with the space-born observations,” in

- Synergies between Ground and Space Based Solar Research - 1st SOLARNET - 3rd EAST/ATST Meeting* (Oslo). Available online at: [http://www.astro.sk/~choc/open/apvv\\_081611/output/presentations/2013\\_solarynet\\_conference\\_oslo/koza\\_comp-s\\_at\\_LSO\\_oslo\\_east\\_conference.pdf](http://www.astro.sk/~choc/open/apvv_081611/output/presentations/2013_solarynet_conference_oslo/koza_comp-s_at_LSO_oslo_east_conference.pdf)
- Kramar, M., Inhester, B., Lin, H., and Davila, J. (2013). Vector tomography for the coronal magnetic field. II. hanle effect measurements. *Astrophys. J.* 775, 25–36. doi: 10.1088/0004-637X/775/1/25
- Kramar, M., Inhester, B., and Solanki, S. K. (2006). Vector tomography for the coronal magnetic field. I. Longitudinal Zeeman effect measurements. *Astron. Astrophys.* 456, 665–673. doi: 10.1051/0004-6361:20064865
- Krieger, A. S., Timothy, A. F., and Roelof, E. C. (1973). A coronal hole and its identification as the source of a high velocity solar wind stream. *Solar Phys.* 29, 505–525. doi: 10.1007/BF00150828
- Kucera, A., Ambroz, J., Gomory, P., Kozak, M., and Rybak, J. (2010). CoMP-S - the coronal multi-channel polarimeter for Slovakia. *Contrib. Astron. Obs. Skalnaté Pleso.* 40, 135–138.
- Lambour, R. L., Coster, A. J., Clouser, R., Thornton, L. E., Sharma, J., and Cott, T. A. (2003). Operational impacts of space weather. *Geophys. Res. Lett.* 30, 1136. doi: 10.1029/2002gl015168
- Laming, J. M. (2004). A unified picture of the fip and inverse fip effects. *Astrophys. J.* 614, 1063–1072. doi: 10.1086/423780
- Laming, J. M. (2009). Non-WKB models of the FIP effect: implications for solar coronal heating and the coronal helium and neon abundances. *Astrophys. J.* 695, 954–969. doi: 10.1088/0004-637X/695/2/954
- Laming, J. M. (2012). Non-WKB models of the FIP effect: the role of slow mode waves. *Astrophys. J.* 744, 115–127. doi: 10.1088/0004-637X/744/2/115
- Laming, J. M. (2015). The FIP and inverse FIP effects in solar and stellar coronae. *Living Rev. Solar Phys.* 12:2. doi: 10.1007/lrsp-2015-2
- Laming, J. M., Moses, J. D., Ko, Y.-K., Ng, C. K., Rakowski, C. E., and Tylka, A. J. (2013). On the remote detection of suprathermal ions in the solar corona and their role as seeds for solar energetic particle production. *Astrophys. J.* 770, 73–84. doi: 10.1088/0004-637X/770/1/73
- Lin, H., and Casini, R. (2000). A classical theory of coronal emission line polarization. *Astrophys. J.* 542, 528–534. doi: 10.1086/309499
- Lin, H., Kuhn, J. R., and Coulter, R. (2004). Coronal magnetic field measurements. *Astrophys. J.* 613, L177–L180. doi: 10.1086/425217
- Lin, H., Penn, M. J., and Tomczyk, S. (2000). A new precise measurement of the coronal magnetic field strength. *Astrophys. J.* 541, L83–L86. doi: 10.1086/312900
- Liu, J., McIntosh, S. W., De Moortel, I., Threlfall, J., and Bethge, C. (2014). Statistical evidence for the existence of Alfvénic turbulence in solar coronal loops. *Astrophys. J.* 797, 7–16. doi: 10.1088/0004-637X/797/1/7
- Liu, Y.-H., Drake, J. F., and Swisdak, M. (2011). The effects of strong temperature anisotropy on the kinetic structure of collisionless slow shocks and reconnection exhausts. part I. particle-in-cell simulations. *Phys. Plasmas* 18, 062110. doi: 10.1063/1.3627147
- Longcope, D. W., Guidoni, S. E., and Linton, M. G. (2009). Gas-Dynamic shock heating of post-flare loops due to retraction following localized impulsive reconnection. *Astrophys. J.* 690, L18–L22. doi: 10.1088/0004-637X/690/1/L18
- Lynch, B. J., Antiochos, S. K., MacNeice, P. J., Zurbuchen, T. H., and Fisk, L. A. (2004). Observable properties of the breakout model for coronal mass ejections. *Astrophys. J.* 617, 589–599. doi: 10.1086/424564
- Malanushenko, A., and Schrijver, C. J. (2013). On anisotropy in expansion of magnetic flux tubes in the solar corona. *Astrophys. J.* 775, 120–135. doi: 10.1088/0004-637X/775/2/120
- Mann, G., Klassen, A., Aurass, H., and Classen, H.-T. (2003). Formation and development of shock waves in the solar corona and the near-sun interplanetary space. *Astron. Astrophys.* 400, 329–336. doi: 10.1051/0004-6361:20021593
- McIntosh, S. W., and De Pontieu, B. (2012). Estimating the “Dark” energy content of the solar corona. *Astrophys. J.* 761, 138–145. doi: 10.1088/0004-637X/761/2/138
- McIntosh, S. W., De Pontieu, B., Carlsson, M., Hansteen, V., Boerner, P., and Goossens, M. (2011). Alfvénic waves with sufficient energy to power the quiet solar corona and fast solar wind. *Nature* 475, 477–480. doi: 10.1038/nature10235
- Morton, R. J., Tomczyk, S., and Pinto, R. (2015). Investigating Alfvénic wave propagation in coronal open-field regions. *Nat. Commun.* 6, 7813. doi: 10.1038/ncomms8813
- Nakariakov, V. M., Ofman, L., DeLuca, E. E., Roberts, B., and Davila, J. M. (1999). TRACE observation of damped coronal loop oscillations: implications for coronal heating. *Science* 285, 862–864. doi: 10.1126/science.285.5429.862
- Ng, C. K., and Reames, D. V. (2008). Shock acceleration of solar energetic protons: the first ten minutes. *Astrophys. J.* 686, L123–L126. doi: 10.1086/592996
- Okamoto, T. J., and De Pontieu, B. (2011). Propagating waves along spicules. *Astrophys. J.* 736, L24–L29. doi: 10.1088/2041-8205/736/2/L24
- Orozco Suárez, D., Asensio Ramos, A., and Trujillo Bueno, J. (2014). The magnetic field configuration of a solar prominence inferred from spectropolarimetric observations in the He I 10830 Å triplet. *Astron. Astrophys.* 566, A46. doi: 10.1051/0004-6361/201322903
- Patsourakos, S., Vourlidas, A., and Stenborg, G. (2013). Direct evidence for a fast coronal mass ejection driven by the prior formation and subsequent destabilization of a magnetic flux rope. *Astrophys. J.* 764, 125–137. doi: 10.1088/0004-637X/764/2/125
- Penn, M. J., H., Lin, S., Tomczyk, D., and Elmore, P., (Judge) (2004). Background-induced measurement errors of the coronal intensity, density, velocity and magnetic field. *Solar Phys.* 222, 61–78. doi: 10.1023/B:SOLA.0000036850.34404.5f
- Pesnell, W. D., Thompson, B. J., and Chamberlain, P. C. (2012). The Solar Dynamics Observatory (SDO). *Solar Phys.* 275, 3–15. doi: 10.1007/s11207-011-9841-3
- Peter, H. (2001). On the nature of the transition region from the chromosphere to the corona of the sun. *Astron. Astrophys.* 374, 1108–1120. doi: 10.1051/0004-6361/20010697
- Peter, H. (2010). Asymmetries of solar coronal extreme ultraviolet emission lines. *Astron. Astrophys.* 521, A51. doi: 10.1051/0004-6361/201014433
- Peter, H., Bingert, S., Klimchuk, J. A., de Forest, C., Curtin, J. W., Golub, L., et al. (2013). Structure of solar coronal loops: from miniature to large-scale. *Astron. Astrophys.* 556, A104. doi: 10.1051/0004-6361/201321826
- Rachmeler, L. A., Gibson, S. E., Dove, J. B., DeVore, C. R., and Fan, Y. (2013). Polarimetric properties of flux ropes and sheared arcades in coronal prominence cavities. *Solar Phys.* 288, 617–636. doi: 10.1007/s11207-013-0325-5
- Rachmeler, L. A., Platten, S. J., Bethge, C., Seaton, D. B., and Yeates, A. R. (2014). Observations of a hybrid double-streamer/pseudostreamer in the solar corona. *Astrophys. J.* 787, L3–L8. doi: 10.1088/2041-8205/787/1/L3
- Rakowski, C. E., and Laming, J. M. (2012). On the origin of the slow speed solar wind: helium abundance variations. *Astrophys. J.* 754, 65–74. doi: 10.1088/0004-637X/754/1/65
- Régnier, S. (2013). Magnetic field extrapolations in the corona: success and future improvements. *Solar Phys.* 288, 481–505. doi: 10.1007/s11207-013-0367-8
- Roberts, B., Edwin, P. M., and Benz, A. O. (1983). Fast pulsations in the solar corona. *Nature* 305, 688–690. doi: 10.1038/305688a0
- Rouillard, A. P., Odstrčil, D., Sheeley, N. R., Tylka, A., Vourlidas, A., Mason, G., et al. (2011). Interpreting the properties of solar energetic particle events by using combined imaging and modeling of interplanetary shocks. *ApJ*, 735, 7–17. doi: 10.1088/0004-637X/735/1/7
- Rybák, J., Ambroz, J., Gomory, P., Habaj, P., Koza, J., Kozak, M., et al. (2013). *Coronal Multi-channel Polarimeter at the Lomnický Peak Observatory: CoMP-S@LSO, Kanzelhoehe Colloquium*, (Treffen), Austria. Available online at: [http://www.astro.sk/~choc/open/apvv\\_0816-11/output/presentations/2013\\_kanzelhoehe\\_colloquium\\_2013/rybak\\_comp-s\\_at\\_lso\\_kso70.pdf](http://www.astro.sk/~choc/open/apvv_0816-11/output/presentations/2013_kanzelhoehe_colloquium_2013/rybak_comp-s_at_lso_kso70.pdf)
- Sakai, J. I., Minamizuka, R., Kawata, T., and Cramer, N. F. (2001). Nonlinear torsional and compressional waves in a magnetic flux tube with electric current near the quiet solar photospheric network. *Astrophys. J.* 550, 1075–1092. doi: 10.1086/319802
- Savage, S. L., McKenzie, D. E., Reeves, K. K., Forbes, T. G., and Longcope, D. W. (2010). Reconnection outflows and current sheet observed with Hinode/XRT in the 2008 April 9 “Cartwheel CME” Flare. *Astrophys. J.* 722, 329–342. doi: 10.1088/0004-637X/722/1/329
- Scherrer, P. H., Bogart, R. S., Bush, R. I., Hoeksema, J. T., Kosovichev, A. G., Schou, J., et al. (1995). The solar oscillations investigation-michelson doppler imager. *Sol. Phys.* 162, 129–188. doi: 10.1007/BF00733429
- Schrijver, C. J., Title, A. M., Berger, T. E., Fletcher, L., Hurlburt, N. E., Nightingale, R. W., et al. (1999). A new view of the solar outer atmosphere by the transition region and coronal explorer. *Sol. Phys.* 187, 261–302. doi: 10.1023/A:1005194519642

- Sturrock, P. A. (1999). Chromospheric magnetic reconnection and its possible relationship to coronal heating. *Astrophys. J.* 521, 451–459. doi: 10.1086/307544
- Testa, P., De Pontieu, B., Martínez-Sykora, J., DeLuca, E., Hansteen, V., Cirtain, J., et al. (2013). Observing coronal nanoflares in active region moss. *Astrophys. J.* 770, L1–L7. doi: 10.1088/2041-8205/770/1/L1
- Thurgood, J. O., and McLaughlin, J. A. (2013). 3D Alfvén wave behaviour around proper and improper magnetic null points. *Astron. Astrophys.* 558, A127. doi: 10.1051/0004-6361/201322021
- Tian, H., Tomczyk, S., McIntosh, S. W., Bethge, C., de Toma, G., and Gibson, S. (2013). Observations of coronal mass ejections with the coronal multichannel polarimeter. *Solar Phys.* 288, 637–650. doi: 10.1007/s11207-013-0317-5
- Tomczyk, S., Card, G. L., Darnell, T., Elmore, D. F., Lull, R., Nelson, P. G., et al. (2008). An instrument to measure coronal emission line polarization. *Solar Phys.* 247, 411–428. doi: 10.1007/s11207-007-9103-6
- Tomczyk, S., and McIntosh, S. W. (2009). Time-distance seismology of the solar corona with CoMP. *Astrophys. J.* 697, 1384–1391. doi: 10.1088/0004-637X/697/2/1384
- Tomczyk, S., McIntosh, S. W., Keil, S. L., Judge, P. G., Schad, T., Seeley, D. H., et al. (2007). Alfvén waves in the solar corona. *Science* 317, 1192–1196. doi: 10.1126/science.1143304
- Tylka, A. J., and Lee, M. A. (2006). A model for spectral and compositional variability at high energies in large, gradual solar particle events. *Astrophys. J.* 646, 1319–1334. doi: 10.1086/505106
- Ugarte-Urra, I., Warren, H. P., and Wineberger, A. R. (2007). The magnetic topology of coronal mass ejection sources. *Astrophys. J.* 662, 1293–1301. doi: 10.1086/514814
- Van Doorsselaere, T., Nakariakov, V. M., and Verwichte, E. (2008). Detection of waves in the solar corona: kink or alfvén? *Astrophys. J.* 676, L73–L75. doi: 10.1086/587029
- Vasheghani Farahani, S., Nakariakov, V. M., and Doorsselaere, T. (2010). Long wavelength torsional modes of solar coronal plasma structures. *Astron. Astrophys.* 517, A29. doi: 10.1051/0004-6361/201014502
- von Steiger, R., Wimmer Schweingruber, R. F., Geiss, J., and Gloeckler, G. (1995). Abundance variations in the solar wind. *Adv. Space Res.* 15, 3–12. doi: 10.1016/0273-1177(94)00013-Q
- Vourlidas, A., Wu, S. T., Wang, A. H., Subramanian, P., and Howard, R. A. (2003). Direct detection of a coronal mass ejection-associated shock in large angle and spectrometric coronagraph experiment white-light images. *Astrophys. J.* 598, 1392–1402. doi: 10.1086/379098
- Wang, T. J., Ofman, L., and Davila, J. M. (2009). Propagating slow magnetoacoustic waves in coronal loops observed by Hinode/EIS. *Astrophys. J.* 696, 1448–1460. doi: 10.1088/0004-637X/696/2/1448
- Warren, H. P., Winebarger, A. R., and Brooks, D. H. (2010). Evidence for steady heating: observations of an active region core with Hinode and TRACE. *Astrophys. J.* 711, 228–238. doi: 10.1088/0004-637X/711/1/228
- Wiegelmann, T., and Sakurai, T. (2012). Solar force-free magnetic fields. *Living Rev. Solar Phys.* 9:5. doi: 10.12942/lrsp-2012-5

**Conflict of Interest Statement:** The authors declare that the research was conducted in the absence of any commercial or financial relationships that could be construed as a potential conflict of interest.

Copyright © 2016 Ko, Moses, Laming, Strachan, Tun Beltran, Tomczyk, Gibson, Auchère, Casini, Fineschi, Knoelker, Korendyke, McIntosh, Romoli, Rybak, Socker, Vourlidas and Wu. This is an open-access article distributed under the terms of the Creative Commons Attribution License (CC BY). The use, distribution or reproduction in other forums is permitted, provided the original author(s) or licensor are credited and that the original publication in this journal is cited, in accordance with accepted academic practice. No use, distribution or reproduction is permitted which does not comply with these terms.



# mxCSM: A 100-slit, 6-Wavelength Wide-Field Coronal Spectropolarimeter for the Study of the Dynamics and the Magnetic Fields of the Solar Corona

Haosheng Lin \*

Institute for Astronomy, University of Hawaii, Pukalani, HI, USA

## OPEN ACCESS

**Edited by:**

Sarah Gibson,  
National Center for Atmospheric  
Research, USA

**Reviewed by:**

Gordon James Duncan Petrie,  
National Solar Observatory, USA  
Jonathan Wesley Curtin,  
NASA, USA

**\*Correspondence:**

Haosheng Lin  
lin@ifa.hawaii.edu

**Specialty section:**

This article was submitted to  
Stellar and Solar Physics,  
a section of the journal  
Frontiers in Astronomy and Space  
Sciences

**Received:** 12 February 2016

**Accepted:** 08 March 2016

**Published:** 30 March 2016

**Citation:**

Lin H (2016) mxCSM: A 100-slit,  
6-Wavelength Wide-Field Coronal  
Spectropolarimeter for the Study of  
the Dynamics and the Magnetic Fields  
of the Solar Corona.

Front. Astron. Space Sci. 3:9.  
doi: 10.3389/fspas.2016.00009

Tremendous progress has been made in the field of observational coronal magnetometry in the first decade of the Twenty-First century. With the successful construction of the Coronal Multichannel Magnetometer (CoMP) instrument, observations of the linear polarization of the coronal emission lines (CELs), which carry information about the azimuthal direction of the coronal magnetic fields, are now routinely available. However, reliable and regular measurements of the circular polarization signals of the CELs remain illusive. The CEL circular polarization signals allow us to infer the magnetic field strength in the corona, and is critically important for our understanding of the solar corona. Current telescopes and instrument can only measure the coronal magnetic field strength over a small field of view. Furthermore, the observations require very long integration time that preclude the study of dynamic events even when only a small field of view is required. This paper describes a new instrument concept that employs large-scale multiplexing technology to enhance the efficiency of current coronal spectropolarimeter by more than two orders of magnitude. This will allow for the instrument to increase the integration time at each spatial location by the same factor, while also achieving a large field of view coverage. We will present the conceptual design of a 100-slit coronal spectropolarimeter that can observe six CELs simultaneously. Instruments based on this concept will allow us to study the evolution of the coronal magnetic field even with coronagraphs with modest aperture.

**Keywords:** corona, magnetic fields, spectropolarimetry, instrumentation

## 1. INTRODUCTION

In the low density, high temperature and highly ionized coronal plasma, magnetic fields suppress cross-field-line motion of charged particles, thereby creating an atmosphere with highly anisotropic local thermodynamic properties, thus shaping the appearance of the corona to closely resemble that of the magnetic field lines. However, large scale flows of charged particles (electric currents) in turn alter the large scale structure of the magnetic fields. Therefore, detailed observations of the behavior of magnetic fields and plasmas during major eruptions, as well as during quiet periods, are the crucial data needed for understanding the interaction between the fields and the coronal plasmas,

and the physics of solar eruptions. While it has been more than a century since the ground-breaking work of Hale (1908) that revealed the magnetic nature of the sun, direct measurement of magnetic fields in the outer layer of the solar atmosphere remains difficult. Much progress has been made in the past two decades in the field of coronal polarimetry to directly measure the polarization of coronal emission lines (CELs) that responds directly to coronal magnetic fields (Casini and Judge, 1999; Lin and Casini, 2000; Lin et al., 2000, 2004). The Coronal Multichannel Polarimeter (CoMP), in particular, can now provide direct measurements of the FeXIII line linear polarization on a daily basis (Tomczyk et al., 2008). Nevertheless, direct inference of the coronal magnetic fields from these measurements remains a challenging task due to the low optical density of the coronal atmosphere.

Recent advancements in scalar and vector tomography based on space EUV intensity and ground intensity and linear polarization data of CELs have further allowed us to make direct inference of the 3D magnetic and thermodynamic structure of the corona from these observations (Kramar et al., 2016). As shown by Kramar et al. (2016), coronal magnetic fields derived from tomographic reconstruction of EUV and white light data for Carrington Rotation 2112, revealed several possible deficiencies in MHD simulated models of the same period, and demonstrated the importance of direct 'observations' for research of coronal magnetic fields.

While we have finally attained the capability to derive the 3D magnetic and thermodynamic structures of the corona from direct observations, their accuracy and applicability are still subject to the limitations of existing instrumentation. For examples, CEL polarimetry at present is only possible from ground-based instrumentation, and with a single sight line from Earth. True tomographic observations that sample the corona from multiple lines of sight (LOS) simultaneously is currently not possible. Therefore, we have relied on the rotation of the Sun to provide the multiple LOS measurements for use with tomographic inversion tools. Accordingly the results from these tomographic inversions are the static component of the coronal fields during the period of the observations. *To resolve the dynamic time scales of solar eruptions, true tomography with simultaneous observations from multiple sight lines is needed.* Next, tomography with only linear polarization input is insensitive to certain magnetic field configurations (Kramar et al., 2013). However, the amplitudes of the circular polarization signals of the CELs are two orders of magnitude lower than that of the linear polarization. Therefore, *the sensitivity of our synoptic coronal polarimeters needs to be greatly improved for tomographic inversion to provide coverage of the full range of coronal magnetic field configurations.* Finally, **Figure 1** shows the solar corona observed in six different CELs with excitation temperatures ranging from 0.5 to 2.2 MK (Habbal et al., 2011). The dramatic difference in the appearance of the corona between ions with low and high ionization temperatures is a manifestation of the (spatial) non-uniformity of the coronal temperature. Therefore, polarization measurements at only one CEL sample only coronal plasma with temperature within a narrow range around the ionization temperature of the spectral line. In order to "see" the

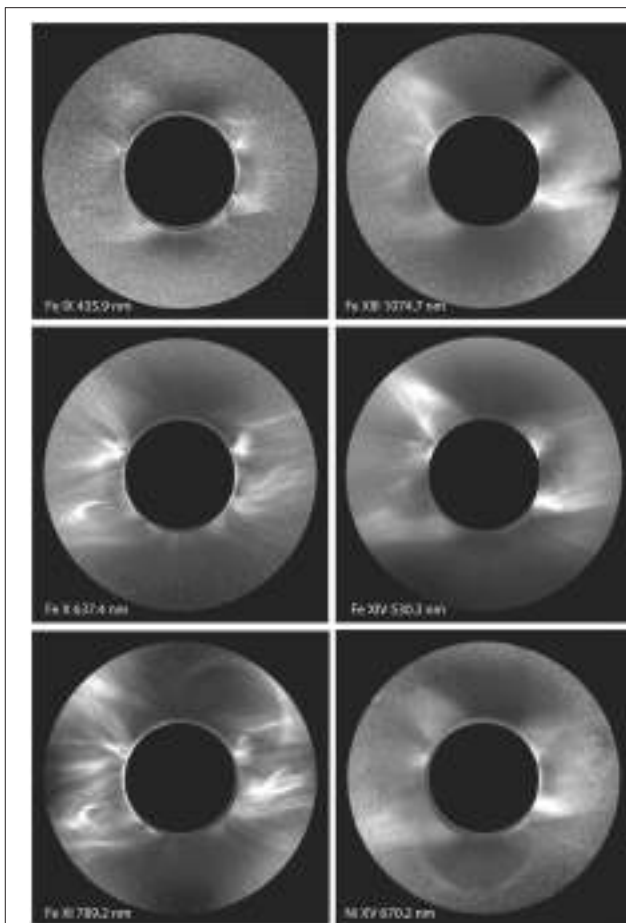


**FIGURE 1 |** The solar corona from the solar limb to about  $2.5 R_{\odot}$  from disk center observed during the 2010 South Pacific total eclipse (Habbal et al., 2011) in six coronal emission lines with temperature ranging from 0.8 to 2.0 MK. Images are courtesy of S. Habbal.

entire corona, *observations at multiple spectral lines spanning a broad range of the coronal temperature is needed.*

Observational coronal magnetometry is a new field that will eventually provide solar physicists the magnetic and thermodynamic structure of the solar corona needed for every aspect of coronal research. Even with its current limitations, this new capability to directly derive the 3D corona magnetic field structure from measurements of signals originating from the corona, as opposed to extrapolations or MHD simulations that rely on information of magnetic fields at the lower boundary layers, is an important new capability that will provide new insight into the physical processes that define the corona. Therefore, it is critically important that we continue to develop and improve our observing capability to provide data with comprehensive coverage in spatial, temporal, polarization, and temperature domains to allow tomographic inversion techniques to yield a complete picture of the corona.

In this paper, we present the conceptual design of a new coronal magnetometer, called the **massively-multiplexed Coronal Spectropolarimetric Magnetometer (mxCSM)**, for the

measurement of the intensities, velocities, and polarizations of the six CELs shown in **Figure 1** simultaneously. This instrument will provide CEL polarization data with sufficient spatial, spectral, and temporal resolution, and spatial, temperature, and velocity field coverage to enable high precision vector tomographic inversion of the coronal magnetic fields. mxCSM adapts the large-scale multiplexing strategy demonstrated by the massively-multiplexed SPECtroheliograph (mxSPEC, Lin, 2014) proof-of-concept instrument. Its optical system consists of a new catadioptric off-axis Gregorian coronagraph and two 100-slit, 3-line spectrographs. It uses six  $4096 \times 4096$  format CCDs and/or IR cameras to observe the six spectral lines simultaneously. With this new design, mxCSM can deliver close to three orders of magnitude improvement in capability over current generation of coronal magnetometers without the use of large aperture telescopes. This conceptual design that will be described in the following sections serves to showcase the potential of the large-scale multiplexing strategy for instrumentations for coronal magnetism research in particular, and for future solar spectroscopic instrumentations in general. More importantly, due to its compact design, mxCSM is ideally suited for deployment in space. We envision that future missions with two or more mxCSMs deployed in circumsolar orbits similar to the Solar Terrestrial Relations Observatory (STEREO) mission will provide multiple LOS measurements to enable true tomographic inversion of the coronal magnetic and thermodynamic structures.

## 2. THE DEVELOPMENT OF MODERN MULTIPLE-SLIT SPECTROGRAPHS

### 2.1. FIRS: The Facility IR Spectropolarimeter

Multi-slit spectroscopy is a simple, yet very effective method of multiplexing spectra from multiple slices of a 2D spatial field onto a 2D array detector. It was first conceived 40 years ago (Martin et al., 1974; Livingston et al., 1980) but had not been widely adapted in the digital age until it was revived by Srivastava and Mathew (1999). Lin (2003), unaware of the historical developments and the new effort in India, independently conceived the design for a multi-slit, multi-wavelength IR spectropolarimeter in late 1990s. Its design goals were to take advantage the large multiplexing capability of modern large-format, high-performance visible and IR focal plane arrays (FPAs) and new high-efficiency narrow passband Dense Wavelength Division Multiplexing (DWDM) filter technology developed for telecommunication applications to improve the imaging capability and operational efficiency of grating-based spectropolarimeters. This design was first realized through the development and construction of the Facility IR Spectropolarimeter (FIRS, Jaeggli et al., 2010) for the Dunn Solar Telescope (DST) of the National Solar Observatory (NSO) in Sunspot, New Mexico. In addition to realizing the potential of the multi-slit design, FIRS also advanced an achromatic reflecting spectrograph design that uses coarsely-ruled echelle grating to allow for observations of multiple spectral lines simultaneously

on the same spectrograph to further increase the operational efficiency of the instrument. FIRS supports observations with a maximum of 4 slits. The primary constraints on the number of slits for FIRS are (1) the relatively modest size of the  $1024 \times 1024$  format IR camera available, (2) the requirements for high spectral resolution (with a spectral sampling size  $\Delta\lambda \approx \lambda/300,000$ ), and (3) substantial Doppler velocity field coverage (e.g.,  $\geq 200$  kms). In order to cover a spectral window of approximately  $\pm 120$  km/s around the spectral lines, 256 pixels per slit were dedicated to record the spectra at each spatial sampling point. Nevertheless, even with a relatively small number of slits, it takes only 190 scan steps to observe a  $150'' \times 75''$  field with  $0.3''$  spatial sampling size, a factor of 4 faster than a single slit instrument.

### 2.2. mxSPEC: The Massively Multiplex Spectroheliograph Concept

For science that requires only low or medium spectral resolution, a large field of view coverage with moderate spatial resolution, multi-slit spectrograph can be reconfigured with low dispersion gratings to accommodate a large number of slits without the reduction of the spectral window (and Doppler velocity field) coverage, thereby greatly reducing the number of scan steps needed to scan the full 2D field. This enables a scanning grating spectrograph to perform 3D imaging spectroscopy with very high temporal resolution. The proof-of-concept instrument, mxSPEC, was assembled at the full-disk port of the DST in 2014 using DST inventory optics, a He I 1083 nm DWDM bandpass isolation filter (BIF) with 1.4 nm bandpass, and a 10 frame per second (fps) Raytheon Virgo 2K  $2048 \times 2048$  IR camera. In this setup, the DST aperture was reduced to 135 mm, and mxSPEC observed the full solar disk with  $1''$  pixel $^{-1}$  spatial sampling. mxSPEC was equipped with a photolithographically etched 49-slit mask. The slits are separated by  $750 \mu\text{m}$  distance, with a slit width of  $12.5 \mu\text{m}$ . The Sun illuminates 34 to 35 of the 49 slits at any given time, while the IR camera sees 41 of the 49 slits. Thus, only 60 scan steps, or less than 8 seconds (including processing overhead) are required to obtain a  $2460 \times 2048 \times 50$  ( $x, y, \lambda$ ) hyper-spectral data cube. The spectrograph yields a  $250 \text{ m}\text{\AA}/\text{pixel}$  spectral sampling size ( $\lambda/\Delta\lambda = 40,000$ ), and a  $\pm 225 \text{ km/s}$  Doppler velocity coverage centered on the nearby Si I 1072.7 nm line. **Figure 2** shows a sample multi-slit full-Sun spectral image from mxSPEC, detailed spectra around a sunspot near the east limb and a full-disk He I 1083 nm line core image constructed from a full disk scan. Image sequences of the whole sun in He I 1083 nm line showing many aspects of chromosphere dynamics are available at <http://www.ifa.hawaii.edu/users/lin/default/mxSPEC.html>.

## 3. THE MASSIVELY-MULTIPLEX CORONAL SPECTROPOLARIMETRIC MAGNETOMETER

In order to observe six spectral lines spanning over two octaves in wavelength simultaneously through a single telescope, an optical system that can project an achromatic image of the sun at the full-disk occulter, as well as at the entrance slits of the spectrographs is needed. Furthermore, the spectrograph also needs to be

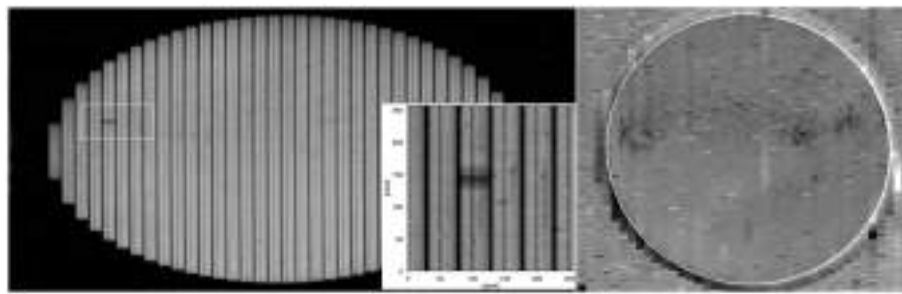


**FIGURE 2 | Left:** 34-slit spectra of the full Sun obtained with the mxSPEC proof-of-concept instrument. Each vertical slice in the image is a horizontally dispersed spectrum. The  $2048 \times 2048$  image was rescaled to a  $2408 \times 1024$  image to better display the slit spectra. Close-up of spectra of a sunspot in the rectangular box in the full-disk spectral image are shown in the insert. **Right:** He I 1083 nm line core image constructed from a full-disk scan. The black and white short horizontal lines are data reduction artifacts due to defective pixels.

achromatic to support multi-wavelength observations. We have designed a new wide-field catadioptric coronagraph based on an off-axis Gregorian telescope, and a 100-slit refractive Czerny-Turner spectrograph that can observe three spectral lines simultaneously. The system is equipped with two spectrographs to support simultaneous observations of six spectral lines. The following sections describe the designs of the coronagraph and the spectrographs.

### 3.1. The Catadioptric Off-Axis Gregorian Coronagraph

#### 3.1.1. The Imaging System of mxCSM Coronagraph

Classical Lyot coronagraphs employ low-scatter, super polished singlet objective lens to minimize the scattered light at the prime focus, and a prime focus occulter to prevent the disk light from traveling further downstream. However, due to the dispersion of the index of reflection, the size and location the solar image formed by the objective lens vary as functions of wavelength. It is therefore difficult to observe more than one spectral line at the same time with the Lyot coronagraphs. The catadioptric optical system of mxCSM overcomes this limitation of the classical Lyot coronagraph. Figures 3–6 shows the ZEMAX layouts of the optical system of mxCSM projected in the Y-Z, X-Y, Z-X plane, and an isometric 3D shaded model, respectively. This optical design is based on a CCD camera with  $4096 \times 4096$  format and  $9 \mu\text{m}$  pixels. The catadioptric off-axis Gregorian coronagraph consists of an aspheric aperture corrector (AC, aperture  $\Phi = 300 \text{ mm}$ ) followed by an off-axis parabolic primary mirror ( $M_1$ ,  $\Phi = 300 \text{ mm}$ , Focal Length  $FL = 800 \text{ mm}$ , Off-Axis Distance  $OAD = 300 \text{ mm}$ ) and a concave off-axis elliptical secondary mirror ( $M_2$ ,  $\Phi = 120 \text{ mm}$ ,  $FL = 244.6 \text{ mm}$ ,  $OAD = 160 \text{ mm}$ , conic  $C = -0.158$ ). A full-disk occulter is placed at the  $M_1$  focus to block disk light. The effective focal length at the Gregorian focus is  $1850 \text{ mm}$ . An entrance aperture stop (AS) placed between AC and  $M_1$ , and a Lyot stop (LS) placed on the image of AS formed by  $M_2$  limit the effective aperture of the telescope. The location of AS is chosen such that the Lyot stop can be located at an accessible location outside of the region with overlapping beams near  $M_2$ . The diameter of AS is oversized to  $275 \text{ mm}$ . Edge diffractions of AS will be blocked by the Lyot stop, which

also limits the effective telescope aperture to  $250 \text{ mm}$ . This design achieves better than  $1''$  spatial resolution within a  $0.375$  degree field ( $1.5 R_\odot$ ) from Fe XIV 530 nm to Si X 1430 nm, as demonstrated by the spot diagram in Figure 7.

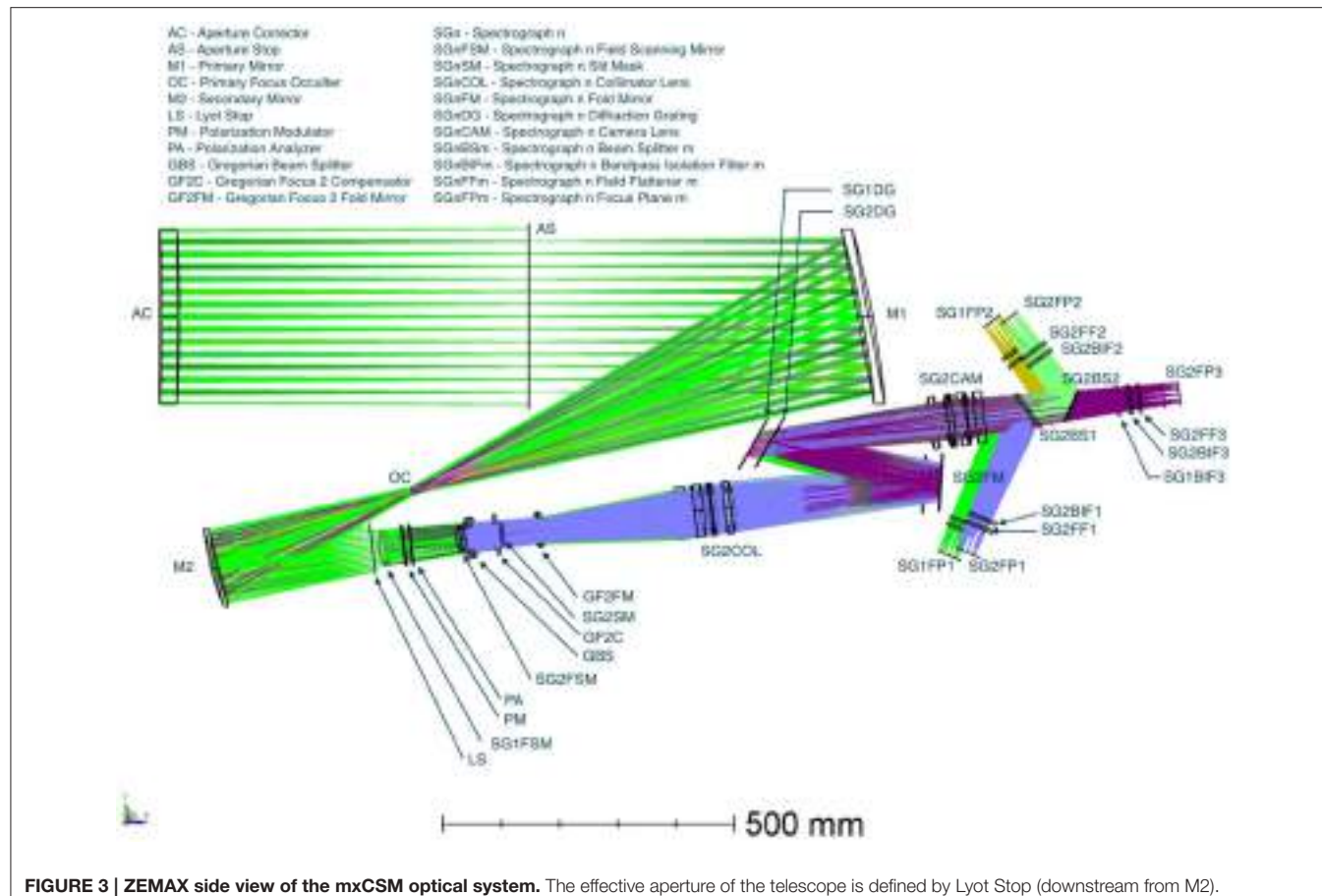
To support simultaneous observations of six spectral lines, a Gregorian beam splitter (GBS) splits the beam coming down from  $M_2$  into two arms. Light with wavelengths shorter than  $750 \text{ nm}$  is reflected again with the spectrograph 1 fold and scan mirror (SG1FSM) to feed the first spectrograph SG1. The transmitted light is reflected by a Gregorian fold mirror (GFM) and then SG2FSM to feed the second spectrograph. SG1FSM and SG2FSM also serve as the field scanning mirrors of the spectrographs.

The optical system of mxCSM is designed for use with CCDs with  $9 \mu\text{m}$  pixels. With an effective focal length of  $1850 \text{ mm}$  at the Gregorian foci, and a 1:1 magnification between the entrance and exit slit focal planes, the spatial sampling size is  $1''$  per pixel. The slit masks, SG1SM and SG2SM of the spectrographs have 100 parallel slits with width of  $9 \mu\text{m}$ , separated by a distance of  $432 \mu\text{m}$ . It takes only 48 scan steps to complete the scanning of the  $1.2 \times 1$  degree field of view (FOV).

For polarization measurements, a simple polarimeter consists of a rotating achromatic  $\lambda/3$  waveplate polarization modulator PM followed by a linear polarizer PA are shown between  $M_2$  and GBS for single-beam polarimetry. For dual beam polarimetry, the linear polarization analyzer PA can be replaced by Wollaston prisms placed near the focal planes of the spectrograph (§ 3.2).

#### 3.1.2. Scattered Light Considerations

The most important aspect of a coronagraph design is the scattered light performance of the optical system. The primary source of instrumental scattered light of a classical Lyot coronagraph is the scattering of disk light off the dusts and imperfections on the surfaces and in the substrate of the objective lens. For ground-based observations, Elmore (2007) has found that the scattered light of the MK4 coronagraph located at Mauna Loa Solar Observatory is dominated by dust particle accumulation on the objective lens of the coronagraphs even immediately after cleaning the objective. As Mauna Loa is one of the best ground-based coronal sites, this finding strongly suggests that for ground-based coronal observations dust control

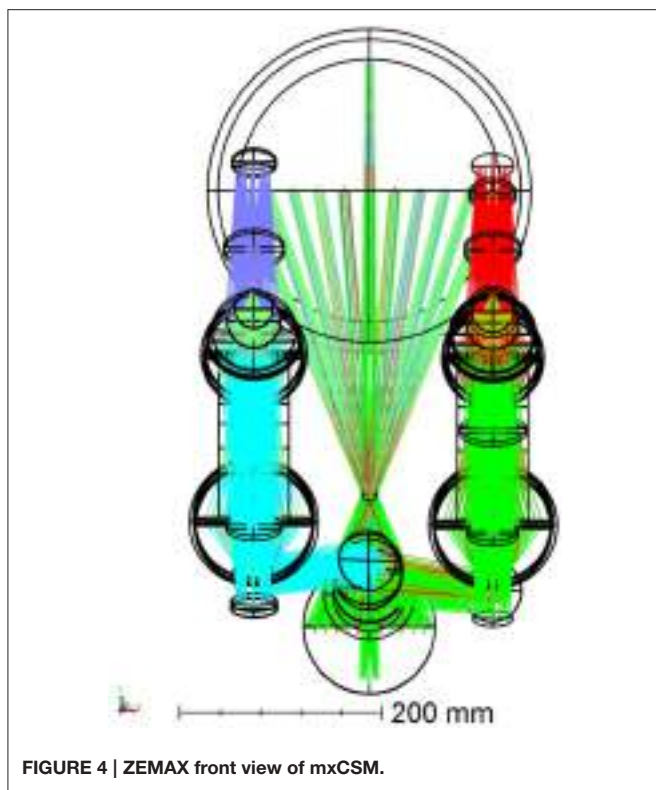


is the most critical element for achieving low scattered light level, provided that the objective of the coronagraph is of sufficient quality. Indeed, a recent scattered light study performed for the COSMO Large Coronagraph project at HAO (Gallagher, 2015) showed that a super polished coronagraph singlet lens with a 0.7 nm root-mean-square (RMS) micro roughness polish over the spatial period from 3 to 0.4 mm produces a scattered light of approximately  $4 \times 10^{-6} I_{\odot}$  at a distance of  $1.1 R_{\odot}$  from disk center and at the wavelength of the Fe XIII 1075 nm coronal emission line. Whereas, the total scattered light produced by the 0.7 nm RMS objective plus contribution from dust accumulation on the objective surface equivalent to a cleanliness level (CL) of CL220 is approximately  $10 \times 10^{-6} I_{\odot}$  at  $1.1 \mu\text{m}$  and  $1.1 R_{\odot}$ . Here  $I_{\odot}$  and  $R_{\odot}$  denote the intensity of the Sun at disk center, and the radius of the Sun, respectively.

For a catadioptric Gregorian telescope, the scattering off the surface of the primary mirror M1 is an additional source of instrumental scattered light. Given identical surface quality, a mirror produces approximately two times the scattered light than a lens (Gallagher, 2015). We estimated that for a catadioptric Gregorian coronagraph, the combined scattered light off the aperture corrector and the primary mirror with 0.4 nm RMS micro roughness on all three optical surface is equal to that of a classical Lyot coronagraph with 0.7 nm RMS surface quality on

the two surfaces of the objective lens. Modern optical fabrication techniques can now produce mirrors with RMS micro roughness well below 0.5 nm. Therefore, while a catadioptric Gregorian coronagraph will need to be polished with a surface micro roughness specification that is almost two times more stringent than that for a lens coronagraph in order to achieve the same instrumental scattered light performance, the cost differential for the additional polishing (which should be a small fraction of the total cost required to build a functional system) is more than compensated by the multi-spectral-line observing capability that the catadioptric optical system enables, and the multitude of improvements in the operational efficiency that it will provide.

With properly controlled instrumental scattered light using super-polished surfaces, the primary source of the instrumental scattered light is the accumulation of dust particles on the optical surfaces upstream of the occulter at the primary focus of the system. Decades of operations of Lyot coronagraphs at the Evans Facility of the National Solar Observatory in Sunspot, New Mexico, Mauna Loa Solar Observatory on the Big Island of Hawaii, Mees Solar Observatory on Haleakala, and other coronal observatories around the world had demonstrated the effectiveness of lens cleaning techniques and the robustness of the super polished lens surfaces to withstand repeated



cleaning without long-term degradation of the scattered light performance of the coronagraphs. On the other hand, while mirror coronagraphs like SOLARC (Kuhn et al., 2003) offer unparalleled wavelength coverage and simultaneous multi-line observations, our experience from operation of SOLARC was that cleaning of its primary mirror is difficult and inevitably scratches the mirror surface and degrades its scattered light performance over time. Therefore, it is important that the primary mirror surface of mxCSM be kept clean to minimize dust contamination. With a catadioptric optical system, the aperture corrector can serve as the window of an air-tight or semi-air-tight enclosure to enclose M1 to eliminate or minimize the need of periodic cleaning of the M1 surface. With comprehensive dust control measure, such as (slightly) clean air over-pressurized dome, the semi-air-tight M1 enclosure, and extended lens tube in front of AC, supplemented with cleaning of the external surface of AC when necessary, low total scattered light can be achieved on a regular basis.

### 3.2. Compact 3-Line Spectrographs

Spectroscopy and spectropolarimetry of CELs are particularly well suited for the mxSPEC concept. In the million-degree corona, the Doppler width of the CELs are of the order of  $\lambda/10,000$ , where  $\lambda$  is the wavelength of the spectral line. Therefore, a spectrograph with only moderate resolution that samples the spectra with about  $\lambda/40,000$  sample size is sufficient. However, in order to observe multiple spectral lines over a large wavelength range simultaneously, an achromatic spectrograph is needed. mxCSM uses two identical (except for the grating angles)

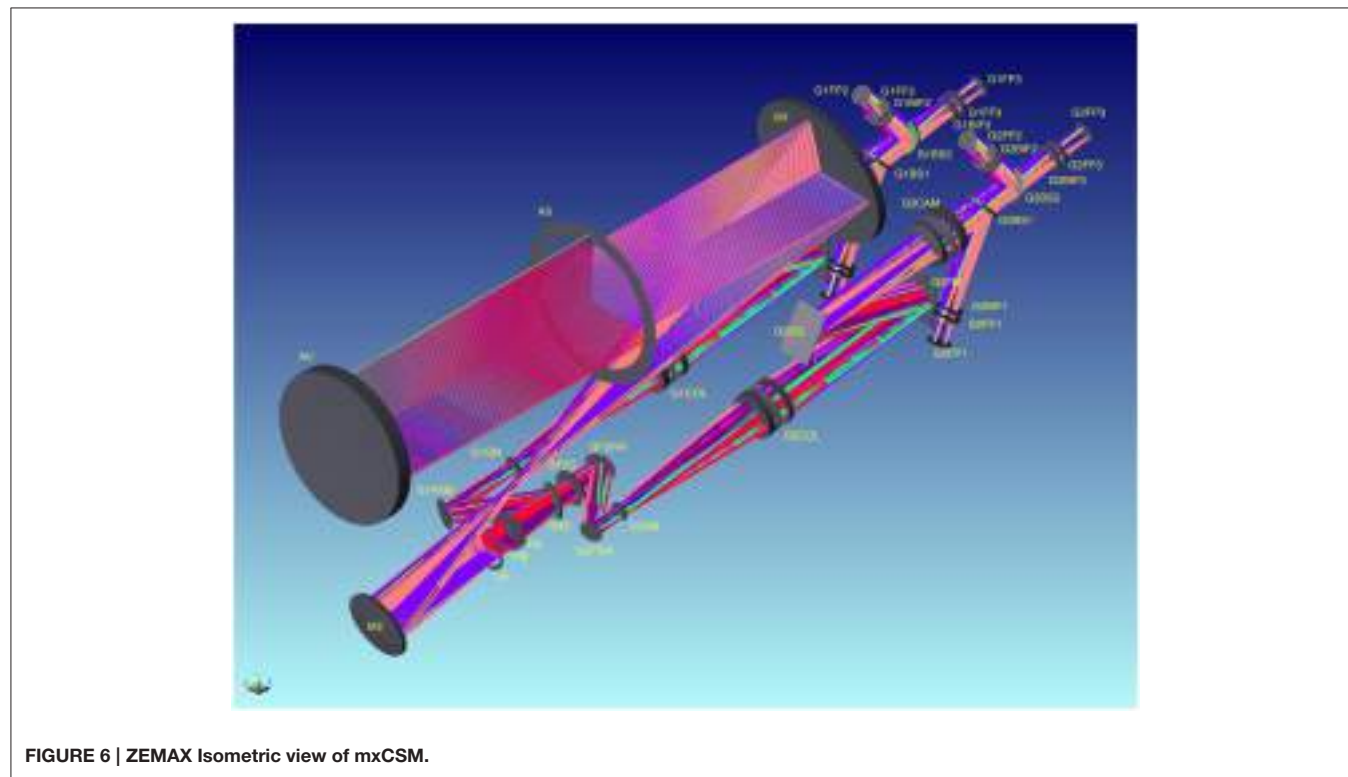
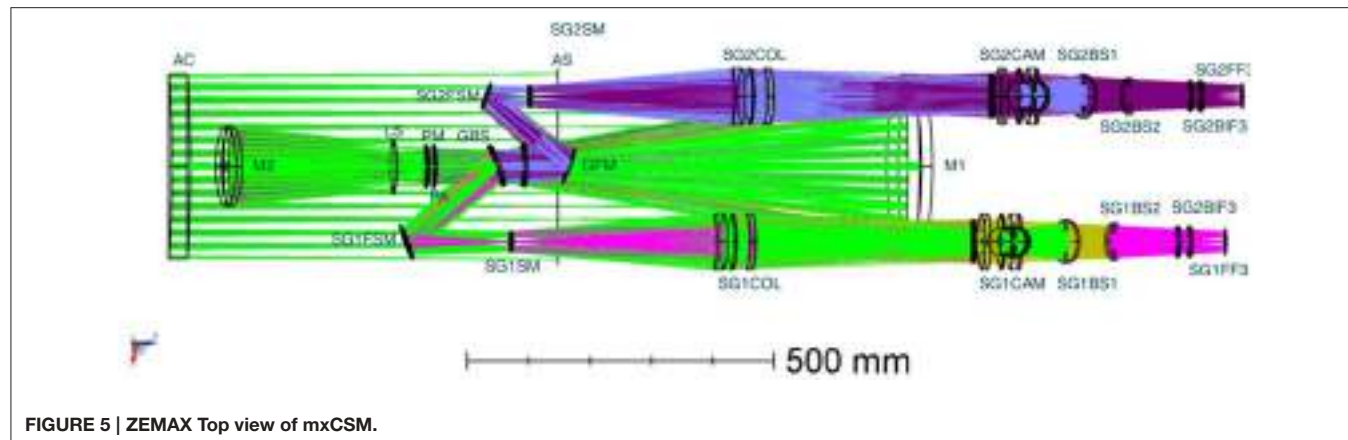
3-line spectrographs for observation of a total of 6 spectral lines simultaneously. The spectrographs are folded refractive Czerny-Turner spectrographs based on a pair of air-spaced achromatic triplet lenses and a medium-resolution diffraction grating with 7.9 line/mm ruling blazed at 26.7 degree. The optical layout of the first spectrograph is shown again in **Figure 8** without the rest of the optical system for clarity. The effective focal length of the air-spaced triplet lenses is 381 mm. The nominal spectrograph angle  $\phi (\equiv \alpha - \beta)$  is set to 20 degree. **Table 1** shows the spectrograph configuration parameters and performance characteristics of the six spectral lines shown in **Figure 1**. The collimator SG1COL forms an image of the pupil approximately 650 mm away from the collimator, where the diffraction grating SG1DG is located. The fold mirror SG1FM and the grating redirect the beam away from the direction of the entrance slit. Due to the coarse-ruling and the moderate blaze angle, most of the wavelengths in the visible and near-IR wavelengths are diffracted in approximately the same angular direction. This allows all the spectra to be formed by a single camera lens with minimal image quality degradation. The camera lens (SG1CAM) is placed one focal length away from the grating to produce a telecentric beam. Two dichroic beam splitters (SG1BS1 and SG1BS2) split the exit beams into three arms with different wavelength bands, allowing for observation of three spectral lines simultaneously. Three ultra-narrow bandpass isolation filters (BIFs) with bandwidth equal to  $\lambda/1000$  centered at the wavelength of the spectral lines are placed in the telecentric beams in the three arms, each followed by a field flattener optimized for each spectral line.

The slit masks of mxCSM will be configured with 100 parallel slits with slit width of  $9 \mu\text{m}$  and slit separation of  $432 \mu\text{m}$  between neighboring slits. Therefore, it will take only 48 scan steps to cover a  $1.2 \times 1$  degree FOV. Due to the anamorphic demagnification of the spectrographs, the images of the entrance slits are separated by  $360 \mu\text{m}$ , or 40 pixels on the CCDs at the exit slit planes. With the 380 mm focal length, 20 degree spectrograph angle, and the 7.9 line/mm grating blazed at 26.7 degree, the  $9 \mu\text{m}$  pixel of the CCD samples the spectra with a sample size of  $\Delta\lambda \approx \lambda/39,000$  for all wavelengths. The width of  $\lambda/1000$  of the 40-pixel spectral windows of each slit thus cover a Doppler velocity window of  $\pm 150 \text{ km/s}$ .

The ultra-narrow bandpass isolation filters will have a flat top transmission profile with a minimum 90% ( $-0.5 \text{ dB}$ ) transmission bandwidth of  $\lambda/2000$ , and a maximum 0.1% ( $-30 \text{ dB}$ ) transmission bandwidth of  $\lambda/1000$  to eliminate crosstalk of spectra from neighboring slits and overlapping orders. The size of the BIFs will be approximately  $50 \times 50 \text{ mm}$ .

### 3.3. Polarimetry Sensitivity Estimates

With the simple optical system, mxCSM will have very high photon throughput. The maximum number of optical surfaces (Spectrograph 2, Arm 3) is 35, excluding the diffraction grating and the bandpass isolation filters. Assuming a nominal 99.5% efficiency for each optical surface using high-performance anti-reflection coating, 70% efficiency for the diffraction grating, 90% efficiency for the BIFs, and 75% quantum efficiency for the



detector, the overall system throughput of the system is about 40%. The expected photon flux in the continuum spectra near the Fe XIII 1075 nm line with a total scattered light (including sky, dust, and instrumental contribution) of  $10 \times 10^{-6} I_{\odot}$ , with different spatial and temporal binning is listed in **Table 2**. Using a circular polarization amplitude of  $1 \times 10^{-3}$  for a 10 G magnetic field, the estimated  $3\sigma$  detection limits of the line-of-sight component of the coronal magnetic field  $B_{3\sigma}$  of mxCSM for the Fe XIII 1075 nm line are 35 G, 12 G, and 4 G, respectively, with spatial resolution of 1'', 3'', and 10'' and temporal resolution of 2 h per map if the scattered light background is  $10 \times 10^{-6} I_{\odot}$ . This is sufficient to measure the coronal magnetic field in most active regions up to  $1.4R_{\odot}$ , based on the experience from the SOLARC

coronagraph. In comparison, it would take a conventional single slit spectropolarimeter a minimum of 26.7 h of observation to obtain one full-polarization map of the  $1.2 \times 1.0$  degree field.

The high polarization sensitivity of the hourly and daily averaged data will also allow us to measure the orientation of the coronal magnetic fields from the orientation of the linear polarization of the CEL at very large distance from the limb. It will also allow us to explore the possibility of measuring the line-of-sight magnetic field strength in quiet regions. These observations will provide the data necessary for tomographic inversion of the coronal magnetic fields.

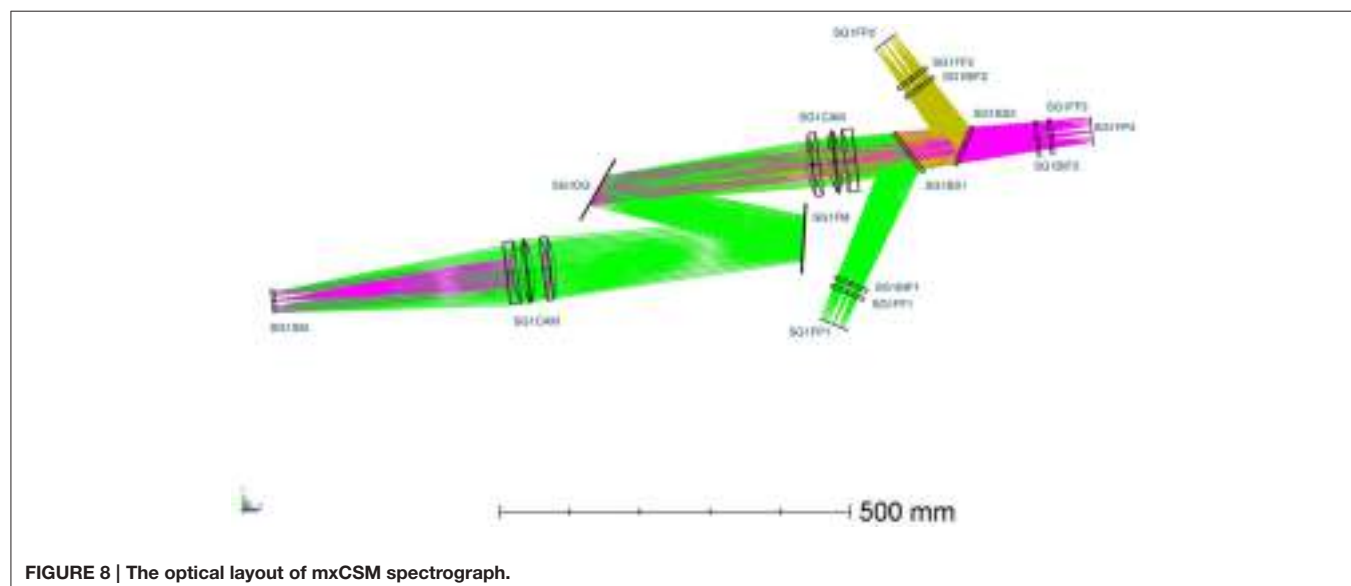
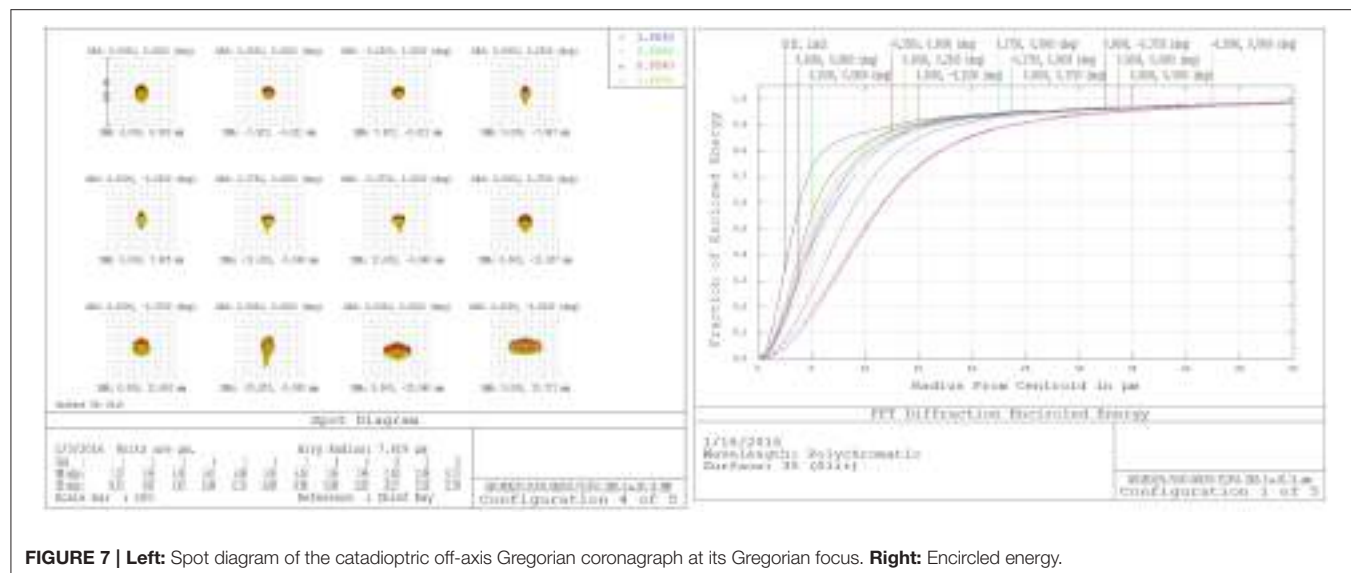


**TABLE 1 |** Instrument characteristics of the mxCSM spectrographs.

Ion	$\lambda$ [nm]	$m$	$\alpha$	$\beta$	$\phi$	$\epsilon$	$\Delta\lambda$ [pm]	$\lambda/\Delta\lambda$	$\Delta V$ [km/s]
Fe IX	436	257	36.701	16.701	20.000	1.00	11	39,114	$\pm 150$
Fe XIV	530	211	36.701	16.638	20.063	0.87	13	39,053	$\pm 150$
Fe X	637	176	36.701	16.775	19.926	0.86	16	39,185	$\pm 150$
Ni XIV	670	167	36.674	16.674	20.000	0.94	17	39,072	$\pm 150$
Fe XI	789	142	36.674	16.742	19.932	0.99	20	39,135	$\pm 150$
Fe XIII	1075	104	36.674	16.601	20.070	0.87	27	39,034	$\pm 150$

$m$  denotes the blazing order of the wavelength, and  $\alpha$  and  $\beta$  are the incident and exit angles of the line with respect to the grating normal, respectively. The first three lines are observed with Spectrograph 1 (SG1) and therefore have identical grating incident angle  $\alpha$ . The second set of lines are observed by SG2. The nominal spectrograph angle  $\phi \equiv \alpha - \beta$  of the spectrographs is 20 degree  $\epsilon$  is the amplitude of the blazing function for each spectral line,  $\Delta\lambda$  denotes the spectral sampling size per pixel, and  $\Delta V$  is the Doppler velocity coverage of each slit for the spectrograph.

**TABLE 2 |** Estimates of continuum photon flux  $N_v$ , normalized photon noise level  $\sigma_P$ ,  $3\sigma$  longitudinal magnetic field detection limit  $B_{3\sigma}$ , and total time  $\Delta T_{map}$  required to scan a  $1.2 \times 1.0$  degree FOV of mxCSM for the Fe XIII 1075 nm line polarimetric observations, assuming a 20% system efficiency, which includes the 50% transmission of the exit linear polarizer of the polarimeter, and a  $10 \times 10^{-6} I_\odot$  scattered light background for coronal observation.

No. Slit	No. Scan step	$\Delta x$	$\Delta t$ [s]	CoAdd	$\Delta T$	$N_v$	$\sigma_P$	$3\sigma_B$	$\Delta T_{map}$
1	4800	1"	20 (2.5 × 8)	1	20 s	66,350	$3.8 \times 10^{-3}$	100 G	26.7 h
					20 s	66,350	$3.8 \times 10^{-3}$	100 G	16 min
					160 s	531,000	$1.4 \times 10^{-3}$	35 G	2 h
100	48	1"	20 (2.5 × 8)	8	600 s	2,000,000	$7.1 \times 10^{-4}$	18 G	8 h
					20 s	600,000	$1.3 \times 10^{-3}$	33 G	16 min
					160 s	4,800,000	$4.6 \times 10^{-4}$	12 G	2 h
100	48	3"	20 (2.5 × 8)	30	600 s	18,000,000	$2.4 \times 10^{-4}$	6 G	8 h
					20 s	6,600,000	$3.8 \times 10^{-4}$	10 G	16 min
					160 s	53,000,000	$1.4 \times 10^{-4}$	4 G	2 h
100	48	10"	20 (2.5 × 8)	30	600 s	200,000,000	$7.1 \times 10^{-5}$	2 G	8 h

The first row of the table shows the estimates for a single-slit instrument for comparison. The spectrograph samples the corona with a  $1'' \times 1''$  sample size.  $\Delta x$  denotes the size of the spatial sampling element, which can be increased by binning the data. The total integration time at each spatial sampling element  $\Delta T$  is calculated from the 2.5 s individual integration, an 8-state modulation sequence, and the number of **averaged polarization sequences** (CoAdd).  $\Delta T_{map}$  is estimated assuming a camera with high speed readout that operates with near 100% duty cycle.  $N_v$  is the total number of photons that each spatial sampling element collects with integration time  $\Delta T$  for each polarimetry measurement.  $\sigma_P (= 1/\sqrt{N_v})$  denotes the amplitude of noise in the continuum of the polarized spectra if the intensity of the continuum spectra is equal to  $10 \times 10^{-6} I_\odot$ .

## 4. SUMMARIES AND DISCUSSIONS

We have presented a conceptual design for a new instrument, optimized for high-temporal resolution spectroscopic measurements of the intensity and polarization of multiple CELs over a very large field of view for research in coronal magnetism. Key technologies that enable this new instrument configuration are (1) large-format focal plane arrays, (2) high-efficiency ultra narrow bandpass isolation filters, and (3) new catadioptric wide-field coronagraph designs. Integration of these technologies enables the implementation of large-scale multiplexing technique to efficiently project the spectra of a very large number of slices of the image plane of the telescope onto multiple focal plane arrays to be recorded simultaneously. The large-scale multiplexing design greatly enhances the capability of the telescope with moderate apertures for observations that require a large field of view coverage. For comparison, the time required for the 25 cm aperture, 6-line, 100-slit coronal spectropolarimeter coronagraph presented in this paper to observe the 1 degree FOV is comparable to that of a 6-m coronagraph equipped with current single-slit, single-wavelength spectropolarimeter. But mxCSM can be constructed with only a fraction of the cost required for the construction of a 6-m class coronagraph.

The high system throughput of this design also makes it an ideal design for future space missions where size and weight of the instruments are severely limited. Finally, we note that although large-scale multiplexing strategy can greatly

enhance the capabilities of a current generation of small aperture telescopes, it should also be implemented for future large ground-based telescope projects. For example, a 1-m class mxCSM would yield a magnetic field sensitivity of 10 G with a  $3''$  spatial sampling and 15 min temporal resolution. This will directly enable study of the evolution of active region coronal magnetic fields during solar flares and coronal mass ejections, and finally allow us to test theoretical models of solar eruptions.

## AUTHOR CONTRIBUTIONS

The author confirms being the sole contributor of this work and approved it for publication.

## FUNDING

The hardware used for the demonstration of the mxSPEC proof-of-concept instrument were acquired with two NSF Major Research Instrument grants, NSF ATM#0421582, and NSF ATM#0923560.

## ACKNOWLEDGMENTS

The author thanks Shadia Habbal for helpful comments and review of the paper, and for graciously providing the 2010 Eclipse data for inclusion in this paper. The author also thanks John W. Harvey and Sarah F. Martin for information on early multiple-slit spectroscopy works.

for magnetic-dipole transitions. *Astrophys. J.* 522, 524–539. doi: 10.1086/307629

Elmore, D. (2007). *TMk4 Scattered Light Analysis*. High Altitude Observatory Coronal Solar Magnetism Observatory Technical Note 10.

## REFERENCES

Casini, R., and Judge, P. G. (1999). Spectral lines for polarization measurements of the coronal magnetic field. II. Consistent treatment of the stokes vector

- Gallagher, D. (2015). *COSMO Stray Light Analysis*. High Altitude Observatory  
Coronal Solar Magnetism Observatory Document 16-COSMOLC-DE-7003.
- Habbal, S. R., Druckmüller, M., Morgan, H., Ding, A., Johnson, J.,  
Druckmüllerová, H., et al. (2011). Thermodynamics of the solar corona  
and evolution of the solar magnetic field as inferred from the total  
solar eclipse observations of 2010 July 11. *Astrophys. J.* 734, 120. doi:  
10.1088/0004-637X/734/2/120
- Hale, G. E. (1908). On the probable existence of a magnetic field in sun-spots.  
*Astrophys. J.* 28, 315. doi: 10.1086/141602
- Jaeggli, S. A., Lin, H., Mickey, D. L., Kuhn, J. R., Hegwer, S. L., Rimmele, T. R., et al.  
(2010). FIRS: a new instrument for photospheric and chromospheric studies at  
the DST. *Mem. Soc. Astronom. Ital.* 81, 763.
- Kramar, M., Inhester, B., Lin, H., and Davila, J. (2013). Vector tomography for the  
coronal magnetic field. II. Hanle effect measurements. *Astrophys. J.* 775, 25.  
doi: 10.1088/0004-637X/775/1/25
- Kramar, M., Lin, H., and Tomczyk, S. (2016). Direct observation of coronal  
magnetic fields by vector tomography of the coronal emission line  
polarizations. *Astrophys. J. Lett.* 819:36. doi: 10.3847/2041-8205/819/2/L36
- Kuhn, J. R., Coulter, R., Lin, H., and Mickey, D. L. (2003). “The SOLARC  
off-axis coronagraph,” in *Innovative Telescopes and Instrumentation for Solar  
Astrophysics*, Vol. 4853 of *Proc. SPIE*, eds S. L. Keil and S. V. Avakyan, 318–326.  
doi: 10.1117/12.460296
- Lin, H. (2003). “ATST near-IR spectropolarimeter,” in *Innovative Telescopes and  
Instrumentation for Solar Astrophysics*, Vol. 4853 of *Proc. SPIE*, eds S. L. Keil  
and S. V. Avakyan, 215–222. doi: 10.1117/12.460374
- Lin, H. (2014). “mxSPEC: a massively multiplexed full-disk spectroheliograph  
for solar physics research,” in *Ground-Based and Airborne Instrumentation for  
Astronomy V*, Vol. 9147 of *Proc. SPIE*, eds S. K. Ramsay, I. S. McLean and H.  
Takami (Montréal, QC), 914712.
- Lin, H., and Casini, R. (2000). A classical theory of coronal emission line  
polarization. *Astrophys. J.* 542, 528–534. doi: 10.1086/309499
- Lin, H., Kuhn, J. R., and Coulter, R. (2004). Coronal magnetic field measurements.  
*Astrophys. J. Lett.* 613, L177–L180. doi: 10.1086/425217
- Lin, H., Penn, M. J., and Tomczyk, S. (2000). A new precise measurement of  
the coronal magnetic field strength. *Astrophys. J. Lett.* 541, L83–L86. doi:  
10.1086/312900
- Livingston, W., Harvey, J., Doe, L. A., Gillespie, B., and Ladd, G. (1980). The  
kitt-peak coronal velocity experiment. *Bull. Astronom. Soc. Ind.* 8, 43.
- Martin, S. F., Ramsey, H. E., Carroll, G. A., and Martin, D. C. (1974). Multi-  
slit spectrograph and H alpha Doppler system. *Solar Phys.* 37, 343–350. doi:  
10.1007/BF00152493
- Srivastava, N., and Mathew, S. K. (1999). A digital imaging multi-slit spectrograph  
for measurement of line-of-sight velocities on the sun. *Solar Phys.* 185, 61–68.  
doi: 10.1023/A:1005189319845
- Tomczyk, S., Card, G. L., Darnell, T., Elmore, D. F., Lull, R., Nelson, P. G., et al.  
(2008). An instrument to measure coronal emission line polarization. *Solar  
Phys.* 247, 411–428. doi: 10.1007/s11207-007-9103-6

**Conflict of Interest Statement:** The author declares that the research was  
conducted in the absence of any commercial or financial relationships that could  
be construed as a potential conflict of interest.

Copyright © 2016 Lin. This is an open-access article distributed under the terms  
of the Creative Commons Attribution License (CC BY). The use, distribution or  
reproduction in other forums is permitted, provided the original author(s) or licensor  
are credited and that the original publication in this journal is cited, in accordance  
with accepted academic practice. No use, distribution or reproduction is permitted  
which does not comply with these terms.

# Advantages of publishing in Frontiers



## OPEN ACCESS

Articles are free to read,  
for greatest visibility



## COLLABORATIVE PEER-REVIEW

Designed to be rigorous  
– yet also collaborative,  
fair and constructive



## FAST PUBLICATION

Average 85 days from  
submission to publication  
(across all journals)



## COPYRIGHT TO AUTHORS

No limit to article  
distribution and re-use



## TRANSPARENT

Editors and reviewers  
acknowledged by name  
on published articles



## SUPPORT

By our Swiss-based  
editorial team



## IMPACT METRICS

Advanced metrics  
track your article's impact



## GLOBAL SPREAD

5'100'000+ monthly  
article views  
and downloads



## LOOP RESEARCH NETWORK

Our network  
increases readership  
for your article

## Frontiers

EPFL Innovation Park, Building I • 1015 Lausanne • Switzerland  
Tel +41 21 510 17 00 • Fax +41 21 510 17 01 • info@frontiersin.org  
[www.frontiersin.org](http://www.frontiersin.org)

## Find us on

